Nonlinear Finite Element Analysis of Influence of Support Geometry on the Punching Shear Behaviour of Reinforced Concrete Slabs

by

Graeme Milligan

A thesis
presented to the University of Waterloo
in fulfillment of the
thesis requirement for the degree of
Doctor of Philosophy
in
Civil Engineering

Waterloo, Ontario, Canada, 2023

© Graeme Milligan 2023

Examining Committee Membership

The following served on the Examining Committee for this thesis. The decision of the Examining Committee is by majority vote.

External Examiner	Stavroula Pantazopoulou, PhD Professor, Civil Engineering York University
Supervisor(s)	Maria Anna Polak, PhD Professor, Civil and Environmental Engineering University of Waterloo
Internal Member	Mahesh Pandey, PhD Professor, Civil and Environmental Engineering University of Waterloo
	Trevor Hrynyk, PhD Assistant Professor, Civil and Environmental Engineering University of Waterloo
Internal-External Member	Kumaraswamy Ponnambalam, PhD Professor, Systems Design Engineering University of Waterloo

Author's Declaration

This thesis consists of material all of which I authored or co-authored: see Statement of Contributions included in the thesis. This is a true copy of the thesis, including any required final revisions, as accepted by my examiners.

I understand that my thesis may be made electronically available to the public.

Statement of Contributions

Graeme Milligan was the sole author of Chapters 1, 2, 3, 4, 5, 9 and 10. These chapters were written under the supervision of Dr. Maria Anna Polak and were not written for publication (though the information contained in Chapter 9 will be submitted for publication in the future). Graeme Milligan was also the sole author of appendices A, B, C, E, F, G, I, J and K, which were also written under the supervision of Dr. Polak.

This thesis consists in part of ten manuscripts written for publication. Exceptions to sole authorship of material are as follows:

Research presented in Chapter 6:

The research presented in Chapter 6 was conducted at the University of Waterloo under the supervision of Dr. Maria Anna Polak in collaboration with Dr. Cory Zurell. The study was designed by Graeme Milligan, Dr. Polak and Dr. Zurell. All finite element modelling, including the determination of the dimensions of the isolated slab-wall specimens, was solely conducted by Graeme Milligan. All data analysis was conducted by Graeme Milligan, and reviewed by Dr. Polak and Dr. Zurell.

Chapter 6 is primarily based on two manuscripts. The first of these manuscripts was co-authored by Graeme Milligan, Dr. Polak and Dr. Zurell, and published in Structural Concrete. The second manuscript was co-authored by Graeme Milligan, Dr. Polak and Dr. Zurell, and at the time of publication of this thesis has been submitted for publication. Discussions related to the load type study and finite element model calibration include information taken from two manuscripts co-authored by Graeme Milligan and Dr. Polak (published in the Proceeding of the *fib* Symposium), and Graeme Milligan, Dr. Polak and Dr. Zurell (published in Engineering Structures), respectively (citations provided below). Graeme Milligan was the lead author of these four manuscripts. The manuscripts were drafted by Graeme Milligan, while Dr. Polak and Dr. Zurell provided editorial and technical feedback prior to submission.

A breakdown of the co-authored content in Chapter 6 is provided below:

- Section 6.1 – This section is a combination of co-authored content taken from the manuscript published in Structural Concrete, the manuscript submitted for publication (Influence of Openings on the Punching Shear Behaviour of Concrete Slabs Supported on Rectangular

Columns and Walls) and sole-authored content. However, all text in this section represents sole-authored content, as any information from the aforementioned manuscripts has been paraphrased and expanded upon in this thesis.

- Sections 6.2.1 and 6.4.2, and subsections 6.2.2.2, 6.4.1.2 – These sections and subsections are largely taken verbatim (other than minor formatting and reference changes to make them consistent with the remainder of this thesis) from the co-authored publication published in Structural Concrete. However, sole-authored content, related to the estimation of the radius of contraflexure and the calculation of the flexural capacity of the connections according to ACI 318 has been added to Section 6.2.1 and subsection 6.4.1.2, respectively.
- Subsections 6.2.2.1 and 6.4.1.1 – These subsections are based on information originally presented in the conference paper published in the Proceedings of the *fib* Symposium (2019). While these subsections are based on this previous co-authored publication, the text contained in this thesis has been paraphrased and expanded.
- Section 6.2.3 – This section is a combination of co-authored content taken from the manuscript published in Structural Concrete and sole-authored content. The sole-authored content is based on research presented in the aforementioned manuscript but has been paraphrased and expanded in this thesis. A brief discussion related to the influence of in-plane forces has also been added for the purpose of this thesis.
- Sections 6.2.4 and 6.4.3 – The information in these sections is largely taken verbatim from a co-authored manuscript which has been submitted for publication (Influence of Openings on the Punching Shear Behaviour of Concrete Slabs Supported on Rectangular Columns and Walls). However, some discussions in Section 6.2.4 have been paraphrased and/or expanded upon in this thesis. Furthermore, some portions of this manuscript are also included in Chapter 8, as will be discussed.
- Section 6.3 – The information related to the calibration of the finite element model has been rewritten for this thesis, though it is primarily based on research previously published in Structural Concrete and Engineering Structures.
- Section 6.5 – This section summarizes the chapter and primary contributions of the presented study. This section represents sole-authored content written for this thesis.

Citations:

G. J. Milligan and M. A. Polak, "Finite Element Analysis of Shear Behaviour of Concrete Slabs Partially Supported on Walls," *Proceedings of the fib Symposium 2019,* pp. 1803-1810, 2019.

G. J. Milligan, M. A. Polak and C. Zurell, "Finite Element Analysis of Punching Shear Behaviour of Concrete Slabs Supported on Rectangular Columns," *Engineering Structures,* vol. 224, p. 111189, 2020. doi:10.1016/j.engstruct.2020.111189

G. J. Milligan, M. A. Polak and C. Zurell, "Finite Element Analysis of Punching Shear Behaviour of Reinforced Concrete Slabs Supported on Walls," *Structural Concrete,* vol. 23, no. 2, pp. 1118-1133, 2022. doi:10.1002/suco.202100692

Manuscript details available at the time of thesis publication for submitted manuscripts:

G. J. Milligan, M. A. Polak and C. Zurell. Influence of Openings on the Punching Shear Behaviour of Concrete Slabs Supported on Rectangular Columns and Walls. (submitted)

Research presented in Chapter 7:

The research presented in Chapter 7 was conducted at the University of Waterloo under the supervision of Dr. Maria Anna Polak in collaboration with Dr. Cory Zurell. Based on an analysis of the FEA results, Graeme Milligan developed the proposed design methods for rectangular slab-column and slab-wall connections in consultation with Dr. Polak and Dr. Zurell. All modelling and data analysis was conducted by Graeme Milligan (though it should be noted that the initial idea for the cut-wall model was proposed by Dr. Zurell). The database of experimental specimens from literature used to verify the proposed design methods for rectangular slab-column connections was also compiled by Graeme Milligan.

Other than Section 7.1.1, the majority of Section 7.1 is taken verbatim (other than minor formatting and reference changes to make it consistent with the remainder of this thesis) from a manuscript co-authored by Graeme Milligan, Dr. Polak and Dr. Zurell. This manuscript is related to alternative punching shear design methods for rectangular slab-column connections. The manuscript, which has been submitted for publication at the time of publication of this thesis (citation details available at the time of thesis submission are provided on the following page), was drafted by Graeme Milligan, with Dr. Polak and Dr. Zurell providing editorial and technical feedback. The information contained in

Section 7.1.1 is based on the information contained in this manuscript but has been paraphrased in this thesis.

Other than the Sections discussed below, the majority of Section 7.2 is taken verbatim from a manuscript co-authored by Graeme Milligan, Dr. Polak and Dr. Zurell. This manuscript, which has also been submitted for publication at the time of publication of this thesis, was drafted by Graeme Milligan, with Dr. Polak and Dr. Zurell again providing editorial and technical feedback.

An overview of modifications to the content of the manuscript made for this thesis is as follows:

- Section 7.2.1 – The majority of this section has been taken verbatim from the co-authored manuscript related to alternative punching shear design methods for slab-wall connections (Punching Shear Design Methods for Reinforced Concrete Slab-Wall Connections). However, some portions of this section have been modified or expanded to make this section consistent with the remainder of this thesis.
- Section 7.2.2 – The information in this section is based on information provided in the previously mentioned manuscript but has been entirely rewritten for this thesis.
- Section 7.2.4 – Most of Section 7.2.4 is taken verbatim from the previously mentioned manuscript, however, the discussions related to the chosen mesh size and connection region modelling have been expanded upon in this thesis. These additional discussions represent sole-authored content.
- Section 7.2.5 – While the cut-wall model is also discussed in the aforementioned manuscript, the discussions related to the toe length study (Subsection 7.2.5.1), gap length study (Subsection 7.2.5.2), opening size study (Subsection 7.2.5.3) and verification of the proposed cut-wall model (Subsection 7.2.5.4) have been significantly expanded in this thesis. Any expansions to the information contained in the manuscript represent sole-authored content. Furthermore, the introduction of this Section has been slightly expanded and modified to make it consistent with the remainder of this thesis.
- Section 7.2.8 – The majority of this section is taken verbatim from the previously mentioned manuscript. However, a comparison of the predicted capacities according to the proposed design method for rectangular columns, which is not included in the manuscript, has been added to this thesis.

Section 7.3, which summarizes the chapter and the contributions of the presented work, is sole-authored content written for this thesis.

Manuscript details available at the time of thesis publication for submitted manuscripts:

G. J. Milligan, M. A. Polak, and C. Zurell. Alternative Punching Shear Design Methods for Concrete Slabs on Rectangular Columns. (submitted)

G. J. Milligan, M. A. Polak, and C. Zurell. Punching Shear Design Methods for Reinforced Concrete Slab-Wall Connections. (submitted)

Research presented in Chapter 8:

The research presented in Chapter 8, which is a compilation of multiple manuscripts (co- or lead-authored by Graeme Milligan), was conducted at the University of Waterloo under the supervision of Dr. Maria Anna Polak. The study was designed by Graeme Milligan with assistance from Dr. Polak. All finite element modelling, other than the calibration of the nonlinear finite element model, was solely conducted by Graeme Milligan. Qing (Paris) Zhang, while serving as an undergraduate research assistant, calibrated the finite element model under the supervision of Dr. Polak and Graeme Milligan. All data analysis was conducted by Graeme Milligan and reviewed by Dr. Polak.

Chapter 8 is largely based on three manuscripts. At the time of publication of this thesis, two of these manuscripts have been published (citations provided below) and one has been submitted for publication (details provided below). Qing (Paris) Zhang was the lead author for one of the previously published manuscripts, though Graeme Milligan also assisted in drafting and editing the manuscript, with Dr. Polak providing additional feedback. The other two manuscripts were drafted by Graeme Milligan, with Dr. Polak providing editorial and technical feedback.

Information from two other previously published manuscripts is also included in Chapter 8 as outlined below (citations provided below). Graeme Milligan was the lead author of both of these manuscripts. Qing (Paris) Zhang assisted in drafting and editing one of the manuscripts, and Dr. Polak provided editorial and technical feedback for both.

A breakdown of the co-authored content in Chapter 8 is provided below:

- Sections 8.1 – The text presented in this section is based on information contained in all the manuscripts listed below, other than that which is focused on rectangular columns and walls.

All text in this section has been rewritten in this thesis based on the information in these manuscripts and represents sole-authored content.

- Section 8.2 – Some of the text in this section is taken verbatim (other than minor formatting and reference changes) from two of the co-authored manuscripts. The first of these co-authored manuscripts (Influence of Openings on the Punching Shear Behaviour of Concrete Slabs Supported on Special-Shaped Columns) has been published in Engineering Structures, whereas the second (Influence of Openings on the Punching Shear Behaviour of Concrete Slabs Supported on Rectangular Columns and Walls) has been submitted for publication. However, the majority of the section has been rewritten for this thesis based on information contained in three co-authored manuscripts. The first of these three manuscripts was co-authored with Professor Polak and has been published in an ACI Symposium Publication. The other two manuscripts are the two previously outlined above (details of both of these manuscripts available at the time of submission of this thesis are provided below). Additional discussions of the connections' flexural reinforcement, which are not included in the aforementioned manuscripts, have also been added for the purposes of this thesis.
- Section 8.3 – The text in subsection 8.3.1 is sole-authored content as it is not taken from any of the manuscripts listed below. The text and figures in subsection 8.3.2 are largely based on that previously published in an ACI Symposium Publication co-authored with Qing Zhang and Dr. Polak (citation provided below). However, the text has been entirely rewritten or expanded on in this thesis, and therefore, represents sole-authored content.
- Section 8.4.1 – This subsection is largely taken verbatim (other than minor formatting and reference changes to make it consistent with the remainder of this thesis) from the co-authored manuscript that has been submitted for publication (Influence of Openings on the Punching Shear Behaviour of Concrete Slabs Supported on Rectangular Columns and Walls). However, discussions related to the estimation of the flexural capacities of the connections according to the ACI provisions, which represent sole-authored content, have been added to this thesis.
- Section 8.4.2 – A significant portion of this subsection is taken verbatim (other than minor changes to formatting, references and removal of some repetitive text when compiled in this thesis) from the co-authored manuscript published in Engineering Structures (citation provided below). However, the discussions related to the predicted load-displacement

responses, crack patterns, shear stress distributions and proposed modifications to existing code provisions represent sole-authored content which is paraphrased from the aforementioned manuscript and expanded with paraphrased material from a manuscript previously published in an ACI Symposium Publication (citation provided below, this manuscript, which was drafted by Graeme Milligan, was co-authored with Professor Polak).

- Sections 8.4.3 and 8.4.4 and 8.4.5 – These subsections are largely verbatim (other than minor formatting and reference changes) from the manuscript published in Engineering Structures (citation provided below).
- Section 8.4.6 – This subsection is primarily sole-authored content, though the three paragraphs directly following Figure 8-35 are taken verbatim (again other than minor changes) from the co-authored manuscript published in Engineering Structures (citation provided below).
- Section 8.5 – This section summarizes the chapter and primary contributions of the presented study. This section represents sole-authored content written for this thesis.

Citation:

Q. Zhang, G. J. Milligan and M. A. Polak, "Nonlinear finite element analysis of punching shear strength of reinforced concrete slabs supported on L-shaped columns," *Budownictwo i Architektura,* vol. 19, no. 4, pp. 125-138, 2020. doi:10.35784/bud-arch.2122.

G. J. Milligan, Q. Zhang and M. A. Polak, "Effect of Support Geometry on the Punching Shear Behaviour of Reinforced Concrete Flat Slabs," *ACI Symposium Publication,* vol. 353, pp. 29-49, 2022.

G. J. Milligan and M.A. Polak, “Influence of Slab Openings on the Punching Shear Behaviour of Reinforced Concrete Slabs Supported on L-Shaped Columns,” *ACI Symposium Publication*, vol. 357, pp. 187-221, 2023.

G. J. Milligan and M. A. Polak, “Influence of Openings on the Punching Shear Behaviour of Concrete Slabs Supported on Special-Shaped Columns,” *Engineering Structures*, vol. 284, pp. 115968, 2023

Manuscript details available at the time of thesis publication for submitted manuscripts:

G. J. Milligan, M. A. Polak and C. Zurell. Influence of Openings on the Punching Shear Behaviour of Concrete Slabs Supported on Rectangular Columns and Walls. (submitted)

Research presented in Appendix D:

The summary of the experimental specimens considered in the verification of the alternative design methods for rectangular slab-column connections in Appendix D is taken verbatim (other than revising the reference numbers to be consistent with the remainder of this thesis) from the appendix of the manuscript which makes up the majority of Section 7.1 (Alternative Punching Shear Design Methods for Concrete Slabs on Rectangular Columns). As previously mentioned, this database was compiled from literature by Graeme Milligan. The appendix was written by Graeme Milligan and reviewed by Dr. Polak and Dr. Zurell.

Research presented in Appendix H:

As mentioned in Appendix H, the sample calculations for L slab-column connections (L-SCCs) are taken verbatim (other than minor formatting and reference changes to make them consistent with the remainder of this thesis) from the appendix of a manuscript co-authored by Graeme Milligan and Dr. Maria Anna Polak (citation provided below). These sample calculations were prepared by Graeme Milligan and reviewed by Dr. Polak. The remainder of Appendix H was sole-authored by Graeme Milligan.

Citation:

G. J. Milligan and M.A. Polak, "Influence of Slab Openings on the Punching Shear Behaviour of Reinforced Concrete Slabs Supported on L-Shaped Columns," *ACI Symposium Publication*, vol. 357, pp. 187-221, 2023.

As lead author of nine of the ten manuscripts that make up the aforementioned chapters and appendices (I served in a partial supervisory role for the manuscript lead-authored by Qing (Paris) Zhang, I was responsible for contributing to the study design, finite element modelling, results analysis and drafting/submitting manuscripts. As discussed above, my co-authors provided guidance throughout my research and provided feedback on the draft manuscripts.

Abstract

Due to their many benefits including ease of construction, open floor plans and reduced cost reinforced concrete flat slabs are one of the most common structural systems. However, these systems, particularly flat slabs supported on columns alone (flat plates) are susceptible to punching shear failures. Punching shear failures are brittle and occur due to the complex state of stress at the intersection of the slab and column. Due to the brittleness of the failure, a punching shear failure of one slab-column connection can lead to the progressive collapse of an entire structure, which makes proper punching shear design essential.

Past research has led to the development of mechanical models and design provisions which can be used to estimate punching shear capacity. However, most of this past research has focused on square or circular slab-column connections, even though alternate support geometries are common. For example, elongated connections, such as rectangular slab-column or slab-wall connections, are commonly used due to lateral force considerations. Additionally, design provisions for special-shaped slab-column connections, such as L-, T-, and cruciform connections, have been included in major worldwide design codes for over 40 years. The existing research database for alternate column geometries is limited, particularly in the case of special-shaped slab-column connections, and thus, there is a need for a comprehensive study of the influence of support geometry on punching shear to allow code committees and practicing engineers to properly understand the behaviour of elongated and special-shaped connections.

In this thesis, a combination of linear elastic finite element analysis (FEA) and calibrated nonlinear FEA (NLFEA), implemented in Abaqus 6.13, was used to study the influence of support geometry on the punching shear behaviour of interior elongated and special-shaped connections without shear reinforcement. In addition to the support geometry, the influence of monotonic uniaxial unbalanced moments, and the presence of slab openings near the connections were also studied, as past research has demonstrated that both of these factors can have a significant negative influence on punching shear behaviour. Due to the overall size of the study, FEA was used in place of experiments due to the large cost and time required to conduct large-scale testing, though past experimental results from literature were used to calibrate the nonlinear finite element models (FEMs).

In the slab-wall study, the punching shear behaviour of interior slab-wall connections (SWCs) without shear reinforcement was studied using a nonlinear FEM implemented in Abaqus/Explicit.

The nonlinear FEM used in the slab-wall study, which was based on the Concrete Damaged Plasticity model (as with all calibrated nonlinear FEMs used in this work), was an extension of a FEM previously developed by the author for an analysis of the punching shear behaviour of interior rectangular slab-column connections (R-SCCs) without shear reinforcement [1]. In this study, the influence of loading conditions (various methods of concentric gravity loading and combined concentric gravity loading and uniaxial monotonic unbalanced moment), wall size (thickness and length) and presence of symmetric slab opening layouts (nonsymmetric opening layouts were not considered due to limitations in available computational resources) on the punching shear behaviour of slab-wall connections were studied. While the FEA predicted that punching shear failures of slab-wall connections could occur before one-way shear failures, the concentric punching shear capacities of the connections, which increased as the wall size increased, were typically higher than the expected load demand in the prototype structure. The unbalanced moment capacities of slab-wall connections were also found to be higher than typical unbalanced moment demands. The punching shear behaviour of interior slab-wall and rectangular slab-column connections with and without slab openings was also compared and found to be similar, though differences do exist and are discussed.

The slab-wall study and the author's previous analysis of rectangular slab-column connections [1] demonstrated that the ACI 318-19 [2] punching shear design provisions were inadequate for elongated connections. Therefore, alternate punching shear design methods were developed. These methods were developed based on the FEA results and verified through comparisons to available experimental results where possible. For interior square and rectangular slab-column connections, three alternative methods, which are intended to replace the existing ACI 318-19 provisions, were proposed. For interior slab-wall connections, which are defined as connections where the maximum support dimension exceeds *14d* (where *d* is the effective slab depth), a simplified design method, in which the slab-wall connection is decomposed into a combination of two-way and one-way shear regions was proposed.

The study of the punching shear behaviour of interior special-shaped slab-column connections (SS-SCCs) is divided into two parts.

In the first part, the concentric punching shear behaviour of special-shaped slab-column connections was analyzed using a nonlinear FEM in Abaqus/Explicit, which was calibrated to experimental results of one square and eight rectangular slab-column connections tested by Hawkins et al. [3]. The influence of column shape (L-, T- or cruciform), column size and influence of slab

openings at various locations around the column on punching capacity was studied. Based on the FEA results, the shear force distribution around special-shaped slab-column connections was found to be non-uniform, particularly for L and T connections, where a significant portion of the load is transferred along the outer edges of the L and base of the T, respectively. However, regardless of column shape, slab openings near special-shaped slab-column connections should be located near the diagonal portion of the critical perimeter assumed in ACI 318-19 [2] or in the region between the column flanges to minimize their influence on punching shear capacity.

In the second part of the special-shaped connection study, the punching shear behaviour of special-shaped slab-column connections subjected to concentric shear and monotonically increasing uniaxial unbalanced moment was analyzed. Since the Hawkins et al. [3] specimens only had flexural reinforcement on one side of the slab, a FEM calibrated to the experimental results of Drakatos et al. [4] (which were tested under combined concentric shear and monotonic or cyclic uniaxial unbalanced moment) was used. Due to limitations in available computational resources, only one column size, and one opening layout, which involved a single square opening located between the column flanges, were considered per column shape (L-, T- and cruciform-shapes). The FEA results demonstrated that slab openings located between the column flanges typically have a minor influence on punching capacity when the moment is applied away from the opening. However, when the moment is applied towards the opening, the openings reduce the punching capacity of the analyzed special-shaped slab-column connections by approximately 10%. Therefore, openings between the column flanges do have some influence on the punching shear capacity of special-shaped slab-column connections subjected to combined unbalanced moment and concentric loading (especially because the moment direction cannot be controlled in most, if not all, practical applications.

It should be noted that in both parts of the special-shaped connection study that rectangular slab-column connections were also analyzed. These additional analyses further expanded the database for elongated connections and helped quantify the benefits of using special-shaped connections in place of rectangular connections. Furthermore, the accuracy of the ACI 318-19 [2] and ACI 421.1R-20 [5] punching shear provisions, for predicting both punching capacity and the influence of slab openings, was evaluated through comparisons to the FEA results in both parts. Concentric punching capacities according to the ACI 421.1R-20 method were typically conservative compared to those from the FEA, though the method is time-consuming and not suitable for iterative design. Therefore, simplified modifications to the ACI 318-19 concentric provisions were proposed for the initial design

of L and T slab-column connections (no modifications were required for cruciform connections). For specimens subjected to combined unbalanced moment and concentric loading, the ACI 421.1R-20 provisions result in very conservative capacity estimates, particularly for connections with slab openings. Additionally, the ACI 421.1R-20 predictions are very inconsistent compared to the NLFEA predictions, which suggests that the ACI 421 method is not accurately capturing the behaviour of slab-column connections subjected to combined unbalanced moment and concentric loading. With respect to the influence of openings, the existing provisions were found to typically overpredict the influence of openings located between the column flanges. Furthermore, the ACI 421.1R-20 provisions were found to not accurately predict the influence of moment direction on punching capacity. Unlike the FEM, ACI 421.1R-20 predicted higher unbalanced moment capacities when the moment was applied toward the opening.

Acknowledgements

Firstly, I would like to thank those who made my doctoral degree possible. Specifically, Professor Maria Anna Polak and Dr. Cory Zurell. Professor Polak for being my supervisor throughout my graduate career, for always trusting my judgement and for providing guidance when I was struggling with my research. Dr. Zurell for providing me with practical insights into portions of my research, chairing my comprehensive exam, assisting with my PhD defense and co-authoring numerous publications with Professor Polak and myself.

I would like to acknowledge the funding I received from the University of Waterloo (Engineering Excellence Fellowship) and the Natural Sciences and Engineering Research Council (NSERC) of Canada (NSERC Postgraduate Scholarship-Doctoral [PGS D]).

I would also like to thank the members of my examining committee Professor Polak, Professor Pantazopoulou, Professor Mahesh Pandey, Professor Trevor Hrynyk and Professor Kumaraswamy Ponnambalam for their time reviewing my thesis and their comments, which greatly improved this thesis.

I also wish to extend my gratitude to all the professors at the University of Waterloo who have helped me during my graduate studies. Professor Jeffrey West, Professor Giovanni Cascante, Professor Scott Walbridge and Professor Pandey for providing me with reference letters for my numerous scholarship applications and my Ph.D. application. Professor Adil Al-Mayah, Professor Daniel Lacroix, Professor Lei Xu, and Professor Polak for giving me the opportunity to assist in undergraduate teaching. Professor Pandey, Professor Hrynyk and Professor Ponnambalam for serving as examiners for my comprehensive exam. Professor David Brush for always providing advice and guidance throughout my undergraduate and graduate studies. Finally, Professor Martin Pei, who spent countless hours teaching me concepts from numerous fields of study including applied mathematics and statistics since my first year at the University of Waterloo, and who provided me with many enjoyable squash matches.

Many thanks also need to be extended to my friends and colleagues for all the help and support throughout my graduate studies. Colin Van Niejenhuis, Stan Fong and Matt Sjaarda for showing me how to excel as a CA/TA. Ryan Barrage and Mickey Laguta for discussing Abaqus problems and assisting in the creation and debugging of numerous Python scripts. Piotr Wiciak, Dominik Kueres, Daniel Lahey, Tyler Hull, Fook-Yee Yang and Philip Lochan for discussing numerous topics and

providing a break from research. Jason May for our numerous chats about life and spending time sharing our favourite games and music. Aaron Lima for always being available to chat, offer advice, provide file backup services and assist me with debugging and correcting numerous computer and software issues. Casey Vanderwerff for providing a constant source of support regardless of circumstances and for sharing in my journey through undergraduate and graduate studies. And Nelson McFadyen, who has been one of my best friends since we met over 20 years ago, for providing support and pro bono video editing services during online teaching terms.

I also need to extend my thanks to my friends from around the world who have provided more support and guidance than I could have ever expected. Gary Muratore and Rick Jones for providing countless hours of entertainment and laughs and providing a much-needed distraction from my studies by playing one of my favourite games over the last three years. Samuel Kellogg, who has been a very close friend since we connected, for providing countless hours of entertainment and laughs discussing wrestling or video games. Like Gary and Rick, Samuel has also been there through times of struggle to offer advice and support. Maaike Jager for being a constant source of support and motivation for over 10 years and for providing me with a safe space to share my thoughts. Jade Faulkner for fostering a welcoming and supportive community while providing hours of entertainment and motivation to assist in completing my thesis. And Elisa Schulte, whose music and willingness to lend an ear helped me persevere through some of the most stressful parts of the final year of my graduate studies. Without all of you, and numerous others not named, my time as a graduate student would have been much less enjoyable, and I greatly appreciate getting to know all of you, though many of us have never met in person.

And I would be remiss if I did not share my appreciation for Joan Thompson. Since we met in September of 2021, Joan’s love and support have been fundamental to my success, and I greatly appreciate her patience as I have worked toward the conclusion of my graduate studies. I look forward to sharing many more memories with you.

Finally, last but not least, I would like to extend my sincerest thanks to my parents, John and Paula Milligan, for their financial and emotional support and for always understanding when I missed or was late to family events due to my research or coursework. Without their teachings and support throughout my life, the successful completion of my doctoral degree would not have been possible. I also need to acknowledge my grandmother, Angela Milligan, who like my parents, has always offered her love and support and shown an interest in my studies.

Dedication

I would like to dedicate this thesis to my parents, John and Paula Milligan, and my grandmother, Angela Milligan.

Table of Contents

Examining Committee Membership ii
Author's Declaration iii
Statement of Contributions iv
Abstract xii
Acknowledgements xvi
Dedication xviii
List of Figures xxv
List of Tables l
Chapter 1 : Introduction 1
1.1 Background 1
1.2 Research Objectives and Problem Statement 4
1.3 Outline 6
Chapter 2 : Punching Shear in Reinforced Concrete Slabs 8
2.1 Introduction 8
2.2 Phenomenon of Punching Shear 8
2.3 Review of Previous Punching Shear Research 10
2.3.1 Introduction 10
2.3.2 Square and Circular Slab-Column Connections 12
2.3.3 Rectangular Slab-Column Connections (R-SCCs) 21
2.3.4 Special-Shaped Slab-Column Connections (SS-SCCs) 29
2.3.5 Slab-Wall Connections (SWCs) 34
2.3.6 Slab-Column Connections With Openings 38
2.3.7 Overview of Finite Element Modelling Methodologies 45
2.3.8 Overview of Previous FEA of Punching Shear in Abaqus at the University of Waterloo 47
2.4 Mechanical Models 53
2.4.1 Kinnunen and Nylander 53
2.4.2 Upper Bound Plasticity Approach 55
2.4.3 Nölting Model 56
2.4.4 Models by Alexander and Simmonds 56
2.4.5 Rankin and Long Yield Line Model 58
2.4.6 Shehata and Regan Model 61

2.4.7 Critical Shear Crack Theory (CSCT) 61
Chapter 3 : Overview of Punching Shear Design Code Provisions 64
3.1 Introduction 64
3.2 Critical Perimeter Concept 64
3.3 ACI 318-19 65
3.3.1 Historical Development 65
3.3.2 Design Provisions for Connections Without Shear Reinforcement 67
3.4 Eurocode 2 71
3.4.1 Historical Development 71
3.4.2 Design Provisions for Connections Without Shear Reinforcement 73
3.5 *fib* Model Code 2010 78
3.5.1 Historical Development 78
3.5.2 Design Provisions for Connections Without Shear Reinforcement 78
3.6 Treatment of Openings 83
Chapter 4 : Overview of the Mechanical Behaviour of Concrete and Its Modelling Using the Concrete Damaged Plasticity (CDP) Model in Abaqus 85
4.1 Overview of Mechanical Behaviour of Concrete 85
4.1.1 Uniaxial Compressive Behaviour 85
4.1.2 Uniaxial Tensile Behaviour 88
4.1.3 Behaviour Under Biaxial or Triaxial Loads 88
4.2 Overview of the Concrete Damaged Plasticity (CDP) Model in Abaqus 89
4.2.1 Modelling of Compressive Behaviour of Concrete 90
4.2.2 Modelling of Tensile Behaviour of Concrete 92
4.2.3 Modelling of Damage 93
4.2.4 Modelling of Plasticity 95
Chapter 5 : Study Overview 105
Chapter 6 : Interior Slab-Wall Connection Study 108
6.1 Motivation 108
6.2 Study Overview 110
6.2.1 Determination of Specimen Dimensions 110
6.2.2 Concentric Load Study 112

6.2.3 Punching Behaviour of Slab-Wall Connections Subjected to Combined Shear and Moment (V+M Study) 115
6.2.4 Influence of Slab Openings on Punching Behaviour of Slab-Wall Connections (Symmetric Opening Study) 117
6.3 FEM Calibration 120
6.3.1 Summary of Experimental Specimens Considered in FEM Calibration 120
6.3.2 Summary of Calibrated FEM 123
6.4 Study Results 128
6.4.1 Concentric Load Study 128
6.4.2 Combined Shear and Unbalanced Moment (V+M Study) 140
6.4.3 Influence of Slab Openings (Symmetric Opening Study) 143
6.5 Summary and Contributions 150
Chapter 7 : Alternative Punching Shear Design Methods for Elongated Connections 152
7.1 Rectangular Slab-Column Connections (R-SCCs) 152
7.1.1 Motivation 152
7.1.2 Numerical and Experimental Database 155
7.1.3 Overview 156
7.1.4 Method 1: Effective Critical Perimeter 157
7.1.5 Method 2: Non-uniform Critical Perimeter Shear Stress Distribution 167
7.1.6 Combined Method 172
7.2 Slab-Wall Connections (SWCs) 175
7.2.1 Motivation 175
7.2.2 Numerical Database 177
7.2.3 Overview 177
7.2.4 Estimation of Load Demand (Tributary Area Study) 178
7.2.5 Decomposition of Wall Into Two-Way and One-Way Shear Regions (Cut-Wall Model) 184
7.2.6 Estimation of Capacity of Two-Way (Toe) Regions 207
7.2.7 Estimation of Capacity of One-Way Regions 212
7.2.8 Summary of the Design Method 215
7.3 Summary and Contributions 216
Chapter 8 : Special-Shaped Slab-Column Connection Study – Concentric Loading 218
8.1 Motivation 218

8.2 Study Overview 220
8.2.1 General Details 220
8.2.2 Rectangular Slab-Column Connection (R-SCC) Study 225
8.2.3 L Slab-Column Connection (L-SCC) Study 228
8.2.4 T Slab-Column Connection (T-SCC) Study 229
8.2.5 Cruciform Slab-Column Connection (X-SCC) Study 230
8.2.6 Investigated Modifications to ACI 318-19 231
8.3 FEM Calibration 232
8.3.1 Summary of Experimental Specimens Considered in Calibration 232
8.3.2 Summary of Calibrated FEM 234
8.4 Study Results 239
8.4.1 Rectangular Slab-Column Connections (R-SCCs) 239
8.4.2 L Slab-Column Connections (L-SCCs) 244
8.4.3 T Slab-Column Connections (T-SCCs) 251
8.4.4 Cruciform Slab-Column Connections (X-SCCs) 256
8.4.5 Comparison of Punching Capacity Predicted by ACI 421.1R-20 and FEA for SS-SCCs 261
8.4.6 Comparison of Results for Different Column Shapes 263
8.5 Summary and Contributions 267
Chapter 9 : Special-Shaped Slab-Column Connection Study – Combined Shear and Unbalanced Moment 269
9.1 Motivation 269
9.2 Study Overview 269
9.3 FEM Calibration 277
9.3.1 Summary of Experimental Specimens Considered in Calibration 278
9.3.2 Summary of FEM Calibration 282
9.3.3 Verification Study 296
9.4 Study Results 301
9.4.1 Concentric Shear Loading (V Only) Specimens 301
9.4.2 Combined Shear and Unbalanced Moment (V+M (Monotonic)) Specimens 306
9.5 Summary and Contributions 322
Chapter 10 : Conclusions and Future Work 324
10.1 Summary 324

10.2 Conclusions of Interior Slab-Wall Connection Study 326
10.2.1 Concentric Load Study 327
10.2.2 Combined Shear and Unbalanced Moment Study (V+M Study) 330
10.2.3 Influence of Slab Openings 331
10.3 Conclusions Related to the Development of Alternative Punching Shear Design Methods 333
10.3.1 Rectangular Slab-Column Connections (R-SCCs) 334
10.3.2 Slab-Wall Connections (SWCs) 336
10.4 Conclusions of Special-Shaped Slab-Column Connection Study – Concentric Shear 337
10.4.1 Rectangular Slab-Column Connections (R-SCCs) 338
10.4.2 General Conclusions for Special-Shaped Slab-Column Connections (SS-SCCs) 340
10.4.3 L Slab-Column Connections (L-SCCs) 341
10.4.4 T Slab-Column Connections (T-SCCs) 342
10.4.5 Cruciform Slab-Column Connections (X-SCCs) 344
10.5 Conclusions of Special-Shaped Slab-Column Connection Study – Combined Shear and Unbalanced Moment 344
10.6 Recommendations for Future Work 347
Letters of Copyright Permission 352
Bibliography 399
Appendix A Calculation of Shear Stress Distribution from Abaqus Results 430
Appendix B Additional Figures from Parametric Study of Isolated Slab-Wall Connections 435
Appendix C Summary of Column Dimensions Considered in Parametric Study of Impact of Column Rectangularity on Punching Shear Conducted During Author's MASc Studies 450
Appendix D Details of Selected Experimental Specimens Which Failed in Punching Considered in Development of Alternative Design Methods for Rectangular Slab-Column Connections 452
Appendix E Supplemental Comparisons of Shear Stress Distribution Predicted by NLFEA And Method 2 for Rectangular Columns 455
Appendix F Additional Load-Displacement Responses, Crack Patterns and Shear Stress Distributions from Parametric Study Using Proposed Cut-Wall Model 460
Appendix G Calculation of Parameters of Critical Perimeters Assumed in ACI 318-19 477
Appendix H Sample Punching Shear Capacity Calculations According to ACI 318-19 and ACI 421.1R-20 for Special-Shaped Slab-Column Connections 481

Appendix I Critical Perimeters Around Slab-Column and Slab-Wall Connections With Slab Openings Analyzed in Chapter 6, Chapter 8, and Chapter 9 According to ACI 318-19 496
Appendix J Predicted Crack Patterns and Shear Stress Distributions – Special-Shaped and Rectangular Slab-Column Connections – Concentric Loading Study 508
Appendix K Additional Load-Deflection Responses, Moment-Deflection Responses, Predicted Crack Patterns and Shear Stress Distributions – Special-Shaped and Rectangular Slab-Column Connections – Combined Shear and Unbalanced Moment Study 541

List of Figures

Figure 1-1: Typical Column Capital and Shearhead Used by Turner [8], (taken from [6]) 1
Figure 1-2: Typical Flat Slabs, a) Flat Slab with Column Capitals and Drop Panels, b) Two-way Slab Supported on Beams, c) Flat Plate, d) Waffle Slab; Acknowledgement: Reinforced Concrete Mechanics and Design, MacGregor and Bartlett (2000) [10], ©2000 Pearson Education Canada Inc., Reproduced with Permission of Pearson Canada Inc. 2
Figure 1-3: Punching Shear Failure Surface; Acknowledgement: Reinforced Concrete Mechanics and Design, MacGregor and Bartlett (2000) [10], ©2000 Pearson Education Canada Inc., Reproduced with Permission of Pearson Canada Inc. 3
Figure 2-1: Typical Tension Surface Cracks After Punching Shear Failure [42], authorized reprint from ACI Structural Journal, Volume 105, Issue 5 (2008) 9
Figure 2-2: Typical Inclined Shear Cracks in Slab After Punching Shear Failure [42], authorized reprint from ACI Structural Journal, Volume 105, Issue 5 (2008) 9
Figure 2-3: Gravity Load Level vs Lateral Drift Capacity of Interior Slab-Column Connections [16, 17, 105] [101]; authorized reprint from ACI 421.2R-10 16
Figure 2-4: Comparison of Experimental Data and Proposed Relationships Between Gravity Shear Ratio (GSR) and Lateral Drift Capacity For Slab-Column Connections Without Shear Reinforcement According to Hueste and Wight [105], ACI 318 (the Relationship used in ACI 318-05 is the Same as that in ACI 318-19) and Robertson and Johnson [14] (Labelled as ND Proposed Drift Limit) [14], authorized reprint from ACI Structural Journal, Volume 103, Issue 3, 2006 17
Figure 2-5: Commonly Assumed Critical Perimeter Shear Stress Distributions for Slab-Column Connections Subjected to Combined Concentric Loading and Unbalanced Moment (Interior Connections), a) Linearly Varying (Elastic Distribution); b) Plastic Redistribution at Ultimate Limit State; c) Plastic Redistribution Based on the Shear Strength of the Slab; Reprinted by permission from: Springer Nature, High Tech Concrete: Where Technology and Engineering Meet, Einpaul et al. [109] ©2018 18
Figure 2-6: Different Failure Locations for Shear Reinforced Slab-Column Connections 20
Figure 2-7: Shear Reinforcement Layouts and Critical Perimeters in ACI 318-19 [2] and Eurocode 2 (2004) [34] 21
Figure 2-8: a) Effective Critical Perimeter Around Elongated Connections According to Model Code 2010 b) Effective Critical Perimeter and One-Way Shear Region Proposed by Setiawan et al. [158]; "Reprinted from Structures, 27, Setiawan, Vollum, Macorini and Izzuddin, Punching of RC slabs

Without Transverse Reinforcement Supported on Elongated Columns, 2048-2068, Copyright (2020), with permission from Elsevier" 26
Figure 2-9: Summary of Slab-Column Connections Tested by Liu and Huang [171]..... 30
Figure 2-10: Comparison of Critical Perimeter Around SS-SCCs Assumed in ACI 318 and Proposed for ACI 318 by Liu and Huang [171] 31
Figure 2-11: L Slab-Column Connections Tested by Pinto et al. [174] (Column Size and Opening Size Consistent Between Specimens) 31
Figure 2-12: Overview of Column Size and Shear Reinforcement Considered by Xue et al. [175] ... 33
Figure 2-13: Transfer of One-Way and Two-Way Shear Forces Near a) Wall Ends b) Wall Corners, Reproduced with Permission from [189] © 2020 *fib*. International Federation for Structural Concrete 34
Figure 2-14: Comparison of Proposed Critical Perimeter for Slab-Wall Connections..... 35
Figure 2-15: Experimental Specimen Tested by Szalwinski [29]..... 36
Figure 2-16: Breakdown of Slab-Wall Corner Connection Into Two-Way, Dummy and One-Way Shear Regions, Adapted from [189] © 2020 *fib*. International Federation for Structural Concrete 38
Figure 2-17: Maximum Recommended Opening Sizes in Various Slab Locations in Lieu of More Advanced Analysis According to ACI 318-19 [2]..... 39
Figure 2-18: Alternative Treatments of Slab Openings Around Slab-Column Connections Suggested in Literature..... 44
Figure 2-19: Example of Crack Pattern for large column rectangularity. $\beta = 5$, $\kappa = 0.990$ (Cracks Visualized Through Contours of Maximum Principal Plastic Strain, Approximate Column Location Shown) [259] 52
Figure 2-20: Typical Shear Stress Distribution Along Column Perimeter, a) Long Side, b) Short Side, $\kappa = 0.990$ [259]..... 52
Figure 2-21: Punching Shear Model by Kinnunen and Nylander [261], Adapted from [261] 54
Figure 2-22: Failure Surface Considered by Braestrup et al. [38] 55
Figure 2-23: Alexander and Simmonds Truss Model, [39] Authorized Reprint from ACI Structural Journal, Volume 84, Issue 3 (1987) 57
Figure 2-24: Curved Compression Strut Used in Bond Model [263], Authorized reprint from ACI Structural Journal, Volume 89, Issue 3 (1992) 58
Figure 2-25: Isolated Slab-Column Specimen Considered by Rankin and Long [266]..... 59

Figure 2-26: Relationship between the critical shear crack width and slab thickness and rotation [11], Authorized reprint from ACI Structural Journal, Volume 105, Number 4 (2008) 62
Figure 3-1: a) Critical Perimeter; b) Shear Stress Distribution for Concentric Loading, ACI 318-19 [2] 67
Figure 3-2: Critical Perimeters Around L, T and Cruciform Columns and Definition of a_n and b_n for Symmetric Columns According to ACI 318-19 69
Figure 3-3: Shear Distribution for Concentric Load and Uniaxial Unbalanced Moment About an Axis Parallel to Maximum Column Dimension, ACI 318-19 70
Figure 3-4: Critical Perimeters Around Shear-Reinforced Connections According to ACI 318-19 and ACI 421.1R-20 71
Figure 3-5: Critical Perimeters Assumed in ENV 1992-1-1 [292] (figure taken from [1]) 72
Figure 3-6: Critical Perimeter for Slab-Column Connections Without Shear Reinforcement Assumed in Eurocode 2 (2004) 74
Figure 3-7: Basic Control Perimeter Assumed in *fib* Model Code 2010 and prEC2 (2020) 80
Figure 3-8: Definition of Reduced Basic Control Perimeter, $b_{1,red}$, to Account for Large Support Size (Model Code 2010) (same perimeter also used in prEC2 (2020)) 80
Figure 3-9: Critical Perimeter Around Large or Rectangular Columns Assumed in Model Code 1978 [53] (taken from [1]) 81
Figure 3-10: Treatment of Slab Openings According to Worldwide Design Codes 83
Figure 4-1: Typical Uniaxial Compressive Stress-Strain Response for Normal Strength Concrete (Note, in Accordance with the Theory of Plasticity "Yielding" Represents When the Material Response Leaves the Elastic Region and Enters the Plastic Region) 86
Figure 4-2: Typical Uniaxial Stress-Strain Responses Assumed in CDP Model, (a) Compression, (b) Tension [313], Used with permission of American Society of Civil Engineers, from Comparative Investigation of Concrete Plasticity Models for Nonlinear Finite-Element Analysis of Reinforced Concrete Specimens, Panahi and Genikomsou, volume 27, issue 2, ©2021; permission conveyed through Copyright Clearance Center, Inc. 91
Figure 4-3: Influence of K_c on the CDP Model Yield Surface in the Deviatoric Plane [315]; Reprinted from Engineering Structures, Vol 132, Alfarah, López-Almansa and Oller, New Methodology for Calculating Damage Variables Evolution in Plastic Damage Model for RC Structures, 70-86, Copyright (2017), with permission from Elsevier 97

Figure 4-4: Influence of K_c on the CDP Model Yield Surface in Three-Dimensional Principal Stress Space (Note, for These Plots f'_t = 4MPa, f'_c = 40MPa, σ_{bo}/σ_{co} = 1.16 and an Initial Yield Stress of $0.4f'_c$ = 16MPa Were Assumed); Reprinted from Archives of Civil and Mechanical Engineering, Vol 19 Issue 4, Wosatko, Winnicki, Polak and Pamin, Role of dilatancy angle in plasticity-based models of concrete, 1268-1283, Copyright (2019), with permission from Elsevier 98
Figure 4-5: Definition of Eccentricity (Denoted as e Instead of ϵ) and the Plastic Potential Function, G, in the $\bar{p} - \bar{q}$ (Meridian) Plane (Note, p and q are Equivalent to $\bar{p}$ and $\bar{q}$, Respectively); Reprinted from Archives of Civil and Mechanical Engineering, Vol 19 Issue 4, Wosatko, Winnicki, Polak and Pamin, Role of dilatancy angle in plasticity-based models of concrete, 1268-1283, Copyright (2019), with permission from Elsevier 100
Figure 4-6: Influence of Eccentricity Parameter (Note, Eccentricity is Denoted as e) on the Plastic Potential Surface, G, in Three-Dimensional Principal Stress Space (Note, for These Plots f'_t = 4MPa and ψ = 30° Were Assumed); Reprinted from Archives of Civil and Mechanical Engineering, Vol 19 Issue 4, Wosatko, Winnicki, Polak and Pamin, Role of dilatancy angle in plasticity-based models of concrete, 1268-1283, Copyright (2019), with permission from Elsevier..... 101
Figure 4-7: Influence of Dilation Angle, ψ, on the Plastic Potential Surface in Three-Dimensional Principal Stress Space for Specimens Tested by Kupfer et al. [308]; Reprinted from Archives of Civil and Mechanical Engineering, Vol 19 Issue 4, Wosatko, Winnicki, Polak and Pamin, Role of dilatancy angle in plasticity-based models of concrete, 1268-1283, Copyright (2019), with permission from Elsevier 102
Figure 5-1: Overview of Remaining Thesis Chapters and key Research Topics in Each..... 105
Figure 6-1: (a) Interior Slab-Wall Connection Analyzed using LEFEA and (b) Estimation of r Perpendicular to Long Side of Wall at the Wall Centerline..... 111
Figure 6-2: Boundary Conditions Used in Determination of Radius of Contraflexure Around Interior Slab-Wall Connection, ¼ Model..... 112
Figure 6-3: Dimensions and Load Locations for Isolated Slab-Wall Specimens (¼ Shown) [324].. 112
Figure 6-4: Boundary Conditions Assumed in Concentric Vertical Load Study [325] 113
Figure 6-5: Boundary Conditions Assumed in Combined Concentric and Unbalanced Moment Study (V+M Study, Top Wall Stub Removed for Clarity) 116
Figure 6-6: Comparison of Predicted Load-Displacement Response (Displacement Measurement Locations Shown in Figure 6-4) For Contact Model and Stub Models (Wall Stubs 800mm Tall in Stub Models), κ = 1.287, Load For Full Isolated Slab-Wall Specimen 117

Figure 6-7: Analyzed Symmetric Opening Layouts Around a) R-SCCs and b) SWCs (Note: ½ of SWCs Shown) 118
Figure 6-8: Boundary Conditions Used in Analysis of R-SCCs with Slab Openings and FEM Calibration 119
Figure 6-9: Dimensions and Load Conditions of Slabs Considered in Calibration [57, 151] 121
Figure 6-10: Comparison of Experimental Results and FEA Predictions for Select Specimens Considered in Calibration, Experimental Results Approximated from Plots in [57, 151] (X and Y Locations Defined in Figure 6-9) [145] 123
Figure 6-11: Hognestad Parabola Assumed in Calibrated FEM used in Chapter 6 [145] 125
Figure 6-12: Hognestad Parabola for f'_c = 44.6MPa used in Calibrated FEM [1] 125
Figure 6-13: Tensile Stress-Crack Width Relationship [327] and Tensile Stress-Strain Relationship [25] used in Calibrated FEM used in Chapter 6 (Note, Crack Width is Equivalent to Crack Displacement) 126
Figure 6-14: Inputted Tensile Stress-Crack Width Relationship for f'_c = 44.6MPa (Note, Crack Width is Equivalent to Crack Displacement) 127
Figure 6-15: Predicted Load-Displacement Response Perpendicular to Long Side of the Wall for Different Load Cases (Vertical Displacement at Slab Edge Perpendicular to Wall Toe [324] 129
Figure 6-16: Predicted Crack Pattern on Tension Surface and Slab Side, c_{min}/d=1.287, Equal Load Plate Loading, Visualized Through Contours of Maximum Principal Plastic Strain 130
Figure 6-17: Predicted Shear Stress Distribution Along Wall Perimeter, 100% of Peak Load, Different Load Conditions; (a) Long Side, (b) Short Side (¼ of Wall Shown) (adapted from [324], Stresses Averaged Over Depth) 131
Figure 6-18: Load-Displacement Response Predicted by FEM for All Slab-Wall Specimens ($\kappa = c_{min}/d$), Displacement Output Locations Shown in Figure 6-4, Load for Full Isolated Slab-Wall Specimen 135
Figure 6-19: Typical Crack Pattern Near Wall Toe, (a) κ = 0.594, (b) κ = 2.970, i) Tension Surface, ii) Slab Side Parallel to Long Side of Wall, iii) Slab Side Parallel to Short Side of Wall (Entire Isolated Slab-Wall Specimen not Shown, Approximate Wall Location Shown in Black on Tension Surface) 136
Figure 6-20: Predicted Shear Stress Distribution Along Wall Perimeter, 100% of Peak Load, κ = 0.792, 1.287, 1.782 and 2.970; (a) Long Side, (b) Short Side (¼ of Wall Shown, Stresses Averaged Over Depth) 137

Figure 6-21: Predicted Shear Stress Distribution Along ACI 318-19 Critical Perimeter, 100% of Peak Load, κ = 0.792, 1.287, 1.782 and 2.970; (a) Long Side, (b) Short Side (¼ of Wall Shown, Stresses Averaged Over Depth) 139
Figure 6-22: Percent of Total Load Carried on Individual Side of Rectangular Column or Walls, Rectangular Column Data Based on Simulations From Milligan et al. [145] (Legend Entries Correspond to κ Values ($\kappa = c_{min}/d$) and Applies to All Three Plots) 140
Figure 6-23: Percentage of Total Load Carried on Different Portions of Support Perimeter for Different Column Geometries and Walls (at Peak Load Predicted by FEA) 140
Figure 6-24: Representative Predicted Load-Displacement and Moment-Displacement Response for Different Vertical Load Levels, κ = 1.287, Displacement Recorded at X-Wall Corner Location (See Figure 6-4) (Pos. X Toe and Neg. X Toe defined in Figure 6-5) 141
Figure 6-25: Predicted Crack Pattern on Tension Surface and Slab Sides (Positive X Toe, see Figure 6-5), i) Tension Surface, ii) Slab Side Parallel to Long Side of Wall, iii) Slab Side Parallel to Short Side of Wall, κ = 1.287, 40% of Vertical Concentric Capacity and Monotonically Increasing Uniaxial Unbalanced Moment (Entire Isolated Slab-Wall Specimen not Shown) 142
Figure 6-26: Comparison of Shear Stress Distribution Along Wall Perimeter at Failure for V and V+M Study, κ = 1.287, ¼ of Wall Shown (a) Long Side of Wall, (b) Short Side of Wall (Note, that $5d \approx$ 1000mm, Stresses Averaged Over Depth) 142
Figure 6-27: Predicted Load-Displacement Responses for R-SCCs with Symmetric Slab Openings (Displacement Outputted at Y-Location Shown in Figure 6-9) 143
Figure 6-28: Predicted Column Perimeter Shear Stress Distributions at Peak Load, R-SCCs with Symmetric Slab Opening Layouts (¼ Column Shown, Stresses Averaged Over Depth) 145
Figure 6-29: Representative Tension Surface Crack Patterns Around R-SCCs in Symmetric Opening Study 145
Figure 6-30: Predicted Load-Displacement Response for SWCs (Displacement Locations shown in Figure 6-4) 147
Figure 6-31: Wall Perimeter Shear Stress Distributions at Peak Load (¼ Wall Shown, Stresses Averaged Over Depth) 148
Figure 6-32: Representative SWC Tension Surface Crack Patterns (¼ Model Shown) 149
Figure 7-1: Comparison of Normalized Nominal Shear Stress Capacity, v_{norm}, Predicted by ACI 318-19 and NLFEA [161] 154
Figure 7-2: Critical Perimeters Assumed in Various Design Codes 158

Figure 7-3: Continuous and Isolated Models Used to Estimate Effective Critical Perimeter 159
Figure 7-4: a) Calculation of Effective Critical Perimeter Length; b) Proposed Effective Critical Perimeter; c) Proposed Nominal Shear Stress (in MPa) 159
Figure 7-5: Comparison of Critical Perimeter Estimates from Design Codes, LEFEA and Method 1 160
Figure 7-6: Example of Calculation of $v_{c,eff1}$ When Using Effective Critical Perimeter Method (Assumed Perimeter Shown in red, Stress Level in MPa) 161
Figure 7-7: Comparison of Shear Stress Along Critical Perimeter at *d/2* Predicted by NLFEA, ACI 318-19 and Method 1, κ = 0.990 (¼ Column Shown, Stresses Averaged Over Depth) 162
Figure 7-8: Comparison of Capacities Predicted by NLFEA [145, 161], ACI 318-19, Method 1, Method 2 and Combined Method 163
Figure 7-9: Comparison of Normalized Nominal Shear Stress Capacity Along ACI 318-19 Critical Perimeter Predicted by NLFEA [145, 161], Various Codes, Method 1 and Method 2, all κ (c_{min}/d ratios) (Note, *fib* Model Code 2010 Results are Based on Level of Approximation IV) 164
Figure 7-10: Comparison of Experimental Capacities and ACI 318-19, Method 1, Method 2 and Combined Method Predictions 165
Figure 7-11: Example of Opening Located in “Ineffective” Region 166
Figure 7-12: Critical Perimeter Shear Stress Distribution Predicted by NLFEA and Method 2 (Assumed Distribution in Purple), κ = 0.990, Rectangular Column (¼ Column Shown, Stresses Averaged Over Depth) 168
Figure 7-13: Critical Perimeter Shear Stress Distribution Along Long Side of Wall Toe (Portion of Wall Within *5d* (≈1000mm) of Wall end) Predicted by NLFEA and Method 2 (Assumed Distribution Shown With Dashed Line), All κ, f'_c = 44.6MPa (Stresses Averaged Over Depth) 168
Figure 7-14: Assumed Shear Stress Distribution for Method 2 Showing Both Linear Region (Two-Way Shear) and Constant Region (One-Way Shear), Distribution Applies to All Connection Sides (Stress Levels in MPa) 169
Figure 7-15: Calculation of $v_{c,eff2}$ for Method 2 When $c_{max} > 6.5d$ and $c_{min} < 6.5d$ (Stress Levels in MPa) 170
Figure 7-16: Comparison of Normalized Nominal Shear Stress Predicted by NLFEA [145, 161], Method 1, and Method 2 and Location of Transition Point Assumed in Combined Method 173
Figure 7-17: Assumed Critical Perimeter and Shear Stress Distributions in Combined Method (Stress Levels in MPa) 174

Figure 7-18: a) Representative Interior SWC Analyzed; b) Details of Isolated SWCs Analyzed (¼ Model Shown) [323]; c) Boundary Conditions in Tributary Area Study 179
Figure 7-19: Comparison of Results Along Y-0 Path (see Figure 7-21a) for Different S4R Sizes, Pin Model, 8x8 Grid; a) Vertical Displacements; b) Sectional Moment (SM1) 180
Figure 7-20: Comparison of Results Along Y-0 Path (see Figure 7-21a) for Different Connection Region Modelling Methodologies, 8x8 Grid; a) Vertical Displacements; b) Sectional Moment (SM1), see Table 7-4 for Definition of Legend Entries 182
Figure 7-21: Example of Output Locations Used When Estimating Tributary Area, Interior SWCs 183
Figure 7-22: Comparison of Theoretical and Estimated Tributary Areas (Red Line: Pin Model; Dashed Black Line: Estimated Theoretical Area; Grey Line: Detailed Model) – Interior SWCs 183
Figure 7-23: Details of Finalized Cut-Wall Model ($d \approx 200$mm for the Analyzed Specimens) 185
Figure 7-24: Overview of Toe Length (λd) Study, Gap Length (μd) set to 1000mm 185
Figure 7-25: Cut-Wall Model Boundary Conditions and Displacement Output Locations (¼ Model Shown) 186
Figure 7-26: Comparison of Predicted Load-Displacement Response at Wall Toe, Cut Wall Study, κ = 1.287 (Gap Length Set to *5d*, no Slab Opening, Predicted Response not cut off at Peak Load) 186
Figure 7-27: Comparison of Predicted Load-Displacement Response at Perp. 1 and Perp. 2 Locations (see Figure 7-25), Cut Wall Study, κ = 1.287 (Gap Length Set to *5d*, no Slab Opening, Predicted Response not cut off at Peak Load) 187
Figure 7-28: Crack Pattern Predicted by Abaqus a) Tension Surface Near Wall Toe, b) Punching Cone on Slab Side Parallel to Long Side of Wall, Cut-Wall Model, *5d* Toe, *5d* Gap, no Slab Opening, κ = 1.287 (Entire SWC not Shown) 188
Figure 7-29: Comparison of Shear Stress Distribution Along Wall Perimeter for Full Wall and Cut-Wall Model (*5d* Toe, *5d* Gap, no Slab Opening), κ = 1.287 (¼ of Wall Shown, Stresses Averaged Over Depth) 188
Figure 7-30: Comparison of Predicted Load-Displacement Response at Wall Toe, Cut Wall Study, κ = 1.980 (Gap Length Set to *5d*, no Slab Opening, Predicted Response cut off at Peak Load) 189
Figure 7-31: Comparison of Crack Pattern From (a) Full Wall and (b) Original Cut-Wall Model, κ = 1.980, i) Tension Surface, ii) Slab Side Parallel to Long Side of Wall, iii) Slab Side Parallel to Short Side of Wall (Entire Isolated Slab-Wall Specimen not Shown 190

Figure 7-32: Percent of Total Load Carried on the Wall Toe (*5d* Toe and Gap Lengths) Throughout the Analyses (Note, Analyses Terminated Before End of Vertical Load Application Step due to Occurrence of Shear Failures) 191
Figure 7-33: Overview of Gap Length (μd) Study, Toe Length (λd) set to 1000mm 192
Figure 7-34: Comparison of Predicted Load-Displacement Response at Wall Toe, Gap Length Study, κ = 1.287 (Toe Length Set to *5d*, no Slab Opening, Predicted Response cut off at Peak Load) 192
Figure 7-35: Comparison of Predicted Crack Pattern at Peak Load in Full Wall and Cut-Wall Models for Different Gap Lengths, κ = 1.287 (No Gap=Full Wall Model; Entire SWC not Shown) 193
Figure 7-36: Side Numbering for Shear Stress Distribution Output – Cut Wall Models 194
Figure 7-37: Influence of Gap Length on Shear Stress Distribution Along Wall Toe and Remaining Wall Perimeter (see Figure 7-36 for Side Numbering Convention, ¼ SWC Shown, Stresses Averaged Over Depth) 195
Figure 7-38: Different Opening Heights Considered and Effective Toe Critical Perimeter Associated with Each According to ACI 318-19 197
Figure 7-39: Comparison of Predicted Load-Displacement Response at Wall Toe, Opening Size Study, κ = 1.287 (Toe Length Set to *5d*, Gap Length set to *2d*, Predicted Response cut off at Peak Load) 197
Figure 7-40: Comparison of Predicted Crack Patterns from Cut-Wall Model with Different Opening Heights (opening width of *0.3d*) and Full wall Models, κ = 1.287 (Entire SWC not Shown) 198
Figure 7-41: Predicted Crack Pattern for Cut Wall Model with Slab Opening (c_{min}+*d* high and *0.5d* wide), κ = 1.287, Top: Slab Side Parallel to Long Side of Wall, Bottom: Tension Surface (Entire SWC not Shown) 199
Figure 7-42: Influence of Opening Size on Shear Stress Distribution Along Wall Toe and Remaining Wall Perimeter (see Figure 7-36 for Side Numbering Convention, ¼ SWC Shown, Stresses Averaged Over Depth) 200
Figure 7-43: Comparison of Predicted Load Displacement Response at Wall Toe from Full Wall, Original Cut-Wall Model (*5d* toe and gap Lengths, no Slab Opening) and Finalized Cut-Wall Model (*5d* toe, *2d* gap, c_{min}+*d* High and *0.5d* Slab Opening), κ = 0.990 201
Figure 7-44: Comparison of Crack Pattern From (a) Full Wall and (b) Finalized Cut-Wall Model, κ = 0.990, i) Tension Surface, ii) Slab Side Parallel to Long Side of Wall, iii) Slab Side Parallel to Short Side of Wall (Entire Isolated Slab-Wall Specimen not Shown 203

Figure 7-45: Comparison of Crack Pattern From (a) Full Wall and (b) Finalized Cut-Wall Model, κ = 1.980, i) Tension Surface, ii) Slab Side Parallel to Long Side of Wall, iii) Slab Side Parallel to Short Side of Wall (Entire Isolated Slab-Wall Specimen not Shown..... 204
Figure 7-46: Comparison of Shear Stress Distribution Along Wall Perimeter from Full Wall and Cut-Wall Models (no Bottom of Toe (Side 3) since c_{min}/d High Opening Removes all Elements), κ = 0.990 (see Figure 7-36 for Side Numbering Convention, ¼ SWC Shown, Stresses Averaged Over Depth) 205
Figure 7-47: Proposed Methods for Estimating Punching Capacity of Toe Regions (Within *5d* of Wall end), 1 Toe Shown 208
Figure 7-48: Comparison of Critical Perimeter Shear Stress Distribution Predicted by NLFEA and Proposed Methods for Estimating Toe Capacity (Entire SWC Not Shown), f'_c =44.6MPa, a) Long Side Within *5d* of Wall End (Wall Toe), b) Short Side (Stresses Averaged Over Depth)..... 208
Figure 7-49: Comparison of Critical Perimeter Shear Stress Distribution Predicted by NLFEA and Proposed Method in One-Way Shear Region (Entire SWC not Shown, Stresses Averaged Over Depth) 212
Figure 7-50: Average Critical Perimeter Shear Stress in One-Way Shear Region Predicted by NLFEA and Proposed Linear Relationship Relating Average Shear Stress to κ..... 213
Figure 7-51: Summary of Proposed Design Method for Interior SWCs (Linear Distribution also Applies to Short Side of Wall)..... 215
Figure 8-1: Assumed Critical Perimeters According to ACI 318-19 [2] and Eurocode 2 [34] Around a) Square/Rectangular Columns, b) L Slab-Column Connections (Effective Loaded Area Assumed in ACI 318-19 Shown with Dashed Blue Line) and c) Shear Reinforced Connections..... 218
Figure 8-2: Overall Layout of Isolated Slab-Column Specimens in Special-Shaped Column Study 221
Figure 8-3: Considered Interior Slab-Column Connections in Continuous Slab System and Conversion to Isolated Specimens for Connections Where Column and Slab Centroid are a) Unaligned and b) Aligned 222
Figure 8-4: Analyzed Column Sizes for Each Column Geometry (Note, for SS-SCCs Each Flange (see Figure 8-5 for the Definition of a Column Flange) has Equal Dimensions) 224
Figure 8-5: Definition of Column Flanges (c_{max} and c_{min}) and Flange Aspect Ratio for SS-SCCs Used in this Work (Column Flange Definition Shown with Hatched Area)..... 224
Figure 8-6: Overview of Specimen Naming Convention Used in Chapter 8..... 225

Figure 8-7: a) Modified Slab Dimensions and Parameters Used in Special-Shaped Column Study (Concentric Loading), b) Representative Boundary Conditions in Special-Shaped Column Study (Concentric Loading) 225
Figure 8-8: Column Dimensions of R-SCCs in This Work 226
Figure 8-9: Overview of Analyzed Slab Opening Layouts in Rectangular Column Study (See Table 8-2 for Parameter Values) 227
Figure 8-10: Column Sizes, and Definition of Side Numbering and Critical Features of L-SCCs in This Work (Column Flange Definition Provided in Figure 8-5) 228
Figure 8-11: Overview of Analyzed Slab Opening Layouts in L Column Study (See Table 8-1 for Parameter Values) 228
Figure 8-12: Column Sizes and Definition of Side Numbering and Critical Features of T-SCCs in This Work (Column Flange Definition Provided in Figure 8-5) 229
Figure 8-13: Overview of Analyzed Slab Opening Layouts in T Column Study (See Table 8-1 for Parameter Values) 229
Figure 8-14: Column Sizes and Definition of Side Numbering and Critical Features of X-SCCs in This Work (Column Flange Definition Provided in Figure 8-5) 230
Figure 8-15: Overview of Analyzed Slab Opening Layouts in Cruciform Column Study (See Table 8-1 for Parameter Values) 230
Figure 8-16: Simplified Modifications to ACI 318-19 Concentric Punching Shear Provisions for Estimating the Punching Shear Capacity of SS-SCCs 231
Figure 8-17: Summary of Experimental Specimens Tested by Hawkins et al. [3] 234
Figure 8-18: General Boundary Conditions Used in FEM Calibration (¼ Models Used in Calibration, Slab 3 Shown) 235
Figure 8-19: Comparison of Load-Displacement Response at D4 and D8 Locations (see Figure 8-17) Measured Experimentally and Predicted by FEA, a) Slab 1 – β = 1, b) Slab 3 – β = 3 (Experimental Data Approximated From Plots Provided by Hawkins et al. [3]) [259] 238
Figure 8-20: Representative Load-Displacement Curves at D4 and D8 Locations for Slabs 1-9 238
Figure 8-21: a) Summary of Experimental Slab Dimensions and Loading Locations [3] b) Modified Slab Dimensions and Load Locations Used in Special-Shaped Column Study (Concentric Loading) [259] 239
Figure 8-22: Predicted Load-Displacement Responses for R-SCCs, Displacement Output Location Shown in Figure 8-2, Negative Displacement is Downwards 241

Figure 8-23: Representative Column Perimeter Shear Stress Distributions for R-SCCs –Peak Load (Stresses Averaged Over Depth) 242
Figure 8-24: Representative Crack Patterns Around R-SCCs with and Without Slab Openings (Grey Regions Have Principal Plastic Strains > 0.02, Approximate Column Location Shown in White) .. 243
Figure 8-25: Predicted Load-Displacement Responses for L-SCCs, Displacement Output Location Shown in Figure 8-2, Negative Displacement is Downwards 245
Figure 8-26: Representative Crack Patterns Around L-SCCs with and Without Slab Openings (Grey Regions Have Principal Plastic Strains > 0.02, Approximate Column Location Shown in White) .. 248
Figure 8-27: Representative Column Perimeter Shear Stress Distributions for L-SCCs –Peak Load (Stresses Averaged Over Depth) 249
Figure 8-28: Examples of Issues with ACI 318-19 Opening Provisions When Column Centroid Falls Within or Near Slab Opening 250
Figure 8-29: Predicted Load-Displacement Responses for T-SCCs, Displacement Output Location Shown in Figure 8-2, Negative Displacement is Downwards 252
Figure 8-30: Representative Crack Patterns Around T-SCCs with and Without Slab Openings (Grey Regions Have Principal Plastic Strains > 0.02, Approximate Column Location Shown in White) .. 254
Figure 8-31: Representative Column Perimeter Shear Stress Distributions for T-SCCs –Peak Load (Stresses Averaged Over Depth) 255
Figure 8-32: Predicted Load-Displacement Responses for X-SCCs, Displacement Output Location Shown in Figure 8-2, Negative Displacement is Downwards 257
Figure 8-33: Representative Crack Patterns Around X-SCCs with and Without Slab Openings (Grey Regions Have Principal Plastic Strains > 0.02, Approximate Column Location Shown in White) .. 259
Figure 8-34: Representative Column Perimeter Shear Stress Distributions for X-SCCs –Peak Load (Stresses Averaged Over Depth) 260
Figure 8-35: Comparison of Percent of Total Load Carried on Each Column Side for Different Column Shapes Predicted by FEA for Specimens Without Slab Openings (Data Recorded at Peak Load) 263
Figure 9-1: Breakdown of Specimen Naming Convention (V Load Type) 271
Figure 9-2: Breakdown of Specimen Naming Convention (V+M Load Type) 271
Figure 9-3: Overview of Column Sizes, Opening Layouts and Moment Directions Considered in SS-SCC Study – Combined Shear and Unbalanced Moment 272

Figure 9-4: Exaggerated Eccentricities for L2x4.6 and T2x4.6 Connections (Location of Slab Centroid not Accurately Shown to Highlight Eccentricity) 274
Figure 9-5: Column Location with Respect to Slab Centerlines for Connections Analyzed in Special-Shaped Connection Study – Combined Shear and Unbalanced Moment (Same Column Location for Specimens Without Openings) 275
Figure 9-6: Overview of Drakatos et al. [4] Experimental Setup for Slabs Subjected to Combined Concentric Shear and Unbalanced Moment, a) Plan View; b) Section A-A; Reprinted from Engineering Structures, 123, Drakatos, Muttoni and Beyer, Internal Slab-Column Connections Under monotonic and cyclic imposed rotations, 501-516, Copyright (2016), with permission from Elsevier 279
Figure 9-7: Example of Specimen Subjected to Combined Concentric Shear and Unbalanced Moment in Test Setup [4]; Reprinted from Engineering Structures, 123, Drakatos, Muttoni and Beyer, Internal Slab-Column Connections Under monotonic and cyclic imposed rotations, 501-516, Copyright (2016), with permission from Elsevier 281
Figure 9-8: Overview of Reinforcement for Slabs Where ρ is approximately equal to 0.8% [4]; Reprinted from Engineering Structures, 123, Drakatos, Muttoni and Beyer, Internal Slab-Column Connections Under monotonic and cyclic imposed rotations, 501-516, Copyright (2016), with permission from Elsevier 281
Figure 9-9: Boundary Conditions Used in FEM Calibration for Concentrically Loaded PD Specimens 283
Figure 9-10: Rotation Output Locations Considered in Chapter 9 285
Figure 9-11: Comparison of Predicted and Measured Vertical Load-Rotation Responses for Concentrically Loaded Specimens, Experimental Responses Approximated from Plots in [4] 286
Figure 9-12: Comparison of Tension Surface Crack Pattern Experimentally Observed and Predicted by Calibrated FEM, Concentrically Loaded Specimen with High Flexural Reinforcement Ratio (PD9); Experimental Crack Pattern Reprinted from Engineering Structures, 123, Drakatos, Muttoni and Beyer, Internal Slab-Column Connections Under monotonic and cyclic imposed rotations, 501-516, Copyright (2016), with permission from Elsevier 287
Figure 9-13: Boundary Conditions Used in FEM Calibration for PD Specimens Subjected to Combined Concentric Loading and Uniaxial Unbalanced Moment (Monotonic Moment) 289

Figure 9-14: Representative Boundary Conditions Used in Special-Shaped Slab-Column Connection Study – Combined Shear and Unbalanced Moment (M1 Direction Shown, Pressure Loads Modified for M2 Direction) 289
Figure 9-15: Comparison of Predicted and Measured Moment-Rotation Responses for PD1, Experimental Responses Approximated from Plots in [4] 290
Figure 9-16: Comparison of Predicted and Measured Moment-Rotation Responses for Specimens Subjected to Combined Concentric Shear and Unbalanced Moment, Finalized Calibrated FEM, Experimental Responses Approximated from Plots in [4] 292
Figure 9-17: Representative Comparison of Experimentally Measured and Numerically Predicted Tension Surface Crack Patterns for Specimens Where ρ is Approximately Equal to 0.8%, PD1 and PD4 Shown (for Experimental Crack Patterns Black and Red Lines Denote Cracks Due to Concentric Load and Unbalanced Moment, Respectively); Experimental Crack Pattern Reprinted from Engineering Structures, 123, Drakatos, Muttoni and Beyer, Internal Slab-Column Connections Under monotonic and cyclic imposed rotations, 501-516, Copyright (2016), with permission from Elsevier 294
Figure 9-18: Representative Comparison of Experimentally Measured and Numerically Predicted Tension Surface Crack Patterns for Specimens Where ρ is Approximately Equal to 1.6%, PD10 and PD12 Shown (for Experimental Crack Patterns Black and Red Lines Denote Cracks Due to Concentric Load and Unbalanced Moment, Respectively); Experimental Crack Pattern Reprinted from Engineering Structures, 123, Drakatos, Muttoni and Beyer, Internal Slab-Column Connections Under monotonic and cyclic imposed rotations, 501-516, Copyright (2016), with permission from Elsevier 295
Figure 9-19: Comparison of Interior Crack Patterns Experimentally Observed and Predicted by Calibrated FEM, Specimens Subjected to Combined Shear and Unbalanced Moment Where ρ is Approximately Equal to 0.8%; Experimental Crack Pattern Reprinted from Engineering Structures, 123, Drakatos, Muttoni and Beyer, Internal Slab-Column Connections Under monotonic and cyclic imposed rotations, 501-516, Copyright (2016), with permission from Elsevier 296
Figure 9-20: Comparison of Predicted Moment-Rotation Response and Moment vs Applied Vertical (Concentric) Load for Low ρ (0.8%) and High ρ (1.56%) Specimens in FEM Calibration Verification Study 299
Figure 9-21: Comparison of Predicted Load-Displacement Responses for Concentrically Loaded R-SCCs and SS-SCCs, Displacement Measurement Locations Shown in Figure 9-5 302

Figure 9-22: Additional Opening Layout Considered for L2x4.6 (200mm Square Opening) – Concentric Loading 303
Figure 9-23: Comparison of Percent of Total Load Carried on Each Column Side for Different Column Shapes Predicted by FEA for Specimens Without Slab Openings (Data Recorded at Peak Load) 305
Figure 9-24: Predicted Moment-Displacement Responses for R-SCCs Subjected to V+M (Monotonic) Loading, Displacement Measurement Locations Shown in Figure 9-5 307
Figure 9-25: Comparison of Unbalanced Moment Capacity of Specimens with Openings to Approximated Capacity Based on Trendline for Specimens Without Openings, R-SCCs 309
Figure 9-26: Predicted Tension Surface Crack Patterns at Failure, R-SCCs (Grey Regions Have Principal Plastic Strains > 0.02) 310
Figure 9-27: Predicted Moment-Displacement Responses for L-SCCs Subjected to V+M (Monotonic) Loading, Displacement Measurement Locations Shown in Figure 9-5 311
Figure 9-28: Comparison of Unbalanced Moment Capacity of Specimens with Openings to Approximated Capacity Based on Trendline for Specimens Without Openings (Note, Trendline Based on M1 and M2 Data), L-SCCs 313
Figure 9-29: Predicted Tension Surface Crack Patterns at Failure, L-SCCs (Grey Regions Have Principal Plastic Strains > 0.02) 314
Figure 9-30: Predicted Moment-Displacement Responses for T-SCCs Subjected to V+M (Monotonic) Loading, Displacement Measurement Locations Shown in Figure 9-5 316
Figure 9-31: Comparison of Unbalanced Moment Capacity of Specimens with Openings to Approximated Capacity Based on Trendline for Specimens Without Openings (Note, Trendline Based on M1 and M2 Data), T-SCCs 317
Figure 9-32: Predicted Moment-Displacement Responses for X-SCCs Subjected to V+M (Monotonic) Loading, Displacement Measurement Locations Shown in Figure 9-5 318
Figure 9-33: Comparison of Unbalanced Moment Capacity of Specimens with Openings to Approximated Capacity Based on Trendline for Specimens Without Openings, X-SCCs 319
Figure 10-1: Examples of Special-Shaped Slab-Column Connections with Unequal Flange Dimensions 349
Figure 10-2: Potential Layout of Additional Diagonal Flexural Reinforcement Which Could be Placed Around Special-Shaped Slab-Column Connections 349

Figure 10-3: Examples of Exterior Openings Which Could be Considered for Special-Shaped Slab-Column Connections Subjected to Combined Concentric Shear and Unbalanced Moment 349
Figure 10-4: Examples of Alternate Moment Directions Which Could be Considered for Rectangular and Special-Shaped Slab-Column Connections Subjected to Combined Concentric Shear and Unbalanced Moment 350

Figure A-1: Overview of AM04 Quarter Model 431
Figure A-2: Top View of Elements Considered in Shear Stress Distribution Calculations 432
Figure A-3: Side View of Elements Considered in Stress Distribution Calculations 433
Figure A-4: Procedure to Calculate Total Stress on a Column of Elements 434

Figure B-1: Predicted Load-Displacement Response Perpendicular to the Long Side of the Wall at the Wall Centerline (X-Wall CL Location, see Figure 6-4), Equal Load Plate Loading, all κ 436
Figure B-2: Predicted Crack Pattern Near Wall Toe, (a) κ = 0.792, (b) κ = 0.990, i) Tension Surface, ii) Slab Side Surface Parallel to Long Side of Wall, iii) Slab Side Parallel to Short Side of Wall, Equal Load Plate Loading (Entire Isolated Slab-Wall Specimen not Shown) 436
Figure B-3: Predicted Crack Pattern Near Wall Toe, (a) κ = 1.485, (b) κ = 1.782, (c) κ = 1.980, i) Tension Surface, ii) Slab Side Surface Parallel to Long Side of Wall, iii) Slab Side Parallel to Short Side of Wall, Equal Load Plate Loading (Entire Isolated Slab-Wall Specimen not Shown) 437
Figure B-4: Predicted Load-Displacement Responses at Selected Locations (see Figure 6-4), Uniformly Distributed Loading (UDL), all κ Values 438
Figure B-5: Comparison of Predicted Load-Displacement Response at Chosen Locations (see Figure 6-4) from Equal Load Plate and UDL Models 440
Figure B-6: Predicted Crack Pattern Near Wall Toe, (a) κ = 0.594, (b) κ = 0.792, (c) κ = 0.990, i) Tension Surface, ii) Slab Side Surface Parallel to Long Side of Wall, iii) Slab Side Parallel to Short Side of Wall, UDL (Entire Isolated Slab-Wall Specimen not Shown) 442
Figure B-7: Predicted Crack Pattern Near Wall Toe, (a) κ = 1.287, (b) κ = 1.485, (c) κ = 1.782, i) Tension Surface, ii) Slab Side Surface Parallel to Long Side of Wall, iii) Slab Side Parallel to Short Side of Wall, UDL (Entire Isolated Slab-Wall Specimen not Shown) 443
Figure B-8: Predicted Crack Pattern Near Wall Toe, (a) κ = 1.980, (b) κ = 2.970, i) Tension Surface, ii) Slab Side Surface Parallel to Long Side of Wall, iii) Slab Side Parallel to Short Side of Wall, UDL (Entire Isolated Slab-Wall Specimen not Shown) 444

Figure B-9: Predicted Shear Stress Distribution Along Wall Perimeter, 100% of Peak Load, all κ; (a) Long Side, (b) Short Side (¼ of Wall Shown), UDL Models (Stresses Averaged Over Depth) 445
Figure B-10: Comparison of Predicted Shear Stress Distribution Along Wall Perimeter for UDL and Equal Load Plate Models, Various Load Levels, κ=1.287; (a) Long Side, (b) Short Side (¼ of Wall Shown, Stresses Averaged Over Depth) 446
Figure B-11: Comparison of Shear Stress at the Corner of Supported Area for Equal Load Plate and UDL Loading, Multiple Load Levels, all κ 447
Figure B-12: Tension Surface Crack Patterns Around Remaining R-SCCs in Symmetric Opening Study 448
Figure B-13: Tension Surface Crack Patterns for Remaining SWCs in Symmetric Opening Study (¼ Model Shown) 449

Figure E-1: Critical Perimeter Shear Stress Distribution Predicted by NLFEA and Method 2 (Assumed Distribution in Purple), κ = 0.594, Rectangular Column (¼ Column Shown, Stresses Averaged Over Depth) 456
Figure E-2: Critical Perimeter Shear Stress Distribution Predicted by NLFEA and Method 2 (Assumed Distribution in Purple), κ = 0.792, Rectangular Column (¼ Column Shown, Stresses Averaged Over Depth) 456
Figure E-3: Critical Perimeter Shear Stress Distribution Predicted by NLFEA and Method 2 (Assumed Distribution in Purple), κ = 1.287, Rectangular Column (¼ Column Shown, Stresses Averaged Over Depth) 457
Figure E-4: Critical Perimeter Shear Stress Distribution Predicted by NLFEA and Method 2 (Assumed Distribution in Purple), κ = 1.485, Rectangular Column (¼ Column Shown, Stresses Averaged Over Depth) 457
Figure E-5: Critical Perimeter Shear Stress Distribution Predicted by NLFEA and Method 2 (Assumed Distribution in Purple), κ = 1.782, Rectangular Column (¼ Column Shown, Stresses Averaged Over Depth) 458
Figure E-6: Critical Perimeter Shear Stress Distribution Predicted by NLFEA and Method 2 (Assumed Distribution in Purple), κ = 1.980, Rectangular Column (¼ Column Shown, Stresses Averaged Over Depth) 458

Figure E-7: Critical Perimeter Shear Stress Distribution Predicted by NLFEA and Method 2 (Assumed Distribution in Purple), κ = 2.970, Rectangular Column (¼ Column Shown, Stresses Averaged Over Depth) 459

Figure F-1: Comparison of Predicted Load-Displacement Response at Wall CL (X-Wall CL, see Figure 7-25 for Displacement Location) for toe and gap Length Studies, κ =1.287, Predicted Response cut off at Peak Load) 461
Figure F-2: Comparison of Predicted Load-Displacement Response at Wall CL (X-Wall CL, see Figure 7-25 for Displacement Location), Opening Size Study, κ = 1.287 (Toe Length Set to *5d*, Gap Length set to *2d*, Predicted Response cut off at Peak Load) 461
Figure F-3: Comparison of Predicted Load Displacement Response at Wall Toe from Full Wall, Original Cut-Wall Model (*5d* toe and gap Lengths, no Slab Opening) and Finalized Cut-Wall Model (*5d* toe, *2d* gap, c_{min}+*d* High and *0.5d* Slab Opening), κ = 0.594 (see Figure 6-4 and Figure 7-25 for Displacement Locations) 462
Figure F-4: Comparison of Predicted Load Displacement Response at Wall Toe from Full Wall, Original Cut-Wall Model (*5d* toe and gap Lengths, no Slab Opening) and Finalized Cut-Wall Model (*5d* toe, *2d* gap, c_{min}+*d* High and *0.5d* Slab Opening), κ = 0.792 (see Figure 6-4 and Figure 7-25 for Displacement Locations) 462
Figure F-5: Comparison of Predicted Load Displacement Response at Wall Toe from Full Wall, Original Cut-Wall Model (*5d* toe and gap Lengths, no Slab Opening) and Finalized Cut-Wall Model (*5d* toe, *2d* gap, c_{min}+*d* High and *0.5d* Slab Opening), κ = 1.485 (see Figure 6-4 and Figure 7-25 for Displacement Locations) 463
Figure F-6: Comparison of Predicted Load Displacement Response at Wall Toe from Full Wall, Original Cut-Wall Model (*5d* toe and gap Lengths, no Slab Opening) and Finalized Cut-Wall Model (*5d* toe, *2d* gap, c_{min}+*d* High and *0.5d* Slab Opening), κ = 1.782 (see Figure 6-4 and Figure 7-25 for Displacement Locations) 463
Figure F-7: Comparison of Predicted Load Displacement Response at Wall Toe from Full Wall, Original Cut-Wall Model (*5d* toe and gap Lengths, no Slab Opening) and Finalized Cut-Wall Model (*5d* toe, *2d* gap, c_{min}+*d* High and *0.5d* Slab Opening), κ = 1.980 (see Figure 6-4 and Figure 7-25 for Displacement Locations) 464
Figure F-8: Comparison of Predicted Load Displacement Response at Wall Toe from Full Wall, Original Cut-Wall Model (*5d* toe and gap Lengths, no Slab Opening) and Finalized Cut-Wall Model

(*5d* toe, *2d* gap, c_{min}+*d* High and *0.5d* Slab Opening), κ = 2.970 (see Figure 6-4 and Figure 7-25 for Displacement Locations) 464
Figure F-9: Comparison of Crack Pattern From (a) Full Wall and (b) Finalized Cut-Wall Model, κ = 0.594, i) Tension Surface, ii) Slab Side Parallel to Long Side of Wall, iii) Slab Side Parallel to Short Side of Wall (Entire Isolated Slab-Wall Specimen not Shown 465
Figure F-10: Comparison of Crack Pattern From (a) Full Wall and (b) Finalized Cut-Wall Model, κ = 0.792, i) Tension Surface, ii) Slab Side Parallel to Long Side of Wall, iii) Slab Side Parallel to Short Side of Wall (Entire Isolated Slab-Wall Specimen not Shown 466
Figure F-11: Comparison of Crack Pattern From (a) Full Wall and (b) Finalized Cut-Wall Model, κ = 1.485, i) Tension Surface, ii) Slab Side Parallel to Long Side of Wall, iii) Slab Side Parallel to Short Side of Wall (Entire Isolated Slab-Wall Specimen not Shown 467
Figure F-12: Comparison of Crack Pattern From (a) Full Wall and (b) Finalized Cut-Wall Model, κ = 1.782, i) Tension Surface, ii) Slab Side Parallel to Long Side of Wall, iii) Slab Side Parallel to Short Side of Wall (Entire Isolated Slab-Wall Specimen not Shown 468
Figure F-13: Comparison of Crack Pattern From (a) Full Wall and (b) Finalized Cut-Wall Model, κ = 2.970, i) Tension Surface, ii) Slab Side Parallel to Long Side of Wall, iii) Slab Side Parallel to Short Side of Wall (Entire Isolated Slab-Wall Specimen not Shown 469
Figure F-14: Comparison of Shear Stress Distribution Along Wall Perimeter from Full Wall and Cut-Wall Models (no Bottom of Toe (Side 3) since c_{min}/d High Opening Removes all Elements), κ = 0.594 (see Figure 7-36 for Side Numbering Convention, ¼ Wall Shown, Stresses Averaged Over Depth) 470
Figure F-15: Comparison of Shear Stress Distribution Along Wall Perimeter from Full Wall and Cut-Wall Models (no Bottom of Toe (Side 3) since c_{min}/d High Opening Removes all Elements), κ = 0.792 (see Figure 7-36 for Side Numbering Convention, ¼ Wall Shown, Stresses Averaged Over Depth) 471
Figure F-16: Comparison of Shear Stress Distribution Along Wall Perimeter from Full Wall and Cut-Wall Models (no Bottom of Toe (Side 3) since c_{min}/d High Opening Removes all Elements), κ = 1.287 (see Figure 7-36 for Side Numbering Convention, ¼ Wall Shown, Stresses Averaged Over Depth) 472
Figure F-17: Comparison of Shear Stress Distribution Along Wall Perimeter from Full Wall and Cut-Wall Models (no Bottom of Toe (Side 3) since c_{min}/d High Opening Removes all Elements), κ = 1.485 (see Figure 7-36 for Side Numbering Convention, ¼ Wall Shown, Stresses Averaged Over Depth) 473
Figure F-18: Comparison of Shear Stress Distribution Along Wall Perimeter from Full Wall and Cut-Wall Models (no Bottom of Toe (Side 3) since c_{min}/d High Opening Removes all Elements), κ = 1.782 (see Figure 7-36 for Side Numbering Convention, ¼ Wall Shown, Stresses Averaged Over Depth) 474

Figure F-19: Comparison of Shear Stress Distribution Along Wall Perimeter from Full Wall and Cut-Wall Models (no Bottom of Toe (Side 3) since c_{min}/d High Opening Removes all Elements), κ = 1.980 (see Figure 7-36 for Side Numbering Convention, ¼ Wall Shown, Stresses Averaged Over Depth)475
Figure F-20: Comparison of Shear Stress Distribution Along Wall Perimeter from Full Wall and Cut-Wall Models (no Bottom of Toe (Side 3) since c_{min}/d High Opening Removes all Elements), κ = 2.970 (see Figure 7-36 for Side Numbering Convention, ¼ Wall Shown, Stresses Averaged Over Depth)476

Figure G-1: Notation Used in Calculation of J and γ_v 478

Figure H-1: Overall Column Dimensions and Values of a_n and b_n According to ACI 318-19 for L2-L-o9 (Effective Load Area Shown with Blue Dashed Line) 482
Figure H-2: Reduced Critical Perimeter According to ACI 318-19 for L2-L-o9 482
Figure H-3: Reduced Critical Perimeter for L2-L-o9 When Diagonal Portion is Neglected..... 483
Figure H-4: Definition of x', $\bar{x}$, y' and $\bar{y}$ axes and Numbering of Critical Points of Assumed Critical Perimeter 485
Figure H-5: a) Determination of $\overline{x_o}$, $\overline{y_o}$ (both Negative for the Example Shown); b) Determination of l_x and l_y and Orientation of Principal Centroidal Axes x and y 487
Figure H-6: Positive Sign Convention for θ, M_{u-x} and M_{u-y} Assumed in ACI 421.1R-20 [5] 489
Figure H-7: Overall Column Dimensions and Values of a_n and b_n According to ACI 318-19 for T2-L-o9 (Effective Load Area Shown with Blue Dashed Line) 490
Figure H-8: Reduced Critical Perimeter According to ACI 318-19 for T2-L-o9 490
Figure H-9: Reduced Critical Perimeter for T2-L-o9 When Diagonal Portion is Neglected..... 491
Figure H-10: Definition of x', $\bar{x}$, y' and $\bar{y}$ axes and Numbering of Critical Points of Assumed Critical Perimeter 493
Figure H-11: a) Determination of $\overline{x_o}$, $\overline{y_o}$ (Negative $\overline{x_o}$ and Positive $\overline{y_o}$ for the Example Shown (T2-L-o9)); b) Determination of l_x and l_y and Orientation of Principal Centroidal Axes x and y 494
Figure H-12: Determination of e_x for T2-L Specimens (Note: e_x is Positive in This Case) 495

Figure I-1: Reduced Critical Perimeters Around Rectangular Slab-Column Connections with Openings According to ACI 318-19 (Radial Approach) 497

Figure I-2: Reduced Critical Perimeters Around Rectangular Slab-Column Connections with Openings According to ACI 318-19 (Straight Projection Approach) 497
Figure I-3: Reduced Critical Perimeters Around Slab-Wall Connections with Openings According to ACI 318-19 (Half-Wall Shown, Radial Approach) 498
Figure I- 4: Reduced Critical Perimeters Around Slab-Wall Connections with Openings According to ACI 318-19 (Half-Wall Shown, Straight Projection Approach) 498
Figure I-5: Reduced Critical Perimeters for Slab-Column Connections with Openings According to ACI 318-19 – R1-S Specimens (Radial Approach) 499
Figure I-6: Reduced Critical Perimeters for Slab-Column Connections with Openings According to ACI 318-19 – R2-S Specimens (Radial Approach) 499
Figure I-7: Reduced Critical Perimeters for Slab-Column Connections with Openings According to ACI 318-19 – R1-L Specimens (Radial Approach) 499
Figure I-8: Reduced Critical Perimeters for Slab-Column Connections with Openings According to ACI 318-19 – R2-L Specimens (Radial Approach) 500
Figure I-9: Reduced Critical Perimeters for Slab-Column Connections with Openings According to ACI 318-19 – R1-S Specimens (Straight Projection Approach) 500
Figure I-10: Reduced Critical Perimeters for Slab-Column Connections with Openings According to ACI 318-19 – R2-S Specimens (Straight Projection Approach) 500
Figure I-11: Reduced Critical Perimeters for Slab-Column Connections with Openings According to ACI 318-19 – R1-L Specimens (Straight Projection Approach) 501
Figure I-12: Reduced Critical Perimeters for Slab-Column Connections with Openings According to ACI 318-19 – R2-L Specimens (Straight Projection Approach) 501
Figure I-13: Reduced Critical Perimeters for Slab-Column Connections with Openings According to ACI 318-19 – L1-S Specimens 501
Figure I-14: Reduced Critical Perimeters for Slab-Column Connections with Openings According to ACI 318-19 – L2-S Specimens 502
Figure I-15: Reduced Critical Perimeters for Slab-Column Connections with Openings According to ACI 318-19 – L1-L Specimens 502
Figure I-16: Reduced Critical Perimeters for Slab-Column Connections with Openings According to ACI 318-19 – L2-L Specimens 502
Figure I-17: Reduced Critical Perimeters for Slab-Column Connections with Openings According to ACI 318-19 – T1-S Specimens 503

Figure I-18: Reduced Critical Perimeters for Slab-Column Connections with Openings According to ACI 318-19 – T2-S Specimens 503
Figure I-19: Reduced Critical Perimeters for Slab-Column Connections with Openings According to ACI 318-19 – T1-L Specimens 504
Figure I-20: Reduced Critical Perimeters for Slab-Column Connections with Openings According to ACI 318-19 – T2-L Specimens 504
Figure I-21: Reduced Critical Perimeters for Slab-Column Connections with Openings According to ACI 318-19 – X1-S Specimens 504
Figure I-22: Reduced Critical Perimeters for Slab-Column Connections with Openings According to ACI 318-19 – X2-S Specimens 505
Figure I-23: Reduced Critical Perimeters for Slab-Column Connections with Openings According to ACI 318-19 – X1-L Specimens 505
Figure I-24: Reduced Critical Perimeters for Slab-Column Connections with Openings According to ACI 318-19 – X2-L Specimens 505
Figure I-25: Reduced Critical Perimeters for R2x7.2o Specimens According to ACI 318-19 (Radial Approach) 506
Figure I-26: Reduced Critical Perimeters for L2x4.6o Specimens According to ACI 318-19 506
Figure I-27: Reduced Critical Perimeters for T2x4.6o Specimens According to ACI 318-19 506
Figure I-28: Reduced Critical Perimeters for X2x4.6o Specimens According to ACI 318-19 507

Figure J-1: Predicted Tension Surface Crack Patterns, R1-S Specimens (Grey Regions Have Principal Plastic Strains > 0.02) 509
Figure J-2: Predicted Tension Surface Crack Patterns, R2-S Specimens (Grey Regions Have Principal Plastic Strains > 0.02) 510
Figure J-3: Predicted Tension Surface Crack Patterns, R1-L Specimens (Grey Regions Have Principal Plastic Strains > 0.02) 511
Figure J-4: Predicted Tension Surface Crack Patterns, R2-L Specimens (Grey Regions Have Principal Plastic Strains > 0.02) 512
Figure J-5: Predicted Tension Surface Crack Patterns, L1-S Specimens (Grey Regions Have Principal Plastic Strains > 0.02) 513
Figure J-6: Predicted Tension Surface Crack Patterns, L2-S Specimens (Grey Regions Have Principal Plastic Strains > 0.02) 514

Figure J-7: Predicted Tension Surface Crack Patterns, L1-L Specimens (Grey Regions Have Principal Plastic Strains > 0.02) 515
Figure J-8: Predicted Tension Surface Crack Patterns, L2-L Specimens (Grey Regions Have Principal Plastic Strains > 0.02) 516
Figure J-9: Predicted Tension Surface Crack Patterns, T1-S Specimens (Grey Regions Have Principal Plastic Strains > 0.02) 517
Figure J-10: Predicted Tension Surface Crack Patterns, T2-S Specimens (Grey Regions Have Principal Plastic Strains > 0.02) 518
Figure J-11: Predicted Tension Surface Crack Patterns, T1-L Specimens (Grey Regions Have Principal Plastic Strains > 0.02) 519
Figure J-12: Predicted Tension Surface Crack Patterns, T2-L Specimens (Grey Regions Have Principal Plastic Strains > 0.02) 520
Figure J-13: Predicted Tension Surface Crack Patterns, X1-S Specimens (Grey Regions Have Principal Plastic Strains > 0.02) 521
Figure J-14: Predicted Tension Surface Crack Patterns, X2-S Specimens (Grey Regions Have Principal Plastic Strains > 0.02) 522
Figure J-15: Predicted Tension Surface Crack Patterns, X1-L Specimens (Grey Regions Have Principal Plastic Strains > 0.02) 523
Figure J-16: Predicted Tension Surface Crack Patterns, X2-L Specimens (Grey Regions Have Principal Plastic Strains > 0.02) 524
Figure J-17: Column Perimeter Shear Stress Distributions at Peak Load – R1-S Specimens (Stresses Averaged Over Depth) 525
Figure J-18: Column Perimeter Shear Stress Distributions at Peak Load – R2-S Specimens (Stresses Averaged Over Depth) 526
Figure J-19: Column Perimeter Shear Stress Distributions at Peak Load – R1-L Specimens (Stresses Averaged Over Depth) 527
Figure J-20: Column Perimeter Shear Stress Distributions at Peak Load – R2-L Specimens (Stresses Averaged Over Depth) 528
Figure J-21: Column Perimeter Shear Stress Distributions at Peak Load – L1-S Specimens (Stresses Averaged Over Depth) 529
Figure J-22: Column Perimeter Shear Stress Distributions at Peak Load – L2-S Specimens (Stresses Averaged Over Depth) 530

Figure J-23: Column Perimeter Shear Stress Distributions at Peak Load – L1-L Specimens (Stresses Averaged Over Depth) 531
Figure J-24: Column Perimeter Shear Stress Distributions at Peak Load – L2-L Specimens (Stresses Averaged Over Depth) 532
Figure J-25: Column Perimeter Shear Stress Distributions at Peak Load – T1-S Specimens (Stresses Averaged Over Depth) 533
Figure J-26: Column Perimeter Shear Stress Distributions at Peak Load – T2-S Specimens (Stresses Averaged Over Depth) 534
Figure J-27: Column Perimeter Shear Stress Distributions at Peak Load – T1-L Specimens (Stresses Averaged Over Depth) 535
Figure J-28: Column Perimeter Shear Stress Distributions at Peak Load – T2-L Specimens (Stresses Averaged Over Depth) 536
Figure J-29: Column Perimeter Shear Stress Distributions at Peak Load – X1-S Specimens (Stresses Averaged Over Depth) 537
Figure J-30: Column Perimeter Shear Stress Distributions at Peak Load – X2-S Specimens (Stresses Averaged Over Depth) 538
Figure J-31: Column Perimeter Shear Stress Distributions at Peak Load – X1-L Specimens (Stresses Averaged Over Depth) 539
Figure J-32: Column Perimeter Shear Stress Distributions at Peak Load – X2-L Specimens (Stresses Averaged Over Depth) 540

Figure K-1: Comparison of Predicted Load-Displacement Responses for Concentrically Loaded R-SCCs in Chapter 9, Displacement Measurement Locations Shown in Figure 9-5 542
Figure K-2: Comparison of Predicted Load-Displacement Responses for Concentrically Loaded L-SCCs in Chapter 9, Displacement Measurement Locations Shown in Figure 9-5 542
Figure K-3: Comparison of Predicted Load-Displacement Responses for Concentrically Loaded T-SCCs in Chapter 9, Displacement Measurement Locations Shown in Figure 9-5 542
Figure K-4: Comparison of Predicted Load-Displacement Responses for Concentrically Loaded X-SCCs in Chapter 9, Displacement Measurement Locations Shown in Figure 9-5 543
Figure K-5: Comparison of Predicted Tension Surface Crack Patterns for Concentrically Loaded R-SCCs in Chapter 9 543

Figure K-6: Comparison of Predicted Tension Surface Crack Patterns for Concentrically Loaded L-SCCs in Chapter 9 544
Figure K-7: Comparison of Predicted Tension Surface Crack Patterns for Concentrically Loaded T-SCCs in Chapter 9 544
Figure K-8: Comparison of Predicted Tension Surface Crack Patterns for Concentrically Loaded X-SCCs in Chapter 9 545
Figure K-9: Column Perimeter Shear Stress Distributions for Concentrically Loaded R-SCCs (Chapter 9) – Peak Load (Stresses Averaged Over Depth) 545
Figure K-10: Column Perimeter Shear Stress Distributions for Concentrically Loaded L-SCCs (Chapter 9) – Peak Load (Stresses Averaged Over Depth) 546
Figure K-11: Column Perimeter Shear Stress Distributions for Concentrically Loaded T-SCCs (Chapter 9) – Peak Load (Stresses Averaged Over Depth) 546
Figure K-12: Column Perimeter Shear Stress Distributions for Concentrically Loaded X-SCCs (Chapter 9) – Peak Load (Stresses Averaged Over Depth) 547
Figure K-13: Predicted Tension Surface Crack Patterns at Failure, T-SCCs (Grey Regions Have Principal Plastic Strains > 0.02) 548
Figure K-14: Predicted Tension Surface Crack Patterns at Failure, X-SCCs (Grey Regions Have Principal Plastic Strains > 0.02) 549

List of Tables

Table 3-1: Values of *k* for Rectangular Columns [34] 75
Table 6-1: Summary of Load Cases Considered [324] 114
Table 6-2: Summary of Isolated Slab-Wall Connections Analyzed 115
Table 6-3: Slab Properties and Comparison of Experimental [57, 151] and FEA Results 122
Table 6-4: Summary of Calibrated FEM [1] 128
Table 6-5: Summary of Concentric Punching Capacities and ACI 318-19 Predictions, Interior SWCs 133
Table 6-6: Predicted Capacities and Opening Influences – R-SCCs 144
Table 6-7: Predicted Capacities and Opening Influences – SWCs 148
Table 7-1: Summary of Isolated Slab-Column Connections in Numerical Database [145, 161] 155
Table 7-2: Selected Databank of Punching Shear Tests for Slabs Without Shear Reinforcement and Supported on Square or Rectangular Columns 156
Table 7-3: Summary of Predictions According to ACI 318-19 and Proposed Methods 165
Table 7-4: Overview of Investigated Connection Region Modelling Methodologies and Notation Used in Figure 7-20 181
Table 7-5: Comparison of Estimated Tributary Areas 184
Table 7-6: Comparison of Predicted Punching Capacities for Interior SWCs by Full Wall and Cut-Wall Models 190
Table 7-7: Comparison of Predicted Capacities of Two-Way Shear Regions, f'_c =44.6MPa 211
Table 7-8: Comparison of Predicted One-Way Shear Region Capacities, f'_c =44.6MPa 214
Table 7-9: Comparison of Predicted Punching Capacities for Interior SWCs 216
Table 8-1: Summary of Column Dimensions, Eccentricities and Opening Details Considered for Studied L, T and Cruciform Slab-Column Connections 223
Table 8-2: Rectangular Slab-Column Connections (R-SCCs) Dimensions and Opening Details 227
Table 8-3: Summary of Experimental Specimens Tested by Hawkins et al. [3] 233
Table 8-4: Summary of Calibrated Model Used in Special Shaped Column Study [259] 236
Table 8-5: Summary of Experimental Program by Hawkins et al. (1971) and FEA Predictions 237
Table 8-6: Comparison of Capacities and Opening Influences Predicted by FEA and ACI 318-19 – R-SCCs 240
Table 8-7: Comparison of Capacities and Opening Influences Predicted by FEA and ACI 318-19 – L-SCCs 246

Table 8-8: Comparison of Capacities and Opening Influences Predicted by FEA and ACI 318-19 – T-SCCs 253
Table 8-9: Comparison of Capacities and Opening Influences Predicted by FEA and ACI 318-19 – X-SCCs 258
Table 8-10: Capacities and Opening Influences Predicted by ACI 421.1R-20 for Analyzed L-SCCs, T-SCCs and X-SCCs 262
Table 8-11: Comparison of Opening Influence Predicted by NLFEA for Different Column Geometries 265
Table 9-1: Overview of Analyzed R-SCCs – SS-SCC Study – Combined Shear and Unbalanced Moment 275
Table 9-2: Overview of Analyzed L-SCCs – SS-SCC Study – Combined Shear and Unbalanced Moment 276
Table 9-3: Overview of Analyzed T-SCCs – SS-SCC Study – Combined Shear and Unbalanced Moment 276
Table 9-4: Overview of Analyzed X-SCCs – SS-SCC Study – Combined Shear and Unbalanced Moment 277
Table 9-5: Summary of Experimental Specimens (Concentric Shear Only [V Only] and Combined Concentric Shear and Monotonic Uniaxial Unbalanced Moment [V+M (Monotonic)]) Tested by Drakatos et al. [4] 280
Table 9-6: Comparison of Specimens Tested by Sagaseta et al. [57, 151] and Drakatos et al. [4] Considered in FEM Calibrations 283
Table 9-7: Summary of Concrete Material Parameters in Calibrated FEM in Chapter 9 283
Table 9-8: Summary of Experimental and FEA Results for Selected PD [4] Specimens 287
Table 9-9: Comparison of Predictions for PD1 From Explicit and Static Analyses (Timestep of Moment Application Step Varied for Explicit Analyses) 291
Table 9-10:Summary of Specimens Considered in FEM Calibration Verification Study 297
Table 9-11: Summary of NLFEA and ACI 318-19 Predictions, FEM Calibration Verification Study 300
Table 9-12: Comparison of Capacities and Opening Influences Predicted by FEA, ACI 318-19 and ACI 421.1R-20 – Concentrically Loaded Specimens 303
Table 9-13: Summary of Predicted Unbalanced Moment Capacities and Approximated Opening Influences, R-SCCs 308

Table 9-14: Summary of Predicted Unbalanced Moment Capacities and Approximated Opening Influences, L-SCCs 312
Table 9-15: Summary of Predicted Unbalanced Moment Capacities and Approximated Opening Influences, T-SCCs 317
Table 9-16: Summary of Predicted Unbalanced Moment Capacities and Approximated Opening Influences, X-SCCs 319
Table 9-17: Unbalanced Moment Capacities Predicted by ACI 421.1R-20 for Analyzed R-SCCs and SS-SCCs Subjected to V+M (Monotonic) Loading 321

Table B-1: Comparison of Predicted Capacities for Analyzed Slab-Wall Connections for Different Load Conditions 439

Table C-1: Summary of 77 Isolated-Slab Column Specimens Simulated During Author's MASc Work [1] 451

Table D-1: Detailed of Selected Databank Specimens Without Shear Reinforcement Which Failed in Punching and are Supported on Square or Rectangular Columns (86 Specimens) 453

Table H-1: Summary of Coordinates of Critical Perimeter About Different axes and Summary of Computed Shear Stress Values at Critical Points for V=388.0kN, Specimen L2-L-o9 486
Table H-2: Summary of Lengths and Centroids of Each Segment of Critical Perimeter With Respect to x' and y' Coordinate System, Specimen L2-L-o9 486
Table H-3: Summary of Coordinates of Critical Perimeter About Different axes and Summary of Computed Shear Stress Values at Critical Points for V=424.0kN, Specimen T2-L-o9 493
Table H-4: Summary of Lengths and Centroids of Each Segment of Critical Perimeter With Respect to x' and y' Coordinate System, Specimen T2-L-o9 493

Chapter 1: Introduction

1.1 Background

Reinforced concrete flat slabs, which were introduced in 1900 by George M. Hill, and popularized by American engineer C.A.P. Turner and Swiss engineer Robert Maillart, are one of the most common structural systems for buildings where open floor plans are essential, such as warehouses, parking garages and office buildings [6]. Due to the lack of an accepted structural analysis method for reinforced concrete flat slabs until 1921, early designs varied greatly in the required amount of flexural reinforcement [7] and usually included large capitals near the supporting columns, to provide additional shear strength [6]. An example of Turner's typical shear capital is shown in Figure 1-1.

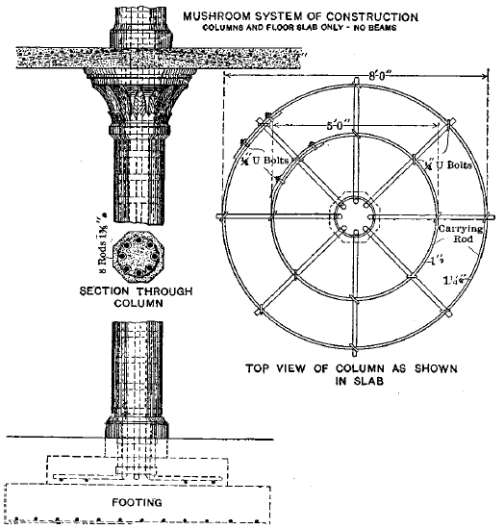


Figure 1-1: Typical Column Capital and Shearhead Used by Turner [8], (taken from [6])

Despite the fact that an accepted method of analysis for flat slabs was not available until 1921, over 1000 flat slab buildings had been constructed worldwide by 1913 [7] due to the many advantages of the system including minimized formwork, reduced floor height and easier installation of architectural finishes. Today, there are four typical flat slab systems, as shown in Figure 1-2, with the system shown in Figure 1-2c, referred to as a flat plate, increasing in popularity as the understanding of flat slabs has improved. Flat plate systems where the slab is either entirely supported on columns or a combination of columns and walls are the focus of the proposed research.

Flat plates have many advantages; however, the lack of supporting members between columns results in a critical region at the connection between the slab and column which is subjected to a

complicated three-dimensional state of stress [9]. This leads to the primary disadvantage of flat plates, which is the possibility of brittle punching shear failures at the slab-column or slab-wall connections.

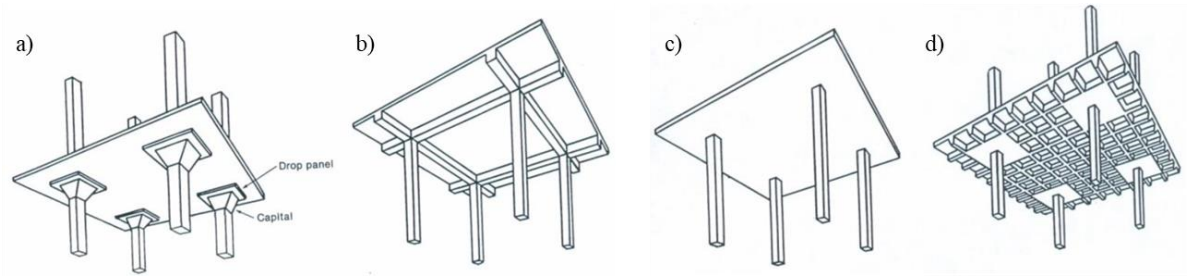


Figure 1-2: Typical Flat Slabs, a) Flat Slab with Column Capitals and Drop Panels, b) Two-way Slab Supported on Beams, c) Flat Plate, d) Waffle Slab; Acknowledgement: Reinforced Concrete Mechanics and Design, MacGregor and Bartlett (2000) [10], ©2000 Pearson Education Canada Inc., Reproduced with Permission of Pearson Canada Inc.

Due to its brittle nature, punching of one connection (a typical punching shear failure surface is shown in Figure 1-3) can lead to the progressive collapse of a structure, and as such punching shear has been studied extensively since the 1950s as the popularity of flat plates has grown [11]. Even with this extensive research, punching failures still occur in practice, either before construction is complete due to insufficient strength of partially cured concrete [12], but also in occupied structures potentially leading to a catastrophic loss of life. For example, the collapse of the Sampoong Department Store in Seoul, South Korea, which occurred due to a punching failure of a 5th-storey slab-column connection, led to the deaths of approximately 500 people [12, 13]. Punching shear failures are also common during earthquake events, due to a deterioration of strength and stiffness due to the cyclic displacements and the additional shear stresses due to the lateral displacements of the structure, which are transferred to the slab-column connection as an unbalanced moment. For example, during the 1985 Mexico City Earthquake over 91 flat plate buildings collapsed, with 44 experiencing significant damage due to punching [14].

The lateral strength and stiffness provided by slab-column frames alone have been shown to be insufficient. Therefore, slab-column systems are typically assumed to not be part of the lateral force resisting system (LFRS) of a structure and are commonly combined with stiff shear walls, which are assumed to carry the entire lateral force caused by wind or earthquake loading [14, 15, 16, 17, 18, 19, 20, 21, 22, 23]. However, the slab-column connections need to have sufficient strength and ductility to sustain the additional shear stresses due to the imposed lateral displacements, which are transferred

to the connection via unbalanced moments, while maintaining their gravity load capacity during and after the extreme loading event. Of the many methods to increase punching shear capacity, which include increasing the concrete compressive strength, slab depth or column size, adding shear capitals or drop panels, only one, the addition of shear reinforcement in the slab, leads to a substantial increase in ductility as well as strength [17, 24].

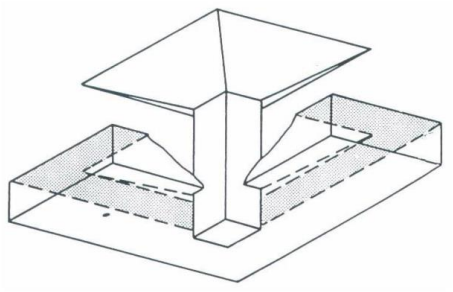


Figure 1-3: Punching Shear Failure Surface; Acknowledgement: Reinforced Concrete Mechanics and Design, MacGregor and Bartlett (2000) [10], ©2000 Pearson Education Canada Inc., Reproduced with Permission of Pearson Canada Inc.

To date, much research effort has been dedicated to the study of the punching shear behaviour of slab-column connections with and without shear reinforcement and subjected to gravity loads only or combined gravity and lateral loads. Most of this research has been experimental, and typically involves testing of isolated slab-column connections, where the portion of the slab included in the test approximates the extent of the negative moment region around the column, due to the cost and facility size required for testing full structures. Numerous researchers have also shown that nonlinear finite element analysis (NLFEA) can be used to study punching shear [1, 25, 26, 27], and is a valuable tool to efficiently expand experimental databases and verify experimental observations. NLFEA also allows quantities which are difficult to measure experimentally, such as the internal crack propagation and shear stress distributions, to be studied, which makes it ideal for punching shear research.

However, as will be discussed in detail, most previous punching shear research has focused on the behaviour of square or circular slab-column connections, even though rectangular slab-column and slab-wall connections (elongated connections) are common in practice. In particular, the punching shear behaviour of slab-wall connections (SWCs) has been largely ignored since the early 1980s [28, 29, 30, 31, 32, 33], even though punching shear failures have been observed in the limited experimental database. Additionally, while less common than elongated connections, punching shear design provisions for special-shaped slab-column connections (SS-SCCs), such as L, T and cruciform

connections, are included in worldwide design codes [2, 34, 35], and have been largely unchanged since their introduction over 40 years ago. While SS-SCCs are uncommon in practice, particularly for interior connections, they could offer architectural benefits, especially if slab openings between the column flanges have a minimal influence on punching capacity. Therefore, the overall goal of this research is to use calibrated, nonlinear, three-dimensional FEA to conduct a comprehensive study of the influence of support geometry on the punching behaviour of reinforced concrete flat plates.

1.2 Research Objectives and Problem Statement

The proposed research has four primary objectives:

1. Summarize historical and current code provisions related to the influence of support geometry on punching shear capacity for slab-column connections without shear reinforcement.
2. Develop calibrated, nonlinear, three-dimensional finite element models (FEMs) which can be used to study the influence of support geometry on the punching shear capacity of isolated slab-column and slab-wall connections (SWCs).
3. Use the calibrated FEMs to conduct parametric studies to analyze the punching shear behaviour of elongated connections (rectangular slab-column and slab-wall connections) and special-shaped slab-column connections (specifically L, T and cruciform columns) with and without slab openings near the connection.
4. Compare the influence of support geometry and slab openings predicted by the nonlinear finite element analysis (NLFEA) with that predicted by worldwide design provisions, with a particular focus on the predictions according to ACI 318-19 [2] (which serves as the basis for CSA A23.3-19 [36]).

Due to their large size, the SWCs are analyzed by expanding the FEM developed during the author's MASc studies. The FEM, implemented in Abaqus/Explicit, was originally calibrated to study the punching shear behaviour of rectangular slab-column connections (R-SCCs) [1]. The specific objectives of the slab-wall connection study are:

1. Summarize past research and design methods related to punching shear of SWCs.

2. Extend the three-dimensional nonlinear FEM developed for the analysis of the punching shear behaviour of R-SCCs under concentric loading to allow for the study of SWCs subjected to concentric loading and combined concentric loading and unbalanced moment.
3. Using the modified calibrated FEM, study the overall punching shear behaviour of interior SWCs of different lengths and thicknesses.
4. Using the modified calibrated FEM, study the influence of slab openings at various locations on the behaviour of interior SWCs.
5. Develop simplified analysis and design methods to estimate the concentric load demand and punching shear capacity of interior SWCs.
6. Provide recommendations for the ideal location of slab openings around interior SWCs from the perspective of concentric punching shear.

The FEMs used in the analysis of SS-SCCs are also extensions of those developed during the author's MASc studies. The first FEM, used to study the punching shear behaviour of special-shaped connections subjected to concentric loading, was calibrated based on the 9 experimental specimens of Hawkins et al. [3], which form the basis for the ACI 318-19 equation relating column geometry and punching capacity. Since the specimens tested by Hawkins et al. [3] are singly reinforced, a second FEM, calibrated to experimental results by Drakatos et al. [4], was used to study the punching behaviour of special-shaped connections subjected to combined shear and unbalanced moment. The specific objectives of the special-shaped column study are:

1. Summarize past research and design methods for punching shear of SS-SCCs, specifically for L-, T- and cruciform columns.
2. Develop nonlinear, three-dimensional FEMs to study the punching shear behaviour of interior SS-SCCs subjected to concentric shear only, or combined concentric shear and unbalanced moment.
3. Use the calibrated FEMs to study the punching behaviour of SS-SCCs for different column sizes and slab openings at various locations around the connection.
4. Use the calibrated FEMs to evaluate the influence of slab openings between the column flanges for SS-SCCs for various load conditions.

5. Evaluate the accuracy of current design provisions for estimating the punching capacity of SS-SCCs, with a particular focus on ACI 318-19 [2] and ACI 421.1R-20 [5]. Simplified provisions suitable for the preliminary design of SS-SCCs will also be presented.
6. Provide recommendations for the ideal location of slab openings around interior SS-SCCs from the perspective of punching shear.

1.3 Outline

The outline of this thesis is as follows:

The introduction of this thesis (Chapter 1) briefly introduces the research problem, overviews the advantages of FEA and outlines the research objectives. The phenomenon of punching shear is further described in Chapter 2. A summary of previous relevant experimental, analytical and finite element studies of punching shear is also provided in Chapter 2. The literature review is primarily focused on interior slab-column and slab-wall connections without shear reinforcement. A summary of major worldwide punching shear design provisions for connections subjected to concentric loading and combined shear and unbalanced moment is provided in Chapter 3. A brief overview of the mechanical behaviour of concrete and the Concrete Damaged Plasticity (CDP) model in Abaqus is provided in Chapter 4. A summary of the overall research program is provided in Chapter 5. Chapter 6 summarizes the research related to the punching shear behaviour of interior SWCs. The study motivation, specimen overview, FEM calibration, and FEA results are discussed. Addressing a gap in the existing literature, the goal of this study was to provide a detailed discussion of the punching shear behaviour of SWCs. As existing design methods and provisions for elongated connections are either inaccurate, or require the use of specialized FEA, alternative punching shear design methods for R-SCCs and SWCs, developed from the numerical results presented herein and in [1], are proposed in Chapter 7. The proposed design methods were developed to address issues with the existing ACI 318-19 provisions for elongated connections, while ensuring the methods were still suitable for hand calculations, as this is one of the primary benefits of the ACI 318 provisions. The methods are also presented in a code-like formulation as they will be submitted to the American Concrete Institute (ACI) for potential adoption in future versions of ACI 318. Chapter 8 summarizes the research related to the punching shear behaviour of interior SS-SCCs subjected to concentric loading. In Chapter 9, the punching shear behaviour of interior SS-SCCs subjected to combined shear and unbalanced moment is discussed. In both Chapters 8 and 9, the study motivation, specimen

dimensions, FEM calibration and FEA results are discussed. Detailed discussions of the punching shear behaviour of rectangular and special-shaped (L-, T- and cruciform) slab-column connections under various load conditions are provided in both chapters. Such discussions are limited in existing literature, particularly in the case of SS-SCCs. In addition to the proposed design methods for rectangular slab-column and slab-wall connections, recommendations for the ideal slab opening location around interior slab-column and slab-wall connections are provided in Chapters 6, 8 and 9. Additionally, based on the FEA results in Chapters 6, 8 and 9, issues with the ACI 318-19 punching shear design provisions, which are representative of current North American practice, are highlighted. Finally, a summary of the research, conclusions and recommendations for future work are provided in Chapter 10.

Chapter 2: Punching Shear in Reinforced Concrete Slabs

2.1 Introduction

This chapter presents an overview of punching shear in reinforced concrete flat plates. Firstly, the phenomenon of punching shear and its consequences are discussed. Secondly, the existing literature related to punching shear, focused on slabs supported on square or circular columns, rectangular columns, special-shaped columns and walls with and without slab openings is reviewed. The review is primarily focused on the punching shear behaviour of interior connections without shear reinforcement, as that is the focus of this thesis, though some relevant studies with shear reinforcement are included, and considers both experimental and numerical research. Thirdly, some historical and current mechanical punching shear models are presented.

2.2 Phenomenon of Punching Shear

As previously shown in Figure 1-2, reinforced concrete flat slabs have many forms. However, as the understanding of the behaviour of reinforced concrete flat slabs has developed, the flat plate (see Figure 1-2c), where the slab is supported on columns alone, has become increasingly popular. While the removal of beams and girders has architectural advantages, it also results in a statical discontinuity at the intersection of the slab and columns. The region common to the slab and column is a D region, and is subjected to a complicated three-dimensional state of stress as all flexural and shear stresses are transferred through the slab column connections [9]. The complicated state of stress and lack of additional supporting members make punching shear failures possible.

Punching shear failure is a brittle failure mode of reinforced concrete flat slabs supported on columns which occurs when the shear stresses due to the applied load exceed the shear strength of the connection. Due to the gravity moment carried by the slab, radial cracks typically form on the tension surface of the slab before punching occurs [10, 37]. As the load on the slab is increased a crack pattern similar to that assumed in the yield-line analysis of two-way slabs forms on the tension surface [10] and internal inclined cracks begin to form due to the significant increase in vertical strains near the slab-column connections [10, 37, 38]. With additional loads, these inclined cracks, which typically have inclinations between 25-30 degrees, extend towards the compression surface of the slab at some distance from the column face [38, 39]. For slab-column connections without shear reinforcement a punching shear failure, which involves a truncated cone of slab concrete and the column punching through the slab (the resulting failure surface is shown in Figure 1-3), occurs when

the applied shear stresses exceed the connection strength, which is a function of the shear carried by the concrete in the compression zone, aggregate interlock along the crack, and dowel action provided by the slab's flexural reinforcement [40]. Representative punching shear crack patterns are provided in Figure 2-1 and Figure 2-2. Even though the slab's longitudinal reinforcement near the slab-column connection typically yields before punching, the overall failure mode is brittle [39, 40, 41]. Due to the brittleness of the failure, a punching shear failure of one connection can lead to the progressive collapse of an entire structure.

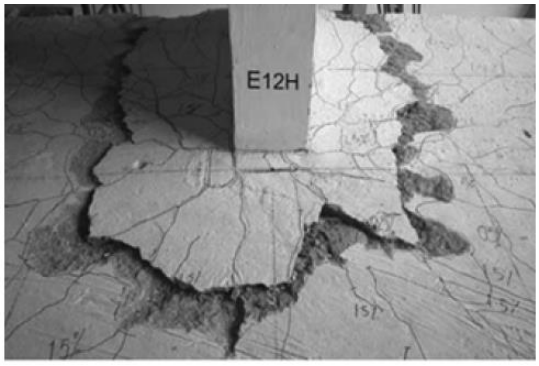


Figure 2-1: Typical Tension Surface Cracks After Punching Shear Failure [42], authorized reprint from ACI Structural Journal, Volume 105, Issue 5 (2008)



Figure 2-2: Typical Inclined Shear Cracks in Slab After Punching Shear Failure [42], authorized reprint from ACI Structural Journal, Volume 105, Issue 5 (2008)

Numerous design parameters, such as column size, column capital size and slab thickness can be governed by punching shear capacity [41]. If the overall capacity of a reinforced concrete flat plate is governed by punching shear, design engineers should be aware that the level of safety and the potential for warnings of failure, between most of the slab and the region of the slab around the

column are not the same due to the brittleness of punching failures compared to ductile flexural slab failure [9] [1].

2.3 Review of Previous Punching Shear Research

2.3.1 Introduction

Initial contributions to punching shear research were made by Talbot (1913), Bach and Graf (1915), Graf (1933 and 1938) and Richart (1948) [43], though these research programs were not focused on punching shear. For example, Talbot tested 114 wall-footing and 83 column-footing connections to study the behaviour of reinforced concrete footings. Based on the results of the 20 column-footing connections which failed in shear, Talbot proposed an equation to estimate the shear capacity of reinforced concrete column-footing connections based on the assumption of uniform shear stress around the connection. Additionally, while Bach and Graf (1915) were focused on investigating the flexural behaviour of reinforced concrete slabs, they observed that some of the slabs which were subjected to central point loads failed due to shear. Following this work, Graf (1933) investigated the shear capacity of reinforced concrete slabs subjected to point loads near the supports through a series of experimental tests. The shear capacity of the slab was found to decrease as the distance between the load and support increased and Graf hypothesized that flexural cracking in the slab influences the slab's shear strength. Further expanding upon this work, Graf published experimental results for eight slab tests, six of which included shear reinforcement in 1938. Like Talbot, Richart (1948) conducted extensive testing of reinforced concrete footings and concluded that footing design may be governed by shear stresses instead of bond stresses [43].

Since these initial studies, much research has been dedicated to studying the punching shear behaviour of reinforced concrete slabs and footings (though footings are not discussed further in this thesis). Much of this past work has been experimental, though as will be discussed, the popularity of FEA for punching shear research is increasing. The results from many past experimental programs are summarized in databases curated by organizations which are focused on advancing concrete research, such as the American Concrete Institute (ACI) or the International Federation for Structural Concrete (*fib*), or independent researchers. However, the vast majority of previous research programs, and therefore the existing databases, are focused on square or circular slab-column connections, even though other connection geometries are common. For example, most of the 550 (note, 150 of the specimens are shear reinforced connections) experimental specimens in the *fib* database [9], which

includes tests from 1954-1999, are for square or circular slab-column connections. A lack of experimental data for alternate column geometries also exists in the ACI 445C database [44], as only 27 of 519 tests are for rectangular slab-column connections (note, this database includes tests from 1938 onwards).

To date, the largest databases for rectangular and special-shaped slab-column connections have been compiled by Paiva et al. [45] and Zhang et al. [46], respectively, though these databases are much smaller than those for square or circular slab-column connections. For example, the database compiled by Paiva et al. [45] contains a total of 131 specimens. However, many of the 131 tests involve square slab-column connections, which serve as reference specimens in the rectangular column studies, or one-way slabs subjected to concentrated loads. The database for special-shaped slab-column connections (SS-SCCs) is even smaller than that for rectangular slab-column connections (R-SCCs) and contains only 32 specimens, some of which failed in flexure or contain shear reinforcement near the slab-column connection.

In this section, previous research related to the punching shear behaviour of reinforced concrete flat slabs supported on square or circular columns, rectangular columns, special-shaped columns and walls will be summarized. As previously mentioned, most historical research has been focused on square or circular slab-column connections, and therefore experimental and numerical research for square or circular slab-column connections is summarized separately in Sections 2.3.2.1 and 2.3.2.2, respectively (note, due to the size of the existing database for these column geometries only select research programs are presented). While significantly less research has been conducted for rectangular slab-column connections, the existing database is large enough that it is also summarized in two sections (see Sections 2.3.3.1 and 2.3.3.2 for a summary of past experimental and numerical research for R-SCCs, respectively).

It should be noted that Sections 2.3.2-2.3.5 are primarily focused on research programs where slab openings are not located in the vicinity of slab-column connections. Past experimental and numerical research related to the influence of slab openings on punching shear behaviour for square, circular and rectangular slab-column connections is presented in Section 2.3.6 (note, the influence of openings on the punching shear behaviour of SS-SCCs is discussed in Section 2.3.4).

2.3.2 Square and Circular Slab-Column Connections

As seen by analyzing the existing experimental databases the punching shear behaviour of reinforced concrete slabs supported on square or circular columns has been studied extensively (though further work is still needed). Some of the largest studies of the punching shear behaviour of square and circular slab-column connections were conducted by Elstner and Hognestad [47], Moe [43], Mowrer and Vanderbilt [48], and Regan [49].

Elstner and Hognestad [47] studied the influence of concrete compressive strength, reinforcing ratio (both tensile and compressive), column size, support conditions, load conditions, tensile reinforcing layout and use of shear reinforcement on punching shear behaviour by testing 39 isolated slab-column connections. The testing program was significant as many of the available American punching shear studies at the time considered footings, which are typically much thicker than floor slabs. As slab tests were limited before the work of Elstner and Hognestad [47], American punching shear design provisions at the time were extrapolated from the results of footing studies, which was questionable as floor slabs typically have lower thickness-to-span ratios and higher shear-to-moment ratios [47].

Building on the work of Elstner and Hognestad [47], Moe [43] tested 43 isolated slab-column connections to study the influence of column size, concentrating tensile reinforcement near the column, shear reinforcement, eccentric loading and slab openings on punching shear behaviour. Based on the experimental results, Moe [43] proposed equations to estimate the punching shear capacity of slab-column connections based on the shear stresses along the column perimeter which were functions of the concrete compressive strength, ratio of the column dimensions to the effective slab depth and flexural capacity of the slab. Moe [43] was also one of the first to demonstrate that properly anchored shear reinforcement could increase the punching shear capacity of slab-column connections and to suggest that column rectangularity would have a negative influence on punching capacity. Moe's work formed the basis of many of the ACI 318 punching shear provisions [50] in ACI 318-63 [51], though modifications were made to these equations as discussed in Section 3.3.1.

Mowrer and Vanderbilt [48] were one of the first to study the influence of lightweight concrete on punching shear capacity. They tested 51 isolated slab-column connections, 43 of which were cast with lightweight concrete. Additional test variables included slab openings, flexural reinforcing ratio, concrete compressive strength, column size and the edge fixity of the isolated connections. Based on their experimental results, Mowrer and Vanderbilt [48] proposed a modified version of Moe's

equation [43] which accounted for the influence of lightweight concrete. Additionally, they proposed a modified isolated slab-column connection test specimen which was believed to better represent the behaviour of a slab-column connection in a continuous structure. Fifteen of these modified isolated slab-column connections were then tested by Vanderbilt [52] to study the influence of column size and column shape on punching shear (only square and circular columns were tested). Shear stress concentrations were observed at the corners of the square columns, and for both the square and circular slab-column connections, the nominal shear stress capacity was found to decrease as the ratio of column size to effective slab depth increased [52].

Regan [49] tested 28 isolated slab-column connections to investigate the influence of flexural reinforcement layout, slab size, slab depth, concrete compressive strength, flexural reinforcing ratio, boundary restraint and size of the loaded area (which is similar to column size). The experimentally measured punching capacities demonstrated that the punching shear design provisions from British design standards, Model Code 1978 [53] and ACI 318-83 [54], whose provisions are largely similar to those in ACI 318-19 [2], to be generally unconservative, overly conservative and conservative, respectively [49]. Regan [49] also concluded that boundary restraint increased punching shear capacity, but could not quantity its influence based on the 28 tests alone.

While the major studies outlined above identified many of the most influential parameters on punching shear behaviour, a significant amount of work has been conducted by other researchers as well. In subsections 2.3.2.1-2.3.2.3, the main findings of some of these studies for square and circular columns will be presented. The punching shear behaviour of connections without shear reinforcement subjected to concentric loading and combined shear and unbalanced moment is addressed in subsections 2.3.2.1 and 2.3.2.2, respectively, whereas the behaviour of shear reinforced connections is addressed in subsection 2.3.2.3. It should be noted that the results and studies presented herein are only a subset of the available literature, and are not exhaustive.

2.3.2.1 Concentric Loading – Connections Without Shear Reinforcement

Since the initial studies outlined above, numerous researchers have studied the punching shear behaviour of square and circular slab-column connections. Due to the cost and facility size required to conduct experimental testing the majority of these tests have also involved isolated slab-column connections (most numerical research also typically involves isolated connections as well due to the high computational cost of larger specimens). These isolated connection tests can typically be classified into two categories, those where the slab is centrally supported (on the column) and loaded

at the slab edges [55, 56, 57, 58, 59], or those where the slab edges are supported and the slab is centrally loaded through the column [60, 61, 62, 63, 64, 65]. Other researchers have focused on the punching shear behaviour of cantilever slabs subjected to concentrated loads [66, 67], or the punching shear behaviour of slab-column connections in multi-bay or continuous flat slab systems [68, 69, 70, 71].

The previous testing and numerical analyses have confirmed that parameters such as the concrete compressive strength, slab flexural reinforcement ratio, column size, slab slenderness, and load conditions have a significant influence on punching shear capacity and behaviour. More recently, research has focused on studying the influence of size effect, high-strength concrete and low flexural reinforcing ratios on punching shear capacity.

Due to the high strength of thick slabs most previous studies involve relatively thin slabs (i.e. d<200mm), even though higher thicknesses are common in practice. However, recently, the influence of slab thickness [56, 58, 62, 72, 73, 74], and size effect [75, 76, 77, 78, 79, 80], on punching shear capacity has become a point of emphasis. While further research is still needed, a significant size effect has been observed for slab-column connections, though the exact relationship and the effective depth at which size effects begin to govern are still under debate (though it is typically in the range of 200-300mm).

In an effort to increase the punching capacity of slab-column connections, the use of high-strength concrete (i.e. $f_c' > 60$MPa) has been proposed. Experimental testing by Marzouk and Hussein [60] and Inácio et al. [65] has demonstrated that the use of high-strength concrete leads to a significant increase in punching shear strength, though the rate of increase is lower than the square root of compressive strength. The strategic use of thin layers of ultrahigh-performance fiber-reinforced concrete (UHPFRC) near the slab-column connections has also been studied recently and has been shown to lead to significant improvements in punching capacity and behaviour, without the need for the entire slab to be cast from high-strength concrete [81, 82, 83].

It should be noted that slab-column connections considered in research are typically heavily reinforced in flexure (i.e. flexural reinforcing ratio greater than 1%). However, in practice, slabs with flexural reinforcement ratios between 0.6-0.8% are common, and research has shown that slabs with flexural reinforcing ratios below approximately 0.7% may not be able to achieve the punching capacities predicted by previous editions of ACI 318 (ACI 318-14 [84] and earlier) [85].

Slabs with flexural reinforcement ratios below 0.7% can experience extensive yielding of the slab reinforcement, resulting in crack patterns similar to that assumed in a yield-line analysis. This crack pattern differs greatly from that observed in typical punching tests of slabs with high flexural reinforcement ratios. In typical punching tests, a series of closely spaced radial cracks or circular fan-type cracks form on the tension surface of the slab in addition to the final circumferential crack which forms due to the critical inclined shear crack. In tests of slabs with low flexural reinforcement ratios, the circular fan-type cracks may not form, and for slabs with very low flexural reinforcing ratios (i.e. 0.3%), the cracks typically form parallel to the column sides, denoting extensive yielding of the slab reinforcement [85]. Due to the extensive yielding of the flexural reinforcement above the column, the flexural cracks can extend through most of the slab thickness and trigger a secondary punching failure, referred to as flexure-induced punching. The study of the punching shear behaviour of slabs with low flexural reinforcement ratios has recently been a point of focus [22, 56, 85, 86, 87, 88, 89, 90, 91, 92], and led to the inclusion of equation 2-1 in ACI-318-19, which specifies the minimum flexural reinforcement above the column to avoid flexure induced punching required when the factored shear stress on the critical section at *d/2*, v_{uv}, exceeds $0.17\phi\lambda_s\lambda\sqrt{f_c'}$.(MPa), $A_{s,min}$ (mm^2)

$$A_{s,min} = [5(v_{uv})(b_{slab})(b_o)]/\left[\phi(\alpha_s)(f_y)\right] \quad \text{2-1}$$

where b_{slab} is equal to the column dimension plus three times the slab thickness (mm), f_y is the yield strength of the flexural reinforcement (MPa) and ϕ is the shear resistance factor [2] (the remainder of the ACI 318-19 punching shear provisions for connections without shear reinforcement are discussed in Section 3.3).

2.3.2.2 Combined Shear and Unbalanced Moment – Connections Without Shear Reinforcement

Even though the impact of unbalanced moment was studied by Elstner and Hognestad [47] and Moe [43], the first studies focused on the impact of unbalanced moment on punching shear capacity were conducted by Hawkins and Corley [93] and Islam and Park [94] [95]. Since these initial studies, many researchers have studied the punching behaviour of slab-column connections without shear reinforcement subjected to eccentric gravity loads or combined gravity and lateral loads.

Past work has shown that the unbalanced moment capacity, drift capacity and ductility of slab-column connections without shear reinforcement are governed by many factors including the gravity load level [4, 15, 23, 96, 97, 98] and loading type (monotonic vs cyclic) [4, 15, 23, 96, 97, 98, 99].

The gravity load level is typically defined in terms of the gravity shear ratio (GSR), which is defined as the ratio of the design shear force, V, to the concentric punching capacity predicted by ACI 318, which is equal to $0.33\sqrt{f_c'}b_o d$ (f_c' in MPa) for square columns where $b_o/d <\approx 20.2$ and $d \leq$ 250mm. It has been shown that as the GSR increases the moment capacity, drift capacity and ductility of slab-column connections without shear reinforcement decrease significantly. This behaviour is important because structural design requires structural members, even those not part of the LFRS, to support gravity loads when subjected to the expected lateral displacements caused by the design earthquake [100, 101, 102]. Historically, a design drift ratio of at least 1.5%, including inelastic deformations, has been recommended for earthquake-resistant structures [16, 96, 101, 103, 104], and interior slab-column connections without shear reinforcement can only achieve this drift ratio if the GSR is less than or equal to 0.4 [16, 17, 101, 105], as shown in Figure 2-3 (curve 1 is for slabs without shear reinforcement).

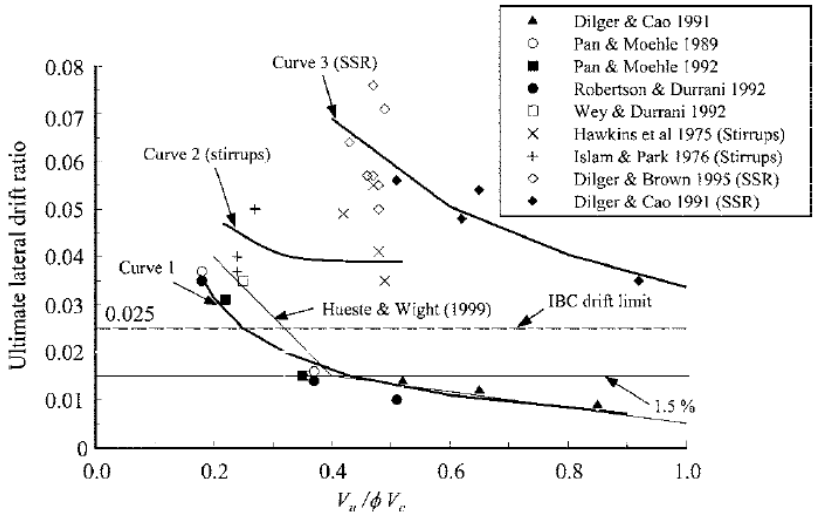


Figure 2-3: Gravity Load Level vs Lateral Drift Capacity of Interior Slab-Column Connections [16, 17, 105] [101]; authorized reprint from ACI 421.2R-10

However, as shown in Figure 2-4, there is still some debate about the relationship between GSR and lateral drift capacity. In ACI 318, a bilinear relationship is assumed, whereas Hueste and Wight [105] and Robertson and Johnson [14] propose trilinear relationships (note, the relationship proposed by Robertson and Johnson [14] is intended to be used for connections without integrity reinforcement). According to ACI 318, all slab-column connections have a minimum lateral drift capacity of 0.5%, with those with a GSR less than 0.6 having higher drift capacities (a linear

relationship between GSR and lateral drift capacity is assumed for GSRs less than or equal to 0.6 as shown in Figure 2-4). On the other hand, both Hueste and Wight [105] and Robertson and Johnson [14] assume that the lateral drift capacity of slab-column connections continues to decrease for GSRs exceeding 0.6 (approaching a minimum of 0.5% and 0% for a GSR of 1.0 in [105] and [14], respectively). Additionally, both methods also assume that punching shear does not govern the allowable drift limit for low GSRs (this is represented by the vertical portion of the trilinear relationships in Figure 2-4. It should also be noted that recent research has shown that the lateral drift capacity is also a function of the flexural reinforcing ratio and effective slab depth and that the existing approaches, which are provided in Figure 2-4, can lead to unsafe estimates of lateral drift capacities for connections where the effective slab depth exceeds 120mm due to size effects [23, 98, 106].

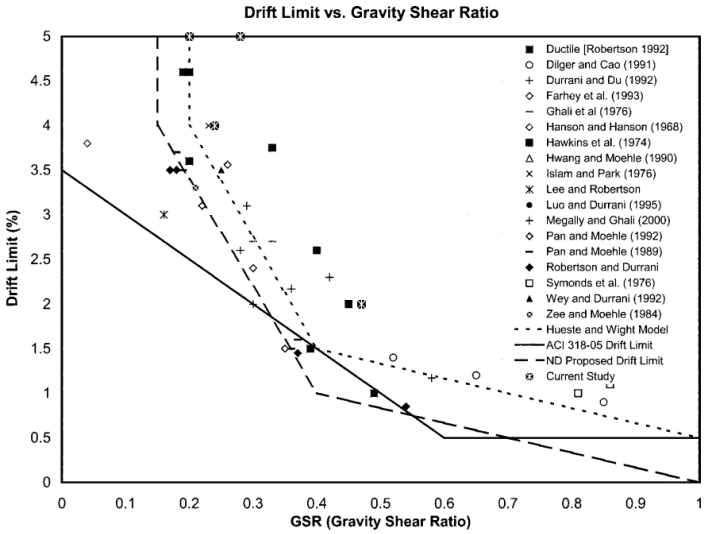


Figure 2-4: Comparison of Experimental Data and Proposed Relationships Between Gravity Shear Ratio (GSR) and Lateral Drift Capacity For Slab-Column Connections Without Shear Reinforcement According to Hueste and Wight [105], ACI 318 (the Relationship used in ACI 318-05 is the Same as that in ACI 318-19) and Robertson and Johnson [14] (Labelled as ND Proposed Drift Limit) [14], authorized reprint from ACI Structural Journal, Volume 103, Issue 3, 2006

Research has also shown that biaxial lateral loading and cyclic lateral loading are more detrimental than uniaxial [15, 97] and monotonic lateral loading [4, 15, 23, 96, 99], respectively, in terms of the loss of moment capacity, connection stiffness and ductility due to the excessive crack widening and

deterioration of the slab concrete near the connection. However, research [97, 107] has also shown that monotonic or cyclic tests of isolated slab-column connections result in very similar backbone curves, with the primary difference being that higher drift levels are achieved in the monotonic tests [108].

Numerous methods to estimate the punching shear capacity of unbalanced slab-column connections subjected to combined shear and unbalanced moment have also been proposed (the methodologies used in North American and European design codes are discussed in Chapter 3). As is done for concentric punching capacity an assumed shear stress distribution along the critical perimeter at a distance from the column face is used to estimate the connection capacity. Three of the most commonly assumed shear stress distributions for connections subjected to combined concentric loading and unbalanced moment are shown in Figure 2-5 and correspond to the following cases:

- A linear variation of shear stress as determined from elastic analysis (Figure 2-5a; note Mast (1970) was one of the first to propose this model, and this type of distribution is used in ACI 318 [2])
- A plastic redistribution of the shear stress at the ultimate limit state (Figure 2-5b; note, this type of distribution is used in Eurocode 2 (2004) [34])
- A plastic redistribution of the critical perimeter shear stresses based on the shear strength of the slab, which varies along the critical perimeter (Figure 2-5c; note, this method was proposed by Sagaseta et al. [57]) [109]

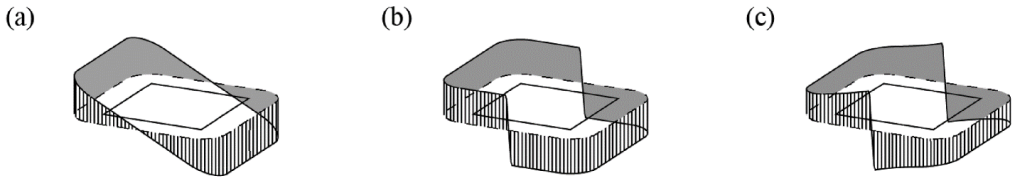


Figure 2-5: Commonly Assumed Critical Perimeter Shear Stress Distributions for Slab-Column Connections Subjected to Combined Concentric Loading and Unbalanced Moment (Interior Connections), a) Linearly Varying (Elastic Distribution); b) Plastic Redistribution at Ultimate Limit State; c) Plastic Redistribution Based on the Shear Strength of the Slab; Reprinted by permission from: Springer Nature, High Tech Concrete: Where Technology and Engineering Meet, Einpaul et al. [109] ©2018

2.3.2.3 Connections with Shear Reinforcement

Due to unreinforced slab-column connections having limited drift capacity and the need for additional gravity capacity for high loads, numerous methods of increasing the shear capacity and ductility of slab-column connections have been studied. In early flat slab designs, shear capitals and drop panels were popular methods of increasing the punching capacity of slab-column connections, but as the cost of labour and formwork increased they became less popular [110]. Additionally, these methods typically only increased punching capacity, without a significant increase in ductility, and as such, brittle punching failures still occurred under combined gravity and lateral seismic loads [17, 111, 112, 113]. As such, the use of shear reinforcement for punching became a focus of study.

Multiple types of shear reinforcement, including but not limited to shearheads [93, 95, 114], stirrups [58, 115, 116, 117, 118, 119, 120], single-leg stirrups [55, 121], lattice girders [122, 123], shear bands [124, 125], prefabricated trusses [126] and shear bolts [24, 127, 128, 129], have been proven to be effective for improving punching shear behaviour. However, due to their ease of installation and anchorage, and extensive research which has demonstrated their effectiveness to increase the shear strength and ductility of slab-column connections subjected to concentric loads [58, 115, 122, 130, 131, 132, 133, 134, 135, 136] or combined concentric loads and unbalanced moment [16, 17, 19, 111, 137, 138, 139, 140, 141, 142], shear studs are currently one of the most commonly used types of shear reinforcement. As shown in Figure 2-3, slab-column connections subjected to combined concentric loading and unbalanced moment reinforced with properly designed stirrups (curve 2) or shear studs (curve 3) are capable of achieving ultimate drift ratios well above the minimum 1.5% commonly specified for seismic design, and above the maximum of 2.5% specified in IBC 2006 [100], regardless of the GSR level [101]. Therefore, ACI 318-19 [2]. requires shear reinforcement for slab-column connections when the GSR exceeds 0.4 and the design lateral drift is greater than 1.5%. Shear studs are commonly preferred over stirrups due to their superior performance which is attributed to their ability to develop the full yield strength of the vertical portion of the stud with minimal slippage. To ensure adequate anchorage, the dimensions of the stud, forged heads and welded base rails should conform to ASTM 1044/1044M [111, 143].

Shear reinforced slab-column connections can fail in three failure modes as shown in Figure 2-6 (calculation of the strength of each failure mode is not discussed herein as all connections analyzed in this work are not shear reinforced). The first mode, referred to as failure inside the shear reinforced zone, is assumed to occur at the same location as an unreinforced slab-column connection. In this

mode, the shear reinforcement crosses the failure crack and provides ductility by restricting the opening of the shear crack, delaying the onset of failure. However, punching failures can also occur beyond the shear reinforced zone, if the shear reinforcement does not extend far enough from the column face, or between the first peripheral line of shear reinforcement and the column face, if the spacing to the first line of shear reinforcement is too large. Both failure modes are brittle because the shear reinforcement is not engaged, and as such, the connection resistance is dependent on the concrete alone. Ideally, the shear strength outside the shear reinforced zone should exceed that inside the shear reinforced zone to ensure ductile failure. Failure between the first line of shear reinforcement and the column face is referred to as the maximum punching capacity and is dealt with in North American practice by specifying a maximum spacing to the first row of shear reinforcement based on the applied shear stress level.

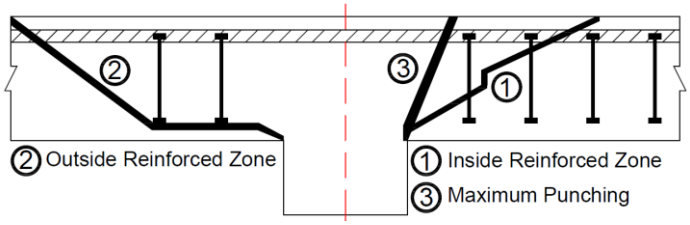


Figure 2-6: Different Failure Locations for Shear Reinforced Slab-Column Connections

The possibility of these different failure modes also calls the optimal shear reinforcement layout into question. In North American practice shear reinforcement is commonly oriented parallel to the column faces in a cruciform layout, as shown in Figure 2-7a, whereas in European practice it is typically arranged in a radial pattern, as shown in Figure 2-7b. The advantage of the cruciform layout is limited interference with the slab longitudinal reinforcement, but depending on the column size and extent of the shear reinforced zone this layout can leave large portions of the connection region unreinforced, potentially leading to lower capacities than predicted by code. In ACI 318-19 the entire outer critical perimeter is assumed to be effective, whereas in Eurocode 2 (2004) the outer critical perimeter is reduced when the spacing between studs on adjacent column faces exceeds *2d* as shown in Figure 2-7a.

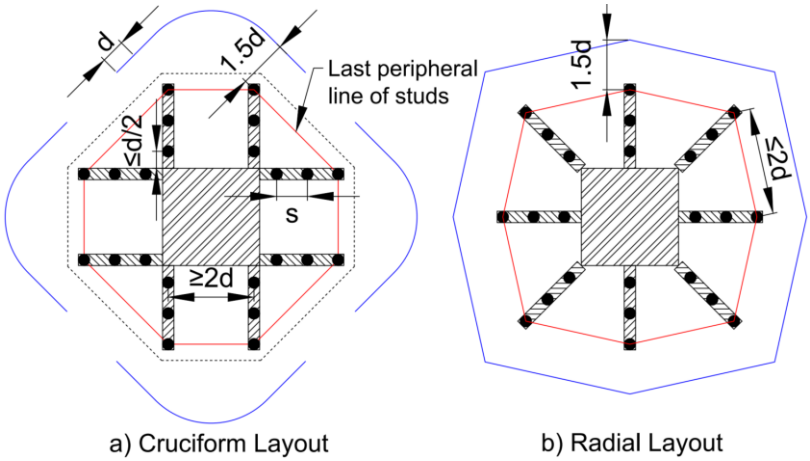


Figure 2-7: Shear Reinforcement Layouts and Critical Perimeters in ACI 318-19 [2] and Eurocode 2 (2004) [34]

In the case of slabs with low flexural reinforcing ratios and cruciform shear stud layouts, Dam and Wight [88] found that the entire outer critical perimeter is not effective, and the diagonal portions should be assumed to have a maximum length of *4d*. The effectiveness of shear studs for slabs with low flexural reinforcement ratios has been questioned [22, 88, 89] as the observed ductility could be due to the yielding of the flexural reinforcement.

2.3.3 Rectangular Slab-Column Connections (R-SCCs)

While Moe [43] included one rectangular slab-column connection in his experimental program, and theorized that column rectangularity would have a negative influence on punching capacity, the first study focused on investigating the influence of column rectangularity on punching shear was conducted by Hawkins et al. [3] (only concentric punching was studied). A total of nine isolated slab-column connections were tested, with the primary variables being the column aspect ratio, which varied from 1 to 4.33, and the loading conditions (one-way or two-way loading). The experimental tests demonstrated that the nominal shear capacity along the critical perimeter decreased as the column aspect ratio, β, increased and therefore, an equation relating the nominal shear capacity to β was added to ACI 318 as discussed in Section 3.3. It should be noted that the nine isolated connections tested by Hawkins et al. [3] were used to calibrate the finite element model used to study the concentric punching shear behaviour of special-shaped slab-column connections with and without openings. Therefore, this experimental program is discussed in greater detail in Section 8.3.1.

Prior to the work of Hawkins et al. [3], Hanson and Hanson [144] also studied the influence of column rectangularity on punching shear. In their landmark study of the punching shear behaviour of slab-column connections subjected to combined concentric shear and unbalanced moment, Hanson and Hanson [144] tested four R-SCCs with an aspect ratio of 2. The tests demonstrated that the use of rectangular columns could result in higher unbalanced moment capacities, but also showed that the column orientation with respect to the moment was important. It should also be noted that the work of Hanson and Hanson [144] was used to derive the γ_v and γ_f parameters used in ACI 318 to quantify the amount of unbalanced moment transferred via shear and flexure, respectively.

Following the work of Hawkins et al. [3] and Hanson and Hanson [144], numerous researchers, including the author [1, 145], have studied the impact of column rectangularity on the punching shear behaviour of slab-column connections. The key observations and conclusions from studies of R-SCCs under concentric loading and combined concentric loading and unbalanced moment are presented in subsections 2.3.3.1 and 2.3.3.2, respectively.

2.3.3.1 Concentric Loading

Experimental research of R-SCCs has primarily involved isolated slab-column connections and has typically focused on the influence of column aspect ratio, loading conditions, flexural reinforcement and slab openings (note, studies related to the influence of slab openings are discussed in Section 2.3.6). This previous testing has confirmed that column rectangularity does have a negative influence on punching shear capacity [146, 147, 148, 149] and that shear stress concentrations exist at the column corners [150, 151]. However, this testing has also shown that the influence of column rectangularity is not dependent on the column aspect ratio alone and that the behaviour of R-SCCs is also dependent on the ratio of the column side dimensions to the effective slab depth [150, 151] (note, the work by Al-Yousif and Regan [150] also suggests that the influence of this ratio is more severe when the slab is primarily bent in one direction), loading conditions [146, 151] and the flexural reinforcing ratio [85].

Additional experimental work has also demonstrated many key observations including but not limited to:

- Shear reinforcement can be used to improve the punching shear strength and ductility of R-SCCs [152]

- The combination of a rectangular column with an aspect ratio of 1.5 and the inclusion of three times as much integrity reinforcement in one orthogonal direction does not lead to a significant improvement in post-punching strength, though it does lower the deflection experienced by the connection [153]
- The highest strains in the flexural reinforcement are typically observed in the reinforcement which crosses the column perimeter [154]
- The one-way shear strength of reinforced concrete slabs subjected to concentrating loading or uniformly distributed loading are different [155]
- R-SCCs lead to lower maximum deflections and bending moments in a flat slab [156]

FEA has also been used to study the punching shear behaviour of R-SCCs. Originally, most studies were linear elastic and were focused on estimating the point at which the connection behaviour is dominated by one-way shear or on estimating the effective critical perimeter length around R-SCCs based on the elastic column and critical perimeter shear stress distributions. However, recently, NLFEA has been used to conduct detailed analyses of the punching shear behaviour of R-SCCs.

In addition to conducting an experimental test of a one-third scale three-bay by three-bay reinforced concrete flat slab, Simmonds [156] also conducted linear elastic finite difference analyses of a typical interior panel of a flat slab structure supported on rectangular columns with fixed widths equal to 5% of the slab span. The numerical results demonstrated that the maximum negative moments in both directions greatly decrease as the columns become increasingly elongated. Furthermore, with increasing column elongation the maximum positive moment in the direction parallel to the maximum column dimension decreased, whereas the moment in the direction parallel to the short sides of the columns slightly increased. Simmonds [156] concluded that this behaviour corresponded to the behaviour of the slab transitioning from two-way to one-way, and that one-way shear became dominant when the ratio of the maximum column dimension to the slab span (c/L ratio) was equal to 0.4. The numerical results were also used to analyze the column perimeter shear stress distributions, and it was found that most of the shear force was transferred by the portions of the connection within a distance equal to the column width from the column corners [156]. It should be noted that analyses by Hartley and El Kafrawy [157], Sagaseta et al. [151] and Setiawan et al. [158] have since confirmed that one-way shear becomes more dominant as the support aspect ratio

increased, though Sagaseta et al. [151] determined that transition point between two-way and one-way shear behaviour occurs when the *c/L* ratio is between 0.35-0.4.

To supplement their experimental testing, Oliveria et al. [146] conducted linear elastic FEA of R-SCCs to study the influence of loading conditions on the column and critical perimeter shear force distributions. The FEM, which was implemented using shell elements in SAP2000, predicted that shear stress concentrations exist at the column corners when the column aspect ratio exceeds 1. Based on the FEA results, and the experimental results for 15 slab-column connections, Oliveria et al. [146] proposed modification factors for the Model Code 1990 [159] provisions (note, Model Code 1990 serves as the basis for Eurocode 2 (2004) [34] as discussed in Section 3.4.1) which were functions of the ratio of the maximum column dimension to the effective slab depth.

Like Oliveria et al. [146], Sagaseta et al. [151] also conducted linear elastic FEA using shell elements to supplement their experimental tests. Using the FEA results, and an equation proposed by Vaz Rodrigues et al. [67], Sagaseta et al. [151] estimated the effective critical perimeter length at *d/2* from the column face. The predicted effective critical perimeter lengths agreed well with those predicted by *fib* Model Code 2010 [35] and an alternate method based on the predicted contact pressures in the FEA proposed by Sagaseta et al. [151]. It should be noted that Shu et al. [26] also used the equation proposed by Vaz Rodrigues et al. [67] to estimate the effective critical perimeter lengths around slab-column connections. However, Shu et al. [26] demonstrated that the equation proposed by Vaz Rodrigues et al. [67] could also be used with NLFEA results of isolated slab-column connections, instead of only linear elastic FEA results for continuous flat plate structures. They also demonstrated that NLFEA based on shell or continuum elements could be used to accurately predict the punching shear behaviour of slab-column connections with various column shapes, slab shapes and reinforcing details [26].

As previously mentioned, NLFEA has recently been used to study the punching shear behaviour of R-SCCs. In addition to the author's previous studies [1, 145, 160, 161], which are summarized in subsection 2.3.8.4, NLFEA of R-SCCs has been conducted in the commercial software ATENA by Sarvaicova et al. [162] and Setiawan et al. [158].

Sarvaicova et al. [162] conducted NLFEA in ATENA to evaluate the accuracy of the Eurocode 2 and Model Code 2010 punching shear provisions (note, both the existing Eurocode 2 provisions, which consider a critical perimeter at *2d* from the column face, and the current draft of the new version of Eurocode 2, which is based on the Critical Shear Crack Theory (CSCT) and considers a

critical perimeter at *d/2* from the column face, were evaluated) and to estimate the effective critical perimeter length around interior slab-column connections with aspect ratios varying from 1-7 under various two-way and one-way loading conditions. Though the NLFEA predicted shear stress concentrations at the column corners, the predicted concentration was not as significant as that assumed when using the effective critical perimeter specified in Model Code 2010 and the newest draft of Eurocode 2 (which is presented in Section 3.5.2). The existing Eurocode 2 provisions, which do not include specific provisions to account for the influence of column rectangularity on concentric punching capacity, were found to lead to the most accurate predictions of punching capacity compared to the NLFEA. Furthermore, as observed by other researchers [146, 151], the punching capacity and failure mode of R-SCCs are strongly dependent on the load conditions.

Finally, Setiawan et al. [158] used three-dimensional NLFEA with continuum elements to extend the study of the punching shear behaviour of interior R-SCCs without shear reinforcement conducted by Sagaseta et al. [151] to connections where the ratio of the maximum column dimension to the effective slab depth (c_{max}/d ratio) is between 6-10, as tests of such elongated connections are limited. In the NLFEA radial cracking dominated near the column corner, whereas tangential cracking dominated along the long side of the columns. This behaviour became more prominent as β increased, and demonstrates the transition from two-way to one-way shear. The increased dominance of one-way shear with increasing column elongation was also supported by the critical perimeter shear stress distributions. Along the critical perimeter, the greatest shear force magnitudes were predicted near the column corners, whereas the shear forces in the portion of the critical perimeter neglected by Model Code 2010 [35] (see Figure 2-8a) were typically low, which suggests that punching around elongated connections is triggered locally around the column ends before the full shear capacity is mobilized elsewhere. However, the shear forces in the portion of the critical perimeter neglected by Model Code 2010 were predicted to increase as β and c_{max}/d increased. For example, for connections where c_{max}/d is less than 6, the portion of the critical perimeter neglected by Model Code 2010 only accounts for approximately 5% of the connection capacity (which validates the critical perimeter assumed in Model Code 2010 for such connections), whereas for a connection where c_{max}/d is equal to 9.9 the neglected regions accounts for approximately 13.44% of the connection capacity. Therefore, when estimating the capacity of very elongated connections ($c_{max}/d > 6$) the contribution of one-way shear should be included. Additionally, Setiawan et al. [158] also noted that a redistribution of shear force from the short to long sides of the connection occurs before the onset of failure (when the applied load exceeds 90% of the peak load), though they

noted that ATENA can overpredict the shear stress redistribution unless a strain based failure criterion is adopted. It should be noted that the conclusions of the work by Setiawan et al. [158] are consistent with the author's previous study of the influence of column rectangularity [1], which is discussed in subsection 2.3.8.4.

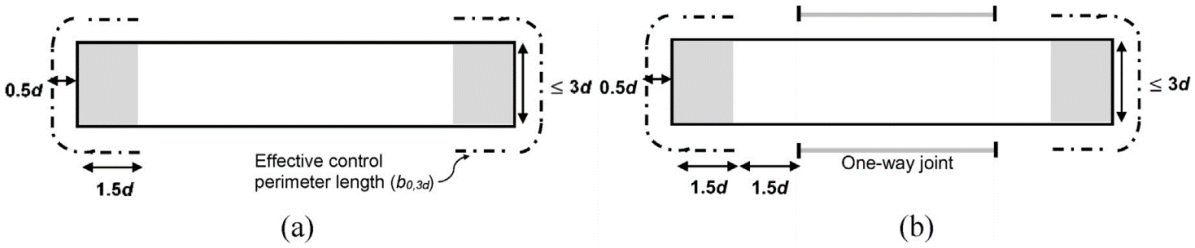


Figure 2-8: a) Effective Critical Perimeter Around Elongated Connections According to Model Code 2010 b) Effective Critical Perimeter and One-Way Shear Region Proposed by Setiawan et al. [158]; "Reprinted from Structures, 27, Setiawan, Vollum, Macorini and Izzuddin, Punching of RC slabs Without Transverse Reinforcement Supported on Elongated Columns, 2048-2068, Copyright (2020), with permission from Elsevier"

Furthermore, while the NLFEA provided valuable insights into the punching shear behaviour of elongated connections, Setiawan et al. [158] noted that it is not practical for typical structural assessments. For large-scale structural assessments, they proposed a model which uses a combination of nonlinear shell elements, joint elements along the critical perimeter at *d/2* from the column face and the Critical Shear Crack Theory (CSCT). The model, denoted the Joint Shell Punching Model (JSPM), has advantages over conventional nonlinear shell element analyses as shear failures can be captured without the need to post-process results. However, based on the NLFEA results, the JSPM was modified to include the contribution of one-way shear along the critical perimeter as discussed in Section 2.3.5.

2.3.3.2 Combined Shear and Unbalanced Moment

Consistent with the observations for R-SCCs subjected to concentric loading, column rectangularity has a negative influence on punching shear behaviour of connections subjected to combined shear and unbalanced moment [163] and results in shear stress concentrations at the column corners [42, 164, 165]. Even though research related to the punching shear behaviour of R-SCCs subjected to combined concentric shear and unbalanced moment is limited [42, 144, 163, 164, 165, 166, 167, 168], rectangular columns are one of the only two column geometries, square being the other, for which

ACI 318-19 includes explicit equations to calculate the shear stress demand along the critical perimeter [166] (the ACI 318-19 punching shear provisions are discussed in Section 3.3.2).

To investigate the influence of column rectangularity and the ratio of the critical perimeter length, b_o, to the effective depth, d, on the punching shear behaviour of slab-edge column connections Sherif et al. [165] tested five half-scale connections. In the tests, the column aspect ratio, β, and the b_o/d ratio varied from 1-2.5 and 6.5-11, respectively, and the vertical load was applied with an eccentricity of 300mm with respect to the column centroid to apply an unbalanced moment to the connection and accurately simulate the loading conditions in a continuous flat plate subjected to gravity loads. In addition to stress concentrations at the column corners, the experimental tests demonstrated that punching capacity (note, all specimens failed in punching) decreases as the b_o/d ratio increases due to a decrease in the amount of confinement provided to the failure surface by the in-plane stresses in the slab. Additionally, the connection ductility was found to decrease as b_o/d decreased and increase as β increased [165].

Five three-quarter scale connections were tested by Tan and Teng [167] to investigate the punching shear behaviour of interior R-SCCs subjected to combined gravity and lateral loads (both uniaxial and biaxial lateral loads) with and without shear reinforcement. The experimental results demonstrated that connections subjected to biaxial unbalanced moments have significantly lower strength, drift capacity, ductility and stiffness than connections subjected to uniaxial unbalanced moments. Additionally, it was observed that interior R-SCCs with an aspect ratio of five (note, the maximum and minimum column dimensions were equal to 900mm and 180mm, respectively) may not be able to sustain a lateral drift ratio of 1.5%, even when the applied gravity load is small. On the basis of their limited tests Tan and Teng [167] recommended a maximum GSR of 0.28 for R-SCCs with a column aspect ratio of 5 and subjected to combined concentric load and biaxial unbalanced moments in order to maintain a lateral drift capacity of 1.5%, unless properly detailed and installed shear reinforcement was provided (shear-reinforced connections were found to achieve lateral drift capacities exceeding 1.5% even when biaxial unbalanced moment was applied). They also noted that the connection strength in the direction perpendicular to the short side of the rectangular column was approximately 1.6 times higher than that in the direction perpendicular to the long side of the column [167].

The punching shear behaviour of rectangular edge-slab column connections was also investigated by Anggadjaja and Teng [42]. Five isolated slab-column connections were tested to investigate the influence of column rectangularity (as with Tan and Teng [167] all columns were 180x900mm),

gravity load level, and unbalanced moment (two specimens were subjected to uniaxial lateral loads and two to biaxial lateral loads) on punching shear behaviour. In all tests, shear stress concentrations near the short sides of the columns were observed, with the shear stress magnitudes decreasing rapidly with increasing distance from the short side, though the use of rectangular columns does have the benefit of increasing the maximum moment magnitude which can be transferred about the strong axis of the column. Additionally, the highest stiffness was observed in the direction parallel to the long side of the column, though the overall connection behaviour is also more brittle in this direction. Consistent with the results of Tan and Teng [167], biaxial unbalanced moments were more detrimental to connection capacity, stiffness, ductility and drift capacity than uniaxial unbalanced moments. Additionally, a lateral drift capacity of 1.5% could not be achieved when biaxial moments were applied unless the gravity load was small. Based on the experimental results, Anggadjaja and Teng [42] recommended a maximum GSR of 0.3 for edge rectangular slab-column connections with an aspect ratio of 5 and subjected to concentric load and biaxial unbalanced moment to ensure a minimum lateral drift capacity of 1.5%.

The influence of cyclic unbalanced moment on the punching shear behaviour of R-SCCs was investigated by Himawan and Teng [168], though unlike the other studies discussed herein, the connections were post-tensioned. Three isolated slab-column connections, also with 180x900mm columns, one subjected to concentric load only, and two subjected to combined concentric load and unbalanced moment (uniaxial and biaxial), were tested. Consistent with the results of Anggadjaja and Teng [42] a higher connection stiffness was observed in the direction perpendicular to the short side of the column. Additionally, it was observed that the shear strength increase due to prestressing was smaller for R-SCCs than for square or circular slab-column connections [168].

Three-dimensional NLFEA was used by Megally and Ghali [166] to study the punching shear behaviour of square and rectangular slab-column connections subjected to combined concentric shear and unbalanced moment. The NLFEA demonstrated that the amount of unbalanced moment transferred to the column through shear is a function of the column aspect ratio and that the shear stresses along the critical perimeter do not vary linearly for connections subjected to combined concentric shear and unbalanced moment. However, the FEA results also demonstrated that assuming a linear critical perimeter shear stress distribution, as done in ACI 318-95 (and ACI 318-19), can lead to reasonable punching capacity predictions if the parameter approximating the portion of the

unbalanced moment transferred to the column through shear, γ_v, is a function of the column aspect ratio [166].

2.3.4 Special-Shaped Slab-Column Connections (SS-SCCs)

To this point in this thesis, the punching shear behaviour of common column geometries (square, rectangular and circular) have been discussed. However, American [169, 170] and European [53] design codes have also included provisions for alternate column geometries (commonly referred to as special-shaped or irregular columns), such as L, T and cruciform columns, since 1977 and 1978, respectively. The basis for these provisions, which have been largely unchanged since their introduction, is unclear, as studies focused on the punching shear behaviour of special-shaped slab-column connections (SS-SCCs) are limited [171, 172, 173, 174, 175].

SS-SCCs are commonly used in post-tensioned flat plate structures [172, 173] and have many potential architectural and structural benefits due to their geometry. For example, when the required column cross-sectional area is large, special-shaped columns can be used instead of square or rectangular columns to better fit the architectural constraints of the structure [174]. Instead of having a large column protruding from an interior partition or exterior wall, special-shaped columns can potentially fit within the existing wall geometry, increasing the useable floor space and improving overall building aesthetics [172, 175]. From a structural perspective, shake table tests of 1/6th scale reinforced concrete flat plate structures have demonstrated that SS-SCCs provide good seismic performance [176]. Additionally, as will be discussed herein, experimental and numerical work has suggested that slab openings located between the column flanges have a minor impact on concentric punching capacity [174], which is beneficial structurally, as typically openings have a large influence on punching capacity as discussed in Section 2.3.6. Locating the openings between the column flanges is also beneficial architecturally as the openings and services can be hidden from view.

To date, the largest study of SS-SCCs was conducted by Liu and Huang [171]. The primary goal of the study was to compare the punching shear behaviour of interior SS-SCCs (specifically L, T and cruciform slab-column connections) and square slab-column connections with equivalent column cross-sectional area or critical perimeter lengths. Two of the eleven slab-column connections were square slab-column connections, with the remaining nine specimens being SS-SCCs (3 specimens per column shape). In addition to varying the column shape and dimensions (the dimensions of the investigated columns are shown in Figure 2-9), the flexural reinforcing ratio was also varied between the specimens. The three specimens with the lowest flexural reinforcement ratio ($\rho = 0.8\%$,

specimens CS3, CT3 and CL3) were governed by flexure, with the remaining eight specimens, where ρ was equal to 1.59% or 1.91%, governed by punching shear. The experimental results demonstrated that SS-SCCs have higher concentric punching capacity and ductility than square slab-column connections of an equivalent cross-sectional area or critical perimeter length, though stress concentrations at the column corners were observed. Additionally, based on the experimental results, Liu and Huang [171] proposed critical perimeters for the punching shear design of SS-SCCs. The proposed critical perimeters for use with the ACI 318 provisions are shown in Figure 2-10 (note, in their analysis Liu and Huang [171] considered ACI 318-95 [177], but the punching shear provisions related to SS-SCCs are identical to those in ACI 318-19 [2], other than not accounting for size effect for connections with effective depths greater than or equal to 250mm). The use of this critical perimeter, which is slightly larger than that assumed in ACI 318 (the calculation of the critical perimeter length according to ACI 318-19 is provided in Appendix G), as shown in Figure 2-10, and a nominal shear stress capacity of $0.33\sqrt{f_c'}$ (MPa) led to conservative estimates of punching capacity.

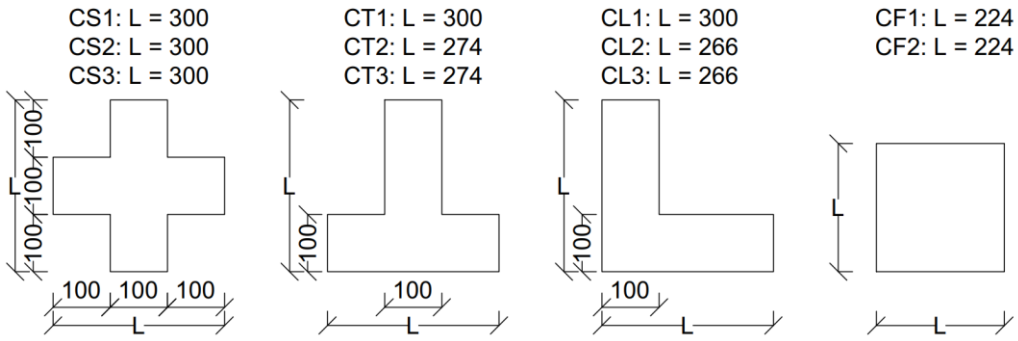


Figure 2-9: Summary of Slab-Column Connections Tested by Liu and Huang [171]

Following the work of Liu and Huang [171] the punching shear behaviour of SS-SCCs was largely ignored (some studies of post-tensioned connections were conducted as will be discussed) until recently becoming an area of renewed research interest. Through a combination of experimental tests and NLFEA of isolated slab-column connections, Pinto et al. [174] studied the influence of slab openings located between the column flanges on the punching shear behaviour of interior L slab-column connections (L-SCCs). Four isolated slab-column connections, three of which had openings between the column flanges (the investigated column sizes and opening details are provided in Figure 2-11), were investigated. Both the experiments and the NLFEA, which was implemented in Abaqus using the Concrete Damaged Plasticity (CDP) model, demonstrated that the investigated opening layouts had a minor influence on the connection behaviour and punching capacity (though it must be

noted that the connections failed in flexural punching instead of pure punching), which suggests that the region between the column flanges is relatively ineffective for L-SCCs. The NLFEM, which was able to accurately predict the connection capacity, load-deflection response and crack patterns, also predicted shear stress concentrations around the column corners, and along the exterior column edges (see Figure 2-11 for the definition of the exterior edges).

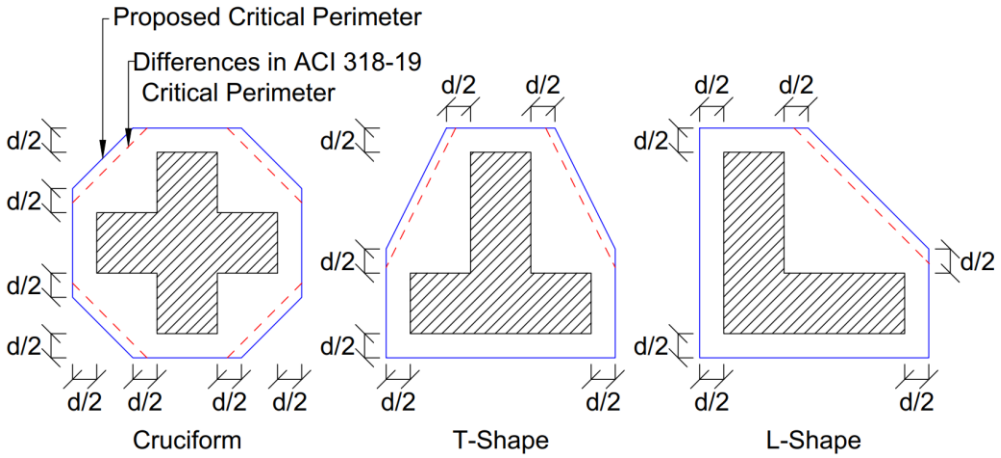


Figure 2-10: Comparison of Critical Perimeter Around SS-SCCs Assumed in ACI 318 and Proposed for ACI 318 by Liu and Huang [171]

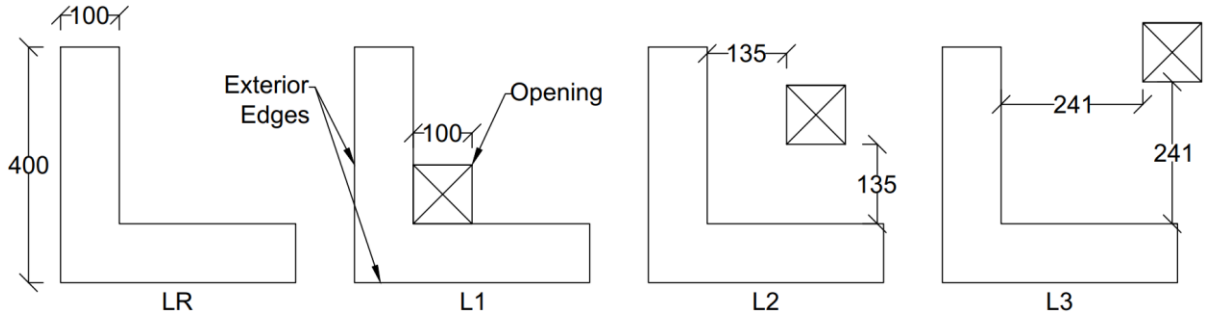


Figure 2-11: L Slab-Column Connections Tested by Pinto et al. [174] (Column Size and Opening Size Consistent Between Specimens)

The experimental capacities were also used to investigate the accuracy of current worldwide punching shear design codes. The punching capacities predicted according to the ACI 318-19 punching shear provisions were conservative and accurate for three of the four specimens. However, when the opening was located adjacent to the column perimeter (specimen L1, see Figure 2-11) the capacity predicted by ACI 318 was very conservative, as the influence of the opening was severely overpredicted (this also occurred for Eurocode 2 (2004) [34] and *fib* Model Code 2010 [35]).

Furthermore, Pinto et al. [174] noted that current worldwide design codes do not include recommendations for the treatment of slab openings when the column centroid falls within the opening (as discussed in Section 3.6, design codes typically recommend neglecting the portion of the critical perimeter bounded by lines which originate from the column centroid and are tangential to the opening boundaries). Therefore, Pinto et al. [174] recommended that future studies focus on investigating the influence of different sizes and locations around the column to improve the accuracy of the opening provisions for SS-SCCs. Additionally, they recommended that future punching shear studies for SS-SCCs focus on corner columns or columns with unequal flange dimensions.

A combination of experimental tests and NLFEA was also used to study the punching shear behaviour of L-SCCs by Xue et al. [175]. In the experimental portion of the work, four half-scale isolated slab-column connections were tested to study the influence of slab thickness, the inclusion of a drop panel (referred to as a column capital by Xue et al. [175]) and the inclusion of shear reinforcement on the punching capacity. Consistent with the results for other column geometries, increasing the slab thickness and inclusion of a drop panel or shear reinforcement, which consisted of inverted T-shaped reinforcement strategically placed around the column as shown in Figure 2-12, lead to a higher punching capacity. Following the experiments, NLFEA, also based on the CDP model and implemented in Abaqus, was used to compare the punching shear behaviour of square and L slab-column connections without drop panels or shear reinforcement. Consistent with the findings of Liu and Huang [171], the predicted capacity and ductility of L-SCCs were higher than that of square slab-column connections with the same area. The NLFEA was also used to evaluate the accuracy of the ACI 318-14 [84] (note, size effect is also not considered in ACI 318-14) punching shear design provisions, which were found to be very conservative for both column geometries. Xue et al. [175] recommended that future studies of SS-SCCs, particularly L-SCCs, consider column flanges with different dimensions than those studied, and with different column flange aspect ratios, as the ratio of the minimum and maximum flange dimensions may influence the punching behaviour of SS-SCCs.

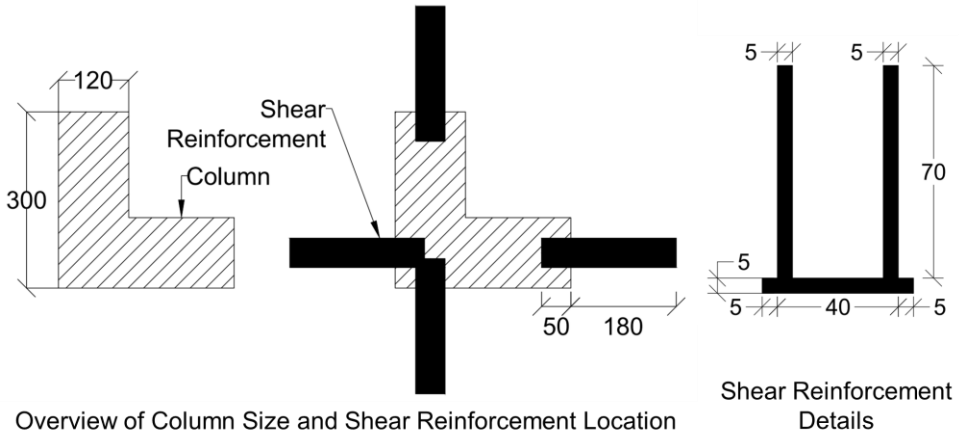


Figure 2-12: Overview of Column Size and Shear Reinforcement Considered by Xue et al. [175]

The remaining studies of the punching shear behaviour of SS-SCCs all involve post-tensioned connections with unbonded tendons. The punching shear behaviour of post-tensioned interior L and T slab-column connections was studied by Abou-Saleh [173] and Cai et al. [172], respectively. In both studies, the interior connections failed in punching shear after the slabs had achieved their flexural capacity and the shear stress distribution around the columns was non-uniform. Both studies also evaluated the applicability of the ACI 318 punching shear provisions for SS-SCCs and noted that changes were necessary to accurately account for the influence of shear reinforcement [172] and slab thickness [173].

Finally, Zhang et al. [46] investigated the flexural capacity of interior isolated slab-column connections where the slab is supported along its edges and concentric loading is applied through the column. Yield line analyses, assuming circular fan failure mechanisms, were used to estimate the flexural capacity of isolated L, T and cruciform slab-column connections. The proposed yield line failure mechanisms for each column geometry were calibrated by comparing the predicted capacity to that of experimental specimens from literature. Based on the proposed yield line models closed formed equations were developed to estimate the flexural capacity of isolated L, T and cruciform slab-column connections. Using these equations, the influences of the flexural reinforcement ratio, column shape and column flange aspect ratio on flexural capacity were studied. It was concluded that the column cross-section shape and flange aspect ratio have a minimal impact on the flexural capacity of isolated slab-column connections, but these findings need to be taken with some skepticism, as some of the experimental results used to calibrate the yield line analyses failed in punching shear, and not flexure.

2.3.5 Slab-Wall Connections (SWCs)

Another common design scenario which has not been sufficiently studied is the punching shear behaviour of flat plates partially supported on walls. Due to the low lateral stiffness of reinforced concrete flat plates supported on columns alone, slabs are typically partially supported on shear walls where the flat slab either acts to couple the shear walls or the shear walls are combined with the slab-column frames to form the lateral force-resisting system [32, 178, 179, 180]. In such structures the shear walls are commonly the stiffest structural component, which causes the shear walls to attract the most load, making the connection between the slab and shear walls essential for the adequate performance of the lateral force-resisting system (LFRS). Additionally, the walls also carry a portion of the gravity (vertical) loading, making the slab-wall connections essential for the overall structural performance. The distribution of shear stresses along the slab-wall interface is not well understood, though it is typically agreed that two-way shear only influences a small region near the end of the wall/wall corner as shown in Figure 2-13, and is dependent on the applied gravity load level. In practice, the shear design of SWCs is commonly neglected due to the length of the connection between the slab and walls [181]. Most of the previous research on SWCs has been focused on studying the moment and deflection response of coupled shear walls [28, 182, 183, 184], estimating the bending stiffness of coupled shear wall systems [185, 186, 187], or on creating analysis methods to predict overall structural response [182, 188].

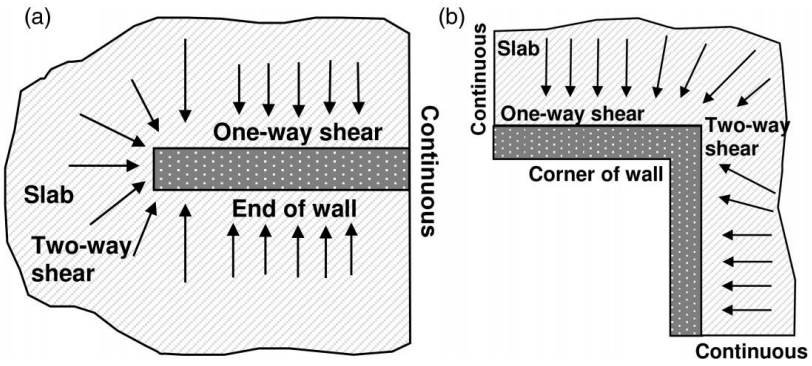


Figure 2-13: Transfer of One-Way and Two-Way Shear Forces Near a) Wall Ends b) Wall Corners, Reproduced with Permission from [189] © 2020 *fib*. International Federation for Structural Concrete

One of the first researchers to study the shear distribution along the slab-wall interface was Chang [28], who used the finite difference method to study the bending moment distribution in a slab of a

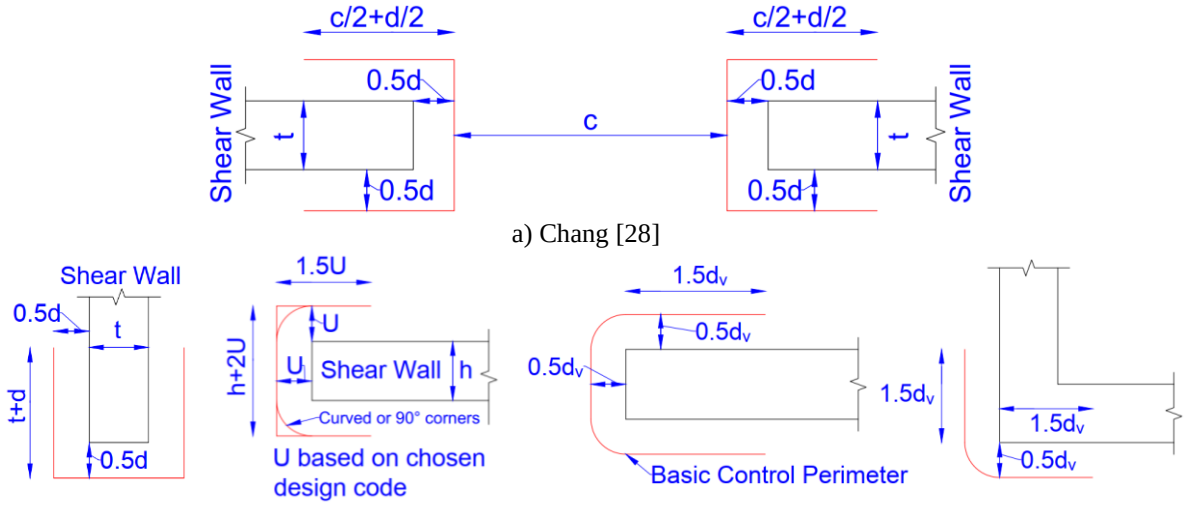
combined flat plate shear wall structure. Chang found that the shear forces in the slab concentrated along the edges of the shear wall near the wall toe at adjacent ends of the opening between the two shear walls. Based on the predicted shear distribution the use of a U-shaped critical perimeter located at *d/2* from the wall face with a total length, $b_{o,wall}$, calculated according to equation 2-2 and shown in Figure 2-14a, was suggested for calculating the punching capacity of the SWC.

$$b_{o,wall} = 2d + t_w + c \qquad 2\text{-}2$$

where t_w is the wall thickness (mm), d is the effective slab depth (mm) and c is half the width of the opening between the shear walls (mm, see Figure 2-14a). Chang also proposed equation 2-3 to calculate the nominal shear load acting on the assumed critical perimeter, v_j (MPa)

$$v_j = R_j/(b_{o,wall} \cdot d) = \frac{\{[(a + 1.5c)/(a - c)]V_j\}}{b_{o,wall} \cdot d} \qquad 2\text{-}3$$

where R_j is the positive idealized reaction (N), and a is equal to the half-width of the opening plus the wall length (mm). The ACI code at the time, ACI 318-63, also assumed a constant shear stress along the critical perimeter located at *d/2* from the wall face but assumed the entire wall to be effective in resisting punching [28]. ACI 318-19 still assumes this same critical perimeter but has since added equations reducing the assumed shear stress value for large column aspect ratios and large ratios of critical perimeter length to effective slab depth, though these equations were calibrated to results from slab-column connections [2], and their applicability to SWCs is unknown.



a) Chang [28]

b) Schwaighofer and Collins [30]

c) Coull and Chee [32]

d) *fib* Model Code 2010 [35]

Figure 2-14: Comparison of Proposed Critical Perimeter for Slab-Wall Connections

Szalwinski [29] used two-dimensional finite element analysis (FEA) to study the impact of bay width, corridor width, wall depth and wall thickness on the effective width and stress distribution in a slab coupling shear walls. To extend the results of the study beyond the linear elastic range, the ¼ scale slab-wall system shown in Figure 2-15, was tested by applying load to one set of walls while keeping the others fixed. During the test, punching shear failures around the wall toes were observed, but the punching was gradual and occurred over a large range of deflections, and after punching had visibly occurred the load-carrying capacity of the assembly did not significantly decrease [29].

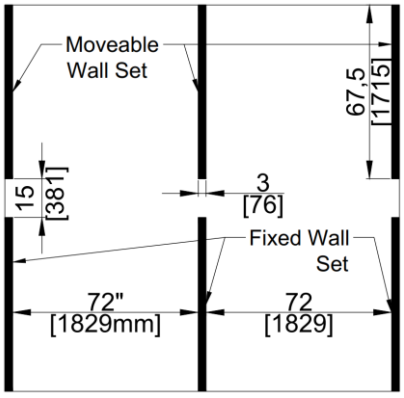


Figure 2-15: Experimental Specimen Tested by Szalwinski [29]

Following the work of Szalwinski [29], Schwaighofer and Collins [30] proposed the effective critical perimeter shown in Figure 2-14b for the punching design of SWCs. The use of a nominal shear capacity of $0.33\sqrt{f_c'}$ (MPa) and the proposed critical perimeter led to a conservative estimate of the experimental capacity reported in [29]. It should be noted that ACI 352.1R-11 refers designers to the work of Schwaighofer and Collins [30] when designing slab-column connections where the column aspect ratio exceeds 3, though no specific recommendations are given [104].

ACI 352.1R-11 also refers to the work of Paulay and Taylor [31] for the design of SWCs [104]. Unlike Szalwinski [29] and Schwaighofer and Collins [30], who applied monotonic loading, Paulay and Taylor [31] tested four ½ scale specimens of slabs coupling shear walls subjected to reversed cyclic lateral loading and gravity load due to self-weight. They found that the inclusion of stirrups, which enclosed the top and bottom longitudinal slab reinforcement near the opening between the two walls, improved the specimen ductility by confining the damaged concrete. However, the inclusion of a structural steel section in the slab near the wall toes was found to be the most promising method to increase both the strength and energy dissipation capacity of the SWC [31].

Coull and Chee [32] analyzed the bending moments and shear forces in a slab coupling a pair of laterally loaded shear walls using a two-dimensional FEA. The shear stresses along the wall perimeter were found to concentrate near the wall toe and corners of the wall, with the remainder of the wall being under very low stress. Coull and Chee proposed the critical perimeter shown in Figure 2-14c [32].

To investigate the impact of numerous strengthening methods for SWCs, Mirza and Lim [33] tested nine coupled slab-wall assemblies subjected to lateral loading simulating earthquakes. Some of the tested specimens failed in punching, and the capacity predictions using the method proposed by Schwaighofer and Collins [30] agreed well with the experimental results for the connections without transverse reinforcement near the wall toe and were conservative for those with transverse reinforcement. Based on the experimental results reinforcing details near the wall toe to control cracking and delay punching were proposed.

Hyun-Ki Choi [190] tested three ½ scale shear walls with openings, two of which also included a portion of the slab around the wall, to study the impact of openings in the shear wall and coupling slabs on the overall behaviour of reinforced concrete shear walls. The shear walls were subjected to lateral loading and a gravity load equal to approximately 10% of the vertical capacity of the walls, and both specimens which included slabs failed in the wall and not in the slab. However, for the specimen which had an opening in the shear wall the slab crack pattern was similar to that observed by Schwaighofer and Collins [30].

Following their study of the punching shear behaviour of R-SCCs [158], previously discussed in Section 2.3.2, Setiawan et al. [189] studied the punching shear behaviour of interior slab-wall corner connections. The first step in their analysis was to extend the three-dimensional nonlinear FEM which had been implemented in ATENA and developed to analyze the punching shear behaviour of R-SCCs, to allow for the analysis of interior slab-wall corner connections. Following the NLFEA, Setiawan et al. [189] applied their previously developed extended joint-shell punching model (JSPM) [158] to estimate the punching capacity of the slab-wall corner connection. As was assumed for R-SCCs, the critical perimeter at *d/2* from the wall face was broken into three regions, as shown in Figure 2-16. The first of these regions, the two-way shear region, extends to a distance of *1.5d* beyond the end of the wall or wall corners to match the critical perimeter assumed in *fib* Model Code 2010 [35]. Beyond this two-way shear region, a *1.5d* long dummy region, which is assumed to have approximately zero shear capacity, and is necessary to avoid overestimating the shear capacity due to

excessive shear redistribution, is assumed. Finally, a one-way shear region is assumed along the remainder of the connection. The extended JSPM was found to predict punching capacities which agreed well with the ATENA results, demonstrating that the method was applicable to elongated connections (rectangular slab-column and slab-wall connections) and slab-wall corner connections, while being much more computationally efficient than three-dimensional NLFEA.

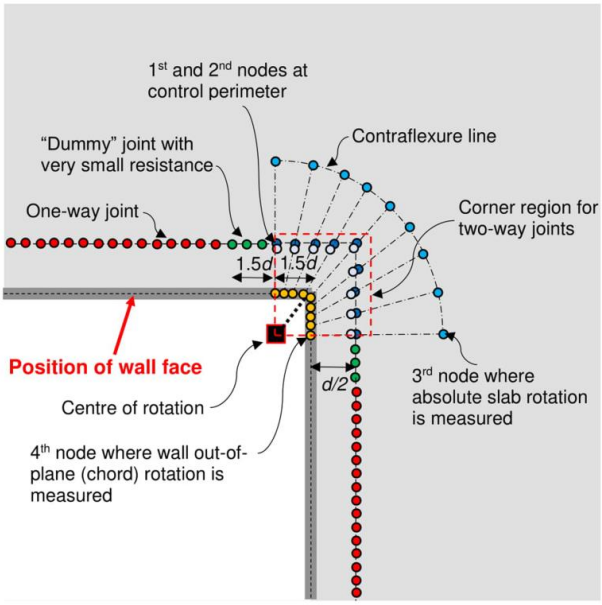


Figure 2-16: Breakdown of Slab-Wall Corner Connection Into Two-Way, Dummy and One-Way Shear Regions, Adapted from [189] © 2020 *fib*. International Federation for Structural Concrete

From the review of the previous studies of SWCs, it is clear that there is a lack of experimental and numerical studies of slab-wall assemblies with dimensions and loading conditions seen in practice. Furthermore, to the author's knowledge, the influence of slab openings on the punching shear behaviour of SWCs has not been studied, even though slab openings near walls are common. Due to the required specimen size experimental testing of these connections is very costly and time-consuming, making three-dimensional FEA an ideal method to study their behaviour.

2.3.6 Slab-Column Connections With Openings

Like the influence of support geometry, where previous work is lacking, the influence of slab openings on punching shear is another research area which is lacking. From a structural perspective, slab openings should be avoided in reinforced concrete flat plate structures as they reduce the

capacity, stiffness, energy dissipation capacity and ductility of slab-column connections. However, slab openings are required for architectural features such as stairwells and elevators, and to route mechanical and electrical services throughout the structure. Based on past research and practical experience, reinforced concrete design codes typically contain recommendations for the maximum allowable opening size in different sections of the slab. For example, as seen in Figure 2-17, ACI 318-19 [2] outlines maximum permitted opening sizes for various slab areas in lieu of more advanced analysis (a summary of the ACI 318-19 punching shear provisions is provided in Section 3.3).

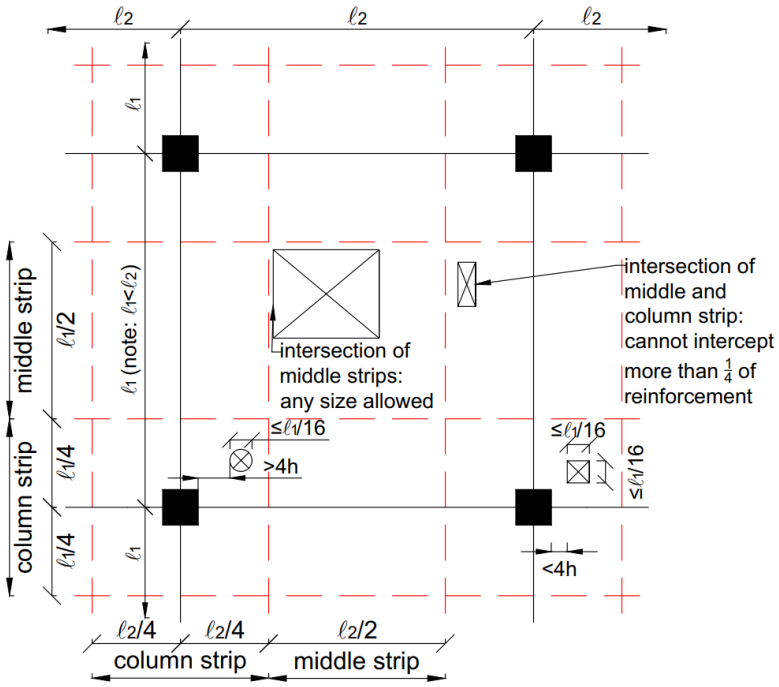


Figure 2-17: Maximum Recommended Opening Sizes in Various Slab Locations in Lieu of More Advanced Analysis According to ACI 318-19 [2]

According to ACI 318-19 [2], openings of any size are permitted in the area common to intersecting middle strips (the definition of middle strips is shown in Figure 2-17), assuming the amount of reinforcement provided is equivalent to that which would be provided if the opening was not present. In the area common to the middle strips and column strips (the definition of a column strip is also provided in Figure 2-17) the maximum opening size is limited by the fact that the opening cannot interrupt more than 1/4th of the reinforcement in either strip. Additionally, an area of reinforcement at least equal to the amount of reinforcement interrupted must be evenly distributed on both sides of the opening. Finally, in the area common to two column strips, the maximum opening

size is limited to 1/8th of the minimum column strip width (the interrupted reinforcement must also be replaced on the sides of the opening in this case as well) [2]. The openings in the area common to two column strips typically are used to route mechanical (HVAC, piping, fire suppression systems etc.) and electrical services throughout the structure. In flat plate structures, due to the lack of additional supporting members, these small openings are typically located in the high-stress regions near the column, and therefore must be accounted for in punching shear design (though the location of openings that must be accounted for when estimating punching capacity varies between design codes as discussed in Section 3.6). In the remainder of this section past research related to quantifying the influence of slab openings on punching shear capacity and behaviour is discussed.

Slab openings near slab-column connections typically have a negative influence on punching shear capacity and behaviour since the removal of concrete near the connection reduces the amount of concrete resisting punching stresses, but also increases the shear stresses in an already highly stressed region. The influence of slab openings on punching shear capacity was originally investigated by Moe [43], Hognestad et al. [191], Mowrer and Vanderbilt [48], Hanson and Hanson [144] and Roll et al. [192] (note, a methodology to account for their negative influence on punching shear by reducing the critical perimeter length was proposed by Di Stasio and Van Buren [193, 194] prior to these initial studies). Even though slab openings near slab-column connections are common, and were found to have a significant influence on punching capacity in the initial studies [43, 48, 144, 191, 192], the influence of slab openings on punching shear behaviour was largely ignored until the late 1990s.

Since the late 1990s, the influence of slab openings on punching shear behaviour has seen renewed research interest, but many areas of study are still lacking, as most of the previous research involves square slab-column connections [61, 195, 196, 197, 198, 199, 200, 201, 202, 203, 204, 205, 206, 207, 208, 209, 210, 211, 212, 213, 214, 215, 216, 217, 218]. For example, research related to the influence openings around rectangular [147, 210, 219, 220, 221, 222, 223, 224, 225] or special-shaped slab-column connections (the only previous study of the influence on SS-SCCs not conducted by the author [174] was discussed in Section 2.3.4) is lacking. Extrapolation of results for square slab-column connections to these other geometries is questionable [147], as it is known that the shear stress distribution around these other geometries is highly non-uniform. Furthermore, the influence of slab openings for interior connections subjected to combined concentric shear and unbalanced moment [144, 146, 203, 204, 209, 210], which is another contributor to stress non-uniformity, is also lacking and needs to be addressed as most connections are subjected to a combination of concentric

shear and unbalanced moment. Finally, the influence of eccentric (which are also referred to as nonsymmetric herein) opening layouts on the punching shear behaviour of interior slab-column connections, which also introduce unbalanced moments to the connection, is also lacking [202, 204, 211, 225]. It should also be noted that the influence of slab openings for edge and corner slab-column connections is also lacking, though such connections are not addressed herein.

It should be noted that most previous studies related to slab openings are experimental. While experiments are fundamental to advancing punching shear research most of the previous studies are limited with respect to the number of specimens, investigated column sizes and investigated opening layouts due to the cost of conducting large-scale testing. Additionally, unavoidable variabilities between experimental specimens can make the identification of the most critical opening layouts difficult. As such, the development of code provisions which accurately account for the influence of slab openings on punching shear is difficult, and a large scatter between the code predictions and experimental capacities exists [225]. Therefore, there is a need to expand the existing databases so that accurate provisions can be developed. Due to increases in available computational resources many recent studies of the influence of slab openings on punching shear behaviour involve the use of NLFEA [200, 201, 203, 204, 205, 208, 209, 213, 222]. Once properly calibrated to experimental results, NLFEA can be used to conduct large studies investigating the influence of slab openings for a consistent set of material and geometric properties in a cost and time-effective manner, which would ideally lead to the development of more accurate code provisions.

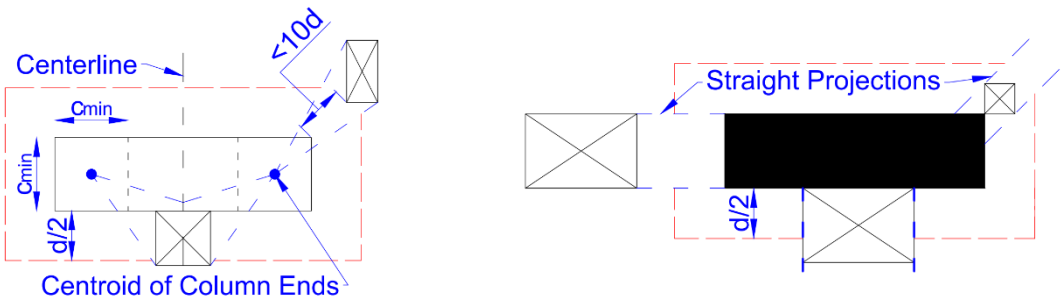
In the previous studies, which again primarily involve square slab-column connections, the following conclusions are typically reached. Firstly, openings near the slab-column connections reduce the connections' punching capacity, stiffness, energy dissipation capacity and ductility [198, 202, 203, 207, 210, 211, 213, 215, 226] (note, the list of references provided is not exhaustive). Secondly, the negative influence of the opening is influenced by many factors, but the opening size and location with respect to the column (distance from the column face and location around the column) are typically the most influential. Experimental tests and NLFEA have shown that slab openings located adjacent and parallel to the column faces have the largest negative influence [198, 203, 204, 210, 226, 227] (though some research has shown that openings located at the column corner can be more detrimental [199]), with the influence of similarly sized openings decreasing with increasing distance from the column [198, 200, 201, 203, 204, 209, 213, 228], with openings located further than $4h$ from the column face having a negligible influence [200, 213, 214].

Most previous opening studies only consider one opening shape (typically circular or square). However, the influence of opening shape on punching shear behaviour was investigated by Ha et al. [199] and Yooprasertchai et al. [214]. Ha et al. [199] tested isolated connections with groups of circular openings oriented in different layouts at various locations around the column. The experimental results demonstrated that the opening orientation is an important parameter when determining the influence of the openings. Placing the maximum dimension of a group of openings perpendicular to the column face reduces the influence of the group of openings compared to when the maximum dimension of the group is parallel to the column face. Additionally, it was found that an L-shaped arrangement of openings around the column corner was more detrimental than a rectangular arrangement of openings parallel to the column face with a similar critical perimeter reduction [199]. Unlike Ha et al. [199], who considered groups of circular openings with different shapes, Yooprasertchai et al. [214] investigated the influence of opening size, location, number of openings and opening shape through 14 isolated slab-column connection tests. Rectangular openings were found to have the largest influence on punching shear behaviour for a consistent distance between the opening and column face, followed by the square and circular openings. While the rectangular openings had the largest area, followed by the square and circular openings, their larger negative influence is also due to the stress concentrations at the opening corners, whereas a more uniform stress distribution exists around circular openings [214]. Recent experimental tests of isolated slab-column connections by El-Shafiey et al. [228] have also demonstrated that circular openings are less detrimental to punching shear capacity than square openings.

The influence of slab openings on the punching shear behaviour of shear-reinforced connections has seen renewed research interest lately. While the experimental database is limited, the available experimental results typically demonstrate that properly installed shear reinforcement can be used to at least partially mitigate the negative influence of slab openings around square and rectangular columns [195, 207, 210, 219, 221, 229]. However, Marques et al. [208] have demonstrated that designers must be cautious when detailing shear reinforcement around slab-column connections with openings. If too many rows of shear reinforcement are provided when openings are present, particularly if openings are located on each side of the column, it is possible to weaken the slab near the connection, making the inclusion of shear reinforcement detrimental to the connection capacity, though this is not reflected in current design codes [208].

The influence of slab openings on the punching shear behaviour of R-SCCs has also seen renewed research interest lately as the use of rectangular columns has become increasingly common. To date, the largest study of the influence of slab openings on the punching shear behaviour of R-SCCs was conducted by Teng et al. [147]. In addition to varying the column aspect ratio (β equals 1, 3 and 5 for 4, 13 and 3 of the specimens, respectively), opening location (adjacent to the short side, adjacent to the long side or at the column corner) and opening orientation, the influence of different load ratios in the two orthogonal directions was also studied. Slab openings were found to reduce connection capacity regardless of their location, but Teng et al. [147] recommended that if openings near R-SCCs cannot be avoided then they should be located along the long side of the connection to minimize their influence. However, due to variations in concrete compressive strength between the specimens (f_c' varied from approximately 33MPa to 43MPa), it is difficult to identify which opening layouts had the largest influence. Based on their experimental results and a database of 223 tests from literature, Teng et al. [147] proposed an alternative equation to estimate the punching shear capacity of slab-column connections.

In addition to proposing an alternative equation to estimate the punching shear capacity, Teng et al. [147] also proposed an alternative method of estimating the influence of slab openings around rectangular columns. Instead of neglecting the portion of the critical perimeter bounded by lines which are tangential to the opening boundaries and originate from the column centroid, which is the method commonly used in most worldwide design codes as discussed in Section 3.6, and herein denoted the radial approach, Teng et al. [147] recommended neglecting the portion of the critical perimeter bounded by lines which are tangential to the opening and originate from the centroid of a hypothetical square column at each end of the rectangular column as shown in Figure 2-18a (note the projections from each end should not extend over the column centerline as shown in Figure 2-18a). This modified radial approach was recommended because Teng et al. [147] observed that as the column becomes increasingly elongated that the portions of the slab around each column end become more independent of one another, and punching shear failures can occur around one end of the connection only, and therefore, the typical radial approach (lines from the column centroid) is not always accurate.



a) Radial Projections from Hypothetical Column Ends (Teng et al., 2004)

b) Straight Projections (Regan, 1974; Borges et al., 2013; Augustin et al., 2020)

Figure 2-18: Alternative Treatments of Slab Openings Around Slab-Column Connections Suggested in Literature

Following the work of Teng et al. [147], most research related to the influence of slab openings on the punching shear behaviour of R-SCCs has primarily considered openings adjacent to the short sides of the connection. One of the largest of these more recent studies was that conducted by Borges et al. [219] in which 13 slab-column connections were tested to study the influence of slab openings and shear reinforcement on the punching behaviour of R-SCCs which an aspect ratio of 3. Ignoring differences in concrete compressive strength, which ranged from 37-42MPa, the inclusion of one or two square slab openings, whose width is equal to the minimum column dimension, adjacent to the short side of the column resulted in approximately 8% and 10% lower punching capacities on average, respectively. Experimental results by other researchers [210, 221, 222, 224] have also demonstrated that openings adjacent to the short sides of R-SCCs typically have a small influence on punching capacity (approximately 10%), even when the opening itself is quite rectangular (the short side of the rectangular opening is adjacent to the short side of the column) [222]. However, recent experimental tests by Santos et al. [225] have shown that openings adjacent to the short sides of R-SCCs can have a significant influence on punching capacity, especially when the opening dimension parallel to the short side of the column exceeds the column dimension. The tests by Santos et al. [225] have also shown that openings adjacent to the long side of R-SCCs can have a significant influence on punching capacity and that the unbalanced moment generated due to the eccentricity of the column and critical perimeter centroids for connections with eccentric slab opening layouts should be accounted for when the opening is large relative to the column [225].

It should be noted that Borges et al. [219] also questioned the use of the typical radial approach for estimating the influence of slab openings around R-SCCs since the radial approach ignores any shear non-uniformity due to a lack of symmetry in the opening layout and assumes that an opening along

the long side of an R-SCC will have a larger influence than if the same opening was located along the short side of the connection. In the opinion of Borges et al. [219], this assumption is questionable due to the shear stress concentrations near the short sides of R-SCCs. Instead of using the radial approach, or the modified radial approach proposed by Teng et al. [147], Borges et al. [219] proposed accounting for the negative influence of slab openings by neglecting the portion of the critical perimeter bounded by straight projections from the opening boundaries, as shown in Figure 2-18b. This approach, herein referred to as the straight projection approach, has also been suggested by other researchers [206, 229], though Borges et al. [219] noted that additional studies are necessary to determine its widespread applicability. Additionally, it has been noted that any unbalanced moment generated due to the eccentricity between the column and critical perimeter centroids may need to be accounted for when using the straight projection approach [219, 229].

Finally, the influence of slab openings on the punching shear behaviour of connections subjected to combined concentric shear and unbalanced moment has also received limited research interest [144, 146, 203, 204, 209, 210], though from the existing literature two key conclusions are drawn. Firstly, the presence of openings leads to higher peak shear stresses for connections subjected to combined concentric shear and unbalanced moment compared to connections without openings [203, 209]. Secondly, and more importantly, previous studies for square [204, 210] and rectangular slab-column connections [210, 220] have demonstrated that slab openings are more detrimental to the connection behaviour when the opening is located on the side of the connection where the shear stresses due to the concentric load and unbalanced moment are additive (the moment is applied towards the opening). On the other hand, when the moment is applied away from the opening, the opening typically has a minor impact on the connection capacity. However, ACI 318-19 [2], Eurocode 2 (2004) [34] and *fib* Model Code 2010 [35] do not include provisions to account for the benefit of locating the opening away from the moment [210], likely because it is not possible to confirm that the moment will not act towards the opening in most practical design situations. It should also be noted that Bursac et al. [210] found the ACI 318-19 punching shear provisions for connections subjected to combined concentric shear and unbalanced moment to result in very conservative capacity predictions for R-SCCs with openings.

2.3.7 Overview of Finite Element Modelling Methodologies

The potential of FEA for punching shear research has long been recognized, but its use was initially limited due to computational resource limitations (the first uses of FEA for punching shear research

occurred in the 1970s). For example, Hawkins et al. [3] used two-dimensional linear elastic FEA to estimate the deflection of experimentally tested connections in 1971. Masterson and Long [230] were also early adopters of FEA for punching shear research and derived equations to estimate the capacity of square and rectangular slab-column connections from the results of two-dimensional linear finite element analyses based on thin plate theory in 1974. Since these initial attempts to use FEA for punching shear research, its popularity has only grown as available computing power, element formulations and the number of commercially available software have increased.

Initially, two-dimensional FEA was used in the analysis of slab-column and footing-column connections [3, 230, 231, 232, 233, 234]. However, since the 1990s, most numerical punching shear research has involved three-dimensional FEA, as two-dimensional analyses are generally not capable of modelling connections with orthogonal reinforcement or which experience nonsymmetrical punching [235]. Additionally, three-dimensional analyses can more accurately model the out-of-plane behaviour of reinforced concrete structures compared to two-dimensional analyses [236].

Three-dimensional FEA can make use of either shell elements or continuum (solid) elements. Shell elements are generally used to conduct global analyses of structures as they typically have a lower number of degrees of freedom, making them more computationally efficient than three-dimensional continuum elements. On the other hand, three-dimensional continuum elements are the preferred choice when conducting a detailed analysis of a small portion of a structure [237], such as an isolated slab-column connection, as FEMs based on continuum elements can be used to conduct detailed studies of cracking and damage [196], though the computational resource demands can be significant as a fine mesh is required near the slab-column connection to get accurate results [238]. Historically, shell element analyses are typically less detailed than those based on continuum elements, as they are generally based on a smeared cracking approach and consider the reinforcement as a layer within the concrete element or by modifying the concrete stiffness. Additionally, classical shell elements struggle with estimating the shear behaviour of disturbed regions, such as those near slab-column connections, due to the fundamental assumptions of thin and thick plate theory [239]. Therefore, recent work has focused on the development of layered shell element formulations [196, 237, 240, 241] or using a combination of joint and shell elements [242] to overcome these issues. Continuum elements do not suffer from these issues, but instead have a high computational demand due to the high number of degrees of freedom per element, and the necessity of using a fine mesh near the slab-

column connection to get accurate results [238]. Additionally, three-dimensional NLFEA using continuum elements typically requires detailed calibration studies.

Initially, studies made use of linear elastic FEA. However, as the desire of engineers and researchers to realistically model structural behaviour under various load conditions has grown so too has the popularity of NLFEA. As shown in Sections 2.3.2-2.3.6 and 2.3.8, NLFEA, which can be based on various concrete material models, is capable of simulating experimental testing schemes and can be used to estimate the influence of parameters which are difficult to measure experimentally [243]. However, the application of NLFEA to punching shear research is not trivial due to the interaction of shear and flexure and the development of localized fracture zones near the slab-column connection as the load is applied [26, 244] and requires a skilled modeller due to the large influence of modelling choices on the results [245].

2.3.8 Overview of Previous FEA of Punching Shear in Abaqus at the University of Waterloo

In this section, an overview of the previous NLFEA of punching shear conducted in Abaqus using the Concrete Damaged Plasticity (CDP) model at the University of Waterloo is provided. The CDP model is a continuum, plasticity, damaged-based model which considers both tensile cracking and compressive crushing of the concrete [235] and has been used by researchers at the University of Waterloo [1, 235, 246, 247] and elsewhere [108, 218, 244, 248, 249, 250, 251, 252, 253, 254] to study punching shear behaviour due to its ability to model concrete behaviour under arbitrary loading states, including cyclic loading. A detailed discussion of the CDP model is provided in Chapter 4.

2.3.8.1 Genikomsou [235]

Genikomsou [235] conducted a comprehensive study of the punching shear behaviour of square slab-column connections using NLFEA, which served as the basis for future punching shear research using Abaqus at the University of Waterloo. First, a detailed investigation into the calibration of the CDP model considering experimental tests of small-scale concrete specimens subjected to combinations of compressive and tensile loads, reinforced concrete beams with and without shear reinforcement and isolated slab-column connections was conducted. Then, a nonlinear FEM was calibrated to the experimental results of an interior square slab-column connection without shear reinforcement tested by Adetifa and Polak [61]. This calibrated FEM was then used to conduct parametric studies focused on investigating the influence of slab openings and compressive membrane action on punching shear

behaviour. In the opening study, openings located at a distance greater than or equal to *4d* from the column face were found to have a minor influence on punching shear behaviour and capacity for both interior and edge square slab-column connections. In the compressive membrane action study, compressive membrane forces, which are present in a continuous flat plate structure, were found to increase the punching capacity and stiffness of interior square slab-column connections. Genikomsou also conducted a detailed study of the punching shear behaviour of square slab-column connections with shear reinforcement. Numerous methods of modelling shear reinforcement in Abaqus were investigated, with one based on an arrangement of linear truss elements recommended for use in future studies [235].

The reader is referred to [235] and the numerous publications by Genikomsou and Polak [25, 200, 255, 256, 257] for further details of the work conducted by Genikomsou.

2.3.8.2 Laguta [246]

Laguta [246] extended the study of square slab-column connections subjected to combined concentric shear and unbalanced moment to interior slab-column connections (note, Genikomsou [235] primarily considered edge slab-column connections subjected to combined concentric shear and unbalanced moment). As done by other researchers at the University of Waterloo, Genikomsou's calibrated model [235] was modified slightly by Laguta [246], since different experimental specimens were considered in the calibration. After calibration, the FEM was used to conduct parametric studies investigating the influence of unbalanced moment on the punching shear behaviour of interior square slab-column connections with flexural reinforcing ratios of 0.5%, 1.0% and 1.5%. Regardless of the flexural reinforcing ratio, the NLFEA predicted a nonlinear relationship between the shear and moment capacity of the connections, whereas worldwide design codes assume a linear relationship. The NLFEA results were also used to analyze the shear stress distribution along the critical perimeter at *d/2* from the column face. Laguta [246] found that the distribution of unbalanced moments to shear and flexural stresses was dependent on the vertical load level and the reinforcing ratio of the slab. As discussed in Section 3.3.2, ACI 318-19 [2] accounts for the distribution of unbalanced moment to flexural and shear stresses through the parameter γ_v, which is equal to 0.4 for interior square slab-column connections. However, the FEA results suggest that γ_v should vary from 0.25-0.4 for connections where the unbalanced moment is low and large, respectively [246].

2.3.8.3 Beaulieu [247]

Further building on the work of Genikomsou [235], Beaulieu [247] extended the study of the punching shear behaviour of shear reinforced slab-column connections. First, the calibration of Genikomsou [235] was modified slightly to improve the agreement between the Abaqus predictions and experimental results. Then, Beaulieu [247] conducted a study to optimize the parameters of the arrangement of truss elements recommended by Genikomsou [235] to model shear reinforcement. After optimizing the arrangement of the truss elements, which was referred to as a shear stud star by Beaulieu [247], three parametric studies were conducted. In the first study, the influence of the number of rows and spacing between the rows of shear reinforcement was investigated. It was found that the total area of shear reinforcement is more influential on punching shear behaviour than the number of rows, and that interstud punching failures do not occur for spacings up to *1.5d*, where *d* is the average effective slab depth. In the second study, the calibrated FEM was used to study the influence of both opening size and the number of openings on the punching behaviour of square slab-column connections with shear reinforcement. The FEA results demonstrated that approximately 90% of the connection capacity can be maintained if the ratio of the opening width to the column width is less than 0.6 or 0.33 for connections with 2 and 4 openings adjacent to the column sides, respectively. In the final study, the influence of anchorage-controlled shear reinforcement, which is a novel type of shear reinforcement proposed by Topuzi [258] to increase the ductility of slab-column connections under seismic loads, on concentric punching capacity is studied. The Abaqus results suggest that the use of anchorage-controlled shear reinforcement, which allows larger crack widths to develop before activation of the shear reinforcement, results in less than a 10% reduction in concentric punching shear capacity [247].

2.3.8.4 Author's Previous NLFEA of Punching Shear Behaviour of R-SCCs Under Concentric Loading [1]

Before undertaking the research program presented in this thesis the author previously analyzed the concentric punching shear behaviour of R-SCCs [1]. First, the calibrated FEM proposed by Genikomsou [235] was used to analyze 5 hypothetical R-SCCs (the slab geometry, reinforcing details and material properties of these connections were chosen to match slab SB1 tested by Adetifa and Polak [61]) and the 9 slab-column connections tested by Hawkins et al. [3]. These initial studies demonstrated that Abaqus and the CDP model could be used to accurately predict the punching shear behaviour of R-SCCs and that the predictions agreed with previous experimental results.

Following the capability study, a nonlinear FEM was calibrated to the experimental results for three square slab-column connections with non-axisymmetric reinforcing layouts [57] and four rectangular slab-column connections (β = 3) with different load conditions [151] (the calibration of this FEM is briefly summarized in Section 6.3.2). This calibrated FEM was then used to conduct a parametric study to analyze the impact of column rectangularity on the concentric punching shear behaviour of interior connections without shear reinforcement. Based on an analysis of historical and current punching shear design provisions the parametric study was focused on investigating the influence of the column aspect ratio, β ($\beta = c_{max} / c_{min}$, where c_{max} and c_{min} are the maximum and minimum column dimensions, respectively) and the ratio of the minimum column dimension to the effective slab depth, d (which is referred to as the relative column size and denoted as κ in [1] and herein). In total, 77 isolated slab-column connections, spanning 8 different κ values, were analyzed. The main conclusions of the parametric study are as follows [1]:

- The FEM typically predicted an increase in punching capacity as the column size and β increased for a constant κ value. This was expected because the critical perimeter length, b_o, increases as β increases for a constant κ.
- The calibrated FEM predicted most of the 77 isolated slab-column connections to fail in punching shear, but one-way shear failures parallel to the long side of the support were predicted when the ratio of the maximum column dimension to the isolated slab length was approximately 0.4. The dominance of one-way shear when the maximum support dimension is equal to approximately 40% of the slab span is supported by analyses of continuous slab systems by Simmonds [156], Hartley and El Kafrawy [157] and Sagaseta et al. [151]. However, the difference between slab-column connections in isolated specimens and continuous structures is also clear, as the corresponding ratio between the maximum column dimension and the slab span in the continuous system is less than approximately 0.2 for the connections predicted to fail in one-way shear.
- The impact of column rectangularity on concentric punching shear capacity is not dependent on the column aspect ratio only and becomes much more severe as κ ($\kappa = c_{min}/d$) increases. The calibrated FEM predicts the relationship between the nominal shear capacity along the critical perimeter and column rectangularity to be approximately linear for each κ value.

- The stiffness of R-SCCs in both orthogonal directions increases as β increases, though the increase in the direction parallel to the long side of the column, which is stiffer, is larger. A higher connection stiffness in the direction parallel to the long side of the column has also been observed experimentally [42, 167, 168].
- As the column rectangularity increases the predicted crack patterns on the tension surface and interior sides of the slab become increasingly non-uniform for all κ values. On the tension surface of the slab, the amount of diagonal cracking decreases and the amount of cracking perpendicular to the long and short sides of the connection increases with increasing β. Additionally, a concentration of cracking near the column corner and the formation of a one-way shear crack along the long side of the support is predicted. The shape of the punching cone on the interior of the slab in both orthogonal directions is also dependent on β. As β increases, the conical crack on the interior side of the slab parallel to the short side of the support decreases in thickness before transitioning into a reverse Z shape (also known as an S shape). The lack of a punching cone on the interior slab side parallel to the long dimension of the support confirms that one-way shear becomes increasingly dominant as β increases. Representative tension surface and interior slab side crack patterns for an R-SCC subjected to concentric loading are provided in Figure 2-19.
- The NLFEA predicted the shear stresses in the slab along the support perimeter to concentrate near the corner and along the short side of the support, which matches previous experimental and numerical results [26, 42, 146, 147, 150, 168, 219]. As κ increased the concentration of shear stresses near the support corner increased, and the concentration along the short side decreased. Along the long side of the connection, the shear stress magnitudes were predicted to decrease rapidly with increasing distance from the corner of the support. Representative column perimeter shear stress distributions at the peak load for R-SCCs subjected to concentric loading are provided in Figure 2-20.

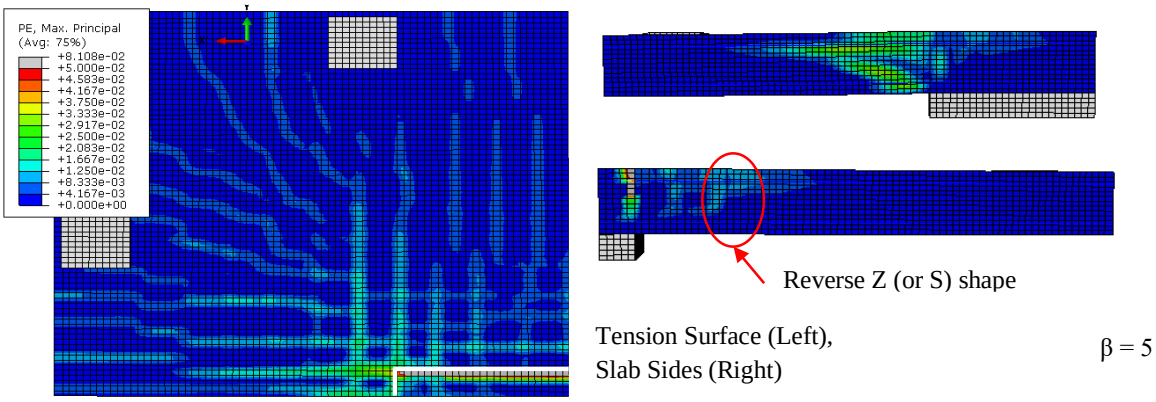


Figure 2-19: Example of Crack Pattern for large column rectangularity. β = 5, κ = 0.990 (Cracks Visualized Through Contours of Maximum Principal Plastic Strain, Approximate Column Location Shown) [259]

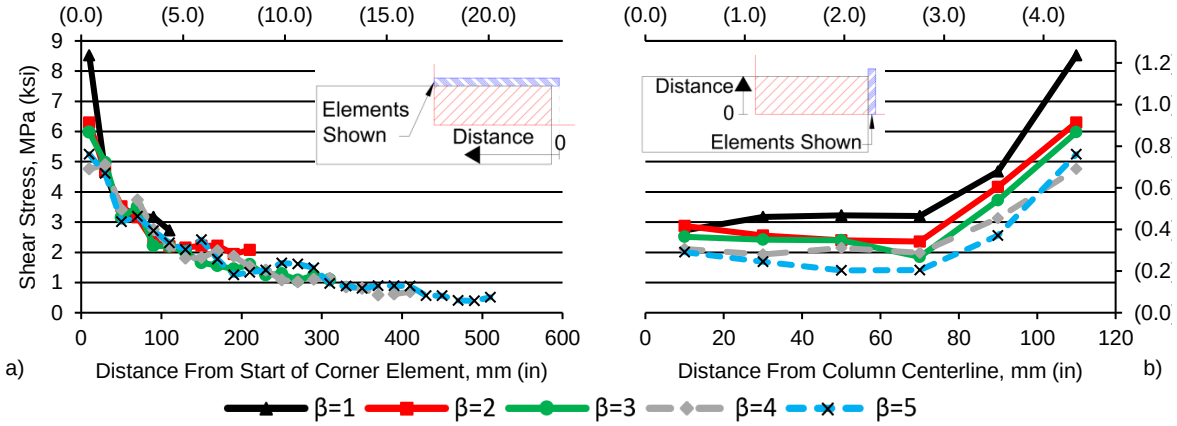


Figure 2-20: Typical Shear Stress Distribution Along Column Perimeter, a) Long Side, b) Short Side, κ = 0.990 [259]

- While not explicitly functions of κ, the punching shear design provisions of Eurocode 2 (2004) [34], *fib* Model Code 2010 [35] and the Critical Shear Crack Theory (CSCT) [11] (note, the Eurocode and Model Code provisions are summarized in Chapter 3) predict a more significant influence of column rectangularity as κ increases. Additionally, unless the b_o/d is very large, ACI 318 [2] predicts small column rectangularity values ($1 < \beta \leq 2$) to have no influence on punching capacity, which does not match the predictions from the calibrated FEM, Eurocode 2 (2004), Model Code 2010 or the CSCT.

- The punching capacities predicted by ACI 318 agree well with those predicted by the FEA for κ values less than 1. For κ values greater than 1 the ACI 318 predictions become increasingly unconservative as κ increases.
- The punching capacities predicted by Eurocode 2 (2004) are generally slightly unconservative compared to those from the FEA, but follow a similar trend and become increasingly accurate as κ increases. The impact of column rectangularity predicted by Model Code 2010 and the CSCT (note, the capacities predicted by both these methods are based on the slab rotations in the two orthogonal directions predicted by the NLFEA) generally agreed well with those predicted by the NLFEA. The CSCT predictions were generally slightly conservative compared to the FEA results, whereas the Model Code 2010 predictions were very conservative.

2.4 Mechanical Models

Supplemental to the large amount of experimental and numerical studies of punching shear much research effort has been dedicated to the development of mechanical models to estimate the punching capacity of slab-column connections. In this section, some of the most popular mechanical models are discussed. Though it should be noted that the list of models presented herein is not exhaustive, and many others exist. For example, models based on fracture mechanics, such as that proposed by Bazant and Cao (1987), modified versions of the Kinnunen and Nylander model, such as though proposed by Georgopoulous (1988, 1989) and Broms (1990), and more recent models such as those proposed in [212] and [260] are not discussed herein. Many of these additional models have not been as widely studied or adopted as those presented herein, but the reader is also referred to CEB Bulletin 168 [38] and *fib* Bulletin 12 [9] for further discussions related to mechanical punching shear models. It should also be noted that the information presented in this section is largely based on that previously presented in the author's MASc thesis [1].

2.4.1 Kinnunen and Nylander

The first mechanical punching shear model which resulted in accurate capacity predictions [9] was the plasticity-based model proposed by Kinnunen and Nylander [261], which is shown in Figure 2-21. The original model, which was proposed in 1960, was developed based on experimental results of circular isolated slab-column specimens with slab ring reinforcement. By 1963, the model had been

modified to allow for the analysis of slabs with orthogonally placed flexural reinforcement and to account for the influence of dowel action [38].

The Kinnunen and Nylander model assumes that a shear crack bounds a truncated cone of slab concrete. The portion of the slab beyond this shear crack is divided into segments which are assumed to rotate rigidly. Between the column face and the base of the shear crack a fictitious conical shell, which is subjected to compressive stresses, is assumed to support the rotating slab segments [38]. A failure criterion, which considers the maximum values of the inclined compressive stress and the tangential compressive strain at the shear crack [9, 262], and the equilibrium of the internal forces, which is dependent on the slab rotation, are used to estimate the ultimate capacity of a slab-column connection [9].

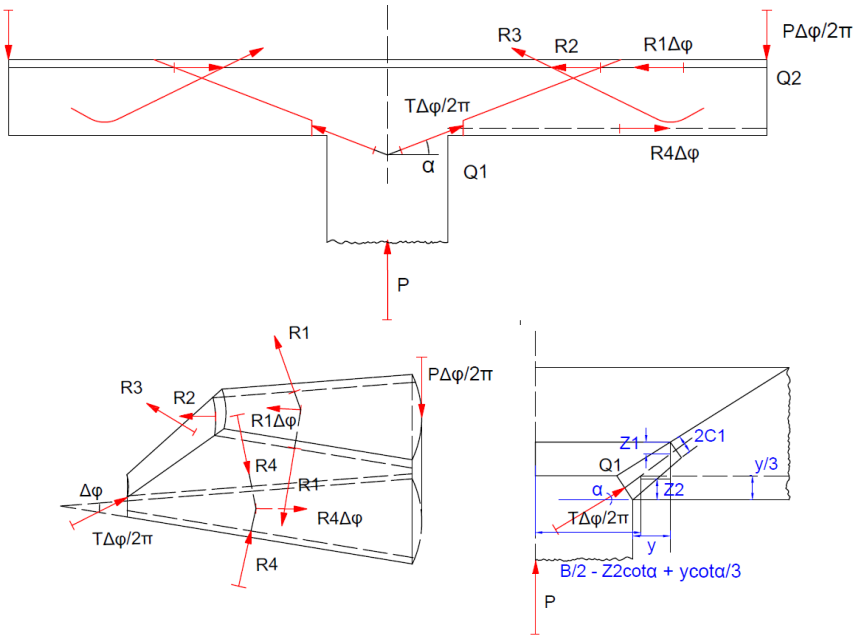


Figure 2-21: Punching Shear Model by Kinnunen and Nylander [261], Adapted from [261]

While the model resulted in accurate punching capacity estimates the assumed failure mode, compression failure of the fictitious conical shell, does not match the experimental observation that punching capacity is related to the concrete's tensile capacity [262]. However, in addition to accurate capacity estimates, the model did have numerous advantages. Firstly, it allowed the flow of forces near the slab-column connection to be visualized [9]. Secondly, it also allowed for the prediction of the connection's failure mode (flexural or punching). Finally, the model could also be used to approximate the slab deformations near the connection [38].

2.4.2 Upper Bound Plasticity Approach

In 1976, an upper-bound plasticity solution to predict the punching capacity of reinforced concrete slabs was proposed by Braestrup, Nielsen, Jensen and Bach. In this approach, the punching capacity of a slab-column connection was calculated by equating the internal work dissipated in the formation of the assumed failure surface shown in Figure 2-22 to the rate of external work due to the applied loading [262]. A modified Coulomb failure criterion and the associated flow rule were used to develop the model's yield criterion [38]

Additional assumptions used in the model's development include:

1. Concrete is assumed to be a rigid, perfectly plastic material [38].
2. All deformations were assumed to occur within the rotation-symmetric failure surface around the slab-column connection [262].
3. The concrete beyond the failure surface was assumed to remain rigid, while the concrete within the failure surface was assumed to punch out of the slab [38].

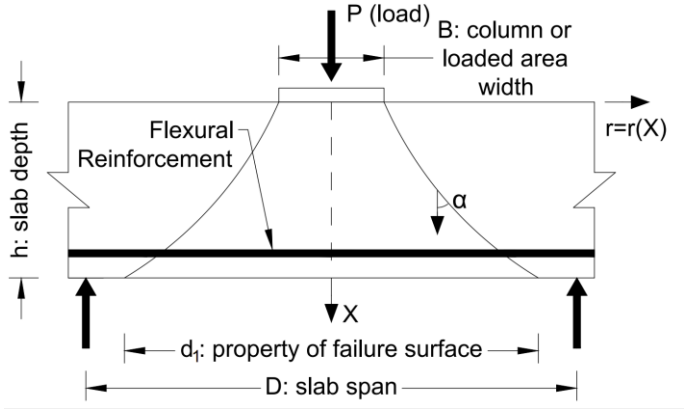


Figure 2-22: Failure Surface Considered by Braestrup et al. [38]

It should be noted that the flexural reinforcement ratio has no impact on the predicted punching capacity since the influence of dowel action is neglected in the model. Additionally, the capacities predicted by the model were found to be strongly dependent on the assumed concrete tensile strength [38].

2.4.3 Nölting Model

A model to estimate the punching shear capacity of reinforced concrete flat slabs, one-way slabs, footings and slabs with eccentrically loaded columns was proposed by Nölting in 1984. In the model, which was based on an inclined compression approach, all inclined cracking in the vicinity of concentrated loads or supports was assumed to be due to punching shear regardless of the reinforcement conditions. Nölting assumed that failure would occur when the diagonal compression strain in the concrete reached a magnitude of -4.5‰. The magnitude of the diagonal compressive strain was a function of the applied load level and also considered the relationship between the applied load and the critical moment at the column or loaded area, the moment and horizontal concrete strains and the inclined and horizontal strains in the concrete. To simplify the use of the model in practice, Nölting provided tabulated moment values for typical slab types and numerical coefficients developed from FEA results for more complicated scenarios [38].

2.4.4 Models by Alexander and Simmonds

In 1987, Alexander and Simmonds proposed the truss model shown in Figure 2-23 to estimate the punching capacity of slab-column connections. Their truss model was an extension of the truss model for edge slab-column connections theorized by Van Dusen in 1985 (note, this model was never fully developed). As shown in Figure 2-23, the model considered a three-dimensional truss composed of linear concrete compressive struts and steel tension ties. The model incorporated both anchoring struts, which were parallel to the plane of the slab, and shear struts, which were inclined with respect to the plane of the slab. Both types of concrete compression struts were assumed to be tied to the column by the strut steel [39].

In order to estimate the punching capacity, the strut steel was assumed to yield. It was also assumed that the in-plane compressive capacity of the concrete struts would never be exceeded. As such, a punching shear failure of a slab-column connection was assumed to occur when the out-of-plane component of the strut force exceeded the resistance provided by the concrete. The concrete's out-of-plane resistance is a function of the tributary width of each rebar, the concrete cover and the concrete's tensile strength and quantifies the ability of the slab to confine the flexural rebar [39].

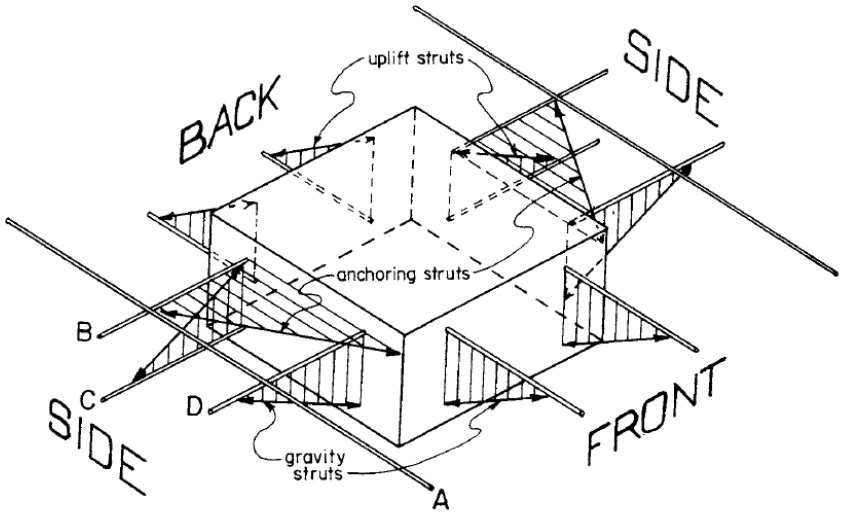


Figure 2-23: Alexander and Simmonds Truss Model, [39] Authorized Reprint from ACI Structural Journal, Volume 84, Issue 3 (1987)

The truss model had numerous advantages including:

1. It explained the load path around slab-column connections.
2. It provided an explanation for the influence of flexural reinforcement on punching capacity.
3. The model could also be used to estimate the capacity of rectangular slab-column connections (R-SCCs) if modification factors were incorporated, and each column face was considered individually [39].

Based on further experiments, Alexander and Simmonds determined that the radial compression struts were not linear, as assumed in the truss model, but were curved, as shown in Figure 2-24, which required the truss model to be modified. In 1992, Alexander and Simmonds proposed an improved version of the truss model, denoted the bond model. The bond model was based on the shear stresses on a critical section and also considered the influence of radial arching action [263, 264].

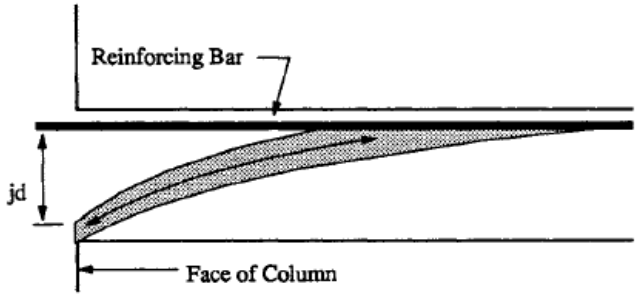


Figure 2-24: Curved Compression Strut Used in Bond Model [263], Authorized reprint from ACI Structural Journal, Volume 89, Issue 3 (1992)

In the bond model, all load is assumed to be carried from the slab to the column by radial strips. The transfer of shear force from the slab to the column is assumed to occur through radial compression arches. The maximum and minimum forces in the arch occur at the column face and where the arch intersects the flexural reinforcement, respectively. The bond model considers the equilibrium and flexural capacity of the radial strips and the shear capacity of the slab quadrants adjacent to the radial strips. A punching shear failure is assumed to occur when the slab is no longer capable of sustaining the force gradients present in the flexural reinforcement, which are limited by either the bond between the rebar and the concrete or the amount of yielding along the rebar's length, in the vicinity of the slab-column connection [263].

While the bond model is an improved version of the truss model, it does have some disadvantages. Firstly, the bond model can only be used for slabs with orthogonally placed flexural reinforcement. Secondly, the bond model cannot properly account for column rectangularity since all force is assumed to be carried by arching action (recall the original truss model could account for column rectangularity). As the support width increases a transition from two-way to one-way action occurs. Therefore, the force transfer mechanism becomes a combination of arching action and beam action as the support becomes increasingly elongated. However, according to Alexander and Simmonds, the bond model should be conservative for the common slab types at the time of its development if the influence of column rectangularity is neglected [263].

2.4.5 Rankin and Long Yield Line Model

Rankin and Long originally proposed a model to estimate the flexural punching capacity and shear punching capacity of typical isolated slab-column connections where the slab is supported near its

edges and the load is applied through a central column, as seen in Figure 2-25, in 1987 [265]. This model considered three failure modes, yielding of the flexural reinforcement, concrete crushing and internal diagonal cracking. Rankin and Long classified failures due to reinforcement yielding or concrete crushing as flexural failures and failures due to internal inclined cracking as shear failures [265].

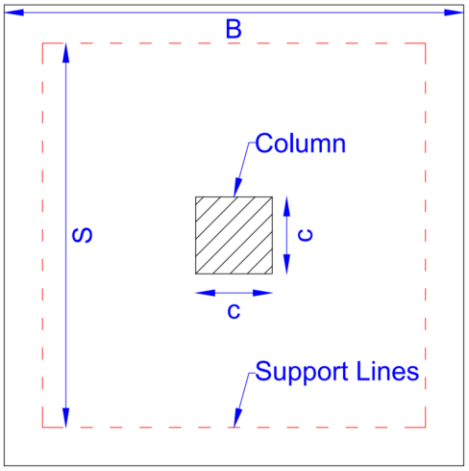


Figure 2-25: Isolated Slab-Column Specimen Considered by Rankin and Long [266]

This model related the punching capacity of a slab-column connection to the flexural behaviour of the slab. For connections where the slab is lightly reinforced for flexure, the failure mode approaches that assumed in the yield line method as failure occurs after widespread yielding of the flexural reinforcement. For connections with heavily reinforced slabs, yielding typically only occurs in a localized region near the connection, and as such, the failure mode is similar to that which occurs for localized concrete compression failure near the column. Therefore, the punching capacity of a slab-column connection should be somewhere between the two extreme values associated with localized concrete compression failure and the development of the full yield line pattern [265].

Rankin and Long have since modified the original model, which is summarized in [1], to include the influence of slab depth and to refine the influence of the slab flexural reinforcement ratio as the original method was found to diverge for low flexural reinforcing ratios [266].

As in the original method the estimated punching capacity of an isolated slab-column specimen is the minimum of the flexural punching strength, P_{vf} (N) and the shear punching strength, P_{vs} (N) [266].

The flexural punching strength of a slab-column specimen similar to that shown in Figure 2-25 can be computed using equation 2-4.

$$P_{vf} = 1.07\left(\frac{200}{d}\right)^{0.1}\left[k_{yl} - \left(k_{yl} - \frac{k_b}{r_f}\right)\frac{M_u}{M_{bal}}\right]M_u \leq 1.07\left(\frac{200}{d}\right)^{0.1}\frac{k_b}{r_f}M_{bal} \quad 2\text{-}4$$

where r_f is a column shape factor equal to 1.15 for square columns, k_{yl} and k_b are factors relating the applied load to the average moment for the formation of an overall yield line mechanism and the average internal moment at the column perimeter respectively, M_u is the ultimate moment resistance of the isolated slab-column specimen (Nmm/mm), M_{bal} is the balanced moment resistance (Nmm/mm), and d is the effective slab depth (mm) [266]. The factors k_{yl} and k_b can be calculated using equations 2-5 and 2-6 respectively for a square slab with a square column (note the model is only applicable to square or circular slab-column connections)

$$k_{yl} = 8\left(\frac{B}{S-c} - 0.172\right) \quad 2\text{-}5$$

$$k_b = \frac{25}{(\log_e \frac{2.5S}{c})^{1.5}} \quad 2\text{-}6$$

where B, S and c are defined as shown in Figure 2-25 [266].

Rankin and Long [266] state that the ultimate moment resistance per unit length, M_u, can be calculated using equation 2-7

$$M_u = \rho f_y d^2\left(1 - 0.59\frac{\rho f_y}{f_c'}\right) \quad 2\text{-}7$$

where ρ is the average flexural reinforcing ratio of the slab, f_y is the yield strength of the flexural reinforcement (MPa) and f_c' is the concrete compressive strength from cylinder tests (MPa).

Equation 2-8, originally proposed by Whitney (1937) is used to calculate the balanced moment resistance per unit length, M_{bal} [266]

$$M_{bal} = 0.333 f_c' d^2 \quad 2\text{-}8$$

The shear punching capacity of a square slab with a square column is calculated using equation 2-9

$$P_{vs} = 1.37(f_c')^{0.45}(c+d)d(100\rho)^{0.2}f_y^{0.05}\left(\frac{200}{d}\right)^{0.18} \quad 2\text{-}9$$

where all variables are defined as in the calculation of P_{vf} [266].

2.4.6 Shehata and Regan Model

An improved version of the Kinnunen and Nylander model [261] was proposed by Shehata and Regan in 1989 [267]. The key improvements made by Shehata and Regan include:

1. The forces generated by dowel action are calculated based on equilibrium instead of assumed.
2. The deformation of the portion of the slab on top of the column and bounded by the shear crack is accounted for.
3. The revised failure criterion is more complete than that proposed by Kinnunen and Nylander [261] [267].

Consistent with the model proposed by Kinnunen and Nylander the slab is divided into rigid segments which are assumed to rotate about a point, denoted the center of rotation., The center of rotation is assumed to be located at the slab's neutral axis at the column face. Before failure occurs, rigid wedge elements, which are bounded by the inclined cracks in the slab and the initial circumferential cracks on the slab surface around the column are assumed to break away from each rigid segment and rotate independently about the center of rotation [267].

The slab rotation, the slab's neutral axis depth, and the inclination of the compressive force at the column face are related to the applied load through three equilibrium states in the radial plane. Failure is defined according to the three conditions outlined below.

1. The front portion of the radial segments, which are subjected to compression, is assumed to fail due to tensile splitting when the inclination of the compression force reaches 20 degrees.
2. If the average radial strain on the compressed face reaches a magnitude of 0.0035 radial concrete crushing is assumed to occur.
3. If the tangential strain at a distance of x from the column face, where x is equivalent to the neutral axis depth, reaches a magnitude of 0.0035 tangential concrete crushing is assumed to occur [267].

2.4.7 Critical Shear Crack Theory (CSCT)

The Critical Shear Crack Theory (CSCT), proposed by Muttoni in 2008 [11], is one of the more recent and widely used mechanical models for estimating punching shear capacity. As with many of

the other mechanical models presented herein, the CSCT relates punching capacity to the slab rotation. According to the CSCT, the punching capacity of a slab-column connection decreases as the rotation of the surrounding slab increases. Mechanically speaking, the punching capacity of a slab-column connection decreases due to the existence of a critical shear crack which propagates through the slab as the applied load increases and eventually intersects the inclined compression struts which transfer the shear force between the slab and supporting column. As the width of the critical crack grows, the shear strength of the inclined compression struts decreases, eventually resulting in the punching shear failure of the connection. The width of the critical shear crack can be estimated by using a relationship proposed by Muttoni and Schwartz [268], which assumes that the crack width is proportional to the product of the slab rotation, ψ, and the effective slab depth, d, as shown in Figure 2-26.

The crack roughness, which is assumed to be a function of the maximum aggregate size, is used to estimate the amount of shear which can be transferred across the critical shear crack. The ability of the critical shear crack to transfer shear force is estimated by dividing the nominal crack width, ψd, by $d_{g0} + d_g$, where d_g and d_{g0} are the maximum aggregate size (mm) and the reference aggregate size of 16mm, respectively, based on findings by Walraven (1981) and Vecchio and Collins (1986). Multiplying the slab rotation by the factor $d/(d_{g0} + d_g)$ also simplifies the formulation of the model as the influence of slab thickness and aggregate size cancel out [11].

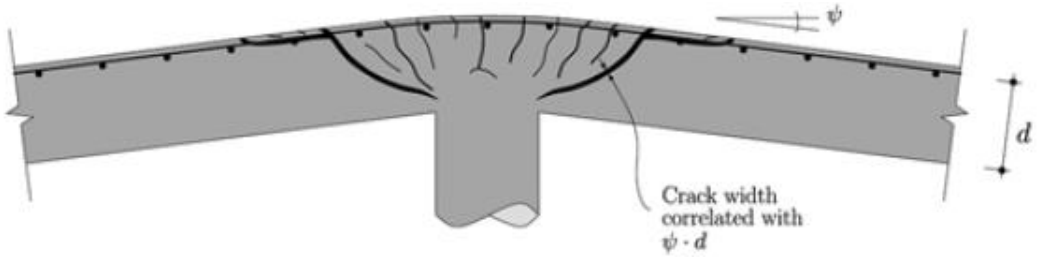


Figure 2-26: Relationship between the critical shear crack width and slab thickness and rotation [11], Authorized reprint from ACI Structural Journal, Volume 105, Number 4 (2008)

To apply the CSCT the load-rotation response of the slab must be estimated. For experimental tests, the slab rotations can either be directly measured or calculated from recorded deflections. In design scenarios, the slab rotation can either be estimated using FEA or simplified equations. If the flexural reinforcement is not consistent in both orthogonal directions the maximum slab rotation should be used to estimate punching capacity [11].

Unlike the other mechanical models presented herein, the CSCT has been adopted in worldwide design codes. For example, earlier versions of the CSCT served as the basis for the Swiss concrete design codes SIA 262 (2003) [269] and SIA 162 (1993) [270]. More recently, the CSCT has also been used in the development of the *fib* Model Code 2010 provisions and the current draft version of the newest iteration of Eurocode 2 (prEC2) [271, 272], as discussed in Section 3.5.

Recently, the CSCT formulation has been extended so that it can be used for shear reinforced slabs (reinforcement installed prior to casting [273], and post-installed shear reinforcement [274]), footings [275] and bridge deck slabs [67], though these modifications are not discussed herein. The CSCT formulation has also been shown to be capable of accounting for size and strain effects [276], membrane effects and slab continuity [277] and to apply to pre-stressed slabs [278], and linearly supported slabs with concentrated loads near the support [279].

.

Chapter 3: Overview of Punching Shear Design Code Provisions

3.1 Introduction

In this chapter, the punching shear design provisions and historical development of ACI 318-19 [2], Eurocode 2 (both the current version, EN 1992-1-1 [34], and the latest draft of the newest version, prEC2 [280]), and *fib* Model Code 2010 [35] are discussed. The punching shear design provisions of CSA A23.3-19 [36] are not discussed herein, since they have the same overall trend as those from ACI 318-19, but typically result in higher predicted capacities due to the differences in resistance factors between the two codes. Since the resistance factors will be set to 1 when comparing the capacities predicted by the design codes and the NLFEA the more conservative ACI 318-19 predictions are considered in this work. Furthermore, as the work in this thesis is focused on connections without shear reinforcement only provisions for connections without shear reinforcement are provided. Issues with the existing code provisions for slab-wall connections (SWCs), special-shaped slab-column connections (SS-SCCs) and slab openings are discussed in Chapters 6-9.

It should be noted that many parameters have been found to influence punching capacity. Some of the most influential parameters include the concrete compressive strength, the slab flexural reinforcement ratio, the effective slab depth, the ratio of critical perimeter length to slab depth and the ratio of shear span to effective depth [281]. However, punching capacity is also influenced by other factors such as the restraint forces generated due to frame action and column geometry [50]. As discussed in the following sections, design codes vary in their treatment of these parameters or do not explicitly account for them at all.

3.2 Critical Perimeter Concept

Even with the large amount of punching shear research that has been conducted, current punching shear design codes differ regarding the parameters assumed to influence punching shear and how to account for these parameters. However, all design codes use the critical perimeter concept to facilitate punching shear design as it allows the punching design of flat plates to be completed using a similar methodology to that used when designing reinforced concrete beams for shear based on the nominal shear stresses acting on a cross-section. In the case of concentrically loaded slab-column connections, the total load demand on the connection is divided by the area of an assumed critical surface. As discussed in this chapter, the location and shape of the critical perimeter vary between codes, though they are commonly vertical rectangular or cylindrical surfaces around the connection. The location

and shape of the critical perimeter assumed in each code are typically based on the experimental observations or mechanical model used to develop the code provisions. The critical perimeter concept was originally introduced by Talbot in 1913. Talbot concluded that the shear capacity of column-footing connections could be accurately estimated by considering the nominal shear stresses along a critical perimeter located at a distance of *d* from the column face, where *d* was the effective footing depth [38].

In the design of concentrically loaded connections without shear reinforcement, the nominal shear stress resistance provided by the concrete, which is assumed to be uniform along the critical perimeter, is compared to the applied shear stress demand, which is also assumed to be uniform. In addition to the different critical perimeters, design codes also predict different values for the shear stress resistance provided by the concrete.

While the critical perimeter concept greatly simplifies the punching shear design process, it does not necessarily represent the complex mechanical behaviour of connections failing in punching. Even so, if proper factors are applied the critical perimeter concept can lead to reasonable estimates of punching shear capacity [38].

3.3 ACI 318-19

3.3.1 Historical Development

The first official concrete design code in the United States was published in 1908 by the National Association of Cement Users (NACU) [282], which since 1920 has been known as the American Concrete Institute (ACI). The first ACI punching shear design provisions were published in 1920 in ACI Standard Specification Number 23 [283]. Unlike current punching provisions, which are based on ultimate strength design, the first punching provisions were based on working stress design. In Standard Specification Number 23, the stresses along two critical sections were compared to allowable stress values, which were fractions of the concrete's compressive strength. The first section was vertical through the slab depth and located at the perimeter of the column capital. The second section, which was assumed to have an inclination of 45 degrees, also originated at the capital perimeter, and the shear stresses along this section were assumed to be transferred by diagonal tension [283].

By 1927, the punching shear design provisions were revised to consider only one critical section. This revised critical section was vertical through the slab depth and was located at a distance of *d*

from the face of the column capital or drop panel [284]. From 1936-1956, the punching provisions were largely unchanged, other than minor modifications to the allowable stress limits and detailing requirements [285, 286].

However, starting in the 1960s, significant changes were made to the ACI 318 punching provisions. ACI 318-63 introduced ultimate strength design provisions, though working stress design was still permitted. Furthermore, ACI 318-63 also introduced modifications to the assumed critical perimeter and allowable stress levels.

Based on recommendations from Joint ASCE-ACI Committee 326, which is now known as Joint ASCE-ACI Committee 426, the critical perimeter in ACI 318-63 [51] was located at a distance of *d/2* from the face of the column or drop panel. This critical perimeter, which has remained unchanged since ACI 318-63, was assumed since available experimental punching shear tests displayed a pyramid-shaped failure surface with an inclination of approximately 45 degrees. This failure surface, which starts at the neutral axis of the slab, is subjected to a complicated state of stress due to the combined action of bending and shear in the vicinity of the slab-column connections. Joint ASCE-ACI Committee 326 believed that punching shear design could be simplified by considering a critical perimeter at *d/2* from the column face, even though this differed from Moe's [43] recommendation [287]. Based on a comprehensive experimental study, Moe [43] developed punching shear design equations which considered the shear stresses along the column perimeter and were functions of a parameter relating the column dimension, *c*, to the effective slab depth, *d* (*c/d* ratio) [43, 287]. Joint ASCE-ACI Committee 326 believed that the use of a critical perimeter at *d/2* from the column face accounted for the influence of the *c/d* ratio. This belief came from the assumption that the shear stress distribution along the critical perimeter at *d/2* was independent of *c/d* because the area of the assumed critical section was proportional to the area of the actual failure surface and because the assumed critical section shared a common point with the failure surface [287].

In ACI 318-63, the ultimate stress resistance provided by the concrete along the critical perimeter at *d/2* from the column was assumed to equal $0.33\sqrt{f_c'}$ (SI units, f_c' in MPa) regardless of the column shape or size [287]. This was the first time that punching shear capacity was related to the $\sqrt{f_c'}$ in ACI 318, and was preferable to the equation which was a function of *c/d* and based on the column perimeter stresses, particularly for irregularly shaped columns or connections with slab openings [191]. As will be discussed in the next subsection, this relationship is still used in ACI 318-19.

Furthermore, ACI 318-63 [51] was the first ACI code to include provisions for shear reinforced connections, slab openings near the columns and to require designers to check both the one-way and two-way shear capacity of two-way slabs. ACI 318-63 also introduced provisions related to the influence of unbalanced moments on punching capacity, though these provisions used an alternate critical perimeter located further from the column.

As will be discussed in the next section, the assumption that the shear stresses along the critical perimeter at *d/2* from the column face were uniform and independent and *c/d* for any column size and shape was found to be invalid. However, research has shown that the use of a critical perimeter at *d/2* from the column face can lead to the most accurate punching capacity estimates [281].

3.3.2 Design Provisions for Connections Without Shear Reinforcement

The critical perimeter assumed in ACI 318-19 is located at a distance of *d/2* from the column face and has 90-degree corners as shown in Figure 3-1a. For slab-column connections without shear reinforcement that are subjected to concentric loading only, the applied shear stress demand, v_f (MPa), and the nominal shear stress resistance provided by the concrete, v_c, along the critical perimeter are assumed to be uniform as shown in Figure 3-1b. As shown in Figure 3-1b, v_f can be calculated using equation 3-1 for concentric load conditions.

$$v_f = V/(b_o d) \quad \text{3-1}$$

where V is the applied shear force (N), b_o is the critical perimeter length (mm) and d is the effective slab depth (mm) [2].

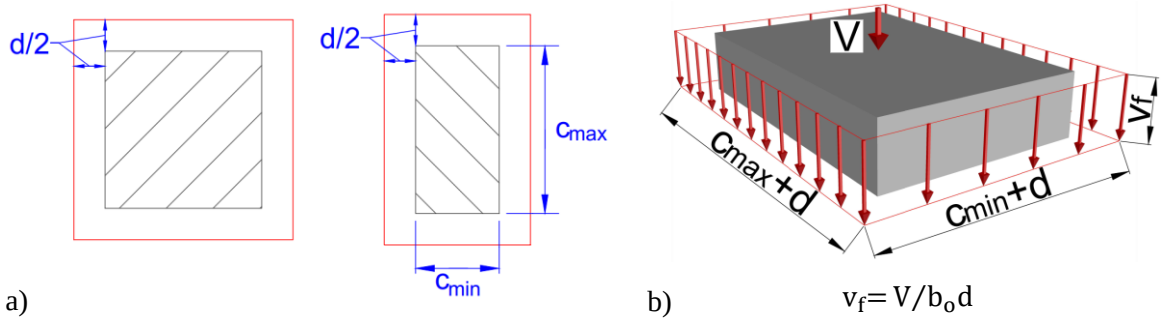


Figure 3-1: a) Critical Perimeter; b) Shear Stress Distribution for Concentric Loading, ACI 318-19 [2]

According to ACI 318-19 slab-column connections without shear reinforcement are predicted to fail in punching when v_c, which is calculated as the minimum of equations 3-2-3-4 (SI units), is less than v_f.

$$v_c = 0.33\lambda\lambda_s\sqrt{f_c'} \quad 3\text{-}2$$

$$v_c = 0.17(1 + 2/\beta)\lambda\lambda_s\sqrt{f_c'} \quad 3\text{-}3$$

$$v_c = 0.083(2 + \alpha_s[d/b_o])\lambda\lambda_s\sqrt{f_c'} \quad 3\text{-}4$$

where λ is a parameter to account for concrete density (1 for normal density), λ_s is the size effect factor, f_c' is the concrete compressive strength (MPa), β is the column aspect ratio, and α_s is a parameter to account for the column's location in the overall structure (40 for interior columns) [2]. While the influence of size effect has long been included in Canadian [36] and European [34] punching shear design provisions, λ_s, which is calculated using equation 3-5, and applies to slabs where *d* exceeds 250mm, was only introduced in ACI 318-19 [2].

$$\lambda_s = \sqrt{2/(1 + 0.004d)} \leq 1 \quad 3\text{-}5$$

As previously discussed, equation 3-2 was introduced in ACI 318-63 [51] and is a modified version of that proposed by Moe [43], based on the assumption that the shear stresses along the critical perimeter at *d/2* from the column face are uniform and independent of column size. This assumption was found to be invalid, and therefore, equations 3-3 and 3-4 were introduced in ACI 318-77 [170] and ACI 318-89 [288], respectively.

Equation 3-3, which was primarily derived from experimental tests of rectangular slab-column connections (R-SCCs) by Hawkins et al. [3], accounts for shear stress concentrations at the corners of rectangular or special-shaped columns [2, 50, 150, 289] by relating v_c to the column aspect ratio, β. The definition of β varies depending on the column/support geometry. For rectangular columns and walls, β is defined as the ratio of the maximum and minimum support dimensions, c_{max} and c_{min}, respectively. Whereas for SS-SCCs, such as L, T and cruciform columns, β is defined as the ratio of a_n to b_n, where a_n and b_n are the longest overall dimension of the assumed effective loaded area, and the largest dimension of the effective loaded area perpendicular to a_n [2]. The assumed effective loaded area and definitions of a_n and b_n for symmetric L, T and cruciform slab-column connections are provided in Figure 3-2.

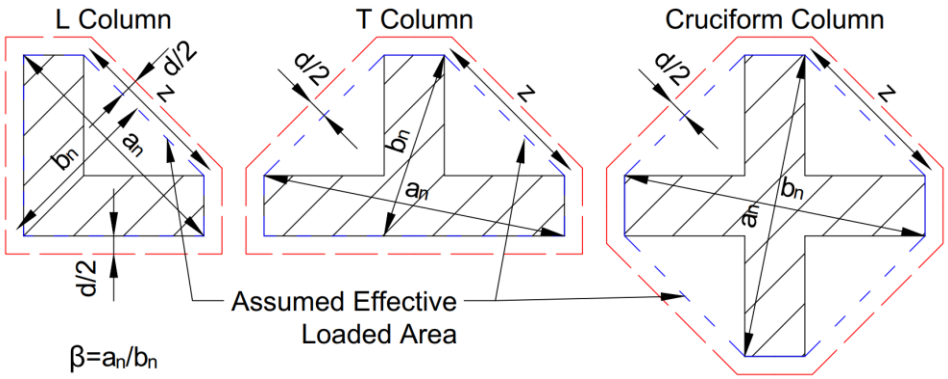


Figure 3-2: Critical Perimeters Around L, T and Cruciform Columns and Definition of a_n and b_n for Symmetric Columns According to ACI 318-19

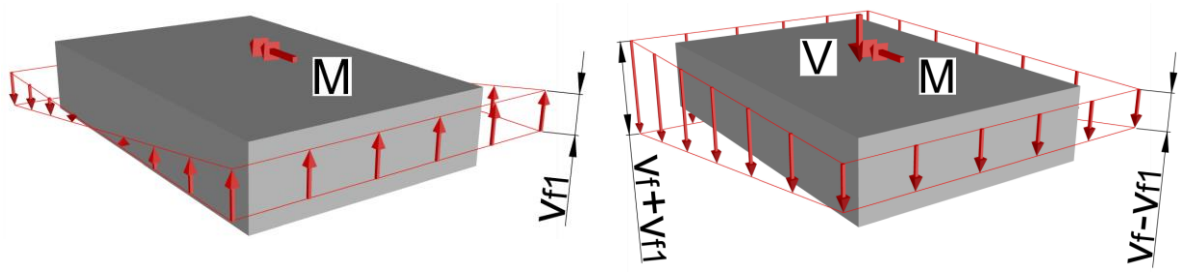
Equation 3-4, which accounts for Vanderbilt's [52] observation that v_c decreases as the b_o/d ratio increases [2], also applies to all column shapes. Unlike other geometries, where the critical perimeter follows the column geometry exactly, the critical perimeter around SS-SCCs, which was first explicitly defined in ACI 318-77 [169, 170], is instead defined to minimize its length as shown in Figure 3-2.

Punching shear design provisions for slab-column connections subjected to combined concentric shear and unbalanced moment (which can be due to unequal gravity loading, lateral loading or eccentricities between the slab, column and critical perimeter centroids) were introduced in ACI 318-63 [51, 287], and modified to their current state in ACI 318-71 [290]. According to ACI 318-19 [2] the applied shear stress demand along the critical perimeter is assumed to vary linearly about the centroid of the critical perimeter. If v_c, which is still assumed to be uniform and calculated as the minimum of equations 3-2-3-4, is greater than or equal to the maximum shear stress along the critical perimeter, $v_{f,max}$ (MPa), the connection is deemed adequate.

ACI 318-19 provides explicit equations to calculate $v_{f,max}$ for square or rectangular slab-column connections without shear reinforcement and slab openings. For example, for the R-SCC subjected to concentric shear and a uniaxial unbalanced moment about an axis parallel to the maximum column dimension shown in Figure 3-3, $v_{f,max}$ can be calculated using equation 3-6.

$$v_{f,max} = \frac{V}{b_o d} + \frac{\gamma_v M_f e}{J} \qquad 3\text{-}6$$

where M_f is the unbalanced moment (Nmm), γ_v is a parameter to account for the amount of unbalanced moment assumed to be transferred by flexure in the slab and eccentric shear, e is the eccentricity (mm) and J is a constant analogous to the polar moment of inertia of the critical perimeter (mm^4) [2].



$v_{f1} = \gamma_v M_f e/J$ $\qquad$ $v_f = V/b_o d + \gamma_v M_f e/J$

Figure 3-3: Shear Distribution for Concentric Load and Uniaxial Unbalanced Moment About an Axis Parallel to Maximum Column Dimension, ACI 318-19

However, for connections where the critical perimeter has an irregular shape, ACI 318-19 does not provide equations for γ_v, J and e. Instead, Clause R8.4.4.2.3 [2] refers designers to ACI 421.1R-20 [5] for calculating $v_{f,max}$. Considering the general case of a connection subjected to combined concentric shear and biaxial unbalanced moments, $v_{f,max}$ is calculated using equation 3-7.

$$v_{f,max} = \frac{V}{b_o d} + \frac{\gamma_{vy} M_{u-y}}{J_{cy}} x + \frac{\gamma_{vx} M_{u-x}}{J_{cx}} y \qquad 3\text{-}7$$

where J_{cx} and J_{cy} are properties of the assumed critical perimeter of any shape, equal to d multiplied by the second moment of perimeter about the x or y axis respectively (mm^4), γ_{vx} and γ_{vy} are factors used to determine the moment about the axes x and y between the slab and column that is transferred by shear stress at the assumed critical perimeter, x and y are coordinates of a point along the assumed critical perimeter with respect to the centroidal principal axes x and y (mm) and M_{u-x} and M_{u-y} are the factored slab moments resisted by the supporting column about the centroidal principal axes x and y of the assumed critical perimeter (Nmm) [5].

While ACI 421.1R-20 is intended for the design of shear-reinforced connections (note, clause R8.4.4.2.3 [2] only explicitly mentions shear-reinforced connections), its provisions can also be applied to connections without shear reinforcement for critical perimeters of any shape. As seen in Figure 3-4, the critical perimeters around shear reinforced square slab-column connections are similar to those around SS-SCCs without shear reinforcement. Therefore, ACI 421.1R-20 can be used to

design connections subjected to combined concentric shear and unbalanced moment, or connections subjected to concentric shear only where an eccentricity between the column and critical perimeter centroids exists (i.e. connections with nonsymmetric slab openings or L and T connections). Sample calculations according to ACI 421.1R-20 for L and T connections with slab openings are provided in Appendix H. Appendix H also includes detailed formulas for calculating γ_v, M_u, J_c and the coordinates of the critical perimeter with respect to the centroidal principal axes according to ACI 421.1R-20 [5].

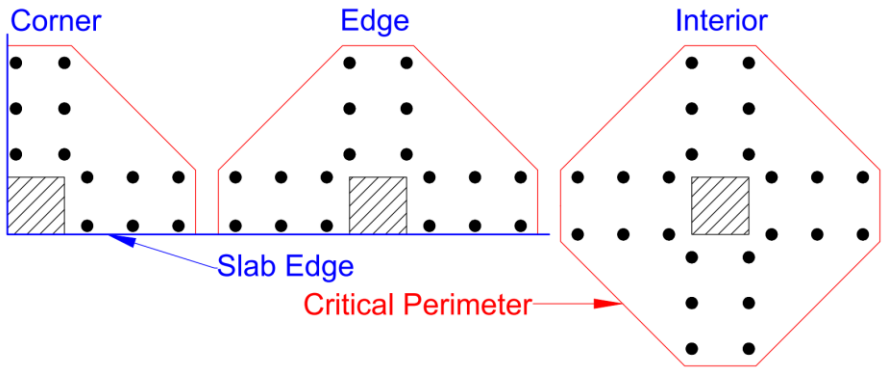


Figure 3-4: Critical Perimeters Around Shear-Reinforced Connections According to ACI 318-19 and ACI 421.1R-20

3.4 Eurocode 2

3.4.1 Historical Development

The primary motivation of the Eurocodes was to allow the same design framework to be used throughout Europe, but still provide individual nations with control over certain parameters such as load levels [291]. The design of concrete structures is addressed in Eurocode 2 (EC2). At the time of writing this thesis a new version of EC2, prEC2 (2020), is in development [271, 272]. However, since this code has not been finalized, both the current version of EC2 [34] (EN 1992-1-1, also known as EC2 (2004)), and prEC2 (2020) [280] are considered.

The original draft of EC2 (2004), ENV 1992-1-1 [292], released in 1991, was primarily influenced by CEB-FIP Model Code 1978 [53] (note, CEB-FIP is now known as *fib*) and four British design standards, BS 8110 – Structural Use of Concrete: Parts 1-3 (1985) and BS 5400-4 – Steel, Concrete and Composite Bridges: Part 4 (1984) [293]. As shown in Figure 3-5a, the critical perimeter in ENV 1992-1-1 was located at a distance of *1.5d* from the column face to match that recommended by the

British standards. To account for the negative influence of column size and aspect ratio on punching shear, a reduced effective critical perimeter, shown in Figure 3-5b, was used when the column dimensions exceeded specific values. While the length of the straight segments of the critical perimeter, which are assumed to carry two-way shear, match those from Model Code 1978 [53], there are fundamental differences. Firstly, the critical perimeter in Model Code 1978 is located at *d/2* from the column face instead of *1.5d*. Secondly, ENV 1992-1-1 neglects the capacity of any regions beyond the two-way shear regions, whereas Model Code 1978 assumes a lower capacity, associated with one-way shear, along the remaining portions of the critical perimeter.

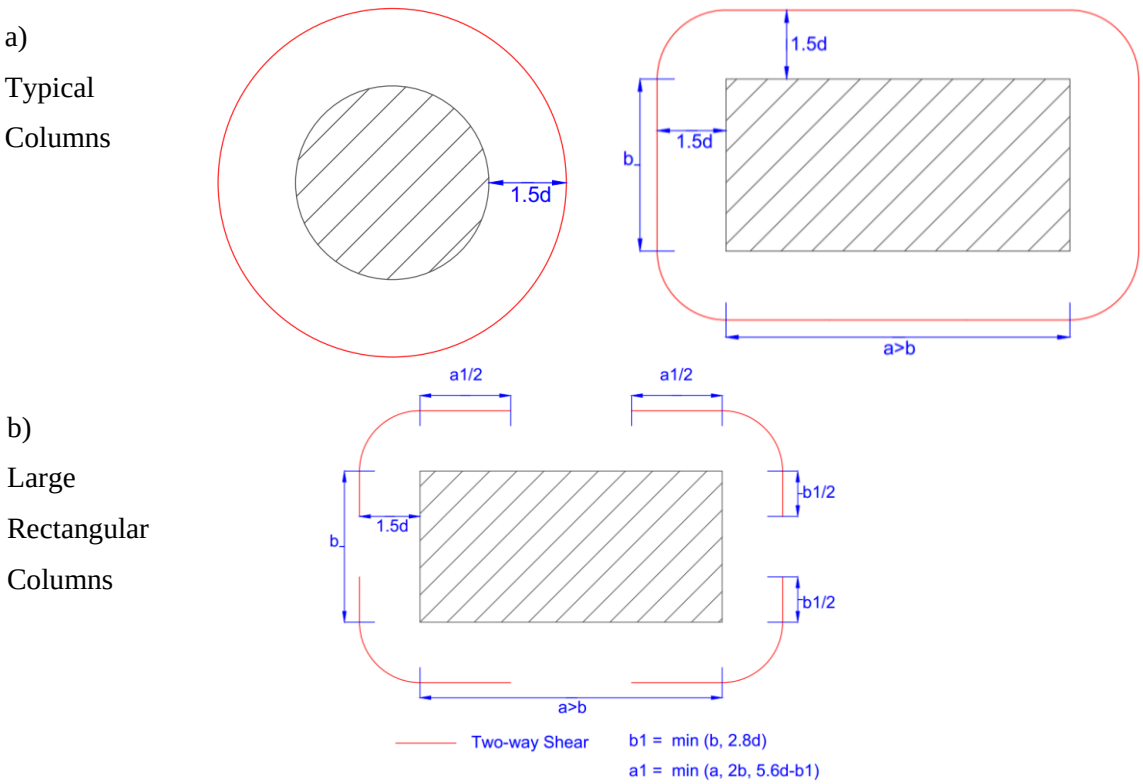


Figure 3-5: Critical Perimeters Assumed in ENV 1992-1-1 [292] (figure taken from [1])

The EC2 (2004) provisions, which are presented in the following section, were primarily based on CEB-FIP Model Code 1990 [159], and are significantly different than those in ENV 1992-1-1 [12, 294, 295]. Firstly, the critical perimeter was relocated to a distance of *2d* from the column face, as shown in Figure 3-6, to match that used in Model Code 1990 [159]. Also, due to the relocation of the critical perimeter, no effective critical perimeter provisions to account for column size and aspect ratio are included in EC2 (2004) [34, 294]. The effective critical perimeter provisions were removed since the shear stresses along the critical perimeter at *2d* were found to be approximately uniform

regardless of column size. Relocating the critical perimeter to a distance of *2d* also had the additional benefit of allowing the punching shear provisions to follow a similar methodology to that used in the design of concrete members without shear reinforcement [294]. Secondly, the equation used to calculate the nominal shear stress capacity along the critical perimeter provided by the concrete (see equation 3-12 in the following subsection) was modified to more closely resemble that used in Model Code 1990, as an error in the derivation of the ENV 1992-1-1 equation, which leads to unconservative predictions for high concrete strengths, was discovered [294].

Recently, work has begun on the newest version of Eurocode 2, prEC2 (2020). Compared to the previous version, Eurocode 2 (2004), prEC2 represents a fundamental change in code philosophy. The punching shear design provisions in the previous Eurocode, EN 1992-1-1, were empirically based (the provisions of Model Code 1990 were primarily derived from the work of Zsutty [296] [271, 297]. On the other hand, the prEC2 provisions are based on the Critical Shear Crack Theory [271, 272], similar to *fib* Model Code 2010 (which is discussed in Section 3.5).

3.4.2 Design Provisions for Connections Without Shear Reinforcement

3.4.2.1 EN 1992-1-1 (Eurocode 2 (2004))

Unlike ACI 318-19 [2] which only requires punching shear checks along critical perimeters at some distance from the column face, EC2 (2004) [34] requires punching shear checks at the column perimeter in addition to those along critical perimeters at some distance from the column face. The critical perimeter in EC2 (2004) differs from that used in ACI 318-19 in two ways. Firstly, for slabs without shear reinforcement, the critical perimeter is located at a distance of *2d* from the column face (representative critical perimeters around interior slab-column connections according to EC2 (2004) are provided in Figure 3-6). Secondly, the corners of the critical perimeter are curved, as shown in Figure 3-6.

According to EC2 (2004) the applied shear stress demand along the considered critical perimeter, v_{Ed} (MPa) can be calculated using equation 3-8.

$$v_{Ed} = \beta V_{Ed}/u_i d \qquad 3\text{-}8$$

where V_{Ed} is the design value of the applied shear force (N), d is the effective slab depth (mm), u_i is the length of the perimeter being considered (mm) and β is a unitless parameter which accounts for stress increases due to eccentric shear or unbalanced moment [34].

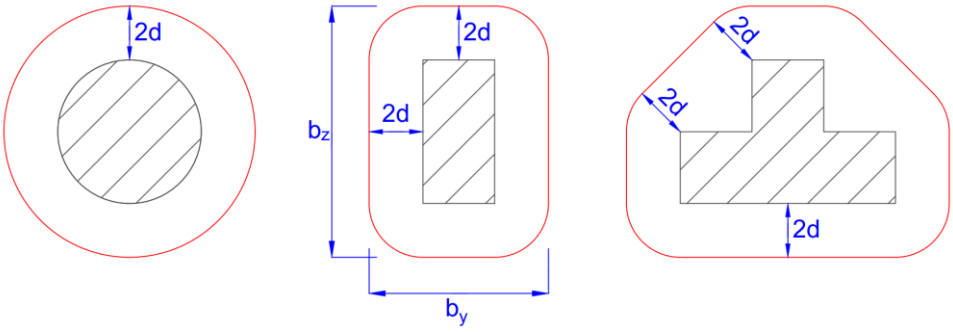


Figure 3-6: Critical Perimeter for Slab-Column Connections Without Shear Reinforcement Assumed in Eurocode 2 (2004)

For a slab-column connection subjected to concentric loading only, β is equal to 1. For connections subjected to combined shear and uniaxial unbalanced moment β can be calculated using equation 3-9, or taken as 1.15 for interior slab-column connections where the lateral stability of the structure is not dependent on the frame action of the flat plate system and the adjacent span lengths do not differ by more than 25%

$$\beta = 1 + k\left(\frac{M_{Ed}}{V_{Ed}}\right)\left(\frac{u_1}{W_1}\right) \quad 3\text{-}9$$

where M_{Ed} is the design value of the internal bending moment (Nmm), u_1 is the length of the critical perimeter at *2d* from the column face (mm), k is a coefficient which is dependent on the column aspect ratio (c_1/c_2) and W_1 is a term which corresponds to the shear stress distribution assumed in EC2 (2004) (mm^2) [34] For R-SCCs, k can be taken from Table 3-1 and W_1 can be calculated using equation 3-10

$$W_1 = (c_1/2)^2 + c_1c_2 + 4c_2d + 16d^2 + 2\pi dc_1 \quad 3\text{-}10$$

where c_1 and c_2 are the column dimensions parallel and perpendicular to the eccentricity of the load, respectively [34]. For interior R-SCCs subjected to combined shear and biaxial unbalanced moments, equation 3-11 can be used to approximate β

$$\beta = 1 + 1.8\sqrt{\left(\frac{e_y}{b_z}\right)^2 + \left(\frac{e_z}{b_y}\right)^2} \quad 3\text{-}11$$

where e_y and e_z are the eccentricities along the *y* and *z* axes (mm), respectively, and b_y and b_z are dimensions of the critical perimeter as shown in Figure 3-6 (mm) [34]. It should be noted that while EC2 (2004) explicitly defines critical perimeters for SS-SCCs, no equations for β or k are provided.

Table 3-1: Values of *k* for Rectangular Columns [34]

c_1/c_2	≤0.5	1.0	2.0	≥3.0
k	0.45	0.60	0.70	0.80

The punching shear resistance along the critical perimeter at *2d* from the column face for a slab-column connection without shear reinforcement, $v_{Rd,c}$ (MPa) can be calculated using equation 3-12

$$v_{Rd,c} = C_{Rd,c}k(100\rho_l f_{ck})^{\frac{1}{3}} \quad 3\text{-}12$$

where f_{ck} is the characteristic concrete compressive strength (MPa), k is the size effect factor, which is calculated as $1 + \sqrt{200/d} \leq 2.0$, where d is the effective slab depth (mm), ρ_l is a term related to the flexural reinforcement of the slab, calculated as $\sqrt{\rho_{ly}\rho_{lz}} \leq 0.02$, where ρ_{ly} and ρ_{lz} are the slab reinforcement ratios for a slab width equal to the column width plus *3d* on each side of the column in each orthogonal direction and $C_{Rd,c}$ is a constant equal to $0.18/\gamma_c$, where γ_c is a safety factor taken from the national annexes (typically equal to 1.5) [34].

Since equation 3-12 approaches 0 as the slab reinforcing ratio approaches 0, which was also an issue with the Model Code 1990 [159], equation 3-13 was added to calculate the minimum punching capacity along the critical perimeter, v_{min} (MPa) [34].

$$v_{min} = 0.035k^{\frac{3}{2}}f_{ck}^{\frac{1}{2}} \quad 3\text{-}13$$

The punching shear resistance along the column perimeter, $v_{Rd,max}$ (MPa), is calculated using 3-14

$$v_{Rd,max} = 0.4[0.6(1 - f_{ck}/250)]f_{cd} \quad 3\text{-}14$$

where f_{cd} is the design concrete strength (MPa), which is calculated as $\alpha_{cc}f_{ck}/\gamma_c$, where α_{cc} is a factor to account for the influence of long-term effects on concrete strength, though its recommended value is 1 [34]. It should be noted that the $1 - f_{ck}/250$ term in equation 3-14 is intended to account for the reduced strength of the compression struts in cracked concrete due to lateral tensile stresses [281, 295].

3.4.2.2 prEC2 (2020)

Unlike EN 1992-1-1, which requires shear stress checks at the column and critical perimeter, prEC2 (2020) only requires checks along the critical perimeter. Additionally, in prEC2, the critical perimeter has been revised to match that used in *fib* Model Code 2010 (note this critical perimeter will be shown in Section 3.5). Therefore, the distance between the column face and critical perimeter has been reduced from *2d* to $0.5d_v$, (note d_v is the shear resisting effective depth, which is commonly equal to the effective slab depth, *d*)

According to prEC2 (2020) the applied shear stress demand along the considered critical perimeter, τ_{Ed} (MPa) can be calculated using equation 3-15

$$\tau_{Ed} = \beta_e \left(\frac{V_{Ed}}{b_{0,5} d_v} \right) \tag{3-15}$$

where V_{Ed} is the design shear force at the critical perimeter (N), $b_{0,5}$ is the length of the critical perimeter located at $0.5d_v$ from the column face (mm) and β_e is a unitless coefficient accounting for the concentration of shear forces [280].

For a slab-column connection subjected to concentric loading only, β is equal to 1. For connections subjected to combined shear and uniaxial unbalanced moment, β can be calculated using equation 3-16, or taken as 1.15 for interior slab-column connections where the lateral stability of the structure is not dependent on the frame action of the flat plate system, the adjacent span lengths do not differ by more than 25%, the slab is subjected to uniformly distributed loads and the moments transferred to the edge and corner columns do not exceed a specified maximum value. For the slab-wall end connections and slab-wall corner connections, β_e is equal to 1.4 and 1.2, respectively.

$$\beta_e = 1 + 1.1 \frac{e_b}{b_b} \tag{3-16}$$

where b_b is the geometric mean of the minimum and maximum overall widths of the critical perimeter (mm), and e_b is the eccentricity (mm), which is calculated using equation 3-17

$$e_b = \sqrt{\left(e_{b,x}\right)^2 + \left(e_{b,y}\right)^2} \tag{3-17}$$

where $e_{b,x}$ and $e_{b,y}$ are the components of the eccentricity of the applied shear force with respect to the critical perimeter centroid (mm) [280].

The punching shear resistance along the critical perimeter at *0.5d_v* from the column face for a slab-column connection without shear reinforcement, $\tau_{Rd,c}$ (MPa) can be calculated using equation 3-18

$$\tau_{Rd,c} = \frac{0.6}{\gamma_v} k_{pb} \left(100 \rho_l f_{ck} \frac{d_{dg}}{d_v}\right)^{\frac{1}{3}} \leq \frac{0.6}{\gamma_v} \sqrt{f_{ck}} \quad 3\text{-}18$$

where f_{ck} is the characteristic concrete compressive strength (MPa), ρ_l is a term related to the flexural reinforcement of the slab, calculated as $\sqrt{\rho_{lx}\rho_{ly}}$, where ρ_{lx} and ρ_{ly} are the slab reinforcement ratios for a slab width equal to the column width plus *3d* on each side of the column in each orthogonal direction, γ_v is a constant used when estimating the punching shear capacity of connections without shear reinforcement (note, the value of γ_v is dependent on the limit state being considered), d_{dg} is a size parameter describing the failure zone roughness which is calculated using equation 3-19 (mm), and k_{pb} is the punching shear gradient enhancement coefficient which is calculated using equation 3-20

$$d_{dg} = \begin{Bmatrix} 16mm + D_{lower} \leq 40 \; when \; f_{ck} \leq 60MPa \\ 16mm + D_{lower}(60/f_{ck})^4 \leq 40 \; when \; f_{ck} > 60MPa \end{Bmatrix} \quad 3\text{-}19$$

where D_{lower} is the smallest permitted value of the upper sieve size *D* in an aggregate for the coarsest fraction of aggregates in the concrete according to EN 206 [280].

$$1 \leq k_{pb} = 3.6 \sqrt{1 - \frac{b_0}{b_{0,5}}} \leq 2.5 \quad 3\text{-}20$$

where b_0 is the length of the column perimeter, which is constructed to minimize its length in the case of SS-SCCs [280].

Like EC2 (2004), prEC2 (2020) also includes an equation to calculate the minimum shear resistance provided by the concrete. If the shear stress demand, τ_{Ed} is less than the minimum resistance, $\tau_{Rdc,min}$ (MPa), which is calculated using equation 3-21, more detailed punching shear checks are not required.

$$\tau_{Rdc,min} = \frac{11}{\gamma_v} \sqrt{\frac{f_{ck} d_{dg}}{f_{yd} d}} \quad 3\text{-}21$$

where f_{yd} is the design value of the yield strength which has been used to design the flexural reinforcement (MPa) and d is the effective flexural depth (mm) [280].

3.5 *fib* Model Code 2010

3.5.1 Historical Development

Unlike ACI 318-19 [2] and EC2 (2004) [34], the Model Codes are not legally binding codes and are instead intended to summarize the current state-of-the-art and to serve as starting points from which countries and code committees can develop design provisions for reinforced concrete design. The most recent Model Code, published by the International Federation for Structural Concrete (*fib*, formally known as CEB-FIP), Model Code 2010 [35], represents the state-of-the-art knowledge regarding material behaviour, analysis and design of concrete structures [35, 298].

Model Code 2010, which is the third published model code, represents a significant change in code philosophy. Unlike Model Code 1978 [53] and Model Code 1990 [159], where the punching provisions were largely derived from empirical results, the Model Code 2010 provisions are based on the Critical Shear Crack Theory (CSCT), which is a mechanical model for punching shear [269, 295, 299, 300] (previously presented in Chapter 2). Secondly, since the punching shear design provisions are mechanically based, Model Code 2010 also introduced a level of approximation (LoA) approach, which provides practitioners with the option to select the level of accuracy required. For preliminary and initial designs, simplified procedures, which are suitable for hand calculations, are provided, whereas more advanced methods are available for the design of critical members or the assessment of existing structures. Four levels of approximation are available for punching shear design. With each increasing LoA the time required for the analysis increases, but the final results should be more accurate and less conservative, though still safe. The LoA approach cannot be implemented into empirically-based codes (like ACI 318-19 and EC2 (2004)) since it requires the provisions to be based on mechanical models so that the relationships between the simplified and complicated models are clear to practitioners [301].

3.5.2 Design Provisions for Connections Without Shear Reinforcement

Unlike ACI 318-19 [2], EC2 (2004) [34], and prEC2 (2020) [280], which are formulated in terms of the critical perimeter shear stresses, *fib* Model Code 2010 is formulated in terms of total shear force capacity. The shear resistance provided by the slab concrete, $V_{Rd,c}$ (N), is calculated using equation 3-22.

$$V_{Rd,c} = k_{\psi}\sqrt{f_{ck}}b_0 d_v \qquad 3\text{-}22$$

where f_{ck} is the characteristic concrete compressive strength (MPa), b_0 is the length of the shear resisting control perimeter (mm), d_v is the shear resisting effective depth (mm, commonly equal to the effective slab depth, *d*) and k_ψ is a parameter dependent on the slab rotation [35].

The shear-resisting control perimeter, b_0, accounts for the non-uniformity of shear stresses along the critical perimeter due to support size, geometrical discontinuities in the slab, unbalanced moment and any concentrated loads near the slab-column connection. In the most general case, b_0 can be calculated using equation 3-23

$$b_0 = V_{Ed}/v_{perp,d,max} \quad 3\text{-}23$$

where V_{Ed} is the design value of the applied shear force (N) and $v_{perp,d,max}$ is the maximum shear force per unit length perpendicular to the basic control perimeter (N/mm), b_1 [35]. The basic control perimeter in Model Code 2010 is located at a distance of $0.5d_v$ from the column face and has curved corners, as shown in Figure 3-7 (note the control perimeters in Figure 3-7 are for slab-column connections only, for the basic control perimeter around SWCs see Figure 2-14d).

However, equation 3-23 requires numerical analysis to determine $v_{perp,d,max}$. In cases without large concentrated loads near the slab-column connection b_0 can be calculated using equation 3-24.

$$b_0 = k_e b_{1,red} \quad 3\text{-}24$$

where k_e is the coefficient of eccentricity, which is calculated using equation 3-25 and $b_{1,red}$ is the reduced basic control perimeter, which accounts for stress concentrations due to the support size and the presence of slab openings near the connection (mm).

$$k_e = 1/\left(1 + \frac{e_u}{b_u}\right) \quad 3\text{-}25$$

where e_u is the eccentricity of the resultant shear force with respect to the centroid of b_1 (mm, note in design the centroid of b_1 can be determined by considering b_1 to have straight corners) and b_u is the diameter of a circle with the same surface as the region inside b_1 (mm). In cases where the lateral stability of the structure is not dependent on the frame action of the flat plate system and where adjacent spans do not differ by more than 25% approximate values of k_e can be used (0.9 for interior columns and 0.75 for wall corners) [35].

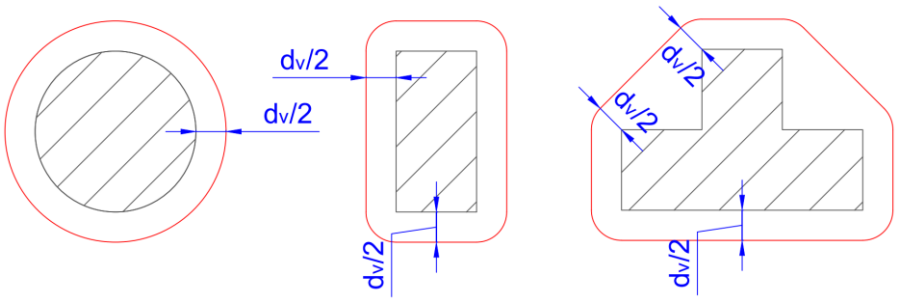


Figure 3-7: Basic Control Perimeter Assumed in *fib* Model Code 2010 and prEC2 (2020)

To account for stress concentrations at the corners of large supports, Model Code 2010 limits the length of the straight portions of the basic control perimeter to a maximum length of $3d_v$ as shown in Figure 3-8. Any portions of the critical perimeter beyond the end of the straight regions are neglected, leading to $b_{1,red}$. It should be noted that Model Code 1978 [53] also used a reduced effective critical perimeter length, shown in Figure 3-9, for the design of large columns, since it was concluded that the use of a critical perimeter at *d/2* from the support face lead to unconservative punching capacity estimates for large columns [302]. However, unlike Model Code 2010, where portions of the control perimeter are assumed to provide no capacity, the effective critical perimeter in Model Code 1978 is divided into two-way shear regions, near the column corners, and one-way shear regions, which are assumed to have a lower capacity [53]. Additionally, as will be discussed in the next subsection, $b_{1,red}$ is further reduced if any slab openings or inserts are located within $5d_v$ of the column face.

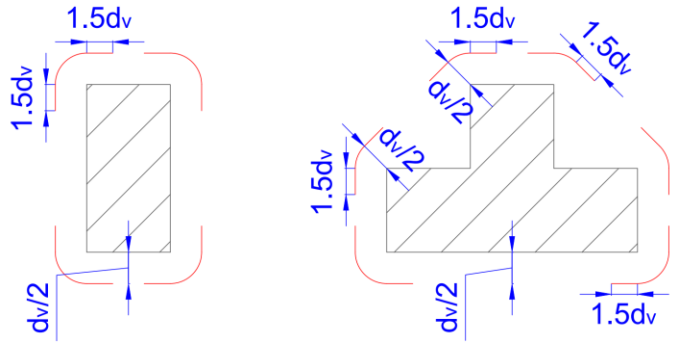


Figure 3-8: Definition of Reduced Basic Control Perimeter, $b_{1,red}$, to Account for Large Support Size (Model Code 2010) (same perimeter also used in prEC2 (2020))

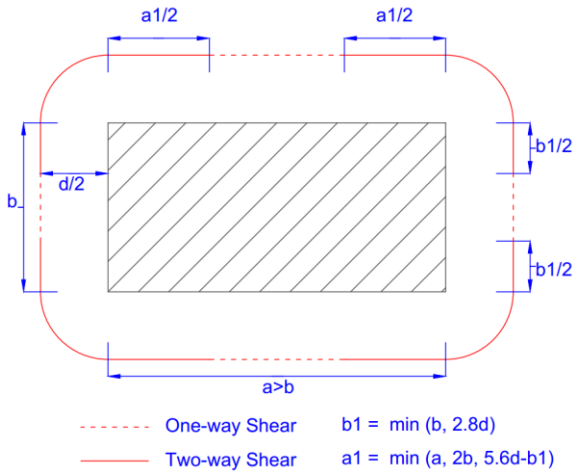


Figure 3-9: Critical Perimeter Around Large or Rectangular Columns Assumed in Model Code 1978 [53] (taken from [1])

The parameter which relates the concrete shear capacity to slab rotation, k_ψ, can be calculated according to equation 3-26.

$$k_\psi = \frac{1}{1.5 + 0.9\psi d k_{dg}} \qquad 3\text{-}26$$

where ψ is the slab rotation (rad) and k_{dg} is a parameter accounting for the maximum aggregate size, d_g (mm), which is calculated according to equation 3-27 [35].

$$k_{dg} = \frac{32}{16 + d_g} \geq 0.75 \qquad 3\text{-}27$$

Model Code 2010 provides four levels of approximation (LoA) to estimate ψ. The first LoA, LoA I, is intended for preliminary design and is based on the assumption that all flexural reinforcement over the support strip yields at failure. Due to this assumption, very large crack widths are assumed, which results in a significantly lower punching capacity according to the CSCT. If a slab-column connection is adequate for punching according to LoA I, the final design will likely be very safe as the overall connection design will be governed by a flexural failure of the slab, and the failure will likely be ductile [299]. According to LoA I, ψ can be calculated using equation 3-28

$$\psi = 1.5 \frac{r_s}{d} \frac{f_{yd}}{E_s} \qquad 3\text{-}28$$

where r_s is the location where the radial bending moment is equal to 0 (mm, typically assumed as approximately 0.22 times the clear span) and f_{yd} and E_s are the yield strength and elastic modulus of the flexural reinforcement (MPa), respectively [35].

LoA II, which is based on a simplified approximation of the moment capacity per unit length of the support strip, has been found to result in fairly accurate punching capacity estimates [11, 269, 299] and is generally recommended for the design of new structures [45, 235]. In LoA II, an analytical equation is used to approximate the moment capacity of the support strip. This analytical equation relates the moment in the support strip to the shear forces in the strip and the moment transferred from the slab to the support region accounting for any eccentricity [299]. According to LoA II, ψ can be calculated according to equation 3-29

$$\psi = 1.5\frac{r_s}{d}\frac{f_{yd}}{E_s}\left(\frac{m_{Ed}}{m_{Rd}}\right)^{1.5} \quad 3\text{-}29$$

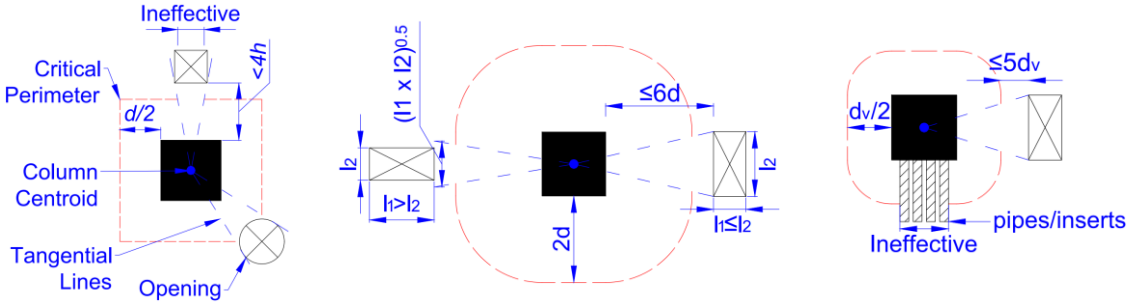
where m_{Ed} is the average moment per unit length for the calculation of the flexural reinforcement in the support strip (Nmm/mm) and m_{Rd} is the design average flexural strength per unit length in the support strip (Nmm/mm). It should be noted that to use LoA II in design ψ must be calculated in both orthogonal directions [35].

LoA III and IV both require numerical analysis to estimate ψ, and therefore, are recommended for use in special cases or in the analysis of existing structures (LoA IV is only recommended in cases where very accurate capacity estimates are required) [235]. Similar to LoA II, LoA III uses an analytical equation to estimate slab rotation, but LoA III allows designers to improve the estimate for ψ by using linear elastic FEA to estimate the slab's moment field, which also improves the estimate of $V_{Rd,c}$. Since the moment is more accurately estimated, ψ is calculated using equation 3-29, but with the coefficient of 1.5 reduced to 1.2 [35, 299]. The reduction of the coefficient in equation 3-29 is equivalent to assuming a stiffer slab response as it results in a smaller rotation, and therefore a smaller crack width and a higher punching capacity [299].

In LoA IV, NLFEA is used to estimate ψ directly [35]. LoA IV is only recommended for slabs with low flexural reinforcing ratios, or where significant moment redistribution is expected, as in other cases predictions according to LoA III and IV will be similar [299] (with those according to LoA IV requiring significantly more time and computational resources). As with all NLFEA, the use of LoA IV requires an experienced practitioner and proper model calibration [299].

3.6 Treatment of Openings

As discussed in Chapter 2, slab openings near a slab-column connection can significantly reduce the connection's punching shear capacity due to the interruption of the stress transfer between the slab and the column, and in the case of nonsymmetric opening layouts, the introduction of an unbalanced moment due to the eccentricity between the lines of action of the applied load and resisting forces [225]. Current punching shear design provisions typically account for the negative influence of slab openings on punching capacity by neglecting the portion of the critical perimeter bounded by lines which originate from the column centroid and are tangent to the opening boundaries as shown in Figure 3-10. As with the use of the critical perimeter concept for punching shear design, the treatment of openings is generally similar between codes, though there are key differences, as discussed below.



a) ACI 318-19 [2] b) Eurocode 2 (2004) [34] c) *fib* Model Code 2010 [35] and prEC2 (2020) [280]

Figure 3-10: Treatment of Slab Openings According to Worldwide Design Codes

Firstly, design codes differ in the location of openings assumed to influence punching shear as shown in Figure 3-10. EC2 (2004) [34] and Model Code 2010 [35] consider openings within *6d* and $5.5d_v$ of the column face, respectively, to negatively influence punching shear (note prEC2 [280] also considers openings within $5.5d_v$). On the other hand, ACI 318-19 [2] considers openings within *4h* of the column face to influence punching shear (note, *d* for slabs is typically between *0.8h-0.9h*, so *4h* is typically between approximately *4.5d-5d*). It should be noted that in all previous versions of ACI 318, between ACI 318-63 [51], where the opening provisions were introduced, and ACI 318-14 [84], openings within *10h* of the column face were assumed to negatively influence punching shear. The distance of *10h*, which was proposed by Hanson and Hanson [144] and is still used in CSA A23.3-19 [36], was revised to *4h* in ACI 318-19 [2] based on the results of NLFEA of slabs with openings by Genikomsou and Polak [200] and has since been verified by other researchers [213, 214].

Secondly, ACI 318-19 does not account for the opening type or orientation with respect to the column whereas European provisions do. As shown in Figure 3-10b, EC2 (2004) includes provisions to account for the opening orientation with respect to the column. When the opening dimension in the radial direction, l_1, exceeds the opening dimension in the transverse direction, l_2 (see Figure 3-10b for definitions of l_1 and l_2), EC2 (2004) considers a larger fictitious transverse dimension equal to $\sqrt{l_1 l_2}$. While Model Code 2010 and prEC2 (2020) do not consider the opening orientation they do consider the opening type. When an opening removes the entire slab depth the neglected portion of the critical perimeter is bounded by lines which originate from the column centroid and are tangent to the opening, which is consistent with ACI 318-19 and EC2 (2004). However, when an opening only partially removes the slab depth, which occurs for internal pipes or inserts, a smaller neglected region, which is bounded by straight projections from the limits of the reduced depth area, as shown in Figure 3-10c, is considered. Therefore, Model Code 2010 and prEC2 (2020) suggest that openings which do not penetrate the entire slab depth have less of a negative influence on punching capacity than those which remove the entire slab depth.

Chapter 4: Overview of the Mechanical Behaviour of Concrete and Its Modelling Using the Concrete Damaged Plasticity (CDP) Model in Abaqus

In this chapter, brief overviews of the short-term behaviour of concrete subjected to compressive and tensile loads are provided in Section 4.1 (note, the information presented in this section is largely based on that originally presented in the author's MASc thesis). Additionally, a summary of the Concrete Damaged Plasticity (CDP) model in Abaqus is provided in Section 4.2. For discussions of the behaviour of concrete under long-term loading (which is influenced by creep and shrinkage) and the other available concrete material models in Abaqus the reader is referred to [10] and [235, 303, 304, 305], respectively. An overview of the general theory of plasticity with respect to concrete modelling is also provided in [235, 305] (detailed discussions of plasticity theory can be found in [306, 307].

4.1 Overview of Mechanical Behaviour of Concrete

4.1.1 Uniaxial Compressive Behaviour

Other than water, the two primary constituents of concrete are cement paste and aggregates (coarse and fine). Both primary constituents are fundamentally linear elastic, brittle materials when subjected to uniaxial compressive loads and typically fracture in the direction perpendicular to the principal tensile strain (which is parallel to the applied load in a uniaxial compression test). Therefore, when concrete is subjected to uniaxial compression, cracks form parallel to the direction of the applied load. However, even though the two primary constituents are linear elastic, brittle materials, the uniaxial compressive stress-strain response of concrete is nonlinear and displays some limited ductility, as shown in Figure 4-1, due to the development of microcracking within the concrete and stress redistributions from cracked to uncracked regions. Two primary types of microcracks exist. The first type, which occurs along the interface of the aggregates and the surrounding cement, is referred to as a bond crack. The second type, which develops in the mortar between the aggregates, is referred to as a mortar crack [10]. In the following paragraphs, the four primary stages of microcracking which occur when concrete is subjected to uniaxial compressive loads are discussed.

As concrete cures, the aggregates restrain the shrinkage of the cement paste, which causes tensile stresses to develop within the concrete matrix. Once large enough, these internal tensile stresses result

in cracks, which are referred to as no-load bond cracks. These no-load bond cracks, which are formed before any additional load is applied to the concrete, have a minimal influence on the uniaxial compressive behaviour of the concrete under low load levels. Even though some cracking has already occurred before any load is applied, the initial portion of the uniaxial compressive stress-strain response is still approximately linear, as shown in Figure 4-1, until the compressive stress reaches a magnitude approximately equal to 30% of the concrete's compressive strength, f_c' [10].

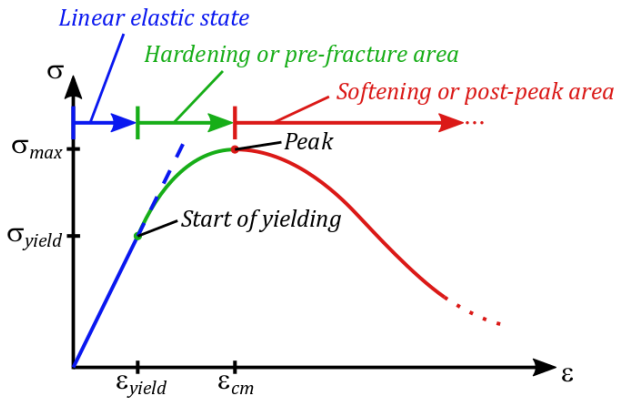


Figure 4-1: Typical Uniaxial Compressive Stress-Strain Response for Normal Strength Concrete (Note, in Accordance with the Theory of Plasticity "Yielding" Represents When the Material Response Leaves the Elastic Region and Enters the Plastic Region)

Bond cracks, which occur when the tensile and shear stress capacity of inclined planes along the cement paste-aggregate interface are exceeded, begin to form when the internal stress in the concrete reaches approximately 30-40% of f_c'. However, since the applied load is still relatively low, and the concrete is largely uncracked, the crack propagation is stable at this stage, and the cracks do not grow in size unless the applied load is increased. Additionally, the formation of bond cracks represents the transition point from linear elastic to nonlinear behaviour (marked as the "start of yielding" in Figure 4-1), as the stresses are now being redistributed from cracked to uncracked regions of the concrete [10].

As the applied uniaxial compressive load reaches approximately 50-60% of the ultimate compressive capacity of the concrete, localized mortar cracks, which occur due to the transverse tensile strains and are parallel to the applied compressive load, form between the previously developed bond cracks. At this stage of loading overall crack propagation is still stable, though the onset of localized mortar cracking is typically referred to as the discontinuity limit [10].

A critical stress level is achieved when the applied load reaches approximately 75-80% of the ultimate load capacity of the concrete. At this point, the uniaxial compressive stress-strain response becomes increasingly nonlinear due to an increase in the number of mortar cracks and the development of a continuous microcracking pattern. At the critical stress level, the overall amount of cracking, the lateral tensile strains and the volumetric strains, which are a function of both the axial compressive strain and the lateral tensile strain, increase rapidly. Additionally, the crack propagation becomes unstable, and cracks continue to grow even when the applied load is kept constant. The ultimate compressive capacity of the concrete, f_c', is achieved when the uncracked regions can no longer carry any additional load. Further loading results in the descending portion of the stress-strain response (which is denoted as the softening or post-peak area in Figure 4-1) where a decrease in stress is observed for an increasing strain [10].

However, the response of the concrete between the critical stress level and f_c' is also dependent on other factors. Firstly, if the concrete is subjected to a compressive stress gradient instead of uniform compressive stress (which occurs in the compression zone of a beam in bending), the onset of unstable crack propagation is delayed as stresses can be redistributed from the regions of highest strain to regions of lower strain. Additionally, if transverse reinforcement is provided within the concrete, the volumetric strains induce pressure on this reinforcement. These pressures resist the lateral expansion of the concrete and delay the occurrence of failure [10] (note, confinement can also be caused by biaxial or triaxial loading).

Some typical trends with respect to the uniaxial compressive behaviour of concrete are as follows [10]:

- The uncracked modulus of elasticity increases as the compressive strength, f_c', increases.
- A parabola can be used to approximate the ascending portion of the uniaxial compressive stress-strain response (the ascending portion includes both the linear elastic state and the hardening or pre-fracture area shown in Figure 4-1), though it must be noted that the ascending portion becomes increasingly linear as f_c' increases.
- As f_c' increases the strain corresponding to f_c', ϵ_c', increases, whereas the maximum strain at failure (end of the softening or post-peak area in Figure 4-1), ϵ_u, decreases.
- The slope of the descending portion of the stress-strain response is also dependent on f_c', and generally increases as f_c' increases. Though for f_c' values less than approximately

40MPa, the slope of the descending region is typically less than that of the ascending region. On the other hand, for high f_c' values (i.e. f_c' > approximately 70MPa), the descending portion is nearly vertical, which demonstrates that high-strength concrete is very brittle and fails shortly after achieving f_c' with limited ductility. It should also be noted that the descending portion of the uniaxial compressive stress-strain response is highly variable and dependent on the testing procedure. Additionally, the maximum compressive strain is a function of the specimen type, loading conditions and loading rate, and tends to be higher if the potential for load redistribution exists at high loads.

4.1.2 Uniaxial Tensile Behaviour

Concrete is much weaker in tension than compression, with the uniaxial tensile strength typically being equal to approximately 8-15% of the uniaxial compressive strength. Due to the low maximum tensile stress, the tensile stress-strain response of concrete is typically approximated as linear, even though the response is slightly nonlinear in reality [10]. As stated by MacGregor and Bartlett [10] "After the tensile strength is reached microcracking occurs in a fracture process zone adjacent to the point of the highest tensile stress, and the tensile capacity of the concrete drops very rapidly with increasing [crack] elongation" (p. 64). Simultaneously, the concrete outside the fracture process zone unloads elastically while the elongations concentrate in the concrete within the fracture process zone. In numerical modelling, it is common to model the uniaxial tensile response of concrete with a tensile stress-crack opening relationship (the inputted relationships for the uniaxial compressive and tensile responses used in the FEMs herein are discussed in Section 6.3.2). In such models, the full formation of a crack corresponds to a tensile capacity of 0 [10].

4.1.3 Behaviour Under Biaxial or Triaxial Loads

The behaviour of concrete under uniaxial conditions is different than its behaviour under biaxial or triaxial conditions. Numerous researchers have studied the mechanical behaviour of concrete under different load conditions, with the most famous being the work of Kupfer, Hilsdorf and Rüsch [308]. A summary of the main conclusions of these studies based on the discussion provided in [10] is provided in the following paragraphs.

As discussed previously, tensile cracking parallel to the direction of the applied load leads to the failure of the concrete under uniaxial compressive loading. However, under biaxial or triaxial compressive loading, the onset of unstable crack propagation is delayed (i.e. the critical stress level is

increased) due to the additional compressive loading delaying crack formation. Therefore, the biaxial or triaxial compressive stress-strain response of concrete is stronger and more ductile than the uniaxial response [10].

On the other hand, the tensile response of concrete is typically not improved by multiaxial loading. For example, when a concrete specimen is subjected to biaxial tensile loading the observed tensile strength is similar to that observed under uniaxial tension, and the failure occurs perpendicular to the direction of the maximum tensile stress. Additionally, a specimen which is subjected to compressive loading in one direction and tension loading in another will usually fail on planes which are perpendicular to the maximum tensile stress at a compressive or tensile load less than the respective uniaxial strengths [10].

4.2 Overview of the Concrete Damaged Plasticity (CDP) Model in Abaqus

The Concrete Damaged Plasticity (CDP) model in Abaqus, which is a continuum, plasticity-based damage model [303], is based on the model proposed by Lubliner et al. [309] and includes the modifications proposed by Lee and Fenves [310] [304]. The CDP model is intended to be used to model concrete and other quasi-brittle materials subjected to monotonic, cyclic or dynamic loading under low confining pressures. A non-associated flow rule (the meaning of associated or non-associated flow is discussed briefly in subsection 4.2.4.3) which considers independent hardening variables in tension and compression is used to model the irreversible damage due to fracturing. With respect to concrete, the model assumes that the two primary failure mechanisms are tensile cracking and compressive crushing. Additionally, isotropic damaged elasticity is combined with isotropic tensile and compressive plasticity to model the inelastic response of concrete.

In addition to the CDP model, which is available in both Abaqus/Standard and Abaqus/Explicit (though the use of viscoplastic regularization to improve convergence is only available in Abaqus/Standard [303]), two other material models for concrete are included in Abaqus. These models are the Smeared Crack Model (SCM), which is available in Abaqus/Standard, and the Brittle Cracking Model (BCM), which is available in Abaqus/Explicit.

The SCM, which is a traditional concrete model [311], is intended to be used to model concrete subjected to primarily monotonic loading under low confining pressures [303]. In the SCM, concrete cracking is assumed to be critical, and therefore, cracking and post-cracking behaviour dominates the modelling. The integration point stresses and a crack detection surface are used to determine if

cracking has occurred. The formation of individual cracks is not tracked in the model. Instead, a smeared crack approach, which involves modifying the stresses and material stiffnesses to account for cracking is used. When the loading primarily leads to compressive principal stresses a simplified elastic-plastic theory, which considers only the first two stress invariants is used. The simplified yield surface used in the SCM, which is based on an associated flow rule and isotropic hardening, is known to lead to inaccurate results in some cases (the third stress invariant would need to be included to make the model more general). Compared to the CDP model, the SCM includes many simplifications with the goal of improving computational efficiency [303, 304].

While the BCM can be used to model concrete (note, it can also be used to model ceramics or brittle rocks) in all types of structures, it is intended for applications where the material response is dominated by tensile cracking. Unlike the CDP model and the SCM, which allow the user to specify the uniaxial compressive stress-strain response, the BCM assumes a linear elastic compression response. As such, the BCM is only suitable for use when the brittle tensile behaviour dominates the response, otherwise, the simplified compression response will lead to inaccurate results.

Therefore, based on the above discussions, previous FEA work at the University of Waterloo [235, 246, 247, 305, 312], and the fact that previous attempts [313] to apply the SCM for punching shear research have been unsuccessful (convergence issues occur due the associated flow rule overestimating the volumetric plastic strains) the CDP model was selected for use in this work (note, the adequacy of the CDP for modelling punching shear has also been demonstrated by many [108, 218, 244, 248, 249, 250, 251, 252, 253, 254]). In the following sections, a brief discussion of the CDP model is provided.

4.2.1 Modelling of Compressive Behaviour of Concrete

The typical shape of the uniaxial compressive stress-strain response assumed in the CDP model is provided in Figure 4-2a.

As discussed in Section 4.1.1, the initial uniaxial compressive response is assumed to be linear elastic until the initial compressive yield stress (which is specified by the user and marks the onset of plastic behaviour), σ_{co}, is reached. To model the linear elastic portion of the response, the user is only required to specify the initial elastic modulus of the undamaged material, E_0, and the Poisson's ratio, ν [303].

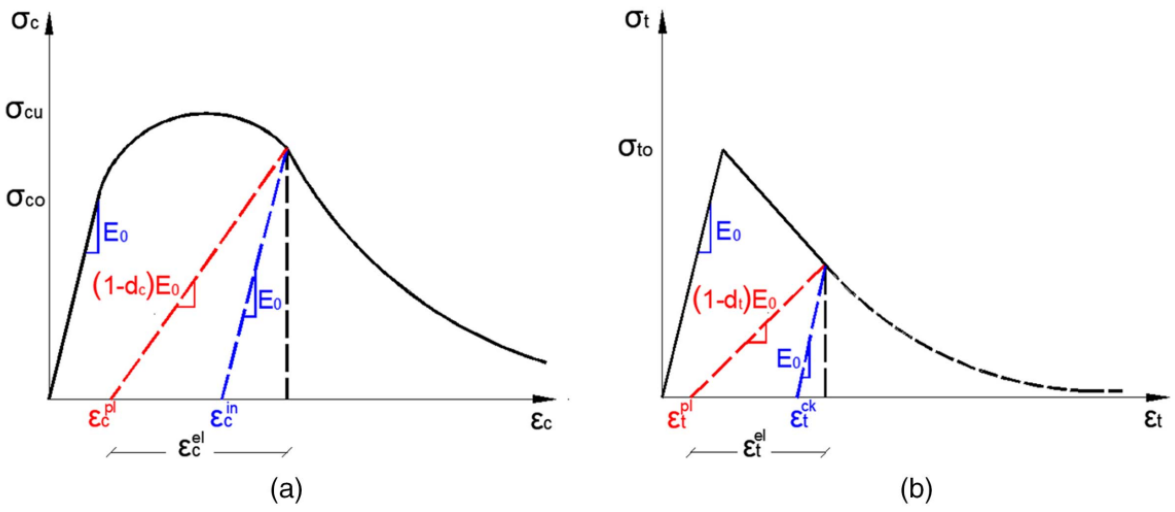


Figure 4-2: Typical Uniaxial Stress-Strain Responses Assumed in CDP Model, (a) Compression, (b) Tension [313], Used with permission of American Society of Civil Engineers, from Comparative Investigation of Concrete Plasticity Models for Nonlinear Finite-Element Analysis of Reinforced Concrete Specimens, Panahi and Genikomsou, volume 27, issue 2, ©2021; permission conveyed through Copyright Clearance Center, Inc.

After the initial yield stress is achieved, the concrete is assumed to undergo work hardening until the ultimate compressive stress, σ_{cu}. After achieving σ_{cu}, the concrete is then assumed to undergo strain-softening. To model the plastic portion of the uniaxial compressive response the user is required to enter tabular data corresponding to the stress-inelastic strain relationship [303]. The inelastic strain for a particular stress level, ϵ_c^{in}, is calculated according to equation 4-1 (a graphical representation of ϵ_c^{in} is provided in Figure 4-2a)

$$\epsilon_c^{in} = \epsilon_c - \epsilon_{0c}^{el} = \epsilon_c - \sigma_c/E_0 \qquad 4\text{-}1$$

where ϵ_c is the total compressive strain, ϵ_{0c}^{el} is the elastic compressive strain corresponding to the undamaged material (which is calculated as σ_c/E_0), σ_c is the compressive stress and E_0 is the initial modulus of elasticity of the undamaged material. Abaqus requires the inputted inelastic strains to be positively increasing values. Additionally, the user is required to specify the initial yield point, which corresponds to an inelastic strain of zero [303]. The specific relationships used to generate the inputted uniaxial compressive stress-strain responses are discussed in Section 6.3.2.

4.2.2 Modelling of Tensile Behaviour of Concrete

The general uniaxial tensile stress-strain relationship assumed in the CDP model is provided in Figure 4-2b.

As was discussed in Section 4.1.2, the uniaxial tensile stress-strain response is assumed to be linear elastic until the peak stress of σ_{to} (see Figure 4-2b). It should be noted that since the CDP model is based on the assumption of isotropic linear elasticity, the same initial undamaged elastic modulus is used for tension and compression (the same Poisson's ratio is also used).

The formation of microcracks is assumed to begin when σ_{to} is reached. After this point, a softening stress-strain response, which causes strain localization to occur in the concrete structure, is used to macroscopically model the crack formation. This softening response, which is referred to as tension stiffening in reinforced concrete, can be modelled using one of three methods in the CDP model [303].

In the first method, the user specifies the tensile stress-cracking strain response directly using tabular data (which is the same method used for the uniaxial compressive data). The tensile cracking strain, ϵ_t^{ck} is calculated according to equation 4-2 (a graphical representation of ϵ_t^{ck} is provided in Figure 4-2b)

$$\epsilon_t^{ck} = \epsilon_t - \epsilon_{0t}^{el} = \epsilon_t - \sigma_t/E_0 \qquad 4\text{-}2$$

where ϵ_t is the total tensile strain, ϵ_{0t}^{el} is the elastic tensile strain corresponding to the undamaged material (which is calculated as σ_t/E_0) and σ_t is the tensile stress [303]. This method has the advantage of allowing the user to control the post-peak tensile response, which allows the CDP model to be tailored to specific applications [305]. However, it must be noted that Abaqus imposes a lower bound on the post-peak tensile magnitude. This lower bound, which is equal to 1% of σ_{to}, and applies regardless of the method used to specify the softening response, is necessary to limit convergence issues when using the CDP model [303, 305]. However, for structures with limited or no reinforcement, directly specifying the post-peak tensile stress-cracking strain response causes the FEA results to be highly mesh sensitive. In such cases, the FEA results will not converge to a unique solution due to increased strain localization with decreasing mesh size [305]. Therefore, Abaqus provides two other methods to model the post-peak tensile response of the concrete.

To reduce the mesh sensitivity of results based on the CDP model, the second method allows the user to specify a tensile stress-cracking displacement response using tabular data (note, in literature

the cracking displacement is also referred to as crack width or crack opening). This method, which is based on the fracture energy proposal by Hillerborg et al. [314], treats the concrete fracture energy, G_f, which according to brittle fracture mechanics defines the energy to open a crack of a unit area, as a material property. Therefore, while this method retains the freedom to customize the post-peak response to a particular application, the post-peak tensile response is defined in terms of a stress-cracking displacement (opening) response instead of a stress-strain response. In this method, the user specifies the post-peak tensile stress-crack displacement response through tabular data. This method was used in this work since previous FEA at the University of Waterloo has shown that this method, and a bilinear post-peak tensile response, is adequate for modelling punching shear behaviour [1, 235, 246, 247]. The specific tensile stress-crack displacement response used in this work is discussed in Section 6.3.2.

The second alternative method to specify the post-peak tensile response also uses a tensile stress-crack displacement relationship, but only requires the user to specify G_f and σ_{to}. Unlike the previous method, which allows the user to input the tensile stress-crack displacement response directly, in this method a linear post-peak response is assumed. The maximum crack displacement corresponding to a complete loss of tensile strength, w_c is calculated according to equation 4-3, assuming that the area under the curve is equal to G_f [303].

$$w_c = [2G_f]/\sigma_{to} \tag{4-3}$$

4.2.3 Modelling of Damage

When the load applied to a concrete specimen in the post-elastic portion of its response is removed the unloading response is weaker (i.e. the elastic stiffness is lower) as shown in Figure 4-2. To quantify this loss of elastic stiffness the CDP model uses two damage variables, d_c and d_t (the physical definitions of d_c and d_t for uniaxial loading are provided in Figure 4-2). The magnitudes of these damage variables vary from 0, which represents an undamaged material, to 1, which represents a material with no remaining strength. Like the uniaxial stress-strain responses, the damage parameters are specified by the user as tabular data. Abaqus then calculates the damage parameters to be used in the simulation according to equations 4-4 and 4-5, respectively,

$$d_c = d_c\left(\tilde{\epsilon}_c^{pl}, \theta, f_i\right); \quad 0 \le d_c \le 1.0 \tag{4-4}$$

$$d_t = d_t\left(\tilde{\epsilon}_t^{pl}, \theta, f_i\right); \quad 0 \le d_t \le 1.0 \tag{4-5}$$

where $\tilde{\epsilon}_c^{pl}$ and $\tilde{\epsilon}_t^{pl}$ are the equivalent compressive and tensile strains, respectively, θ is the temperature and f_i are other predefined field variables [303] (note, temperature and other field variables are not considered in this work).

As shown in equations 4-4 and 4-5, d_c and d_t are functions of the plastic strains. However, Abaqus requires the user to specify the damage parameters in terms of inelastic or cracking strains. Therefore, Abaqus must convert the user-defined strain values to plastic strains.

Equation 4-6 is used to convert the user-defined inelastic compressive strains, $\tilde{\epsilon}_c^{in}$, into plastic compressive strains, $\tilde{\epsilon}_c^{pl}$ [303].

$$\tilde{\epsilon}_c^{pl} = \tilde{\epsilon}_c^{in} - \frac{d_c}{(1-d_c)}\frac{\sigma_c}{E_0} \tag{4-6}$$

If a stress-strain relationship is specified for the uniaxial tensile response equation 4-7 is used to convert the user-defined cracking tensile strains, $\tilde{\epsilon}_t^{ck}$, into plastic tensile strains, $\tilde{\epsilon}_t^{pl}$ [303].

$$\tilde{\epsilon}_t^{pl} = \tilde{\epsilon}_t^{ck} - \frac{d_t}{(1-d_t)}\frac{\sigma_t}{E_0} \tag{4-7}$$

On the other hand, if the uniaxial tensile response is specified using one of the two stress-cracking displacement relationships, the inputted cracking displacements, u_t^{ck}, are converted to plastic cracking displacements, u_t^{pl}, using equation 4-8

$$u_t^{pl} = u_t^{ck} - \frac{d_t}{(1-d_t)}\frac{\sigma_t l_0}{E_0} \tag{4-8}$$

where l_0 is the specimen length, which is assumed to equal 1.0 [303].

It should be noted that care must be taken when defining damage using the CDP model. Excessive damage can lead to significant convergence issues due to the creation of singularities. Therefore, the Abaqus user manual [303] recommends a maximum damage parameter magnitude of 0.99 (which is equivalent to a 99% loss in stiffness).

If damage parameters are specified (which is not necessary) the uniaxial compressive and tensile stress-strain responses are calculated according to equations 4-9 and 4-10, respectively.

$$\sigma_c = (1-d_c)E_0\left(\epsilon_c - \tilde{\epsilon}_c^{pl}\right) \tag{4-9}$$

$$\sigma_t = (1-d_t)E_0\left(\epsilon_t - \tilde{\epsilon}_t^{pl}\right) \tag{4-10}$$

As previously discussed, when concrete is subjected to uniaxial loads cracking will occur. This cracking reduces the total area which is available to transfer load, leading to an increase in the effective stress experienced by the concrete [304, 305]. Equations 4-11 and 4-12 are used to calculate the effective compressive stress, $\bar{\sigma}_c$, and effective tensile stress, $\bar{\sigma}_t$, respectively. These effective stresses, which are denoted the uniaxial effective cohesion stresses, control the size of the yield and loading surfaces within the plasticity portion of the CDP model [303, 305].

$$\bar{\sigma}_c = \frac{\sigma_c}{(1-d_c)} = E_0\left(\epsilon_c - \tilde{\epsilon}_c^{pl}\right) \quad 4\text{-}11$$

$$\bar{\sigma}_t = \frac{\sigma_t}{(1-d_t)} = E_0\left(\epsilon_t - \tilde{\epsilon}_t^{pl}\right) \quad 4\text{-}12$$

It should be noted that the above discussion of damage was focused on uniaxial conditions for simplicity. While damage parameters are also applicable to three-dimensional stress states, the mathematics are more complex and are not presented herein as damage is not considered in this work. Damage was not considered in this work following the recommendation of Genikomsou [235], though many other studies, including, but not limited to, [174, 249, 250], have also demonstrated that the inclusion of damage parameters is not necessary when modelling punching shear under monotonic conditions in Abaqus. Neglecting damage also has the additional benefit of simplifying the FEMs used herein. Therefore, only the plasticity portion of the CDP model is considered, and the inelastic strains are equal to the plastic strains in this work. Additionally, the CDP model also allows the user to specify stiffness recovery parameters for specimens which are subjected to cyclic loading. As all specimens in this work are subjected to monotonic loading only, these stiffness reduction factors were not considered; therefore, the corresponding mathematics are not presented herein. For a detailed discussion of the stiffness reduction parameters and the use of damage for three-dimensional stress states, the reader is referred to [303, 304, 310].

4.2.4 Modelling of Plasticity

The three primary components of plasticity models are the yield function, the hardening rule, and the plastic flow rule [305]. The details of each of these components are discussed in the following three subsections. Finally, viscoplastic regularization, which is available in Abaqus/Standard to improve convergence when using the CDP model, is discussed in subsection 4.2.4.4.

4.2.4.1 Yield Function

The CDP model uses the yield function proposed by Lubliner et al. [309], including the modifications to account for different strength evolutions in tension and compression proposed by Lee and Fenves [310] [303]. When expressed in terms of effective stresses, the CDP model yield function takes the form shown in equation 4-13, with the parameters α, β and γ defined according to equations 4-14, 4-15 and 4-16, respectively.

$$F = \frac{1}{1-\alpha}\left(\bar{q} - 3\alpha\bar{p} + \beta\left(\tilde{\epsilon}^{pl}\right)\langle\hat{\bar{\sigma}}_{max}\rangle - \gamma\langle-\hat{\bar{\sigma}}_{max}\rangle\right) - \bar{\sigma}_c\left(\tilde{\epsilon}_c^{pl}\right) \quad 4\text{-}13$$

$$\alpha = \frac{(\sigma_{bo}/\sigma_{co}) - 1}{2(\sigma_{bo}/\sigma_{co}) - 1}; 0 \leq \alpha \leq 0.5 \quad 4\text{-}14$$

$$\beta = \frac{\bar{\sigma}_c\left(\tilde{\epsilon}_c^{pl}\right)}{\bar{\sigma}_t\left(\tilde{\epsilon}_t^{pl}\right)}(1-\alpha) - (1+\alpha) \quad 4\text{-}15$$

$$\gamma = \frac{3(1-K_c)}{2K_c - 1} \quad 4\text{-}16$$

In equations 4-13 - 4-16, $\bar{\sigma}_c\left(\tilde{\epsilon}_c^{pl}\right)$ and $\bar{\sigma}_t\left(\tilde{\epsilon}_t^{pl}\right)$ are the effective compression and tensile cohesion stresses, respectively (note, $\bar{\sigma}_c\left(\tilde{\epsilon}_c^{pl}\right)$ is a function of the equivalent compressive plastic strain, $\tilde{\epsilon}_c^{pl}$, and $\bar{\sigma}_t\left(\tilde{\epsilon}_t^{pl}\right)$ is a function of the equivalent tensile plastic strain, $\tilde{\epsilon}_t^{pl}$), σ_{bo} is the initial equibiaxial compressive yield stress, σ_{co} is the initial uniaxial compressive yield stress, $\bar{q}$ is the Mises equivalent stress (note, $\bar{q} = \sqrt{\frac{3}{2}\bar{S}:\bar{S}} = \sqrt{3J_2}$, where J_2 is the second deviatoric stress invariant), $\bar{p}$ is the effective hydrostatic pressure stress (note, $\bar{p} = -I_1/3$, where I_1 is the first stress invariant) and $\hat{\bar{\sigma}}_{max}$ is the maximum principal effective stress [303, 305]. It should also be noted that the Macauley bracket $\langle\cdot\rangle$ is calculated as follows: $\langle x\rangle = \frac{1}{2}(|x| + x)$ [235].

The parameter α represents a material constant, and as seen in equation 4-14, is a function of the ratio of σ_{bo} to σ_{co}. Experimental tests have demonstrated that σ_{bo}/σ_{co} typically ranges from 1.1 to 1.16, corresponding to α values between 0.08 and 0.12 [304, 309]. In the tests of Kupfer et al. [308] the compressive strengths of specimens subjected to equal biaxial compression were 16% higher than those subjected to uniaxial compression, and therefore, the default value of σ_{bo}/σ_{co} in the CDP model in Abaqus is 1.16 [305] (the default value of α is therefore 0.12).

The parameter γ is also a material constant that only influences the yield function in states of triaxial compression (i.e. $\hat{\bar{\sigma}}_{max} < 0$) [304]. As shown in equation 4-16, γ is a function of the

parameter K_c, which is the ratio of the second stress invariant on the tensile meridian, $q(TM)$, to that on the compression meridian, $q(CM)$, for any given value of the hydrostatic pressure, $\bar{p}$, which results in a negative maximum principal stress. In Abaqus, the default value of K_c is 2/3 (which corresponds to γ = 3), though the user can specify any value greater than 0.5 and less than or equal to 1.0. It should be noted that the use of a constant value for K_c is not contradicted by experimental tests [304, 309] and these tests have also shown that K_c typically ranges from 0.64 to approximately 0.8 [309]. Additionally, K_c values of 0.5 and 1.0 result in yield surfaces which are equal to the Rankine yield surface and the Von Mises surface, respectively [315].The influence of K_c on the yield surface in the deviatoric plane and in three-dimensional stress space is shown in Figure 4-3 and Figure 4-4, respectively.

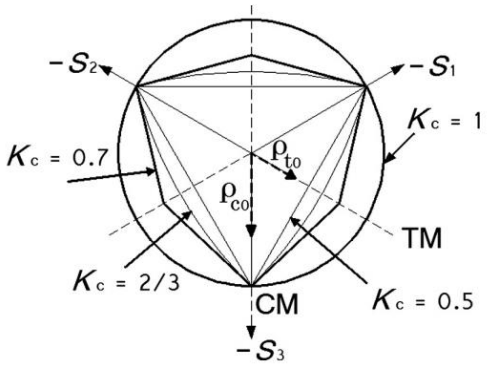
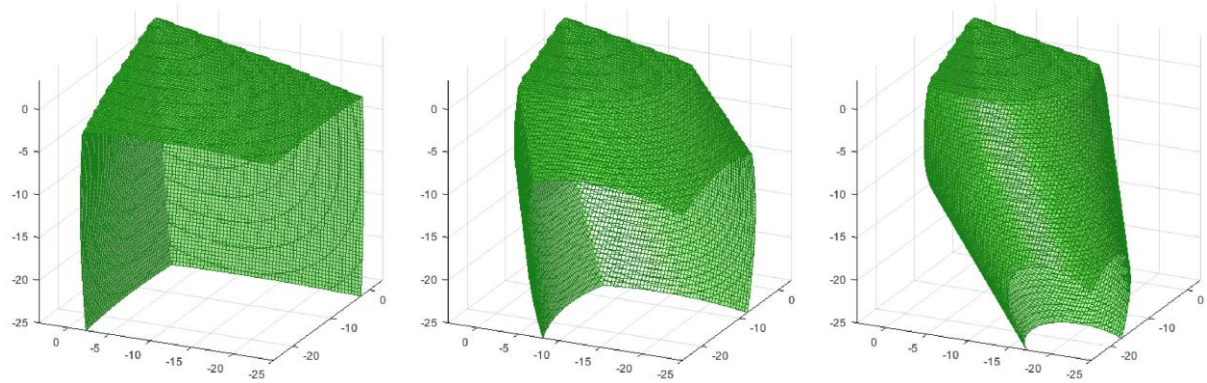


Figure 4-3: Influence of K_c on the CDP Model Yield Surface in the Deviatoric Plane [315]; Reprinted from Engineering Structures, Vol 132, Alfarah, López-Almansa and Oller, New Methodology for Calculating Damage Variables Evolution in Plastic Damage Model for RC Structures, 70-86, Copyright (2017), with permission from Elsevier

As shown in Figure 4-3, when K_c is equal to 1.0 the yield surface has a circular shape within the deviatoric plane. However, it is well known that the shear strength of concrete under biaxial compression (equal compressive stresses in the two principal axes with zero stress in the third principal direction) and triaxial compression are different [305]. Therefore, according to Yu et al. [316], a yield surface which accurately represents the experimentally observed behaviour of concrete should include the influence of the third deviatoric stress invariant and have a non-circular shape in the deviatoric plane [305]. For all simulations in this work, the default value of K_c (2/3) is assumed, which results in the yield surface having a non-circular shape within the deviatoric plane as shown in Figure 4-3, and is within the range of experimental values reported by Lubliner et al. [309].



(a) $K_c = 0.6$. (b) $K_c = 0.8$. (c) $K_c = 1.0$.

Figure 4-4: Influence of K_c on the CDP Model Yield Surface in Three-Dimensional Principal Stress Space (Note, for These Plots f'_t = 4MPa, f'_c = 40MPa, σ_{bo}/σ_{co} = 1.16 and an Initial Yield Stress of $0.4f'_c$ = 16MPa Were Assumed); Reprinted from Archives of Civil and Mechanical Engineering, Vol 19 Issue 4, Wosatko, Winnicki, Polak and Pamin, Role of dilatancy angle in plasticity-based models of concrete, 1268-1283, Copyright (2019), with permission from Elsevier

4.2.4.2 Hardening

In the original model proposed by Lubliner et al. [309], an isotopic hardening rule was used. However, due to the use of a single damage parameter, their model was adequate for monotonic loading only due to the different damage processes experienced by concrete under tension and compression loads. Therefore, Lee and Fenves [310] modified the model to make it adequate for both monotonic and cyclic loading by including two independent damage parameters, one for compression and one for tension. Therefore, in the CDP model in Abaqus, two hardening variables, $\tilde{\epsilon}_c^{pl}$ and $\tilde{\epsilon}_t^{pl}$, which are denoted the compressive and tensile equivalent plastic strains, respectively, control the evolution of the yield and loading surfaces [304, 309]. The equations used to calculate $\tilde{\epsilon}_c^{pl}$ and $\tilde{\epsilon}_t^{pl}$ were previously presented in Section 4.2.3.

4.2.4.3 Plastic Flow Rule

The link between the yield surface, denoted herein as *F*, and the stress-strain relationship is represented by the flow rule [306] [305]. In plasticity, the flow rule can either be "associated" or "non-associated." For associated flow rules, the plastic potential surface (also referred to as flow potential function), *G*, has the same shape as the current yield or loading surface (i.e. $F = G$). In other words, when using an associated flow rule the plastic flow is connected to the yield criterion and the

plastic flow develops normal to the loading/yield surface. If two different functions are used for *F* and *G* and these surfaces do not coincide (i.e. $F \neq G$) the flow rule is considered non-associated and the plastic flow develops normal to *G* [317] [305].

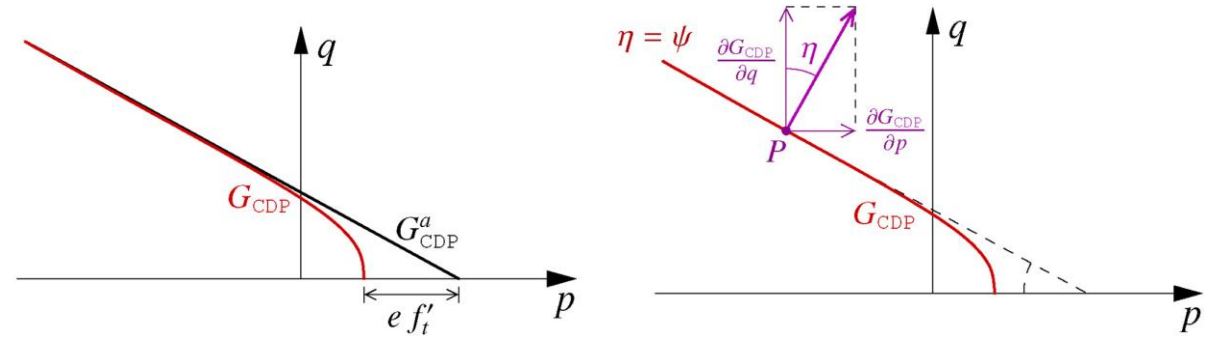
In the past, attempts have been made to model concrete behaviour using an associated flow rule. However, the associated flow rule is not valid to model the full response of concrete and can lead to large discrepancies between the predictions and experimental measurements [318] [305]. Additionally, the assumptions of the associated flow rule are violated since concrete initially contracts before it experiences dilation when subjected to compression loading (this behaviour results in an inflection point in the stress-volumetric strain response which violates the associated flow rule [305]). Therefore, since concrete (and other frictional materials) experience significant volume changes when subjected to loading, a non-associated flow rule, which can adequately control dilatancy, must be used [307, 310]. Equation 4-17 expresses the non-associated plastic potential flow rule used in the CDP model in the effective stress space

$$\dot{\epsilon}^{pl} = \dot{\lambda}\frac{\partial G(\bar{\sigma})}{\partial \bar{\sigma}} \tag{4-17}$$

where $\dot{\epsilon}^{pl}$ is the plastic strain rate, G is the flow potential function (also known as the plastic potential function) and $\dot{\lambda}$ is the scalar hardening parameter (plastic consistency parameter [310]) which is greater than or equal to 0 [304, 309]. Since the yield surface has the geometric shape of two combined Drucker-Prager type functions, a Drucker-Prager type function is also used for the flow potential function [310]. In the $\bar{p} - \bar{q}$ plane, the specific Drucker-Prager hyperbolic function used for *G* in the CDP model is expressed according to equation 4-18 (a graphical representation of *G* in the $\bar{p} - \bar{q}$ plane is provided in Figure 4-5)

$$G = \sqrt{(\epsilon\sigma_{to}\tan\psi)^2 + \bar{q}^2} - \bar{p}\tan\psi \tag{4-18}$$

where ψ is the dilation angle of the concrete measured in the *p*-*q* plane at high confining pressure, σ_{to} is the uniaxial tensile stress at failure specified by the user and ϵ is the eccentricity, which is discussed in further detail below (note, ϵ is also commonly denoted as *e* in literature). It should be noted that *G* is a continuous and smooth function, and is formulated such that the flow direction is always uniquely defined. Finally, *G* asymptotically approaches the linear Drucker-Prager flow potential function at high confining pressures and intersects the hydrostatic axis at 90° [303].



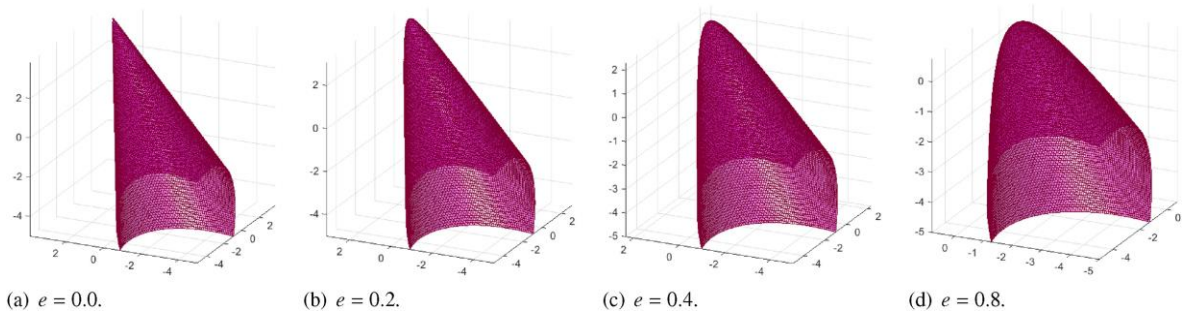
(a) Function and its asymptote. (b) Gradient of G_{CDP} in point P.

Figure 4-5: Definition of Eccentricity (Denoted as e Instead of ϵ) and the Plastic Potential Function, G, in the $\bar{p} - \bar{q}$ (Meridian) Plane (Note, p and q are Equivalent to $\bar{p}$ and $\bar{q}$, Respectively); Reprinted from Archives of Civil and Mechanical Engineering, Vol 19 Issue 4, Wosatko, Winnicki, Polak and Pamin, Role of dilatancy angle in plasticity-based models of concrete, 1268-1283, Copyright (2019), with permission from Elsevier

As shown in Figure 4-5, the shape of the flow potential function, G, in the meridional plane is hyperbolic. The shape of this hyperbola is controlled by the user-inputted eccentricity parameter. The eccentricity parameter is typically a small positive value that "expresses the rate of approach of the plastic potential hyperbola to its asymptote" [319]. In simpler terms, the eccentricity parameter is the length of a line segment along the hydrostatic axis between the vertex of the hyperbola and its center (intersection of the asymptotes of the hyperbola) [319]. As the eccentricity parameter approaches 0 the flow potential function approaches a straight line in the $\bar{p} - \bar{q}$ plane. On the other hand, higher eccentricity values correspond to an increased curvature of the flow potential function, which implies that the dilation angle increases rapidly with decreasing confining pressure. In Abaqus, the default value for the eccentricity parameter is 0.1, which corresponds to the assumption that the dilation angle is constant for a wide range of confining pressures. It should be noted that specifying eccentricity values much lower than the default can lead to convergence issues due to the very tight localized curvature of the flow potential function where it intersects the $\bar{p}$ axis [303]. The influence of different eccentricity values on the plastic flow potential function in three-dimensional principal stress space is shown in Figure 4-6.

G is also dependent on the inputted value of the dilation angle, ψ. "This angle is a material property that is a measure of the inclination of the flow potential function within the meridional plane relative to the hydrostatic pressure axis at high confining pressures" [305]. As shown in Figure 4-7, the

assumed value for the dilation angle has a significant influence on the flow potential function, with increased values of ψ leading to broader flow potential functions. Therefore, the assumed dilation angle has a significant influence on the predicted response of concrete specimens (particularly the stress-strain and strain-dilation responses), as demonstrated by Wosatko et al. [320] in their analyses of the specimens tested by Kupfer et al. [308]. Wosatko et al. [320] also demonstrated that even for low values of the dilation angle that the CDP model can overpredict the influence of dilatancy. Additionally, with respect to slab-column connections, higher dilation angles lead to a more ductile response, an increased dominance of flexure on the predicted response, and cause the predicted crack patterns to diffuse [320].



(a) $e = 0.0$. (b) $e = 0.2$. (c) $e = 0.4$. (d) $e = 0.8$.

Figure 4-6: Influence of Eccentricity Parameter (Note, Eccentricity is Denoted as e) on the Plastic Potential Surface, G, in Three-Dimensional Principal Stress Space (Note, for These Plots f'_t = 4MPa and ψ = 30° Were Assumed); Reprinted from Archives of Civil and Mechanical Engineering, Vol 19 Issue 4, Wosatko, Winnicki, Polak and Pamin, Role of dilatancy angle in plasticity-based models of concrete, 1268-1283, Copyright (2019), with permission from Elsevier

It should also be noted that G can alternatively be expressed according to equation 4-19

$$G = \sqrt{2J_2} + \alpha_p I_1 \tag{4-19}$$

where I_1 and J_2 are the stress invariants, and α_p is the dilatancy parameter in the Drucker-Prager plastic potential function [235]. In literature, α_p has been defined to range between 0.2 and 0.3 [310, 321, 322]. Considering the asymptote line to G, equation 4-20 was derived by Genikomsou [235] to verify the acceptable range of dilation angles for use in Abaqus.

$$\tan(\psi) = 3.67\alpha_p \tag{4-20}$$

Using equation 4-20, the acceptable range for the dilation angle is 36.3°-47.8°, which corresponds to α_p values of 0.2 and 0.3, respectively. Both of these values are less than the maximum value of 56.3° permitted in Abaqus [303].

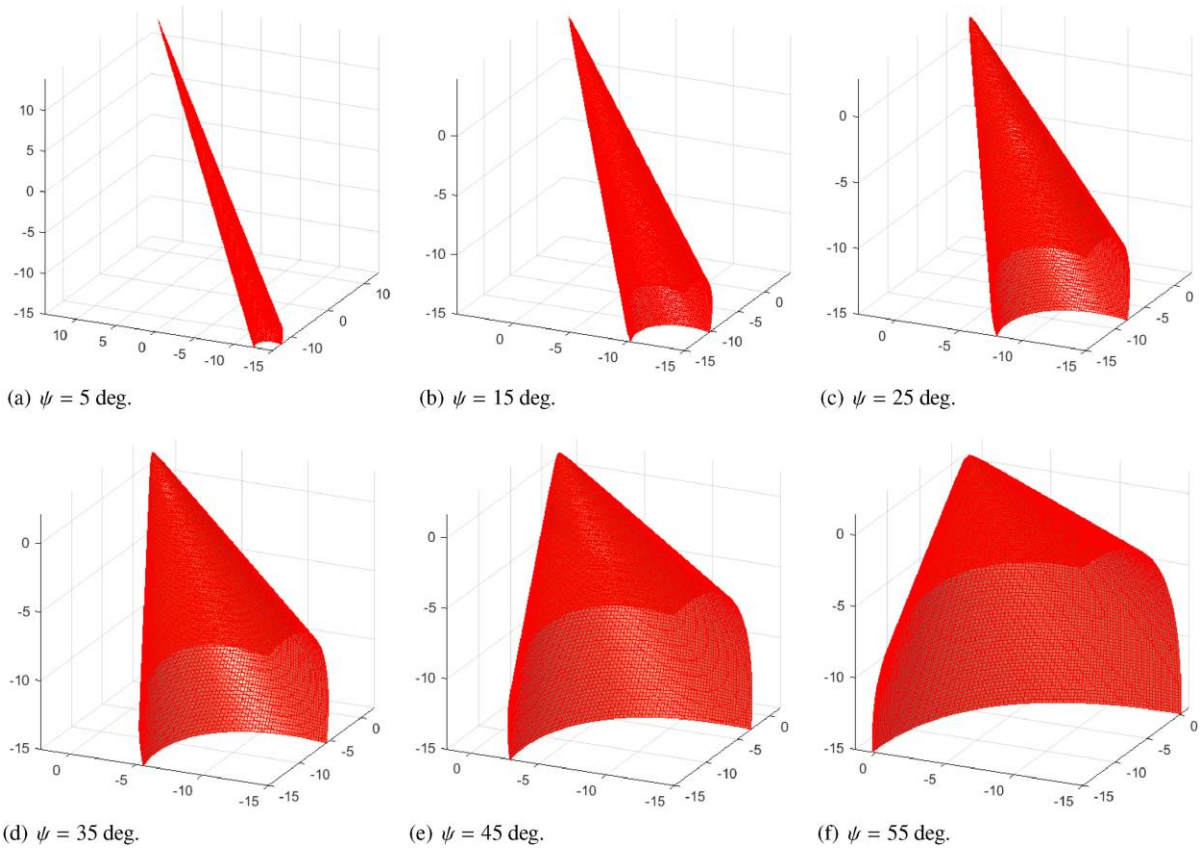


Figure 4-7: Influence of Dilation Angle, ψ, on the Plastic Potential Surface in Three-Dimensional Principal Stress Space for Specimens Tested by Kupfer et al. [308]; Reprinted from Archives of Civil and Mechanical Engineering, Vol 19 Issue 4, Wosatko, Winnicki, Polak and Pamin, Role of dilatancy angle in plasticity-based models of concrete, 1268-1283, Copyright (2019), with permission from Elsevier

4.2.4.4 Viscoplastic Regularization

Convergence issues can occur when using implicit analysis programs, like Abaqus/Standard, to analyze materials which exhibit softening behaviour and stiffness degradation [303]. In particular, materials which have a drastic change in slope at the peak uniaxial tensile stress, such as concrete,

typically lead to significant convergence issues [305]. Viscoplastic regularization is typically used to partially mitigate these convergence issues.

When using the CDP model in Abaqus/Standard (note, the majority of the analyses herein are conducted in Abaqus/Explicit so viscoplastic regularization does not apply), viscoplasticity can be used to permit stresses outside of the yield surface. To include viscoplastic regularization in the analysis a positive non-zero value can be specified for the viscosity parameter, μ. By default, analyses in Abaqus/Standard do not include viscoplastic regularization (μ = 0). When a non-zero value is specified for μ the viscoplastic strain rate, $\dot{\epsilon}_v^{pl}$ is calculated according to equation 4-21 (which is based on a generalization of the Duvant-Lions regularization approach)

$$\dot{\epsilon}_v^{pl} = \frac{1}{\mu}\left(\epsilon^{pl} - \epsilon_v^{pl}\right) \tag{4-21}$$

where μ is the viscosity parameter which represents the relaxation time of the viscoplastic system, ϵ_v^{pl} is the viscoplastic strain and ϵ^{pl} is the plastic strain calculated in the inviscid backbone model (note, the inviscid solution corresponds to that without viscoplastic regularization) [303].

The use of viscoplastic regularization also requires the calculation of a viscous stiffness degradation variable, d_v.

$$\dot{d}_v = \frac{1}{\mu}(d - d_v) \tag{4-22}$$

where d is the degradation variable calculated in the inviscid backbone model [303].

And finally, the stress-strain relationship in the viscoplastic model is calculated according to equation 4-23

$$\sigma = (1 - d_v)D_0^{el} : \left(\epsilon - \epsilon_v^{pl}\right) \tag{4-23}$$

where D_0^{el} is the initial (undamaged) elasticity matrix [303].

If a non-zero value has been specified for μ, the FEA results will be based on the viscoplastic parameters ϵ_v^{pl} and d_v. In order to not negatively impact the accuracy of the results, the viscosity parameter must be small with respect to the iteration time increment of the analysis (μ should be less than approximately 15% of the iteration time increment [235]). However, the iteration time increment is typically unknown and varies throughout the analysis. Therefore, several values of the viscosity parameter must be investigated to ensure accurate results. As μ approaches 0 the calculated solution

approaches the plastic solution considering no viscosity. Whereas when μ becomes increasingly large compared to the iteration time increment the calculated solution approaches the elastic solution [305].

Chapter 5: Study Overview

As shown in Figure 5-1, the remainder of this thesis is focused on presenting the results of three studies (Chapters 6, 8 and 9) and proposing alternate punching shear design methods for elongated connections (rectangular slab-column and slab-wall connections) (Chapter 7). To improve the clarity of Chapters 6, 8 and 9, the study motivation, specimen overview, relevant linear elastic and nonlinear FEMs and study results are presented in each chapter (compared to separate calibration and results chapters). Additionally, the primary contributions of this thesis are summarized at the end of each chapter.

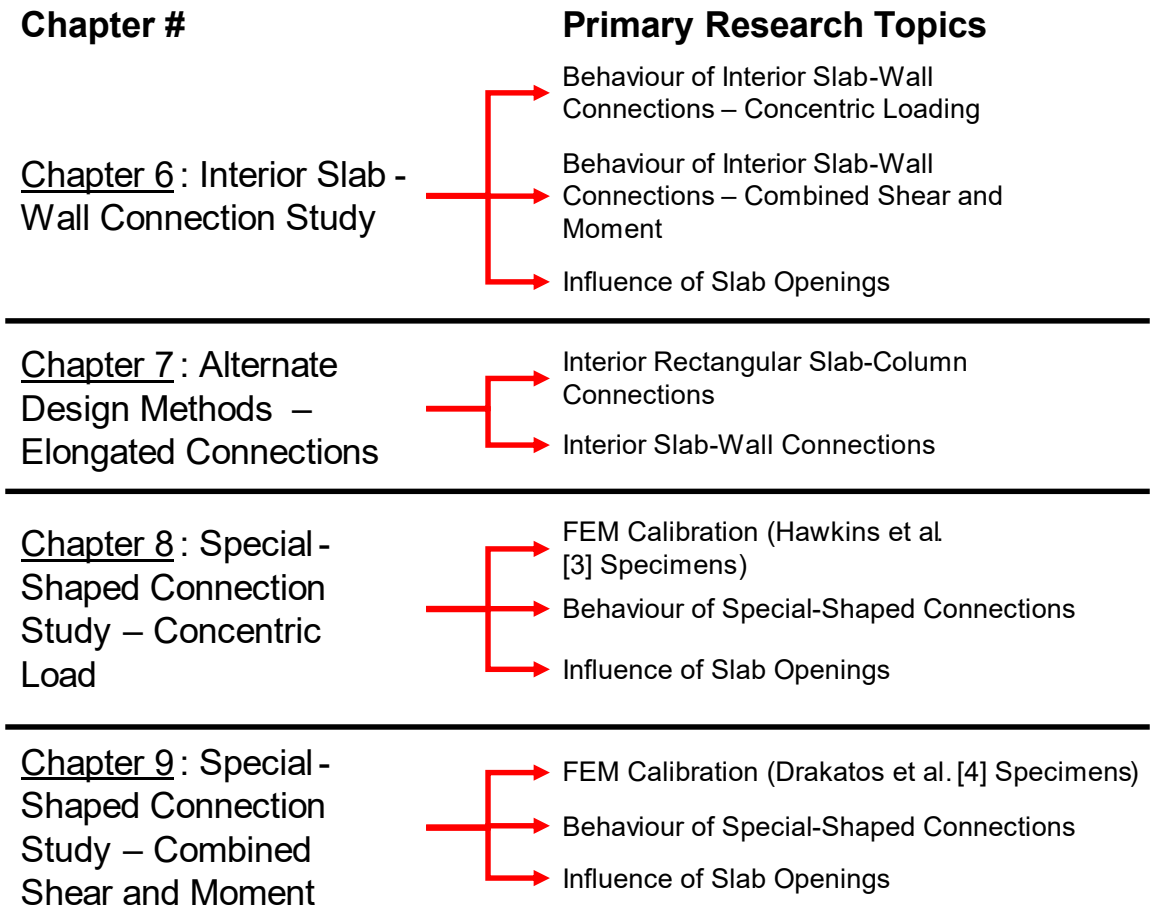


Figure 5-1: Overview of Remaining Thesis Chapters and key Research Topics in Each

In Chapter 6, the punching shear behaviour of interior slab-wall connections (SWCs) is discussed. The slab-wall connection study is primarily focused on the punching shear behaviour of interior SWCs under various loading conditions. The influence of slab openings on the behaviour of SWCs

subjected to concentric loading is also investigated and compared to that for rectangular slab-column connections (R-SCCs).

It should be noted that only a brief overview of the nonlinear FEMs used in the slab-wall connection study is presented in Chapter 6. The nonlinear FEM used in the analysis of the behaviour of SWCs and the R-SCCs with symmetric slab opening layouts is that which was calibrated during the author's MASc studies. As such, the calibrated FEM is only summarized, and a detailed discussion of the calibration process is provided in [1].

The results in Chapter 6 and [1] have demonstrated that the ACI 318-19 provisions can overpredict the concentric punching shear capacity of elongated connections (rectangular slab-column and slab-wall connections). Therefore, alternate punching shear design methods, intended for adoption in ACI 318-19 [2], for R-SCCs and SWCs (elongated connections) are proposed in Chapter 7. As will be discussed, the NLFEA results presented herein and in [1] were used to develop the proposed design methods, which were then verified through comparisons to existing design provisions and available experimental results.

In Chapter 8, the punching shear behaviour of special-shaped slab-column connections (SS-SCCs), specifically L, T and cruciform connections, with or without slab openings and subjected to concentric loading is investigated. The calibration of the FEM, to the experimental results of Hawkins et al. [3], and the influence of the slight modifications made to the specimen geometry before conducting the special-shaped connection study are discussed. Further information related to the FEM calibration can also be found in [1], as the FEM was partially calibrated during the author's MASc studies. The punching capacities predicted by the ACI 318-19 [2] concentric punching provisions, ACI 421.1R-20 [5] and the NLFEA are compared to evaluate the accuracy of existing North American design provisions for SS-SCCs. Modifications to the concentric provisions to approximate the influence of unbalanced moment for preliminary design purposes are also investigated as the ACI 421.1R-20 method is time-consuming and not suitable for iterative design. Additionally, the influences of openings around SS-SCCs and R-SCCs are compared to further quantify the benefits of using SS-SCCs.

In Chapter 9, the punching shear behaviour of rectangular, L, T and cruciform slab-column connections with and without slab openings and subjected to constant vertical loading and monotonically increasing unbalanced moment is investigated. Since the specimens tested by Hawkins et al. [3] only had flexural reinforcement at the top of the slab (which corresponds to the tension side

of the slab under concentric loading for the experimental boundary conditions) the nonlinear FEM used in Chapter 9 was calibrated to the experimental specimens tested by Drakatos et al. [4]. As will be discussed, these tests were conducted to study the punching shear behaviour of square slab-column connections subjected to combined concentric loading and unbalanced moment, and therefore, included flexural reinforcement on both sides of the slab. Since the specimen geometry and method of applying vertical load are identical to those used in the experiments to calibrate the FEM used in Chapter 6, which were tested by Sagaseta et al. [57, 151], the calibration of most of the FEM parameters is not presented. However, the results of a calibration verification study and the calibration of parameters such as the step time used in Abaqus/Explicit are discussed. The primary goal of the study presented in Chapter 9 was to determine if slab openings between the flanges of L, T and cruciform connections also have a minor influence on punching behaviour when the connection is subjected to combined concentric loading and unbalanced moment. As was done in Chapter 8, R-SCCs are also analyzed to study the benefit of using SS-SCCs over more common column shapes.

Chapter 6: Interior Slab-Wall Connection Study

6.1 Motivation

As outlined in Chapter 2, the punching shear behaviour of reinforced concrete flat slabs has been studied extensively due to the brittleness of the failure and the popularity of flat slab structures. To date, most existing research has involved experimental testing and has been primarily focused on slabs supported on square or circular columns, even though slabs supported on rectangular columns and walls are common. Even though rectangular slab-column and slab-wall connections are common, much less research effort has been dedicated to studying their punching shear behaviour. The work presented in this chapter, focused on the punching shear behaviour of slab-wall connections (SWCs), is an extension of the study of the punching shear behaviour of rectangular slab-column connections (R-SCCs) conducted during the author's MASc work.

In this chapter, the punching shear behaviour of interior SWCs subjected to concentric vertical loading and combined concentric vertical loading and uniaxial unbalanced moment is studied using NLFEA. Due to the large size of SWCs experimental testing of such connections is very time-consuming and costly. Once properly calibrated, NLFEA can be used to predict commonly measured quantities such as punching capacity, connection stiffness and external crack patterns. However, NLFEA also allows quantities which are difficult to measure experimentally, such as the internal crack propagation and shear stress distribution, to be studied. Finally, unlike experiments, where variations in material parameters between large-scale specimens are unavoidable, NLFEA allows studies to be conducted for a consistent set of material parameters.

While reinforced concrete flat plates, where the slab is directly supported on columns, are very efficient gravity load-resisting systems, they struggle with resisting lateral loads due to the flexibility of the system. Therefore, as previously discussed, flat plates are typically combined with other structural elements, such as shear walls, which serve as the primary lateral force-resisting elements. In these combined flat plate shear wall structures, the slab-column connections are typically designed to resist gravity loading only, while the shear walls are designed to resist both gravity and lateral loading. As such, the SWCs are essential to the performance of both the gravity and lateral force-resisting systems and must be properly designed.

The shear behaviour of SWCs has received limited research interest, even though the limited experimental tests have demonstrated that punching shear failures can occur [29, 30, 33]. Additionally, the shear stress distribution along the wall perimeter and critical perimeter at *d/2* from

the wall face is not yet well understood.

As was shown in Figure 2-14, researchers have proposed critical perimeters which can be used to estimate the punching shear capacity of SWCs based on past numerical and experimental research. However, this past research has not led to the inclusion of specific punching shear design provisions for SWCs in most major North American [2] or European [34] design codes. Of major current design codes, only *fib* Model Code 2010 [35] contains specific punching shear provisions for SWCs. Model Code 2010 specifies an effective critical perimeter to be used when estimating the punching capacity of SWCs, as shown in Figure 2-14d, but does not provide references or justification for how this perimeter was determined (note, the new draft of Eurocode 2, prEC2 [280], also includes the same provisions for SWCs as Model Code 2010). As discussed in Section 3.3.2, in North American punching shear design provisions, the shear capacity of a connection is a function of the column aspect ratio, β (ratio of maximum and minimum column dimensions), and the ratio of the critical perimeter length, b_o, to the effective slab depth, d. Even though the provisions were derived from limited tests of elongated or large columns, no upper bounds for β or the b_o/d ratio are currently specified. Therefore, as currently formulated, the provisions are also applicable for the punching shear design of SWCs. However, Joint ACI-ASCE Committee 352 (Joints and Connections in Monolithic Concrete Structures) recommends that designers refer to the work of Schwaighofer and Collins [30] and Paulay and Taylor [31] when designing slab-column connections when β exceeds 3 [104]. Therefore, the accuracy of the ACI 318-19 punching shear provisions for estimating the capacity of SWCs needs to be evaluated.

Furthermore, most previous research related to the influence of slab openings on punching shear capacity has also been focused on square or circular slab-column connections. Extrapolation of these results, and the code provisions related to the influence of slab openings derived from them, which were presented in Section 3.6, to elongated connections such as rectangular slab-column and slab-wall connections is questionable. Unlike square columns, where each side of the connection transfers an approximately equal amount of the load when no opening is present, the force distribution around elongated connections is non-uniform [145, 259, 323], and as the support becomes increasingly elongated, more load is transferred along the long sides of the connection, reaching a maximum of approximately 45% per long side according to the NLFEA presented herein.

Additionally, while it is known that the long sides of rectangular columns transfer a significant portion of the load, most punching shear research of R-SCCs with openings involve openings near the

short side of the connection. Therefore, one of the primary goals of this work is to study the influence of slab openings adjacent to the long side of elongated supports. The influence of the opening location along the long side is also studied due to the non-uniformity of the force distribution along the support perimeter.

As will be discussed in this chapter and Chapter 7, the punching shear capacity of very elongated connections ($\beta > 20$) without slab openings, such as SWCs, is very high. However, the FEA also suggests that approximately 40-50% of the total load is transferred by the region within $5d$ of each end of the wall (wall toes). Therefore, depending on their location, openings in the vicinity of SWCs could significantly reduce punching capacity.

6.2 Study Overview

6.2.1 Determination of Specimen Dimensions

The majority of available experimental punching shear tests are for isolated slab-column connections since they are easier to test than full slab systems, and because they result in conservative punching capacity estimates as the influence of compression membrane action and moment redistribution is typically neglected. As such, punching shear design provisions are primarily based on the results of isolated connection tests [25]. Therefore, in order to evaluate the applicability of ACI 318-19 punching provisions for SWCs, isolated SWCs should be analyzed. In this work, isolated SWCs, representing the interior SWC shown in Figure 6-1a, were analyzed. The use of isolated specimens also provides the additional benefits of reducing the required computational resources (analysis of full flat plate systems with solid three-dimensional elements is still currently infeasible due to the time required to complete even one analysis run) and allowing the results of this study to be compared with those from the previous rectangular column study [145, 161].

Since no isolated slab-wall specimens exist in the current experimental database, the radius of contraflexure around a SWC had to be estimated as discussed herein (the procedure used to estimate the radius of contraflexure is also discussed in [324]). Since the FEM used in this study was originally calibrated for interior slab-column connections, the interior SWC shown in Figure 6-1a was considered. Linear elastic FEA (LEFEA) was used to estimate the deflected shape of a quarter of the slab system shown in Figure 6-1a when the slab was subjected to a uniformly distributed gravity load (the boundary conditions used in this analysis are provided in Figure 6-2). To account for cracking, the Poisson's ratio of the concrete was assigned a value of 0 in this model. Using the nodal

deflections predicted by Abaqus, the radius of contraflexure, r, was estimated for eight different wall sizes (the details of the 8 isolated SWCs are discussed in Section 6.2.2.2 and are presented in Table 6-2) at various points along the wall with the three locations shown in Figure 6-1a and Figure 6-3 being critical. The radius of contraflexure was found to increase as the wall thickness, c_{min}, and ratio of wall thickness to effective slab depth (denoted as κ in this work ($\kappa=c_{min}/d$) to be consistent with the previous rectangular column studies [145, 161]) increased, leading to the use of the slab dimensions shown in Figure 6-3, which are based on the estimated r for the connection where κ is equal to 2.970. As demonstrated in Figure 6-1b, r was defined as the maximum distance from the wall centreline where the magnitude of the first derivative of the deflected shape was within 1% of its maximum value (note, this procedure was used to estimate r since the estimated radius of contraflexure values for interior square columns were typically slightly lower than those commonly reported in literature [$0.2L$ or $0.22L$, where L is the centerline distance between columns]). The location of the maximum of the first derivative of the deflected shape is equivalent to the inflection point of the deflected shape, which is synonymous with the location where the slab moment changes from negative to positive. Since the FEA only provides discrete values for the deflected shape at each location, the central difference approximation was used to numerically differentiate the predicted deflected shape, considering all nodal deflections at the location where r was estimated. This analysis resulted in the overall specimen dimensions shown in Figure 6-3 (a quarter of the isolated SWC is shown). Note, during the analysis of the tributary area of interior SWCs, which is discussed in Section 7.2.4, the moment magnitudes were verified to be approximately 0 near the estimated radius of contraflexure, confirming the validity of the methodology presented herein.

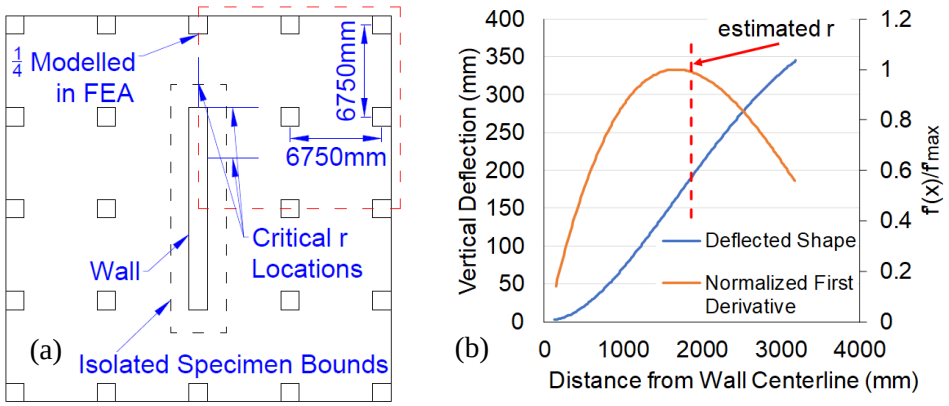


Figure 6-1: (a) Interior Slab-Wall Connection Analyzed using LEFEA and (b) Estimation of *r* Perpendicular to Long Side of Wall at the Wall Centerline

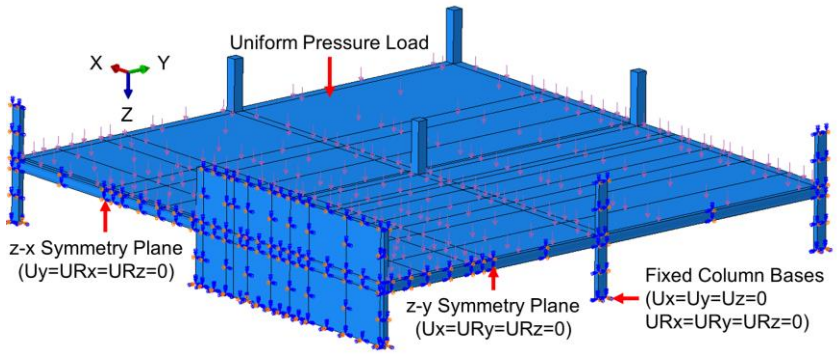


Figure 6-2: Boundary Conditions Used in Determination of Radius of Contraflexure Around Interior Slab-Wall Connection, ¼ Model

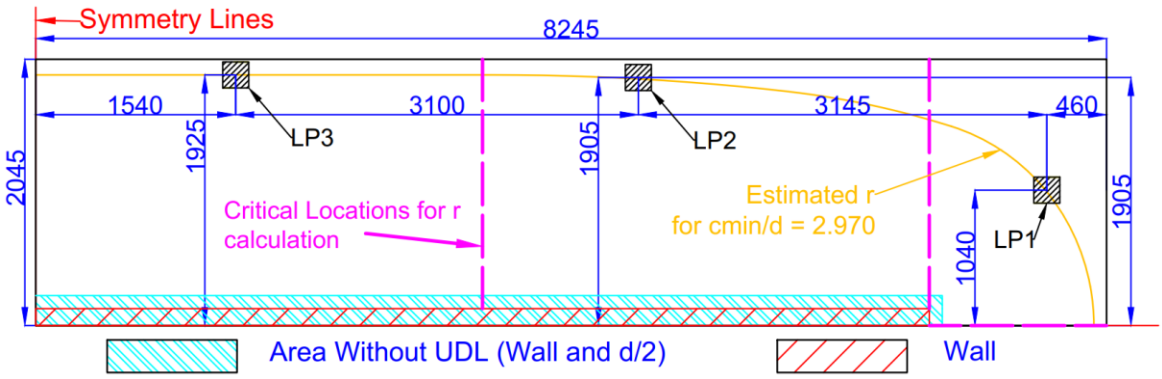


Figure 6-3: Dimensions and Load Locations for Isolated Slab-Wall Specimens (¼ Shown) [324]

6.2.2 Concentric Load Study

Despite the fact that SWCs are typically subjected to a combination of concentric vertical loading and unbalanced moment, the punching shear behaviour of SWCs under concentric vertical loading was studied first. The general boundary conditions assumed in the concentric load study are provided in Figure 6-4 (quarter models were used in the concentric load study to take advantage of symmetry). The concentric load study was divided into two parts, as discussed in the following subsections.

Note, in both parts of the concentric load study, and the V+M study introduced in Section 6.2.3, the flexural reinforcement on the tension and compression sides of the slab (under concentric loading) consisted of 16mm diameter bars spaced at 125mm on center (o/c) in both directions and 12mm

diameter bars spaced at 125mm o/c in both directions, respectively. This reinforcement is the same as that used in the AM series slabs tested by Sagaseta et al. [151]. As discussed in Section 6.3, the AM series slabs were used to calibrate the nonlinear FEM used in this chapter. Therefore, the same reinforcement was used in all specimens analyzed herein, other than the PT series slabs [57], which were also considered in the FEM calibration (the reinforcement of the PT slabs is discussed in Section 6.3.1).

Additionally, as discussed in Section 6.3.2, perfect bond was assumed in the FEM. Therefore, the influence of anchorage details of the slab reinforcement in the vicinity of the SWC was not studied herein. However, in practice, proper anchorage of the slab reinforcement near the SWCs is essential, as improper detailing could lead to slip of the reinforcement, particularly in the flexural reinforcement normal to the length of the wall, potentially lowering the overall connection strength.

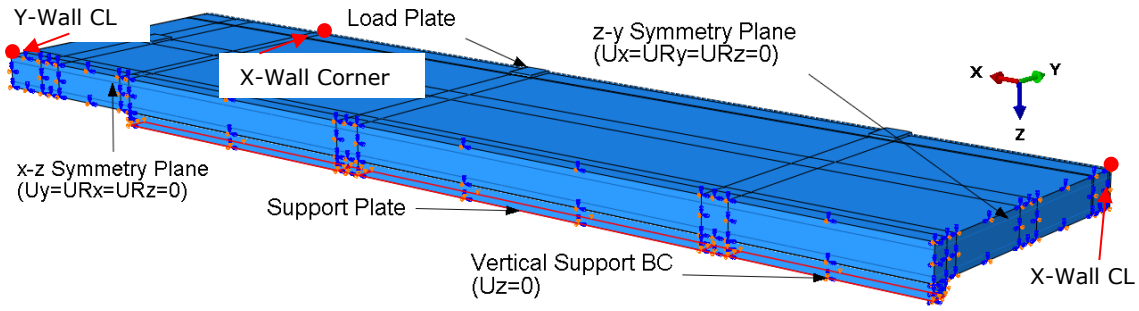


Figure 6-4: Boundary Conditions Assumed in Concentric Vertical Load Study [325]

6.2.2.1 Load Type Study

The first part of the concentric load study, denoted the Load Type Study, was focused on studying the impact of the four load cases summarized in Table 6-1 on the predicted response of an interior isolated SWC with a wall thickness of 260mm (κ=1.287 for the SWC, thickness chosen to match the minimum column dimension of the experimental specimens considered in the FEM calibration) and a wall length of 13760mm (considering the interior connection shown in Figure 6-1a). For the first three load cases, the slab was loaded via three load plates, whose locations are shown in Figure 6-3. These load cases were investigated to study the impact of the different loading conditions near the wall toe compared to along the rest of the wall. In the fourth load case, the load plates were removed, and a uniformly distributed vertical load was applied to the slab surface beyond *d/2* from the wall face, as shown in Figure 6-3.

Table 6-1: Summary of Load Cases Considered [324]

Model	Load Plate Magnitude (MPa)		
	Load Plate 1	Load Plate 2	Load Plate 3
Equal Plate Loads	7.75	7.75	7.75
High Short-Side Load	15.5	7.75	7.75
Unequal Load Plates	5.05	7.75	7.67
Uniformly Distributed Load	0.12MPa (applied on top of slab beyond *d/2* as shown in Figure 6-3)		

6.2.2.2 Parametric Study – Influence of Connection Size (Wall Length and Thickness) (V Study)

The second part of the concentric load study, denoted the V Study, involved a parametric study of the influence of wall length and thickness on the punching shear behaviour of interior SWCs. In the V Study, the 8 SWCs summarized in Table 6-2 were subjected to monotonically increasing concentric vertical loading until failure. The concentric vertical load was applied to the connection through three equally loaded 200x200mm load plates located along the radius of contraflexure (the location of the plates matches that used in the Load Type Study). This loading condition is similar to that used in many isolated slab-column tests and similar to that used in the experimental tests used to calibrate the FEM (as discussed in Section 6.3). A series of equally loaded load plates located along the radius of contraflexure was also used by Setiawan et al. [189] in their NLFEA of isolated interior slab-wall-corner connections subjected to vertical loading. For all specimens where κ was less than 2.970, a traction with a magnitude of 7.75MPa was applied to each load plate. For the connection where κ equals 2.970, an increase traction magnitude of 8.5MPa was required in order to observe failure.

It should be noted that the V Study was also conducted for the uniformly distributed load case from the Load Type Study. The results of this load condition are not presented in the body of this thesis as the results of the equal load plate study are typically representative of those for both load cases, and the equal load plate condition is more representative of the load conditions in typical isolated slab-column connection tests (note, results for the uniformly distributed load case and a discussion of key differences between the results for connections subjected to concentric loading from equally load plates or uniformly distributed loading are provided in Appendix B).

Table 6-2: Summary of Isolated Slab-Wall Connections Analyzed

Wall dimensions (mm)			Loading Conditions	
κ (c_{min}/d)	Length (c_{max})	Thickness (c_{min})	V (Concentric Vertical Load)	V+M (Combined Concentric Vertical Load and Uniaxial Unbalanced Moment)
0.594	13620	120	Monotonically Increased to Failure	-
0.792	13660	160		-
0.990	13700	200		-
1.287	13760	260		40% or 65% of Concentric Vertical Capacity + Monotonically Increasing M
1.485	13800	300		-
1.782	13860	360		-
1.980	13900	400		-
2.970	14100	600		-

f_c'=44.6MPa, d_{avg}=202mm, ρ_t=0.75%, 16mm diameter bars (f_y=516MPa) at 125mm on center both directions (tension side), 12mm diameter bars (f_y=526MPa) at 125mm on center both directions (compression side), slab depth (h)=250mm to match properties of slab AM04 tested by Sagaseta et al. [151]

6.2.3 Punching Behaviour of Slab-Wall Connections Subjected to Combined Shear and Moment (V+M Study)

In the V+M Study, the punching shear behaviour of isolated SWCs subjected to combined shear and uniaxial unbalanced moment about an axis parallel to the short side of the wall is studied. Unlike the V study, where 8 SWCs were analyzed, only the SWC where κ equals 1.287 was analyzed in the V+M study (reinforcing details are provided in Section 6.2.2 and Table 6-2). The decision to analyze only 1 SWC was made due to the large amount of computational resources required to complete these analyses, even when taking advantage of symmetry and using half-models as shown in Figure 6-5, and due to the fact that the unbalanced moment capacity of the connection was found to be quite high, as will be discussed in Section 6.4.2. In the V+M study, the SWC is first subjected to a constant vertical load level (equal to 40% or 65% of the concentric capacity of the connection determined in the V study) and then a monotonically increasing uniaxial unbalanced moment is applied until connection failure.

Due to the application of unbalanced moment, half models are required in the V+M study. The boundary conditions used in the V+M study are provided in Figure 6-5). As shown in Figure 6-5, the unbalanced moment is applied to the connection by applying equal and opposite vertical traction loads to the slab faces parallel to the short side of the wall. This method was necessary since the isolated slab-wall specimens are supported at the base of the wall stub, which is common in isolated

slab-column tests, and matches the experimental conditions of the PT [57] and AM [151] series slabs used to calibrate the FEM. Note, due to the use of isolated specimens no in-plane forces were considered herein. However, it should be noted that a higher connection capacity and stiffness would be expected in a continuous flat plate structure, due to the presence of in-plane compression forces which are developed due to slab continuity.

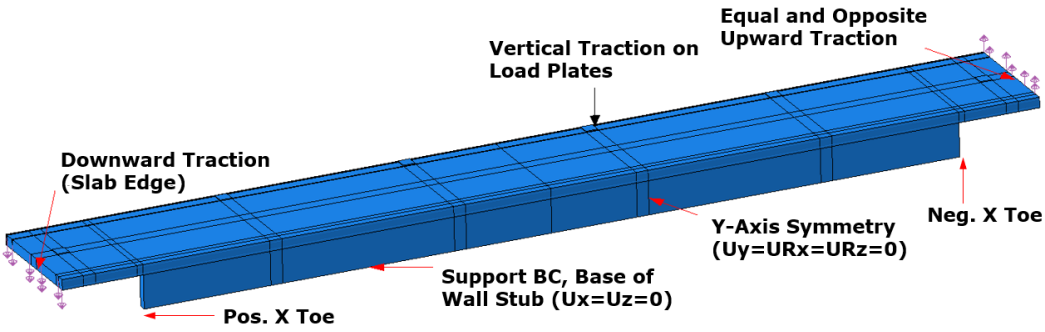
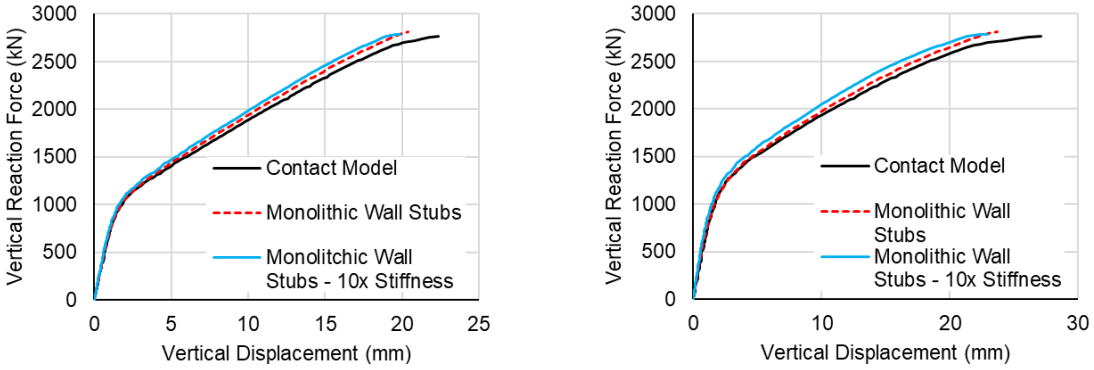


Figure 6-5: Boundary Conditions Assumed in Combined Concentric and Unbalanced Moment Study (V+M Study, Top Wall Stub Removed for Clarity)

In the V Study, the slab and supporting wall are modelled separately and the interaction between the slab and wall is modelled using a "hard" contact which allows separation of the contact surfaces. As such the slab is free to rotate off of the supporting wall, which matches the experimental conditions of the specimens considered in the calibration [57, 151]. However, this results in only the outer edge of the supporting wall being effective in transferring loads between the slab and the wall. To improve the stability of the numerical solution in the V+M Study, the supporting wall and slab are modelled monolithically, which allows some tensile force to be transferred between the slab and wall. As with the supporting plate in the V Study, the supporting wall stub is modelled as linear elastic. However, the stiffness of the supporting wall stub was increased by a factor of 10 to ensure that the stub's deformations do not influence the slab's behaviour. This change in the support conditions and supporting stub stiffness was found to have a minor impact on the predictions of the V Study as shown in Figure 6-6.



(a) Vertical Displacement Measured Perpendicular to Long Side at Wall Toe (X-Wall Corner)

(b) Vertical Displacement Measured Perpendicular to Short Side at Wall Toe (Y-Wall CL)

Figure 6-6: Comparison of Predicted Load-Displacement Response (Displacement Measurement Locations Shown in Figure 6-4) For Contact Model and Stub Models (Wall Stubs 800mm Tall in Stub Models), κ = 1.287, Load For Full Isolated Slab-Wall Specimen

6.2.4 Influence of Slab Openings on Punching Behaviour of Slab-Wall Connections (Symmetric Opening Study)

The primary goal of the Symmetric Opening Study was to analyze the impact of slab openings on the punching shear behaviour of interior SWCs. However, to allow for a direct comparison of the behaviour of R-SCCs and SWCs seven R-SCCs were also analyzed, as shown in Figure 6-7. Of the seven R-SCCs, one was a reference specimen without an opening, which was identical to AM04 tested by Sagaseta et al. [151], and six had slab openings as shown in Figure 6-7a.

Based on the slab shear stress distributions along the column perimeter for the reference specimen [1] opening layouts 1R and 2R were expected to cause the largest punching capacity reductions since the removed parts of the connection were under the highest shear stress. Layout 5R and 6R were hypothesized to have the lowest influence as the openings are in a low shear stress region, with layout 6R being less detrimental than 5R due to the opening orientation.

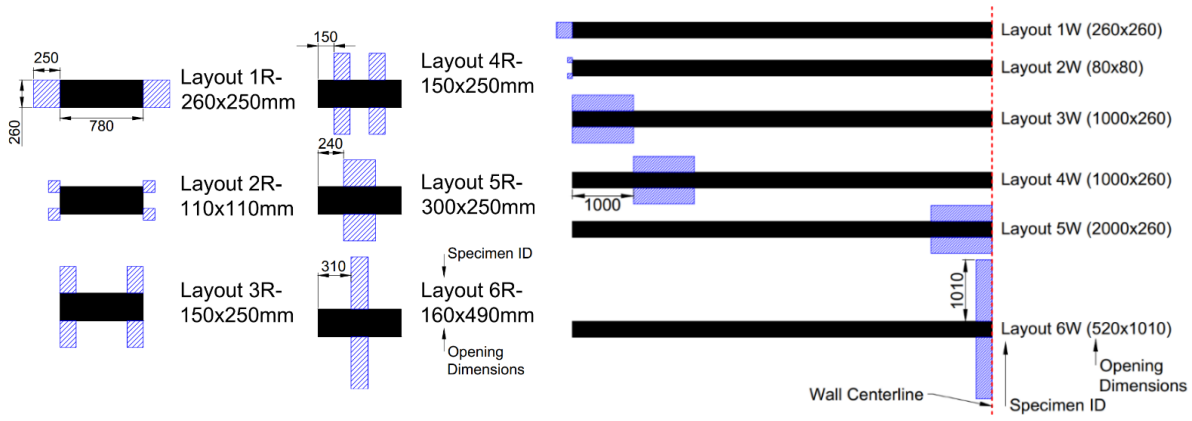


Figure 6-7: Analyzed Symmetric Opening Layouts Around a) R-SCCs and b) SWCs (Note: ½ of SWCs Shown)

The influence of slab openings on the punching shear behaviour of interior SWCs was analyzed considering the isolated SWC with a length of 13760mm, a width of 260mm (to match the considered R-SCC) and a κ value of 1.287. The influence of the six opening layouts shown in Figure 6-7b on the punching behaviour of this connection was analyzed. Symmetric opening layouts were considered to allow quarter models to be used (which was necessary to reduce the required computational resources).

Layouts 1W and 2W are similar to layouts 1R and 2R, but with modified opening dimensions due to the differences in specimen dimensions and load plate locations between the rectangular column and wall specimens. Layouts 1W and 2W were hypothesized to result in significant capacity reductions due to the removal of high-shear stress regions. Layouts 3W through 6W were used to analyze the ideal location and orientation of large openings along the long side of the wall. Layout 3W was expected to cause the largest capacity reduction as the openings remove the long sides of the toe region, which carries a significant portion of the load. Layouts 4W, 5W and 6W were hypothesized to have a minor influence on connection capacity as they are located further than $5d$ from the wall end and are located in low-shear stress regions.

The boundary conditions used in the analysis of the R-SCCs, shown in Figure 6-8, match those used in the FEM calibration and in the author's previous parametric study of the influence of column rectangularity on punching shear behaviour [1]. As with the interior SWCs, symmetric slab opening layouts are considered to allow quarter models to be used (the influence of nonsymmetric slab opening layouts on the punching shear behaviour of R-SCCs is studied in Sections 8.4.1, 9.4.1 and 9.4.2.1). For the isolated SWCs, the slab is loaded through equally loaded load plates located along

the approximate radius of contraflexure. Therefore, the boundary conditions used in the analysis of the influence of slab openings on the punching shear behaviour of interior SWCs are the same as those provided in Figure 6-4. The influence of slab openings on the punching shear behaviour of interior SWCs subjected to combined concentric shear and unbalanced moment is not analyzed due to the high computational demand associated with the use of half models.

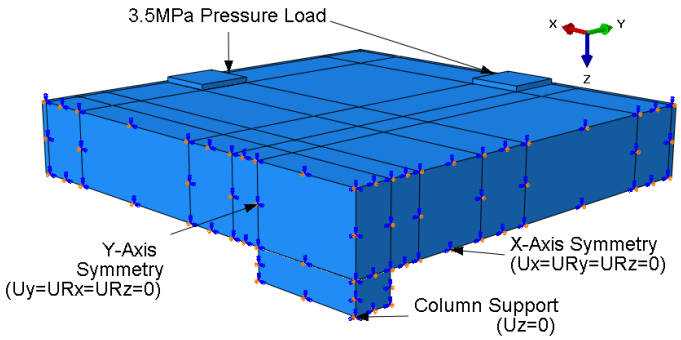


Figure 6-8: Boundary Conditions Used in Analysis of R-SCCs with Slab Openings and FEM Calibration

As with the other studies presented in this chapter the material parameters (f_c' = 44.6MPa, f_y = 516MPa (tension side reinforcement), f_y = 526MPa (compression side reinforcement) d = 202mm) and reinforcement details (tension side: 16mm diameter bars at 125mm o/c, both directions; compression side: 12mm diameter bars at 125mm o/c, both directions) were based on slab AM04 [151].

In addition to studying the influence of slab openings on the punching shear behaviour of elongated connections, this study is also used to evaluate the accuracy of the radial and straight projection approaches to estimate the negative influence of openings on the punching capacity of elongated connections. For the R-SCCs and SWCs the punching capacities are estimated considering reduced critical perimeters according to the existing ACI 318-19 opening provisions (radial approach) and the straight projection approach suggested by Regan [229], Borges et al. [219] and Augustin et al. [206] (see Figure 2-18).

Finally, it should be noted that in all specimens with openings additional rebar is equally distributed around the openings to replace the flexural reinforcement interrupted by the openings (this was also done for the specimens in Chapter 8 and Chapter 9).

6.3 FEM Calibration

Since experimental tests of SWCs are exceptionally limited, as discussed in Section 2.3.5, the FEM originally calibrated during the author's MASc research [1] to study the punching shear behaviour of interior R-SCCs was extended to study the punching shear behaviour of SWCs. Detailed discussions of the FEM calibration are provided in [1, 145, 161, 326], and therefore, only a concise summary of the FEM calibration is provided herein. It should be noted that Setiawan et al. [189] also used a similar procedure of extending a FEM originally calibrated to study the punching shear behaviour of R-SCCs to study SWCs. Furthermore, the summary provided in this section is largely based on discussions previously published in [145, 161, 323].

6.3.1 Summary of Experimental Specimens Considered in FEM Calibration

The calibrated FEM used to study the punching shear behaviour of interior rectangular slab-column and slab-wall connections was calibrated considering experimental results for seven isolated slab-column connections. Of the seven considered slabs, four are from the AM series [151] and three are from the PT series [57]. The AM series slabs were tested to study the influence of the loading conditions and column aspect ratio on punching shear [151], whereas the PT series slabs were tested to study the influence of non-axisymmetric flexural reinforcement arrangements on punching shear [57]. The seven slabs were selected for the calibration since they have the same overall geometry (3000mm square in plan and 250mm thick as shown in Figure 6-9), but had different concrete compressive strengths, flexural reinforcement arrangements and loading conditions. In all seven tests, the supporting column was simulated using a steel plate, and as shown in Figure 6-9, the AM series slabs were supported on rectangular plates with an aspect ratio of 3 [151] and the PT series slabs were supported on square steel plates with a side length of 260mm [57]. Concentric vertical loading was applied through steel plates located along the approximate radius of contraflexure, as shown in Figure 6-9.

Since the original purpose of the calibration was to study the influence of column rectangularity on punching shear, slab AM04 was the primary specimen used to calibrate the FEM parameters (this is also why the material properties of slab AM04 are used for all rectangular slab-column and slab-wall connection simulations discussed in Section 6.4). After calibrating the FEM to the experimental results of slab AM04, the FEM's ability to accurately predict the response of slab-column connections with different loading conditions, support dimensions and flexural reinforcement layouts was verified by modelling the remaining 6 slabs considered in the calibration.

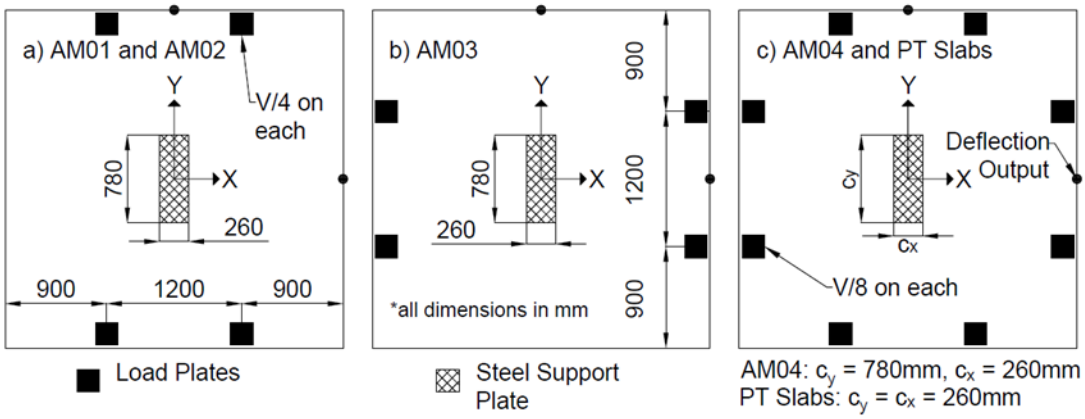


Figure 6-9: Dimensions and Load Conditions of Slabs Considered in Calibration [57, 151]

The material properties, flexural reinforcement details and comparison of the experimental measurements and FEM predictions are provided in Table 6-3. Comparisons of the predicted load-rotation responses in the X- and Y-directions (see Figure 6-9 for the definition of the X- and Y-directions) for slabs AM02-AM04 and PT22 are provided in Figure 6-10 (comparison of the measured and predicted responses for AM01, PT31 and PT32 are provided in [160, 326]. Based on the comparison of the experimental results and FEM predictions in Table 6-3 and Figure 6-10, the calibrated FEM was found to be capable of accurately predicting the response of slab-column connections which failed in punching shear. Furthermore, the strong correlation between the experimental results and the FEM predictions for slabs AM01 and AM02 is also of particular importance for the slab-wall connection study. Since slab AM01 and AM02 are subjected to one-way loading parallel to the long side of the connection, their behaviour is dominated by one-way shear parallel to the long side of the columns. Due to the length of SWCs, the influence of one-way shear parallel to the long side of the wall is expected to be significant, even for two-way loading conditions. Therefore, it is important that the FEM is capable of accurately predicting one-way shear behaviour. The strong agreement between the experimental and FEA results for AM01 and AM02 suggests that the FEM is capable of accurately predicting one-way shear behaviour.

Table 6-3: Slab Properties and Comparison of Experimental [57, 151] and FEA Results

Slab	f_c' MPa	d_{avg} mm	Tensile Flexural Reinforcement[c,d]		Experimental Results[b]			FEA Results		
			ρ_x-ρ_y (%)	f_{yx}-f_{yy} (MPa)	V_{exp} kN	ψ_x mRad	ψ_y mRad	V_{FEA} kN	ψ_x mRad	ψ_y mRad
AM01	44.0	214	0.75[a]	516-516	950	1.3	28.6	963.4	4.6	24.4
AM02	39.7	208	0.75[a]	516-516	919	5.2	26.3	926.0	5.0	20.6
AM03	42.2	203	0.75[a]	516-516	883	46.8	3.6	742.1	21.8	3.9
AM04	44.6	202	0.75[a]	516-516	1067	17.6	16.8	997.7	15.9	16.4
PT22	67.0	196	0.82-0.82	552-552	989	14.4	16.7	908.3	13.8	13.8
PT31	66.3	212	1.48-1.48	540-540	1433	9.5	11.6	1225.0	9.3	9.3
PT32	40.0	215	1.46-0.75	540-558	1157	10	12	961.4	8.9	12.2

[a]only average flexural reinforcement ratio reported for AM series
[b]experimental rotations from AM series estimated from plots in Sagaseta et al. [151]
[c]AM series flexural reinforcement: 16mm and 12mm diameter bars spaced at 125mm both directions on the tension and compression sides of the slab, respectively
[d]PT series flexural reinforcement (tension side): 16mm diameter bars at 125mm both directions (PT22), 20mm diameter bars at 100mm both directions (PT31), 20mm diameter bars at 100mm (PT32, x direction, see Figure 6-9) and 16mm diameter bars at 125mm (PT32, y direction, see Figure 6-9); (compression side): 10mm diameter bars with same spacing as tension reinforcement
Note: all spacings specified as on center (o/c)

However, it needs to be noted that the calibrated FEM was not able to accurately predict the experimental response of slab AM03, which failed in flexure, for loads exceeding approximately 600kN. The large deviation between the FEA and experimental results for higher load magnitudes is likely due to the simplified material modelling for the flexural reinforcement. As discussed in the next section, a simplified linear-elastic perfectly-plastic stress-strain response was assumed for the flexural reinforcement since the focus of the FEM was predicting punching shear behaviour, and the flexural capacity of slab AM04, was much higher than its punching capacity. The use of this simplified model results in accurate predictions for connections whose behaviour is governed by shear, and as such, the FEA results for SWCs must be carefully studied to ensure that the connections are not predicted to be governed by flexure.

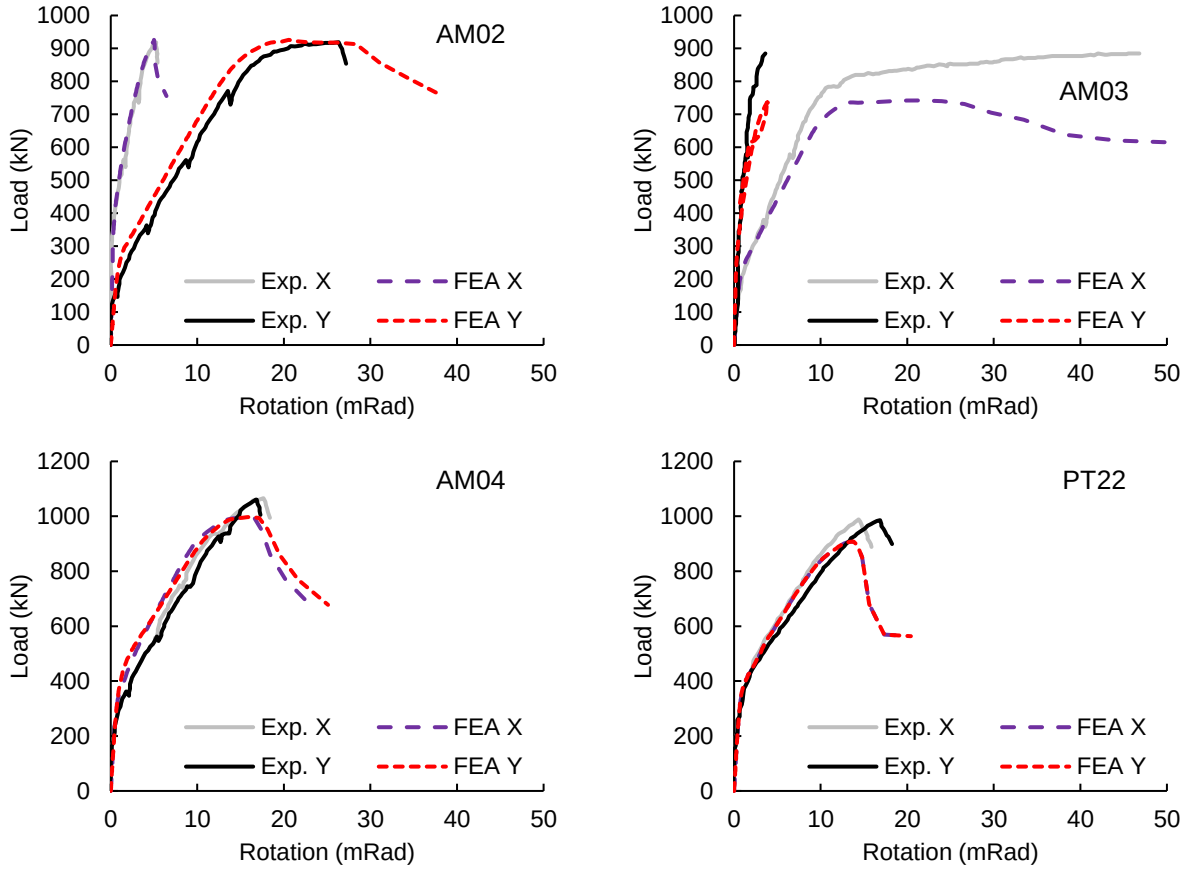


Figure 6-10: Comparison of Experimental Results and FEA Predictions for Select Specimens Considered in Calibration, Experimental Results Approximated from Plots in [57, 151] (X and Y Locations Defined in Figure 6-9) [145]

6.3.2 Summary of Calibrated FEM

As previously shown in Figure 6-8, quarter models were used in the calibration to take advantage of symmetry (other than for PT32 where a half model was required due to the non-axisymmetric flexural reinforcement arrangement). Instead of applying the boundary conditions directly to the slab geometry, the steel load and support plates used in the experiments were included in the FEM based on the results of a boundary condition study [1, 326]. The interaction between these plates and the slabs was modelled using the general contact algorithm in Abaqus/Explicit. Between the top of the supporting plate, which is intended to simulate the column (or the wall for the SWCs analyzed herein) and the base of the slab, a hard contact, which allows the contact surfaces to separate was used. Between the base of the loading plates and the top of the slab, a cohesive contact, which does not

allow the contact surfaces to separate, was used. Both contacts were also defined to limit the penetration of the contact surfaces into one another [303]. To ensure uniform load application, pressure loads were applied to the top of each load plate in the FEM, as shown in Figure 6-8.

A dynamic/explicit solution procedure in Abaqus/Explicit, which accounted for nonlinear geometric effects, was used for all NLFEAs presented in this chapter due to the use of the general contact algorithm and force-based loading. While Abaqus/Explicit was developed to conduct dynamic analyses, it can also be used to conduct quasi-static analyses if the magnitude of the inertial forces is low. Due to its formulation, a quasi-static analysis in Abaqus/Explicit is typically more computationally efficient than a similar general static analysis in Abaqus/Standard. For example, a general static analysis of slab AM04 took approximately 23 hours in Abaqus/Standard, whereas a quasi-static analysis, which resulted in similar predictions [1], took approximately 4 hours in Abaqus/Explicit [161].

Following the work of Genikomsou [235], three-dimensional, eight-node, reduced-integration hexahedral elements, with default hourglassing controls (C3D8R) were used to discretize the concrete slab, steel load plates and steel support plates. Also consistent with the work of Genikomsou [235], three-dimensional, two-node truss elements (T3D2) were used to discretize the flexural reinforcement. A perfect bond between the concrete slab and the flexural reinforcement was assumed, and this was modelled by embedding the T3D2 elements into the C3D8R elements of the slab using the embedded constraint in Abaqus. Based on the results of a mesh sensitivity study [1, 326], a global mesh size of 20mm was used in the calibration, and in all simulations presented in this chapter. Therefore, a total of 13 C3D8R elements were provided through the slab depth, which greatly exceeds the minimum of 5 recommended when using reduced integration elements [25].

Due to its versatility, the compressive and tensile behaviour of the concrete was modelled using the Concrete Damaged Plasticity (CDP) model, which was discussed in detail in Chapter 4. For all slabs where the concrete compressive strength was less than 60MPa, which includes all slabs in this thesis other than PT22 and PT31, the Hognestad parabola shown in Figure 6-11 was used to model the uniaxial compressive response of the concrete (the specific Hognestad parabola for slab AM04 which is used for all FEAs presented in Section 6.4 is provided in Figure 6-12). As shown in Figure 6-11, the post-peak portion of the Hognestad parabola was terminated at a compressive stress of approximately $0.4f_c'$ to limit numerical issues which occur when the post-peak response is extended to a stress near 0. For PT22 and PT31, where f_c' exceeded 60MPa, the uniaxial compressive stress-

strain response proposed by Thorendfeldt, Tomaszewicz and Jensen (1987), which is valid for f_c' values less than or equal to 125MPa [10], was used.

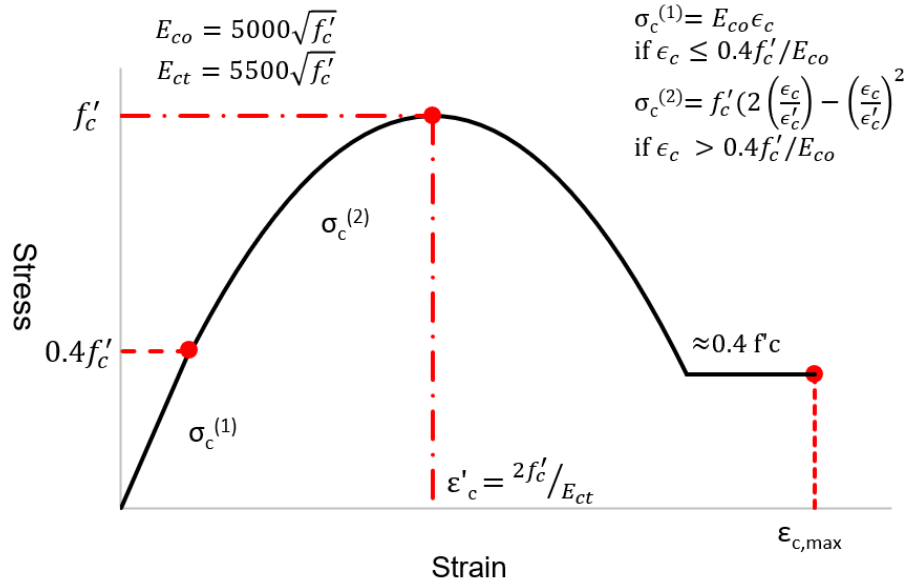


Figure 6-11: Hognestad Parabola Assumed in Calibrated FEM used in Chapter 6 [145]

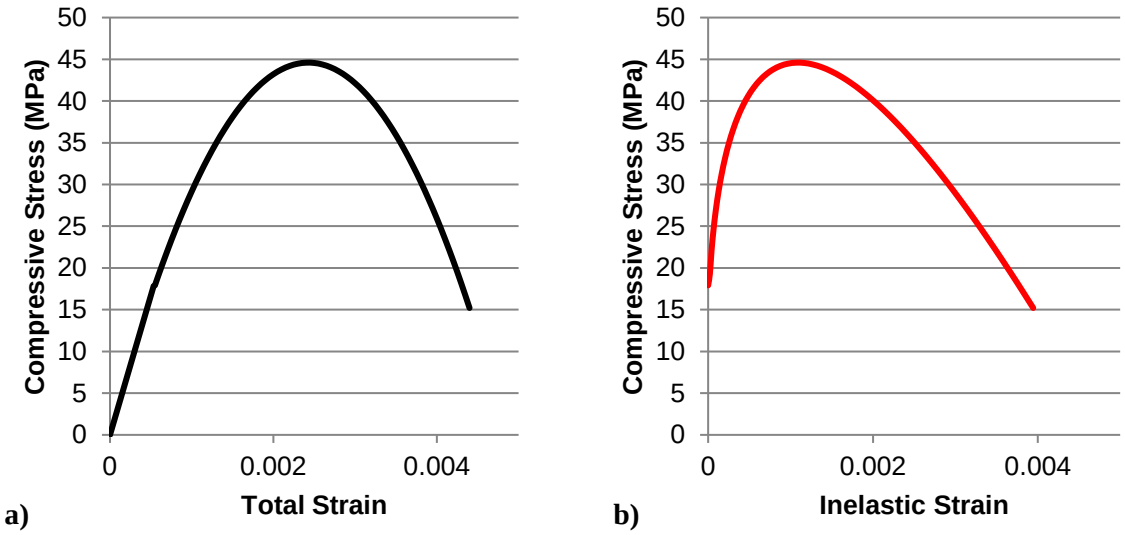


Figure 6-12: Hognestad Parabola for f'_c = 44.6MPa used in Calibrated FEM [1]

The peak tensile strength of the concrete, f_t', which was not provided in [57, 151], was estimated using equation 6-1

$$f_t' = 0.33\sqrt{f_c'} \qquad 6\text{-}1$$

Prior to achieving f_t', the tensile stress-strain response of the concrete was assumed to be linear elastic. To reduce the mesh sensitivity of the FEM, post-peak tension softening was incorporated using the bilinear tensile stress-crack width relationship proposed by Petersson [327] (note, Genikomsou [235] demonstrated that this bilinear relationship is adequate for modelling punching shear and is more computationally efficient than the exponential relationship proposed by Cornelissen et al. [328]), shown in Figure 6-13, instead of directly inputting a post-peak tensile stress-strain response. To use the relationship proposed by Petersson [327] the concrete's fracture energy must be estimated. Based on the results of another sensitivity study [1, 326], the concrete fracture energy was calculated according to equation 6-2, which is taken from Model Code 1990 [159]

$$G_f = G_{f0}(f_{cm}/f_{cmo})^{0.7} \qquad 6\text{-}2$$

where G_{f0} is the base fracture energy (which is a function of the maximum aggregate size) (N/mm), f_{cm} is the mean concrete compressive strength (MPa), which was calculated as the characteristic concrete strength, f_{ck}, plus 8MPa, and f_{cmo} is equal to 10MPa [159]. Using the relationships presented in Figure 6-13, Abaqus then automatically converts the inputted tensile stress-crack width response into a tensile stress-strain response based on the characteristic length of each element (for C3D8R elements the characteristic length is the cubic root of the element volume [25])

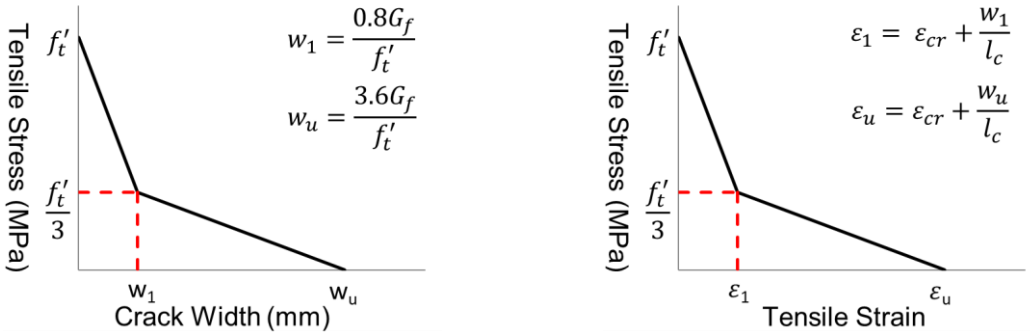


Figure 6-13: Tensile Stress-Crack Width Relationship [327] and Tensile Stress-Strain Relationship [25] used in Calibrated FEM used in Chapter 6 (Note, Crack Width is Equivalent to Crack Displacement)

Tensile Stress (MPa)	Crack Width (mm)
2.204	0.0
0.735	0.0341
0*	0.1533

*Abaqus sets the minimum stress at 10^{-2} times the initial stress

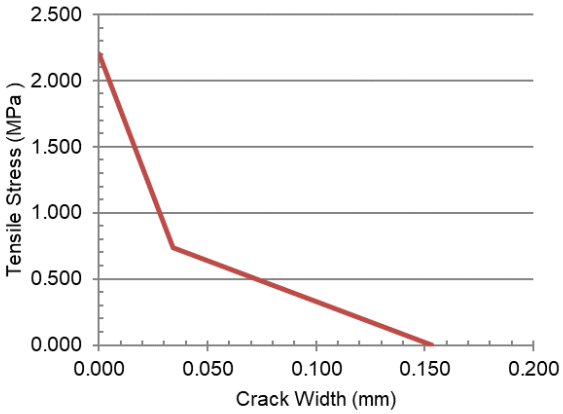


Figure 6-14: Inputted Tensile Stress-Crack Width Relationship for f'_c = 44.6MPa (Note, Crack Width is Equivalent to Crack Displacement)

Other than the user-defined compressive and tensile stress-strain responses, the CDP also requires values for numerous other parameters. The most influential of these parameters, which are summarized in Table 6-4, is the dilation angle. Based on a sensitivity study [1, 326], a dilation angle of 45 degrees was found to lead to the best correlation between the FEA and experimental results, and therefore, is used for all simulations presented in this chapter. Other than the dilation angle, the CDP also requires the user to specify the eccentricity, ϵ, viscosity parameter (which is not used in Abaqus/Explicit), μ, ratio of initial equibiaxial compressive yield stress to initial compressive yield stress, σ_{bo}/σ_{co}, ratio of second stress invariant on the tensile meridian to the stress invariant on the compressive meridian, K_c, and the concrete's Poisson ratio, ν. Consistent with other punching shear research [25, 81, 108, 251, 253, 320, 329], the default values of 0.1, 1.16 and 0.667 were used for ϵ, σ_{bo}/σ_{co} and K_c, respectively. A value of 0 was inputted for ν, which is a common assumption in the nonlinear analysis of cracked concrete structures. However, it should be noted that specifying ν as 0 or 0.2 has a minor impact on the predicted results, especially outside of the linear elastic range.

The final required input parameter of the calibrated FEM was the stress-strain response of the flexural reinforcement. As previously discussed, a linear-elastic perfectly-plastic stress-strain relationship in compression and tension was assumed for the flexural reinforcement, since the primary goal of the calibrated FEM was to study punching shear behaviour. As the elastic modulus and Poisson's ratio of the rebar were not provided [57, 151], the typical values of 200000MPa and 0.3 were assumed, respectively. The yield strengths of the flexural reinforcement in the FEM,

summarized in Table 6-4, were based on that provided in [57, 151] (note, in all models in Section 6.4 the yield strength of the flexural reinforcement was set to match that of slab AM04).

A summary of the concrete and steel parameters in the calibrated FEM used in this chapter is provided in Table 6-4.

Table 6-4: Summary of Calibrated FEM [1]

Calibrated Model – Concrete Specific Parameters		
Material Model – Concrete Damaged Plasticity Dilation Angle – 45° Eccentricity* – 0.1 σ_{bo}/σ_{co}* – 1.16 Damage Parameters – N.A.	Uniaxial Compression Model – Hognestad Parabola $E_c = 5000\sqrt{f_c'}$ (33392MPa for all simulations in Section 6.4) Poisson's Ratio (ν) – 0 Tension Model – Bilinear tensile stress-crack width/displacement [327] G_f – Calculated according to Model Code 1990 [159] (0.093N/mm all simulations in Section 6.4)	Element Size – 20mm Element Type – C3D8R *Abaqus Default Value

Calibrated Model – Steel Specific Parameters		
	Load/Support Plates	Flexural Rebar
Material Model	Linear Elastic	Linear Elastic-Perfectly Plastic
Elastic Modulus, E	200000MPa	200000MPa
Poisson's Ratio, ν	0.3	0.3
Yield Strength, f_y	–	516MPa (tension side), 526MPa (compression side)
Element Type	C3D8R	T3D2 (embedded in concrete)
Element Size	20mm	20mm
Effective Depth	–	202mm (tension side), 43.55mm (compression side)

6.4 Study Results

6.4.1 Concentric Load Study

6.4.1.1 Load Type Study

As shown in Figure 6-15, the loading conditions have a significant impact on the predicted stiffness and capacity of interior SWCs. For the load plate models, the predicted punching capacity and stiffness decreased as the magnitude of the load on the plate near the wall toe increased. This was expected since it is well known that shear stresses in a slab concentrate near the short side and corners of square or rectangular columns [324]. A similar stress concentration was observed by Sagaseta et al. [151] when comparing the results of slabs AM01 and AM02, which had higher loads near the short

sides of the column, to slab AM04, which had equal loads on all sides. The model subjected to a uniformly distributed load (UDL) on the slab surface was found to display a much higher capacity and stiffness [324], which is consistent with experimental observations for square slab-column connections subjected to uniformly distributed loading [330, 331]. The higher capacity of the SWC subjected to UDL is likely due to the different combination of moment and out-of-plane shear under this load condition than in the load plate simulations. As will be shown when discussing the wall perimeter shear stress distribution, a larger portion of the total load appears to be transferred via one-way shear for the SWC subjected to a UDL, likely due to the different bending response of the slab.

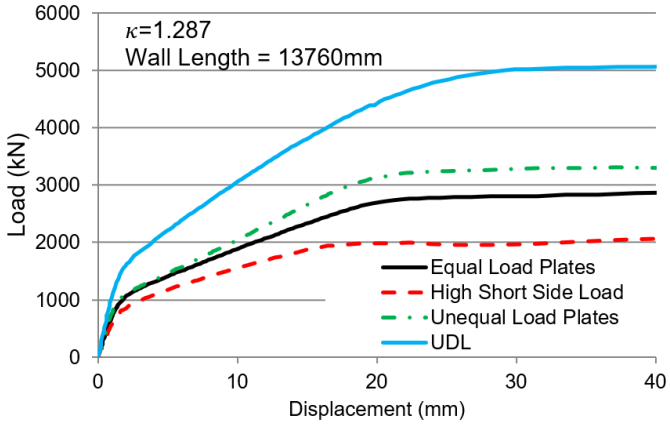
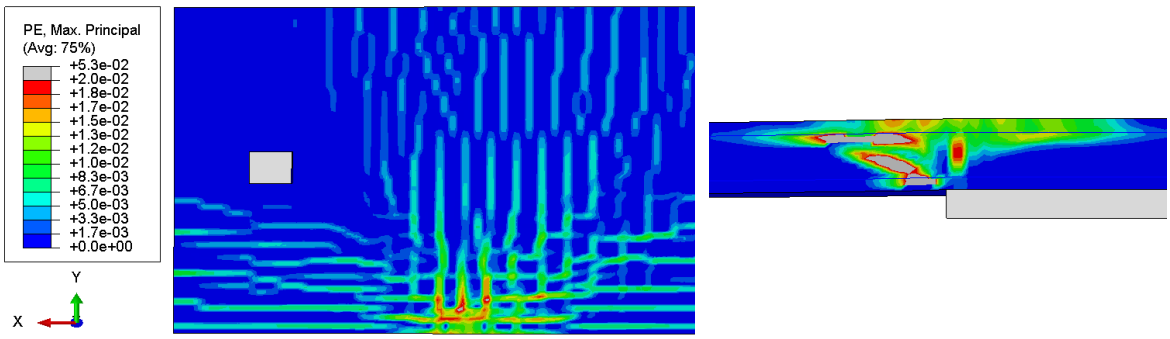


Figure 6-15: Predicted Load-Displacement Response Perpendicular to Long Side of the Wall for Different Load Cases (Vertical Displacement at Slab Edge Perpendicular to Wall Toe [324]

Looking at the predicted load-displacement responses provided in Figure 6-15, it is not clear that a punching failure has occurred. For an isolated slab-column specimen a severe drop in load-carrying capacity is commonly observed at punching, whereas, in the isolated slab-wall models the load capacity reaches a horizontal plateau. However, if the deflected shape and crack pattern, visualized through the contours of maximum principal plastic strain, predicted by Abaqus are analyzed it is clear that a punching failure has occurred as shown in Figure 6-16. The tension surface crack pattern shown in Figure 6-16 is similar to that observed for isolated R-SCCs failing in punching with a large concentration of cracking at the wall toe. Additionally, punching cones are observed on the interior surface of the slab in both orthogonal directions at the wall toe. Similar horizontal plateaus in the load-displacement response, and an increased load-capacity post-punching, were also observed in experimental tests of coupled SWCs under lateral loading by Szalwinski [29].

It should be noted that an analysis of the reinforcement stresses suggests that the flexural capacity of the SWCs is not governing the overall connection response. While some yielding of the slab reinforcement does occur, this yielding is limited to the reinforcement which crosses the wall perimeter and is typically constrained to a very small region near the end of the wall. Even though yielding of this reinforcement initiates before the formation of the punching shear failure, the load carrying capacity of connection continues to increase between the onset of yielding and punching failure. This increase in capacity suggests that the connection capacity is not governed by flexure.

In addition to analyzing the crack pattern and the deflected shape, the onset of failure can be estimated by identifying when the predicted and expected reaction forces begin to deviate. Since force-based traction boundary conditions, which are defined based on undeformed geometry and do not follow the slab rotation, were used to load the slab, static equilibrium can be used to calculate the expected reaction force. At failure, the SWC will no longer be able to support the applied load and the difference between the predicted and expected reaction forces will rapidly increase. It should be noted that for the remainder of this thesis the predicted load-displacement responses are cut off at the point where the predicted and expected reaction forces begin to deviate (unless otherwise noted).



a) Tension Surface b) Punching Cone on Slab Side

Figure 6-16: Predicted Crack Pattern on Tension Surface and Slab Side, c_{min}/d=1.287, Equal Load Plate Loading, Visualized Through Contours of Maximum Principal Plastic Strain

The predicted shear stress distributions in the slab along the wall perimeter for each of the four load cases are provided in Figure 6-17 (note, the methodology used to calculate the shear stress distributions from the FEA results is discussed in Appendix A). For all four load cases, the peak shear stress occurs at the corner of the wall toe, and the overall shape of the shear stress distribution is similar. Additionally, the peak shear stress magnitude at failure and the overall shape of the shear stress distribution are similar to those observed in the author's numerical study of slabs supported on

rectangular columns [1, 145, 160, 324]. However, it should be noted that there are two significant differences in the predicted shear stress distribution along the long side of the wall for the load plate and UDL models (these differences occur for all analyzed specimens as discussed in Appendix B). Firstly, as seen in Figure 6-17a, while the shear stresses near the end of the wall for the connection subjected to UDL decrease significantly with increasing distance from the wall end, they do not approach a magnitude of approximately 0, as observed for the load plate specimens. Secondly, the shear stress magnitudes along the wall perimeter, particularly those beyond the low shear stress region (approximately *5d* from the wall end), are typically higher for the connection subjected to UDL. The higher shear stresses beyond the low shear stress region suggest an increased influence of one-way shear when the SWC is subjected to a UDL (as discussed in subsection 6.4.1.2 and Section 7.2.5 this region of approximately constant stress is assumed to be associated with one-way shear).

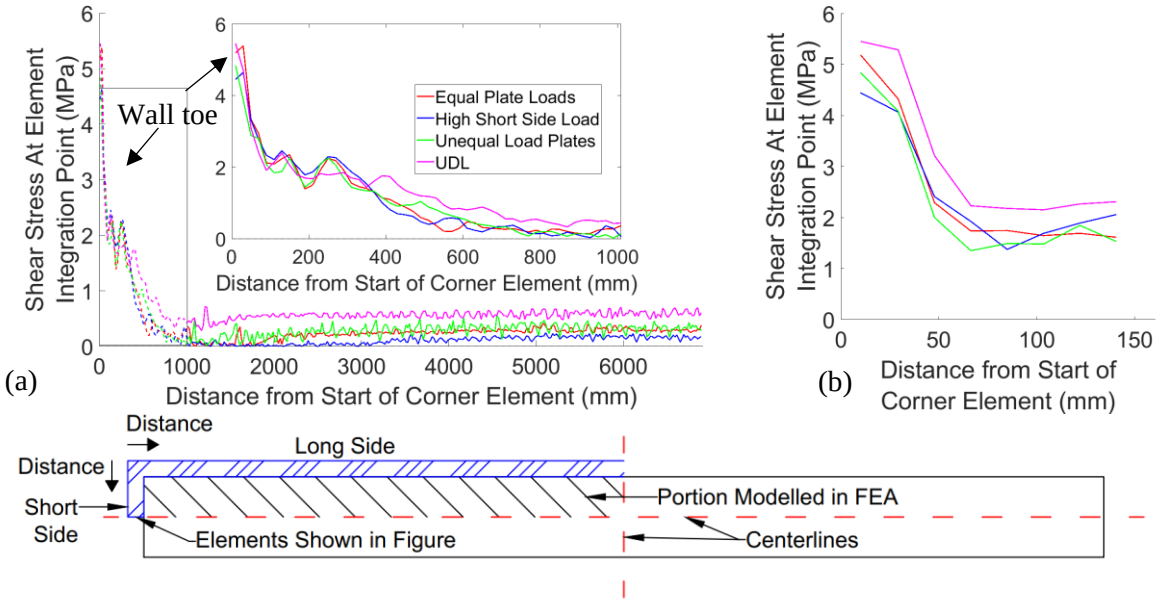


Figure 6-17: Predicted Shear Stress Distribution Along Wall Perimeter, 100% of Peak Load, Different Load Conditions; (a) Long Side, (b) Short Side (¼ of Wall Shown) (adapted from [324], Stresses Averaged Over Depth)

6.4.1.2 Parametric Study (V Study)

The V Study is an extension of the rectangular column study previously conducted by the author during their MASc studies [1, 145, 161]. The majority of trends discussed in this section were found to be consistent with those observed in the rectangular column study (which were briefly summarized

in subsection 2.3.8.4). This similarity suggests that the behaviour of R-SCCs and SWCs are related. However, as will be highlighted in this section, there are differences in their behaviour, particularly in the predicted brittleness of the failure and the shear stress distribution along the support and critical perimeters.

The FEA predicted all eight SWCs to fail in punching, whereas ACI 318-19 predicted one-way shear failures parallel to the short side of the wall as shown in Table 6-5 (note, that all provided shear capacities are for the full specimen and not the ¼ model analyzed in the NLFEA). The ACI 318-19 punching provisions, derived from tests of isolated slab-column connections [25], predict punching capacities that are on average 2.36 times greater than those predicted by the FEA. As in the previous rectangular column study [259], this overprediction is due to the assumption of a constant shear stress capacity along the entire critical perimeter length, which is larger than the shear stress predicted by the FEA along the majority of the critical perimeter, particularly along the long side of the wall. The one-way shear capacity predicted by ACI 318-19 parallel to the long side of the wall, which is the direction of dominant one-way shear behaviour predicted by the FEA, is also higher than the FEA predicted capacity for all eight specimens, though only 1.29 times greater on average. The one-way shear capacity predicted by ACI 318-19 parallel to the short side of the wall is much lower than the FEA predicted capacity, further demonstrating that ACI 318-19 does not accurately capture the behaviour of SWCs. It should be noted that the one-way shear capacities were calculated based on the isolated specimen dimensions (8245mm × 2 for failure along the long side and 1905mm × 2 for failure along the short side), instead of the distance between support centerlines in the prototype structure shown in Figure 6-1a (the bounds of isolated specimen used in the one-way shear calculations are also shown in Figure 6-1a). It should also be noted that the strength reduction factor, ϕ, was set equal to 1.0 when calculating the punching and one-way shear capacities according to ACI 318-19.

Note, the flexural capacity of the SWCs according to ACI 318-19 were not considered when evaluating the accuracy of the ACI provisions since the FEM predicts all analyzed SWCs to be governed by shear. While some yielding of the slab's flexural reinforcement is predicted in the FEA, this yielding is typically constrained to the reinforcement which crosses the wall perimeter and is near the end of the wall. Additionally, after initial yielding, the load carrying capacities of the connections continues to increase until the formation of the localized punching failures near the wall ends. Therefore, in the author's opinion, the behaviour of the analyzed SWCs is governed by shear, and the

accuracy of the ACI 318-19 shear provisions should be evaluated. While a lower capacity may be predicted according to the flexural provisions, this would still result in ACI 318-19 being inaccurate, because the failure mode is not correctly predicted. As such, only the punching and one-way shear provisions were evaluated herein. A similar reasoning is also applied when considering the specimens analyzed in Section 6.4.2, Section 6.4.3, Chapter 8 and Chapter 9.

Table 6-5: Summary of Concentric Punching Capacities and ACI 318-19 Predictions, Interior SWCs

	Wall Parameters (mm)			V_{FEA} (kN)	$V_{ACI\ 318\text{-}19}$ (kN)	
κ (c_{min}/d)	Thickness (c_{min})	Length (c_{max})	Aspect Ratio, β	(Full Model)	Punching Shear[(a)]	One-way Shear[(a)]
0.594	120	13620	113.5	2595.3	6601.7	
0.792	160	13660	85.4	2699.9	6676.9	
0.990	200	13700	68.5	2729.8	6752.3	
1.287	260	13760	52.9	2764.1	6865.8	3781.7[(b)]
1.485	300	13800	46.0	2869.9	6941.7	938.0[(c)]
1.782	360	13860	38.5	3148.5	7056.0	
1.980	400	13900	34.8	3316.0	7132.4	
2.970	600	14100	23.5	3727.4	7517.3	

[(a)] Strength reduction factor, ϕ, set equal to 1.0 when calculating ACI 318-19 shear capacities
[(b)] Assuming one-way failure along the long side of the wall (matches dominant direction of one-way shear predicted by FEA)
[(c)] Assuming one-way failure along the short side of the wall
d_{avg}=202mm, f_c'=44.6MPa, h=250mm, reinforcement details presented in Section 6.2.2
Expected wall axial load: ≈1837kN for a superimposed dead load (SDL) of 2kPa and a live load (LL) of 2.4kPa, ≈2362kN for a SDL of 2kPa and a LL of 4.8kPa.
Expected wall axial load calculated assuming a dead load (DL) factor of 1.2, a live load factor of 1.6, and a self-weight of 6kPa; tributary area for interior slab-wall connection shown in Figure 6-1a = 6.75m x 20.25m = 136.7m^2 [load factors based on ASCE/SEI 7-16 [332]]
(Note: expected wall axial loads according to NBCC 2015 [333] are 1860kN and 2350kN for LL values of 2.4kPa and 4.8kPa, respectively [dead load factor 1.25, live load factor 1.5])

While the FEA predicts the SWCs to fail in punching, in practice punching shear failures of SWCs, in particular those leading to catastrophic connection or structural failure, are exceptionally rare, if not nonexistent. The lack of punching shear failures of SWCs in practice, even without the widespread use of a consistent design method, is likely due to two factors. Firstly, reinforced concrete two-way slabs are highly redundant structures and, unlike slab-column connections, there is a large potential for shear and moment redistribution around SWCs due to the overall connection size. As such, it is likely that the shear forces usually transferred through the slab near the end of the wall can be transferred to another part of the connection and catastrophic failure is avoided. Secondly, as shown in Table 6-5, the nominal shear capacities of SWCs are very high, and in many cases greatly

exceed the expected structural load demands. It should be noted that when a strength reduction factor, ϕ, of 0.75, which is used for shear failures according to ACI 318-19 [2], is applied to the punching capacities predicted by Abaqus the factored punching capacities are lower than the expected load demands calculated according to North American building codes [332, 333] when κ ($\kappa = c_{min}/d$) is less than 1.782 (narrow walls) and the design live load is 4.8kPa which suggests that punching shear failures would occur. In reality, these connections would likely be adequate in service due to the additional capacity provided by compressive membrane action provided by the surrounding slab in a continuous system and due to the fact that the factored load demands assumed in design rarely occur in service. Therefore, concentric punching failures of SWCs without a large, concentrated load near the wall toe (end) or a large opening in the slab in the vicinity of the wall are unlikely. However, understanding the behaviour of SWCs is essential due to the importance of these connections for the performance of both the gravity and lateral load-carrying capacity of reinforced concrete structures and to avoid serviceability issues, such as excessive cracking, due to localized punching failures around the wall ends. Additionally, understanding the shear stress distribution along the wall perimeter can assist in determining the ideal locations for slab openings or large concentrated loads in the vicinity of SWCs.

The predicted load-displacement responses for the full specimens at the slab edge parallel to the short side of the wall at the wall corner (X-Wall Corner) and parallel to the long side of the wall along the wall centerline (Y-Wall CL) for all eight SWCs are provided in Figure 6-18 (see Figure 6-4 for displacement output locations). The overall capacity and stiffness were typically found to increase as κ and the wall size (thickness and length) increased. The stiffness increase parallel to the long side of the wall was found to be the largest. However, unlike experimental or numerical results for isolated slab-column connections, the occurrence of brittle punching shear failures for the isolated SWCs is not identifiable from the predicted load-displacement responses due to a plateau in the predicted reaction force at the onset of punching. A similar plateau in load-carrying capacity was observed by Szalwinski [29] in an experimental test of a coupled SWC subjected to lateral loading. However, due to the use of a force-based loading and a dynamic/explicit solution procedure in the finite element model, the accuracy of the predicted post-peak response is questionable due to the large increase in kinetic and total energies after the occurrence of punching failures near the wall toe. As such, the predicted load-displacement responses provided in Figure 6-18 have been terminated at the peak load, which was identified based on the overall equilibrium and energy balance in the FEM, and the predicted plateau in the reaction force is not shown.

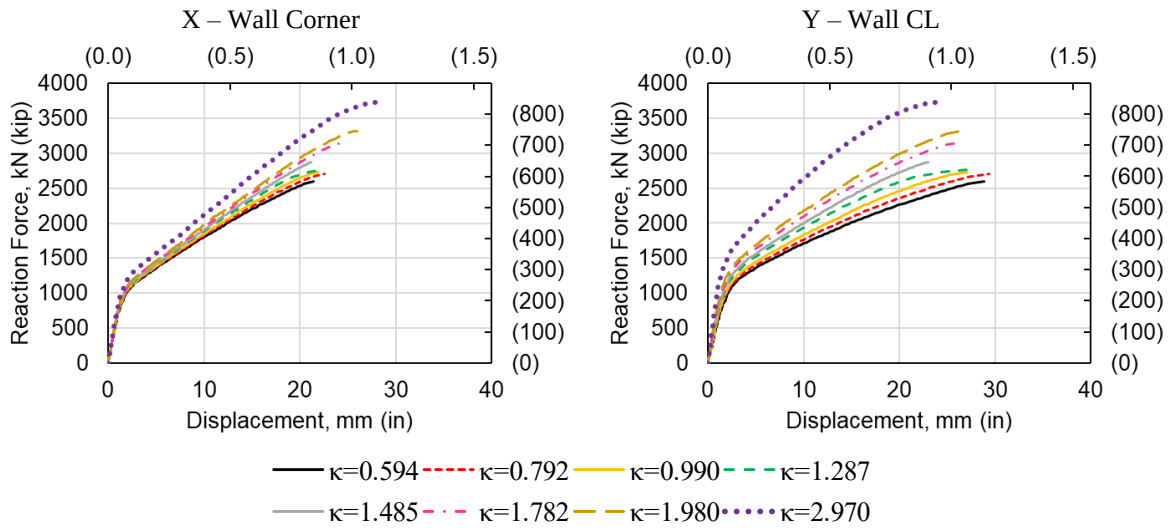


Figure 6-18: Load-Displacement Response Predicted by FEM for All Slab-Wall Specimens ($\kappa = c_{min}/d$), Displacement Output Locations Shown in Figure 6-4, Load for Full Isolated Slab-Wall Specimen

To identify the occurrence of punching shear failures in the slab-wall study the model equilibrium, energy balance, predicted crack patterns and deflected shape are analyzed. The crack patterns on the tension surface of the slab near the wall toe and on the slab sides for the SWCs where κ equals 0.594 and 2.970, which are considered representative of the crack patterns for all investigated κ values, are provided in Figure 6-19. On the tension surface of the slab, a concentration of cracking at the wall toe was predicted and the extent of cracking near the wall toe increased as κ increased. Additionally, diagonal cracks which originate from the corner of the support form on the tension surface of the slab in addition to cracks perpendicular to the long and short sides of the wall. As κ is increased, the one-way shear cracks parallel to the long side of the wall increase in size and density, demonstrating that one-way shear behaviour becomes more dominant for larger wall thicknesses and lengths. This behaviour also demonstrates that the support aspect ratio is less influential for low κ values since one-way shear behaviour is not as dominant for the SWCs studied with low κ values but high β values.

Consistent trends are also observed in the predicted crack patterns on the slab sides. As κ is increased, the punching cone on the slab side parallel to the long side of the wall becomes thinner and more inclined due to the increased dominance of one-way shear. On the slab side parallel to the short side of the wall, punching cones are also observed, confirming the influence of two-way shear on the slab behaviour near the wall toe.

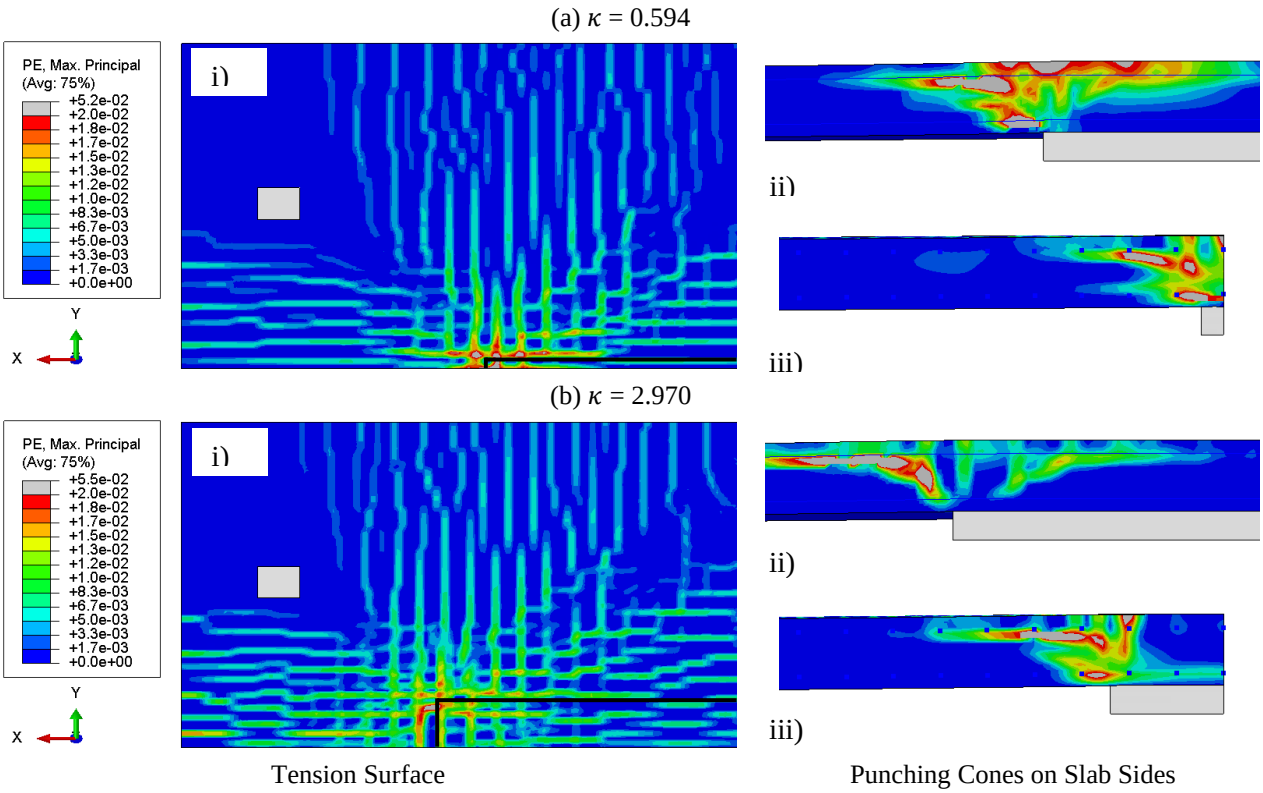


Figure 6-19: Typical Crack Pattern Near Wall Toe, (a) κ = 0.594, (b) κ = 2.970, i) Tension Surface, ii) Slab Side Parallel to Long Side of Wall, iii) Slab Side Parallel to Short Side of Wall (Entire Isolated Slab-Wall Specimen not Shown, Approximate Wall Location Shown in Black on Tension Surface)

The shear stress distribution along the wall perimeter at 100% of the estimated punching load for κ values of 0.792, 1.287, 1.782, and 2.970 (considered representative of all eight κ values), are provided in Figure 6-20 (note, the methodology used to calculate the shear stress distributions from the FEA results is discussed in Appendix A). The shear stress magnitudes along the short side of the wall, and near the wall corner, were much higher than those along the majority of the long side of the wall. Additionally, the concentration of shear stress near the corner of the wall increased as κ increased. A similar shear stress concentration was predicted by Coull and Chee [32] in their two-dimensional FEA of a pair of laterally loaded shear walls coupling a slab. Along the long side of the wall, the shear stress magnitudes decreased rapidly as the distance from the wall corner increased, though the shear stress magnitudes at a set distance from the wall corner were similar between all κ values. The peak shear stresses along the wall perimeter typically occurred at the wall corner, and had magnitudes between 5-7MPa, which are similar to those predicted in the rectangular column study

(conducted during the author's MASc studies) [145]. Unlike the shear stress distributions in the rectangular column study, the shear stress magnitudes on the long side of the wall approached a magnitude of approximately 0 at a distance of approximately *5d* from the wall toe (≈1000mm), before increasing slightly to an approximately constant value along the remainder of the wall. This zero-stress region is assumed to denote the end of the region where two-way shear has a significant impact on the slab behaviour. The influence of two-way shear being confined to a small region near the end of an elongated column or wall has also been suggested by Setiawan et al. [158, 189]. In their model used to predict the punching capacity of slab-column and slab-wall connections, which was previously discussed in Section 2.3.5, the region influenced by two-way shear is assumed to have a length of *1.5d* to match that assumed in Model Code 2010 [35]. Additionally, their model includes a *1.5d* long region between the two-way and one-way shear regions which is assumed to be under very low stress [158, 189]. Therefore, the one-way shear region is assumed to start at a distance of *3d* from the end of the support, which is smaller than the length of *5d* suggested by the Abaqus results presented herein. However, it should be noted that the model proposed by Setiawan et al. [158, 189] is based on the shear stresses along the critical perimeter located at *d/2* from the column/wall face and not the column/wall perimeter.

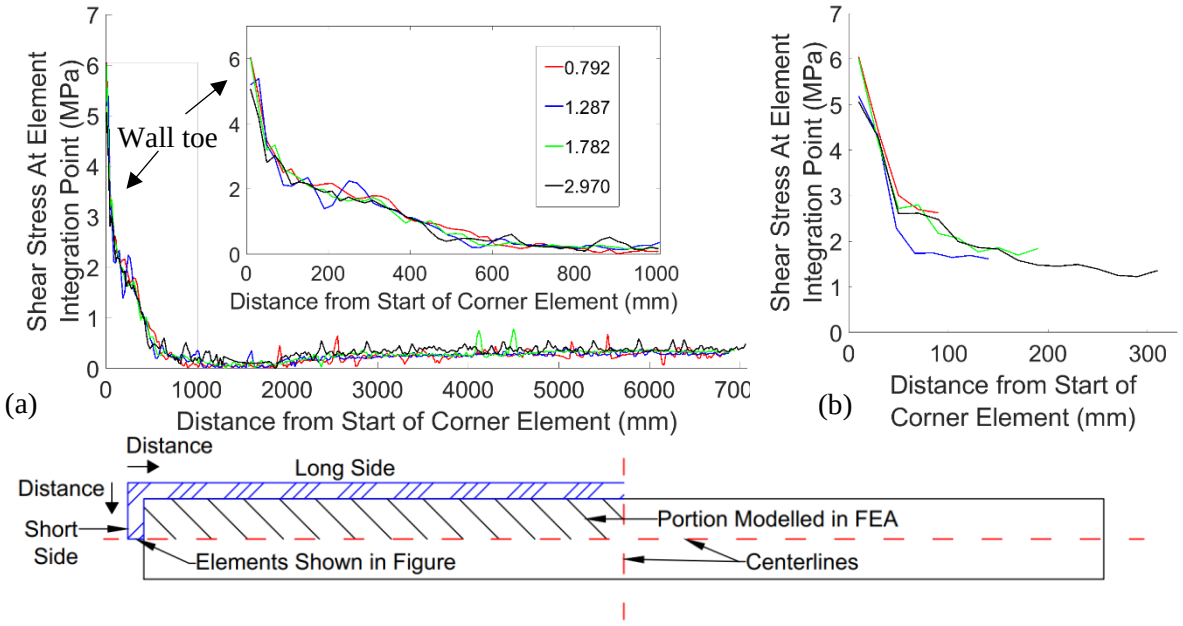


Figure 6-20: Predicted Shear Stress Distribution Along Wall Perimeter, 100% of Peak Load, κ = 0.792, 1.287, 1.782 and 2.970; (a) Long Side, (b) Short Side (¼ of Wall Shown, Stresses Averaged Over Depth)

The shear stress distributions along the ACI 318-19 critical perimeter at 100% of the estimated punching load predicted by the FEA for the same κ values as Figure 6-20 are provided in Figure 6-21. As expected, the shear stress distribution along the critical perimeter is non-uniform. Along the long side of the wall, two shear stress concentrations are predicted, the first being at the corner of the critical perimeter, and the second at the approximate location of the wall toe. The shear stress magnitudes along the long side near the wall toe and along the short side of the wall are similar to those observed in the rectangular column study. The minimum shear capacity along the critical perimeter in ACI 318-19 is equal $0.17\sqrt{f_c'}$ (MPa), which is the one-way shear capacity of concrete according to ACI 318-19 [2]. As seen in Figure 6-21, this assumed shear capacity is much higher than that predicted by the FEA along the majority of the long side of the wall. This overprediction in shear stress capacity along the critical perimeter is the primary reason why the ACI 318-19 provisions are unconservative compared to the FEA predictions. It should be noted that the shear stresses along the critical perimeter predicted by the FEA in the one-way shear region (*>5d* from the wall toe) are those at the occurrence of punching at the wall toe. Therefore, the predicted shear stresses in the one-way shear region may not be representative of those which would be developed at the occurrence of a one-way shear failure parallel to the long side of the wall without punching at the toe. This may be the reason why the ACI 318-19 one-way shear provisions overpredict the capacity parallel to the long side of the wall (see Table 6-5). However, as shown in Table 6-5, the punching capacities predicted by ACI 318-19 (recall the strength reduction factor, ϕ, was set to 1.0) are much higher than those predicted by the FEA so revisions to the code provisions are required to account for punching around walls. While a punching shear failure of a SWC is unlikely to lead to the failure of the entire connection, and potentially the structure, it is important that designers have an accurate estimate of the connection's punching capacity. Exceeding the punching capacity of a SWC would likely lead to serviceability issues as localized punching failures around the wall ends would lead to significant cracking in the region influenced by two-way shear. This cracking would be a serviceability issue as the safety of the structure, which is likely adequate, would be questioned. Additionally, excessive cracking around the wall ends due to localized punching failures would also damage services installed within or on the slab, again leading to serviceability issues.

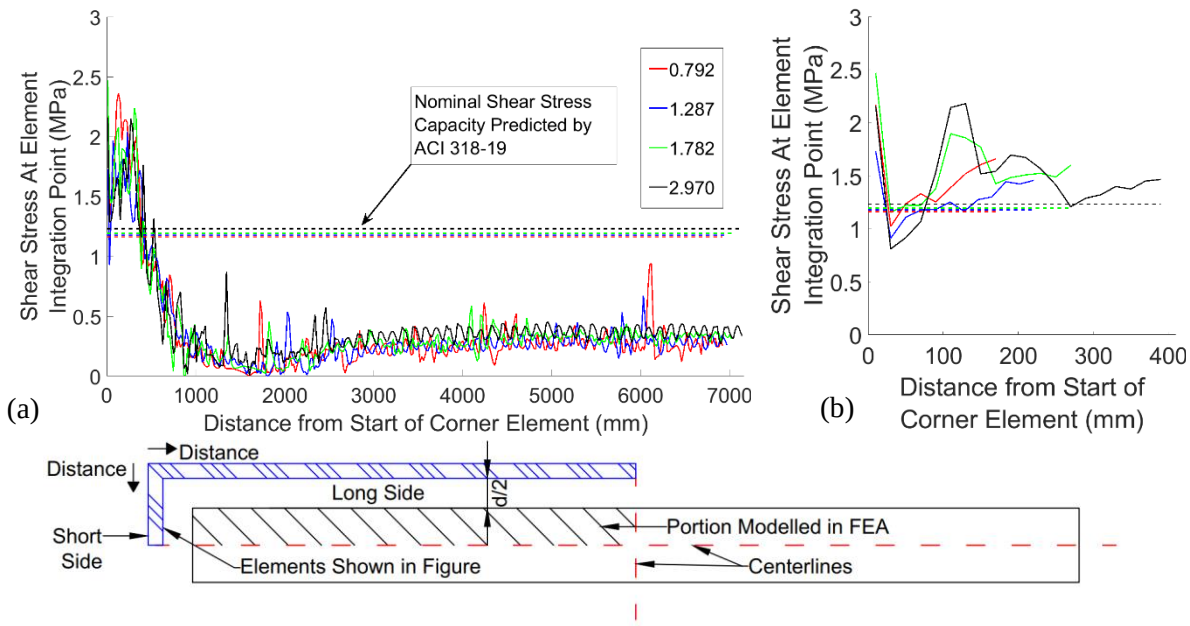


Figure 6-21: Predicted Shear Stress Distribution Along ACI 318-19 Critical Perimeter, 100% of Peak Load, κ = 0.792, 1.287, 1.782 and 2.970; (a) Long Side, (b) Short Side (¼ of Wall Shown, Stresses Averaged Over Depth)

Combining the results of the current study with the previous study of R-SCCs [1], it becomes clear that an increased portion of the total load is transferred along the long side of the supporting column or wall as the support becomes more elongated as shown in Figure 6-22 and Figure 6-23. Based on an analysis of the crack patterns and shear stress distributions along the column perimeter predicted by the FEA at the peak load level, the majority of the load along the long side of the column is transferred through one-way shear, with two-way shear influencing the stress distribution near the end of the column or wall only. Therefore, one-way shear behaviour has a large impact on the overall shear behaviour of elongated slab-column or slab-wall connections.

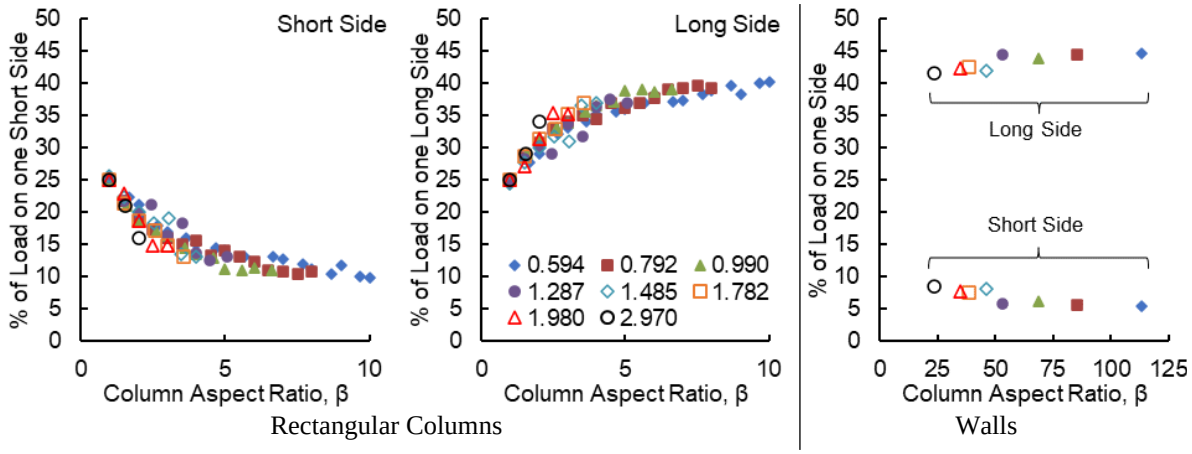


Figure 6-22: Percent of Total Load Carried on Individual Side of Rectangular Column or Walls, Rectangular Column Data Based on Simulations From Milligan et al. [145] (Legend Entries Correspond to κ Values ($\kappa = c_{min}/d$) and Applies to All Three Plots)

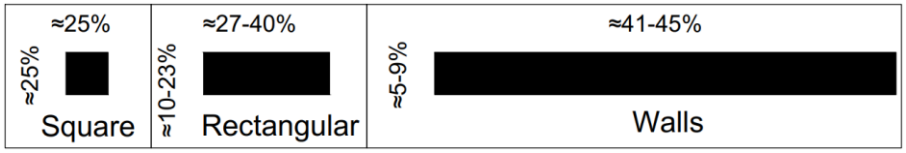


Figure 6-23: Percentage of Total Load Carried on Different Portions of Support Perimeter for Different Column Geometries and Walls (at Peak Load Predicted by FEA)

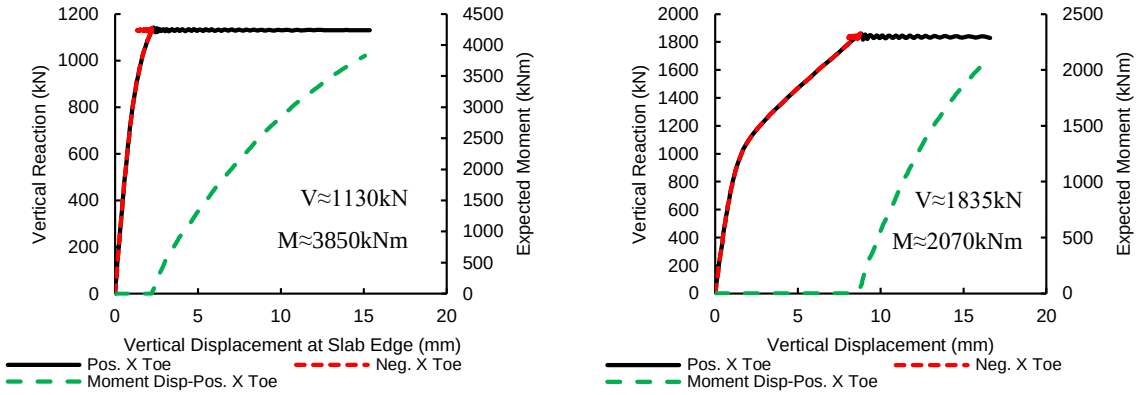
6.4.2 Combined Shear and Unbalanced Moment (V+M Study)

The predicted load-displacement and the approximated moment-displacement relationships for the two vertical load levels in the V+M Study are provided in Figure 6-24 (note, as was done for the predicted load-displacement responses in the V Study, see Figure 6-18, the data provided in Figure 6-24 has been terminated at the predicted peak load/moment). The exact moment applied to the connection cannot be determined since force-based tractions were used to introduce the unbalanced moment, which was necessary to ensure that the forces applied on the opposite slab faces were equal in magnitude, which could not be easily achieved with displacement-based loads. As such, the moment applied to the connection is estimated by multiplying the expected magnitude of the traction at each time step by the undeformed area of the slab side (the tractions were defined considering the undeformed geometry) and the distance between the two opposite slab sides (16.49m).

The predicted moment capacity of the SWC where κ equalled 1.287 was approximately 3850kNm and 2070kNm when the connection was subjected to concentric vertical loads of 1130kN (40% of

concentric capacity) and 1835kN (65% of concentric capacity) respectively. As with many of the vertical concentric punching capacities in the V Study, the predicted unbalanced moment capacities for an individual SWC are much higher than the unbalanced moment, which would be transferred between a slab and a wall in typical structures.

The predicted crack pattern for the SWC subjected to 40% of its concentric capacity, which is similar to the crack pattern for the specimen subjected to a higher vertical load level, is provided in Figure 6-25. For both vertical load levels, a punching shear failure occurred at the wall toe where the shear stresses due to concentric vertical loading and unbalanced moment are additive. However, unlike the crack patterns in the V Study, the formation of one-way shear cracks parallel to the long side of the wall was not observed in the V+M Study as seen in Figure 6-25.



(a) 40% V_{conc}+M (b) 65% V_{conc}+M

*at Positive X Wall Toe the Shear Stresses Due to V and M are additive (see Figure 6-5)

Figure 6-24: Representative Predicted Load-Displacement and Moment-Displacement Response for Different Vertical Load Levels, κ = 1.287, Displacement Recorded at X-Wall Corner Location (See Figure 6-4) (Pos. X Toe and Neg. X Toe defined in Figure 6-5)

In addition to the similarity of the tension surface crack pattern near the wall toe, other than the lack of one-way shear cracks, the shear stress distribution along the wall perimeter at the peak unbalanced moment on the half of the wall where the shear stresses due to the concentric vertical load and unbalanced moment are additive were similar in overall shape and magnitude as shown in Figure 6-26. This similarity in the shear stress distribution along the wall perimeter for both specimens in the V+M Study and the specimen where κ equalled 1.287 in the V Study suggests that the same portion of the wall is effective for transferring both concentric vertical loads and unbalanced moment

between the slab and the wall, and that punching shear failures are initiated at a similar shear stress magnitude regardless of the loading condition.

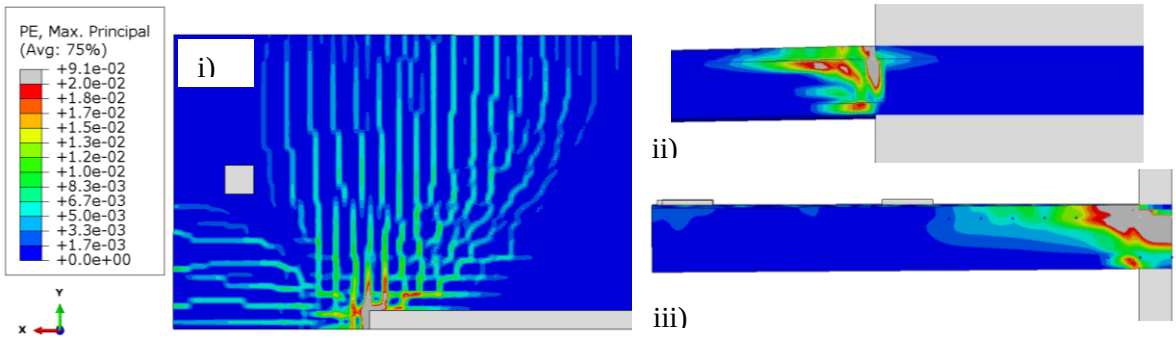


Figure 6-25: Predicted Crack Pattern on Tension Surface and Slab Sides (Positive X Toe, see Figure 6-5), i) Tension Surface, ii) Slab Side Parallel to Long Side of Wall, iii) Slab Side Parallel to Short Side of Wall, κ = 1.287, 40% of Vertical Concentric Capacity and Monotonically Increasing Uniaxial Unbalanced Moment (Entire Isolated Slab-Wall Specimen not Shown)

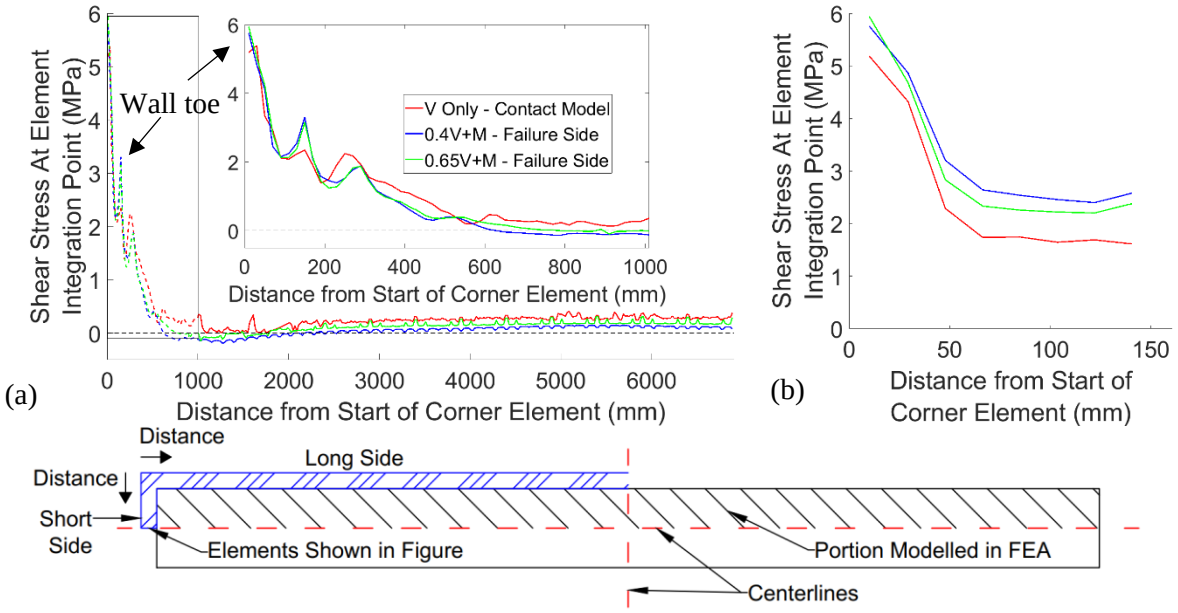


Figure 6-26: Comparison of Shear Stress Distribution Along Wall Perimeter at Failure for V and V+M Study, κ = 1.287, ¼ of Wall Shown (a) Long Side of Wall, (b) Short Side of Wall (Note, that $5d \approx$ 1000mm, Stresses Averaged Over Depth)

6.4.3 Influence of Slab Openings (Symmetric Opening Study)

6.4.3.1 Rectangular Slab-Column Connections (R-SCCs)

The FEA predicted all seven R-SCCs to fail in punching shear. Slab openings led to a reduction in connection capacity and stiffness. As shown in Figure 6-27, the stiffness reduction was approximately the same for the six opening layouts.

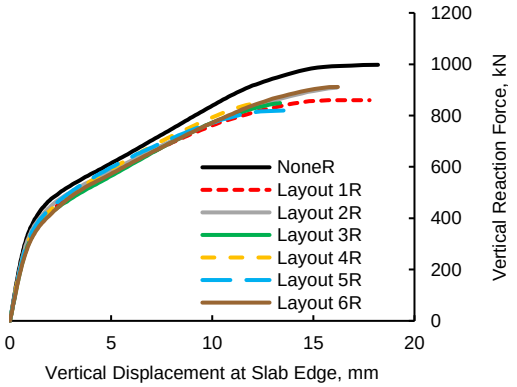


Figure 6-27: Predicted Load-Displacement Responses for R-SCCs with Symmetric Slab Openings (Displacement Outputted at Y-Location Shown in Figure 6-9)

The FEA predicted punching capacities and opening influences are provided in Table 6-6. As hypothesized, opening layouts 1R and 2R led to significant capacity reductions, but the influence of openings along the long side of the connection was larger than expected, and typically exceeded that of openings along the short side or near the column corners. Layout 5R resulted in the largest capacity reduction, approximately 17.8%, but layouts 3R and 4R had a similar impact (approximately 15% reduction). The predictions for layouts 3R through 5R demonstrate that, regardless of location, openings adjacent to the long side of rectangular columns can have a significant impact. However, the opening orientation is important as layout 6R, which has a large opening centered on the long side of the column but oriented such that the short dimension of the opening is parallel to the adjacent column side, resulted in the smallest capacity reduction, approximately 8.7%.

The slab shear stress distributions at the peak load along the column perimeter are provided in Figure 6-28, and they provide insight into why long-side openings have such a large influence. As discussed previously, with increasing support aspect ratio the portion of the total load transferred along the short sides decreases. For the analyzed column (260x760mm), approximately 34% and 16% of the peak load is transferred along each long and short side respectively. Therefore, portions of the

connection which transfer most of the load are removed when openings are along the long sides. Furthermore, when the opening is adjacent to the long side, but near the column centerline, as in layouts 4R and 5R, the portion of the connection which is subjected to low shear stress is removed, which limits any potential shear stress redistribution from the highly stressed regions near the column corners.

Table 6-6: Predicted Capacities and Opening Influences – R-SCCs

ID	V_{FEA} (kN)	β	mm b_o [a]	$V_{ACI}^{(A)}$ (kN)	$V_{ACI}^{(B)}$ (kN)	V_{ACI}/V_{FEA} (A)	(B)	Opening Impact FEA	ACI(A)	ACI(B)
NoneR	997.7		2880	1100.8	1100.8	1.10	1.10	-	-	-
Layout 1R	859.9		2227	851.1	902.0	0.99	1.05	-13.8	-22.7	-18.1
Layout 2R	908.7		2233	853.7	764.4	0.94	0.84	-8.9	-22.5	-30.6
Layout 3R	848.7	3.0	1234	471.8	871.5	0.56	1.03	-14.9	-57.1	-20.8
Layout 4R	848.6		1399	534.9	871.5	0.63	1.03	-14.9	-51.4	-20.8
Layout 5R	820.1		1818	695.1	871.5	0.85	1.06	-17.8	-36.9	-20.8
Layout 6R	911.4		2314	884.4	978.5	0.97	1.07	-8.7	-19.7	-11.1
					Avg.	0.86	1.03			

(A) Radial approach; (B) Straight projection approach; [a] b_0 applies to radial approach only ($V_{ACI}^{(A)}$);
Note: Material safety factors (ϕ) set to 1 for V_{ACI} (concentric provisions);

Openings along the long side of the column typically led to higher shear stresses along the short side, and higher peak shear stresses along the column perimeter. Regardless of location, openings along the long side of the column typically result in lower shear stress magnitudes along most of the long side. When openings are located along the short side of the connection, the shear stress magnitudes along the long side typically increase, particularly in the high shear stress region near the column ends.

Representative tension surface crack patterns for R-SCCs are provided in Figure 6-29, and are consistent with those predicted for R-SCCs with nonsymmetric slab openings, which are discussed in Sections 8.2.2 and 8.4.1. Unless interrupted by openings adjacent to the long side, significant one-way shear cracks form parallel to the long side of the column. Diagonal cracking, which is associated with two-way shear, only occurs in regions near the column ends. Furthermore, significant crack concentrations are predicted near the openings.

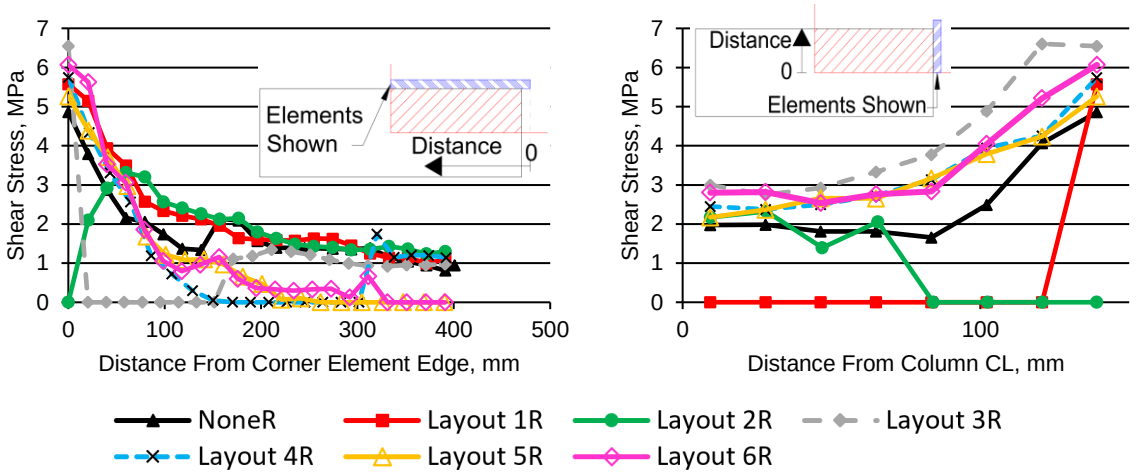


Figure 6-28: Predicted Column Perimeter Shear Stress Distributions at Peak Load, R-SCCs with Symmetric Slab Opening Layouts (¼ Column Shown, Stresses Averaged Over Depth)

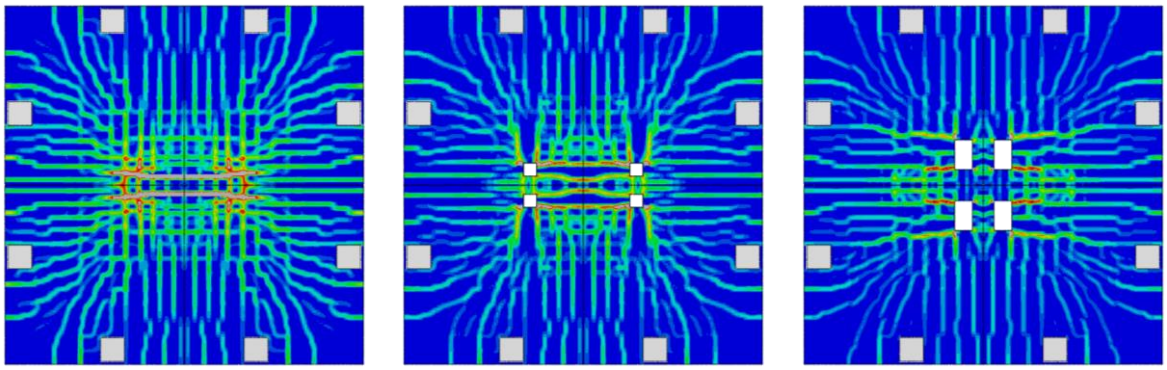


Figure 6-29: Representative Tension Surface Crack Patterns Around R-SCCs in Symmetric Opening Study

The ACI 318-19 predicted punching capacities and opening influences based on the radial approach are also provided in Table 6-6 ($V_{ACI}^{(A)}$). In terms of punching capacity, ACI 318-19 is unconservative compared to the FEA (and to the experimental capacity of 1067kN [151]) for the specimen without an opening but is conservative for all opening specimens. The ACI 318-19 predicted punching capacities for the opening specimens are conservative compared to the FEA because ACI 318-19 greatly overpredicts the opening influences, particularly when the openings are adjacent to the long side of the column. For layouts 3R through 5R, ACI 318-19 predicts capacity reductions between approximately 37-57%, whereas the FEA predicted reductions are between

approximately 15-18%. Therefore, the radial approach is not adequate for the six R-SCCs analyzed herein.

The ACI 318-19 predicted punching capacities and opening influences based on the straight projection approach are also provided in Table 6-6 ($V_{ACI}^{(B)}$). Unlike predictions based on the radial approach, the punching capacities predicted using the straight projection approach are typically only slightly unconservative compared to the FEA (only the capacity of layout 2R is underpredicted). However, the predicted opening influences agree much better with the FEA results for all layouts, other than layout 2R where the opening influence is greatly overpredicted. For example, the capacity reductions for opening layouts 3R through 5R are identical and close to that predicted by the FEA using the straight projection method. Additionally, the influence of layout 6R is accurately predicted. Therefore, the use of the straight projection approach appears to better capture the influence of openings located along the long side of the connection compared to the radial approach when the connection behaviour is dominated by punching.

Since all the critical perimeters in this study are symmetric, no unbalanced moment is generated and the ACI 421.1R-20 method does not need to be applied.

6.4.3.2 Slab-Wall Connections (SWCs)

The FEA predicted all seven SWCs to fail in punching around the wall end (wall toe), though one-way shear cracking parallel to the long side of the wall was also predicted for most connections. Slab openings reduce capacity and stiffness. For openings near the wall toe, specifically large openings within *5d* of the toe (layout 3W), the capacity and stiffness reductions are severe as shown in Figure 6-30. However, due to the overall connection size, the stiffness reduction is usually limited to a region near the opening, with the load-displacement response away from the opening being similar to that for a specimen without an opening.

The FEA predicted punching capacities and opening influences for the SWCs are provided in Table 6-7. As hypothesized, layout 3W resulted in the largest capacity reduction, approximately 39% compared to the reference specimen, which is logical considering approximately 50% of the total connection load is carried by the wall toes (region within *5d* of the wall end) and for the specific SWC analyzed, the long sides of the toes carry approximately 80% of the load transferred through the toes. Unlike the previously analyzed R-SCCs with symmetric slab opening layouts, openings at other locations adjacent to the long side of the wall, which are all located at distances greater than *5d* from

the start of the toe, resulted in insignificant capacity reductions. Limited influence of openings along the long side of the connection which do not begin at the end of the support is consistent with the results for the large R-SCCs with nonsymmetric slab openings discussed in Sections 8.2.2 and 8.4.1 (R1-L and R2-L specimens). For layouts 4W through 6W, the predicted capacities are slightly higher than that for the reference specimen, but these slight capacity increases are likely due to mesh differences between the models. Results based on the CDP model are mesh size dependent, and due to the assumed tensile constitutive relationship for the concrete, which is a function of fracture energy, smaller elements are slightly stronger than larger elements. Due to the size of the SWCs, small mesh changes can lead to small capacity increases, and therefore, the results for layouts 4W through 6W demonstrate that these openings have a very minor influence on connection behaviour. Consistent with the R-SCCs, openings near the short side of the wall can lead to significant capacity reductions, though for the analyzed SWC small openings located near the wall corners were more detrimental than openings which remove the entire short side.

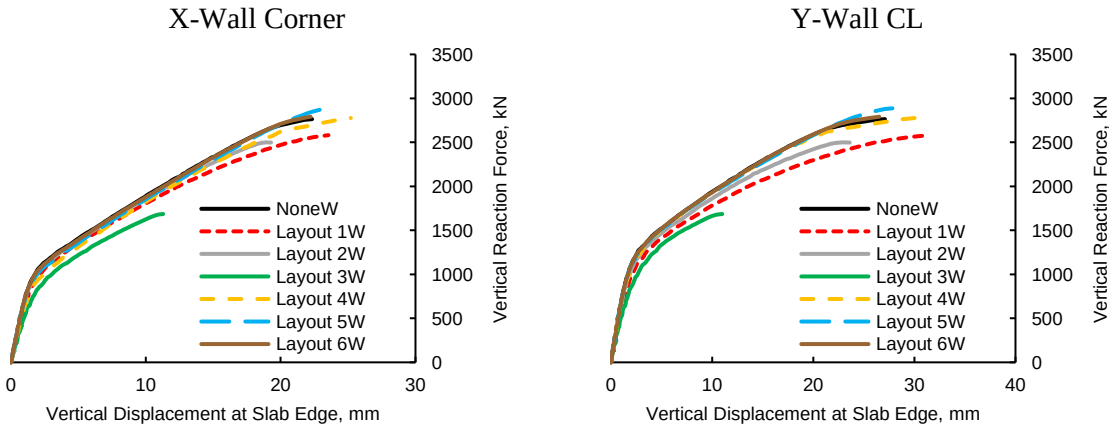


Figure 6-30: Predicted Load-Displacement Response for SWCs (Displacement Locations shown in Figure 6-4)

The slab shear stress distributions along the wall perimeter at the peak load for the seven SWCs are provided in Figure 6-31. While slab openings typically result in stress concentrations near the openings, the overall influence of openings on the wall perimeter shear stress distribution is much less significant than observed for R-SCCs. Along most of the wall perimeter, the overall shape and magnitudes of the shear distribution are similar in the regions without openings. Consistent with the rectangular column results, openings adjacent to the long side of the connection typically result in

higher shear stress magnitudes along the short side of the connection, especially when the opening is close to the wall toe.

Table 6-7: Predicted Capacities and Opening Influences – SWCs

ID	V_{FEA} (kN)	β	mm b_o [a]	$V_{ACI}^{(A)}$ (kN)	$V_{ACI}^{(B)}$ (kN)	V_{ACI}/V_{FEA} (A)	(B)	Opening Impact FEA	ACI(A)	ACI(B)
NoneW	2764.1		28840	6863.9	6863.9	2.48	2.48	-	-	-
Layout 1W	2581.9		28312	6738.4	6740.2	2.61	2.61	-6.6	-1.8	-1.8
Layout 2W	2498.4		28511	6785.7	6711.6	2.72	2.69	-9.6	-1.1	-2.2
Layout 3W	1685.9	52.9	14398	3426.8	5911.9	2.03	3.51	-39.0	-50.1	-13.9
Layout 4W	2777.1		12129	2886.7	5911.9	1.04	2.13	+0.5	-57.9	-13.9
Layout 5W	2886.5		21763	5179.6	5911.9	1.79	2.05	+4.4	-24.5	-13.9
Layout 6W	2791.7		27000	6426.0	6616.4	2.30	2.37	+1.0	-6.4	-3.6
					Avg.	2.14	2.55			

(A) Radial approach; (B) Straight projection approach; [a] b_0 applies to radial approach only ($V_{ACI}^{(A)}$);
Note: Material safety factors (ϕ) set to 1 for V_{ACI}; V_{ACI} based on concentric punching shear provisions, one-way shear capacity neglected as focus is studying the predicted opening influence

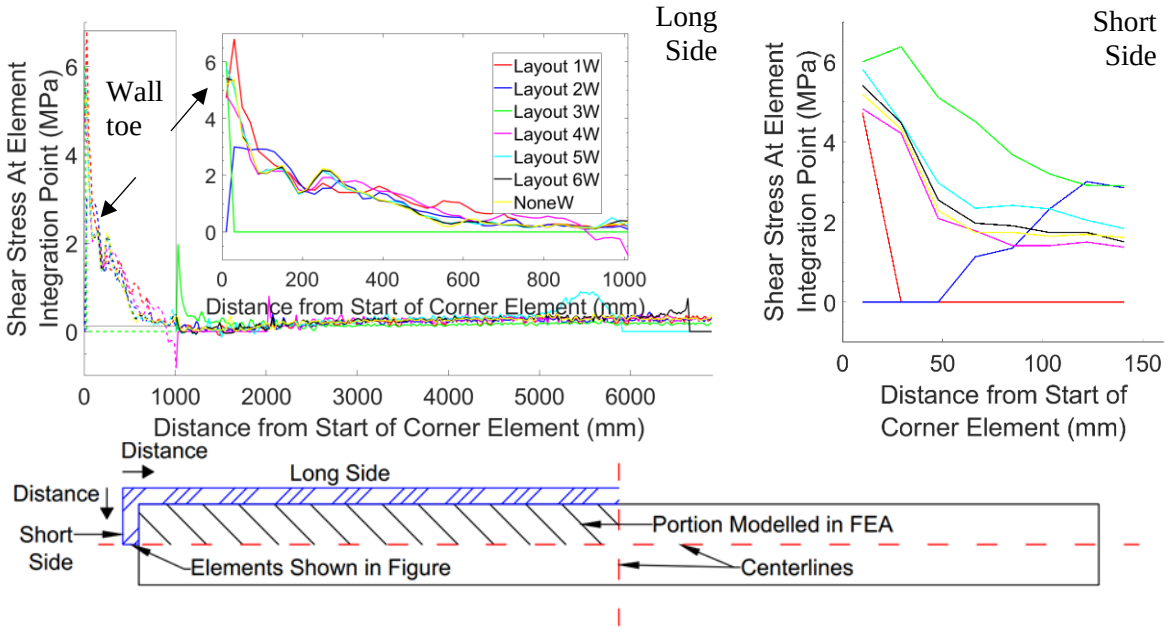


Figure 6-31: Wall Perimeter Shear Stress Distributions at Peak Load (¼ Wall Shown, Stresses Averaged Over Depth)

Representative tension surface crack patterns for the analyzed SWCs are provided in Figure 6-32. Unlike rectangular columns, the influence of the openings, other than layout 3W, on the crack patterns was minor. Compared to the other specimens, the full crack pattern does not develop for the

specimen with opening layout 3W, as shown in Figure 6-32, likely due to the much lower capacity, and because the openings have rendered the toe region relatively ineffective. For the other specimens, the predicted crack patterns are similar to those for the reference specimen, other than the crack concentrations near the opening. Additionally, for layouts 5W and 6W, limited or no cracking is predicted in the portion of the slab bounded by straight projections from the opening perpendicular to the long side of the wall, which demonstrates that the portion of the wall near the opening is not transferring load.

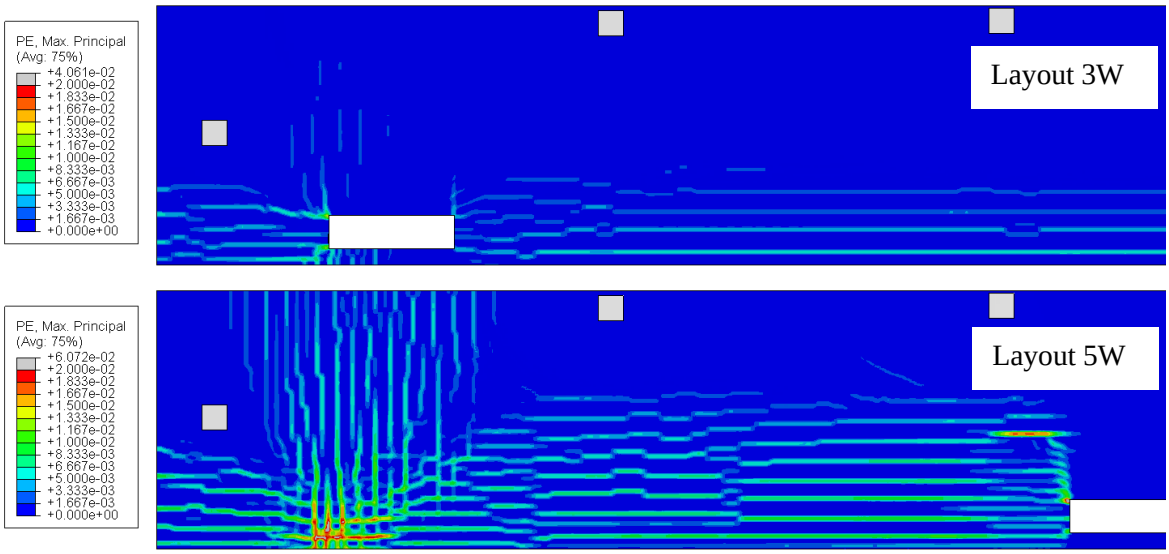


Figure 6-32: Representative SWC Tension Surface Crack Patterns (¼ Model Shown)

The punching capacities and opening influences predicted by ACI 318-19 based on the radial approach are provided in Table 6-7 ($V_{ACI}^{(A)}$). As noted by Milligan et al. [323], and discussed in subsection 6.4.1.2, the punching capacities predicted by ACI 318-19 are much higher than those from the FEA, due to ACI 318-19 predicting a higher shear stress magnitude along most of the critical perimeter. Therefore, the focus of this work is evaluating the opening influences predicted by ACI 318-19, and as seen in Table 6-7, the radial approach does not accurately predict the influence of slab openings around SWCs. Only for layouts 3W and 6W are the predicted opening influences reasonable compared to the FEA. For other openings along the long side (layouts 4W and 5W), ACI 318-19 predicts very large capacity reductions, which contradicts the FEA. For openings along the short side of the wall (layout 1W and 2W), ACI 318-19 underpredicts the opening influences, which further demonstrates that the radial approach is not adequate for SWCs.

Punching capacities and opening influences predicted by ACI 318-19 based on the straight projection approach are also provided in Table 6-7 ($V_{ACI}^{(B)}$). While the use of straight projections does reduce the predicted influence of layouts 4W through 6W, their influence is still overpredicted. Furthermore, the influence of layout 3W, which is the most critical, is now greatly underpredicted, which is unacceptable. Therefore, the straight projection approach is not suitable to account for the influence of slab openings around large interior SWCs.

6.5 Summary and Contributions

As discussed in Section 2.3.5, SWCs are essential to the structural performance of flat plate structures as they are a key component of both the gravity and lateral force resisting systems. While punching shear failures around SWCs have occurred in some of the previous studies [29, 30, 33], past research focussed on the punching shear behaviour of SWCs is limited. Furthermore, due to a lack of existing research, punching shear design provisions for SWCs are limited, or not included in worldwide concrete design codes. Therefore, the primary contribution of this chapter is a study on the punching shear behaviour of SWCs under various loading conditions. Based on the NLFEA results, detailed discussions of the capacity, stiffness, cracking, failure mechanisms and shear stress distribution around interior SWCs are provided. These discussions, which are lacking in the existing literature, are of fundamental importance to practicing engineers and should allow future designs of SWCs to be improved.

Additional contributions are summarized below. The influence of slab openings on the punching shear behaviour of R-SCCs and SWCs under concentric loading was also analyzed using NLFEA. Detailed discussions of the influence of various slab openings on the capacity, stiffness, cracking, failure mechanisms and shear stress distribution around elongated connections are provided. Furthermore, recommendations for the least desirable locations of openings around interior R-SCCs and SWCs are provided. These recommendations can assist designers in minimizing the negative influence of slab openings on the punching shear behaviour of elongated connections.

The accuracy of the ACI 318-19 shear provisions for elongated connections was also evaluated. Based on comparisons to the FEA predictions, the ACI 318-19 provisions were found to be very unconservative for SWCs. While punching failures of SWCs are not expected to lead to catastrophic structural failures due to the high potential for shear and moment redistribution after the formation of a localized punching failure near the wall ends, accurate estimates of connection capacity are essential

to avoid serviceability issues due to excessive cracking. Additionally, based on the findings of this work, it is clear that the ACI 318 opening provisions require revisions, as the influence of slab openings around elongated connections is not accurately predicted.

Chapter 7: Alternative Punching Shear Design Methods for Elongated Connections

7.1 Rectangular Slab-Column Connections (R-SCCs)

7.1.1 Motivation

As discussed in Chapter 2, a significant amount of punching shear research, the majority of which involved experimental tests of isolated slab-column connections, has been conducted. However, the current literature does not adequately address all parameters which influence punching behaviour. Some parameters, such as column rectangularity (aspect ratio, β), have not been as extensively studied as others, though recently the punching shear behaviour of rectangular slab-column [145, 151, 158, 161] and slab-wall connections [189, 323] have seen renewed interest. Quantifying the negative influence of column rectangularity on punching capacity, and the development of accurate, yet simple, code provisions is essential since rectangular columns are commonly used in flat plate structures as they reduce the slab clear span in the direction parallel to the maximum column dimension and provide additional lateral stiffness to the structural system [151]. While research has demonstrated that column rectangularity has a negative influence on punching capacity [3, 146, 147], a consensus on how to accurately estimate this influence has not been reached.

The NLFEA of 77 interior slab-column connections without shear reinforcement or slab openings subjected to concentric loading, conducted during the author's MASc studies (previously summarized in subsection 2.3.8.4), confirmed that the shear stress distribution along the column perimeter and critical perimeter at *d/2* from the column face are non-uniform around square and rectangular columns. The NLFEA also predicted shear stress concentrations along the short sides and near the corners of rectangular columns, which matches experiments [42, 52, 146, 147, 150, 151]. Most importantly, the NLFEA demonstrated that concentric punching capacity is strongly influenced by both β and the relative column size, κ ($\kappa = c_{min}/d$, where c_{min} and d are the minimum column dimension and effective slab depth, respectively) [145, 161].

Worldwide punching shear design provisions for rectangular columns differ greatly [145, 161], and current North American and European design provisions can predict significantly different punching shear capacities for a particular slab-column connection, particularly when κ exceeds 1 [161]. In addition to predicting different capacities, North American and European design codes differ in the methodology used to account for column rectangularity as discussed in Chapter 3. ACI 318-19 [2]

includes explicit equations to account for the column aspect ratio and size. On the other hand, the influence of these parameters is implicitly included in Eurocode 2 (2004) [34] and *fib* Model Code 2010 [35], through the use of a critical perimeter located at *2d* from the column face and an effective critical perimeter, respectively. While no major codes explicitly account for the influence of κ on punching capacity, even though its influence has been acknowledged by many researchers [43, 48, 50, 59, 145, 146, 150, 151], the author previously demonstrated that both Eurocode 2 (2004) and Model Code 2010 implicitly account for this parameter and predict an influence similar to that predicted by the NLFEA. The ACI 318-19 predictions, however, were strongly dependent on β and largely independent of κ as shown in Figure 7-1 [1, 161]. Note, the vertical axis in Figure 7-1 represents a normalized nominal shear capacity along the critical perimeter, v_{norm}, which is calculated using equation 7-1, and will be used throughout this section to evaluate the proposed design methods for rectangular slab-column connections (R-SCCs)

$$v_{norm} = V_{calc} / \left[b_{o,ACI} d \sqrt{f_c'} \right] \quad 7\text{-}1$$

where V_{calc} is the predicted shear capacity (N), $b_{o,ACI}$ is the length of the ACI 318-19 critical perimeter (mm) and f_c' is the concrete compressive strength (MPa).

As seen in Figure 7-1, the ACI 318-19 [2] predictions are unconservative compared to the NLFEA results [145, 161] for κ values greater than 1. Also, ACI 318-19 predicts the relationship between β and v_{norm} to be curved, whereas the NLFEA predicts an approximately linear relationship (for each κ). Therefore, the ACI 318 design provisions should be modified to better account for the influence of β and κ. However, it is desirable to keep the methods simple, and to minimize the changes to the existing provisions to ensure that the proposed methods can be easily adopted. Additionally, any proposed methods should not drastically reduce the punching capacities predicted for small (typical) sized columns as punching failures are not widespread in practice, demonstrating the adequacy of the existing provisions for many typical cases.

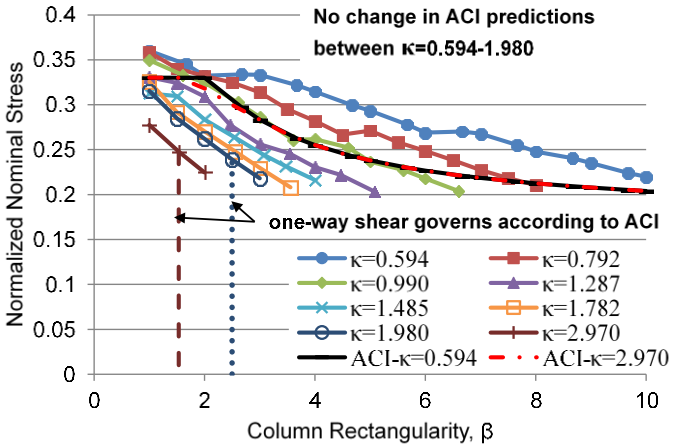


Figure 7-1: Comparison of Normalized Nominal Shear Stress Capacity, v_{norm}, Predicted by ACI 318-19 and NLFEA [161]

While recent research has led to the development of robust and accurate methods to estimate the concentric punching shear capacity of elongated connections (rectangular slab-column [158] and slab-wall [189] connections), these methods require the use of FEA and may not be feasible for common design scenarios. Therefore, there is a need for simplified design methods which are suitable for use in common design scenarios, but also accurately account for the influence of both β and κ on the concentric punching capacity of interior slab-column connections without reinforcement.

In this section, three alternative methods to estimate the concentric punching shear capacity of interior R-SCCs without shear reinforcement, which implicitly account for the influence of β and κ are presented. The previous NLFEA results for 77 interior slab-column connections [145, 161] serve as the basis for the proposed methods. The punching capacities predicted by the proposed methods are compared to those of the NLFEA and ACI 318-19 [2]. The normalized nominal shear capacities along the critical perimeter, v_{norm}, predicted by the FEA, proposed methods and various design codes are also compared. The accuracy of the proposed methods is also studied by considering 86 experimental punching shear tests from literature. Punching shear design methods for slab-wall connections (SWCs), which are extensions of the proposed methods for R-SCCs, are presented in Section 7.2.

7.1.2 Numerical and Experimental Database

During the development of the R-SCC design methods, two separate databases were considered. The first database is the 77 slab-column connections previously simulated by the author using the calibrated FEM presented in Chapter 6 to study the influence of β and κ on punching capacity [145, 161]. Of the 77 specimens, which are summarized in Table 7-1, 69 are slabs supported on rectangular columns ($\beta > 1$). Taking advantage of symmetry these specimens were analyzed using quarter models similar to that shown in Figure 7-3b. The geometric and material properties of the 77 hypothetical specimens were based on slab AM04 [151] and are summarized in Table 7-1 (the column dimensions for each individual specimen are provided in Appendix C).

The second database is made up of 113 experimental tests taken from the Joint ASCE-ACI 445C punching shear database [44], a database of shear tests of slabs supported on rectangular columns compiled by Paiva et al. [45] and various other publications (references are provided in Table 7-2). Of the 113 specimens, which are summarized in Table 7-2, 86 failed in punching, and these 86 are considered in the development of the design methods (details of the 86 specimens are provided in Appendix D). β exceeded 2 in 57 specimens. The issue with this experimental database, and with most experimental punching shear research, is that most of the slabs are relatively thin. Only 12 of the 113 specimens have effective slab depths (d) exceeding 135mm. Therefore, any proposed methods which are functions of d may be overly conservative. Additionally, most of the column aspect ratios are relatively small ($\beta \leq 5$).

Table 7-1: Summary of Isolated Slab-Column Connections in Numerical Database [145, 161]

κ (c_{min}/d ratio)	# of slabs	Min. β	Max. β	Maximum column size	
				mm	in
0.594	19	1.0	10.000	120x1200	4.72x47.24
0.792	15	1.0	8.000	160x1280	6.30x50.39
0.990	12	1.0	6.600	200x1320	7.87x51.97
1.287	9	1.0	5.077	260x1320	10.23x51.97
1.485	7	1.0	4.000	300x1200	11.81x47.24
1.782	6	1.0	3.556	360x1280	14.17x50.39
1.980	5	1.0	3.000	400x1200	15.75x47.24
2.970	3	1.0	2.000	600x1200	23.62x47.24

Note: f_c'=44.6MPa, d_{avg}=202mm, ρ_t=0.75%, 16mm diameter bars (f_y=516MPa) at 125mm o/c in both directions (tension side), 12mm diameter bars (f_y=526MPa) at 125mm o/c in both directions (compression side), slab thickness=250mm, slab properties and reinforcing match those from slab AM04 tested by Sagaseta et al. [151]

Table 7-2: Selected Databank of Punching Shear Tests for Slabs Without Shear Reinforcement and Supported on Square or Rectangular Columns

Researcher	#	$f'c$ [MPa]	d [mm] [(b)]	β (c_{max}/c_{min})	κ (c_{min}/d)
Hawkins et al. [3]	9	22.7-32.0	117.3-120.7	1-4.33	0.95-2.60
Oliveria et al. [146]	15	54-67	106-109	1-5	1.10-1.13
Regan and Rezai-Jorabi [155]	3	29-31	79	1.33-1.5	0.95-1.27
Teng et al. [147]	3	35.8-40.2	102.8-107.3	1-5	1.86-1.95
Al-Yousif and Regan [150]	4	23.0-25.7[(a)]	80	1-5	1.25-3.75
Elstner and Hognestad [47]	7	13.7-37.4	114.5	1	2.22-3.11
Lima Neto [334]	4	41-47	95-102	1-1.13	1.47-1.58
Forsell and Holmberg [335]	3	17.6	104-112	2.43-12	0.24-1.30
Carvalho [336]	3	50-52	85-86	1-5	0.99-1.00
Damascenco [337]	8	39.7-42	89.3-99.7	1-7	0.85-0.95
Vihena et al. [338]	6	51.2-55.2	65-67	1-5	1.27-1.31
Moraes Neto [339]	3	39.4-40.9	86.5-87.5	1-5	0.97-0.98
Mouro [340]	8	22-29	90-94	1-4	1.06-2.66
Borges [341]	8	36.2-44.7	139-164	1.67-4	0.94-1.44
Sagaseta et al. [151]	4	39.7-44.6	202-214	3	1.21-1.29
Vanderbilt [52]	9	45.6-53.6	38.1	1	2.00-8.00
Urban [342]	13	18.3-36.8	90-104	1-4.13	0.81-3.23
Yitzhaki [343]	1	14.7[(a)]	82	2	2.45
Moe [43]	1	27.6	114.3	3.01	1.33
Rosenthal [344]	1	17.4[(a)]	80	1.89	2.86

[(a)]$f'c$ estimated as cube strength divided by 1.15; [(b)]all effective depths less than 250mm (10") therefore size effect in ACI 318-19 [2] does not apply
Note: #: number of slabs, $f'c$: concrete compressive strength, d: effective slab depth, β: column aspect ratio, κ=c_{min}/d: ratio of minimum column dimension to effective slab depth;

7.1.3 Overview

In the following sections, three proposed methods for the design of square or rectangular slab-column connections subjected to concentric vertical loading without shear reinforcement or slab openings near the connection are presented. The intent of the proposed methods is to replace the equations for v_c in ACI 318-19 [2], which do not accurately capture the influence of β and κ as previously discussed. The first method, denoted Method 1, uses an effective critical perimeter, the length of which was estimated using linear elastic finite element analysis (LEFEA), to implicitly account for the influence of β and κ on punching capacity. The second method, denoted Method 2, uses a non-uniform shear stress distribution along the critical perimeter to account for the influence of β and κ. The non-uniform shear stress distribution was determined based on the previous NLFEA results for 77 slab-column connections [145, 161]. The third method, denoted the Combined Method, uses both Method 1 and 2 depending on the length of the maximum column dimension. The development,

implementation in design, comparisons to the numerical and experimental databases and advantages/disadvantages of each method are discussed.

7.1.4 Method 1: Effective Critical Perimeter

7.1.4.1 Development

Designing slab-column connections for punching shear by using an effective critical perimeter instead of a reduced nominal shear capacity, as is currently done in North America, is supported by research which has shown that shear stresses in the slab concentrate along the short side and at the corner of rectangular supports [26, 42, 52, 145, 146, 147, 150, 151]. As shown in Figure 7-2, effective critical perimeters for punching shear design have been suggested in historical European design codes, but to date have not been widely adopted in Eurocode 2 (EC2) [34] (note, the latest draft of Eurocode 2, prEC2 [280], proposes the same effective critical perimeter as *fib* Model Code 2010 [35]). Additionally, these historical codes do not provide the reasoning or research supporting the specified perimeters.

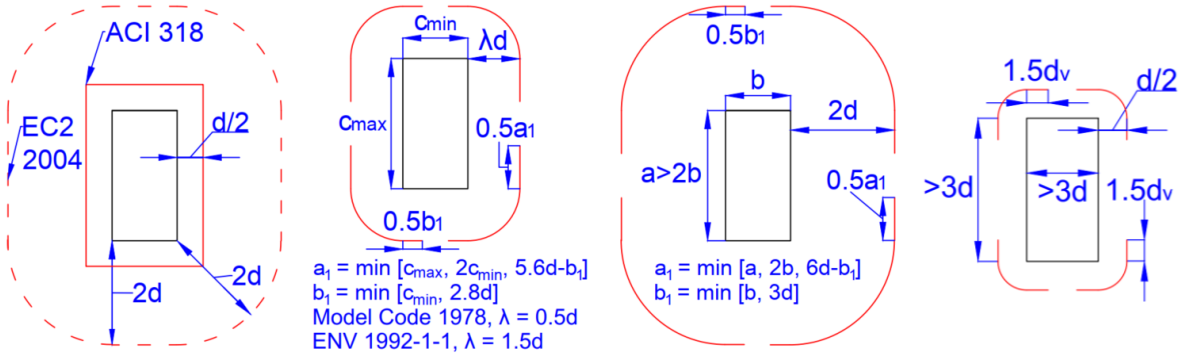
Research has shown that both LEFEA [66, 67, 151] and NLFEA [26] can be used to estimate the effective critical perimeter around square and rectangular columns. LEFEA has the advantage of lower computational demand and typically results in conservative critical perimeter length estimates, since shear stress redistribution due to concrete cracking and reinforcement yielding are neglected. Equation 7-2, which has been adopted in [35, 151, 345], can be used to estimate the effective critical perimeter around a column or loaded area, $b_{o,elast}$, based on LEFEA results.

$$b_{o,elast} = V/v_{el,max} \tag{7-2}$$

where V is the applied shear force, and $v_{el,max}$ is the maximum value of shear force per unit length along the critical perimeter calculated from the LEFEA results [67].

However, when estimating the effective critical perimeter length using LEFEA the concrete's shear modulus must be reduced to 1/8th of its elastic value to account for the concrete's reduced torsional stiffness due to cracking [66]. To input a reduced shear modulus in Abaqus the "Engineering Constants" elasticity definition is used, which allows the user to specify the elastic modulus, shear modulus and Poisson's ratio in three orthogonal directions based on an assigned material orientation. Additionally, the use of shell elements and continuous slab models where the columns are fixed to the slab are recommended [67, 151]. The use of continuous models, similar to that shown in Figure 7-3a

where all columns have the same geometry, to estimate the effective critical perimeter length was originally planned. Due to the use of continuum elements, these models were very inefficient. Therefore, the use of isolated slab-column models created during the previous parametric study of the influence of column rectangularity on punching capacity [145], similar to those in Figure 7-3b, where the slab is not fixed to the column, was investigated. The validity of using isolated slab-column models to estimate effective critical perimeter lengths has been previously demonstrated [26].



a) ACI 318-19 [2] and Eurocode 2 (2004) [EC2] [34]

b) Model Code 1978 [53] and ENV 1992-1-1 [292]

c) DIN EN 1992-1-1/NA(D) [German Annex to EC2] [346]

d) *fib* Model Code 2010 [35] and prEC2 (2020) [280]

Figure 7-2: Critical Perimeters Assumed in Various Design Codes

To estimate the effective critical perimeter length around square and rectangular columns, equation 7-2 was applied to both the short and long sides of the column (following the recommendation of [151]), as shown in Figure 7-4a, using the predicted shear stress distributions at *d/2* from the column face, which were calculated from the LEFEA results using a Python post-processing script as described in [1] (the details are the Python post-processing script have also been reproduced in Appendix A). As seen in Figure 7-5, the estimated critical perimeter lengths from the continuous models, where the slab is fixed to the columns, and the isolated models, where the slab is free to rotate off the column, are similar with a maximum difference of approximately 7% for column aspect ratios of 9 and 10 for a κ value of 0.594. Additionally, the MC 2010 [35] effective critical perimeter length agreed well with that estimated from the LEFEA results. Based on the critical perimeter lengths estimated using the LEFEA, the effective critical perimeter shown in Figure 7-4b is proposed for the design of interior slab-column connections. This effective perimeter is similar to that in MC 2010 [35], but the length of the straight portions measured from the column corners is lower (*1.125d* for the proposed perimeter as seen in Figure 7-4b vs *1.5d* for MC 2010) due to the use of 90-degree

corners to match ACI 318-19 [2], which are approximately 27% longer than the curved corners in MC 2010 [35].

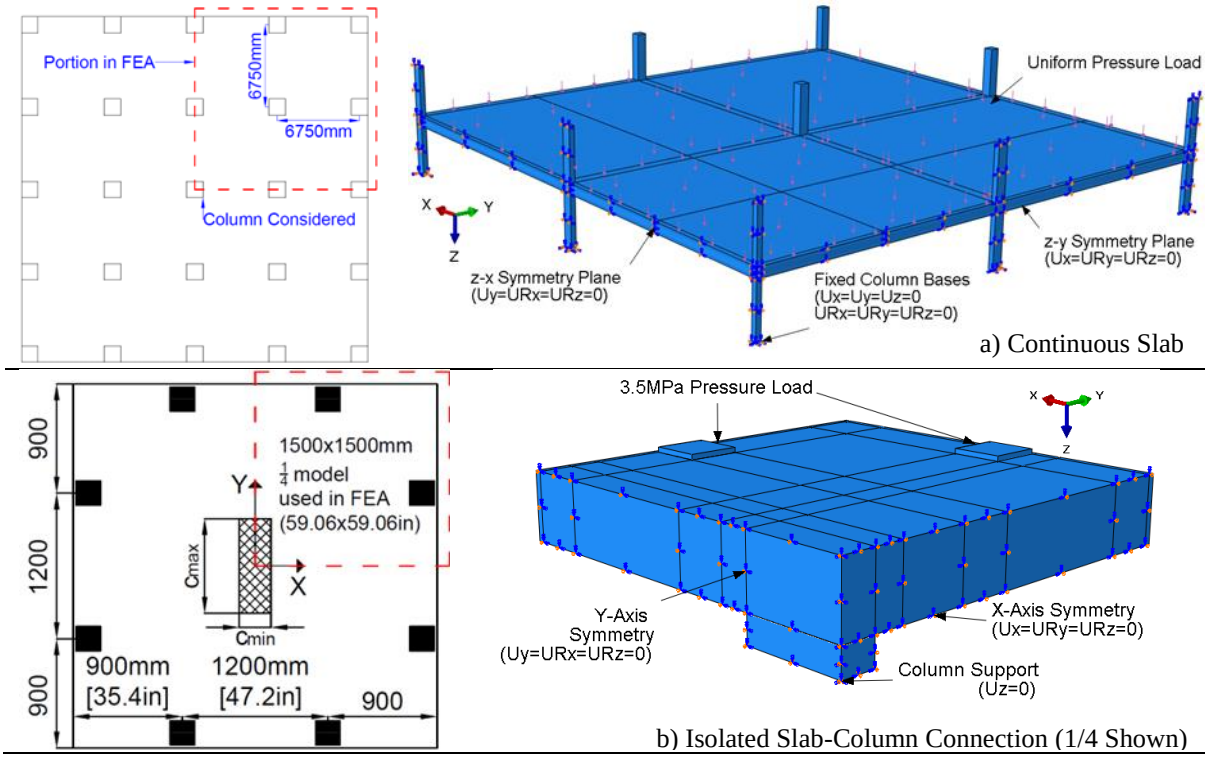


Figure 7-3: Continuous and Isolated Models Used to Estimate Effective Critical Perimeter

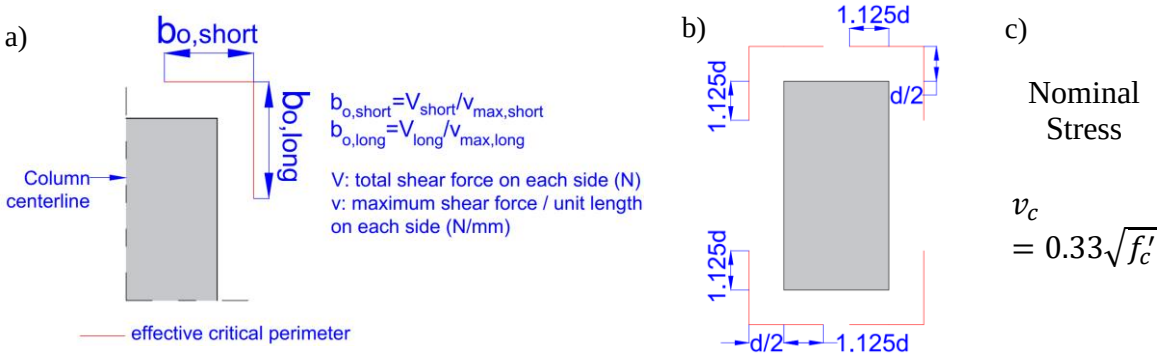


Figure 7-4: a) Calculation of Effective Critical Perimeter Length; b) Proposed Effective Critical Perimeter; c) Proposed Nominal Shear Stress (in MPa)

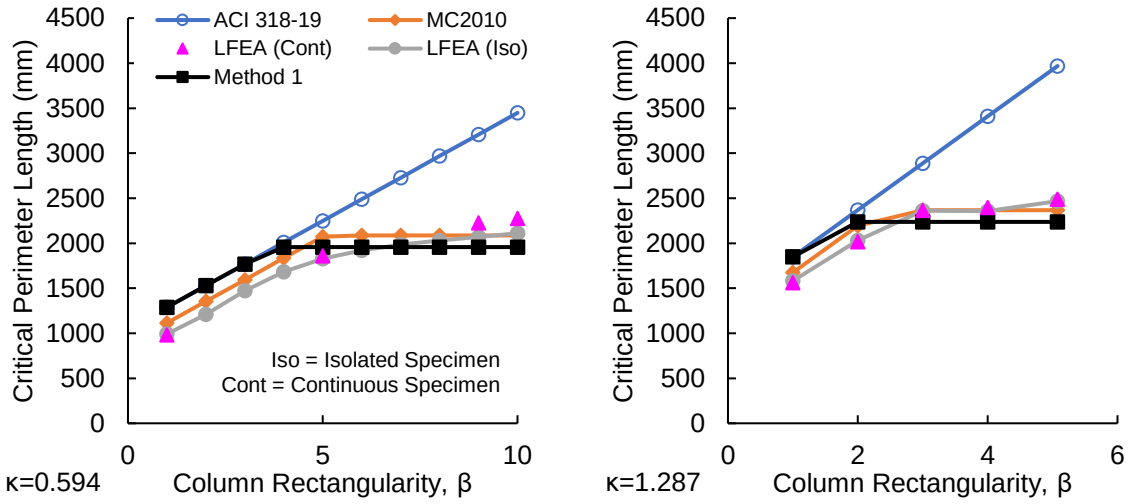


Figure 7-5: Comparison of Critical Perimeter Estimates from Design Codes, LEFEA and Method 1

7.1.4.2 Implementation

According to Method 1, the concentric punching capacity of a slab-column connection, V_c (N), can be calculated according to equation 7-3 (SI units, f_c' in MPa),

$$V_c = \left(0.33\sqrt{f_c'}\right)\left(b_{o,eff}\right)d \qquad 7\text{-}3$$

where $b_{o,eff}$ is the effective critical perimeter length (mm), which is determined according to Figure 7-4b. If V_c exceeds the required shear demand, V_f, the connection is adequate.

However, North American punching shear design typically considers shear stresses instead of force. For a slab-column connection subjected to concentric vertical loading the required shear stress demand, v_f (MPa), is calculated according to equation 7-4, assuming the critical perimeter shear stresses to be constant.

$$v_f = V_f / b_o d \qquad 7\text{-}4$$

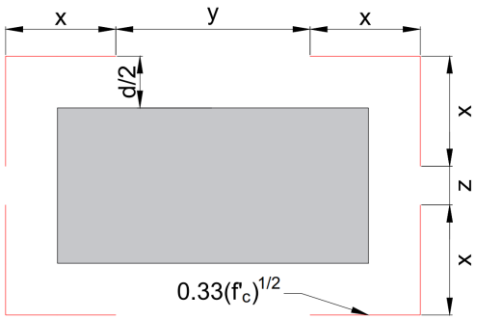
where b_o is the total critical perimeter length ($b_o = 2(c_{max} + d) + 2(c_{min} + d)$). v_f is then compared to the concrete shear resistance, v_c, and connections where $v_c \geq v_f$ are adequate. To follow a similar procedure for Method 1, the weighted average of the assumed shear stress distribution, $v_{c,eff1}$ (MPa), is calculated. For example, for a connection where both c_{max} and c_{min} exceed *2.25d* Equation 7-5 can be used to calculate $v_{c,eff1}$.

$$v_{c,eff1} = \frac{0.33\sqrt{f_c'}(8x) + 0(2y) + 0(2z)}{8x + 2y + 2z} \quad \text{7-5}$$

where x is the effective length of the critical perimeter measured from each column corner (x=*1.625d* when c_{max} and c_{min} exceed *2.25d*), and y and z are the lengths of the ineffective regions on one long and short side of the connection, respectively (a graphical representation of x, y and z is provided in Figure 7-6). It should be noted that the denominator of Equation 7-5 is equal to the total critical perimeter length assumed in ACI 318. In the case that both c_{max} and c_{min} do not exceed *2.25d*, similar equations to calculate $v_{c,eff1}$ can be derived by considering the effective critical perimeter lengths along the short and long sides separately (i.e. replacing the $8x$ term with two separate terms).

If $v_{c,eff1} \geq v_f$, the connection is adequate. $v_{c,eff1}$ also allows Method 1 to be used for connections with shear reinforcement or subjected to combined concentric shear and unbalanced moment through combination with the existing provisions. However, the adequacy of Method 1 for these connections is not studied herein.

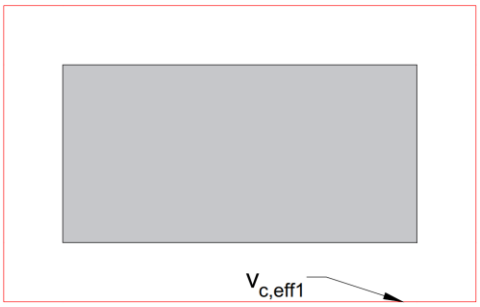
In essence, the proposed effective critical perimeter and nominal shear stress of $0.33\sqrt{f_c'}$ (MPa) replace the equations for v_c in ACI 318-19. All slabs in the numerical and experimental databases have effective depths of less than 250mm and as such λ_s, was neglected. For slabs where *d* exceeds 250mm, the assumed shear stress along the effective perimeter ($0.33\sqrt{f_c'}$ [MPa]) should be multiplied by λ_s (see equation 3-5 in Section 3.3.2).



$$v_{c,eff1} = \frac{0.33\sqrt{f_c'}(8x) + 0(2y) + 0(2z)}{8x + 2y + 2z}$$

where $8x + 2y + 2z = b_o$

a) Calculation of $v_{c,eff1}$



b) Resulting Constant Shear Stress Distribution

Figure 7-6: Example of Calculation of $v_{c,eff1}$ When Using Effective Critical Perimeter Method (Assumed Perimeter Shown in red, Stress Level in MPa)

7.1.4.3 Database Comparison

Comparison with NLFEA: As seen in Figure 7-7, the assumed effective critical perimeter and constant shear stress magnitude do not reflect the shear stress distribution along the perimeter at *d/2* from the column face predicted by the NLFEA (note, the methodology used to calculate the shear stress distributions from the FEA results is discussed in Appendix A). While the shear stresses are higher along the short sides of the column and along the long sides near the column ends, they are not constant. However, Method 1 does result in accurate punching capacity predictions compared to the NLFEA for the 77 connections, as shown in Figure 7-8. On average, the Method 1 predictions are within 10% of those from the FEM for all 8 κ values (minimum V_{calc}/V_{FEA}=0.85, maximum V_{calc}/V_{FEA}=1.07), whereas ACI 318-19 is unconservative compared to the NLFEA when κ is greater than approximately 1.

The normalized nominal shear capacities along the ACI 318 critical perimeter, v_{norm}, for Method 1, the NLFEA and various design codes are compared in Figure 7-9. The v_{norm} values for Method 1 agree well with those from the FEM [145, 161] and are typically conservative. Additionally, Method 1 implicitly accounts for the influence of κ as v_{norm} decreases for a constant β as κ increases, which matches the NLFEA results. Method 1 also predicts v_{norm} to decrease for column aspect ratios between 1 and 2 for κ values greater than or equal to 1.782. A decrease in v_{norm} for these small aspect ratios with increasing κ was also predicted by the NLFEA, EC2 (2004) and MC 2010 (though for all κ values) [161].

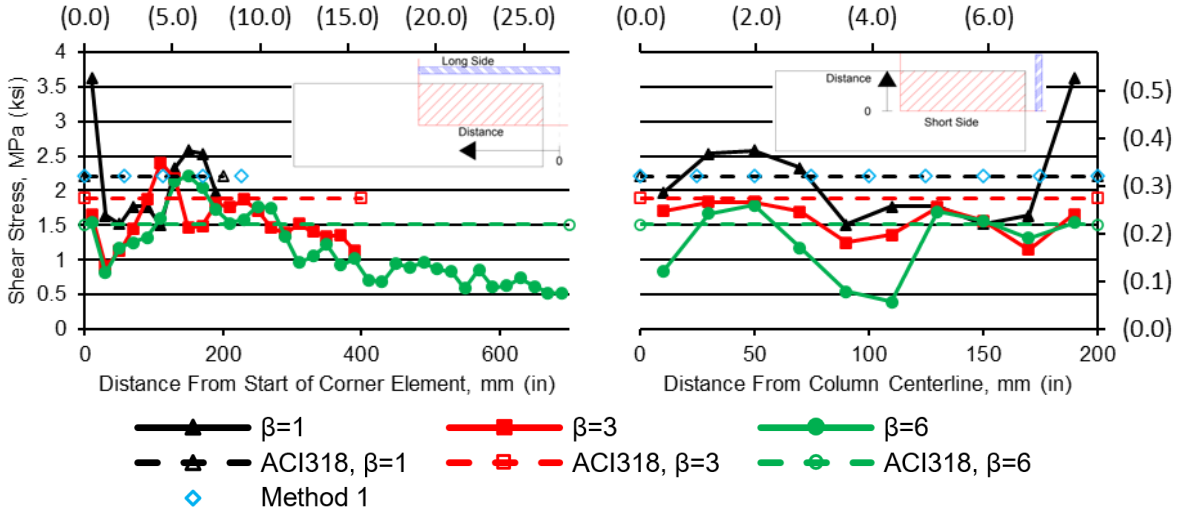


Figure 7-7: Comparison of Shear Stress Along Critical Perimeter at *d/2* Predicted by NLFEA, ACI 318-19 and Method 1, κ = 0.990 (¼ Column Shown, Stresses Averaged Over Depth)

However, Method 1 becomes overly conservative as the connection becomes increasingly elongated (for $\beta > 5$). As the connection becomes more elongated, the length of the neglected portion increases and the contribution of one-way shear to connection's capacity, which is significant and neglected when using Method 1, increases.

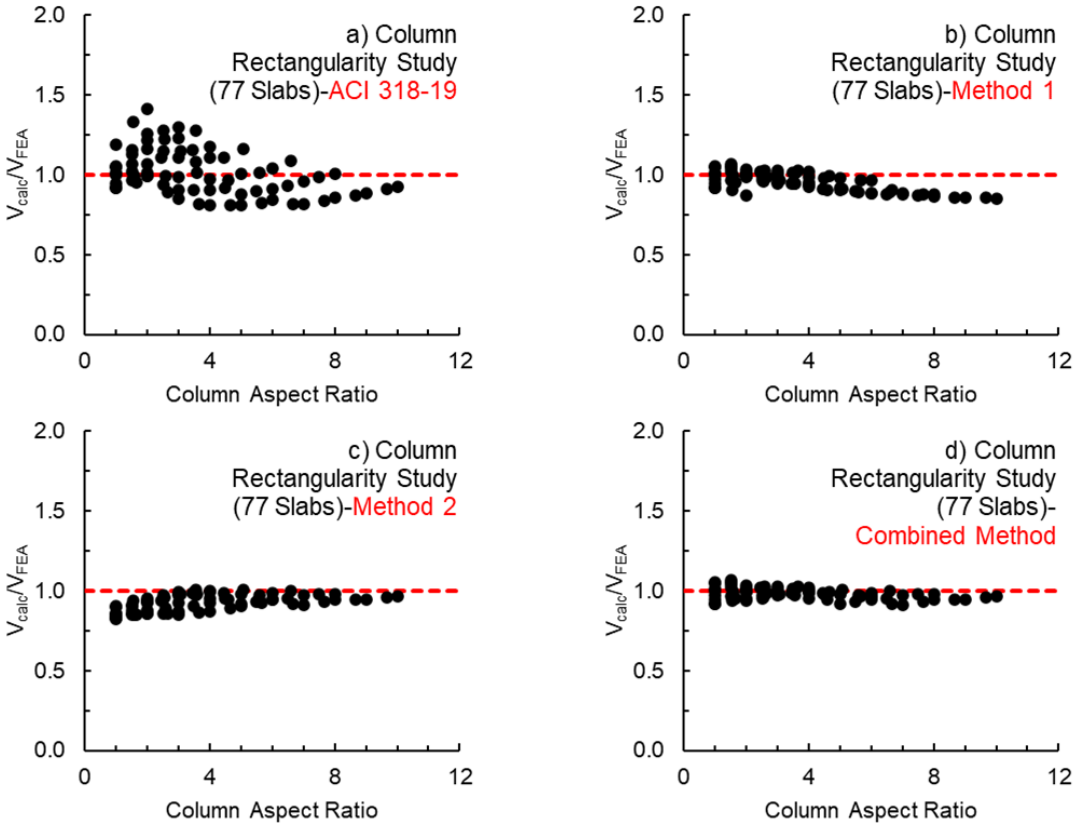


Figure 7-8: Comparison of Capacities Predicted by NLFEA [145, 161], ACI 318-19, Method 1, Method 2 and Combined Method

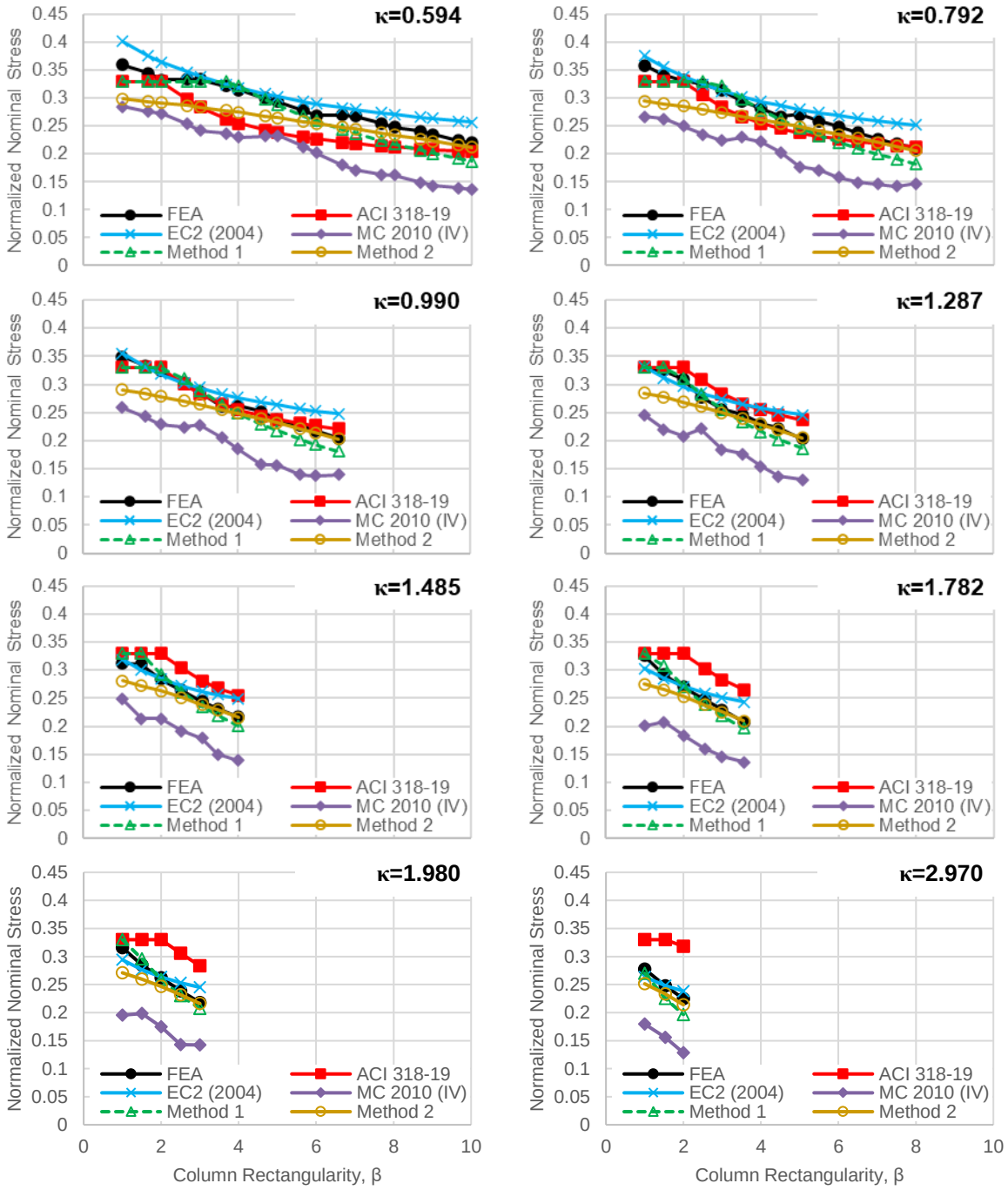


Figure 7-9: Comparison of Normalized Nominal Shear Stress Capacity Along ACI 318-19 Critical Perimeter Predicted by NLFEA [145, 161], Various Codes, Method 1 and Method 2, all κ (c_{min}/d ratios) (Note, *fib* Model Code 2010 Results are Based on Level of Approximation IV)

Comparison with Experimental Database: A comparison of the experimental and predicted capacities according to ACI 318-19 and Method 1 is provided in Figure 7-10 and Table 7-3. As seem in Figure 7-10, the predictions from ACI 318-19 and Method 1 are typically conservative. However, on average, Method 1 is slightly more conservative (average V_{calc}/V_{exp} of 0.682 compared to 0.764 for ACI 318-19). Additionally, Method 1 is conservative for the 86 experimental specimens, whereas ACI 318 is unconservative for 6 specimens, with a maximum overprediction of 28.8%.

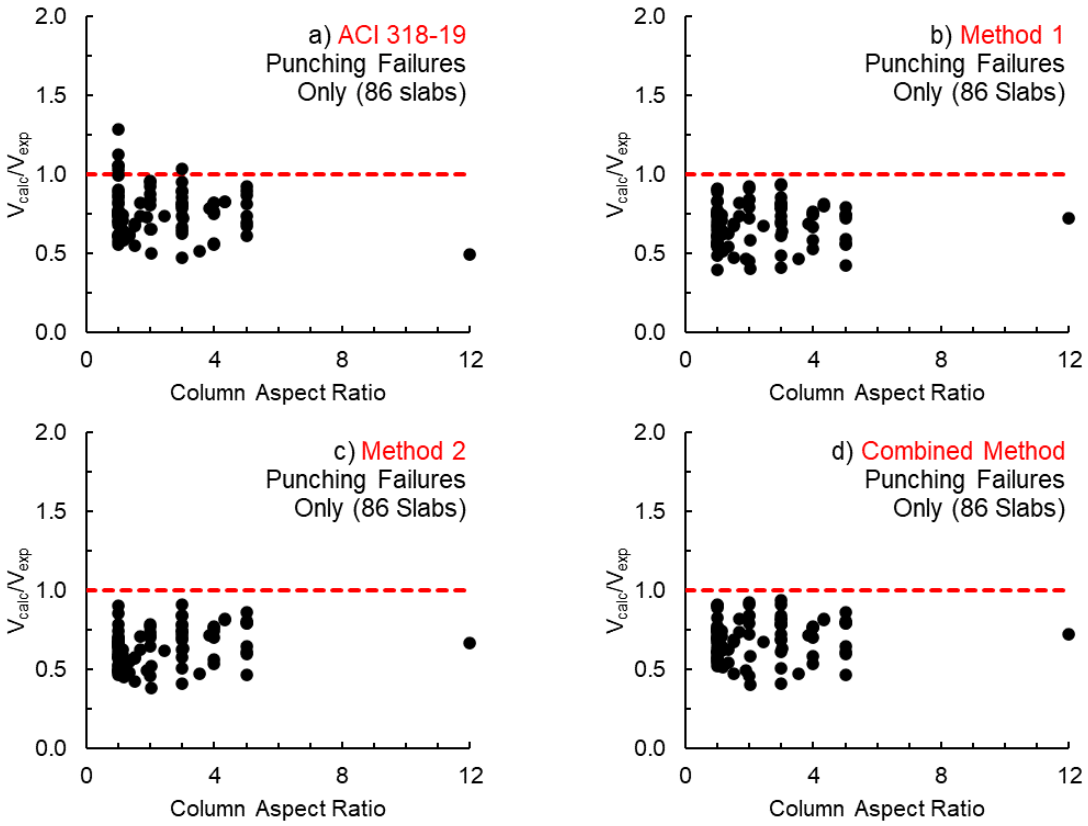


Figure 7-10: Comparison of Experimental Capacities and ACI 318-19, Method 1, Method 2 and Combined Method Predictions

Table 7-3: Summary of Predictions According to ACI 318-19 and Proposed Methods

V_{calc}/V_{exp}	ACI 318-19	Method 1	Method 2	Combined
Min.	0.471	0.396	0.380	0.404
Max.	1.288	0.935	0.913	0.935
Avg.	0.764	0.682	0.643	0.696
COV	0.198	0.199	0.193	0.186
# Overpredictions	6	0	0	0

Note: Material safety factors (ϕ) set to 1 when calculating capacity according to ACI 318-19

7.1.4.4 Advantages and Disadvantages

Advantages: Method 1 has numerous advantages. Firstly, it is simple to use and implicitly accounts for the influence of β and κ ($\kappa = c_{min}/d$). Secondly, the effective critical perimeter agrees well with the predictions from the LEFEA and with the *3d* method from MC 2010 [35]. Thirdly, the punching capacities predicted using Method 1 agree well with the NLFEA results and are conservative compared to the experimental results for R-SCCs. Finally, Method 1 and ACI 318-19 predict the same capacity for connections with column dimensions less than or equal to *2.25d* and $b_o/d \leq \approx 20.2$, which is extremely beneficial as the safety of the existing provisions for such connections has been demonstrated in practice.

Disadvantages: However, Method 1 does have disadvantages. Firstly, the assumed constant shear stress distribution along a portion of the critical perimeter does not match the shear stress distribution predicted by the NLFEA. Secondly, Method 1 becomes overly conservative as the slab-column connections become more elongated since the contribution of one-way shear (which is significant for elongated columns) is neglected. This problem also exists in MC 2010. Thirdly, the use of an effective critical perimeter may suggest that openings can be located in the "ineffective" regions, as shown in Figure 7-11, without negatively influencing punching capacity. This is untrue and complicates the treatment of slab openings near the connection (though $v_{c,eff1}$ can be calculated to allow the existing provisions to be used). Finally, as discussed in Section 7.2, when Method 1 is applied to the design of SWCs, a different effective critical perimeter is needed to estimate the punching capacity of the toe. This requires the distinction between a wall and a rectangular column to be defined.

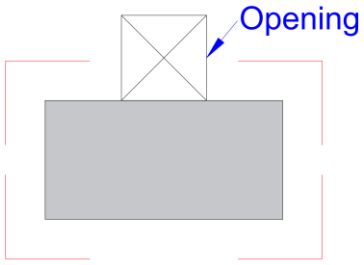


Figure 7-11: Example of Opening Located in "Ineffective" Region

7.1.5 Method 2: Non-uniform Critical Perimeter Shear Stress Distribution

7.1.5.1 Development

As discussed in Section 7.1.4, an effective critical perimeter with a constant shear stress magnitude does not accurately represent the critical perimeter shear stress distribution. While it can lead to accurate punching capacity predictions for relatively small columns, neglecting the contribution of one-way shear leads to overly conservative predictions for increasingly elongated connections. Additionally, based on experiments, Teng et al. [147] concluded that the assumption of uniform stress along the critical perimeter at $d/2$ from the column face is unreasonable for R-SCCs. Therefore, an alternative method of representing the critical perimeter shear stress distribution should be investigated. Considering the critical perimeter shear stress distributions at the peak load around rectangular columns and along the long side of the wall in the toe region (region within $5d$ of the wall end as discussed in the Section 7.2) (representative distributions are provided in Figure 7-12 and Figure 7-13, respectively, with additional plots for rectangular columns provided in Appendix E) it is observed that the NLFEA [259, 323] generally predicts the shear stresses to decrease approximately linearly with increasing distance from the corner of the critical perimeter. Additionally, the shear stress magnitudes are approximately equal at a consistent distance from the corner of the critical perimeter for different β and κ values. Furthermore, the shear stress magnitudes approach an approximately constant value at a consistent distance from the corner of the critical perimeter. As shown in Appendix E, these observations are consistent for all 8 κ values in the rectangular column study (further discussions of the shear stress distribution around SWCs are provided in Section 7.2).

Therefore, it appears that the shear stress distribution around interior elongated connections can be represented through a combination of a linear and constant stress regions. Based on the predicted shear stress distributions, the linear and constant stress regions are assumed to represent the portions of the connection influenced by two-way and one-way shear respectively.

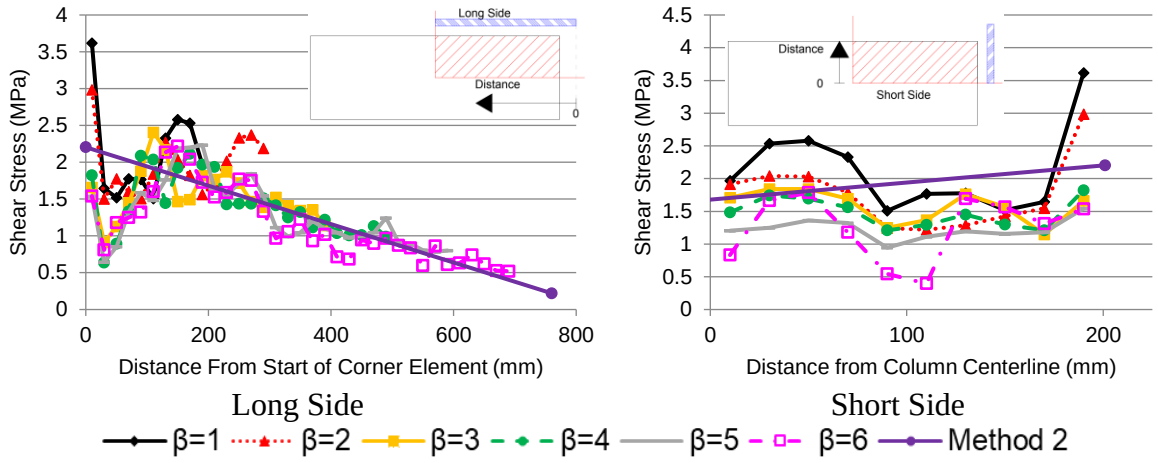


Figure 7-12: Critical Perimeter Shear Stress Distribution Predicted by NLFEA and Method 2 (Assumed Distribution in Purple), κ = 0.990, Rectangular Column (¼ Column Shown, Stresses Averaged Over Depth)

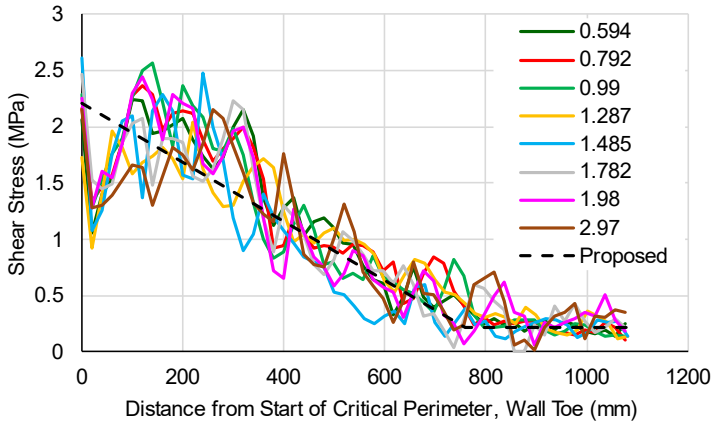


Figure 7-13: Critical Perimeter Shear Stress Distribution Along Long Side of Wall Toe (Portion of Wall Within *5d* (≈1000mm) of Wall end) Predicted by NLFEA and Method 2 (Assumed Distribution Shown With Dashed Line), All κ, f'_c = 44.6MPa (Stresses Averaged Over Depth)

7.1.5.2 Implementation

The details of the assumed shear stress distribution, which applies to all sides of the slab-column connection, are provided in Figure 7-14.

Based on the presented shear stress distributions and those provided in Appendix E, the maximum length of the linear region is specified as *3.75d* (*3.75d*≈760mm for the considered specimens). The

maximum shear stress magnitude in the linear region is once again assumed as $0.33\sqrt{f_c'}$ (MPa) to match the maximum value in ACI 318-19 [2]. However, this value also agrees well with the shear stress magnitudes predicted by the NLFEA.

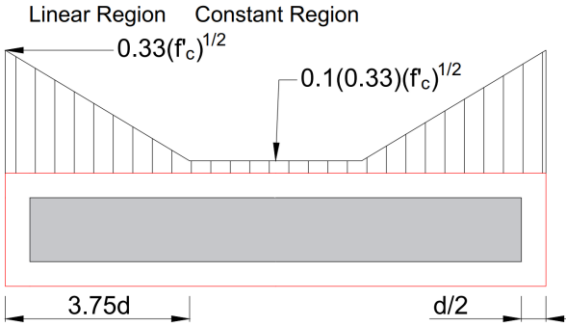
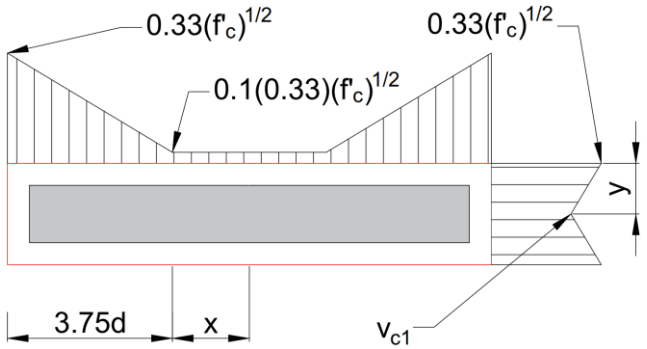


Figure 7-14: Assumed Shear Stress Distribution for Method 2 Showing Both Linear Region (Two-Way Shear) and Constant Region (One-Way Shear), Distribution Applies to All Connection Sides (Stress Levels in MPa)

For any column sides longer than *6.5d*, a constant shear region is assumed beyond the linear regions, as shown in Figure 7-14. To conservatively fit the shear stress magnitudes predicted by the NLFEA, the shear stress magnitude in the constant stress region is specified as $0.1(0.33\sqrt{f_c'})$ (MPa), which is 10% of the assumed two-way shear stress.

The proposed shear stress distribution also applies to the short sides of the connection as shown in Figure 7-15. For any connection where the side lengths are less than *6.5d*, the shear stress magnitude at the center of the column can be determined through linear interpolation, as shown in Figure 7-15. As shown in Figure 7-12, the use of the linear distribution along the short sides agrees with the NLFEA, which predicts the shear stress magnitudes to typically decrease towards the column centerline on the short side. However, while the assumed linear distribution better captures the overall trend of the NLFEA results compared to Method 1, the shear stress magnitude along the short side can still be overestimated. However, the overprediction of the short side stresses did not result in any capacity overpredictions compared to the NLFEA or experimental results, as will be discussed.

To apply Method 2 in practice, the weighted average of the shear stress distribution can be calculated using a similar procedure to that used for Method 1. By calculating the weighted average of the assumed shear stress distribution, an equivalent uniform shear stress distribution, $v_{c,eff2}$, can be determined. If $v_{c,eff2} \geq v_f$, the connection is adequate.



$$v_{c.eff2} = \frac{4 \cdot \left(\left[0.33\sqrt{f_c'} + 0.1(0.33)\sqrt{f_c'}\right]/2\right) \cdot 3.75d + 4 \cdot 0.1(0.33)\sqrt{f_c'} \cdot x + 4 \cdot \left(\left[0.33\sqrt{f_c'} + v_{c1}\right]/2\right) \cdot y}{4 \cdot 3.75d + 4 \cdot x + 4 \cdot y}$$

*v_{c1} determined via linear interpolation, $v_{c,eff2}$ to be multiplied by λ_s if $d > 250$mm

$v_f = V/b_o d \rightarrow if\ v_{c,eff2} \geq v_f \rightarrow ok!$

Figure 7-15: Calculation of $v_{c,eff2}$ for Method 2 When $c_{max} > 6.5d$ and $c_{min} < 6.5d$ (Stress Levels in MPa)

Equation 7-6 can be used to calculate $v_{c,eff2}$ for a rectangular slab-column connection where $c_{max} + d$ exceeds *7.5d* and $c_{min} + d$ is less than *7.5d*

$$v_{c,eff2} = \frac{4\left(\left[0.33\sqrt{f_c'} + 0.1(0.33)\sqrt{f_c'}\right]/2\right)3.75d + 4(0.1)(0.33)\sqrt{f_c'}(x) + 4\left(\left[0.33\sqrt{f_c'} + v_{c1}\right]/2\right)y}{4(3.75d) + \dot{4}x + 4y} \qquad 7\text{-}6$$

where x is the is the distance between the column centerline and end of the linear region, y is the length of the linear region along the short side of the connection (note, graphical representations of x and y are provided in Figure 7-15) and v_{c1} is the shear stress magnitude at the centerline of the short side of the connection, which can be determined using linear interpolation. Note that the denominator of Equation 7-6 is equal to the total critical perimeter length assumed in ACI 318. Similar equations can also be derived for connections where both $c_{max} + d$ and $c_{min} + d$ are either greater than or less than *7.5d* by calculating the weighted average of the critical perimeter shear stress distribution. As with Method 1, the ACI 318-19 [2] size effect factor (see equation 3-5 in Section 3.3.2) would need to be applied when calculating $v_{c,eff2}$ for any slabs where *d* exceeds 250mm.

7.1.5.3 Database Comparison

Comparison with NLFEA: The punching capacities predicted by ACI 318-19, Method 1 and Method 2 for the 77 numerical specimens are provided in Figure 7-8. The agreement between the FEA results and the Method 2 predictions is generally quite good. On average, the predicted capacities are within

10% of those predicted by the NLFEA (minimum V_{calc}/V_{FEA} = 0.82, maximum = 1.01). This was expected as the shear stress distribution was derived from the NLFEA results. Unlike Method 1, which becomes increasingly conservative as the columns become more elongated, Method 2 becomes more accurate as the columns elongate. However, Method 2 becomes more conservative with decreasing column size. For square columns with side lengths less than or equal to *2.25d*, Method 2 predicts lower capacities than ACI 318-19 and Method 1 method due to the assumed shear stress distribution. This could be problematic in practice, as the adequacy of such columns has been demonstrated.

Comparing the normalized nominal shear stress capacities predicted by Method 2, which are also provided in Figure 7-9, to those from the NLFEA confirms the trends discussed above. For small columns, the Method 2 predictions are well below those predicted by the NLFEA. However, as the column aspect ratio increases, the difference between the predictions from the NLFEA and Method 2 decreases. For the elongated columns (the transition point between small and elongated columns is defined in Section 7.1.6.1), the Method 2 predictions match well with those from the NLFEA as shown in Figure 7-9.

As with Method 1, Method 2 implicitly accounts for the impact of κ ($\kappa = c_{min}/d$) as a decreased normalized nominal shear stress capacity is predicted for a constant β as κ is increased, which matches the NLFEA [145, 161]. Method 2 also predicts a decrease in the normalized nominal shear stress capacity for column rectangularities between 1 and 2 for all κ values. This matches the NLFEA results [161] and European design codes [34, 35], and is an improvement over Method 1.

Comparison with Experimental Database: A comparison of the experimental capacities and Method 2 predictions is also provided in Figure 7-10 and Table 7-3. As seen in Figure 7-10, Method 2 is conservative for all 86 experimental specimens and is typically more conservative than ACI 318-19. Method 2 was also found to be slightly more conservative than Method 1 (average V_{calc}/V_{exp} of 0.643 for Method 2 compared to 0.682 for Method 1). Method 2 is typically more conservative than ACI 318-19 and Method 1 since most of the experimental connections are thin and have small effective depths.

7.1.5.4 Advantages and Disadvantages

Advantages: Compared to Method 1, Method 2 has numerous advantages. Firstly, the assumed shear stress distribution agrees well with that predicted by the NLFEA for both rectangular columns and wall toes (regions within *5d* of the wall end). The assumed shear stress distribution also allows the contribution of one-way shear to the connection capacity to be accounted for. Secondly, though a nonlinear shear stress distribution is used, the assumed critical perimeter length matches that used in North American design codes [2, 36]. Though not studied herein, it is anticipated that Method 2 could more accurately account for the influence of slab openings since both the opening size and location are considered through the use of a non-uniform shear distribution along the critical perimeter. Finally, as shown in Section 7.2, Method 2 is also applicable to the punching design of wall toes.

Disadvantages: The largest issue is that Method 2 can be overly conservative for small square columns and columns with low aspect ratios. Predictions for these small columns, which are common in practice, can be much lower than those from ACI 318-19, which is problematic as the adequacy of ACI 318 for these connections has been verified through years of use. Additionally, the use of a non-uniform shear stress distribution may be problematic even though it can be converted to a uniform distribution through the calculation of $v_{c,eff2}$. For connections with dimensions less than or equal to *6.5d*, or with slab openings near the connections, linear interpolation is required to determine the shear stress distribution before calculating $v_{c,eff2}$.

7.1.6 Combined Method

7.1.6.1 Development

Both Method 1 and Method 2 struggle with different column geometries. Due to neglecting the contribution of one-way shear, Method 1 becomes overly conservative as the column becomes more elongated. On the other hand, Method 2 is most accurate for elongated columns but can be overly conservative for small columns, due to the assumed linear stress distribution. Comparing the normalized nominal shear stresses predicted by the NLFEA, Method 1 and Method 2, which were presented in Figure 7-9, there appears to be a transition point between the two methods. For column rectangularities less than the transition point Method 1 accurately reflects the NLFEA predictions, whereas for the larger rectangularities Method 2 is more accurate. Converting the horizontal axis in Figure 7-9 from β to c_{max}, as shown in Figure 7-16, reveals that the transition point is approximately constant for different κ values. For κ values less than or equal to 1.485, the transition point occurs

when c_{max} is between approximately 760 and 800mm. For larger κ values the transition point occurs when c_{max} is between approximately 900-1000mm (with Method 2 typically being more conservative than Method 1 for smaller c_{max} values). Therefore, the transition point in the Combined Method was assumed to occur when c_{max} exceeds *3.75d* (approximately 760mm for the analyzed specimens) for all κ values.

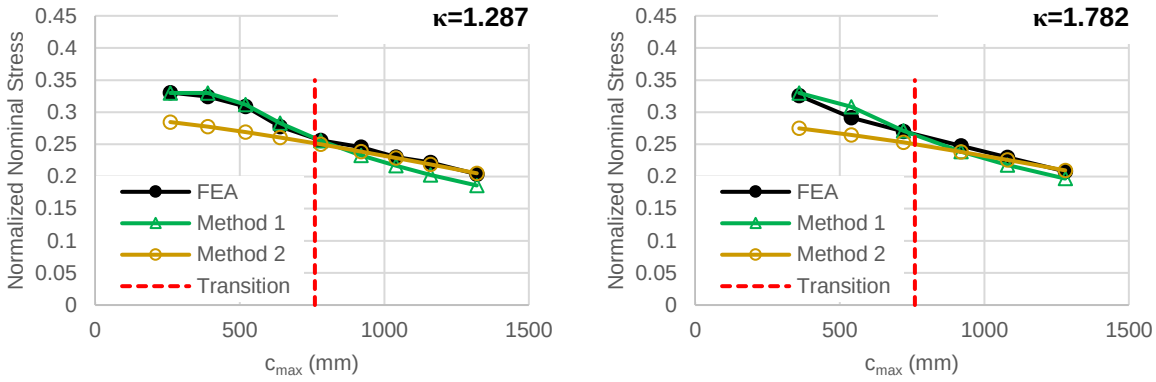
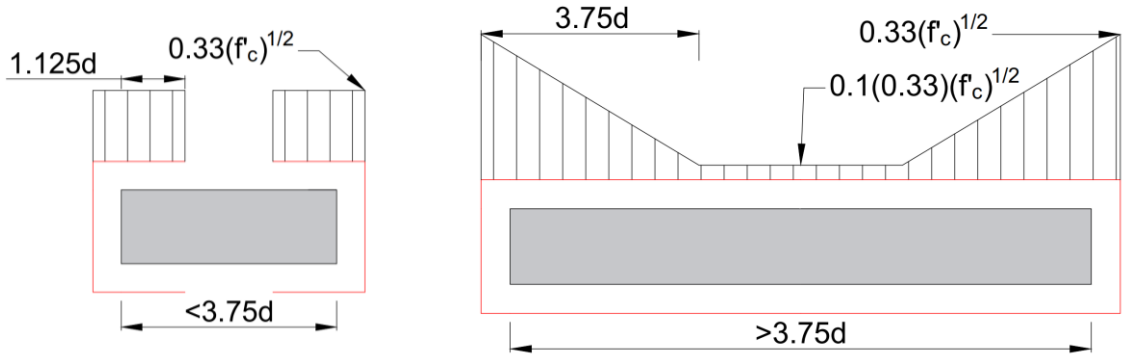


Figure 7-16: Comparison of Normalized Nominal Shear Stress Predicted by NLFEA [145, 161], Method 1, and Method 2 and Location of Transition Point Assumed in Combined Method

7.1.6.2 Implementation

The implementation of the Combined Method is dependent on the maximum column dimension, c_{max}, as shown in Figure 7-17. The connection's punching capacity is estimated using Method 1 when c_{max} is less than *3.75d* and Method 2 when c_{max} is greater than or equal to *3.75d*. As discussed in Section 7.2, when c_{max} exceeds *14d* the column is treated as a wall, and a design procedure which breaks the wall into a two-way shear (toe region) and one-way shear regions is necessary (the Combined Method is overly conservative for connections where c_{max} exceeds *14d*, as discussed in Section 7.2.8).



Method 1 (Effective Critical Perimeter), $c_{max} < 3.75d$

Method 2 (3.75d Linear Method), $c_{max} \geq 3.75d$

Figure 7-17: Assumed Critical Perimeter and Shear Stress Distributions in Combined Method (Stress Levels in MPa)

7.1.6.3 Database Comparison

Comparison with NLFEA: A comparison of the predicted capacities from the Combined Method and the NLFEA is also provided in Figure 7-8. As expected, the predictions from the Combined Method display exceptional agreement with the NFLEA results [145, 161]. The Combined Method predictions are accurate for all considered κ and β values.

Additionally, the Combined Method results in normalized nominal shear stresses which agree very well with the NLFEA. However, since Method 1 is used for columns where c_{max} is less than *3.75d*, the negative influence of column rectangularity for small β values predicted by the NLFEA is not captured for κ values less than 1.782. However, this issue, which was originally discussed when presenting Method 1, does not result in significantly unconservative predictions for the analyzed connections, and matches the ACI 318-19 predictions.

Comparison with Experimental Database: A comparison of the experimental capacities and Combined Method predictions is also provided in Figure 7-10 and Table 7-3. As expected, the Combined Method is conservative for all 86 experimental specimens, and is typically more conservative than ACI 318-19 (6% lower on average). The Combined Method is also slightly less conservative than Method 1 and Method 2 (average V_{calc}/V_{exp} of 0.696 compared to 0.682 and 0.643 respectively as seen in Table 7-3). The Combined Method also has the lowest coefficient of variation (COV).

7.1.6.4 Advantages and Disadvantages

Advantages: Using a combination of Method 1 and Method 2 has numerous advantages. By using the Combined Method, accurate predictions for both small and elongated columns can be made. The Combined Method also predicts the same capacity as ACI 318-19 for columns with side lengths less than or equal to *2.25d* and $b_o/d \leq \approx 20.2$, which is beneficial, as discussed previously. Also, the confusion as to the distinction between a rectangular column and a wall is removed, as once one of the connection dimensions exceed *3.75d* the linear stress distribution is triggered (when the total connection length exceeds *14d* the wall design procedure presented Section 7.2, but the punching capacity of the toe region is still estimated using a procedure similar to Method 2).

Disadvantages: The primary disadvantage of the Combined Method would be potential confusion regarding the treatment of openings. However, as previously discussed, the calculation of $v_{c,eff1}$ or $v_{c,eff2}$ would allow the ACI 318-19 opening provisions to be used.

7.2 Slab-Wall Connections (SWCs)

7.2.1 Motivation

While punching shear failures of SWCs may not result in catastrophic structural failures, due to the failure being primarily confined to regions near the wall ends (wall toes), accurate shear capacity estimates for SWCs are essential due to the importance of the SWCs for both the gravity and lateral force resisting systems. Additionally, accurate capacity estimates will also help avoid excessive cracking near the wall toes, which could lead to serviceability issues. As demonstrated in Chapter 6, the ACI 318-19 punching shear provisions and one-way shear provisions are inadequate for estimating the concentric shear capacity of SWCs with or without slab openings. Additionally, while alternative methods for estimating the punching shear capacity of SWCs have been proposed in research (see Figure 2-14), most of these methods are for lateral loads only. Only the method recently proposed by Setiawan et al. [189], which involves decomposing the SWC into two-way and one-way shear regions accounts for concentric loading. While this method is accurate and robust, it requires the use of two-dimensional nonlinear layered shell elements, joint elements along the critical perimeter at *d/2* from the connection face and application of the critical shear crack theory (CSCT) to estimate the punching capacity of SWCs, making it unsuitable for hand calculations and common design scenarios. Furthermore, methods which are suitable for hand calculations are essential as such methods are frequently used by engineers to perform design checks on analysis done by computer or

to fill the analysis gaps in commonly used design software. Therefore, there is a need for simplified provisions which can accurately estimate the concentric punching shear capacity of SWCs.

Furthermore, as discussed in Chapter 6, while the punching behaviour of SWCs subjected to concentric loading is similar to that of R-SCCs there are key differences, which suggests that the punching shear design of R-SCCs and SWCs should differ.

The first key difference in the behaviour of SWCs compared to slab-column connections is the brittleness of the failure. The nonlinear finite element model (FEM) predicted all 8 interior SWCs (loaded with load plates) to punch around the end of the wall (wall toe), though significant one-way shear cracking in the slab parallel to the long side of the wall was also predicted. Even though the SWCs were predicted to fail in punching, the predicted load-displacement responses did not display a clear softening branch after the onset of punching, which differs from the typical response of slab-column connections. The lack of a clear softening branch, which was also observed in experimental tests of coupled SWCs subjected to lateral loads [29], suggests that punching failures of SWCs may not lead to catastrophic structural collapse. Due to the large size of SWCs, the potential for shear and moment redistribution is high, so shear forces which are typically transferred through the end of the wall can likely be redistributed to other portions of the connection after the onset of punching.

The second key difference is observed in the support perimeter shear stress distribution. As for R-SCCs [145], the highest shear stresses in the slab occur along the short side of the wall and near the corner of the wall along the long side. The shear stress concentration in this area increased as κ increased [323]. Two-dimensional FEA of a pair of laterally loaded shear walls coupled by a slab also predicted shear stress concentrations near the wall corners [32]. Consistent with the predictions for R-SCCs [145] the shear stresses along the long side of the SWCs decreased rapidly with increasing distance from the wall corner, though the shear stress magnitudes at a consistent distance from the wall corner were similar for all κ values. Furthermore, the shear stresses along the long side of the wall approach a magnitude of approximately 0MPa at a distance of approximately *5d* from the wall toe ($5d \approx 1000$mm for the analyzed specimens) before increasing slightly and approaching an approximately constant value along the remainder of the wall. This zero-stress region was not predicted in the NLFEA of R-SCCs [145], and is assumed to denote the end of the region influenced by two-way shear. The influence of two-way shear being limited to a small region near the end of very elongated columns or walls has also been suggested by Setiawan et al. [158, 189], though their analysis was based on the shear stress distribution along the critical perimeter at *d/2* from the support

face. The region of approximately constant stress along the remainder of the wall is assumed to be the region dominated by one-way shear [323]. As will discussed herein, the shear stress distributions along the critical perimeter at *d/2* from the wall face predicted by Abaqus also suggest that the wall should be designed considering separate two-way and one-way shear regions.

In this section, a simplified design method to estimate the punching shear capacity of interior SWCs without shear reinforcement subjected to concentric vertical loading is presented. The proposed design method is an extension of that proposed for R-SCCs in Section 7.1 and is intended to be used when the maximum support dimension is greater than or equal to *14d* (the choice of this transition point is discussed in Section 7.2.5). As discussed herein, the proposed design method is developed and verified considering the NLFEA results for SWCs presented in Chapter 6. The proposed method is similar to that proposed by Setiawan et al. [189] in the fact that the SWC is decomposed into two-way regions, near the ends of the wall, and one-way shear regions, but is suitable for hand calculations.

7.2.2 Numerical Database

As discussed in Chapter 2, punching shear tests of SWCs subjected to concentric loading are nonexistent in the existing experimental database. Therefore, the design methods presented herein were developed and verified considering the FEA results for the 8 SWCs subjected to concentric loading through equally loaded load plates, presented in subsection 6.4.1.2. Due to the lack of other data these 8 connections were reanalyzed as part of this work with a reduced concrete strength (note, the flexural reinforcement of these specimens matches that discussed in Section 6.2.2). Other than a reduced capacity due to the lower concrete compressive strength (30MPa vs 44.6MPa) the overall behaviour of these specimens was similar to that presented in subsection 6.4.1.2.

7.2.3 Overview

In the following sections, the proposed methods for estimating the applied load demand and the punching shear capacity of interior SWCs without shear reinforcement subjected to concentric vertical loading are presented. As with the methods for R-SCCs presented in Section 7.1, the proposed method is intended for application in ACI 318 and therefore, the maximum assumed shear stress magnitude is $0.33\sqrt{f_c'}$ (MPa).

Firstly, an estimate of the tributary area of interior SWCs based on the results of linear elastic FEA is discussed. Shell element modelling of continuous slab systems similar to those shown in Figure

7-18a was used to study the tributary area around interior SWCs. General recommendations regarding the tributary area of interior SWCs when the slab is subjected to uniform vertical loading are provided.

Secondly, a method to estimate the punching capacity of interior SWCs is presented. The SWC is broken into two regions, one near the wall toes which is assumed to be dominated by two-way shear, and the remainder of the wall which is assumed to be dominated by one-way shear.

The proposed method for the punching design of interior SWCs is intended to apply to connections with a maximum dimension greater than or equal to *14d* (the determination of this transition point is discussed). For connections of this size, the methods presented in Section 7.1 could be used to estimate the connection capacity, but generally become increasingly conservative as the influence of one-way shear is underpredicted as shown.

7.2.4 Estimation of Load Demand (Tributary Area Study)

In the design of reinforced concrete flat plates subjected to uniform gravity loading the applied load on each slab-column connection is typically estimated as the product of the tributary area of each column and the applied loading. For slabs supported on columns alone, the tributary area of each column (other than first interior columns), which is defined by the lines of zero shear in the slab, can be accurately estimated by considering the area surrounding each column bounded by the slab centerlines. A similar methodology could also be used to estimate the punching shear demands of interior SWCs, but an estimate of the tributary area of SWCs is needed. Ideally, the tributary area of interior SWCs could also be calculated as the area surrounding the wall bounded by the slab centerlines, but the validity of this assumption needs to be verified.

In this work, linear elastic finite element analysis (LEFEA) is used to estimate the location of the lines of zero shear around interior SWCs when the slab is subjected to uniform gravity loading. Two slab layouts are considered. The first layout, shown in Figure 7-18a, is identical to that used to determine the dimensions of the isolated SWCs analyzed in Chapter 6, and represents a structure with a centrally located SWC and 4 slab bays in each direction (4x4 Grid). The SWC is also centrally located in the second layout, but 2 slab bays have been added in all directions, resulting in a total of 8 slab bays in the horizontal and vertical directions (8x8 Grid). In both layouts the centerline distance between columns is 6750mm, the slab is 250mm thick and all columns are square. To study the influence of support width on tributary area the analysis was conducted for 200mm (κ=0.594) and

600mm (κ=2.970) support widths. Due to the large structure size, shell element modelling was used to reduce the required computational demand.

Two variations of the linear elastic FEM were implemented in Abaqus. In the first, denoted the Pin Model, the columns and walls were simulated as pin supports at the column centroid and a line of pin supports along the wall centerline, respectively. In the second, denoted the Detailed Model, the supporting columns and wall are modelled using beam and shell elements, respectively. Representative boundary conditions used in the Detailed Model are provided in Figure 7-18b, and are similar to those used by Setiawan et al. [189] in the analysis of slab-wall corner connections. Also based on [189], the Detailed Model included the full column and wall height (3m) above and below the slab. It should be noted that in both models, the loading is applied to the slab only, and not the regions which are common to the supports and the slab. Additionally, no rebar is included.

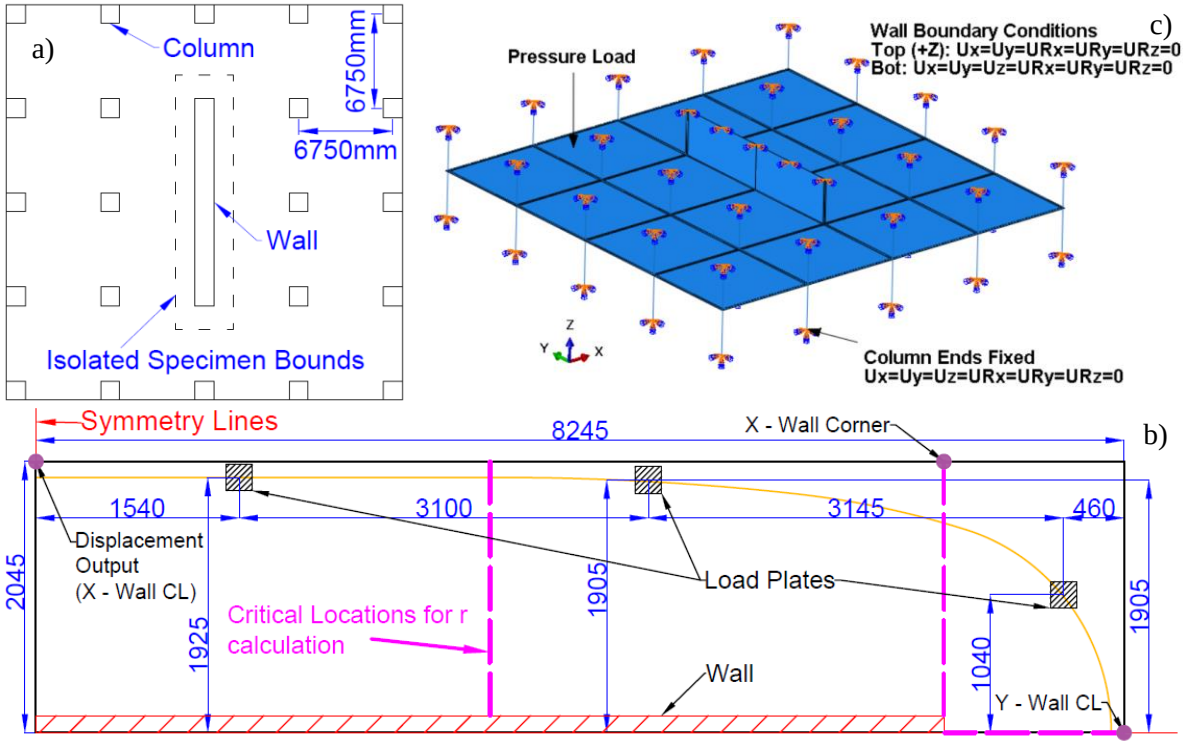


Figure 7-18: a) Representative Interior SWC Analyzed; b) Details of Isolated SWCs Analyzed (¼ Model Shown) [323]; c) Boundary Conditions in Tributary Area Study

The concrete was modelled as a linear elastic, isotropic, homogeneous material. A Poisson's ratio of 0.2 was used for the concrete, and the elastic modulus, E_c, was calculated using equation 7-7 [36] assuming f_c' as 45MPa and a concrete density, γ_c, of 2300kg/m^3.

$$E_c = \left(3300\sqrt{f_c'} + 6900\right)(\gamma_c/2300)^{1.5} \quad \text{7-7}$$

To approximate the influence of cracking, the elastic modulus of the slab and the supporting columns/walls was reduced to 25% and 70%, respectively, of the value determined using equation 7-7. These reduced elastic moduli values are in line with recommendations for member properties in CSA A23.3-19 [36] when determining slenderness effects for reinforced concrete structures.

Shell element, S4R, which is a four noded (6 degrees of freedom per node), reduced integration, homogenous, general purpose, conventional shell element that can account for thin and thick plate behaviour [303, 304], was used to model the slab and wall. The S4R elements were integrated during the analysis using a Simpson's rule with 7 section points through the element thickness. Mesh sizes from 20-130mm were investigated. As shown in Figure 7-19a (which is representative of the trends along all analyzed paths [see Figure 7-21a for the location of each analyzed path]), the assumed mesh size had no influence on the predicted slab displacements. In terms of the sectional moments, the influence of the assumed mesh size was also minor, other than the fact that the peak moment at the column centroid or wall centerline increased with decreasing mesh size, as shown in Figure 7-19b. This was expected due to the formation of stress concentrations at these locations, but had no influence on the overall behaviour. A global mesh size of 100mm was selected for all analyses. Quadratic beam element, B32, was used to model the columns in the Detailed Model (a 100mm mesh size was also used for the B32 elements to match that used for the slab). The FEM was also formulated to account for nonlinear geometric effects.

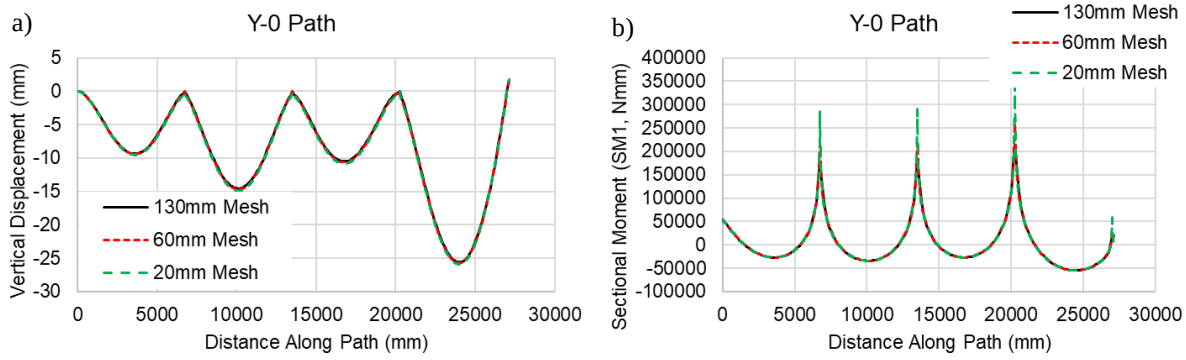


Figure 7-19: Comparison of Results Along Y-0 Path (see Figure 7-21a) for Different S4R Sizes, Pin Model, 8x8 Grid; a) Vertical Displacements; b) Sectional Moment (SM1)

Multiple methods of modelling the connection regions between the slab and supporting columns/walls were investigated (see Table 7-4 for an overview of the investigated methodologies),

but the connection region modelling was found to have a minor influence on the LEFEA results as shown in Figure 7-20a (note the results for this path are representative of those for all other analyzed paths [see Figure 7-21a for the location of each analyzed path]). The shape of the displacement profile along each analyzed path was found to be similar regardless of the methodology used to model the connection region. While the use of a very stiff connection region did result in lower overall displacements, the location of the maximum displacement was still approximately the same. As with the slab displacements, the methodology used to model the connection region also had a minor influence on the sectional moments along each path as shown in Figure 7-20b. In terms of the span moments the chosen methodology had no influence. The use of a very stiff connection regions did result in higher peak moments at the column and wall, but these higher peak moments had no influence on the predicted tributary area. Therefore, for simplicity, the portions of the slab common to the supports were modelled with a very stiff material (elastic modulus equal to $10E_c$, methodology 4 in Table 7-4), instead of introducing rigid links between the slab and the support centerlines.

Table 7-4: Overview of Investigated Connection Region Modelling Methodologies and Notation Used in Figure 7-20

#	Methodology Description	Figure 7-20 Notation
1	No explicit modelling of connection region between slab and wall/column. Wall represented by line of pins along wall centerline (CL).	PinnedWall
2	No explicit modelling of connection region between slab and column. Shell elements representing wall tied to shell elements of slab along wall centerline. Elastic modulus of wall elements set to $0.7E_c$ to represent uncracked wall.	ShellWallCL
3	Same overall methodology as method 2, but elastic modulus of wall elements set to $0.35E_c$ to represent cracked wall.	SoftShellWallCL
4	Shell elements representing wall (elastic modulus = $0.7E_c$) tied to shell elements of slab along wall centerline. Portion of slab common to slab and wall modelled with very stiff elements (elastic modulus = $10E_c$)	StiffConnReg
5	No explicit modelling of connection region between slab and column. Shell elements representing wall tied to shell elements of slab along outer edge of wall as recommended by Setiawan et al. [189]	ShellWellOuter
6	Use of structural distributed coupling constraint in Abaqus to join nodes of slab elements within region common to slab and wall to nodes of wall elements. This method could only be used to model the column regions since it is not possible to couple to more than one master node, and therefore, it was not studied further.	NA

*similar methodologies used to model connection region between column and slab

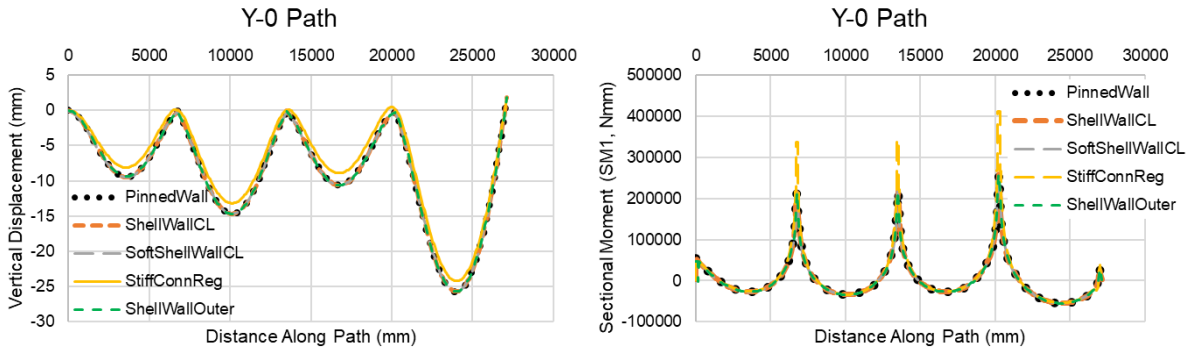
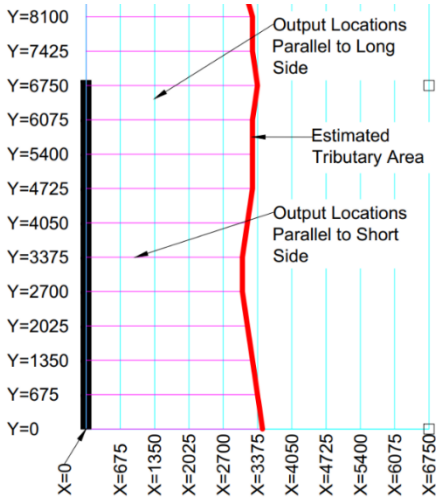


Figure 7-20: Comparison of Results Along Y-0 Path (see Figure 7-21a) for Different Connection Region Modelling Methodologies, 8x8 Grid; a) Vertical Displacements; b) Sectional Moment (SM1), see Table 7-4 for Definition of Legend Entries

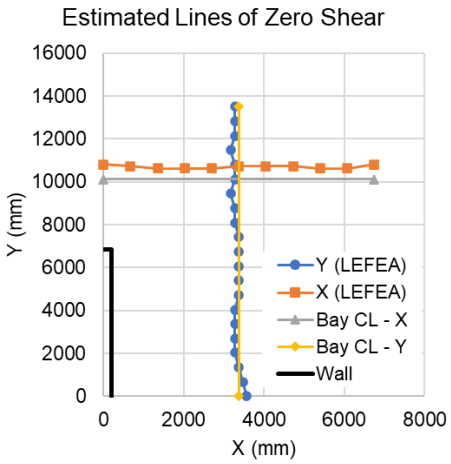
To estimate the tributary area around interior SWCs the location of the lines of zero shear in the slab bays surrounding the SWC were calculated. The locations of the lines of zero shear, which correspond to the location of the maximum positive span moment, were found by calculating the location of the maximum of the second derivative of the deflected shape predicted by Abaqus. Since the deflected shape predicted by Abaqus is discrete, as a result of the finite element method, the deflected shape was differentiated using the central difference method (note: the stability of the central difference method governed the global mesh size). The locations of the lines of zero shear were calculated at *0.1L* increments (675mm) in the X- (parallel to the long side of the wall) and Y- (parallel to the short side of the wall) directions, as shown in Figure 7-21a, with a linear variation between the calculated points assumed as shown in Figure 7-21. The tributary area of the SWC is determined by combining the lines of zero shear in the X- and Y- directions, as shown in Figure 7-21b and Figure 7-22.

As seen in Figure 7-22 and Table 7-5, the tributary areas determined from the Pin and Detailed Models agree well, with those from the Detailed Model typically being slightly larger. Both models also demonstrate that the influence of support width on tributary area is minor. The tributary areas determined from the LEFEA results or based on the slab centerlines (theoretical values in Figure 7-22 and Table 7-5) agree well, with those based on the LEFEA being slightly larger (maximum difference of approximately 4.5% for the Detailed Model). Parallel to the long side of the wall, the locations of the line of zero shear determined from the LEFEA results agree well with those based on the slab centerlines. Parallel to the short sides of the wall, the location of the lines of zero shear determined from the LEFEA results also agree well with the slab centerlines for the 8x8 grid. However, for the

4x4 Grid, the LEFEA predicts the lines of zero shear to be slightly farther than the slab centerline, particularly for the Pin Model, likely because the wall is the first interior support in this direction for this grid size. Overall, the tributary areas calculated based on the slab centerlines or from the LEFEA results agree well, as seen in Table 7-5, and therefore, for simplicity, it is recommended that the tributary area around interior SWCs can be calculated based on the slab centerlines for uniform load conditions. However, for first interior supports, or cases where pattern live loading is to be considered, the tributary area calculated from the slab centerlines should be increased in line with best engineering practices. For non-uniform load conditions or nonsymmetric structural layouts LEFEA using shell elements can also be used to estimate the tributary area around SWCs.

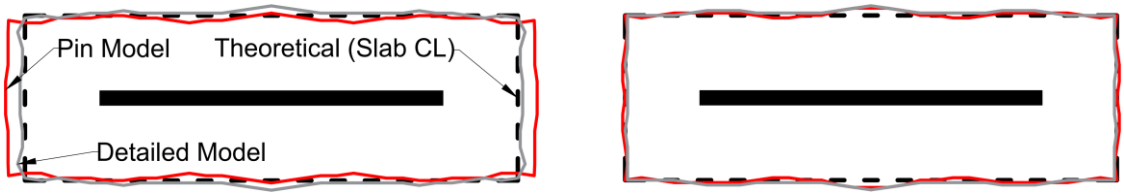


a) Considered output locations for tributary area estimation (All considered locations parallel to short side not shown)



b) Comparison of estimated and theoretical tributary areas, 200mm supports, 8x8 grid, (¼ wall shown, CL=Centerline)

Figure 7-21: Example of Output Locations Used When Estimating Tributary Area, Interior SWCs



a) 4x4 grid – 600mm supports

b) 8x8 grid – 600mm supports

Figure 7-22: Comparison of Theoretical and Estimated Tributary Areas (Red Line: Pin Model; Dashed Black Line: Estimated Theoretical Area; Grey Line: Detailed Model) – Interior SWCs

Table 7-5: Comparison of Estimated Tributary Areas

Grid Size	Support Width (mm)	Tributary Area Estimates (m^2)			% Difference[(d)]
		Theoretical[(a)]	Pin Model[(b)]	Detailed Model[(b,c)]	
4x4	200	136.7	139.6	142.3	4.13
	600	136.7	140.7	142.9	4.56
8x8	200	136.7	138.3	139.5	2.06
	600	136.7	139.2	140.7	2.94

[(a)] Theoretical values calculated assuming tributary area bounded by slab centerlines [(b)] Areas calculated using AutoCAD; [(c)] Model with both columns (beam elements) and walls (shell elements) included; [(d)] Percent difference between theoretical and detailed model results

7.2.5 Decomposition of Wall Into Two-Way and One-Way Shear Regions (Cut-Wall Model)

Originally, it was intended to develop a punching shear design method for SWCs which would use existing design software. Since most design codes do not include punching shear design provisions for SWCs, this would require the SWCs to be approximated by two hypothetical "columns", which are used to represent the toe regions which are governed by two-way shear, and the remaining portion of the wall which is dominated by one-way shear as shown in Figure 7-23. This process of decomposing the SWC into two-way and one-way shear components is referred to as the cut-wall model, and also requires slab openings to be introduced adjacent to the inner short sides of the toe columns, as shown in Figure 7-23. These openings are introduced to limit the critical perimeter considered by the software to that which exists for the actual SWC. The existing punching provisions for slab-column connections would then be used to verify the punching capacity of the toe regions.

However, due to the fact that existing commercial punching shear design software would overpredict the capacity of the toe regions, as will be discussed, the cut-wall model was only implemented in Abaqus. Even though the author did not implement the cut-wall model in commercial punching shear design software, the model was fundamental to the development of the wall design method proposed herein, which is presented in Sections 7.2.6-7.2.8.

In the following subsections the procedures used to estimate the toe length, λd, gap length, μd, and opening details are discussed. These parameters need to be selected such that the cut-wall model accurately captures the behaviour of the toe regions, without greatly impacting the overall response of the SWC. As will be discussed, λd and μd were determined using nonlinear FEMs which did not include the slab openings adjacent to the inner short sides of the toes, but the selected values were confirmed when analyzing the finalized cut-wall specimens as discussed in subsection 7.2.5.4.

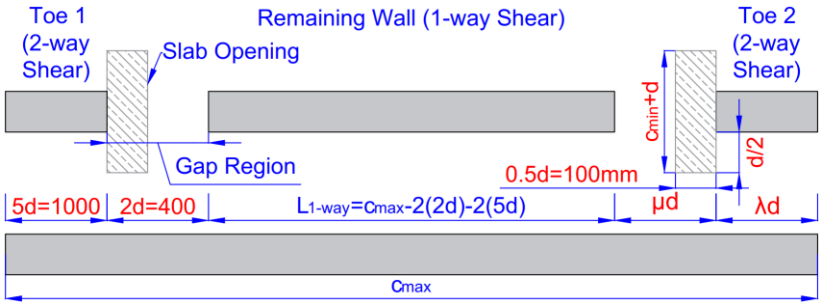


Figure 7-23: Details of Finalized Cut-Wall Model (*d* ≈ 200mm for the Analyzed Specimens)

7.2.5.1 Toe Length Study

The first iteration of the cut-wall model was focused on determining the required toe length for the SWC where κ equalled 1.287 (c_{min}=260mm, f_c'=44.6MPa). Five toe lengths, varying from *1d* to *5d* (where *d* was approximated as 200mm instead of 202mm) were studied, assuming a constant gap length of *5d*, as shown in Figure 7-24. The maximum length of *5d* was chosen to allow the Schwaighofer and Collins [30] method for estimating toe capacity (see Figure 2-14b), which assumes a critical perimeter length of approximately *4d* (800mm) parallel to the long sides of the toe for the specimen where κ equals 2.970, to be evaluated, and also is the beginning of the region of approximately zero shear stress along the wall perimeter predicted by the NLFEA [323]. The boundary conditions used in the toe length study, which are representative of those in all cut-wall models in Abaqus, are shown in Figure 7-25. The boundary conditions used in the NLFEA of the cut-wall specimens are identical to those used for the full SWCs, other than the additional horizontal constraint on the inner face of the wall toe, which is required to restrict the displacement of the toe parallel to its length (this displacement is restricted by the remainder of the wall in the full wall specimens).

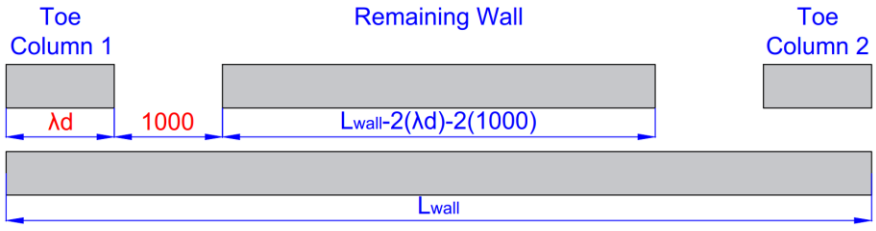


Figure 7-24: Overview of Toe Length (*λd*) Study, Gap Length (*μd*) set to 1000mm

In the following paragraphs, the results of the toe length study are presented. Detailed comparisons of the predicted capacities, load-displacement responses, crack patterns and wall perimeter shear

stress distributions in the slab at the peak loads from the cut-wall and full wall models are provided.

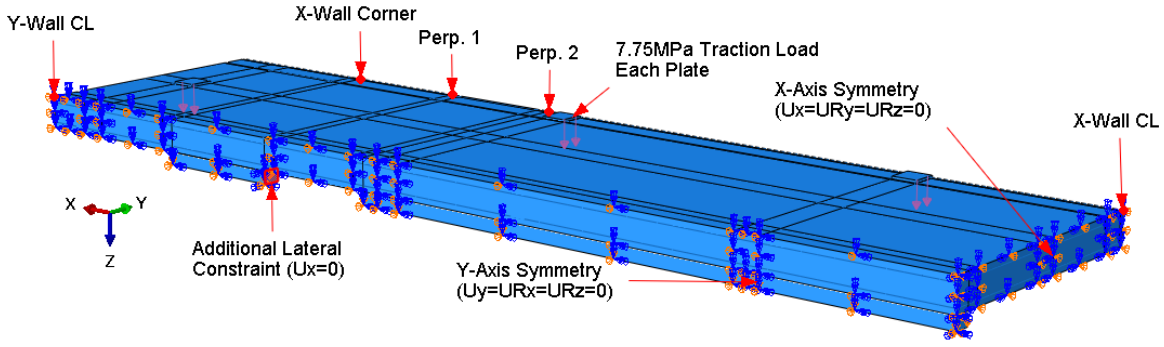
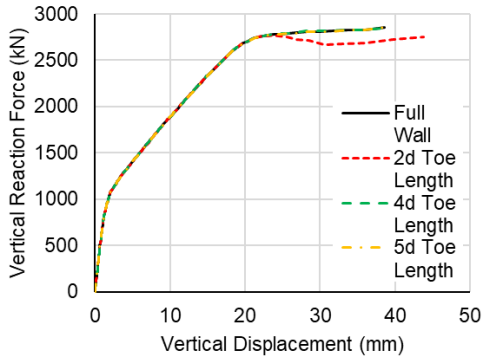
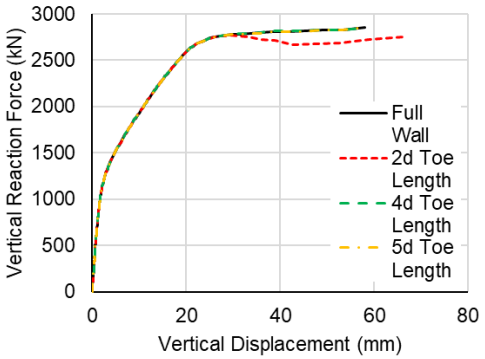


Figure 7-25: Cut-Wall Model Boundary Conditions and Displacement Output Locations (¼ Model Shown)

Load-Displacement Comparison: A comparison of the predicted load-displacement response at the X-Wall Corner and Y-Wall CL locations (see Figure 7-25) for toe lengths of *2d*, *4d* and *5d* and the full wall model where κ=1.287 is provided in Figure 7-26. As seen in Figure 7-26, the difference between the cut-wall model results and the full wall model results decreases as the assumed toe length increases, with toe lengths greater than or equal to *4d* resulting in a nearly identical overall response. However, if one considers the load-displacement response perpendicular to the long side of the wall at the inner end of the toe (Perp. 1 location, see Figure 7-25) and at the start of the remaining wall (Perp. 2 location, see Figure 7-25), a toe length of *5d* leads to better agreement with the full model results compared to a toe length of *4d*, as shown in Figure 7-27.



Perpendicular to Long Side – Wall Toe (X-Wall Corner)



Perpendicular to Short Side – Y-Wall CL

Figure 7-26: Comparison of Predicted Load-Displacement Response at Wall Toe, Cut Wall Study, κ = 1.287 (Gap Length Set to *5d*, no Slab Opening, Predicted Response not cut off at Peak Load)

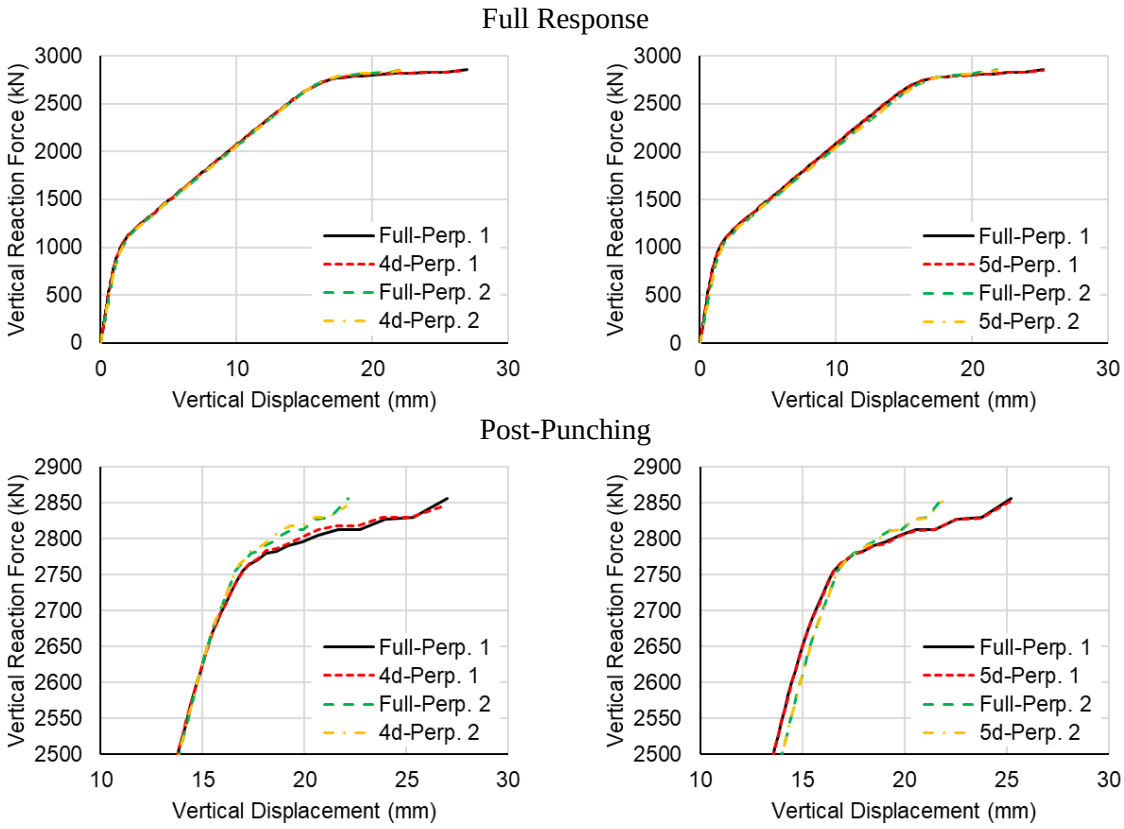
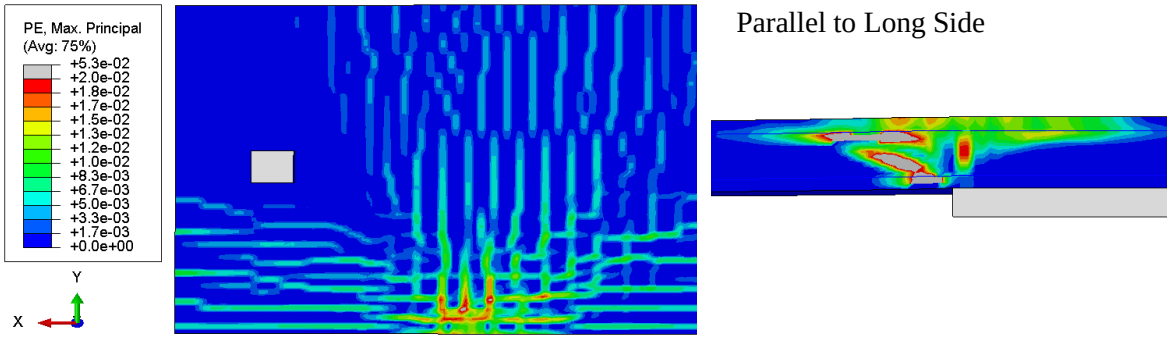


Figure 7-27: Comparison of Predicted Load-Displacement Response at Perp. 1 and Perp. 2 Locations (see Figure 7-25), Cut Wall Study, κ = 1.287 (Gap Length Set to *5d*, no Slab Opening, Predicted Response not cut off at Peak Load)

Crack Pattern Comparison: The use of a toe length of *5d* was also found to minimize the impact on the predicted crack pattern. By comparing Figure 6-16 (full-wall model) and Figure 7-28 (cut-wall model), it is clear that the use of a *5d* wall toe (and *5d* gap) leads to a nearly identical crack pattern on the tension surface of the slab and on the slab interior.



a) Tension Surface b) Punching Cone on Slab Side

Figure 7-28: Crack Pattern Predicted by Abaqus a) Tension Surface Near Wall Toe, b) Punching Cone on Slab Side Parallel to Long Side of Wall, Cut-Wall Model, *5d* Toe, *5d* Gap, no Slab Opening, κ = 1.287 (Entire SWC not Shown)

Shear Stress Distribution Comparison: The use of a toe length of *5d* was also found to minimize the impact on the predicted shear stress distribution along the wall perimeter (note, the methodology used to calculate the shear stress distributions from the FEA results is discussed in Appendix A). For smaller toe lengths a concentration of shear stress along the inner short side of the toe and the short side of the remaining wall was observed, which does not match the behaviour of a full wall. For a toe length of *5d*, the peaks in this region are minimized, and the stress distribution along the long side of both the toe and the remaining portion of the wall and the outer short side of the wall toe (short side of the full wall) are similar to those predicted in the full wall model, as shown in Figure 7-29.

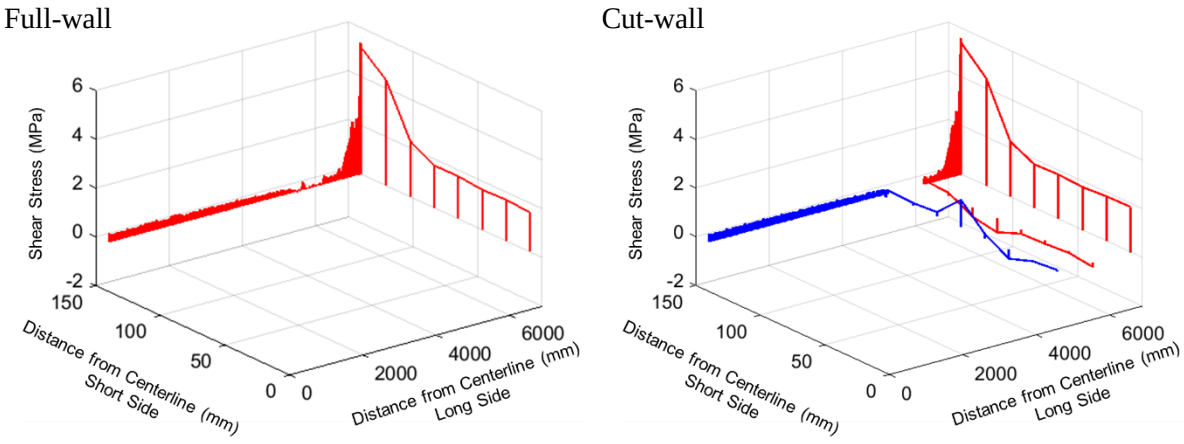
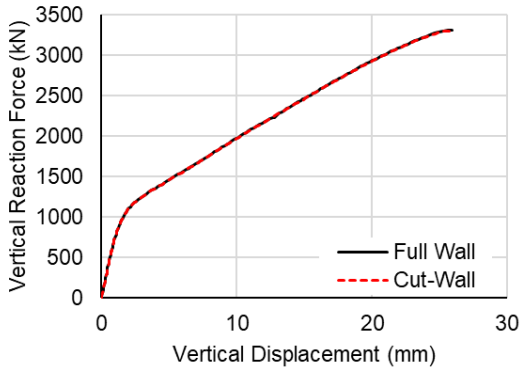


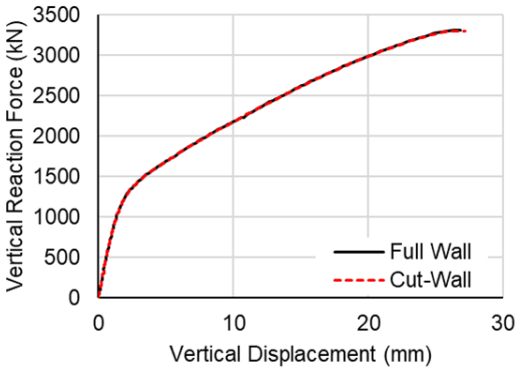
Figure 7-29: Comparison of Shear Stress Distribution Along Wall Perimeter for Full Wall and Cut-Wall Model (*5d* Toe, *5d* Gap, no Slab Opening), κ = 1.287 (¼ of Wall Shown, Stresses Averaged Over Depth)

Recommended Toe Length: Based on the above analysis, a minimum toe length of *5d* is recommended for use in the cut-wall model, as it has been found to minimize the difference in the overall connection behaviour (load-displacement, crack patterns and shear stress distribution) between the full and cut-wall models. Additionally, the recommended toe length of *5d* also encompasses the entire high stress region near the wall toe along the critical perimeter and wall perimeter.

Analysis of Remaining SWCs: After determining that a minimum toe length of *5d* was required to minimize the difference in the results of the cut-wall and full-wall models, the remaining 7 slab-wall specimens (see Table 6-2) were analyzed using the cut-wall model. As expected, the difference in the results between the cut-wall and full wall models were minor. Comparisons of the predicted load-displacement response, and crack patterns for the specimen where κ=1.980 are provided in Figure 7-30 and Figure 7-31, respectively. The capacities predicted by the full-wall and cut-wall models for all 8 interior SWCs is provided in Table 7-6. The capacities predicted by the cut-wall model agree well with those from the full wall models for all specimens, which a maximum difference of 1.43% (underprediction). A comparison of the stress distribution along the wall perimeter from the full wall and cut-wall models with *5d* toe and gap lengths is not provided herein. However, a comparison of the stress distributions from the full-wall and finalized cut-wall model is provided in subsection 7.2.5.4 and Appendix F.



Perpendicular to Long Side – Wall Toe (X-Wall Corner)



Perpendicular to Short Side – Y-Wall CL

Figure 7-30: Comparison of Predicted Load-Displacement Response at Wall Toe, Cut Wall Study, κ = 1.980 (Gap Length Set to *5d*, no Slab Opening, Predicted Response cut off at Peak Load)

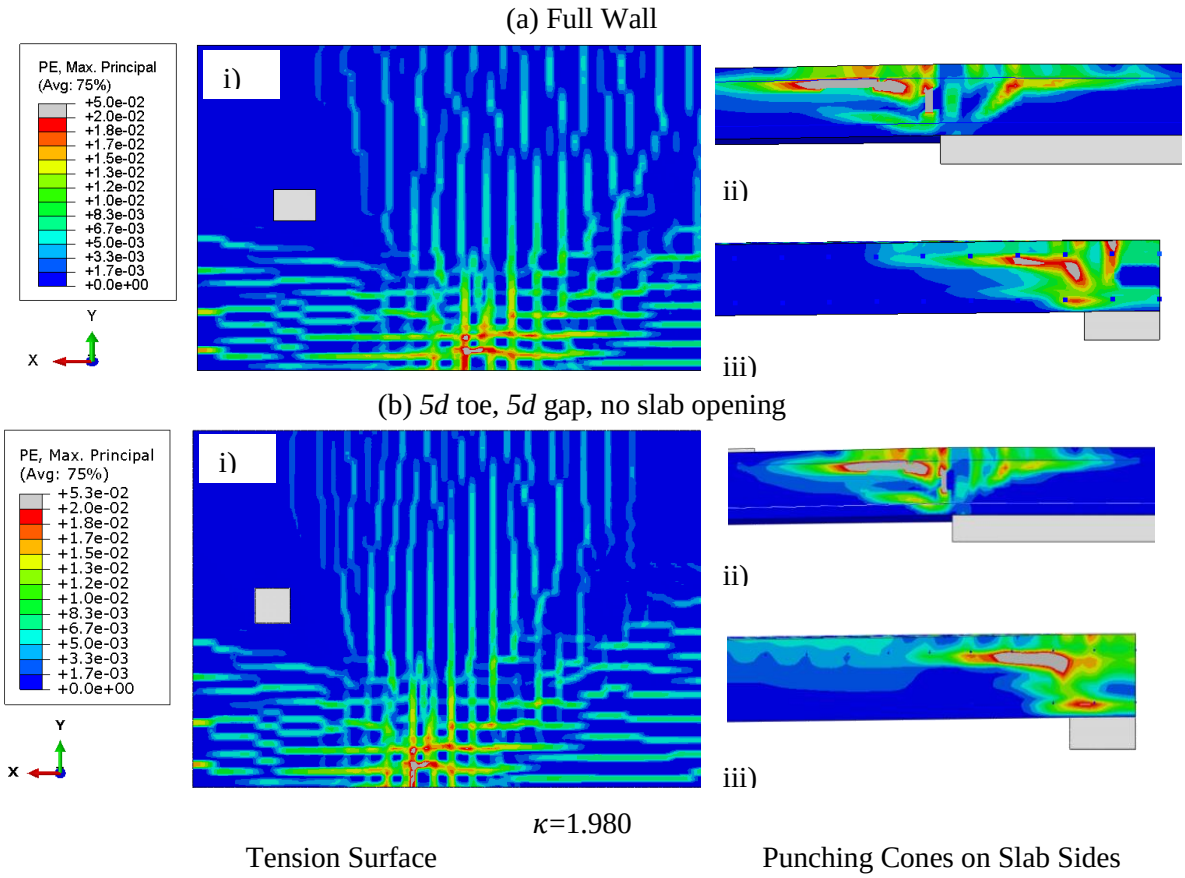


Figure 7-31: Comparison of Crack Pattern From (a) Full Wall and (b) Original Cut-Wall Model, κ = 1.980, i) Tension Surface, ii) Slab Side Parallel to Long Side of Wall, iii) Slab Side Parallel to Short Side of Wall (Entire Isolated Slab-Wall Specimen not Shown

Table 7-6: Comparison of Predicted Punching Capacities for Interior SWCs by Full Wall and Cut-Wall Models

Wall Parameters (mm)				V_{FEA} (kN)			
κ (c_{min}/d)	Thickness (c_{min})	Length (c_{max})	Aspect Ratio, β	Full Wall	Cut-Wall[(A)]	Cut-Wall[(B)]	Cut-Wall[(C)]
0.594	120	13620	113.5	2595.3	2577.1	-	2544.9
0.792	160	13660	85.4	2699.9	2686.6	-	2675.9
0.990	200	13700	68.5	2729.8	2728.0	-	2740.6
1.287	260	13760	52.9	2764.1	2724.7	2723.7	2764.8
1.485	300	13800	46.0	2869.9	2869.1	-	2800.9
1.782	360	13860	38.5	3148.5	3141.2	-	3156.7
1.980	400	13900	34.8	3316.0	3301.3	-	3261.6
2.970	600	14100	23.5	3727.4	3719.3	-	3697.9

[(A)] *5d* toe, *5d* gap, no slab opening model; [(B)] *5d* toe, *2d* gap, no slab opening model; [(C)] *5d* toe, *2d* gap, *0.5d* wide and c_{min}+*d* high slab opening at inner toe faces

Percent of Total Load Carried by Toe (Full and Cut-Wall Models): Additionally, the results for all 8 specimens with *5d* toe lengths were used to study the portion of the total load applied to the connection carried by the wall toe and the remainder of the wall based on the reaction forces calculated by Abaqus. As seen in Figure 7-32, when the slab is loaded through three equally loaded load plates approximately 50% of the total load applied to the SWC is carried by the toe. For models subjected to a UDL on the slab surface beyond *d/2* from the wall face, approximately 40% of the total load was carried by the toe. In both cases it is found that a significant portion of the total connection load is carried by the toe region, supporting the use of a cut-wall model made up of two toes and a remaining wall portion. It should be noted that UDL load case analyses were not conducted for other iterations of the cut-wall model.

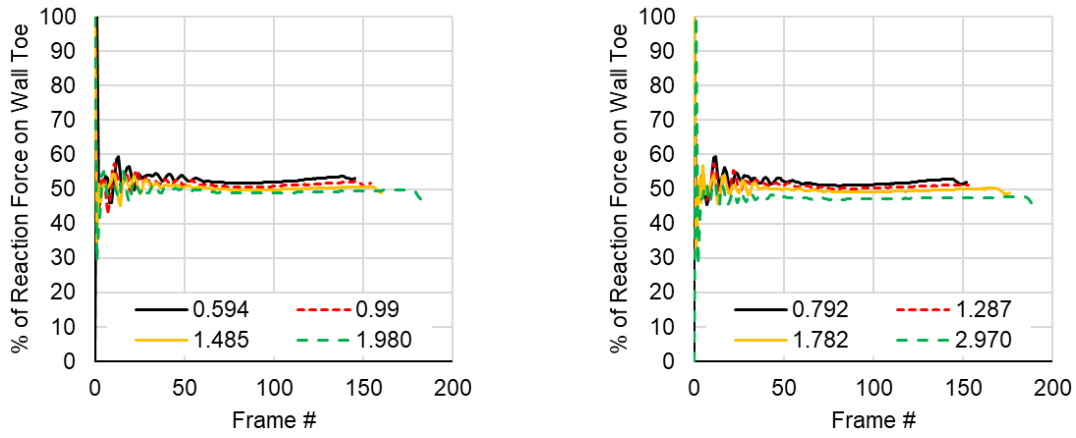


Figure 7-32: Percent of Total Load Carried on the Wall Toe (*5d* Toe and Gap Lengths) Throughout the Analyses (Note, Analyses Terminated Before End of Vertical Load Application Step due to Occurrence of Shear Failures)

7.2.5.2 Gap Length Study

Next, the gap length, between the toe columns (each *5d* in length as shown in Figure 7-33) and the remainder of the wall, μd, was studied, as it was assumed that a gap length of *5d* may be too large for less stiff slabs (slabs with lower thicknesses or concrete compressive strengths). Again, the SWC where κ was equal to 1.287 was analyzed, considering six gap lengths, *0.5d*, *1d*, *2d*, *3d*, *4d* and *5d*. A minimum gap length of *0.5d* was considered to provide room for the introduction of the required slab opening.

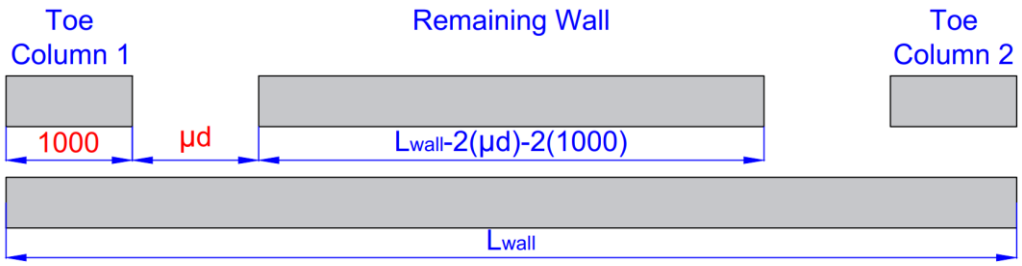


Figure 7-33: Overview of Gap Length (μd) Study, Toe Length (λd) set to 1000mm

As will be discussed in the following paragraphs, the assumed gap length had a minor influence on the predicted load-displacement response and crack patterns but did influence the shear stress distribution along the wall perimeter.

Load-Displacement Comparison: As seen in Figure 7-34, the assumed gap length was found to have a very minor influence on the predicted load-displacement response of the SWC where κ was equal to 1.287. Regardless of the assumed gap length, the predicted capacity and stiffness are nearly identical until the occurrence of punching failure.

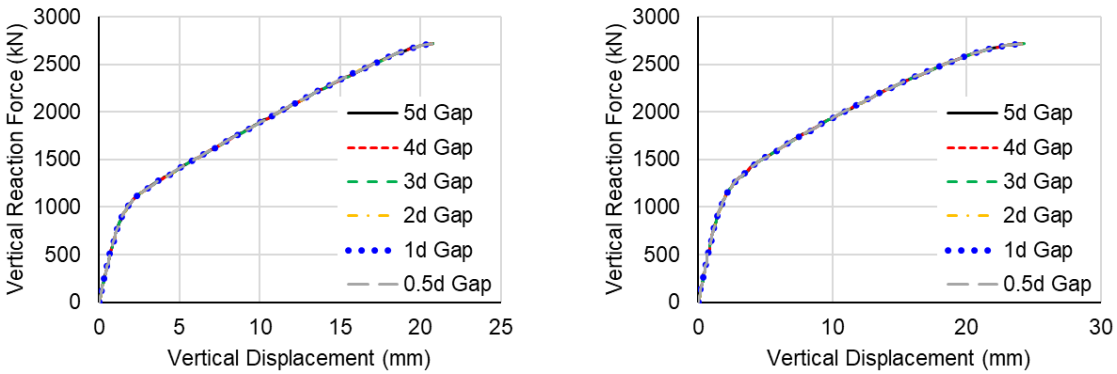


Figure 7-34: Comparison of Predicted Load-Displacement Response at Wall Toe, Gap Length Study, κ = 1.287 (Toe Length Set to *5d*, no Slab Opening, Predicted Response cut off at Peak Load)

Crack Pattern Comparison: As with the predicted load-displacement response, the assumed gap length was not found to significantly impact the predicted crack pattern, as seen in Figure 7-35. On both the tension surface and slab interior, there was no major change in the crack patterns (i.e. no changes in overall pattern or areas of strain concentration compared to the full wall model). It should

be noted that the crack patterns provided in Figure 7-35 are taken at the peak load for each model, hence the discrepancy in output frames between the full wall model and cut-wall models.

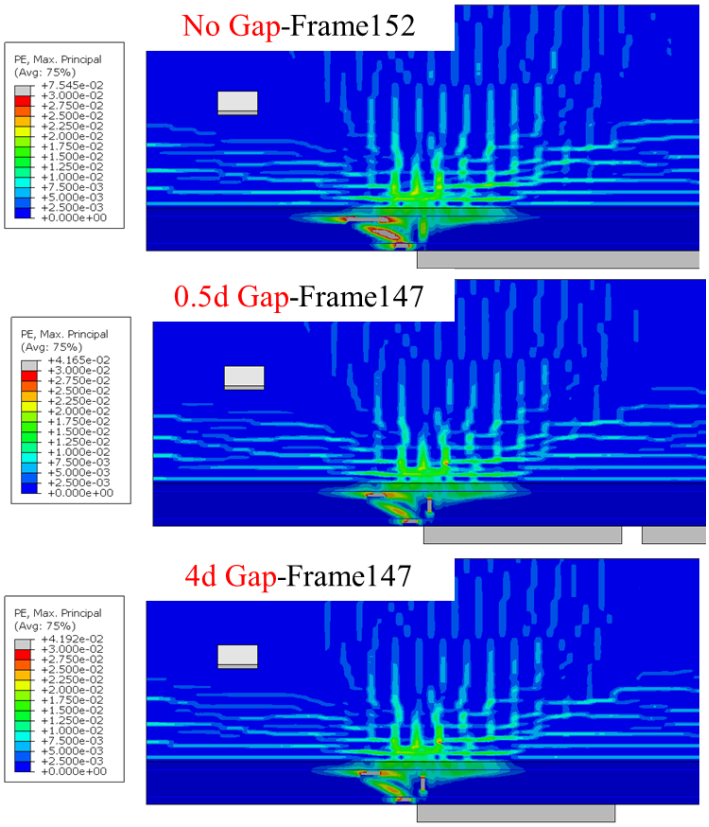


Figure 7-35: Comparison of Predicted Crack Pattern at Peak Load in Full Wall and Cut-Wall Models for Different Gap Lengths, κ = 1.287 (No Gap=Full Wall Model; Entire SWC not Shown)

Shear Stress Distribution Comparison: The influence of the assumed gap length on the shear stress distribution along the wall toe perimeter (sides 1-3 in Figure 7-36) was also found to be minor, as seen in Figure 7-37. Regardless of the assumed gap length, the shear stress distribution around the wall toe has a very similar shape and a similar magnitude at all locations. Unlike the use of different toe lengths, which resulted in increased peak shear stress values along the inner face of the wall toe (side 3), the use of different gap lengths does not result in higher peak shear stress values on this face.

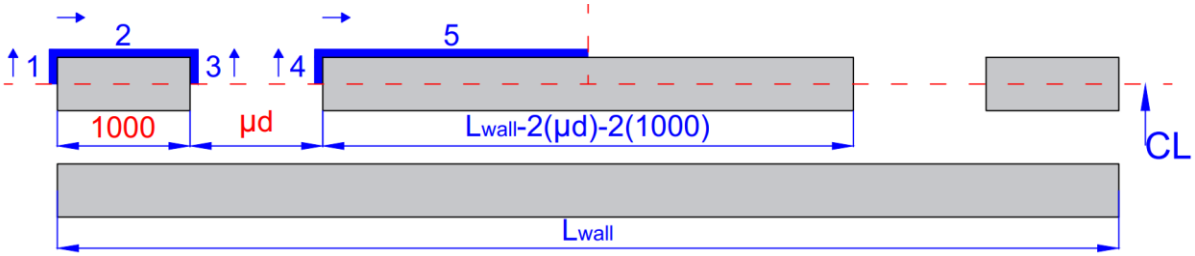


Figure 7-36: Side Numbering for Shear Stress Distribution Output – Cut Wall Models

The assumed gap length was found to influence the shear stress distribution on the remaining portion of the wall (sides 4 and 5 in Figure 7-36). On the long side of the remaining wall (side 5), the influence of gap length was quite minor, with the overall shape and magnitude of the shear stress distribution along the wall perimeter being similar to that from the full wall model. However, on the short side of the remaining wall, side 4, the peak shear stresses were influenced by the assumed gap length. For gap lengths greater than or equal to *3d*, the largest magnitudes of the peak shear stresses along this side of the wall were typically observed and exceeded 1MPa (which is approximately 2x larger than that observed in the constant shear stress zone on side 5). The use of a gap length of *0.5d* also displayed higher peak shear stresses suggesting that the gap between the wall toe and the remaining portion of the wall was too small. A gap length of *2d* was found to result in the lowest shear stress magnitudes along the short side of the remaining wall, as seen in Figure 7-37. Therefore, a gap length of *2d* was selected for implementation in Abaqus as shear stress concentrations should not exist in these areas in the cut-wall models to accurately reflect the behaviour of the full SWC

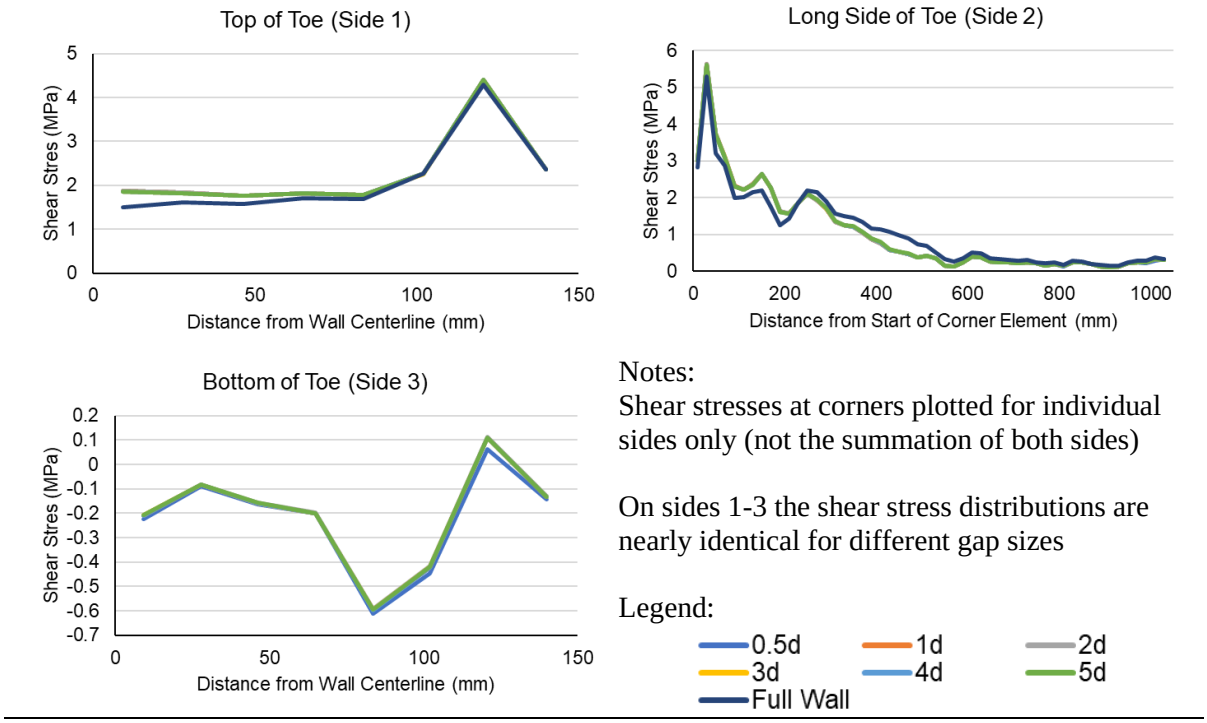


Figure 7-37: Influence of Gap Length on Shear Stress Distribution Along Wall Toe and Remaining Wall Perimeter (see Figure 7-36 for Side Numbering Convention, ¼ SWC Shown, Stresses Averaged Over Depth)

Recommended Gap Length: Based on the analysis of the predicted load-displacement response, crack patterns and shear stress distribution presented above a gap length of *2d* is recommended for use in the cut-wall models with a toe length of *5d*. However, it should be noted that a gap length of *2d* may lead to inaccurate results if the cut-wall model is implemented in commercial punching shear software. For example, if the cut-wall model is implemented in commercial software for the purpose

of estimating the load on the wall it may be necessary to increase the gap length to account for program defaults or the chosen mesh size.

Analysis of Remaining SWCs: Analysis of the remaining seven isolated interior SWC was not completed for a toe length of *5d* and gap length of *2d*. This analysis was not done since the results for the cut-wall model with a *5d* wall toe and *2d* gap were similar to those with a *5d* toe and *5d* gap, which were compared to the full wall results for all 8 specimens in the previous section. However, an analysis of all 8 SWCs was completed for the finalized cut wall models with toe lengths of *5d*, gap lengths of *2d* and slab openings with a width of *0.5d* and height of $c_{min}+d$, as discussed in subsections 7.2.5.3 and 7.2.5.4.

7.2.5.3 Opening Size Study.

After completion of the toe length and gap length studies, it was determined that in order to make use of the cut-wall model in commercial software that the critical perimeter along the inner edge of the wall toe region needed to be neglected to result in conservative estimates of the punching capacity of the toe. As such, the influence of including a slab opening adjacent to the inner end of the wall toe was investigated. Worldwide design codes typically deal with openings by reducing the critical perimeter assumed to resist punching, and therefore the inclusion of a slab opening near the inner end of the toe region should result in this portion of the critical perimeter being neglected.

As will be discussed in this section, the use of both considered opening heights (see Figure 7-38) was found to result in the cut-wall model predicting similar behaviour to the full wall model. However, the opening height of $c_{min}+d$ was chosen for all future analyses as it removes the entire critical perimeter along the inner end of the wall toe, resulting in the cut-wall model shown in Figure 7-23. Additionally, the use of opening widths of *0.3d* and *0.5d* were investigated, with a width of *0.5d* being selected since it extends to the critical perimeter and resulted in a similar response as will be discussed. However, any opening width smaller than *0.5d* can likely be used as the opening width does not impact the reduction in critical perimeter considered by ACI 318-19 for the chosen opening location and orientation.

In the following paragraphs, the impact of the assumed opening height and width on the predicted load-displacement response, crack patterns and shear stress distribution along the wall perimeter is discussed. Based on the presented results, an opening size is recommended for use in the cut-wall model.

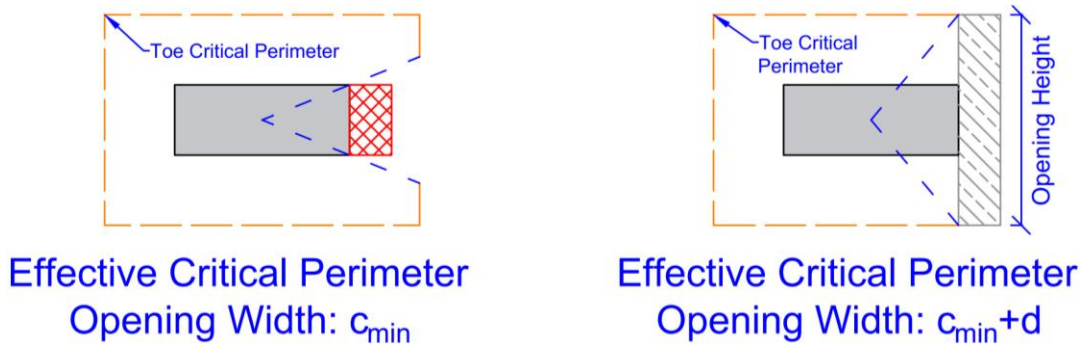


Figure 7-38: Different Opening Heights Considered and Effective Toe Critical Perimeter Associated with Each According to ACI 318-19

Load-Displacement Comparison: As seen in Figure 7-39, the inclusion of a slab opening of either of the investigated heights or widths was found to have a minor influence on the overall load-displacement response of the SWC. Though the models with openings were typically predicted to have a slightly lower capacity (which was expected since a portion of the slab and rebar transferring load were removed) compared to the full wall model, the change in capacity was typically on the order of a magnitude of a few percent. The lack of influence of the slab opening suggests that the portion of the slab removed is indeed ineffective in transferring load (as suggested by the low shear stresses along the toe and remaining wall perimeter in this region), which confirms that this critical perimeter should be neglected in design software.

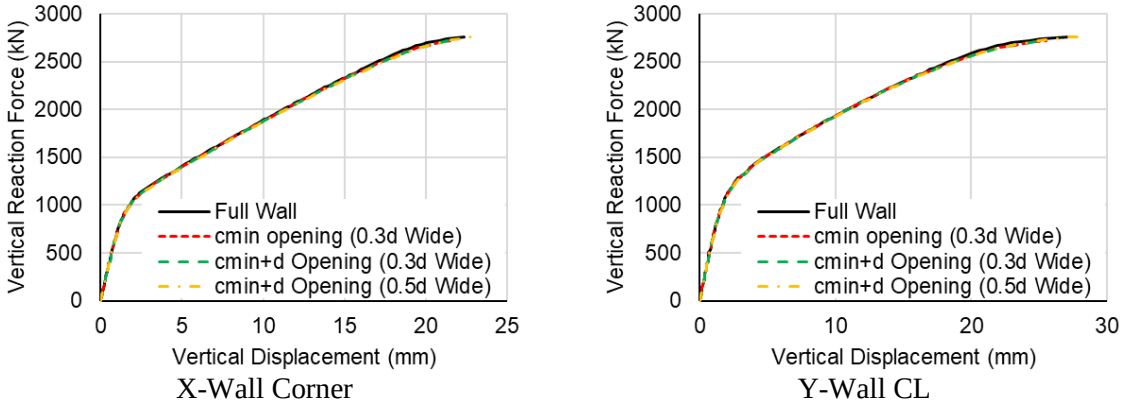


Figure 7-39: Comparison of Predicted Load-Displacement Response at Wall Toe, Opening Size Study, κ = 1.287 (Toe Length Set to *5d*, Gap Length set to *2d*, Predicted Response cut off at Peak Load)

Crack Pattern Comparison: As was observed for different gap lengths, the assumed opening height generally had a minor influence on the tension surface and interior crack patterns predicted by Abaqus, as shown in Figure 7-40. However, for the cut-wall model with a slab opening height equal to the wall thickness, a strain concentration was predicted at the top of the opening, as seen in Figure 7-40. Therefore, an analysis of the crack patterns suggests that an opening height equal to the wall thickness plus the effective slab depth should be used.

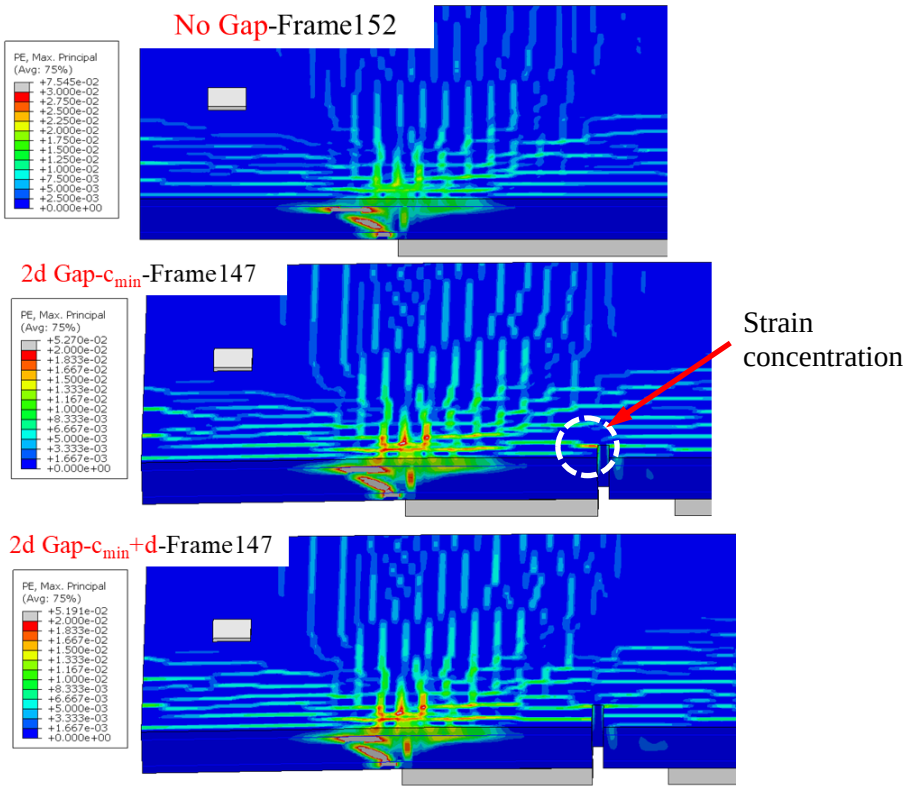


Figure 7-40: Comparison of Predicted Crack Patterns from Cut-Wall Model with Different Opening Heights (opening width of *0.3d*) and Full wall Models, κ = 1.287 (Entire SWC not Shown)

In the original opening size study, an opening width of *0.3d* (60mm) was used. However, for simplicity, it was desirable to revise the opening width to *0.5d* (100mm). Due to the long runtime of the simulations, only the connection with an opening height equal to $c_{min}+d$ was completed for an opening width (parallel to the long side of the wall) of *0.5d*. Comparing Figure 7-40 and Figure 7-41, it is observed that the use of this increased opening width does not affect the predicted crack patterns. Additionally, the use of this increased opening width was found to not influence the predicted load-

displacement response, as shown in Figure 7-39. Therefore, it was decided to use an opening width of *0.5d* for the cut-wall model parametric analysis discussed in subsection 7.2.5.4.

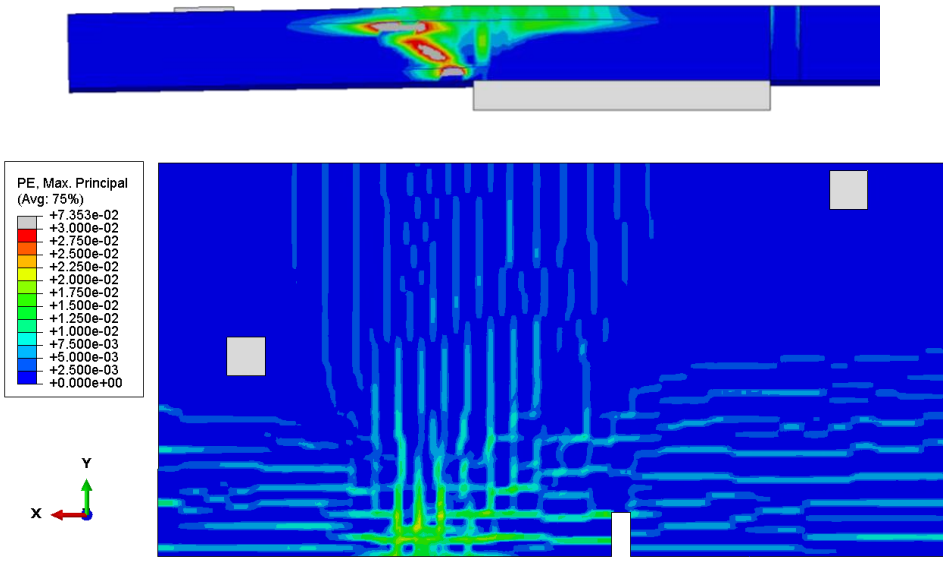


Figure 7-41: Predicted Crack Pattern for Cut Wall Model with Slab Opening (c_{min}+*d* high and *0.5d* wide), κ = 1.287, Top: Slab Side Parallel to Long Side of Wall, Bottom: Tension Surface (Entire SWC not Shown)

Shear Stress Distribution Comparison: The influence of the assumed opening size on the shear stress distribution along the wall toe perimeter (sides 1-3, see Figure 7-36) and along the remaining wall (sides 4 and 5, see Figure 7-36) was also analyzed. The influence of the opening height was found to be minor on the shear stress distributions along sides 1 and 2 of the wall toe, as seen in Figure 7-42. Regardless of the opening size, the predicted shear stress magnitudes and shape of the distribution were similar to those predicted for the cut-wall model without a slab opening and the full wall model. On the inner face of the wall toe (side 3), the use of an opening height equal to the wall thickness (c_{min}) led to a high peak shear stress value of approximately 2MPa. Looking at the short side of the remaining wall (side 4), the use of an opening height equal to the wall thickness led to higher shear stress values than those observed in the cut-wall model without a slab opening, or the model with an opening height equal to c_{min}+*d* (though the shear stress magnitudes are typically <1MPa). For an opening height equal to c_{min}+*d*, higher shear stresses than those in the model without an opening are observed, but the maximum magnitude is less than 0.4MPa.

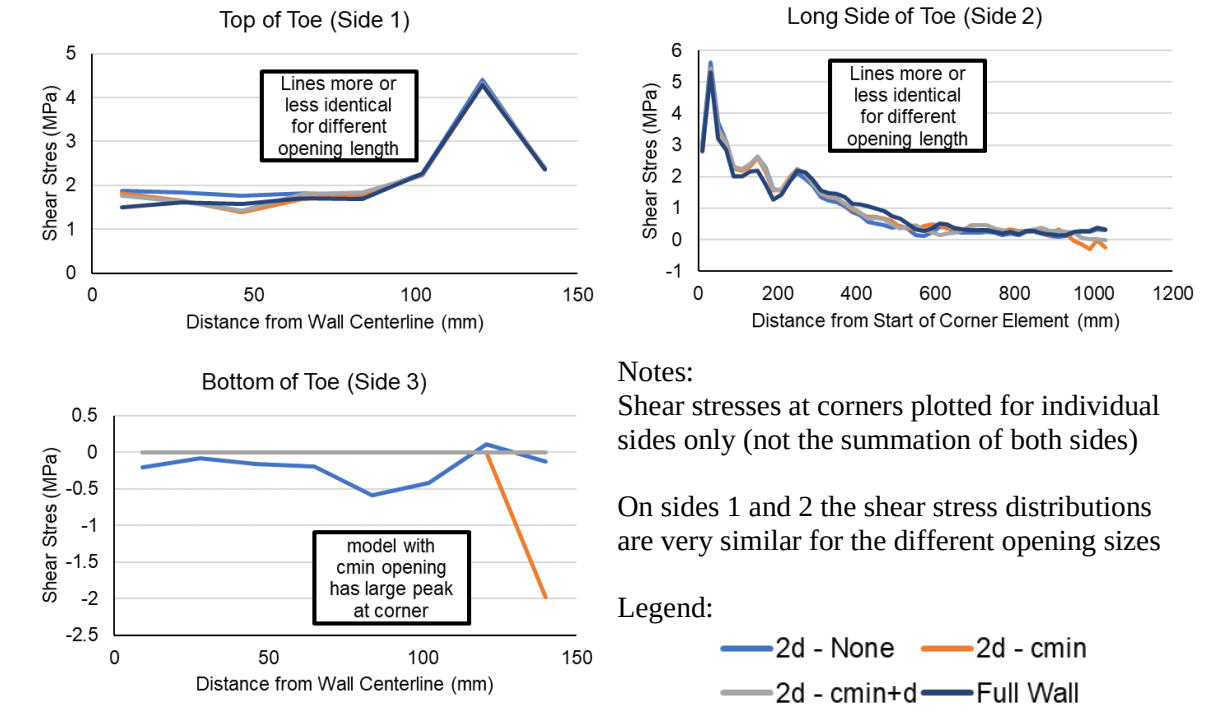


Figure 7-42: Influence of Opening Size on Shear Stress Distribution Along Wall Toe and Remaining Wall Perimeter (see Figure 7-36 for Side Numbering Convention, ¼ SWC Shown, Stresses Averaged Over Depth)

Recommended Opening Size: Based on the analysis presented above (in particular the analysis of the shear stress distribution and crack patterns), an opening height of $c_{min}+d$ and an opening width of $0.5d$ (though smaller can likely be used without issue) is recommended for use in the cut-wall model.

7.2.5.4 Verification of Proposed Cut-Wall Model

Before developing a design method based on the cut-wall model, an additional verification study was conducted. This verification study consisted of analyzing the remaining seven SWCs with the proposed cut-wall model (*5d* toe, *2d* gap, *0.5d* wide and $c_{min}+d$ high opening) to verify that the proposed model was applicable to all 8 SWCs, and not just the connection where κ equalled 1.287. In this section, the predicted load-displacement responses, punching capacities, crack patterns and shear stress distributions along the wall perimeter at the peak load are analyzed. Representative figures are provided herein, and additional figures for the remaining SWCs are provided in Appendix F.

Load-Displacement Comparison: A summary of the predicted capacity for the full wall models, original cut-wall models (*5d* toe and gap, no slab opening) and the proposed cut-wall models (*5d* toe, *2d* gap and $c_{min}+d$ high and *0.5d* wide slab opening) is provided in Table 7-6. On average, the predictions from the proposed cut-wall model with a slab opening are within 1.1% of the predictions from the full-wall study, with a maximum error of approximately 2.4% (κ=1.485), suggesting that the cut-wall model can be used for all 8 slab-wall specimens. However, a detailed analysis of the predicted load-displacement response, crack patterns and shear stress distributions along the wall perimeter must be conducted to verify the applicability of the cut-wall model.

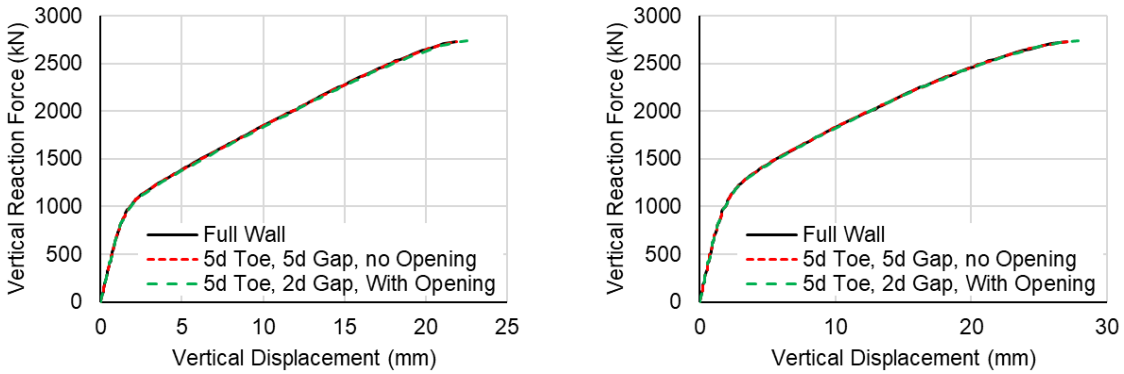


Figure 7-43: Comparison of Predicted Load Displacement Response at Wall Toe from Full Wall, Original Cut-Wall Model (*5d* toe and gap Lengths, no Slab Opening) and Finalized Cut-Wall Model (*5d* toe, *2d* gap, $c_{min}+d$ High and *0.5d* Slab Opening), κ = 0.990

A comparison of the load-displacement response from the full wall models, original cut-wall model and proposed cut-wall model for the specimens where κ=0.990, which is representative of the trends for all κ values studied, is provided in Figure 7-43 (additional plots are provided in Appendix F). As

seen in Figure 7-43, the proposed cut-wall model results in a similar load-displacement response to the original cut-wall model, and to the full-wall model. As discussed above, the use of the proposed cut-wall model results in a slight difference in capacity, likely due to the inclusion of the slab opening and cutting of some of the slab flexural reinforcement.

Crack Pattern Comparison: A comparison of the predicted crack patterns in the vicinity of the end of the wall from the full wall models, original cut-wall model and proposed cut-wall model for the specimens where κ=0.990 and 1.980, which are representative of the trends for all κ values studied, is provided in Figure 7-44 and Figure 7-45, respectively. As was observed for the predicted load-displacement responses, the crack patterns from the finalized cut-wall models are similar to those from the full wall models. The observed cracking on the tension surface displays similar patterns and the cracks extend to similar distances from their origins. The primary difference is the interruption of some of the one-way shear cracks parallel to the long side of the wall due to the inclusion of the slab opening. However, the one-way shear cracks are observed to continue on the other side of the opening, showing that the inclusion of the opening at the inner face of the toe is not strongly influencing the specimen behaviour. The shape and inclination of the punching cones on the slab sides are also similar between the full wall and cut-wall models.

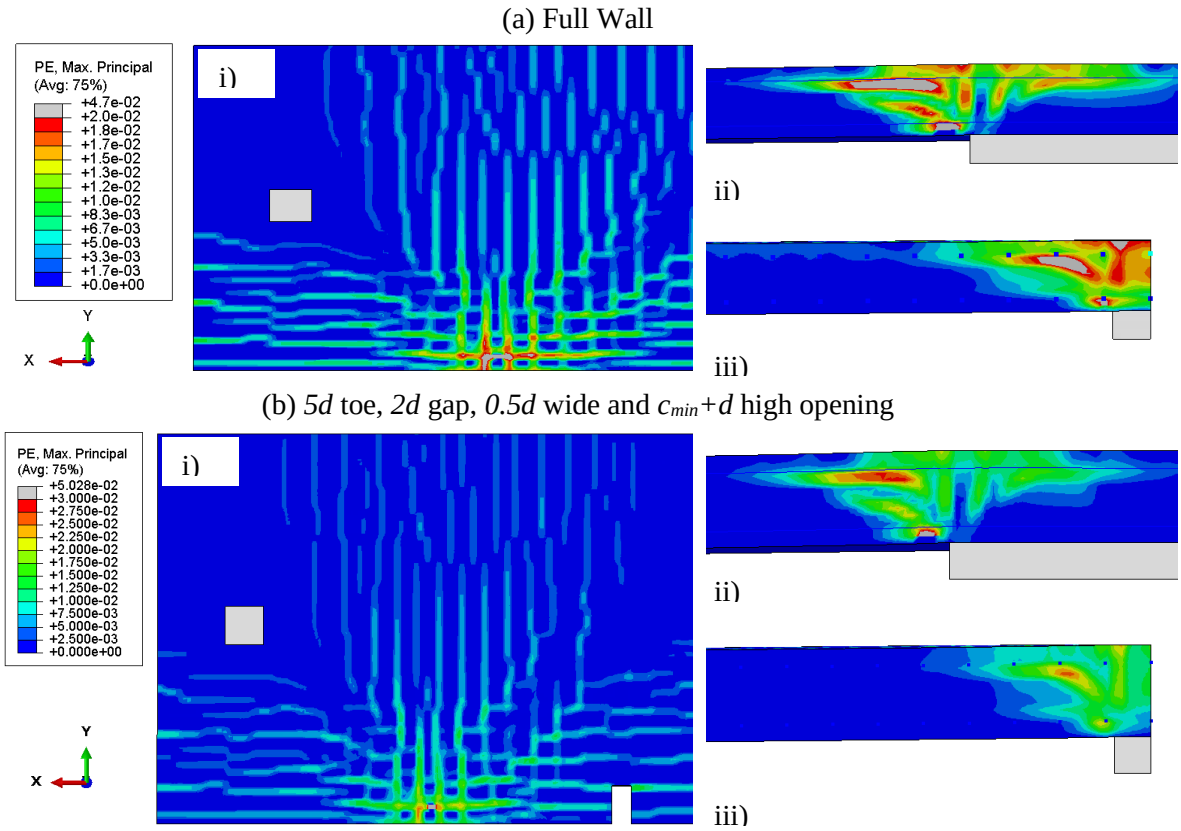


Figure 7-44: Comparison of Crack Pattern From (a) Full Wall and (b) Finalized Cut-Wall Model, κ = 0.990, i) Tension Surface, ii) Slab Side Parallel to Long Side of Wall, iii) Slab Side Parallel to Short Side of Wall (Entire Isolated Slab-Wall Specimen not Shown

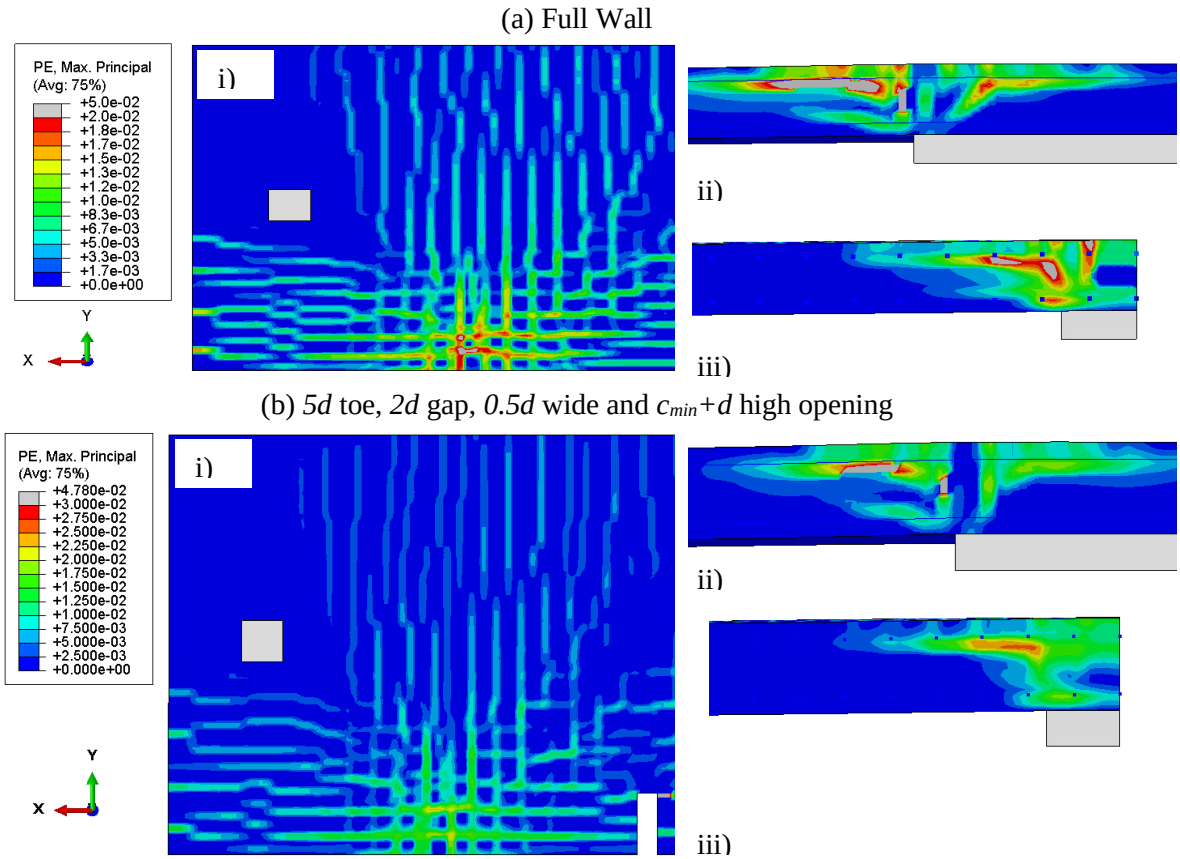


Figure 7-45: Comparison of Crack Pattern From (a) Full Wall and (b) Finalized Cut-Wall Model, κ = 1.980, i) Tension Surface, ii) Slab Side Parallel to Long Side of Wall, iii) Slab Side Parallel to Short Side of Wall (Entire Isolated Slab-Wall Specimen not Shown

Shear Stress Distribution Comparison: Finally, a comparison of the shear stress distribution along the wall perimeter from the full wall models, original cut-wall model and proposed cut-wall model for the specimens where κ=0.990, which is representative of the trends for all κ values studied, is provided in Figure 7-46 (additional figures for other κ values are provided in Appendix F). Along the top short side (side 1) and the long side of the wall toe (side 2), the shear stress distributions predicted from the cut-wall model and the full wall models are typically very similar. For all κ values, the predicted shear stress distributions on these sides of the toe follow very closely to those from the full-wall model, and a similar peak shear stress magnitude is predicted. For a κ value of 2.970, the exact shape of the shear stress distribution is not the same between both models (there is a slight deviation starting at a distance of approximately 300mm from the wall toe) but a similar peak shear stress magnitude

and the overall trend is observed. The similarity in the shear stress distribution between the cut-wall and full wall models suggests that the cut-wall model does accurately represent the behaviour of the wall toe in an isolated SWC.

Due to the use of an opening height equal to $c_{min}+d$, there is no stress distribution along the inner edge of the wall toe (side 3), as all elements along this side have been entirely removed. As expected, the shear stress magnitudes along the short side of the remainder of the wall (side 4) are typically low (less than 0.3MPa in many cases with a maximum of 0.7MPa observed when κ=1.980). Therefore, the chosen gap length and opening size appear acceptable for all eight SWCs studied.

Finally, the shear stress distributions along the long side of the remaining wall (side 5) typically have similar magnitudes between the full wall and cut-wall models. However, the exact distribution shapes do not match along the entire length, but this is primarily because 400mm of the wall has been removed in the cut-wall model, and this load must be transferred elsewhere along the long side.

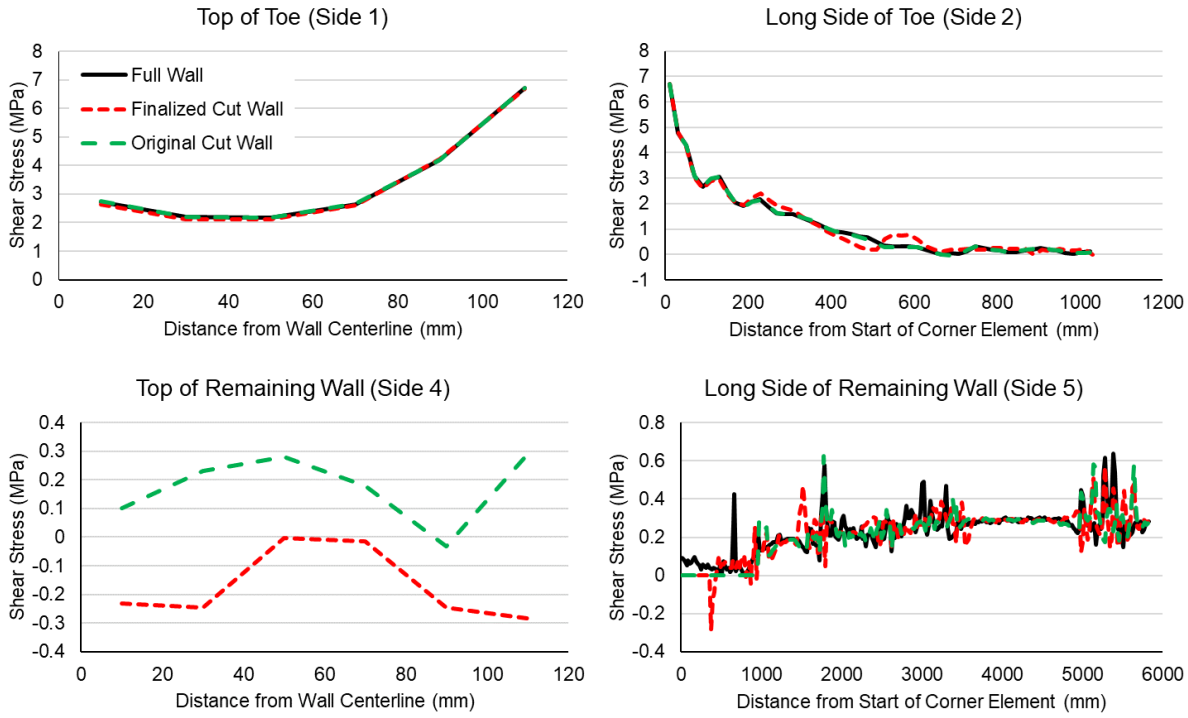


Figure 7-46: Comparison of Shear Stress Distribution Along Wall Perimeter from Full Wall and Cut-Wall Models (no Bottom of Toe (Side 3) since c_{min}/d High Opening Removes all Elements), κ = 0.990 (see Figure 7-36 for Side Numbering Convention, ¼ SWC Shown, Stresses Averaged Over Depth)

7.2.5.5 Key Findings

While not implemented in commercial punching shear design software, as the toe capacity would be greatly overpredicted as discussed in the next section, the results in Table 7-6 demonstrate that when combined with calibrated NLFEA the cut-wall model can be used to accurately estimate the overall punching capacity of interior SWCs subjected to concentric gravity loading, and the distribution of load to the two-way and one-way shear regions. Additionally, the development of the cut-wall models provided valuable insight into the punching behaviour of SWCs and contributed to the development of the proposed design method.

The cut-wall model demonstrated that interior SWCs can be designed by decomposing the connection into a combination of two-way shear regions near the wall ends, and a one-way shear region representing the remainder of the connection. While the length of two-way shear regions can be relatively small compared to the overall connection length, these regions transfer a significant portion of the load. The NLFEA of the cut-wall specimens predicted that a significant amount of the total load was transferred through the toe regions. For a toe length of *5d*, approximately 50% and 40% of the total load was transferred through the toe regions when the connection was loaded through load plates along the radius of contraflexure or a uniformly distributed gravity load applied on the slab surface beyond *d/2* from the wall face, respectively. Therefore, the contribution of two-way shear to the shear capacity of elongated connections is significant, and openings near the toe regions should be avoided, as they can significantly reduce connection capacity.

The cut-wall models also demonstrated that a small portion of SWCs is relatively ineffective in transferring load. This portion, which is represented by the *2d* long gap region in the cut-wall model, is assumed to be the region where the load transfer mechanism is transitioning from a combination of two-way and one-way shear near the wall ends, to purely one-way shear along the remainder of the wall. Therefore, based on the cut-wall model dimensions, SWCs are defined as connections where the maximum support dimension, c_{max} (a graphical representation of c_{max} is provided in Figure 7-23), is greater than or equal to *14d*, otherwise they should be designed as elongated columns as outlined in Section 7.1. The punching shear design of these connections should be conducted using the procedure outlined in the following sections. For the considered flat plate structure (see Figure 7-18a) *14d* is approximately equal to 2800mm and based on a column centerline distance (L) of 6750mm, a support is defined as a wall when c_{max}/L is approximately equal to 0.415. This value agrees with previous

numerical work which has shown that one-way shear behaviour dominates when c_{max}/L exceeds approximately 0.35-0.4 [151, 156].

It should be noted that the proposed design methods were developed considering the NLFEA results for the isolated SWCs loaded through load plates. This load condition was considered as it is similar to that used in the majority of experimental and numerical analyses of slab-column connections. However, the proposed design methods would also conservatively predict the capacity of the connections subjected to uniformly distributed gravity loading.

7.2.6 Estimation of Capacity of Two-Way (Toe) Regions

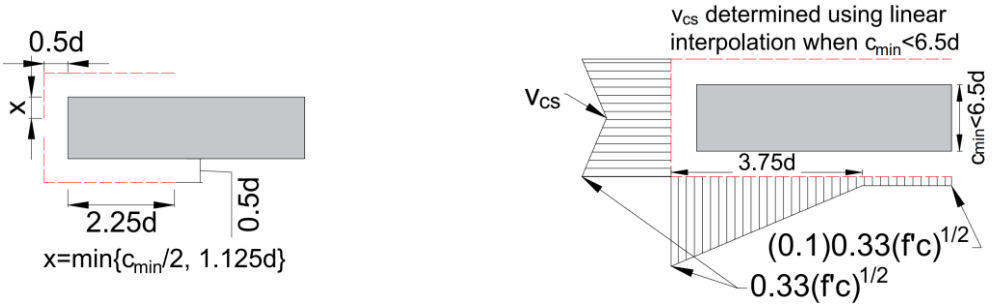
7.2.6.1 Development

After determining the load applied to the SWC using the tributary area method (or another acceptable method), the punching shear capacity of the SWC needs to be estimated. Based on the cut-wall model, the wall should be decomposed into two distinct regions, two-way shear regions at each end of the wall, which have a length of *5d*, and a one-way shear region for the remainder of the wall.

Two methods to estimate the punching capacity of the two-way shear regions (wall toes) are presented. The methods are similar to those proposed in Section 7.1 for the punching shear design of R-SCCs, but modifications have been made to account for the difference in the behaviour of wall toes and rectangular columns. Methods to estimate the shear capacity of the one-way shear region are presented in Section 7.2.7.

The first method for estimating toe capacity, denoted Method 1W, uses an effective critical perimeter to account for the shear stress concentrations at the outer ends of each toe. Along the effective critical perimeter, shown in Figure 7-47a, a constant nominal shear stress capacity of $0.33\sqrt{f_c'}$ (MPa) is assumed (this matches the maximum value in ACI 318-19 [2] and suggested by Schwaighofer and Collins [30] for the punching design of wall toes). The effective length of the critical perimeter beyond the toe corners, *2.25d*, is identical to that proposed for the design of R-SCCs (Method 1 in Section 7.1). However, along the long sides of the toe, the effective critical perimeter has been concentrated at the outer end of the toe, as shown in Figure 7-47a, as the shear stresses along the long side near the inner short side of the toe are very low as shown in Figure 7-48. This differs from the behaviour of rectangular columns where stress concentrations exist at both column ends. Additionally, no critical perimeter parallel to the inner short side of the toe is considered, as in reality

the toe region and remainder of the wall are continuous, and therefore, no perimeter would be considered in this region.



a) Method 1W (Effective Critical Perimeter) b) Method 2W (Linear Stress Distribution)

Figure 7-47: Proposed Methods for Estimating Punching Capacity of Toe Regions (Within *5d* of Wall end), 1 Toe Shown

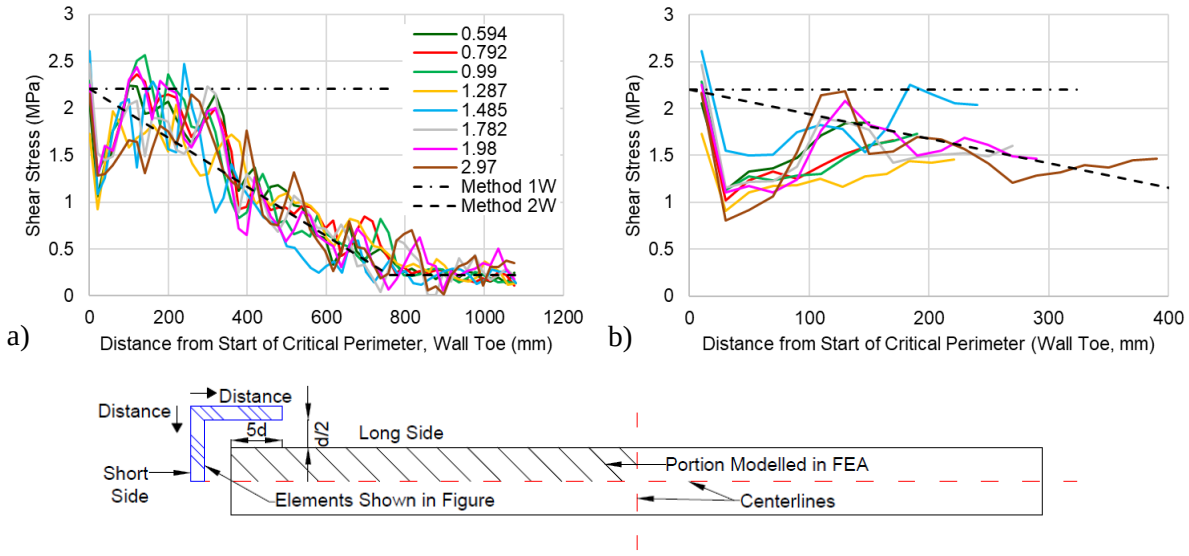


Figure 7-48: Comparison of Critical Perimeter Shear Stress Distribution Predicted by NLFEA and Proposed Methods for Estimating Toe Capacity (Entire SWC Not Shown), f'_c =44.6MPa, a) Long Side Within *5d* of Wall End (Wall Toe), b) Short Side (Stresses Averaged Over Depth)

The wall toe critical perimeter shear stress distributions predicted by the NLFEA and Method 1W for the 8 SWCs (f_c'=44.6MPa) are provided in Figure 7-48. As for R-SCCs (see Section 7.1), an effective critical perimeter and a constant nominal shear stress capacity do not represent the shear stress distribution predicted by the NFLEA. However, Method 1W does accurately predict the punching capacity of the toes and the assumed nominal shear stress capacity agrees well with the maximum shear stress magnitude predicted by the NFLEA.

The second method for estimating toe capacity, denoted Method 2W, uses a combination of linear and constant shear stress regions to better represent the critical perimeter shear stress distribution. As in Method 1W, the maximum shear stress capacity is equal to $0.33\sqrt{f_c'}$, but this shear capacity is assumed to decrease linearly over a distance of *3.75d* to a minimum value of $0.1(0.33)\sqrt{f_c'}$ (MPa), as shown in Figure 7-47b. The assumed shear stress distribution, which was originally derived for the punching shear design of R-SCCs (Method 2 in Section 7.1), applies to the long sides and the outer short side of the toe (wall end). However, differing from the design of R-SCCs, where the linear distribution applies to both ends of the column with a constant stress region in between, the linear distribution only applies to the outer end of the toe as shown in Figure 7-47b. Additionally, no critical perimeter parallel to the inner short side of the toe is considered. As in Method 1W, these changes were made to account for the differences in behaviour between wall toes and rectangular columns.

A comparison of the wall toe critical perimeter shear stress distributions predicted by the NLFEA and Method 2W for the 8 SWCs (f_c'=44.6MPa) is also provided in Figure 7-48. As briefly discussed in Section 7.1, the assumed shear stress distribution accurately captures the shear stress distribution along the long side of the toes predicted by the NFLEA for all κ values (similar agreement was also found when the SWCs were analyzed with f_c'=30MPa). The shear stress magnitudes along the long side are highest at the end of the toe, and decrease approximately linearly with increasing distance from the short side of the critical perimeter, before approaching a region of approximately constant stress. The assumed distribution also predicts the shear stresses along the short side to decrease towards the column centerline, which matches the NLFEA. While the magnitude of the shear stresses along the short side is typically overpredicted by Method 2W this did not lead to any unconservative capacity estimates.

7.2.6.2 Implementation

Unlike the ACI 318-19 [2] punching shear design provisions for slab-column connections, which are formulated in terms of a nominal shear stress capacity along the critical perimeter, the proposed punching shear design equations for interior SWCs are formulated in terms of total force. The proposed design method is not formulated in terms of stress due to the SWC being decomposed into multiple regions.

According to Method 1W the punching capacity of the toe (two-way shear) regions, V_{2-way} (N), can be calculated using equation 7-8 (SI units)

$$V_{2-way} = 0.33\sqrt{f_c'}\left(b_{o,toe-1W}\right)(d) \quad 7\text{-}8$$

where $b_{o,toe-1W}$ is the critical perimeter for both toes according to Method 1W (mm, see Figure 7-47a), which is calculated using equation 7-9

$$b_{o,toe-1W} = 2[2(2.25d + 0.5d) + 2(x + 0.5d)] \quad 7\text{-}9$$

where x is the length of the effective regions parallel to the short side of the toe calculated as the minimum of $c_{min}/2$ and *1.125d* (mm, see Figure 7-47a).

The punching capacity of the toe regions according to Method 2W can be calculated by integrating the non-uniform shear stress distribution shown in Figure 7-47b. Alternatively, the non-uniform distribution can be converted to a uniform distribution by calculating the weighted average of the shear stress distribution, $v_{c,eff}$ (MPa). For a SWC with a wall thickness less than or equal to *6.5d*, $v_{c,eff}$ can be calculated using equation 7-10 (note equation 7-10 is based on the critical perimeter shear stress distribution for one toe)

$$v_{c,eff} = \frac{2\left(\frac{\left[0.33\sqrt{f_c'} + 0.1(0.33)\sqrt{f_c'}\right]}{2}\right)3.75d + 2(0.1)(0.33)\sqrt{f_c'}(1.75d) + 2\left(\frac{\left[0.33\sqrt{f_c'} + v_{cs}\right]}{2}\right)y}{5.5d(2) + (c_{min} + d)} \quad 7\text{-}10$$

where y is equal to $(c_{min} + d)/2$ and v_{cs} is the shear stress magnitude at the centerline of the short side, which can be determined using linear interpolation. Once $v_{c,eff}$ is known, equation 7-11 (SI units) can be used to calculate the punching capacity of the toe regions according to Method 2W

$$V_{2-way} = v_{c,eff}\left(b_{o,toe-2W}\right)(d) \quad 7\text{-}11$$

where $b_{o,toe-2W}$ is the critical perimeter of both toes according to Method 2W (mm), which is calculated using equation 7-12.

$$b_{o,toe-2W} = 2[2(5d + 0.5d) + (c_{min} + d)] \quad 7\text{-}12$$

7.2.6.3 Comparison to NLFEA

A comparison of the toe capacities predicted by the FEA (full wall models), ACI 318-19, the Schwaighofer and Collins method (see Figure 2-14b in Section 2.3.5) [30], Method 1W and Method 2W for the SWCs where f_c'=44.6MPa is provided in Table 7-7.

ACI 318-19 accurately predicts the punching capacity of the wall toes when the nominal shear stress capacity along the critical perimeter is calculated based on the aspect ratio and critical

perimeter for the full SWC. However, as will be discussed in Section 7.2.7, the capacity of the remainder of the wall is greatly overpredicted, which results in ACI 318-19 greatly overpredicting the capacity of the SWCs compared to the NLFEA. If the nominal shear stress capacity is calculated considering the aspect ratio and critical perimeter of the toes only, ACI 318-19 greatly overpredicts the toe capacity (average V_{calc}/V_{FEA} ratio of 1.295), which is why the author did not implement the cut-wall model, presented in Section 7.2.5, in commercial design software as originally intended.

Table 7-7: Comparison of Predicted Capacities of Two-Way Shear Regions, f'_c =44.6MPa

	Predicted Toe Load (kN)					V_{calc}/V_{FEA}			
κ	FEA (Full Wall)	ACI 318	Schwaighofer and Collins [30]	Method 1W	Method 2W	ACI 318	Schwaighofer and Collins [30]	Method 1W	Method 2W
0.594	1389.9	1187.4	860.1	1275.9	1064.1	0.854	0.619	0.918	0.766
0.792	1420.9	1213.0	966.9	1311.5	1092.5	0.854	0.681	0.923	0.769
0.990	1421.1	1238.7	1073.8	1347.1	1120.0	0.872	0.756	0.948	0.788
1.287	1414.6	1277.6	1234.0	1400.5	1159.7	0.903	0.872	0.990	0.820
1.485	1453.9	1303.7	1340.9	1436.1	1185.1	0.897	0.922	0.988	0.815
1.782	1578.5	1343.3	1501.1	1489.6	1221.7	0.851	0.951	0.944	0.774
1.980	1641.4	1369.8	1608.0	1525.2	1245.0	0.835	0.980	0.929	0.758
2.970	1767.9	1505.1	2142.2	1573.7	1348.8	0.851	1.212	0.890	0.763
					Avg.	0.865	0.874	0.941	0.782
					Min	0.835	0.619	0.890	0.758
					Max	0.903	1.212	0.990	0.820

Note: Nominal shear stress capacity based on aspect ratio and critical perimeter of full SWC and material safety factors set to 1 when calculating ACI 318-19 capacity

The accuracy of the method proposed by Schwaighofer and Collins [30], which is recommended by Joint ASCE-ACI Committee 352 for the punching design of connections where β exceeds 3 [104], varies with κ. For very thin walls ($\kappa <\approx 0.8$) the method significantly underpredicts the toe capacity (≈30% lower than the NLFEA), whereas for thick walls ($\kappa \approx 3$) the capacity is overpredicted (≈20% higher than the NLFEA). Therefore, the Schwaighofer and Collins method is not recommended for estimating the punching capacity of the toe regions.

While Method 1W accurately predicts the toe capacity (average V_{calc}/V_{FEA} ratio of 0.941), the method does not accurately represent the shear stress distribution around the wall toe, as discussed previously. Additionally, the use of Method 1W would make the wall design method inconsistent with that proposed for R-SCCs (see Section 7.1). Therefore, Method 2W is recommended for estimating the punching capacity of the toe regions. While the Method 2W predictions are more conservative, as seen in Table 7-7 (average V_{calc}/V_{FEA} ratio of 0.782), Method 2W more accurately

represents the shear stress distribution in the toe regions, particularly along the long side of the toes, and is consistent with the punching shear design method proposed for R-SCCs (c_{max}<*14d*).

7.2.7 Estimation of Capacity of One-Way Regions

7.2.7.1 Development

The final component of the punching shear design method for interior SWCs is an estimate of the capacity of the one-way shear region shown in Figure 7-23. Note, in the proposed design method the connection's capacity in the gap region shown in Figure 7-23 is neglected. This is conservative and makes the proposed design method and cut-wall model consistent.

Representative shear stress distributions along the long side of the critical perimeter at *d/2* from the wall face for interior SWCs (f_c'=44.6MPa) are provided in Figure 7-49. From the distributions provided in Figure 7-49, and those for the other κ values, two clear trends are observed. Firstly, the shear stresses in the one-way shear region, which begins at a distance *7.5d* of from the start of the critical perimeter (approximately 1500mm for the analyzed specimens), are approximately constant. Secondly, the shear stress magnitudes in the one-way shear region typically increase as κ increases.

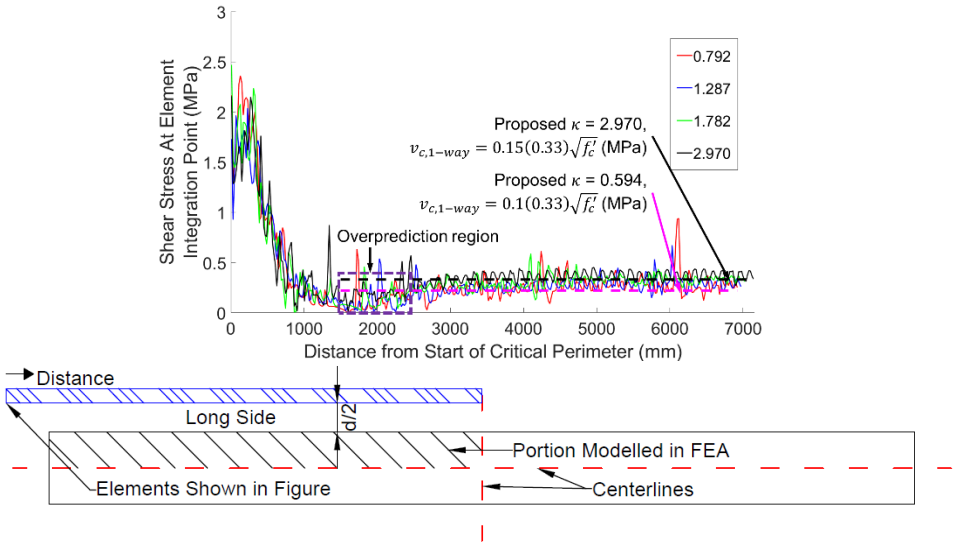


Figure 7-49: Comparison of Critical Perimeter Shear Stress Distribution Predicted by NLFEA and Proposed Method in One-Way Shear Region (Entire SWC not Shown, Stresses Averaged Over Depth)

Therefore, the capacity of the one-way shear region can be estimated using a constant shear stress distribution, whose magnitude is dependent on κ. The average shear stress magnitudes in the one-way shear region (the stresses in the toe and gap region are neglected) for the 8 interior SWCs where f_c'=44.6MPa are provided in Figure 7-50. It was observed that the average shear stress in the one-way shear region is approximately linearly related to κ as shown in Figure 7-50. The calculated average shear stress is approximately equal to $0.1(0.33)\sqrt{f_c'}$ and $0.15(0.33)\sqrt{f_c'}$ (MPa) for κ equal to 0.594 and 2.970, respectively.

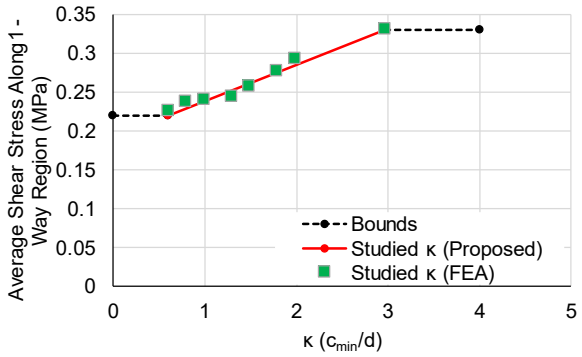


Figure 7-50: Average Critical Perimeter Shear Stress in One-Way Shear Region Predicted by NLFEA and Proposed Linear Relationship Relating Average Shear Stress to κ

7.2.7.2 Implementation

Therefore, the shear capacity of the one-way shear region, V_{1-way} (N) is calculated using equation 7-13, assuming a constant shear stress distribution

$$V_{1-way} = v_{c,1-way}(2L_{1-way})(d) \quad 7\text{-}13$$

where L_{1-way} is the length of the one-way shear region according to Figure 7-23 (mm, $L_{1-way} = c_{max} - 14d$ for the chosen toe and gap lengths) and $v_{c,1-way}$ is the assumed shear stress (MPa). For κ values less than or equal to 0.594, $v_{c,1-way}$ is equal to $0.1(0.33)\sqrt{f_c'}$ (the linear relationship between κ and $v_{c,1-way}$ is not continued for κ values smaller than 0.594 to match the minimum shear stress magnitude assumed in the toe region and in the design of R-SCCs (see Section 7.1). For κ values greater than or equal to 2.970, $v_{c,1-way}$ is equal to $0.15(0.33)\sqrt{f_c'}$ (the maximum value of $v_{c,1-way}$ is capped at the value for κ=2.970 to be conservative as the validity of the assumed linear

relationship for larger κ values is unknown). For intermediate κ values between 0.594 and 2.970, $v_{c,1-way}$ is determined through linear interpolation.

As seen in Figure 7-50, the upper and lower bounds, and the linear relationship between $v_{c,1-way}$ and κ accurately reflect the average shear stress in the one-way shear region predicted by the NLFEA. However, the assumed constant shear stress values can overpredict the shear stress magnitudes at the beginning of the one-way shear region, as shown in Figure 7-49, but these overpredictions did not lead to unconservative capacity estimates.

7.2.7.3 Comparison to NLFEA

The capacities of the one-way shear region predicted by the NLFEA, ACI 318-19 and the proposed wall design method are provided in Table 7-8 (note, the NLFEA and ACI 318-19 predictions include the capacity of the gap region shown in Figure 7-23). As expected, ACI 318-19 greatly overpredicts the capacity of the one-way shear region (average V_{calc}/V_{FEA} of 3.907), due to the fact that the nominal shear stress capacities predicted by ACI 318-19 (based on the geometry of the full SWC) are much higher than those predicted by the NLFEA as discussed in [323] and subsection 6.4.1.2. The proposed wall design method is conservative for all 8 SWCs where f_c' equals 44.6MPa with an average V_{calc}/V_{FEA} ratio of 0.793, and has a similar accuracy for all 8 specimens (minimum and maximum V_{calc}/V_{FEA} ratios of 0.760 and 0.826, respectively), confirming the applicability of the method for different wall sizes.

Table 7-8: Comparison of Predicted One-Way Shear Region Capacities, f'_c =44.6MPa

	Predicted One-Way Region Capacity (kN)			V_{calc}/V_{FEA}	
κ	FEA	ACI	Proposed	ACI	Proposed
0.594	1205.5	5414.3	960.9	4.492	0.797
0.792	1279.0	5464.0	1004.6	4.272	0.785
0.990	1308.7	5513.6	1048.7	4.213	0.801
1.287	1349.4	5588.2	1115.3	4.141	0.826
1.485	1416.0	5638.0	1160.1	3.982	0.819
1.782	1570.0	5712.7	1227.8	3.639	0.782
1.980	1674.6	5762.6	1273.3	3.441	0.760
2.970	1959.5	6012.2	1505.4	3.068	0.768
			Avg.	3.907	0.793
			Min	3.068	0.760
			Max	4.492	0.826

Note: FEA and ACI 318-19 predictions include the capacity of *2d* gap region (see Figure 7-23); Nominal shear stress capacity based on aspect ratio and critical perimeter of full SWC and material safety factors set to 1 when calculating ACI 318-19 capacity

7.2.8 Summary of the Design Method

A summary of the proposed wall design method, which applies to connections where c_{max} is greater than or equal to *14d*, is provided in Figure 7-51 (half wall shown, linear shear stress distribution also applies to the short side of the toes). The punching capacity of an interior SWC, V_{wall}, is the sum of the capacities of the two-way (V_{2-way}) and one-way shear regions (V_{1-way}). If V_{wall} exceeds the applied shear demand, which can be estimated using the tributary area method (or another acceptable method) as discussed in Section 7.2.4, the interior SWC is adequate for punching shear.

The punching capacities predicted by the NLFEA, ACI 318-19, the Combined Method for R-SCCs (presented in Section 7.1) and the proposed wall design method for the 8 interior SWCs are provided in Table 7-9. The proposed wall design method is conservative for all specimens (average V_{calc}/V_{FEA} ratio of 0.787 and 0.771 for connections where f_c' equals 44.6MPa and 30MPa, respectively) and typically predicts higher capacities than the Combined Method for rectangular columns due to the higher shear stress magnitudes in the one-way shear region. The Combined Method for rectangular columns is also conservative for analyzed SWCs (average V_{calc}/V_{FEA} ratio of 0.754 and 0.740 for connections where f_c' equals of 44.6MPa and 30MPa, respectively) but becomes overly conservative as κ increases because the shear stress in the one-way shear region is set to a constant value of $0.1(0.33)\sqrt{f_c'}$ regardless of κ. However, as the Combined Method for rectangular columns does not neglect the capacity of the connection in the gap region (see Figure 7-23) it can predict slightly higher capacities than the wall design method when κ is less than 1.

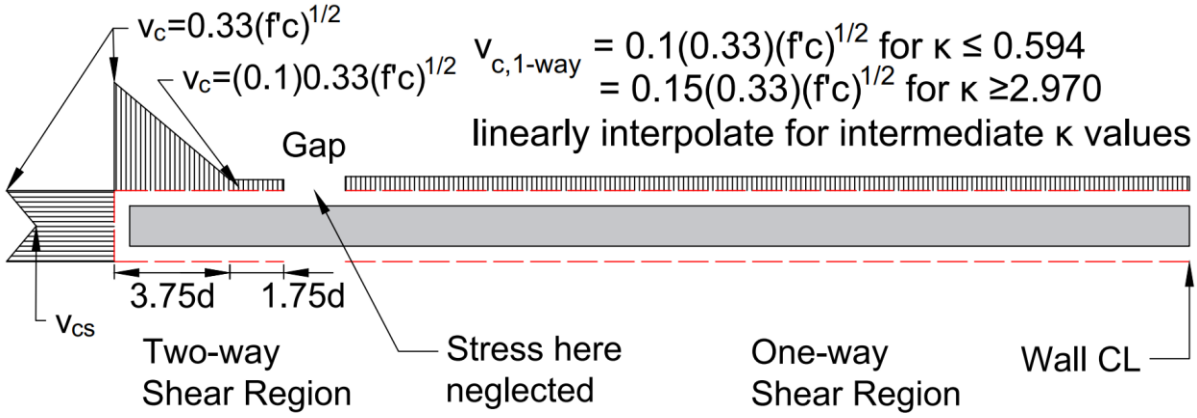


Figure 7-51: Summary of Proposed Design Method for Interior SWCs (Linear Distribution also Applies to Short Side of Wall)

Table 7-9: Comparison of Predicted Punching Capacities for Interior SWCs

		Wall Parameters			Predicted Punching Shear Capacity (kN)				
	κ, c_{min}/d	Thickness, c_{min} (mm)	Length, c_{max} (mm)	Aspect Ratio, β	V_{FEA}, Full Wall	V_{FEA}, Cut Wall	V_{ACI}	$V_{proposed}$ (rect. column)	$V_{proposed}$ (Wall)
f'_c=44.6 MPa [323]	0.594	120	13620	113.5	2595.3	2544.9	6601.7	2096.9	2025.0
	0.792	160	13660	85.4	2699.9	2675.9	6676.9	2128.9	2097.1
	0.990	200	13700	68.5	2729.8	2740.6	6752.3	2160.0	2168.7
	1.287	260	13760	52.9	2764.1	2764.8	6865.8	2205.0	2275.0
	1.485	300	13800	46.0	2869.9	2800.9	6941.7	2234.0	2345.2
	1.782	360	13860	38.5	3148.5	3156.7	7056.0	2275.9	2449.5
	1.980	400	13900	34.8	3316.0	3261.6	7132.4	2302.7	2518.3
	2.970	600	14100	23.5	3727.4	3697.9	7517.3	2424.3	2854.2
f'_c=30 MPa	0.594	120	13620	113.5	2134.2	-	5414.4	1719.8	1660.8
	0.792	160	13660	85.4	2208.7	-	5476.1	1746.0	1719.9
	0.990	200	13700	68.5	2296.6	-	5537.9	1771.5	1778.6
	1.287	260	13760	52.9	2300.8	-	5631.0	1808.4	1865.8
	1.485	300	13800	46.0	2440.4	-	5693.3	1832.2	1923.4
	1.782	360	13860	38.5	2632.5	-	5787.0	1866.6	2008.9
	1.980	400	13900	34.8	2765.8	-	5849.6	1888.6	2064.4
	2.970	600	14100	23.5	3212.1	-	6165.3	1988.3	2340.9

Note: Capacity predicted by ACI 318-19 based on punching shear provisions, One-way shear capacity predicted by ACI 318-19 (assuming one-way shear failure parallel to the long side of the wall) equal to 3781.7kN and 3101.6kN for f'_c equal to 44.6MPa and 30MPa, respectively; Material safety factors set to 1 when calculating capacities according to ACI 318-19;

It should be noted that all considered SWCs had effective depths less than 250mm. Therefore, the size effect factor, λ_s, introduced in ACI 318-19 [2] did not apply. For any connections where the effective depth exceeds 250mm, the recommended shear stress magnitudes (in the two-way and one-way shear regions) should be multiplied by λ_s (see equation 3-5 in Section 3.3.2).

7.3 Summary and Contributions

The author's previous analyses of R-SCCs and SWCs, which were presented in [1], subsection 2.3.8.4 and Chapter 6, have demonstrated that the ACI 318-19 shear provisions are inadequate, and unconservative in many cases, for elongated connections. Therefore, the primary contribution of this chapter was to present alternative concentric punching shear design methods for elongated connections. The proposed design methods for R-SCCs and SWCs are presented in a code-like formulation and will be submitted to ACI for potential adoption in future versions of ACI 318.

Additional detailed contributions are as follows. Three alternative methods to estimate the concentric punching shear capacity of interior R-SCCs without shear reinforcement are presented in

Section 7.1. Unlike the ACI 318-19 provisions, the proposed methods accurately account for the influence of both the column aspect ratio, β, and the relative column size, κ ($\kappa = c_{min}/d$). As discussed in this chapter, the proposed methods show good agreement with the FEA predictions for the 77 hypothetical slab-column connections analyzed during the author's MASc studies [1], and display similar accuracy to the ACI 318-19 provisions for 86 experimentally tested slab-column connections, though the proposed methods are slightly more conservative on average.

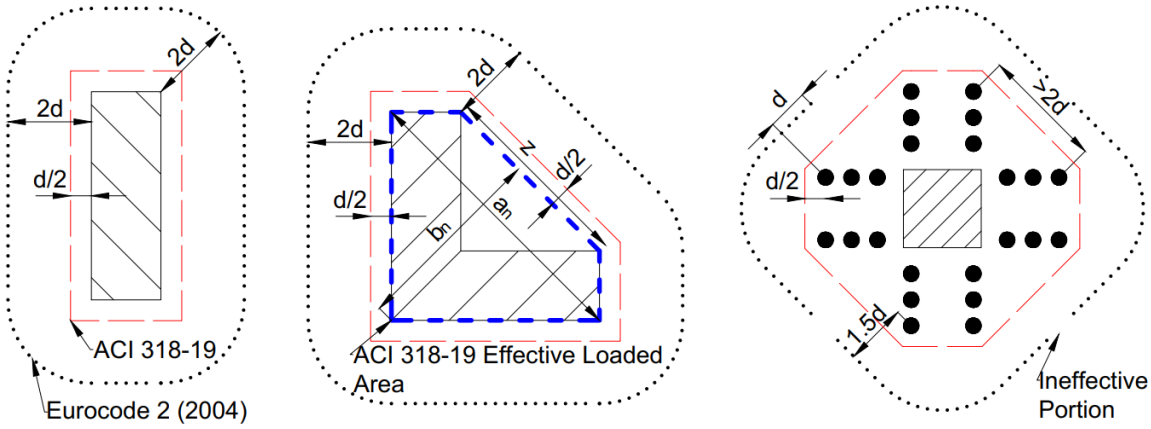
A concentric punching shear design method for interior SWCs without shear reinforcement is presented in Section 7.2. The proposed method is an extension of those proposed for R-SCCs and accounts for the differences in the punching shear behaviour of R-SCCs and SWCs. Based on extensive FEAs, a SWC, which is defined as a connection where the maximum column dimension is greater than or equal to *14d* (where *d* is the effective slab depth), can be designed by decomposing the connection into two-way and one-way shear regions. Unlike the existing ACI 318-19 provisions, which overpredict the connection capacity and shear stress magnitudes along the majority of the wall, as discussed in subsection 6.4.1.2, the proposed method results in conservative capacity estimates and accurately represents the critical perimeter shear stress distribution. Additionally, it was shown that the tributary area method can be used to estimate the applied load demand on interior SWCs.

It should be noted that the design methods for R-SCCs and SWCs proposed herein are suitable for hand calculations, unlike other design methods for elongated connections recently proposed in literature [158, 189], which require specialized FEA and use the Critical Shear Crack Theory (CSCT).

Chapter 8: Special-Shaped Slab-Column Connection Study – Concentric Loading

8.1 Motivation

Another area of punching shear research which has been neglected, even though it has been accounted for in North American [170] and European [53] design provisions since 1977 and 1978, respectively, is the punching shear behaviour of special-shaped slab-column connections (SS-SCCs) (which are also commonly referred to as irregular slab-column connections) such as L, T and cruciform connections. The limited experimental studies which do exist suggest that these connections provide good seismic performance [176] and possess higher strength and ductility than conventional square slab-column connections [171]. Even though previous research is limited, design provisions for SS-SCCs are included in worldwide design provisions [2, 34, 35] and are largely the same as those introduced in the late 1970s. The basis for these provisions, particularly the critical perimeter, which does not follow geometry as is assumed for square, circular and rectangular columns, as shown in Figure 8-1, is unclear, and their accuracy needs to be verified.



a) Regular Slab-Column Connections

b) Unreinforced L Slab-Column Connections

c) Shear Stud Reinforced Slab-Column Connections, Cruciform Layout

Figure 8-1: Assumed Critical Perimeters According to ACI 318-19 [2] and Eurocode 2 [34] Around a) Square/Rectangular Columns, b) L Slab-Column Connections (Effective Loaded Area Assumed in ACI 318-19 Shown with Dashed Blue Line) and c) Shear Reinforced Connections

Unlike Model Code 2010 [35] and prEC2 (2020) [280], current North American [2] and European [34] design provisions assume that the diagonal portion of the critical perimeter is fully effective (as no limitation on the diagonal distance between the column flanges, labelled as *z* in Figure 8-1b is

specified). However, similar to rectangular slab-column and slab-wall connections, the shear stress distribution around SS-SCCs is expected to be non-uniform, and shear stress concentrations are expected near the column corners. Due to these stress concentrations, it is hypothesized that the diagonal portions of the critical perimeter between the column flanges will not be fully effective. This hypothesis is supported by recent experimental and numerical research of the punching shear behaviour of L slab-column connections (L-SCCs) by Pinto et al. [174]. Current European punching shear design provisions for shear reinforced connections, where the shear reinforcement is arranged in a cruciform layout, also support this hypothesis. According to Eurocode 2 (2004), when the diagonal distance between shear reinforcement on adjacent column sides exceeds *2d*, the length of the diagonal portion of the critical perimeter should be reduced to account for the large region of unreinforced concrete around the column, as shown in Figure 8-1c. Logically, a similar reduction should also apply to the large unreinforced regions between the flanges of SS-SCCs without shear reinforcement when *z* exceeds *2d*, though no mention of this is made in Eurocode 2 (2004).

If the diagonal portion of the critical perimeter is indeed ineffective, locating slab openings in the region between the column flanges would be beneficial from both a structural and architectural perspective, as the influence of opening on punching capacity would be minimized, while allowing the openings and services to be hidden from view. The ability to minimize the impact of openings would also be a significant benefit of SS-SCCs, as slab openings greatly reduce the punching capacity of square and rectangular slab-column connections (R-SCCs), as discussed in subsections 2.3.6 and 6.4.3.1.

In this chapter, a three-dimensional nonlinear FEM, implemented in Abaqus/Explicit 6.13 and based on the CDP model, is used to study the punching shear behaviour of L, T and cruciform slab-column connections. As discussed herein, the FEM was calibrated to the experimental results of R-SCC tests by Hawkins et al. [3] (note, the study of L columns by Pinto et al. [174] was not available at the time of calibration). The calibrated FEM is used to study the influence of column shape, column size, and presence of slab openings on the punching behaviour of interior L, T and cruciform slab-column connections without shear reinforcement subjected to concentric loading. As will be discussed, many of the analyzed opening layouts involve openings located between the column flanges. The punching behaviour of R-SCCs with similar opening layouts is also studied to help quantify the benefits of using SS-SCCs. The FEM-predicted punching capacities and opening influences are also used to evaluate the ACI 318-19 punching shear provisions.

8.2 Study Overview

8.2.1 General Details

In this chapter, the punching shear behaviour of R-SCCs and SS-SCCs is analyzed. The study focuses on the influence of three parameters, the column geometry, the column size and the presence of slab openings near the connections.

As shown in Figure 8-2, isolated slab-column connections representing interior columns are analyzed. Since the study is focused on the connection behaviour under concentric loading, the centroids of the column and isolated slab are aligned, which corresponds to the column centroid being aligned with the column gridlines in the continuous structure, as shown in Figure 8-3b. If the centroids are unaligned, as shown in Figure 8-3a, an unbalanced moment needs to be accounted for when estimating the connection capacity according to ACI 318-19. It should be noted that as shown in Table 8-1, small eccentricities between the column and slab centroids exist for most of the L slab-column connections (L-SCCs) and T slab-column connections (T-SCCs). These small eccentricities were necessary for mesh uniformity and to minimize mesh differences between the models for different column geometries, as results based on the CDP model are mesh size dependent. The influence of these minor eccentricities, which have magnitudes between 3.75mm and 11.3mm, on the overall specimen behaviour was negligible (a maximum reduction in punching capacity of 1.5% was predicted by the FEA for the specimens without openings).

For each column geometry, four column sizes are analyzed, as shown in Figure 8-4 (note, all analyzed SS-SCCs are symmetric). For the SS-SCCs, the column flange dimensions (the definitions of a column flange for L, T and cruciform slab-column connections are provided in Figure 8-5) were chosen such that the aspect ratio of each flange, β_{fl} ($\beta_{fl} = c_{max}/c_{min}$ where c_{max} and c_{min} are defined in Figure 8-5), exceeded two, but the overall column aspect ratio according to the ACI 318-19 definition of β for SS-SCCs ($\beta = a_n/b_n$, a_n and b_n were previously defined in Figure 3-2) were less than two (note, the column flange dimensions are summarized in Figure 8-4 and Table 8-1). By sizing the columns this way, the applicability of the alternate definition of the column aspect ratio, β, for special-shaped columns ($\beta = a_n/b_n$ as discussed in Section 3.3.2) can be studied. Due to this alternate definition of β the nominal shear stress capacities along the critical perimeter predicted by ACI 318-19 as a function of the column aspect ratio (equation 3-3) will always be larger for a SS-SCC than that for a R-SCC with the same size as each column flange. Additionally, regardless of the

column flange dimensions, β will always equal 1 for doubly symmetric cruciform slab-column connections (X-SCCs). It should be noted that the column sizes for the SS-SCCs are further divided into two categories, small (100x330 and 200x420mm flanges) and large (100x600 and 200x600mm flanges).

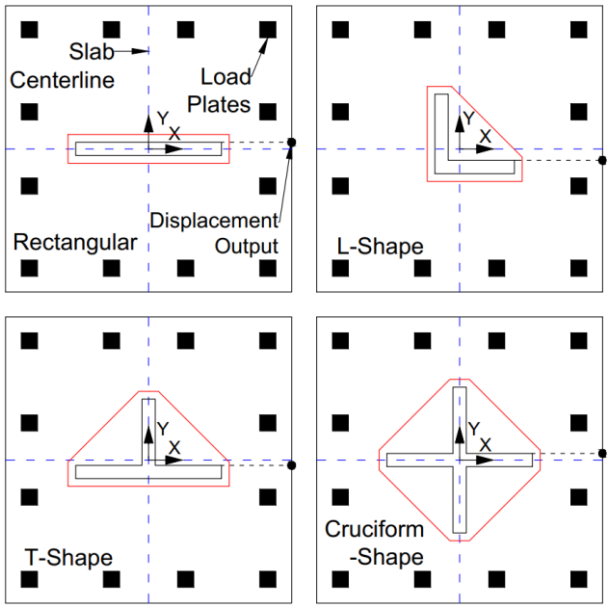


Figure 8-2: Overall Layout of Isolated Slab-Column Specimens in Special-Shaped Column Study

The maximum and minimum dimensions of the R-SCCs were chosen to match the maximum dimension and flange widths of the SS-SCCs, respectively. The R-SCCs are also divided into small (100x560 and 200x640mm columns) and large (100x1100 and 200x1000mm columns) sizes. An overview of the specimen naming convention used in this chapter is provided in Figure 8-6.

The analyzed specimens with openings represent cases where the opening is accounted for in the structural design. Therefore, additional flexural reinforcement is distributed equally on each side of the opening to replace any flexural reinforcement interrupted by the opening. As will be shown in the following sections, many of the investigated opening layouts around the SS-SCCs involve openings located between the column flanges. If the influence of these opening layouts on punching capacity is minor, this confirms that the diagonal portion of the critical perimeter is largely ineffective in transferring load between the slab and column.

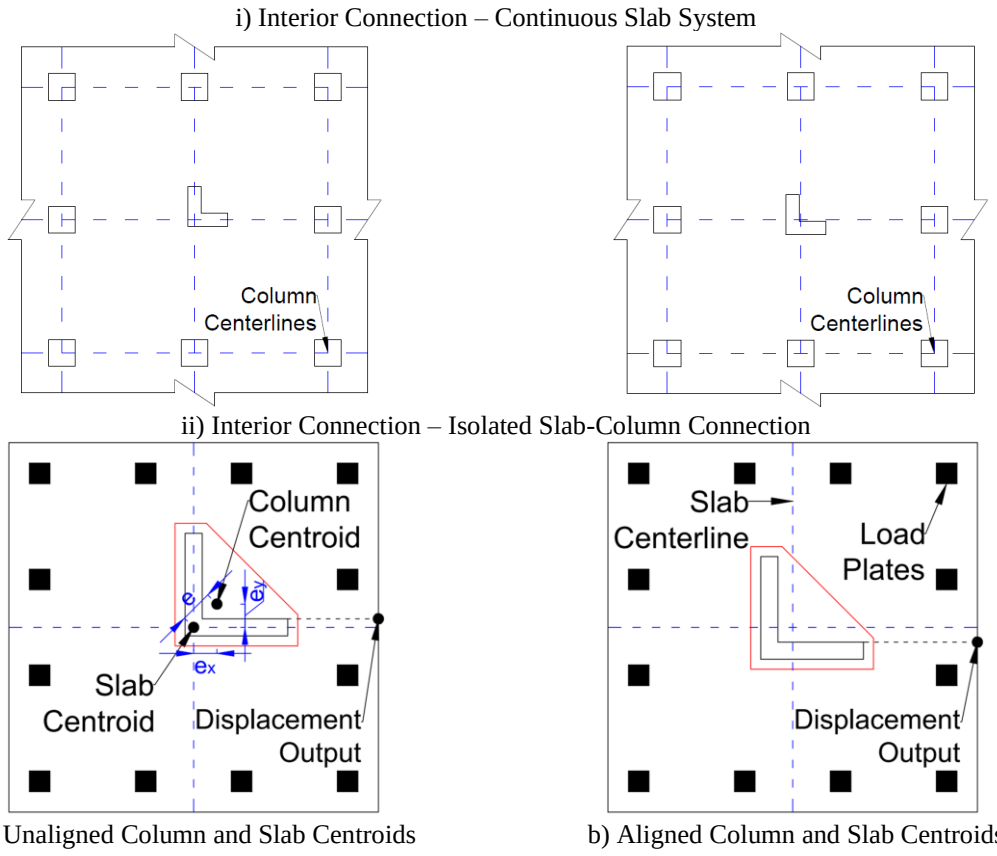


Figure 8-3: Considered Interior Slab-Column Connections in Continuous Slab System and Conversion to Isolated Specimens for Connections Where Column and Slab Centroid are a) Unaligned and b) Aligned

The general specimen geometry and representative boundary conditions used in the analysis of the punching shear behaviour of R-SCCs and SS-SCCs with and without slab openings are provided in Figure 8-7 (note, the boundary conditions are applied directly to the specimen geometry). As will be discussed in Section 8.3, slight modifications were made to the experimental specimen geometry after the FEM calibration to improve mesh uniformity. These small modifications had a minor impact on the predicted capacities for the specimens tested by Hawkins et al. [3] (which were considered in the calibration) [259, 347]. The material parameters and flexural reinforcement in the special-shaped column study are based on Slab 1 tested by Hawkins et al. [3] (discussed in Section 8.3). For the analysis of the R-SCCs and SS-SCCs, the loading conditions also differ from those used in the experiments by Hawkins et al. [3], as an equal load magnitude is applied to each load plate. The modifications to the loading conditions were made after the calibration was completed and were done

so that each side of the slab is subjected to equal loading instead of two sides of the slab being subjected to lower loads, as was done in the experiments [3].

Table 8-1: Summary of Column Dimensions, Eccentricities and Opening Details Considered for Studied L, T and Cruciform Slab-Column Connections

ID[a]	c_{max}[b]	c_{min}[b]	e_x[c,d]	e_y[c,d]	e[c,d]	x_1[b]	y_1[b]	x_2[b]	y_2[b]
V1-S-0	330	100	-8/0/0	-8/-8/0	-11.3/-8/0	-	-	-	-
V1-S-o1						190	190	[e]	[e]
V1-S-o2[f]						190	190	[e]	[e]
V1-S-o3						190	190	[e]	[e]
V1-S-o4						120	120	110	110
V1-S-o5						190	190	[e]	[e]
V1-S-o6[f]						190	190	[e]	[e]
V2-S-0	420	200	8/0/0	8/-6/0	11.3/-6/0	-	-	-	-
V2-S-o1						180	180	[e]	[e]
V2-S-o2[f]						180	180	[e]	[e]
V2-S-o3						180	180	[e]	[e]
V2-S-o4						180	180	120	120
V2-S-o5						180	180	[e]	[e]
V2-S-o6[f]						180	180	[e]	[e]
V2-S-o7						400	200	[e]	[e]
V1-L-0	600	100	-6/0/0	-6/3.75//0	-8.5/3.75/0	-	-	-	-
V1-L-o8						400	100	[e]	[e]
V1-L-o9						400	100	[e]	[e]
V1-L-o10						120	120	[e]	[e]
V1-L-o11						120	120	280/290/290[d]	280/280/290[d]
V2-L-0	600	200	0/0/0	0/6/0	0/6/0	-	-	-	-
V2-L-o8						320	100	[e]	[e]
V2-L-o9						320	100	[e]	[e]
V2-L-o10						120	120	[e]	[e]
V2-L-o11						120	120	240	240

[a] V is a placeholder which is replaced by L, T and X for the L, T and cruciform studies respectively; [b] See Figure 8-11, Figure 8-13 and Figure 8-15 for definition of c_{max}, c_{min}, x_1, y_1, x_2 and y_2 for L-SCCs, T-SCCs and X-SCCs, respectively; [c] See Figure 8-2 for definition of x and y axes (used to measure e_x, e_y and e); [d] XX/YY/ZZ, XX = Value for L column, YY = Value for T column, ZZ = Value for cruciform column; [e] See Figure 8-11, Figure 8-13 and Figure 8-15 for opening location for L-SCCs, T-SCCs and X-SCCs, respectively; [f] specimens not included in cruciform study

It should be noted that the slabs tested by Hawkins et al. [3] did not include any flexural reinforcement on the compression side of the slab (under concentric loading). Therefore, in this study, only the tension side of the slabs is reinforced. For all R-SCCs and SS-SCCs analyzed as part of this study, the tension side reinforcement consists of #5 bars (diameter of approximately 15.9mm, yield strength of 414MPa) spaced at 152mm (6") on center in both directions. An effective depth of 117mm

is assumed, based on Slab 1 tested by Hawkins et al. [3], resulting in an average flexural reinforcing ratio of approximately 1.12%. Note, all reinforcement is placed symmetrically with respect to the slab centerline.

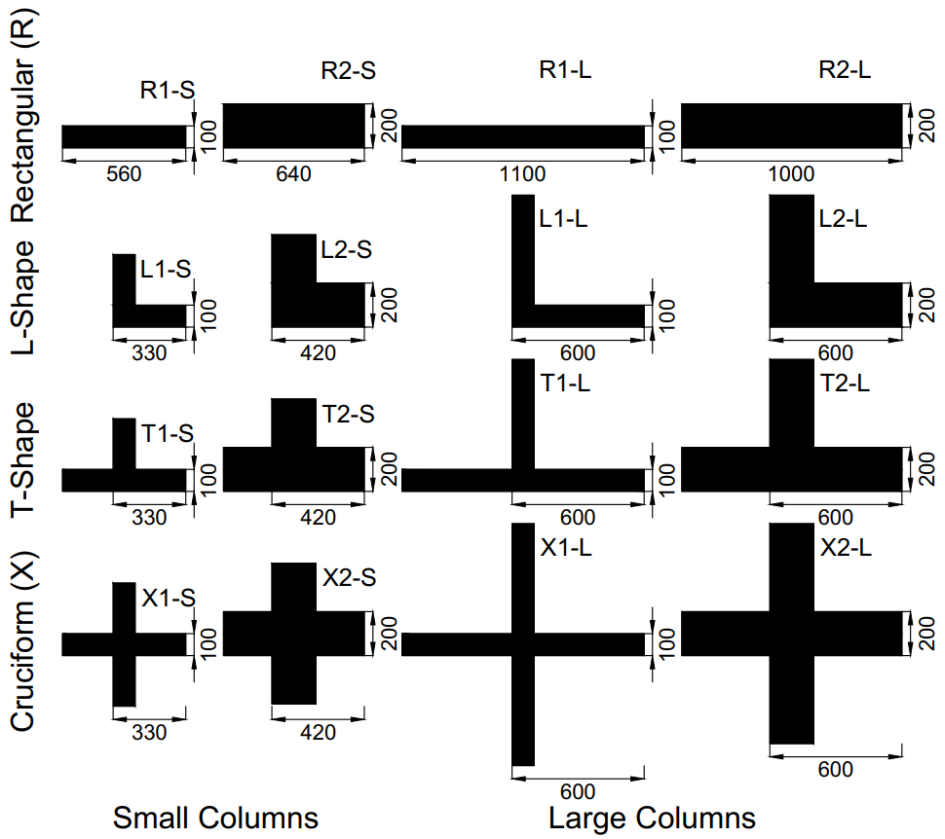


Figure 8-4: Analyzed Column Sizes for Each Column Geometry (Note, for SS-SCCs Each Flange (see Figure 8-5 for the Definition of a Column Flange) has Equal Dimensions)

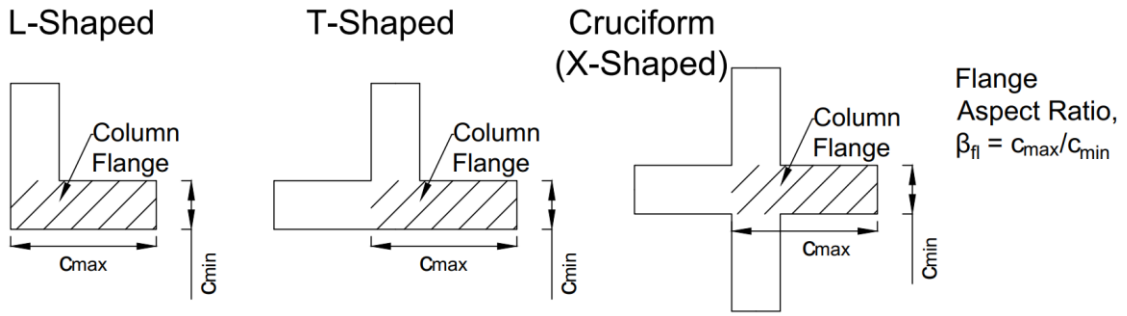


Figure 8-5: Definition of Column Flanges (c_{max} and c_{min}) and Flange Aspect Ratio for SS-SCCs Used in this Work (Column Flange Definition Shown with Hatched Area)

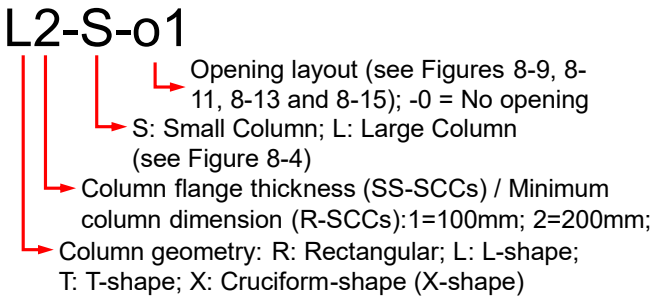
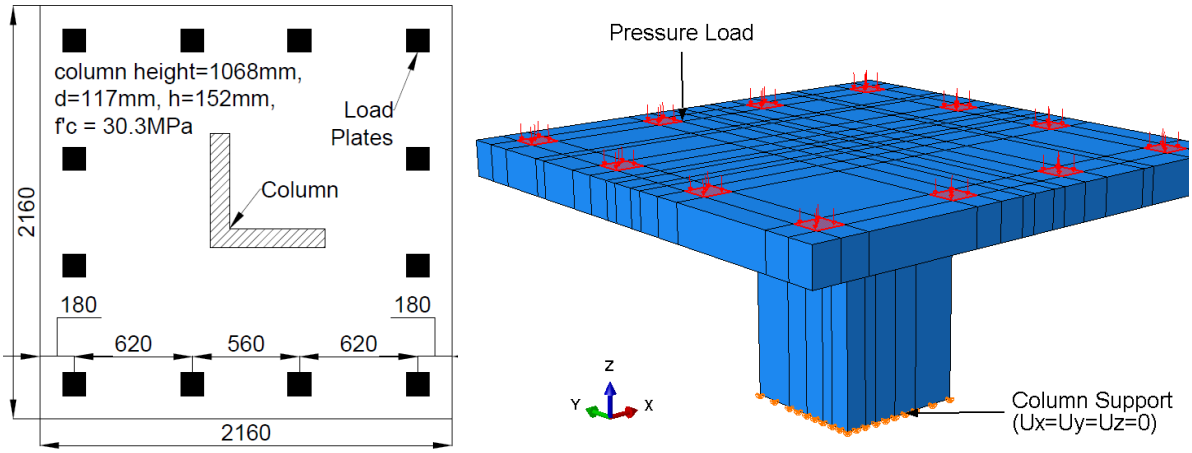


Figure 8-6: Overview of Specimen Naming Convention Used in Chapter 8



a) Overview of Specimens Considered in Special-Shaped Column Study

b) Representative Boundary Conditions in Special-Shaped Column Study (Full Specimen Modelled)

Figure 8-7: a) Modified Slab Dimensions and Parameters Used in Special-Shaped Column Study (Concentric Loading), b) Representative Boundary Conditions in Special-Shaped Column Study (Concentric Loading)

8.2.2 Rectangular Slab-Column Connection (R-SCC) Study

As previously discussed, four different column sizes were investigated in the R-SCC study (the analyzed column sizes are shown in Figure 8-8). The behaviour of the two smaller column sizes (R1-S and R2-S) was expected to be dominated by punching shear, as the ratio of the maximum column dimension, c_{max}, to the isolated specimen length, L_{iso}, was much less than 0.4 and the behaviour of the two larger column sizes (R1-L and R2-L), was expected to be governed by one-way shear, as c_{max}/L_{iso} exceeded 0.4 [145].

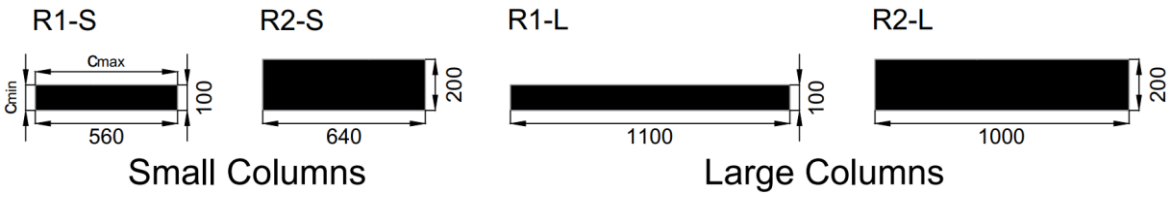


Figure 8-8: Column Dimensions of R-SCCs in This Work

Details of the investigated opening layouts are provided in Table 8-2 and Figure 8-9, and the reduced critical perimeters according to ACI 318-19 for the analyzed R-SCCs are provided in Appendix I. Since the influence of openings along the long side of R-SCCs was found to be significant in the opening study presented in subsection 6.4.3.1, most of the investigated openings are located near the long side of the connection. However, for the large column specimens, the influence of locating the opening at the intersection of the long and short side, or at a short distance away from the short side is also investigated. For all specimens other than R1-L-o9r and R2-L-o9r, the opening size and location matches that considered in the L-SCC, T-SCC and X-SCC studies to allow a comparison of the behaviour of rectangular and special-shaped slab-column connections. Therefore, a consistent naming convention is used between column geometries. However, due to symmetry some opening layouts were not analyzed in the R-SCC study. For example, the results for R2-S-o3 and R2-S-o6 would be identical as the opening location is the same for both specimens, other than the fact that the openings are on opposite column sides.

Table 8-2: Rectangular Slab-Column Connections (R-SCCs) Dimensions and Opening Details

ID	c_{max}[a]	c_{min}[a]	x_1[b]	y_1[b]	x_2[b]	y_2[b]
R1-S-0	560	100	-	-	-	-
R1-S-o1			190	190	50	[c]
R1-S-o3			190	190	50	[c]
R1-S-o4			120	120	160	110
R1-S-o5			190	190	50	[c]
R2-S-0	640	200	-	-	-	-
R2-S-o1			180	180	100	[c]
R2-S-o3			180	180	100	[c]
R2-S-o4			180	180	220	120
R2-S-o5			180	180	100	[c]
R2-S-o7			400	200	[c]	[c]
R1-L-0	1100	100	-	-	-	-
R1-L-o8			400	100	50	[c]
R1-L-o9r			400	100	150	[c]
R1-L-o10			120	120	50	[c]
R1-L-o11			120	120	340	290
R2-L-0	1000	200	-	-	-	-
R2-L-o8			320	100	100	[c]
R2-L-o9r			320	100	180	[c]
R2-L-o10			120	120	100	[c]
R2-L-o11			120	120	240	240

[a]See Figure 8-8 for definition of c_{max} and c_{min}; [b]see Figure 8-9 for definition of x_1, y_1, x_2 (measured from column centerline) and y_2; [c]see Figure 8-9 for opening location

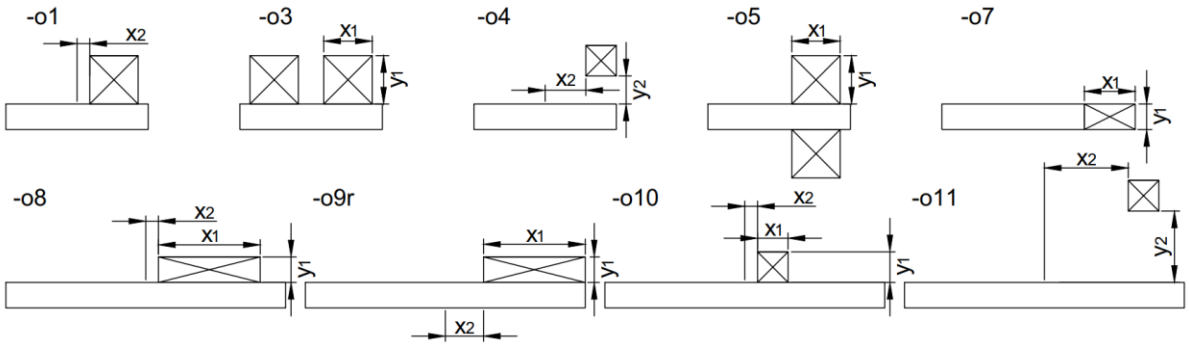


Figure 8-9: Overview of Analyzed Slab Opening Layouts in Rectangular Column Study (See Table 8-2 for Parameter Values)

8.2.3 L Slab-Column Connection (L-SCC) Study

The four different column sizes analyzed in the L-SCC study are shown in Figure 8-10. The analyzed L-SCCs are symmetric about the line $y=x$ (considering the column geometry only). A total of 25 isolated interior connections, 21 of which have slab openings at various locations near the connection, were analyzed. Details of the analyzed opening layouts are provided in Figure 8-11 and Table 8-1. The reduced critical perimeters according to ACI 318-19 for the analyzed L-SCCs are provided in Appendix I.

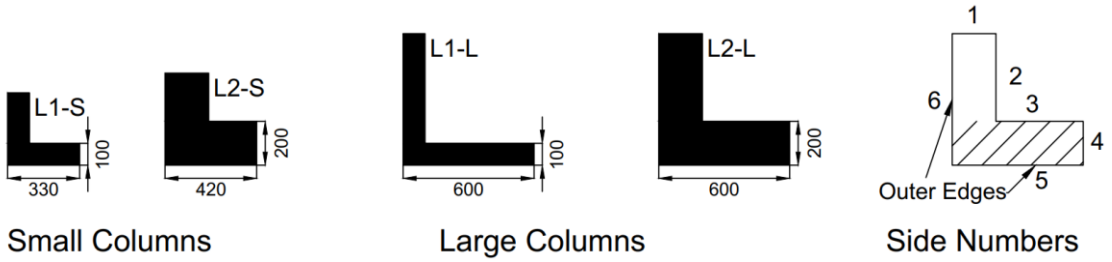


Figure 8-10: Column Sizes, and Definition of Side Numbering and Critical Features of L-SCCs in This Work (Column Flange Definition Provided in Figure 8-5)

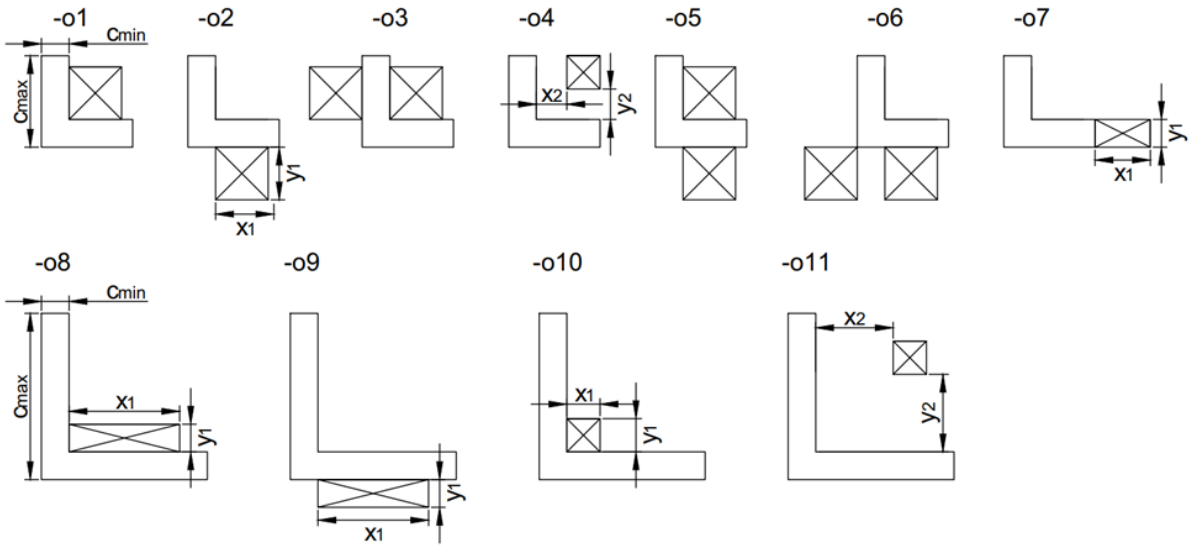


Figure 8-11: Overview of Analyzed Slab Opening Layouts in L Column Study (See Table 8-1 for Parameter Values)

8.2.4 T Slab-Column Connection (T-SCC) Study

The four different column sizes analyzed in the T-SCC study are shown in Figure 8-12. A total of 25 isolated interior connections, 21 of which have slab openings at various locations near the connection, were analyzed. Details of the analyzed opening layouts are provided in Figure 8-13 and Table 8-1. The reduced critical perimeters according to ACI 318-19 for the analyzed T-SCCs are provided in Appendix I.

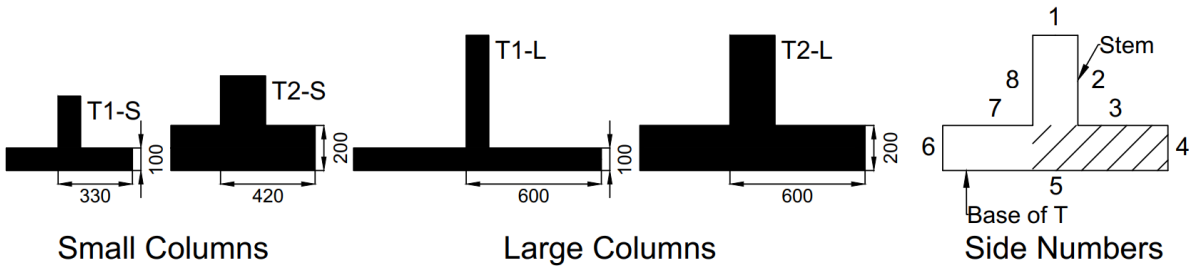


Figure 8-12: Column Sizes and Definition of Side Numbering and Critical Features of T-SCCs in This Work (Column Flange Definition Provided in Figure 8-5)

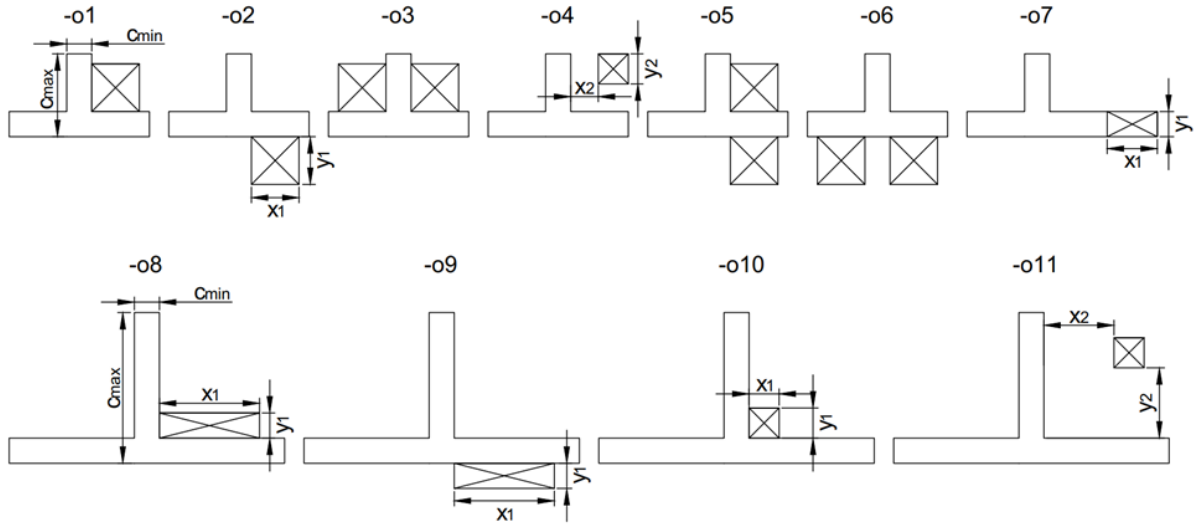


Figure 8-13: Overview of Analyzed Slab Opening Layouts in T Column Study (See Table 8-1 for Parameter Values)

8.2.5 Cruciform Slab-Column Connection (X-SCC) Study

The four different column sizes analyzed in the X-SCC study are shown in Figure 8-14. A total of 21 isolated interior connections, 17 of which have slab openings at various locations near the connection, were analyzed. Details of the analyzed opening layouts are provided in Figure 8-15 and Table 8-1. The reduced critical perimeters according to ACI 318-19 for the analyzed X-SCCs are provided in Appendix I.

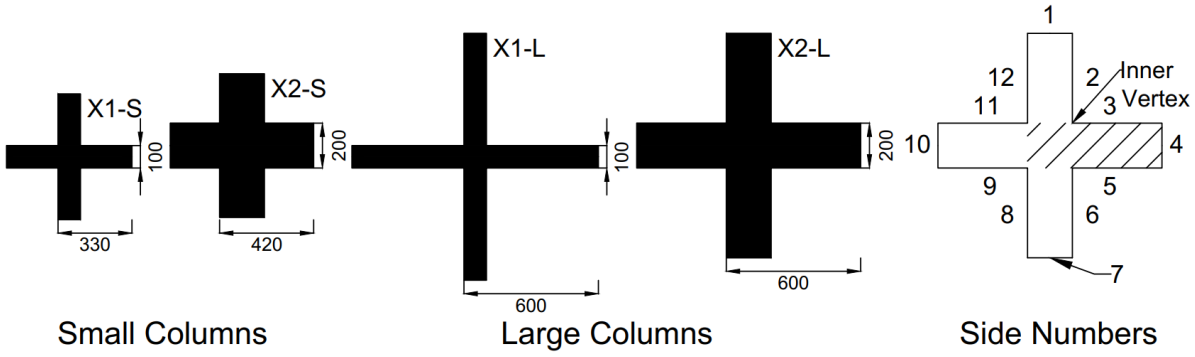


Figure 8-14: Column Sizes and Definition of Side Numbering and Critical Features of X-SCCs in This Work (Column Flange Definition Provided in Figure 8-5)

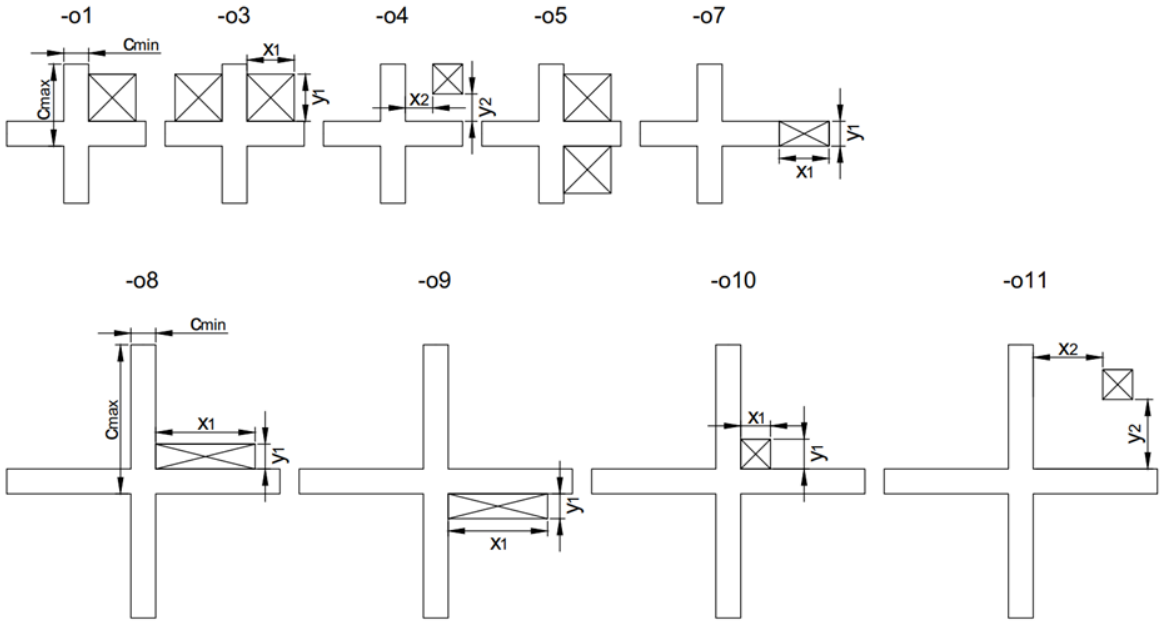


Figure 8-15: Overview of Analyzed Slab Opening Layouts in Cruciform Column Study (See Table 8-1 for Parameter Values)

8.2.6 Investigated Modifications to ACI 318-19

For the analyzed SS-SCCs the critical perimeters for specimens with and without openings will have an irregular shape (critical perimeters according to ACI 318-19 for all analyzed specimens are provided in Appendix I). Additionally, other than the R-SCCs and X-SCCs without openings, the centroids of the critical perimeter and column will be unaligned necessitating the use of ACI 421.1R-20 [5] to estimate the punching shear capacity of the connections (to account for the unbalanced moment). However, application of the ACI 421.1R provisions is complicated and time-consuming (though typically conservative for all column geometries as shown herein), and therefore the provisions are not suitable for preliminary design, particularly for connections with slab openings. Therefore, there is a need for the development of simplified provisions which can be used in the preliminary design of SS-SCCs. Ideally, small modifications to the concentric punching shear provisions (assumption of uniform stress along the critical perimeter) could be made to approximate the influence of the unbalanced moment. These modified concentric provisions could then be used to facilitate preliminary design before detailed calculations using the ACI 421.1R-20 method are completed. Therefore, two modifications to the ACI 318-19 concentric provisions, shown in Figure 8-16, are investigated. Sample calculations using these modifications, and the unmodified ACI 318-19 and ACI 421.1R-20 provisions, are provided in Appendix H.

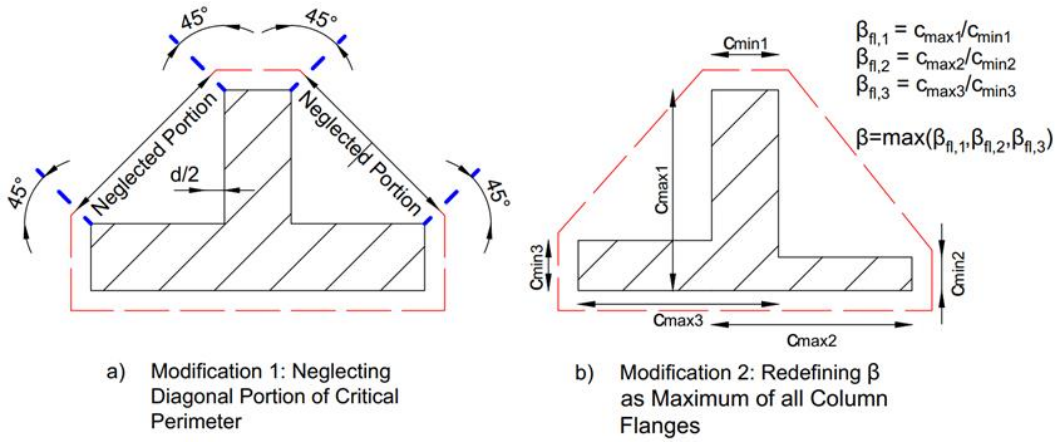


Figure 8-16: Simplified Modifications to ACI 318-19 Concentric Punching Shear Provisions for Estimating the Punching Shear Capacity of SS-SCCs

Modification 1 involves neglecting the diagonal portion of the critical perimeter, as shown in Figure 8-16a, when calculating b_o and v_c. If the diagonal portion of the critical perimeter is ineffective, modification 1 should result in more accurate punching capacity estimates. Modification

2 involves using the existing critical perimeter definition but redefining β for SS-SCCs as the maximum aspect ratio of the individual column flanges which make up the connection, as shown in Figure 8-16b, instead of a_n/b_n. Modification 2 would remove the previously discussed inconsistency in the definition of β for rectangular and SS-SCCs. No other changes are made to ACI 318-19 for both modifications.

For the R-SCCs, the use of straight projections to estimate the negative influence of slab openings on punching capacity is again investigated. No other modifications are studied for R-SCCs.

8.3 FEM Calibration

As previously discussed, when the special-shaped slab-column connection study was initiated the experimental tests of L-SCCs by Pinto et al. [174] were not yet published. As such, the FEM used in this study was calibrated considering experimental tests of R-SCCs by Hawkins et al. [3], This experimental program, which is briefly summarized in Section 8.3.1, forms the basis of the ACI 318-19 equation relating the nominal shear stress capacity, v_c, to the column aspect ratio, β.

It should be noted that the FEM calibration was conducted by Qing (Paris) Zhang, during an undergraduate research assistantship under the supervision of the author and Dr. Polak. The original FEMs of the Hawkins et al. specimens [3], developed during the author's MASc work [1], served as the starting point for the calibration conducted by Qing Zhang. The final calibrated input parameters proposed by Qing Zhang were verified by the author. As such, only the finalized calibrated FEM, which is presented in Section 8.3.2, is summarized herein. Discussions related to the determination of material parameters, such as dilation angle and fracture energy, are not provided as these studies were conducted by Qing Zhang.

8.3.1 Summary of Experimental Specimens Considered in Calibration

In their study of the influence of column rectangularity on punching shear capacity, Hawkins et al. [3] tested the nine isolated slab-column connections summarized in Table 8-3. The nine isolated slab-column connections represented interior connections in a flat slab structure where the columns are spaced at 4.5m (15') on center. As shown in Figure 8-17, the nine isolated slabs were 2.1m (7') square in plan, 152mm (6") thick, and supported on a 104cm (41") tall central column stub (note, the Hawkins et al. [3] specimens were constructed based on the imperial system of units so all metric units provided herein are converted from the original imperial values). The aspect ratio of the analyzed columns varied from a minimum of 1 to a maximum of 4.33 [3].

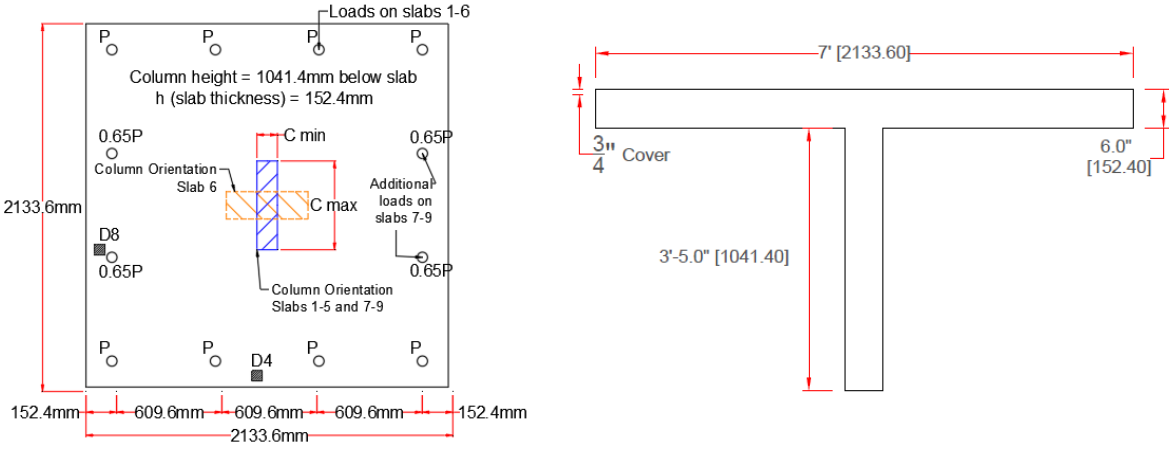
In addition to varying the column aspect ratio, Hawkins et al. [3] also investigated the influence of the slab loading conditions. For slabs 1 through 6, only two edges of the slab were loaded, as shown in Figure 8-17. Therefore, slabs 1 through 6 were loaded in one-way action. For slabs 1 through 5, the two loaded slab edges were parallel to the short side of the column, and for slab 6, the column was rotated 90 degrees such that the loaded slab edges are parallel to the long side of the column. Slabs 7 through 9 were loaded in two-way action. However, equal loading was not applied to all slab sides. For slabs 7 through 9, the loads on the two slab edges parallel to the long side of the column had load magnitudes equal to 65% of the loads applied on the slab edges parallel to the short side of the column [3].

Table 8-3: Summary of Experimental Specimens Tested by Hawkins et al. [3]

Slab	c_{min} (mm)	c_{max} (mm)	β	f_c' (MPa)[(a)]	ρ_{avg}	d_{avg} (mm)
1	304.8	304.8	1.0	30.3/29.6	1.12	117.3
2	203.2	406.4	2	26.3/28.1	1.12	117.3
3	152.4	457.2	3	32.0/29.9	1.12	117.3
4	114.3	495.3	4.33	31.0/29.3	1.12	117.3
5	152.4	457.2	3	26.9/27.4	[(b)]	117.3
6	152.4[(c)]	457.2[(c)]	3	22.7/24.8	1.12	117.3
7	152.4	457.2	3	25.9/26.1	0.87	117.3
8	114.3	495.3	4.33	26.1/24.7	0.81	120.65
9	152.4	304.8	2	29.5/27.1	0.77	120.65

[(a)] XX/YY where XX and YY correspond to the strength of the concrete used to cast the portion of the slab around the slab column connection and the average strength of the four batches used to cast the specimen respectively; [(b)] 4 additional #5 bars added to top reinforcing layer in central 45.7cm (18") of slab; [(c)] Column rotated 90 degrees compared to other slabs (see Figure 8-17)

The flexural reinforcement in the slabs consisted of #4 (diameter of approximately 12.7mm) or #5 (diameter of approximately 15.9mm) bars manufactured according to ASTM A432. The reported yield strengths of the #4 and #5 bars were approximately 412MPa (59.7ksi) and 414MPa (60ksi), respectively. In all slabs, the flexural reinforcement was spaced at 152mm (6") on center and placed such that it was symmetric about the slab centerline with the outer reinforcement layer parallel to the long side of the column [3].



Plan View

Elevation View (Parallel to Short Side of Column, Dimension Inside [ ] are in mm)

Figure 8-17: Summary of Experimental Specimens Tested by Hawkins et al. [3]

All nine specimens tested by Hawkins et al. [3] failed in punching shear (though the experimental shear capacity of slabs 1 and 6 slightly exceeds the theoretical flexural capacity of the slabs). The punching capacity of the connections was found to decrease with increasing column aspect ratio [3]. A decrease in punching capacity with increasing column rectangularity is logical in this case since the column perimeter was fixed at a constant length of 122cm (48") for all slabs other than slab 9, where the column perimeter was equal to 91cm (36"). Therefore, with increasing column rectangularity the overall column cross-sectional area was decreased.

Hawkins et al. [3] also observed that as the column aspect ratio increased, that the failure became more abrupt, and the size of the punching cone decreased. They also observed that the punching capacity of the slabs loaded in two-way action was only slightly lower than those loaded in one-way action [3].

8.3.2 Summary of Calibrated FEM

As was done in the slab-wall connection study, the calibrated FEM used in the concentrically loaded special-shaped connection study was implemented in Abaqus/Explicit. However, unlike the FEM presented in Section 6.3, where the slab, support plates, and load plates were modelled separately, the supporting columns were directly extruded from the slab in the FEMs of the Hawkins et al. [3] specimens and the analyzed R-SCCs and SS-SCCs presented in Section 8.2. This was done to match the experimental conditions, where the column and slab were cast together. Since details of the experimental setup were not provided, the boundary conditions were applied directly to the slab

geometry, as shown in Figure 8-18 (a pin support was assumed at the base of the column stub). Furthermore, since the size of the load plates was not specified, the loading was applied over 120mm square regions, as shown in Figure 8-18, though the assumed loading area size had a minimal influence of the FEA results, assuming the region was large enough to avoid concrete crushing. In the FEM calibration, quarter models were used to take advantage of symmetry, though it should be noted that full specimen geometry was modelled when analyzing the R-SCCs and SS-SCCs in the parametric study due to the presence of nonsymmetric slab opening layouts.

Again, consistent with the calibrated FEM used in Chapter 6, the concrete and steel reinforcement were meshed with C3D8R and T3D2 elements, respectively. A mesh sensitivity study conducted by Qing Zhang confirmed that a mesh size of 20mm was also adequate for the Hawkins et al. [3] specimens. Perfect bond between the concrete and rebar was again assumed, and implemented using the embedded region constraint in Abaqus. The influence of bond was approximated through the inclusion of tension stiffening in the tensile constitutive relationship for the concrete.

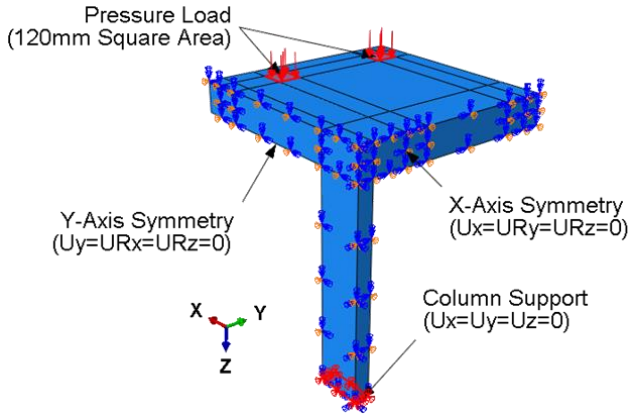


Figure 8-18: General Boundary Conditions Used in FEM Calibration (¼ Models Used in Calibration, Slab 3 Shown)

A summary of the calibrated FEM used in the concentrically loaded special-shaped connection study is provided in Table 8-5. The majority of the parameters used in the calibrated model are identical to those used in Chapter 6 and Chapter 9, though the dilation angle and fracture energy have been modified in order to improve the agreement between the FEA predictions and experimental results. Based on the calibration conducted by Qing Zhang, the dilation angle was reduced from 45° to 42° and the concrete fracture energy was set to 0.08N/mm. The inputted value for the fracture energy is approximately equal to the average fracture energy for the 9 slabs tested by Hawkins et al.

[3] according to Model Code 1990 [159], based on strength of the concrete used to cast the region near the slab column connection (first concrete strength listed in Table 8-3). The choice to use one fracture energy for all 9 slabs tested by Hawkins et al. [3] was made to limit the variability between models. It should also be noted that unlike the FEMs in Chapter 6 and Chapter 9, where the Poisson's ratio of the concrete is inputted as 0 to represent cracked concrete, in the FEMs herein, a concrete Poisson's ratio of 0.2 is specified, based on the calibration conducted by Qing Zhang. The influence of the higher Poisson's ratio on the FEA results in the uncracked and cracked conditions was very minor.

Once again, the steel flexural reinforcement was modelled as linearly elastic-perfectly plastic. For simplicity, all flexural reinforcement was modelled assuming a yield strength of 414MPa. Note, the yield strength of the four #5 rebars near the slab centerline in slab 5 was listed as 412MPa by Hawkins et al. [3], but this slight discrepancy is expected to have no influence on the FEA predictions.

Table 8-4: Summary of Calibrated Model Used in Special Shaped Column Study [259]

Calibrated Model – Concrete Specific Parameters		
Material Model – Concrete Damaged Plasticity Dilation Angle – 42° Eccentricity* – 0.1 σ_{bo}/σ_{co}* – 1.16 K_c* – 0.667	Uniaxial Compression Model – Hognestad Parabola $E_c = 5000\sqrt{f_c'}$ (MPa) Poisson's Ratio (ν) – 0.2 Tension Model – Bilinear tensile stress-crack width/displacement [327] G_f =0.08 N/mm **	Element Size – 20 mm Element Type – C3D8R Damage Parameters – N.A. *Abaqus Default Value **G_f approximately equal to average of 9 Hawkins et al. [3] specimens according to [159]

A comparison of the shear capacities measured experimentally (V_{exp}) and predicted by the calibrated FEA ($V_{FEA}^{(a)}$) are provided in Table 8-5. On average, the capacities predicted by the calibrated FEM are 6.7% lower than that measured experimentally, with maximum under and overpredictions of 15.1% and 2.0%, respectively.

The load-displacement responses predicted by the calibrated FEA for slabs 1 and 3, which were loaded in one-way action, at the D4 and D8 locations (see Figure 8-17), are compared to the experimentally measured responses in Figure 8-19 (it should be noted that the experimental responses provided by Hawkins et al. [3] do not extend to the listed experimental capacities). As observed for the calibrated FEM used in the slab-wall study, the response predicted by the FEA is initially stiffer than that measured experimentally, likely due to the initial stiffness of the Hognestad Parabola used to

model the compressive stress-strain response of the concrete, and the omission of temperature and shrinkage cracking in the FEM. However, as the load is increased, and the amount of cracking increases, the stiffness predicted by the FEA approaches that measured experimentally.

Table 8-5: Summary of Experimental Program by Hawkins et al. (1971) and FEA Predictions

Slab	Column Dimensions, c_{min} x c_{max} (mm) Original	Modified	f'c[(c)] (MPa)	d (mm)[(e)]	V_{exp} (kN)	V_{FEA} (kN) [(a)]	[(b)]
1	304.8x304.8	320x320	30.3[(d)]	117.3	383.9[(f)]	326.0	336.8
2	203.2x406.2	200x400	26.3	117.3	351.4	331.3	332.2
3	152.4x457.2	160x480	32.0	117.3	333.2	339.9	351.8
4	114.3x495.3	120x480	31.0	117.3	330.5	331.8	337.2
5	152.4x457.2	160x480	26.9	117.3	355.0	325.8	332.6
6	152.4x457.2	160x450	22.7	117.3	335.8[(f)]	300.9	308.2
7	152.4x457.2	160x480	25.9	117.3	319.8	297.7	307.3
8	114.3x495.3	120x480	26.1	120.65	314.5	292.5	298.4
9	152.4x304.8	160x320	29.5	120.65	315.4	285.0	287.7

[(a)] FEA predicted capacity considering specific slab parameters
[(b)] FEA predicted capacity considering modified loading and dimensions
[(c)] concrete strength of region used to cast region near connection, see first value in Table 8-3
[(d)] assumed concrete strength for the special-shaped column specimens
[(e)] slab thickness, *h*, of 152.4mm and column height of 1041.4mm in original calibration, *h* and column height modified to 152mm and 1068mm respectively and *d*=117mm for V_{FEA}[(b)] and special-shaped column study
[(f)] Experimental specimens failed in punching after exceeding flexural capacity predicted using yield line analysis according to Hawkins et al. [3]

The predicted load-displacement responses at the D4 and D8 locations (see Figure 8-17) for the remaining slabs loaded in one-way action (slabs 2, 4, 5 and 6) and all slabs loaded in two-way action (slabs 7 through 9) are compared in Figure 8-20. For the slabs loaded in one-way action, the FEA predicts a higher stiffness in unloaded direction (D8 response), which matches the experimental measurements. For the slabs loaded in two-way action, the FEA predicts an approximately equal stiffness in both directions. The experimental measurements for slab 7 (the experimental measurements for slabs 8 and 9 were not provided by Hawkins et al. [3]) also displayed an approximately equal stiffness in both directions, though the stiffness in the D4 direction was slightly larger.

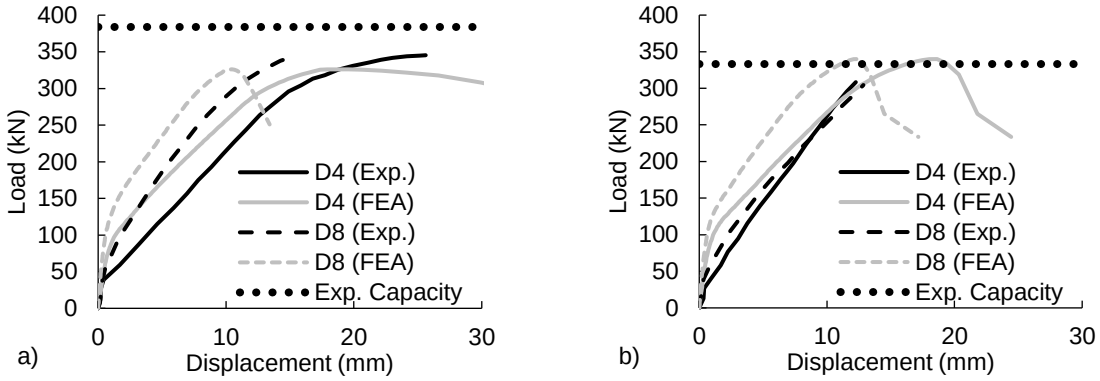
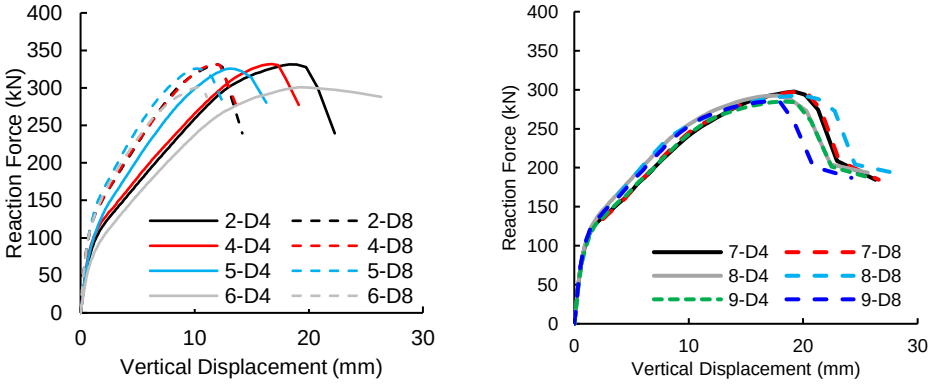


Figure 8-19: Comparison of Load-Displacement Response at D4 and D8 Locations (see Figure 8-17) Measured Experimentally and Predicted by FEA, a) Slab 1 – β = 1, b) Slab 3 – β = 3 (Experimental Data Approximated From Plots Provided by Hawkins et al. [3]) [259]



a) Slabs 1-6 (One-way Shear) b) Slabs 7-9 (Two-way Shear)

Figure 8-20: Representative Load-Displacement Curves at D4 and D8 Locations for Slabs 1-9

Based on the comparison of the predicted load-displacement responses and shear capacities, it was concluded that the calibrated FEM was accurately predicting the behaviour of the slabs tested by Hawkins et al. [3]. As such, the calibrated FEM was used to conduct the study of the concentric punching shear behaviour of R-SCCs and SS-SCCs outlined in Section 8.2. However, before conducting this study, the specimen geometry was modified slightly, as outlined in Figure 8-21 and Table 8-5, to improve mesh uniformity as results based on the CDP model are mesh size dependent. However, to minimize changes in overall behaviour, which could have a negative impact on the FEM calibration, some dimensions, such as slab thickness and effective depth, were only slightly modified. A comparison of the predicted shear capacities for the original ($V_{FEA}^{(a)}$) and modified ($V_{FEA}^{(b)}$)

specimen geometry is provided in Table 8-5. As seen in Table 8-5, the impact of the modifications slab dimensions and loading locations was minor for the 9 slabs tested by Hawkins et al. [3].

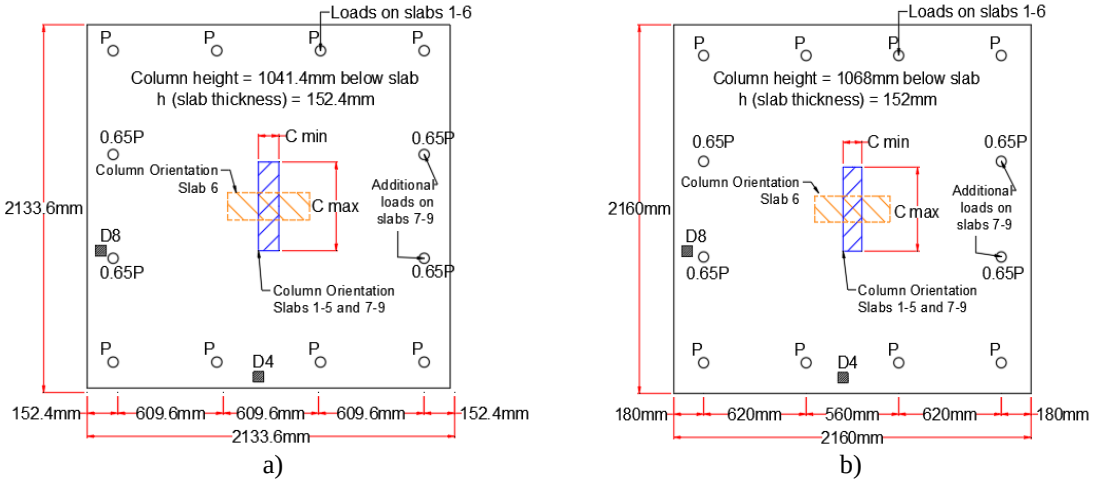


Figure 8-21: a) Summary of Experimental Slab Dimensions and Loading Locations [3] b) Modified Slab Dimensions and Load Locations Used in Special-Shaped Column Study (Concentric Loading) [259]

8.4 Study Results

8.4.1 Rectangular Slab-Column Connections (R-SCCs)

The FEA predicted the eleven small column specimens (R1-S and R2-S) to fail in punching shear, whereas most of the ten large column specimens (R1-L and R2-L) were predicted to fail in one-way shear or a combination of one-way shear and punching shear (failure modes are provided in Table 8-6). Interestingly, R1-L-o9r and R2-L-o9r are predicted to initially punch around the end of the column closest to the opening before experiencing a one-way shear failure parallel to the long side of the column. This supports the conclusion by Teng et al. [147] that punching can occur around one end for increasingly elongated supports.

Table 8-6: Comparison of Capacities and Opening Influences Predicted by FEA and ACI 318-19 – R-SCCs

ID	kN V_{FEA}	β	mm b_o [e]	V_{ACI} (kN) (A)	V_{ACI} (kN) (B)	V_{421} (kN)	V_{ACI}/V_{FEA} (A)	V_{ACI}/V_{FEA} (B)	$\frac{V_{421}}{V_{FEA}}$	Opening Impact (%) FEA	ACI(A)	ACI(B)	421
R1-S-0[a]	323.1		1788	265.7	265.7	265.7[f]	0.82	0.82	0.82	-	-	-	-
R1-S-o1[a]	286.4		1434	213.1	237.4	160.7	0.74	0.83	0.56	-11.3	-19.8	-10.6	-39.5
R1-S-o3[a]	252.9	5.6	1080	160.5	209.2	86.8	0.63	0.83	0.34	-21.7	-39.6	-21.3	-67.3
R1-S-o4[a]	321.8		1660	246.7	247.8	232.6	0.77	0.77	0.72	-0.4	-7.2	-6.7	-12.4
R1-S-o5[a]	255.6		1080	160.5	209.2	93.1	0.63	0.82	0.36	-20.9	-39.6	-21.3	-65.0
						Avg.	0.72	0.81	0.56				
R2-S-0[a]	389.2		2148	382.2	382.2	382.2[f]	0.98	0.98	0.98	-	-	-	-
R2-S-o1[a]	354.6		1803	320.7	350.1	257.8	0.90	0.99	0.73	-8.9	-16.1	-8.4	-32.5
R2-S-o3[a]	318.0	3.2	1458	259.3	318.1	182.0	0.82	1.00	0.57	-18.3	-32.1	-16.8	-52.4
R2-S-o4[a]	366.6		2006	356.3	360.8	335.8	0.97	0.98	0.92	-5.8	-6.6	-5.6	-12.1
R2-S-o5[a]	320.9		1458	259.3	318.1	188.3	0.81	0.99	0.59	-17.6	-32.1	-16.8	-50.7
R2-S-o7[a]	352.2		1911	340.1	346.6	294.5	0.97	0.98	0.84	-9.5	-11.0	-9.3	-22.9
						Avg.	0.91	0.99	0.77				
R1-L-0[b]	398.1		2868	371.1	371.1	371.1[f]	0.93	0.93	0.93	-	-	-	-
R1-L-o8[c]	370.5		2255	291.8	319.3	209.0	0.79	0.86	0.56	-6.9	-21.4	-13.9	-43.7
R1-L-o9r[d]	329.6	11.0	2315	299.5	319.3	219.8	0.91	0.97	0.67	-17.2	-19.3	-13.9	-40.8
R1-L-o10[b]	371.1		2531	327.5	355.6	296.9	0.88	0.96	0.80	-6.8	-11.8	-4.2	-20.0
R1-L-o11[c]	401.2		2801	362.5	355.6	358.1	0.90	0.89	0.89	+0.8	-2.3	-4.2	-3.5
						Avg.	0.88	0.92	0.77				
R2-L-0[b]	429.4		2868	439.6	439.6	439.6[f]	1.02	1.02	1.02	-	-	-	-
R2-L-o8[c]	406.0		2363	362.2	390.6	280.8	0.89	0.96	0.69	-5.4	-17.6	-11.2	-36.1
R2-L-o9r[d]	375.7	5.0	2405	368.7	390.6	290.5	0.98	1.04	0.77	-12.5	-16.1	-11.2	-33.9
R2-L-o10[b]	429.7		2591	397.2	421.2	365.3	0.92	0.98	0.85	+0.1	-9.6	-4.2	-16.9
R2-L-o11[d]	434.4		2771	424.7	421.2	415.0	0.98	0.97	0.96	+0.7	-3.4	-4.2	-5.6
						Avg.	0.96	1.00	0.86				

(A) Radial approach; (B) Straight projection approach; [a] punching shear failure; [b] one-way shear failure (parallel to long side); [c] simultaneous one-way (parallel to long side) and punching shear failure; [d] punching around end near opening, then one-way shear failure parallel to long side; [e] b_0 applies to radial approach only (V_{ACI}(A) and V_{421}); [f] No unbalanced moment due to lack of opening; Note: Material safety factors (ϕ) set to 1 for V_{ACI} (concentric provisions) and V_{421} (421.1R-20);

The predicted load-displacement responses for the twenty-one R-SCCs are provided in Figure 8-22. Slab openings near the R-SCCs led to a reduced connection stiffness and capacity. The results for opening layouts -o9r demonstrate that the stiffness reduction is largest when the opening begins at the end of the column.

The FEA-predicted shear capacities and opening influences are provided in Table 8-6. As expected, openings near the column reduce the connection's punching capacity. R1-L-o11, R2-L-o10 and R2-L-o11, whose predicted capacities are 0.8%, 0.1% and 0.7% higher than the respective reference specimens without openings, are the only exceptions. These small capacity increases are likely due to

meshing differences between the models and demonstrate that these openings have a very minor impact on the connection's punching capacity. Similar small capacity increases are also observed for some of the SS-SCCs discussed in the following sections.

Based on the results presented in Table 8-6, most of the investigated opening layouts are found to have a minor influence on connection capacity for the large columns, likely because the overall connection behaviour is one-way shear dominated. Only when the opening is adjacent to the long side and starts at the column end, as in R1-L-o9r and R2-L-o9r, are significant capacity reductions predicted. Therefore, such openings should be avoided, particularly for very elongated connections which are one-way shear-dominated (i.e. c_{max} ≥≈35-40% of the slab span between column centerlines [151, 156] or when c_{max} ≥≈40% of L_{iso} [145]). Openings adjacent to the long side result in significant capacity reductions for the small columns. Looking specifically at R2-S, openings adjacent to the long side are predicted to have more of a negative influence on punching capacity than openings on the short side.

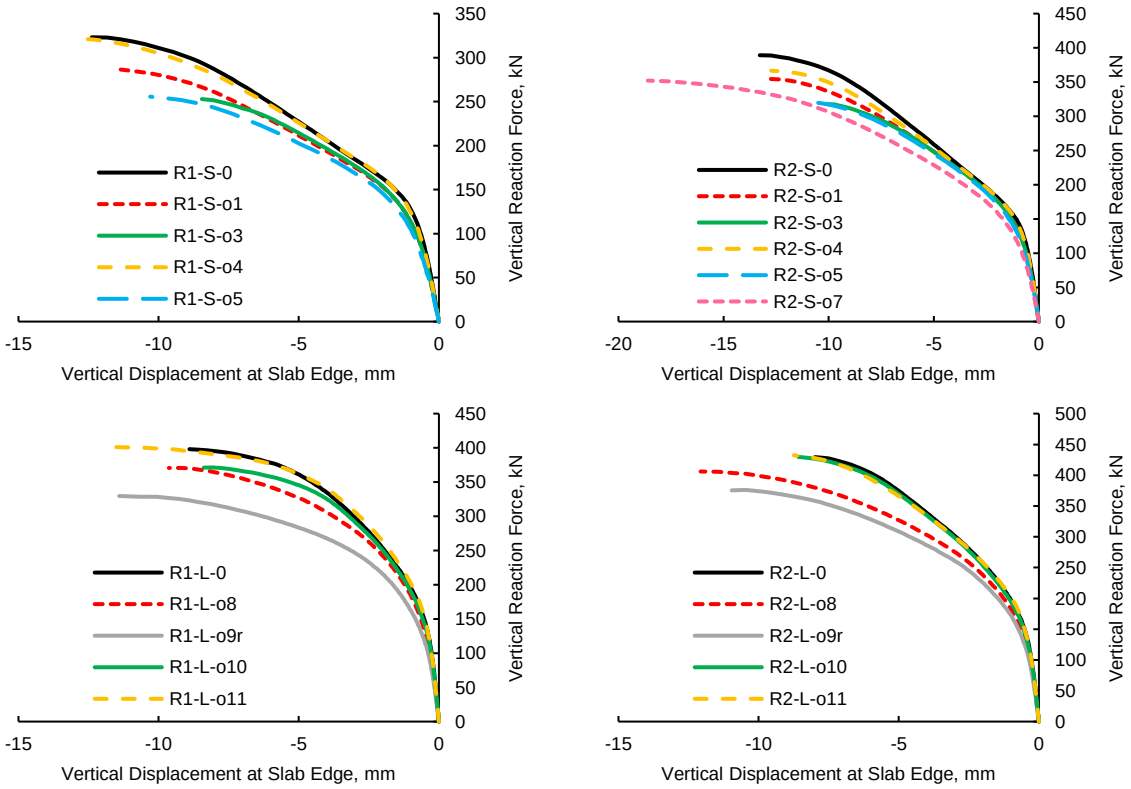


Figure 8-22: Predicted Load-Displacement Responses for R-SCCs, Displacement Output Location Shown in Figure 8-2, Negative Displacement is Downwards

Representative slab shear stress distributions along the column perimeter at the peak load are provided in Figure 8-23 (note, the methodology used to calculate the shear stress distributions from the FEA results is discussed in Appendix A) and these distributions support the finding that openings adjacent to the long side result in large punching capacity reductions. For connections without openings, or with openings located away from the long sides of the column, shear stress concentrations near the column corners and short sides are observed. Along the long sides, the shear stress magnitudes rapidly decrease towards the column centerline, which demonstrates that one-way shear is the dominant method of force transfer along the long sides. Openings adjacent to the long side of the column influence the shear stresses on both sides of the column. On the side with the opening, shear stresses tend to concentrate near the opening, and on the opposite side, the shear stress magnitudes are typically reduced compared to the specimen without an opening, particularly in the region bounded by straight projections from the opening.

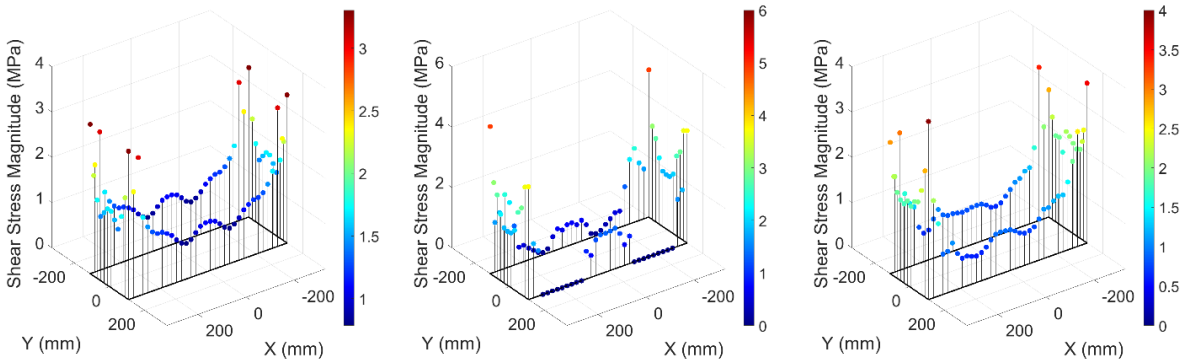
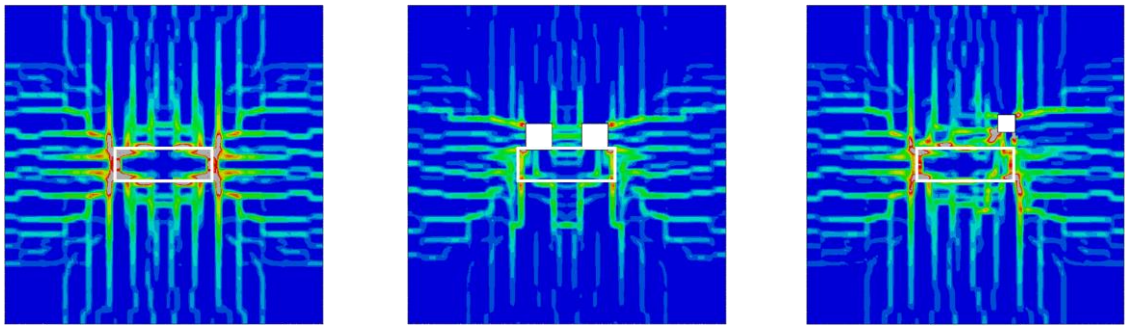


Figure 8-23: Representative Column Perimeter Shear Stress Distributions for R-SCCs –Peak Load (Stresses Averaged Over Depth)

Representative tension surface crack patterns for the analyzed R-SCCs are provided in Figure 8-24. Regardless of the failure mode, significant one-way shear cracking parallel to the long side of the connection is typically predicted, with the regions of diagonal cracking, which are associated with two-way shear, being constrained to regions near the column ends. As expected, nonsymmetric opening layouts lead to nonsymmetric crack patterns, and openings adjacent to the long side of the column interrupt the formation of one-way shear cracks in this region. For connections with openings, significant crack concentrations are predicted near the opening, with the additional cracking near the opening typically confined to a region which is approximately bounded by the additional rebar around the opening.



R2-S-0 R2-S-o3 R2-S-o4

Figure 8-24: Representative Crack Patterns Around R-SCCs with and Without Slab Openings (Grey Regions Have Principal Plastic Strains > 0.02, Approximate Column Location Shown in White)

The shear capacities and opening influences predicted by the ACI 318-19 concentric punching shear provisions using the radial approach are also provided in Table 8-6 ($V_{ACI}^{(A)}$). On average, the predicted shear capacities are conservative compared to the FEA for all specimens, though the failure mode for some of the large columns is incorrectly predicted, as ACI 318-19 predicts all specimens to be governed by punching shear. Additionally, the opening influences predicted by ACI 318-19 are conservative compared to the FEA for all specimens, though the influence of openings adjacent to the long side of the connection is typically significantly overpredicted for the small columns. Furthermore, due to the use of the radial approach, ACI 318-19 predicts openings which start at the column end and are adjacent to the long side of the column to have less of an impact than those which are adjacent to the long side but not placed at the start of the column. This contradicts the FEA, which predicted openings which start at the end of the column to have a much more significant impact (this can be clearly seen comparing the results of R1-L-o9r and R1-L-o8). Therefore, some improvements to the radial approach should be made to improve its accuracy for openings adjacent to the long side of elongated supports.

Punching capacities and opening influences predicted by the ACI 318-19 concentric punching shear provisions using the straight projection approach are also provided in Table 8-6 ($V_{ACI}^{(B)}$). The punching capacities based on the straight projection approach are typically slightly higher than those based on the radial approach, though the predictions are still conservative compared to the FEA on average for the four column sizes. For the small columns, the opening influences based on the straight projection approach generally agree well with the FEA, though they can be slightly unconservative. However, the straight projection approach does not accurately capture the influence of the opening's

location along the long side, particularly for very elongated columns. Therefore, the straight projection method is only suitable for specimens which are strongly dominated by punching shear behaviour.

Due to the nonsymmetric opening layouts, the centroids of the critical perimeter and the column are not aligned, and therefore, an unbalanced moment should be accounted for when calculating punching capacity according to ACI 318-19 [2]. For irregularly-shaped critical perimeters, ACI 318-19 Clause R8.4.4.2.3 refers designers to ACI 421.1R-20 [5] (a detailed discussion of the ACI 421.1R-20 method was previously provided in Section 3.3.2, and sample calculations are provided in Appendix H for L-SCCs and T-SCCs). Punching capacities and opening influences predicted by ACI 421.1R-20 using the radial approach are also provided in Table 8-6 (V_{421}) (calculations based on the straight projection approach were not completed as the straight projection approach was found to not be generally applicable as discussed previously). ACI 421.1R-20 also predicts all connections to be governed by punching shear and the predicted capacities and opening influences are much more conservative than those from the concentric provisions. Therefore, it appears that is it not necessary to account for the misalignment of the column and critical perimeter centroids due to nonsymmetric slab opening layouts for R-SCCs.

Note, consistent with the SWC study discussed in subsection 6.4.1.2, the flexural capacities of the analyzed R-SCCs (and all SS-SCCs analyzed in this chapter) according to ACI 318-19 were not calculated as the FEA predicts all connections to be governed by shear in the author's opinion. While some yielding of the slab's flexural reinforcement does occur, this yielding typically occurs in the reinforcement which intersects the column perimeter, and the load carrying capacity of the connections continues to increase after initial yielding, suggesting that flexural capacity is not governing. Therefore, only the ACI shear provisions were evaluated herein when estimating the connection capacity. Similar reasoning also applies to the analyses presented in Chapter 9.

8.4.2 L Slab-Column Connections (L-SCCs)

The FEA predicted all 25 L slab-column connections (L-SCCs) to fail in punching shear. In all simulations, some yielding of the slab's flexural reinforcement occurred but was typically limited to the reinforcement which intersected or was near the column perimeter. Similar yielding commonly occurs in experimental punching shear tests, and therefore, none of the analyzed SS-SCCs were assumed to be governed by flexure.

The predicted load-displacement responses for the 25 L-SCCs are provided in Figure 8-25. Again, slab openings near the slab-column connection reduced the overall connection capacity and stiffness. Furthermore, the location of the opening with respect to the column is again an important parameter. The influence of interior openings between the column flanges was predicted to be relatively minor, whereas openings located along the outer edges of the connection (sides 5 and 6, see Figure 8-10) result in significant reductions in connection capacity and stiffness.

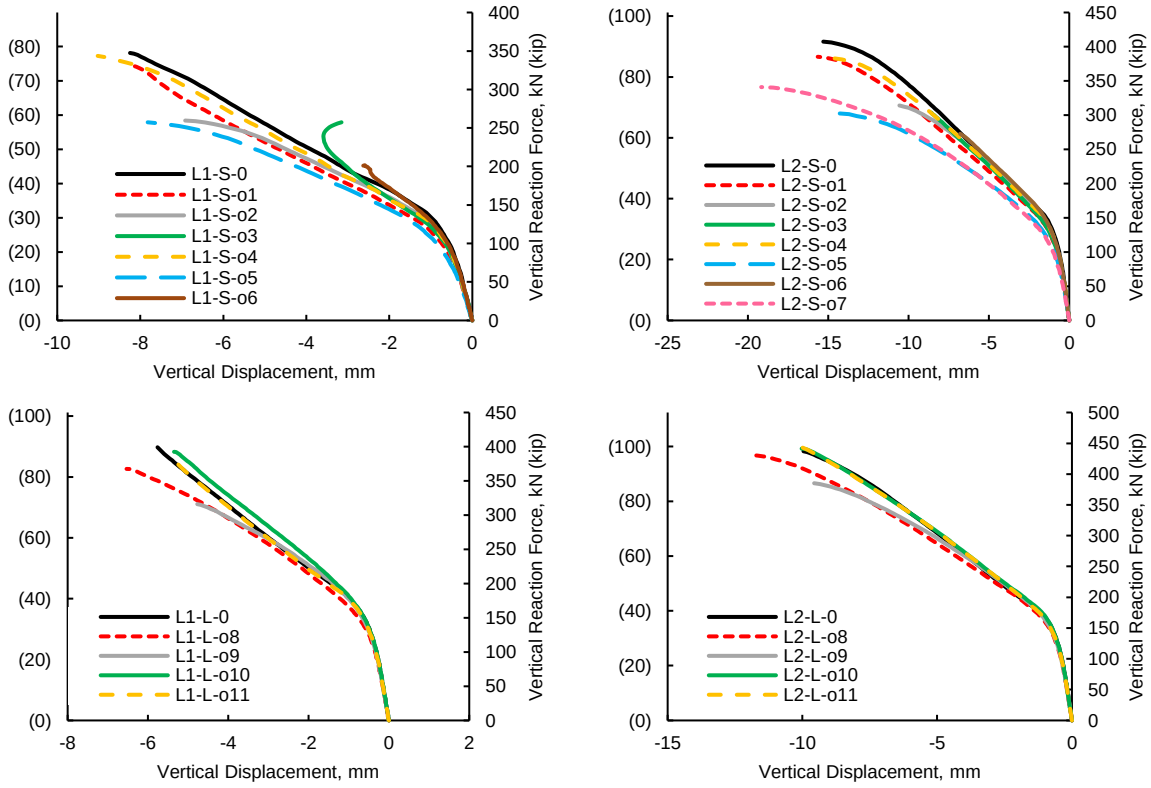


Figure 8-25: Predicted Load-Displacement Responses for L-SCCs, Displacement Output Location Shown in Figure 8-2, Negative Displacement is Downwards

The FEA predicted punching capacities and opening influences are provided in Table 8-7. As expected, openings near the column reduce the connection's punching capacity. From Table 8-7, it is observed that both the opening size and location have a significant impact on the punching capacity. For both the small (L1-S and L2-S) and large (L1-L and L2-L) columns, openings that are between the column flanges either along sides 2 and 3 of the column (-o1, -o4, -o8 and -o10, see Figure 8-10), or near the diagonal portion of the critical perimeter (-o11), result in much smaller punching capacity reductions (note, minor influences of openings in these regions were also observed and predicted by

Pinto et al. [174]) than similar-sized openings along the outer edges (sides 5 and 6) of the connection (-o2, -o6, and -o9). By moving the opening to the outer edges of the connection the opening's negative influence is at least tripled. Looking at the -o6 specimen results, it is clear that multiple openings along the outer connection edges should be avoided, as the most severe capacity reductions are predicted.

Table 8-7: Comparison of Capacities and Opening Influences Predicted by FEA and ACI 318-19 – L-SCCs

	kN		mm	V_{ACI} (kN)			V_{ACI}/V_{FEA}			Opening Impact (%)			
ID	V_{FEA}	β	b_o[(b)]	(A)	(B)	(C)	(A)	(B)	(C)	FEA	(A)	(B)	(C)
L1-S-0	347.4		1633	347.1	267.7	287.2	1.00	0.77	0.83	-	-	-	-
L1-S-o1[(a)]	332.2		1633	347.1	267.7	287.2	1.04	0.81	0.86	-4.4	-	-	-
L1-S-o2	259.7		1349	286.7	207.2	237.2	1.10	0.80	0.91	-25.3	-17.4	-22.6	-17.4
L1-S-o3[(a)]	257.4	1.535	1349	286.7	207.2	237.2	1.11	0.81	0.92	-25.9	-17.4	-22.6	-17.4
L1-S-o4	343.6		1479	314.3	267.7	260.0	0.91	0.78	0.76	-1.1	-9.5	-	-9.5
L1-S-o5[(a)]	257.4		1349	286.7	207.2	237.2	1.11	0.81	0.92	-25.9	-17.4	-22.6	-17.4
L1-S-o6	201.6		1131	240.4	161.0	198.9	1.19	0.80	0.99	-42.0	-30.7	-39.9	-30.7
						Avg.	1.07	0.79	0.88				
L2-S-0	407.5		1999	424.9	348.4	424.9	1.04	0.86	1.04	-	-	-	-
L2-S-o1	385.3		1617	343.7	343.7	343.7	0.89	0.89	0.89	-5.4	-19.1	-1.3	-19.1
L2-S-o2	314.1		1739	369.6	293.1	369.6	1.18	0.93	1.18	-22.9	-13.0	-15.9	-13.0
L2-S-o3	303.7	1.355	1357	288.4	288.4	288.4	0.95	0.95	0.95	-25.5	-32.1	-17.2	-32.1
L2-S-o4	382.9		1853	393.8	348.4	393.8	1.03	0.91	1.03	-6.0	-7.3	-	-7.3
L2-S-o5	302.5		1357	288.4	288.4	288.4	0.95	0.95	0.95	-25.8	-32.1	-17.2	-32.1
L2-S-o6	272.8		1503	319.4	243.0	319.4	1.17	0.89	1.17	-33.1	-24.8	-30.3	-24.8
L2-S-o7	341.0		1752	372.3	295.9	372.3	1.09	0.87	1.09	-16.3	-12.4	-15.1	-12.4
						Avg.	1.04	0.91	1.04				
L1-L-0	393.7		2555	523.3	382.4	373.0	1.33	0.97	0.95	-	-	-	-
L1-L-o8[(a)]	367.6		2555	523.3	382.4	373.0	1.42	1.04	1.01	-6.6	-	-	-
L1-L-o9	316.1	1.714	2030	431.3	270.4	296.3	1.36	0.86	0.94	-19.7	-17.6	-29.2	-20.6
L1-L-o10[(a)]	392.6		2555	523.3	382.4	373.0	1.33	0.97	0.95	-0.3	-	-	-
L1-L-o11	392.2		2423	509.2	382.4	353.7	1.30	0.98	0.90	-0.4	-2.7	-	-5.2
						Avg.	1.35	0.96	0.95				
L2x6-0	437.1		2614	529.6	425.0	476.9	1.21	0.97	1.09	-	-	-	-
L2-L-o8[(a)]	431.3		2614	529.6	425.0	476.9	1.23	0.99	1.11	-1.3	-	-	-
L2-L-o9	385.2	1.5	2209	469.4	338.9	403.0	1.22	0.88	1.05	-11.9	-11.4	-20.3	-15.5
L2-L-o10[(a)]	441.4		2614	529.6	425.0	476.9	1.20	0.96	1.08	+1.0	-	-	-
L2-L-o11	446.9		2479	515.2	425.0	452.4	1.15	0.95	1.01	+2.3	-2.7	-	-5.1
						Avg.	1.20	0.95	1.07				

[(A)] Considering entire critical perimeter length, [(B)] Diagonal portion of critical perimeter neglected, [(C)] Considering full critical perimeter and $\beta=c_{max}/c_{min}$ (see Figure 8-11 for definition of c_{max} and c_{min}), [(a)] Critical perimeter reduction unclear, [(b)] b_o applies to V_{ACI}[(A)] and V_{ACI}[(C)] only; Note: Material safety factors set to 1 when calculating V_{ACI}

Representative tension surface crack patterns for L-SCCs with and without openings are provided in Figure 8-26. Considering the specimens without openings, there is substantial cracking parallel to the outer edges of the connection (sides 5 and 6), regardless of the column size. These cracks, which originate from the column corner shared by sides 5 and 6, demonstrate that a significant amount of load is transferred along these column sides. Additional crack concentrations are also typically predicted around the short sides of each column flange. The crack concentrations near the short sides are typically less severe than those along sides 5 and 6, which demonstrates that while the short sides of the connection do transfer some of the load, they are less effective than the outer edges (Pinto et al. [174] also observed this). Furthermore, even though diagonal cracking in the region between the column flanges is predicted, the significant crack concentrations along the outer edges and short sides suggest that the majority of load transfer is not occurring in the region between the column flanges.

The trends in the predicted tension surface crack patterns for the specimens with slab openings are also consistent between column sizes. For all specimens with openings, crack concentrations around the openings are predicted, with these cracks typically propagating along the additional rebar placed around the opening. For specimens with openings located between the column flanges, such as L2-S-o1 and L2-L-o10, the predicted crack patterns near the opening differ from those predicted for the specimens without an opening. Away from the opening, the predicted cracks in the specimen with an opening are similar to those in the specimen without an opening. On the other hand, openings located on the outer edges of the column (column sides 5 and 6) significantly influence the crack patterns around the entire slab-column connection. When the opening is located along the outer edges of the column, severe crack concentrations near the opening are predicted, along with large crack concentrations along the outer edge of the column without an opening. Additionally, the FEA predicts fewer cracks to form in the region between the column flanges and perpendicular to the column sides. Finally, when an opening is located on the corner shared by sides 5 and 6 of the connection, as in specimen L2-S-o6, limited cracking is predicted in the slab quadrant supported by this corner of the L-shape only, which demonstrates that this region of the slab has become largely ineffective. Therefore, openings at the outer corner of the connection should be avoided wherever possible.

Representative shear stress distributions along the column perimeter at the peak load for L-SCCs, with and without openings, are provided in Figure 8-27. The distributions confirm that all sides of L-SCCs are not equally effective and that a significant amount of the total load is carried along the outer edges of the connection (Pinto et al. [174] also observed this), as the shear stress magnitudes are

typically the highest along column sides 5 and 6 (see Figure 8-10), with approximately 27.4-29.8% of the total load carried along each of these sides for the connections without openings. The short sides of each flange (sides 1 and 4) are the next most effective portions and carry between approximately 10.0-15.4% of the total load on each side. The interior sides of the connection (sides 2 and 3), which carry between approximately 7.2-10.2% of the load, are the least effective, and there is typically a region of very low stress near the inner vertex of the connection (intersection of sides 2 and 3). Therefore, when considering concentric punching capacity, slab openings near L-SCCs should be between the flanges. If the openings must be very close to the column, they should be placed as close as possible to the inner vertex to minimize the opening's negative influence on punching capacity.

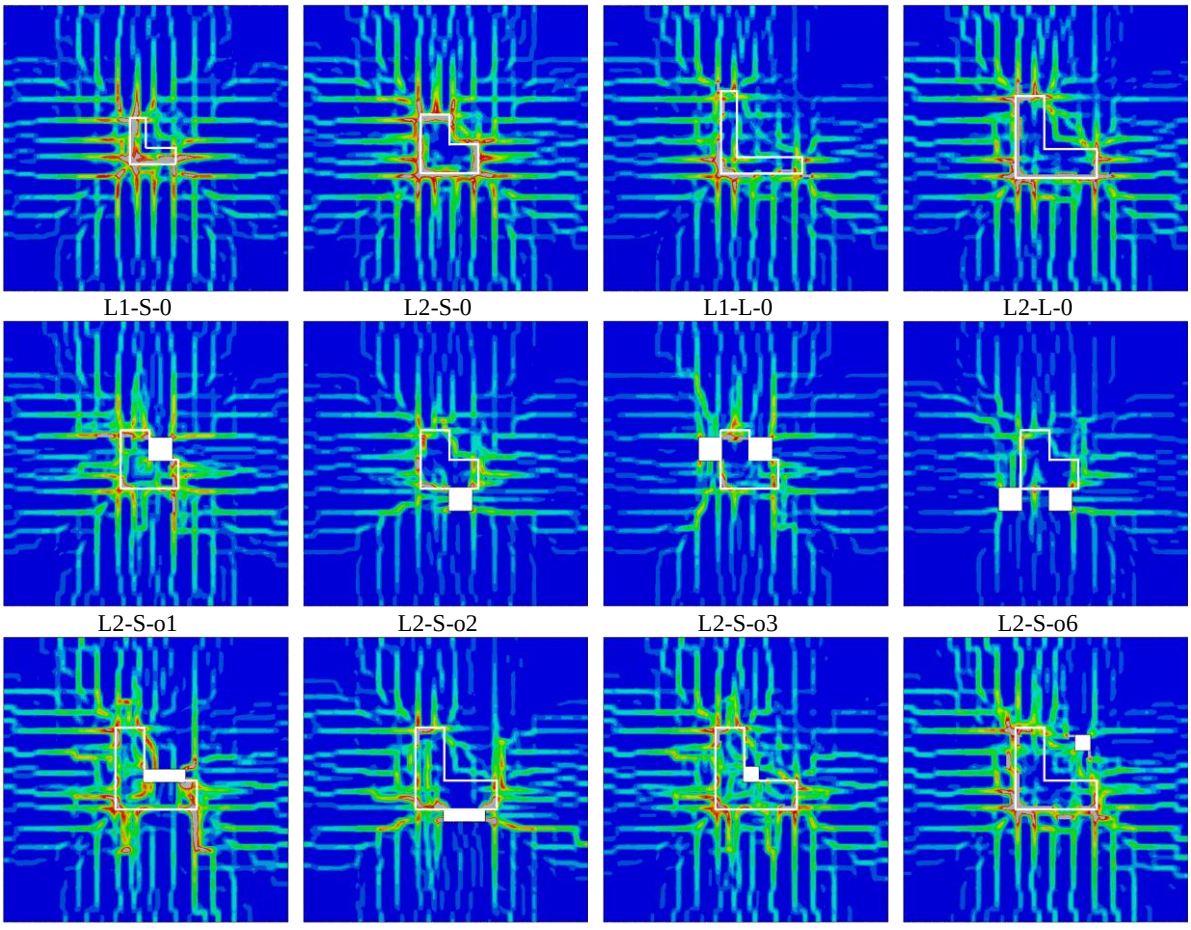


Figure 8-26: Representative Crack Patterns Around L-SCCs with and Without Slab Openings (Grey Regions Have Principal Plastic Strains > 0.02, Approximate Column Location Shown in White)

It is also important to note that as observed in slabs supported on rectangular and square columns [26, 42, 145, 146, 147, 150, 151, 158, 259], shear stress concentrations occur at the column corner as shown in Figure 8-27. With increasing distance from the column corners, the predicted shear stress magnitudes typically decrease, which demonstrates that the entire column perimeter is not equally effective in transferring load between the slab and column. Similar behaviour was also observed for T-SCCs and X-SCCs.

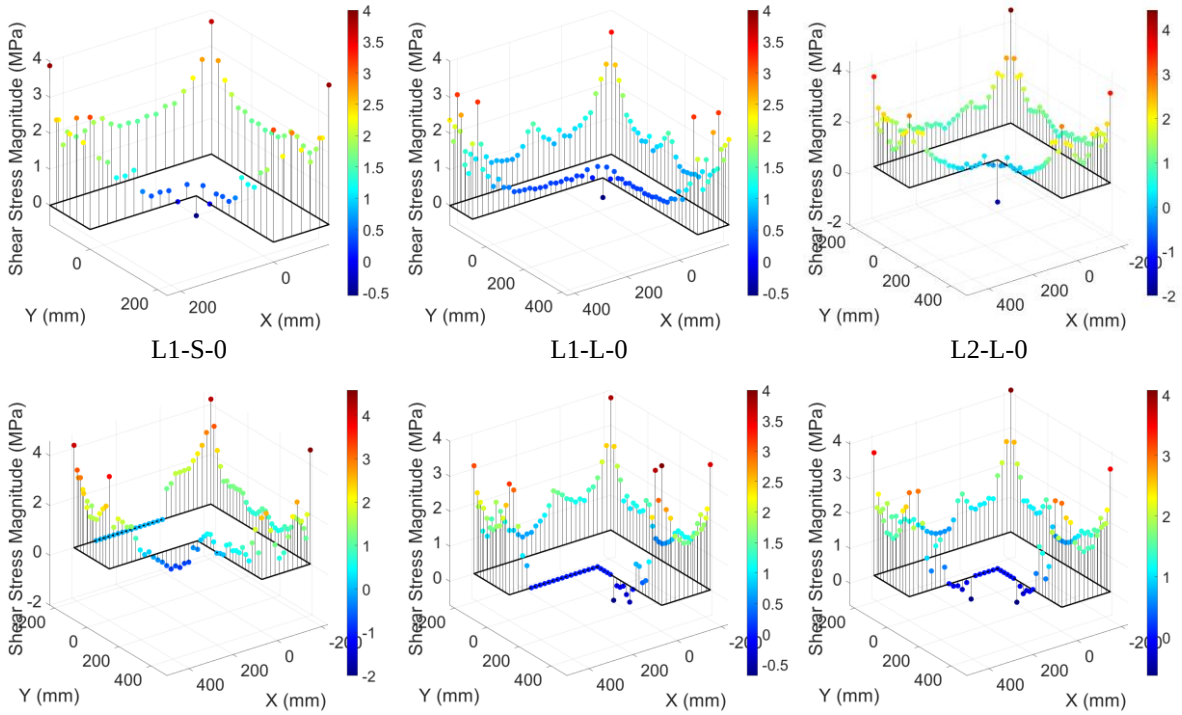


Figure 8-27: Representative Column Perimeter Shear Stress Distributions for L-SCCs –Peak Load (Stresses Averaged Over Depth)

As previously discussed, the majority of studies related to the influence of openings on punching shear capacity are for square slab-column connections. Therefore, design provisions for openings are largely derived considering square slab-column connections. As such, there is no guidance for cases when the column centroid falls within or very close to the slab opening. As shown in Figure 8-28, when the column centroid falls beyond the opening but very close to it, the existing provisions can require exceptionally large critical perimeter reductions. These large reductions in the critical perimeter length, and by extension the connection's punching capacity, contradict the FEA results for

special-shaped connections which demonstrate that these openings have a relatively minor influence on punching capacity. In the case where the column centroid falls within the opening, which is also demonstrated in Figure 8-28, the code provides no guidance into the required critical perimeter reduction. Based on the analysis of T and cruciform columns presented in the following sections, both of these cases seem to only occur for L columns where the opening is located near or at the interior corner shared by column sides 2 and 3 (see Figure 8-10). For both of these cases, no reduction was applied when computing the capacity of L-SCCs according to ACI 318-19 (unmodified and modified concentric provisions) presented in Table 8-7, or ACI 421.1R-20 (note, the ACI 421 predictions for all SS-SCCs are presented in Section 8.4.5 [see Table 8-10]).

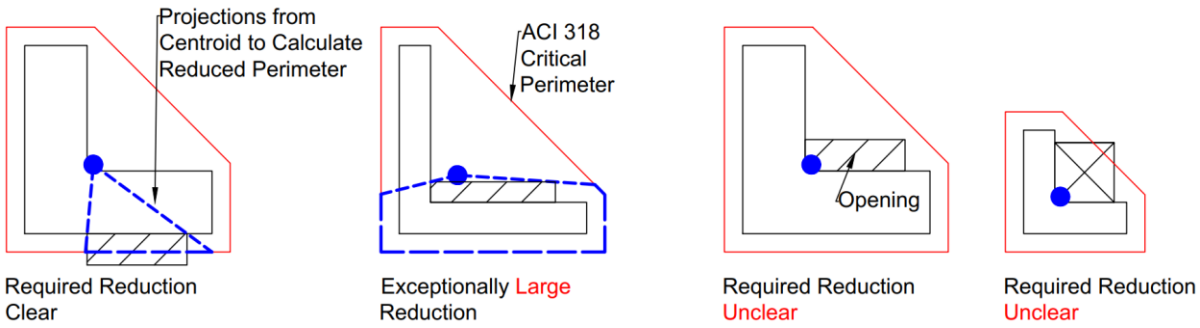


Figure 8-28: Examples of Issues with ACI 318-19 Opening Provisions When Column Centroid Falls Within or Near Slab Opening

The ACI 318-19 predictions are also provided in Table 8-7 ($V_{ACI}^{(A)}$). The concentric provisions are fairly accurate for the L1-S and L2-S specimens (small columns), with average overpredictions of 7% and 4%, respectively. However, for the L1-L and L2-L specimens (large columns), they are generally unconservative, with average overpredictions of 35% and 20%, respectively. Importantly, the opening influences predicted by ACI 318-19 do not agree well with those predicted by the FEA. In terms of exterior openings along sides 5 and 6, the concentric provisions generally underpredict the influence of the opening compared to the FEA. Furthermore, for interior openings, the required critical perimeters are either unclear (as discussed in the preceding paragraph), which partly influences the large average overpredictions for the L1-L and L2-L specimens, or in cases where the reductions are clear, result in very large capacity reductions, which contradicts the FEA.

The ACI predictions using modifications 1 and 2 are also provided in Table 8-7 ($V_{ACI}^{(B)}$ and $V_{ACI}^{(C)}$ respectively). Modification 1 results in punching capacities which are conservative on average for all column sizes, with only one minor overprediction for L1-L-o8 (4%), and generally reduces the

difference between the opening influence predicted by the FEA and ACI 318. Modification 2 generally improves ACI 318's accuracy in terms of punching capacity, though the predictions are unconservative on average for the L2-S and L2-L specimens. Redefining β did not remedy any issues in terms of the predicted opening influences for the analyzed L-SCCs. Therefore, modification 1 is recommended for the preliminary design of L-SCCs, though in cases where an unbalanced moment due to loading or eccentricity of the slab and column centroids exists, the initial column size determined via this method should be increased slightly as discussed in [348]. The use of modification 1 for L-SCCs is supported by the predicted column perimeter shear stress distributions which demonstrated that the interior sides of the connection (column sides 2 and 3) are relatively ineffective in transferring load. If these two column sides are relatively ineffective (which is supported by the findings of Pinto et al. [174]), then the diagonal portion of the critical perimeter is also ineffective, and therefore should not be accounted for when estimating punching capacity.

8.4.3 T Slab-Column Connections (T-SCCs)

The FEA predicted the 15 small column specimens (T1-S and T2-S) to fail in punching shear, whereas most of the 10 large column specimens (T1-L and T2-L) failed in a combination of punching shear and one-way shear parallel to the long dimension of the base of the T (column side 5, see Figure 8-14). It should be noted that T1-L-0 and T1-L-o10 were predicted to fail in one-way shear parallel to column side 5 and T2xL-o9 and T2-L-o10 were predicted to fail in punching shear.

The predicted load-displacement responses for the 25 T slab-column connections (T-SCCs) are provided in Figure 8-29. Consistent with the other column geometries, openings near the column reduce the connection capacity and stiffness.

The FEA results, summarized in Table 8-8, demonstrate that openings between the column flanges have less influence on punching capacity than openings along the long dimension of the base of the T (side 5). Typically, the influence of openings between the column flanges is minor, though for relatively small columns (T1-S) openings between the flanges can lead to significant capacity reductions (9.4% capacity reduction for T1-S-o1). Openings along the long dimension of the base of the T should be avoided whenever possible as a large portion of the total load is transferred along column side 5.

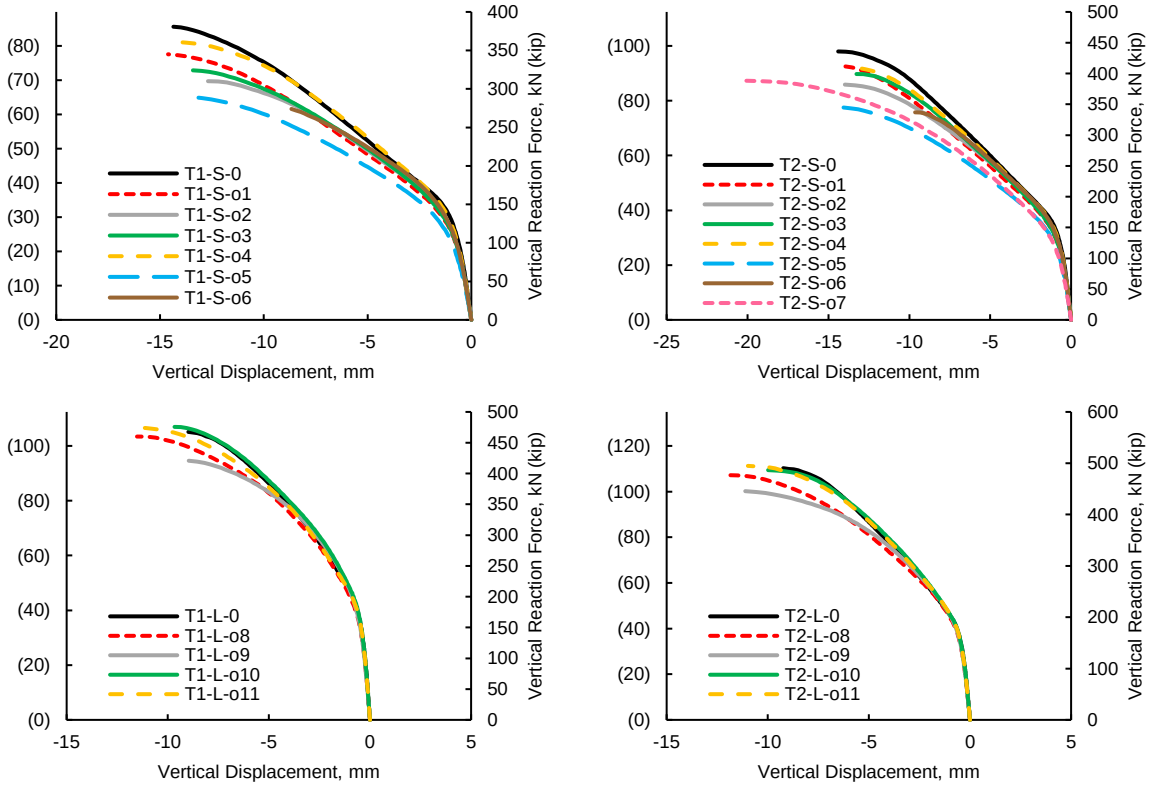


Figure 8-29: Predicted Load-Displacement Responses for T-SCCs, Displacement Output Location Shown in Figure 8-2, Negative Displacement is Downwards

Representative tension surface crack patterns for T-SCCs are provided in Figure 8-30. For the specimens without openings, severe cracking is predicted along the long side (side 5) and the short sides of the base (sides 4 and 6), which suggests that regardless of the failure mode that a significant amount of the load is transferred through the base of the T, primarily through one-way shear along side 5. Diagonal cracking between the short sides of the base and stem of the T is also predicted for the specimens without openings, suggesting that the region between the column flanges is at least partly effective in transferring load.

Openings significantly influence the crack patterns. Nonsymmetric opening layouts, even those which have a minor influence on connection capacity, lead to nonsymmetric cracking. Additionally, cracks concentrate near the opening regardless of its location. When the openings are between the column flanges the diagonal cracking joining the base and stem is interrupted and the cracks propagate towards the opening instead. Consistent with the punching capacities, openings along side 5 influence the crack patterns the most. Openings along side 5 interrupt the one-way shear cracks

parallel to side 5 and cause significant crack concentrations near the opening and less cracking around the corners of the base of the T (intersections of sides 4 and 5 and 5 and 6). Therefore, openings along side 5 interrupt the one-way shear transfer mechanism along the long dimension of the base, which is one of the largest contributors to the capacity of T-SCCs.

Table 8-8: Comparison of Capacities and Opening Influences Predicted by FEA and ACI 318-19 – T-SCCs

	kN		mm	V_{ACI} (kN)			V_{ACI}/V_{FEA}			Opening Impact (%)			
ID	V_{FEA}	β	b_o [(a)]	(A)	(B)	(C)	(A)	(B)	(C)	FEA	(A)	(B)	(C)
T1-S-0	380.8		1938	412.0	253.1	340.8	1.08	0.66	0.90	-	-	-	-
T1-S-o1	345.0		1543	327.9	248.1	271.3	0.95	0.72	0.79	-9.4	-20.4	-2.0	-20.4
T1-S-o2	310.0		1609	341.9	183.1	282.9	1.10	0.59	0.91	-18.6	-17.0	-27.7	-17.0
T1-S-o3	324.1	1.697	1147	243.8	243.1	201.7	0.75	0.75	0.62	-14.9	-40.8	-3.9	-40.8
T1-S-o4	361.2		1781	378.4	253.1	313.1	1.05	0.70	0.87	-5.1	-8.1	-	-8.1
T1-S-o5	289.5		1213	257.8	178.1	213.3	0.89	0.62	0.74	-24.0	-37.4	-29.6	-37.4
T1-S-o6	274.0		1279	271.9	113.0	224.9	0.99	0.41	0.82	-28.1	-34.0	-55.4	-34.0
						Avg.	0.97	0.64	0.81				
T2-S-0	435.8		2290	486.7	333.9	486.7	1.12	0.77	1.12	-	-	-	-
T2-S-o1	413.1		1942	412.6	332.2	412.6	1.00	0.80	1.00	-5.2	-15.2	-0.5	-15.2
T2-S-o2	382.0		1971	418.8	266.0	418.8	1.10	0.70	1.10	-12.4	-13.9	-20.3	-13.9
T2-S-o3	399.1	1.524	1593	338.5	330.5	338.5	0.85	0.83	0.85	-8.4	-30.4	-1.0	-30.4
T2-S-o4	410.2		2140	454.7	333.9	454.7	1.11	0.81	1.11	-5.9	-6.6	-	-6.6
T2-S-o5	345.1		1622	344.8	264.3	344.8	1.00	0.77	1.00	-20.8	-29.2	-20.8	-29.2
T2-S-o6	337.0		1651	351.0	198.1	351.0	1.04	0.59	1.04	-22.7	-27.9	-40.7	-27.9
T2-S-o7	388.4		2054	436.4	283.6	436.4	1.12	0.73	1.12	-10.9	-10.3	-15.1	-10.3
						Avg.	1.04	0.75	1.04				
T1-L-0	467.5		3242	596.8	367.9	473.3	1.28	0.79	1.01	-	-	-	-
T1-L-o8	460.0		2213	470.4	248.8	323.1	1.02	0.54	0.70	-1.6	-21.2	-32.4	-31.7
T1-L-o9	420.7	1.833	2667	535.3	245.7	389.4	1.27	0.58	0.93	-10.0	-10.3	-33.2	-17.7
T1-L-o10	475.7		2151	457.2	248.8	314.0	0.96	0.52	0.66	+1.7	-23.4	-32.4	-33.6
T1-L-o11	474.9		3101	581.6	367.9	452.6	1.22	0.77	0.95	+1.5	-2.5	-	-4.4
						Avg.	1.15	0.64	0.85				
T2-L-0	490.4		3159	587.9	410.4	576.5	1.20	0.84	1.18	-	-	-	-
T2-L-o8	476.9		2744	543.5	406.2	500.7	1.14	0.85	1.05	-2.7	-7.6	-1.0	-13.1
T2-L-o9	445.6	1.667	2692	538.0	311.2	491.3	1.21	0.70	1.10	-9.1	-8.5	-24.2	-14.8
T2-L-o10	486.6		2728	541.8	409.9	497.7	1.11	0.84	1.02	-0.8	-7.9	-0.1	-13.7
T2-L-o11	494.9		3017	572.8	410.4	550.6	1.16	0.83	1.11	+0.9	-2.6	-	-4.5
						Avg.	1.16	0.81	1.09				

[(A)] Considering entire critical perimeter length, [(B)] Diagonal portion of critical perimeter neglected, [(C)] Considering full critical perimeter and $\beta=c_{max}/c_{min}$ (see Figure 8-13 for definition of c_{max} and c_{min}), [(a)] b_o applies to $V_{ACI}^{(A)}$ and $V_{ACI}^{(C)}$ only; Note: Material safety factors set to 1 when calculating V_{ACI}

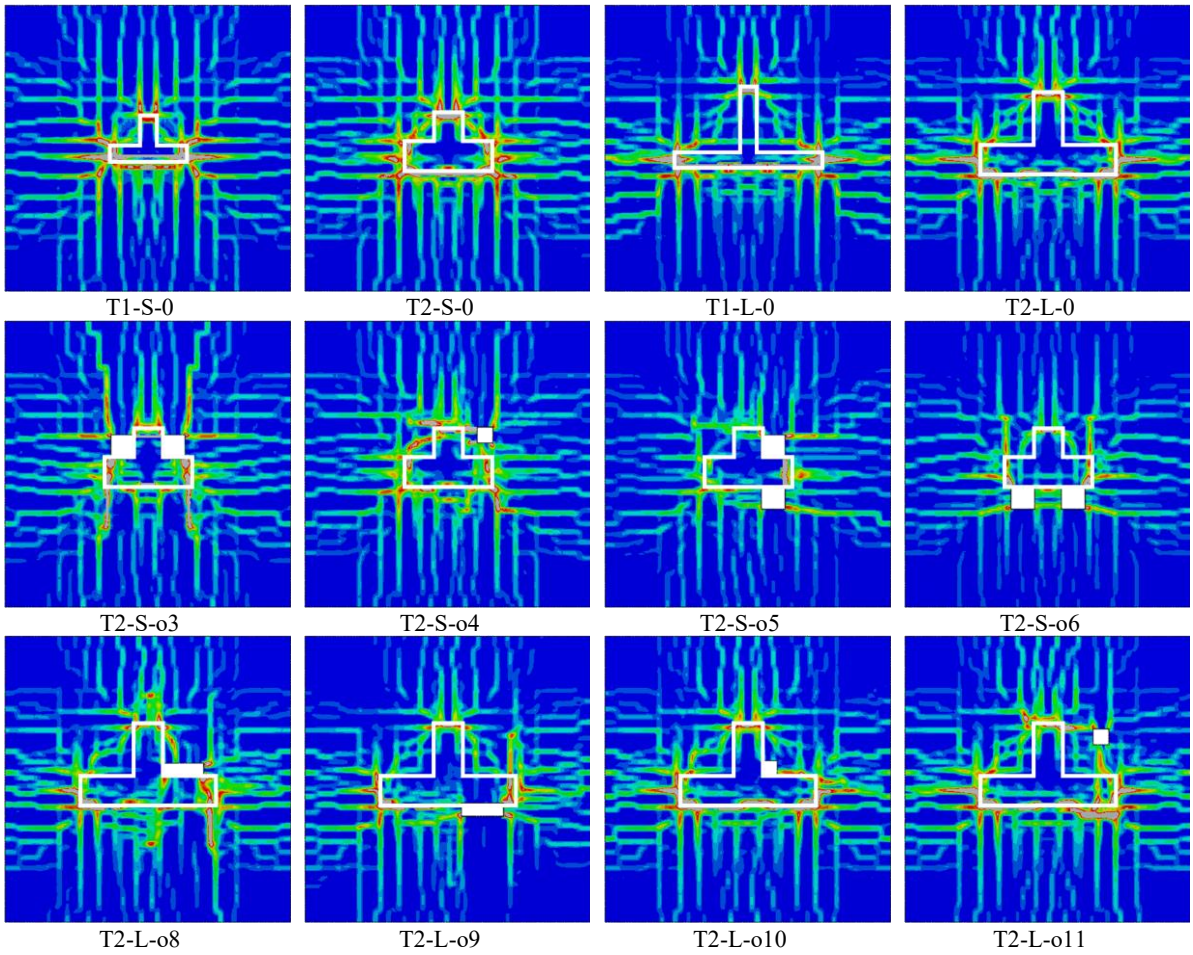


Figure 8-30: Representative Crack Patterns Around T-SCCs with and Without Slab Openings (Grey Regions Have Principal Plastic Strains > 0.02, Approximate Column Location Shown in White)

Representative column perimeter shear stress distributions at the peak load are provided in Figure 8-31. The distributions confirm that a significant amount of the total load is carried along the base of the T, as the shear stress magnitudes are typically the highest along column sides 4, 5 and 6. Additionally, significant load transfer occurs at the end of the stem, with the portion of the connection near the inner vertices being relatively ineffective. Openings along side 5 also had the most significant impact on the predicted distributions, whereas openings between the column flanges were less influential as low shear stress regions were removed.

Therefore, openings around T-SCCs should be located between the column flanges. Ideally, the openings should be near the diagonal of the critical perimeter, but if they must be adjacent to the column, they should be near the inner vertices of the connection to minimize their negative influence.

The unmodified ACI 318-19 predictions are also provided in Table 8-8 ($V_{ACI}^{(A)}$). For the T1-S and T2-S specimens (small columns), ACI 318-19 is quite accurate, with average $V_{ACI}^{(A)}/V_{FEA}$ ratios of 0.97 and 1.04, respectively. For the T1-L and T2-L specimens (large columns), ACI 318-19 is generally unconservative compared to the FEA, with average overpredictions of 15% and 16%, respectively. ACI 318-19 typically overpredicts the influence of interior openings but is fairly accurate for openings along the outer edges of the base of the T (column sides 4, 5 and 6). Therefore, while some revisions to ACI 318-19 are required to account for the benefit of locating openings between the column flanges, the ACI 318-19 opening provisions appear adequate for T-SCCs. It should be noted that unlike some of the L-SCCs, application of the ACI 318-19 opening provisions was clear for all 25 T-SCCs.

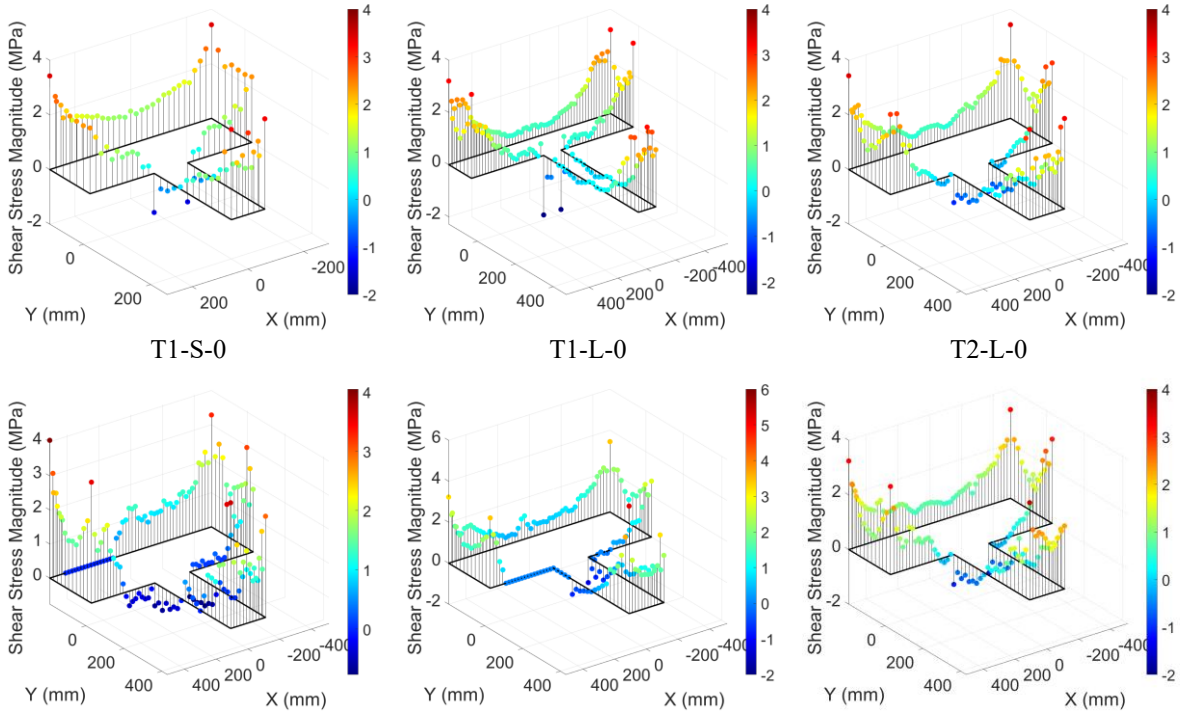


Figure 8-31: Representative Column Perimeter Shear Stress Distributions for T-SCCs –Peak Load (Stresses Averaged Over Depth)

The ACI 318-19 predictions using modifications 1 and 2 are also provided in Table 8-8 ($V_{ACI}^{(B)}$ and $V_{ACI}^{(C)}$ respectively). Modification 1 generally results in very conservative estimates, with average $V_{ACI}^{(B)}/V_{FEA}$ ratios of 0.64, 0.75, 0.64 and 0.81, respectively, which suggests that the diagonal portion of the critical perimeter is at least partially effective for T-SCCs. Punching capacities using modification 2 are higher than those using modification 1 and are typically slightly more conservative than those from the unmodified version of ACI 318-19, other than for the T2-S specimens where both the modified and unmodified predictions are the same. Redefining β also changed the predicted influence of some openings. In particular, the opening influences for the T1-L and T2-L specimens are larger because v_c is now governed by β (equation 3-3) instead of the b_o/d ratio (equation 3-4). Therefore, in the preliminary design of T-SCCs the use of the concentric provisions and modification 2 is recommended.

The use of modification 2 for T-SCCs is logical based on the FEA results. As discussed previously, the most significant cracking and highest shear stresses occur near the base of the T, which is likely the most elongated portion of the connection. Furthermore, the cracking and stress distributions along column sides 4, 5 and 6 are similar to those predicted around rectangular slab-column connections (R-SCCs) in previous analyses by the authors [145, 259]. However, due to the stem of the T, the influence of the elongation is likely less severe than that observed for R-SCCs, which is why the aspect ratio should be defined as the maximum of the individual flanges, and not the maximum of the base and the stem.

8.4.4 Cruciform Slab-Column Connections (X-SCCs)

The load-displacement responses for the 21 X-SCCs, which were predicted to fail in punching shear, are provided in Figure 8-32, and the FEA results are summarized in Table 8-9. Most of the openings in the X-SCC study are located between the column flanges, and these openings have a very minor influence on concentric punching capacity with a maximum reduction of approximately 7.2% predicted when two openings are placed between the flanges (X1-S-o3 or X1-S-o5). The largest capacity and stiffness reductions were predicted when the opening was along the short side of one of the column flanges (X2-S-o7), which confirms that openings in the vicinity of X-SCCs should be between the column flanges, but away from the short sides of the connection.

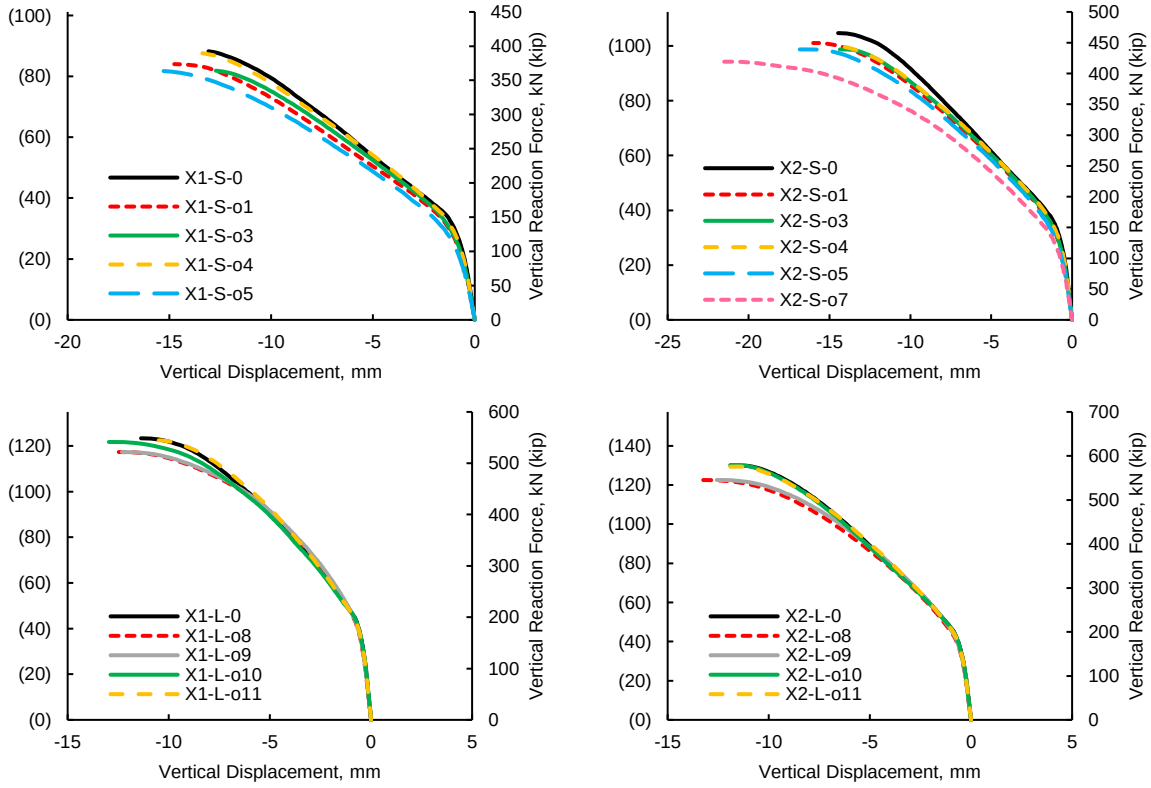


Figure 8-32: Predicted Load-Displacement Responses for X-SCCs, Displacement Output Location Shown in Figure 8-2, Negative Displacement is Downwards

Representative tension surface crack patterns are provided in Figure 8-33. For X-SCCs severe cracking around the intersection of short and long sides is predicted, particularly for the connections without openings. There is significant diagonal cracking in the regions between the column flanges, which suggests that a large portion of these regions are effective in transferring load.

Again, openings significantly impact the predicted cracking. Firstly, non-symmetric slab openings result in non-symmetric crack patterns and crack concentrations on the side of the connection with the opening, even when the opening has a minor influence on the connection capacity (see X2-S-o4 and X2-L-o11 in Figure 8-33). Secondly, large openings located between the column flanges interrupt the diagonal cracking between the column flanges adjacent to the opening as the cracks instead propagate towards the opening (see X2-L-o8 and X2-L-o9).

Table 8-9: Comparison of Capacities and Opening Influences Predicted by FEA and ACI 318-19 – X-SCCs

	kN		mm	V_{ACI} (kN)			V_{ACI}/V_{FEA}			Opening Impact (%)			
ID	V_{FEA}	β	b_o [e]	(A)	(B)	(C)	(A)	(B)	(C)	FEA	(A)	(B)	(C)
X1-S-0	392.5		2089	443.9	126.2	367.3	1.13	0.32	0.94	-	-	-	-
X1-S-o1	373.7		1708	362.9	123.3	300.3	0.97	0.33	0.80	-4.8	-18.2	-2.3	-18.2
X1-S-o3	364.1	1.0	1327	281.9	120.4	233.2	0.77	0.33	0.64	-7.2	-36.5	-4.6	-36.5
X1-S-o4	389.7		1930	410.1	126.2	339.3	1.05	0.32	0.87	-0.7	-7.6	-	-7.6
X1-S-o5	364.2		1327	281.9	120.4	233.2	0.77	0.33	0.64	-7.2	-36.5	-4.6	-36.5
						Avg.	0.94	0.33	0.78				
X2-S-0	465.7		2432	510.2	211.2	510.2	1.10	0.45	1.10	-	-	-	-
X2-S-o1	449.5		2095	445.3	211.2	445.3	0.99	0.47	0.99	-3.5	-12.7	-	-12.7
X2-S-o3	439.0	1.0	1759	373.8	211.2	373.8	0.85	0.48	0.85	-5.7	-26.7	-	-26.7
X2-S-o4	446.2		2280	484.5	211.2	484.5	1.09	0.47	1.09	-4.2	-5.0	-	-5.0
X2-S-o5	439.1		1759	373.8	211.2	373.8	0.85	0.48	0.85	-5.7	-26.7	-	-26.7
X2-S-o7	419.1		2196	466.6	160.9	466.6	1.11	0.38	1.11	-10.0	-8.5	-23.8	-8.5
						Avg.	1.00	0.46	1.00				
X1-L-0	548.7		3616	636.8	126.2	527.9	1.16	0.23	0.96	-	-	-	-
X1-L-o8	521.9		2990	569.9	124.8	436.5	1.09	0.24	0.84	-4.9	-10.5	-1.1	-17.3
X1-L-o9	521.9	1.0	2900	569.9	124.8	436.5	1.09	0.24	0.84	-4.9	-10.5	-1.1	-17.3
X1-L-o10	541.4		3090	580.5	126.2	451.0	1.07	0.23	0.83	-1.3	-8.8	-	-14.6
X1-L-o11	544.4		3471	621.3	126.2	506.7	1.14	0.23	0.93	-0.8	-2.4	-	-4.0
						Avg.	1.11	0.23	0.88				
X2-L-0	578.5		3450	619.1	211.2	619.1	1.07	0.37	1.07	-	-	-	-
X2-L-o8	545.2		2992	570.1	211.2	546.0	1.05	0.39	1.00	-5.8	-7.9	-	-11.8
X2-L-o9	545.4	1.0	2992	570.1	211.2	546.0	1.05	0.39	1.00	-5.7	-7.9	-	-11.8
X2-L-o10	579.2		3088	580.3	211.2	563.6	1.00	0.36	0.97	+0.1	-6.3	-	-9.0
X2-L-o11	575.3		3306	603.6	211.2	603.2	1.05	0.37	1.05	-0.5	-2.5	-	-2.6
						Avg.	1.04	0.37	1.02				

[A] Considering entire critical perimeter length, [B] Diagonal portion of critical perimeter neglected, [C] Considering full critical perimeter and $\beta=c_{max}/c_{min}$ (see Figure 8-15 for definition of c_{max} and c_{min}), [a] b_o applies to $V_{ACI}^{(A)}$ and $V_{ACI}^{(C)}$ only; Note: Material safety factors set to 1 when calculating V_{ACI}

Representative column perimeter shear stress distributions at the peak load are provided in Figure 8-34. The predicted distributions for the specimens without openings confirm that all sides of X-SCCs transfer a significant portion of the load, with most load transfer occurring near the flange ends along both the short and long sides of the connection.

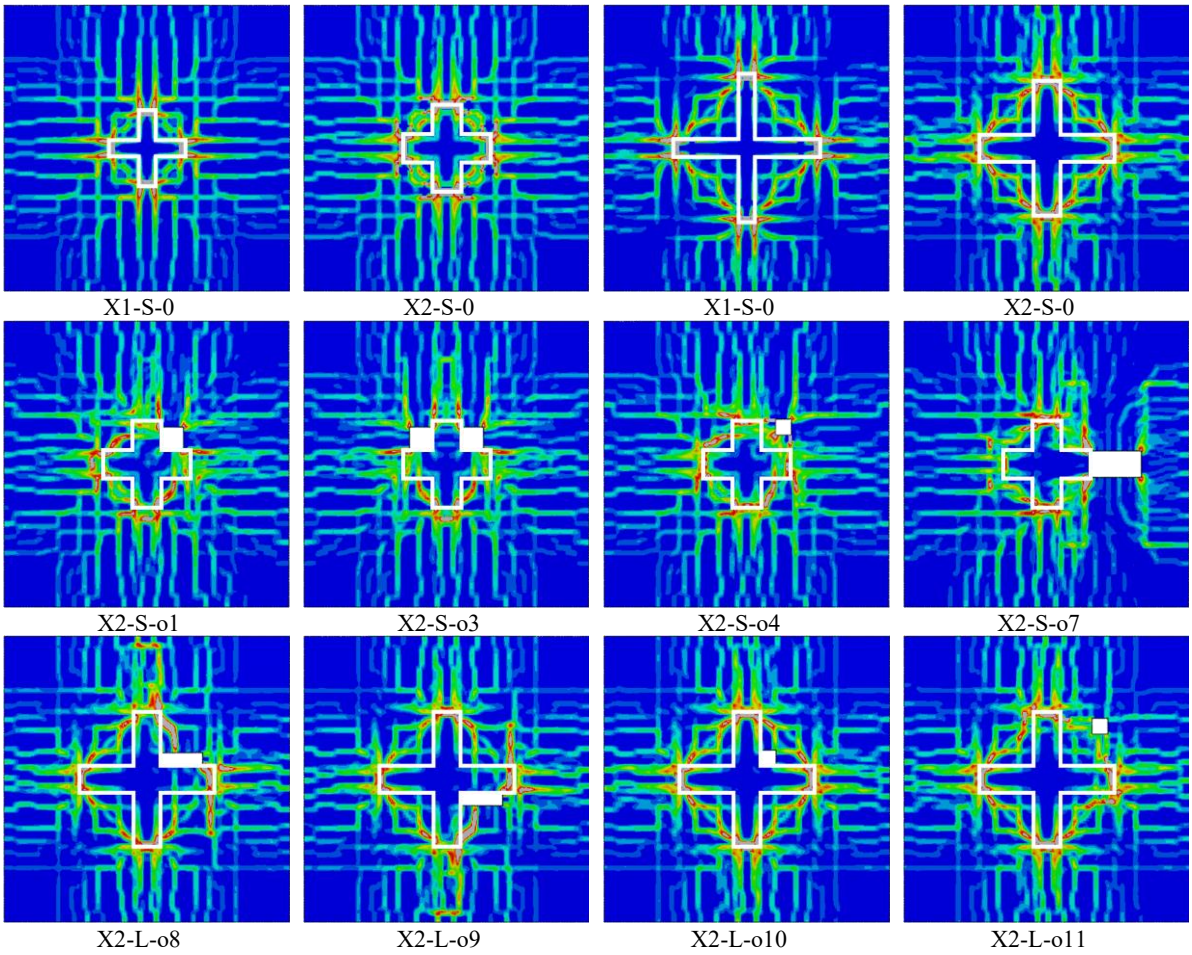
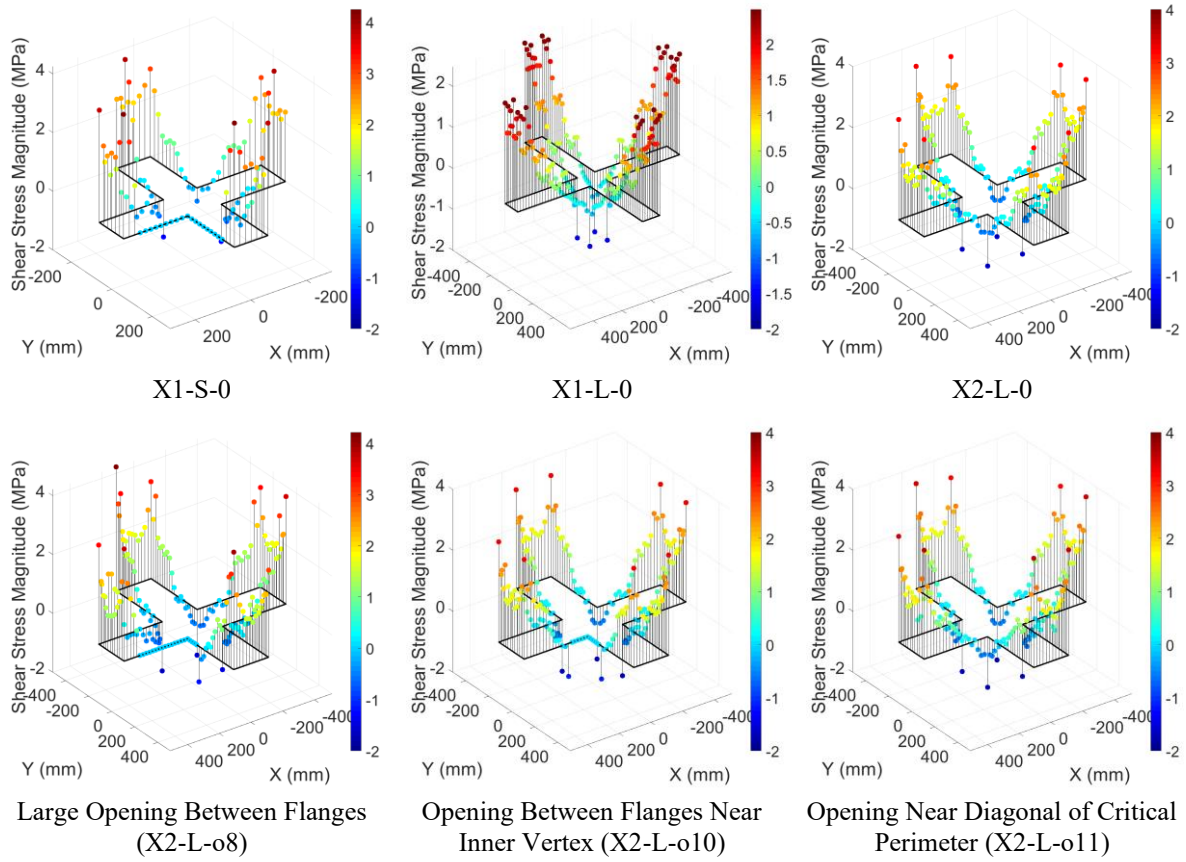


Figure 8-33: Representative Crack Patterns Around X-SCCs with and Without Slab Openings (Grey Regions Have Principal Plastic Strains > 0.02, Approximate Column Location Shown in White)

Again, the opening location influences the effect of the opening on the predicted shear stress distributions. Openings between the column flanges, either near the diagonal portion of the critical perimeter, or close to the inner vertices of the connection, have a minor impact as the removed areas are typically under low shear stress. It should be noted that the potential for shear stress redistribution around X-SCCs is likely high due to the connection size and because all column sides are effective in transferring load.



X1-S-0 | X1-L-0 | X2-L-0

Large Opening Between Flanges (X2-L-o8) | Opening Between Flanges Near Inner Vertex (X2-L-o10) | Opening Near Diagonal of Critical Perimeter (X2-L-o11)

Figure 8-34: Representative Column Perimeter Shear Stress Distributions for X-SCCs –Peak Load (Stresses Averaged Over Depth)

The unmodified ACI 318-19 predictions are also provided in Table 8-9. ($V_{ACI}^{(A)}$). On average, ACI 318-19 and the FEA agreed well for all investigated column sizes. For the X1-S and X2-S specimens (small columns), the concentric provisions are conservative on average, whereas for the X1-L and X2-L specimens (large columns) the predictions are slightly unconservative, with average overpredictions of 11% and 4%, respectively. Regarding opening influences, ACI 318-19 is generally conservative compared to the FEA, with only the opening influence in X2-S-o7 being slightly underpredicted. Application of the opening provisions was clear for all X-SCCs.

However, the accuracy of the ACI 318-19 opening provisions seems to be dependent on the column size. For the large columns, the ACI 318-19 opening influences are conservative, but reasonable, compared to the FEA. Whereas, for the small columns, ACI 318-19 severely overpredicts the influence of interior openings, showing that revisions to the opening provisions are required for X-SCCs.

The ACI 318-19 predictions using modifications 1 and 2 are also provided in Table 8-9 ($V_{ACI}^{(B)}$ and $V_{ACI}^{(C)}$ respectively). Modification 1 resulted in overly conservative predictions. Additionally, many of the investigated openings are predicted to have no influence, which is incorrect. Therefore, a large portion of the diagonal region of the critical perimeter is likely effective for X-SCCs and modification 1 should not be used. Other than the X2-S specimens, modification 2 resulted in more conservative punching estimates than the unmodified concentric provisions. This was expected as β is equal to one when using the a_n/b_n definition, which results in v_c never being governed by β regardless of the flange dimensions (for X-SCCs with equal column flanges). It should be noted that similar to square slab-column connections each side of X-SCCs are effective in transferring load between the slab and the column, as will be discussed in Section 8.4.5. Therefore, the alternate definition of β for SS-SCCs appears to be a good approximation for X-SCCs. Furthermore, modification 2 also increases the predicted influence of each opening layout for the large columns (X1-L and X2-L), as v_c is now governed by β (equation 3-3). However, as previously discussed, the unmodified ACI 318-19 provisions appear to be fairly accurate for X-SCCs. Therefore, neither modification is recommended when using the concentric provisions for preliminary design.

8.4.5 Comparison of Punching Capacity Predicted by ACI 421.1R-20 and FEA for SS-SCCs

As shown in the previous sections, the ACI 318-19 concentric punching shear provisions can result in conservative punching shear capacity estimates for SS-SCCs (assuming the proposed modifications are used for L-SCCs and T-SCCs). However, for the connections with openings, an unbalanced moment, which exists due to the eccentricity between the column and critical perimeter centroids, needs to be accounted for when estimating the connections' capacity according to ACI 318 (this unbalanced moment is in addition to that due to loading or any eccentricity between the column centroid and column gridlines in the continuous structure). However, ACI 318-19 only provides equations for square or rectangular columns without openings subjected to combined concentric load and unbalanced moment and therefore, the ACI 421.1R provisions, which are applicable to any column geometry, must be used to estimate the connection capacity.

As seen in Table 8-10, the punching capacities predicted according to ACI 421.1R-20 (V_{421}) typically agreed well with those predicted by the FEA, though the predictions for the L1-L, L2-L and T2-L specimens were 7%, 6% and 3% unconservative on average. Therefore, while complicated, the ACI 421.1R-20 method is adequate for estimating the punching capacity of SS-SCCs and should be

used to confirm the preliminary designs determined using the proposed modifications to the concentric punching provisions outlined in the previous sections. However, while more accurate than the concentric provisions overall, ACI 421.1R-20 still typically overpredicts the influence of openings located between the column flanges of SS-SCCs (though the influence of exterior openings for L-SCCs and T-SCCs are typically well predicted).

Table 8-10: Capacities and Opening Influences Predicted by ACI 421.1R-20 for Analyzed L-SCCs, T-SCCs and X-SCCs

ID	V_{421} (kN)	$\frac{V_{421}}{V_{FEA}}$	OI[a] (%)	ID	V_{421} (kN)	$\frac{V_{421}}{V_{FEA}}$	OI[a] (%)	ID	V_{421} (kN)	$\frac{V_{421}}{V_{FEA}}$	OI[a] (%)
L1-S-0	298.5	0.86	-	T1-S-0	391.3	1.03	-	X1-S-0[b]	443.9	1.13	-
L1-S-o1[c]	298.5	0.90	-	T1-S-o1	273.8	0.79	-30.0	X1-S-o1	294.1	0.79	-33.8
L1-S-o2	226.4	0.87	-24.2	T1-S-o2	254.4	0.82	-35.0	-	-	-	-
L1-S-o3[c]	226.4	0.88	-24.2	T1-S-o3	175.4	0.54	-55.2	X1-S-o3	180.5	0.50	-59.3
L1-S-o4	291.0	0.85	-2.5	T1-S-o4	352.7	0.98	-9.9	X1-S-o4	385.6	0.99	-13.1
L1-S-o5[c]	226.4	0.88	-24.2	T1-S-o5	155.0	0.54	-60.4	X1-S-o5	180.5	0.50	-59.3
L1-S-o6	129.9	0.64	-56.5	T1-S-o6	176.3	0.64	-54.9	-	-	-	-
	Avg.	0.84			Avg.	0.76			Avg.	0.78	
L2-S-0	418.3	1.03	-	T2-S-0	473.0	1.09	-	X2-S-0[b]	510.2	1.10	-
L2-S-o1	286.8	0.74	-31.4	T2-S-o1	361.0	0.87	-23.7	X2-S-o1	383.7	0.85	-24.8
L2-S-o2	321.1	1.02	-23.2	T2-S-o2	337.2	0.88	-23.7	-	-	-	-
L2-S-o3	230.3	0.76	-44.9	T2-S-o3	276.9	0.69	-41.5	X2-S-o3	289.4	0.66	-43.3
L2-S-o4	378.4	0.99	-9.6	T2-S-o4	435.8	1.06	-7.9	X2-S-o4	459.7	1.03	-9.9
L2-S-o5	230.3	0.76	-44.9	T2-S-o5	253.6	0.73	-46.4	X2-S-o5	289.4	0.66	-43.3
L2-S-o6	236.0	0.87	-43.6	T2-S-o6	262.6	0.78	-44.5	-	-	-	-
L2-S-o7	317.8	0.93	-24.0	T2-S-o7	371.7	0.96	-21.4	X2-S-o7	419.9	1.00	-17.7
	Avg.	0.89			Avg.	0.88			Avg.	0.88	
L1-L-0	423.3	1.08	-	T1-L-0	562.8	1.20	-	X1-L-0[b]	636.8	1.16	-
L1-L-o8[c]	423.3	1.15	-	T1-L-o8	248.8	0.54	-55.8	X1-L-o8	467.8	0.90	-26.5
L1-L-o9	301.7	0.95	-28.7	T1-L-o9	385.9	0.92	-31.4	X1-L-o9	467.8	0.90	-26.5
L1-L-o10[c]	423.3	1.08	-	T1-L-o10	234.3	0.49	-58.4	X1-L-o10	506.1	0.93	-20.5
L1-L-o11	426.6	1.09	+0.8	T1-L-o11	542.3	1.14	-3.6	X1-L-o11	604.3	1.11	-5.1
	Avg.	1.07			Avg.	0.86			Avg.	1.00	
L2-L-0	471.8	1.08	-	T2-L-0	568.4	1.16	-	X2-L-0[b]	619.1	1.07	-
L2-L-o8[c]	471.8	1.09	-	T2-L-o8	479.5	1.01	-15.6	X2-L-o8	496.1	0.91	-19.9
L2-L-o9	388.0	1.01	-17.8	T2-L-o9	424.0	0.95	-25.4	X2-L-o9	496.1	0.91	-19.9
L2-L-o10[c]	471.8	1.07	-	T2-L-o10	479.1	0.98	-15.7	X2-L-o10	529.0	0.91	-14.6
L2-L-o11	477.2	1.07	+1.2	T2-L-o11	530.0	1.07	-6.8	X2-L-o11	585.1	1.02	-5.5
	Avg.	1.06			Avg.	1.03			Avg.	0.96	

[a] OI: Opening Impact, [b] Capacity based on concentric provisions as column, slab and critical perimeter centroids aligned, [c] Critical perimeter reduction unclear; Note: Material safety factors set to 1 when calculating $V_{421;}$ Diagonal portion of critical perimeter included and β defined as a_n/b_n when calculating $V_{421;}$ V_{FEA} provided in Table 8-7, Table 8-8 and Table 8-9 for L-SCCs, T-SCCs and X-SCCs, respectively

8.4.6 Comparison of Results for Different Column Shapes

The percentage of the total load transferred along each column side at the peak load for the analyzed R-SCCs, L-SCCs, T-SCCs and X-SCCs without slab openings are provided in Figure 8-35. For all considered column geometries, the shear force distribution along the column perimeter is non-uniform. From Figure 8-35, it is clear why openings between the column flanges typically have a minor impact on the punching capacity of SS-SCCs, as the openings are typically removing the least effective portions of the connections. Figure 8-35 also demonstrates why openings along the long side of R-SCCs, outer edges of L-SCCs (sides 5 and 6, see Figure 8-10) and the base of T-SCCs (sides 4, 5 and 6, see Figure 8-12) lead to significant reductions in punching capacities. Openings in these regions are removing the portions of the connection which typically transfer the largest portion of the load applied to the connection, and therefore, the connection's punching capacity is significantly reduced.

As discussed in Chapter 6, most of the load applied to R-SCCs is transferred through the long sides of the connection, with the short sides carrying a significantly smaller portion of the load. Based on the predicted crack patterns and shear stress distributions one-way shear again appears to be the significant mechanism of force transfer along the long sides, though two-way shear does influence the shear stress distribution near the column ends. Due to the influence of two-way shear, shear stress concentrations are predicted along the short sides and along the long sides near the column ends.

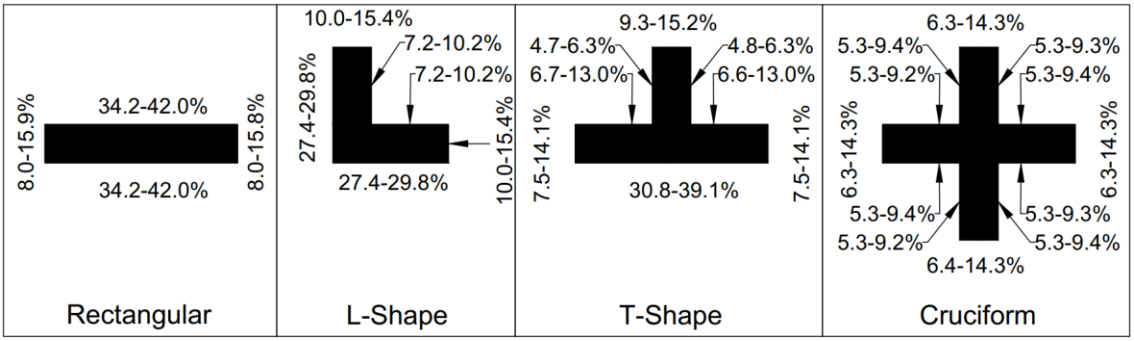


Figure 8-35: Comparison of Percent of Total Load Carried on Each Column Side for Different Column Shapes Predicted by FEA for Specimens Without Slab Openings (Data Recorded at Peak Load)

For L-SCCs, the inner sides of the connection (sides 2 and 3) are quite ineffective compared to the outer edges (sides 5 and 6). Based on the predicted crack patterns (which are provided in Section

8.4.2 and Appendix J), one-way shear is the dominant force transfer mechanism along column sides 5 and 6, even though the connection fails in punching.

For T-SCCs, most of the total load is transferred through the base of the T, particularly along the outer edges (column sides 4, 5 and 6). Similar to L-SCCs, the most heavily loaded side, side 5, is dominated by one-way shear. Both the short side of the stem, column side 1, and the inner edges of the base, column sides 3 and 7, are relatively effective in transferring load. The least effective portion of T-SCCs are the vertical portions of the stem, column sides 2 and 8, with most of the load transfer along these sides occurring near the short sides of the stem.

The least non-uniform shear force distribution is predicted for X-SCCs, with each side carrying a similar portion of the load. While the inner column sides are slightly less effective than the outer sides (short sides of each flange, column sides 1, 4, 7 and 10, see Figure 8-14), there are no overly dominant sides. Therefore, the influence of one-way shear on the behaviour of the analyzed X-SCCs is assumed to be minor.

A comparison of the opening influences predicted by the FEA for consistent opening locations between column shapes is provided in Table 8-11. Based on the predicted opening influences, it appears that the structural benefit of using a SS-SCC over a R-SCC when openings are present is dependent on the column size and the opening's location with respect to the column. If the opening would be located along the outer edges of the L (sides 5 and 6), or the base of the T (sides 4, 5 and 6) a R-SCC or X-SCC should be used. However, if the opening would be located in the region between the column flanges than the use of a SS-SCC over a R-SCC is always beneficial. While the influence of the opening on the concentric punching capacity of a R-SCC or a SS-SCC may be similar in some cases, SS-SCCs still have the additional benefit of allowing the openings and services to be hidden from view if the opening is located in the region between the column flanges.

For the large column specimens (see Table 8-11), the predicted influence of each opening layout around the analyzed R-SCCs is similar to or slightly lower than that around the analyzed SS-SCCs. Therefore, considering just the reduction in concentric punching capacity due to the opening, and not the overall connection capacity, there is not a significant structural benefit of using a SS-SCC over a R-SCC, regardless of opening location, when the overall shear behaviour of the R-SCC is strongly influenced by one-way shear (i.e. $c_{max}/L >$ approximately 0.4 as discussed in Chapter 7).

However, for the small column specimens (see Table 8-11), whose behaviour is dominated by punching shear (i.e. $c_{max}/L <$ approximately 0.4), there can be a significant structural benefit of using a SS-SCC over a R-SCC. This benefit is dependent on both the opening location with respect to the column and the column shape, as discussed in the subsequent paragraphs.

Table 8-11: Comparison of Opening Influence Predicted by NLFEA for Different Column Geometries

	Opening Layout	Predicted Opening Influence			
		R1-S	L1-S	T1-S	X1-S
Small Columns	-o1	-11.3	-4.4	-9.4	-4.8
	-o2	-11.3[a]	-25.3	-18.6	-4.8[a]
	-o3	-21.7	-25.9	-14.9	-7.2
	-o4	-0.4	-1.1	-5.1	-0.7
	-o5	-20.9	-25.9	-24.0	-7.2
	-o6	-21.7[b]	-42.0	-28.1	-7.2[b]
		R2-S	L2-S	T2-S	X2-S
	-o1	-8.9	-5.4	-5.2	-3.5
	-o2	-8.9[a]	-22.9	-12.4	-3.5[a]
	-o3	-18.3	-25.5	-8.4	-5.7
	-o4	-5.8	-6.0	-5.9	-4.2
	-o5	-17.6	-25.8	-20.8	-5.7
	-o6	-18.3[b]	-33.1	-22.7	-5.7[b]
	-o7	-9.5	-16.3	-10.9	-10.0
Large Columns		R1-L	L1-L	T1-L	X1-L
	-o8	-6.9	-6.6	-1.6	-4.9
	-o9	-6.9[c]	-19.7	-10.0	-4.9
	-o10	-6.8	-0.3	+1.7	-1.3
	-o11	+0.8	-0.4	+1.5	-0.8
		R2-L	L2-L	T2-L	X2-L
	-o8	-5.4	-1.3	-2.7	-5.8
	-o9	-5.4[c]	-11.9	-9.1	-5.7
	-o10	+0.1	+1.0	-0.8	+0.1
	-o11	+0.7	+2.3	+0.9	-0.5

(a) Due to symmetry the results for layout -o1 and -o2 would be identical and are included for comparison with the L-SCCs and T-SCCs results; (b) Due to symmetry the results for layout -o3 and -o6 would be identical and are included for comparison with the L-SCCs and T-SCCs results; (c) Due to symmetry the results for layout -o8 and -o9 would be identical and are included for comparison with the SS-SCCs results

When a single square opening is located within the region between the column flanges, the decrease in connection capacity predicted by the FEA for SS-SCCs is smaller than that for R-SCCs with the same slab opening, as seen in Table 8-11 (-o1 layout). However, in the case that the same single square opening is placed on the opposite side of the column, such that it would be located on the outer edge of a L-SCC or the base of T-SCC (-o2 layout), the use of L-SCC or T-SCC over a R-SCC is not recommended, as these connections are predicted to have a larger capacity reduction than that for the R-SCC. In these cases, X-SCCs are recommended for use as they result in a smaller reduction in punching capacity than a R-SCC with a similarly located opening.

For two square openings located along the same long side of the R-SCC (-o3 and -o6 layouts), the benefits of using a SS-SCC are again dependent on the column geometry and opening location. In these cases, it is not beneficial to use a L-SCC since one or both of the openings will be located along the outer column sides. Since these column sides transfer the majority of load for L-SCCs, placing openings here results in significant reductions in punching capacity. As seen in Table 8-11, the predicted reductions for L-SCCs exceed those for R-SCCs for the -o3 and -o6 opening layouts. Using a T-SCC is beneficial if the two openings are located between the column flanges (layout -o3). If both of the openings are placed along the outer edge of the base of the T (-o6 layout), the use of a T-SCC is more detrimental than a R-SCC, since a significant portion of the load is transferred along the base of the T. Based on the analyzed specimens, the use of X-SCC over a R-SCC always seems to be advantageous when the two openings are located along the long side of the rectangular column, as the openings have a significantly lower impact on the capacity of the X-SCC.

If the two openings are located near the end of the column (R-SCC) or flange end (SS-SCC) but on opposite column sides (-o5 layout) the use of R-SCCs, L-SCCs and T-SCCs, all result in significant capacity reductions. In such cases, a X-SCC, where the opening is located as close as possible to the inner column vertices, if it must be adjacent to the column, or as close as possible to the diagonal portion of the critical perimeter, is recommended, as the expected reduction in punching capacity is lower than that expected for other column geometries.

Based on the results in Table 8-11, there appears to be no benefit of using a SS-SCC in the case where a small square opening is located near the diagonal portion of the effective loaded area for the SS-SCC assumed in ACI 318-19 (-o4 or -o11 layouts). In this case, the openings are sufficiently far from the column so that there is no structural benefit of using a SS-SCC in place of a R-SCC.

Finally, though more work is required to investigate the benefits of using SS-SCCs compared to R-SCCs when the openings are located on the short side of the rectangular column/column flanges, the results for opening layout -o7 suggest that there is no significant benefit of using a T or cruciform column when the opening is located along the short side of the base.

8.5 Summary and Contributions

Specific code provisions for SS-SCCs were added to ACI 318 in the late 1970s and have not been modified since their introduction. Due to a lack of previous studies, as discussed in Section 2.3.4, the punching shear behaviour of these connections, and the accuracy of these provisions, is unknown. Therefore, the primary contribution of this chapter was to study the concentric punching shear behaviour of interior SS-SCCs, specifically L-, T- and cruciform-shaped columns. Based on NLFEA results, detailed discussions of the connection capacity, stiffness, cracking, failure mechanisms and column perimeter shear stress distributions around interior SS-SCCs are provided. The influence of the column size and the presence of slab openings on the behaviour of the investigated slab-column connection geometries were also studied. As current literature does not provide discussions of the punching shear behaviour of SS-SCCs, the provided discussions are beneficial to practicing engineers, and can lead to improved designs.

Specific contributions are summarized below. In addition to the analyses of SS-SCCs, R-SCCs were also analyzed in this chapter to compare the punching shear behaviour of SS-SCCs and more common column geometries. As was done when analyzing SS-SCCs, connections with and without slab openings were considered. The same opening locations investigated for the SS-SCCs were used to determine potential situations where the use of a SS-SCC in place of a R-SCC is beneficial. Additionally, most existing studies related to the influence of slab openings on the punching shear behaviour of R-SCCs involve openings located along or near the short sides of the connection, as discussed in Section 2.3.6. Therefore, the specimens analyzed herein greatly expand the existing database of R-SCCs with slab openings, and allow for a detailed discussion of the punching shear behaviour of such connections, for a consistent set of geometric and material parameters.

The FEA results were also used to evaluate the accuracy of the existing ACI provisions for R-SCCs and SS-SCCs subjected to concentric loading with and without slab openings. For the analyzed R-SCCs, the ACI 318-19 concentric punching shear provisions were found to be generally conservative. However, for SS-SCCs, the ACI 318-19 concentric provisions were found to be inaccurate or

unconservative in many cases, especially for the two largest column sizes studied. Due to the presence of slab openings, and eccentricities between the column and critical perimeter centroids for many of the specimens, the concentric punching capacities were also estimated according to ACI 421.1R-20. The more general provisions of ACI 421.1R-20 were found to be overly conservative for R-SCCs, though they were typically accurate and conservative for the analyzed SS-SCCs. However, as the ACI 421.1R-20 method is time consuming for hand calculations, simplified design methods for SS-SCCs were developed as part of this work. These simplified methods can be used to expedite the iterative design process, before conducting final verification with ACI 421.1R-20 in order to satisfy current ACI requirements.

Finally, based on the FEA results, recommendations for locations to avoid placing slab openings around each column geometry are provided. These recommendations are of great value to practicing engineers as openings, which can have a significant negative influence on the punching behaviour of slab-column connections, are typically required in structures. Furthermore, the presented work has demonstrated that the ACI opening provisions do not accurately predict the influence of openings around R-SCCs and SS-SCCs. While the provisions are generally overly conservative, they are unconservative in some cases and cannot be applied when the column centroid falls within the opening, as discussed. Therefore, the work presented herein has highlighted issues with the existing provisions which should be corrected in future versions of ACI 318.

Chapter 9: Special-Shaped Slab-Column Connection Study – Combined Shear and Unbalanced Moment

9.1 Motivation

The results presented in Chapter 8 have demonstrated that slab openings located along the outer edges of SS-SCCs have a significant influence on the concentric punching shear capacity of interior connections and should be avoided whenever possible. On the other hand, openings located between the column flanges were typically found to have a minor influence on the concentric punching shear capacity of interior SS-SCCs (particularly L, T and cruciform connections), and to be less detrimental than similarly placed openings around R-SCCs, particularly for T-SCCs and X-SCCs. However, in practice, most (if not all) interior connections will be subjected to a combination of concentric shear and unbalanced moment due to unequal slab spans or pattern live loading. Therefore, it is necessary to determine if openings located between the column flanges also have a minor influence on the punching shear behaviour of SS-SCCs under such load conditions.

As such, the influence of openings between the column flanges on the punching shear behaviour of SS-SCCs subjected to a constant concentric gravity load and a monotonically increasing uniaxial unbalanced moment is studied herein (the chosen gravity load levels and moment directions are discussed in Section 9.2). As with the concentric study in Chapter 8, the punching shear behaviour of R-SCCs and SS-SCCs (L, T and cruciform connections) without shear reinforcement are compared.

Finally, while ACI 421.1R-20 [5] was found to lead to conservative predictions of concentric punching shear capacity for SS-SCCs in Chapter 8, the accuracy of the provisions for SS-SCCs subjected to combined concentric shear and unbalanced moment needs to be studied. Furthermore, the accuracy of ACI 421.1R-20 for R-SCCs with slab openings subjected to combined concentric shear and unbalanced moment also needs to be studied.

9.2 Study Overview

In this chapter, the punching shear behaviour of interior SS-SCCs with or without slab openings and without shear reinforcement under combined concentric shear and uniaxial unbalanced moment is studied. To the author's knowledge, previous studies of the punching shear behaviour of SS-SCCs under combined shear and unbalanced moment, which is a common loading condition for interior connections, are extremely limited or non-existent. While there is a need to study the punching shear behaviour of SS-SCCs under combined concentric shear and monotonically or cyclically increasing

unbalanced moment, only monotonically increasing unbalanced moments are considered in this work due to limitations in available computational resources (note, the concentric shear force magnitude is kept constant during the application of the unbalanced moment). As will be discussed in Section 9.3, it was necessary to increase the analysis timestep length in Abaqus/Explicit when applying the unbalanced moment in the calibrated FEM in order to get accurate results. The use of a dynamic explicit solution procedure with an increased analysis timestep length was approximately as computationally efficient as a static/general analysis. As such, the computational demand for each simulation in this chapter is much larger than those presented in Chapter 8, which limited the overall study size.

Additionally, in the author's opinion, the punching shear behaviour of connections subjected to combined concentric shear and monotonically increasing unbalanced moment should be well understood before conducting analyses with cyclically increasing unbalanced moment, due to the additional difficulties introduced by force reversals.

As will also be discussed in Section 9.3, the FEM used in Chapter 8 to analyze the punching shear behaviour of SS-SCCs under concentric shear only, which was calibrated to the experimental results of Hawkins et al. [3], could not be used to study the punching shear behaviour of SS-SCCs under combined concentric shear and uniaxial unbalanced moment. This FEM could not be used due to the lack of flexural reinforcement on the bottom surface of the slab (which corresponds to the compression surface of the slab under concentric loading for the load conditions considered in Chapter 8). Therefore, the nonlinear FEM used in this chapter was calibrated to the experimental specimens of Drakatos et al. [4], which in addition to being larger in plan and thicker than those tested by Hawkins et al. [3], have reinforcement on both faces of the slabs and were tested under combined shear and unbalanced moment (both monotonically and cyclically increasing moments).

The naming conventions for the specimens subjected to concentric loading only ("V" load type) and combined concentric shear and monotonically increasing uniaxial unbalanced moment ("V+M" load type) are provided in Figure 9-1 and Figure 9-2, respectively. Note, it was necessary to first analyze the connections under concentric loading only to quantify the influence of each opening layout, and to determine the maximum concentric capacity of each connection. The maximum concentric capacity of each connection was required to determine the vertical load levels in the V+M specimens (the vertical load level in the V+M specimens is represented by the gravity shear ratio (GSR)).

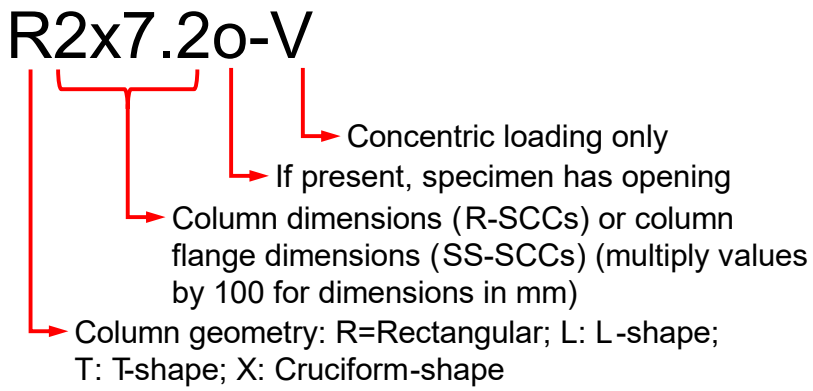


Figure 9-1: Breakdown of Specimen Naming Convention (V Load Type)

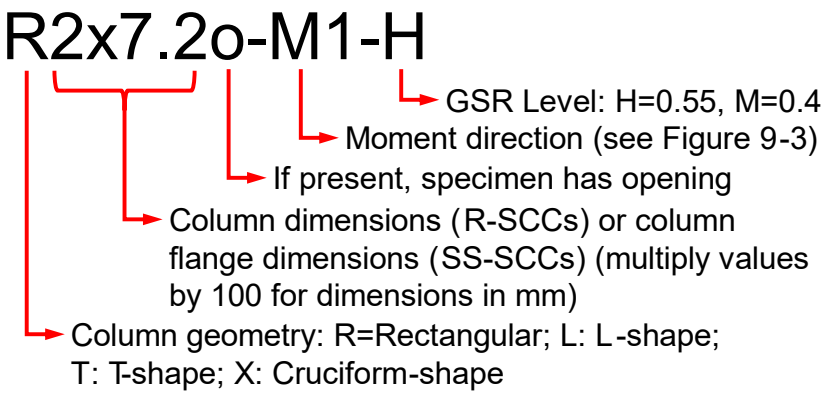


Figure 9-2: Breakdown of Specimen Naming Convention (V+M Load Type)

As was done in Chapter 8, the behaviour of R-SCCs and SS-SCCs (L-SCCs, T-SCCs, and X-SCCs) are compared. However, due to the high computational resource demands, only one column size and one opening layout were analyzed for each column geometry as shown in Figure 9-3. The rectangular column size, 200x720mm, was selected such that the concentric capacity of the R-SCC was of similar magnitude to that of the square slab-column connections tested by Drakatos et al. [4]. Additionally, for this column size, the ratio of the maximum column dimension, c_{max}, to the isolated specimen length, L_{iso}, was equal to 0.24, so the connection behaviour should be dominated by punching shear instead of one-way shear. Furthermore, this column size corresponds to a κ value of approximately 1, which is representative of connections in the experimental database and in actual structures. Consistent with the SS-SCCs analyzed in Chapter 8, all column flanges have equal dimensions

(200x460mm, the definition of a column flange is also consistent with that used in Chapter 8). Since openings along the outer edges of SS-SCCs were found to have a significant influence on concentric punching capacity in Chapter 8, it was anticipated that these openings would also have a significant impact on the unbalanced moment capacity of the connection. Therefore, to reduce the required number of simulations, exterior opening layouts were not considered, and only one interior layout, which is shown in Figure 9-3, was considered for each column geometry. The opening size, 200mm square, was chosen such that the opening removed a similar amount of the connection to that for layout -o1 in the small column study presented in Chapter 8.

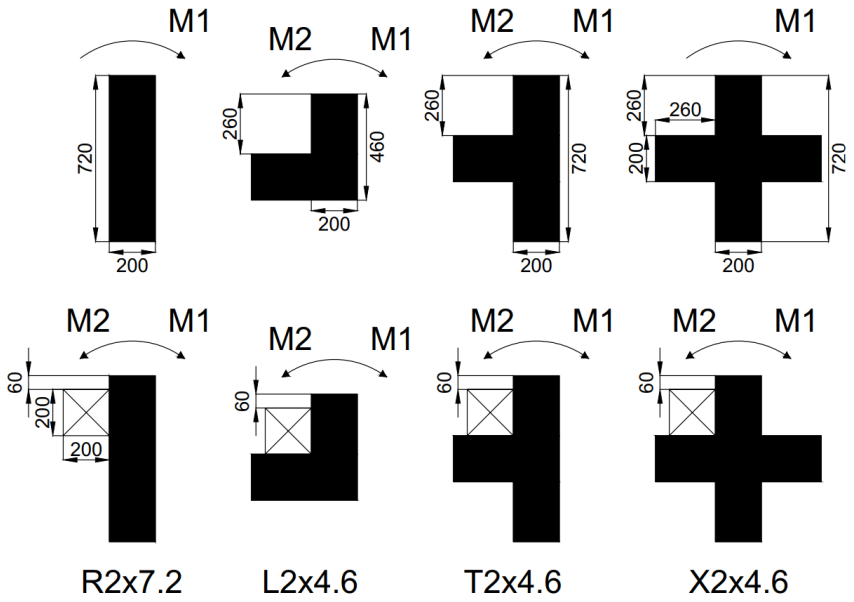


Figure 9-3: Overview of Column Sizes, Opening Layouts and Moment Directions Considered in SS-SCC Study – Combined Shear and Unbalanced Moment

For the connections subjected to V+M loading two moment directions are considered, as shown in Figure 9-3 (note, for the analyzed R-SCC and X-SCC without openings the results for the M1 and M2 directions are mirror images of one another, as the connections are doubly symmetric, so only the M1 direction is considered). For the specimens with openings, the moment directions correspond to an unbalanced moment which is applied away from the opening (M1) and towards the opening (M2), respectively. Based on previous experimental and numerical analysis of square or rectangular slab-column connections subjected to combined concentric shear and unbalanced moment [204, 210, 220], it is anticipated that the slab openings will have less of an impact on the connection behaviour and capacity when the moment is applied away from the opening (M1).

Furthermore, for the V+M specimens, two gravity shear ratios (GSRs) are considered. The lower level, denoted by a M at the end of the specimen ID (as outlined in Figure 9-2), corresponds to a GSR of 0.4, which is the allowable upper limit for connections without shear reinforcement according to ACI 318-19, as discussed in Section 2.3.2. While ACI 318 does not permit higher GSRs without shear reinforcement, a higher GSR of 0.55, denoted by an H at the end of the specimen ID, is also investigated. The choice to study the connection behaviour under a higher GSR instead of a lower one was made for two reasons. Firstly, it was desirable to study the connection behaviour under a more extreme situation. Secondly, as discussed in Sections 6.3, 8.3 and 9.3, the response predicted by the NLFEA is typically initially stiffer than that observed experimentally, with the predicted stiffness approaching that observed experimentally as the load increases. For low GSRs, the calibrated FEM will typically underpredict the influence of the concentric shear force, as shown in Section 9.3.2, which could lead to incorrect conclusions. Therefore, the choice to analyze the behaviour of R-SCCs and SS-SCCs when subjected to GSRs exceeding 0.4 was made.

Commonly, the GSR is defined as the ratio of the applied concentric load (gravity load) to the concentric punching capacity predicted by ACI 318. However, the punching capacities predicted by ACI 318-19 [2] for R-SCCs and SS-SCCs can be inaccurate, as previously shown in Chapter 7 and Chapter 8. Therefore, in this study, the GSR was defined as the ratio of the applied concentric load to the maximum concentric punching capacity of each connection predicted by the calibrated FEM. Additionally, it must be noted that the applied vertical load levels differ between the connections with and without openings. Since the connections with openings have a slightly lower concentric punching shear capacity, the applied vertical loads for the connections with openings subjected to V+M loading are also slightly lower (the vertical load levels for each specific connection are provided in Section 9.4.2) to maintain consistent GSRs between the specimens with and without openings.

The material properties and reinforcing details of the analyzed isolated slab-column connections are the same as those for specimen PD4 tested by Drakatos et al. [4] (the experimental program of Drakatos et al. [4] is summarized in Section 9.3.1). Therefore, the tensile and compressive flexural reinforcing ratios, ρ and ρ', respectively, are equal to 0.8% and 0.35%. The corresponding reinforcement on tension and compression sides of the slab (sides classified considering concentric load conditions) consists of 16mm diameter bars spaced at 125mm on center (o/c) in both directions and 10mm diameter bars spaced at 100mm o/c in both directions, respectively. Furthermore, the effective slab depth is 201mm, the steel yield strength is 507MPa, and the concrete compressive

strength is 39MPa. Analyses were not conducted for higher flexural reinforcement ratios to reduce the number of simulations and since these levels of flexural reinforcement are not representative of typical slabs in practice. It should also be noted that the additional edge reinforcement included in the experimental tests for connections subjected to combined shear and unbalanced moment (this reinforcement is also discussed in Section 9.3.1) was included in all specimens analyzed herein (other than PD7 and PD9 during the FEM calibration to match the experimental conditions [4]). The inclusion of the additional edge reinforcement in the concentric specimens was done to make the slab flexural reinforcement consistent between the V and V+M load cases (which differs from the experiments in [4]).

Finally, as was done in Chapter 8, small eccentricities between the column and slab centroids were introduced for the analyzed L-SCCs and T-SCCs to improve mesh uniformity. For the L2x4.6 connections the eccentricities in both the $\bar{x}$ and $\bar{y}$ directions are equal to -3mm. For the T2x4.6 connections, the eccentricities in the $\bar{x}$ and $\bar{y}$ directions are equal to -1mm and 0mm, respectively (see Figure 9-4 for an exaggerated view of the eccentricities and the axes used to define positive and negative eccentricity and Figure 9-5 for an overview of the analyzed specimens for all column geometries). While the FEA predicts the influence of these eccentricities to be minimal, these eccentricities were accounted for when calculating the specimen capacity according to ACI 421.1R-20 [5].

Summaries of the analyzed R-SCCs, L-SCCs, T-SCCs, and X-SCCs are provided in Table 9-1, Table 9-2, Table 9-3 and Table 9-4, respectively. In total, 8 RSSCs, 10 L-SCCs, 10 T-SCCs and 8 X-SCCs were analyzed.

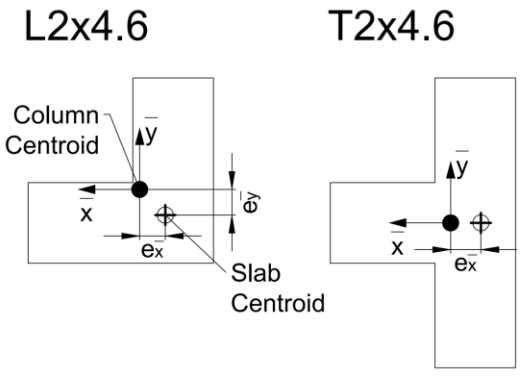


Figure 9-4: Exaggerated Eccentricities for L2x4.6 and T2x4.6 Connections (Location of Slab Centroid not Accurately Shown to Highlight Eccentricity)

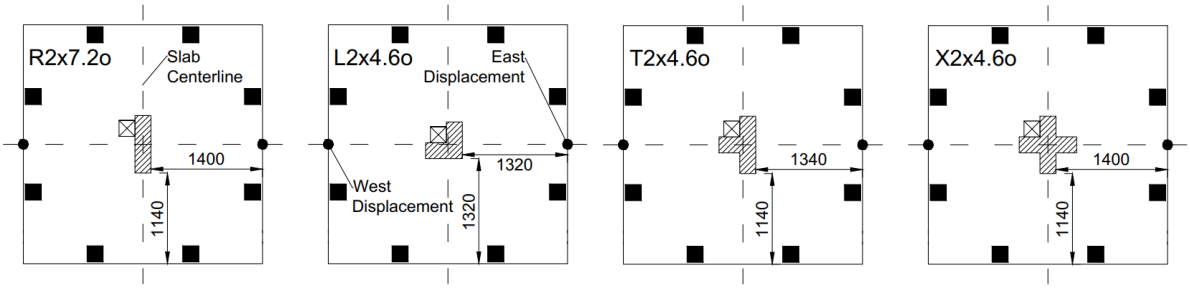


Figure 9-5: Column Location with Respect to Slab Centerlines for Connections Analyzed in Special-Shaped Connection Study – Combined Shear and Unbalanced Moment (Same Column Location for Specimens Without Openings)

Table 9-1: Overview of Analyzed R-SCCs – SS-SCC Study – Combined Shear and Unbalanced Moment

Specimen ID[a]	Load Type[b]	Opening[c]	GSR[d]	Moment Direction[e]
R2x7.2-V	V	N	-	-
R2x7.2o-V	V	Y	-	-
R2x7.2-M1-H	V+M	N	0.55	M1
R2x7.2-M1-M	V+M	N	0.4	M1
R2x7.2o-M1-H	V+M	Y	0.55	M1
R2x7.2o-M2-H	V+M	Y	0.55	M2
R2x7.2o-M1-M	V+M	Y	0.4	M1
R2x7.2o-M2-M	V+M	Y	0.4	M2

[a] See Figure 9-1 and Figure 9-2 for the breakdown of the specimen naming convention; [b] V: Concentric Shear Only, V+M: Combined Concentric Shear and Unbalanced Uniaxial Moment; [c] N: no opening, Y: one 200x200mm square opening (see Figure 9-3 for location); [d] Gravity Shear Ratio, defined as $V_{applied}/V_{FEA}$, for V+M opening specimens, V_{FEA} based on V specimen with opening; [e] See Figure 9-3 for moment direction, for R-SCC specimens without openings M1 and M2 results would be the same, so only M1 considered; Note: f_c'=39.0MPa, d=201mm, ρ=0.80%

Table 9-2: Overview of Analyzed L-SCCs – SS-SCC Study – Combined Shear and Unbalanced Moment

Specimen ID[a]	Load Type[b]	Opening[c]	GSR[d]	Moment Direction[e]
L2x4.6-V	V	N	-	-
L2x4.6o-V	V	Y	-	-
L2x4.6-M1-H	V+M	N	0.55	M1
L2x4.6-M2-H	V+M	N	0.55	M2
L2x4.6-M1-M	V+M	N	0.4	M1
L2x4.6-M2-M	V+M	N	0.4	M2
L2x4.6o-M1-H	V+M	Y	0.55	M1
L2x4.6o-M2-H	V+M	Y	0.55	M2
L2x4.6o-M1-M	V+M	Y	0.4	M1
L2x4.6o-M2-M	V+M	Y	0.4	M2

[a] See Figure 9-1 and Figure 9-2 for the breakdown of the specimen naming convention; [b] V: Concentric Shear Only, V+M: Combined Concentric Shear and Unbalanced Uniaxial Moment; [c] N: no opening, Y: one 200x200mm square opening (see Figure 9-3 for location); [d] Gravity Shear Ratio, defined as $V_{applied}/V_{FEA}$, for V+M opening specimens, V_{FEA} based on V specimen with opening; [e] See Figure 9-3 for moment direction; Note: f_c'=39.0MPa, d=201mm, ρ=0.80%

Table 9-3: Overview of Analyzed T-SCCs – SS-SCC Study – Combined Shear and Unbalanced Moment

Specimen ID[a]	Load Type[b]	Opening[c]	GSR[d]	Moment Direction[e]
T2x4.6-V	V	N	-	-
T2x4.6o-V	V	Y	-	-
T2x4.6-M1-H	V+M	N	0.55	M1
T2x4.6-M2-H	V+M	N	0.55	M2
T2x4.6-M1-M	V+M	N	0.4	M1
T2x4.6-M2-M	V+M	N	0.4	M2
T2x4.6o-M1-H	V+M	Y	0.55	M1
T2x4.6o-M2-H	V+M	Y	0.55	M2
T2x4.6o-M1-M	V+M	Y	0.4	M1
T2x4.6o-M2-M	V+M	Y	0.4	M2

[a] See Figure 9-1 and Figure 9-2 for the breakdown of the specimen naming convention; [b] V: Concentric Shear Only, V+M: Combined Concentric Shear and Unbalanced Uniaxial Moment; [c] N: no opening, Y: one 200x200mm square opening (see Figure 9-3 for location); [d] Gravity Shear Ratio, defined as $V_{applied}/V_{FEA}$, for V+M opening specimens, V_{FEA} based on V specimen with opening; [e] See Figure 9-3 for moment direction; Note: f_c'=39.0MPa, d=201mm, ρ=0.80%

Table 9-4: Overview of Analyzed X-SCCs – SS-SCC Study – Combined Shear and Unbalanced Moment

Specimen ID[a]	Load Type[b]	Opening[c]	GSR[d]	Moment Direction[e]
X2x4.6-V	V	N	-	-
X2x4.6o-V	V	Y	-	-
X2x4.6-M1-H	V+M	N	0.55	M1
X2x4.6-M1-M	V+M	N	0.4	M1
X2x4.6o-M1-H	V+M	Y	0.55	M1
X2x4.6o-M2-H	V+M	Y	0.55	M2
X2x4.6o-M1-M	V+M	Y	0.4	M1
X2x4.6o-M2-M	V+M	Y	0.4	M2

[a] See Figure 9-1 and Figure 9-2 for the breakdown of the specimen naming convention; [b] V: Concentric Shear Only, V+M: Combined Concentric Shear and Unbalanced Uniaxial Moment; [c] N: no opening, Y: one 200x200mm square opening (see Figure 9-3 for location); [d] Gravity Shear Ratio, defined as $V_{applied}/V_{FEA}$, for V+M opening specimens, V_{FEA} based on V specimen with opening; [e] See Figure 9-3 for moment direction, for X-SCC specimens without openings M1 and M2 results would be the same, so only M1 considered; Note: f_c'=39.0MPa, d=201mm, ρ=0.80%

9.3 FEM Calibration

The FEM used in Chapter 8 was calibrated to the experimental results of concentric punching shear tests of square and rectangular slab-column connections by Hawkins et al. [3]. However, since these specimens only have flexural reinforcement on the tension side of the slab (under concentric loading), the calibrated FEM from Chapter 8 is not suitable for the analysis of connections subjected to combined concentric shear and unbalanced moment. Therefore, a new calibrated FEM was needed in order to study the punching shear behaviour of R-SCCs and SS-SCCs subjected to combined concentric shear and uniaxial unbalanced moment.

As will be discussed, the FEM was calibrated to the experimental results of the PD series. The PD series, which was tested by Drakatos et al. [4], and is briefly summarized in the next section, was focused on studying the punching shear behaviour of square slab-column connections under combined concentric shear and uniaxial unbalanced moment. Since the slabs in the PD [4], AM [151] and PT [57] series have the same overall dimensions and vertical load application method, the calibrated FEM used in the analysis of elongated connections (Chapter 6) served as the basis for the calibrated FEM used herein. As will be discussed, most of the parameters of the calibrated FEM are identical to those used in the FEM in Chapter 6, with only modifications to the boundary conditions

and timestep used in the explicit analysis being required to accurately predict the response of the PD series slabs.

9.3.1 Summary of Experimental Specimens Considered in Calibration

Drakatos et al. [4] tested thirteen square slab-column connections. Of these thirteen specimens, two (PD7 and PD9) were subjected to concentric vertical load only (V only), six (PD1, PD3, PD4, PD5, PD10 and PD12) were subjected to combined concentric vertical load and monotonically increasing uniaxial moment (V+M (monotonic)) and five (PD2, PD6, PD8, PD11 and PD13) were subjected to combined concentric vertical load and cyclically increasing uniaxial unbalanced moment (V+M (cyclic)). As shown in Figure 9-6, the slabs were 3000mm square in plan, 250mm thick and supported by a 390mm square column (which was simulated by steel plates) [4].

As previously discussed, experimental programs focused on the behaviour of SS-SCCs subjected to combined concentric vertical load and unbalanced moment are very limited [176]. Therefore, the decision was made to focus on the punching shear behaviour of SS-SCCs subjected to concentric vertical load and monotonically increasing unbalanced moment only, as this behaviour should be studied in depth before considering cyclically applied unbalanced moments. Therefore, only the two specimens subjected to concentric vertical load only and the six specimens subjected to combined concentric vertical load and monotonically increasing unbalanced moment, which are summarized in Table 9-5, were considered in the FEM calibration.

In addition to the load conditions, the eight slabs considered in the calibration vary with respect to the top (tensile side under concentric loading for the experimental setup) flexural reinforcement ratio, bottom (compressive side under concentric loading for the experimental setup) flexural reinforcement ratio, vertical load levels (for the V+M (monotonic) specimens) and material properties (the concrete compressive strengths and yield strengths of the flexural reinforcement for each specimen are summarized in Table 9-5). Two top flexural reinforcement ratios (ρ), approximately 0.8% and 1.6%, and two bottom flexural reinforcement ratios (ρ'), approximately 0.35% and 0.75%, were considered. For the specimens where ρ and ρ' were equal to approximately 0.8% and 0.35%, respectively, the steel reinforcement at the top and bottom surfaces of the slab consisted of 16mm diameter bars spaced at 125mm o/c in both directions and 10mm diameter bars spaced at 100mm o/c in both directions, respectively (note, this is the same reinforcement used in the analyses discussed in Sections 9.3.3 and 9.4). For the specimens where ρ and ρ' were equal to approximately 1.6% and 0.75%, respectively,

the steel reinforcement at the top and bottom surfaces of the slab consisted of 20mm diameter bars spaced at 100mm in both directions and 14mm diameter bars spaced at 100mm in both directions, respectively. It should be noted that for all specimens subjected to combined concentric vertical load and unbalanced moment that the rebar layers with the largest level arms were positioned perpendicularly to the unbalanced moment vector [4]. The vertical load levels were defined in terms of the GSR, which for the experimental specimens, was equal to the ratio of the applied vertical force to the concentric punching capacity predicted by ACI 318-19 (using a critical perimeter with ninety-degree corners), and varied from 0.26-0.85 for the analyzed specimens.

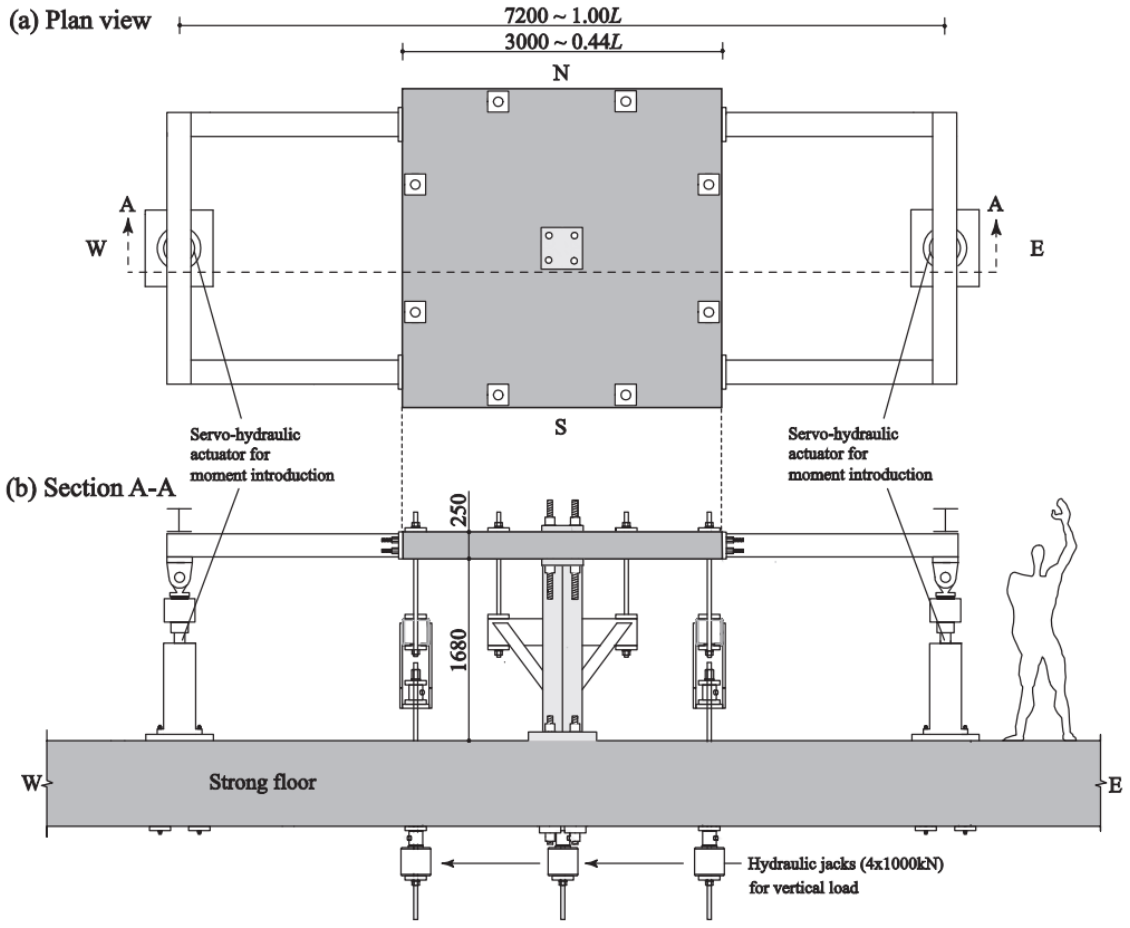


Figure 9-6: Overview of Drakatos et al. [4] Experimental Setup for Slabs Subjected to Combined Concentric Shear and Unbalanced Moment, a) Plan View; b) Section A-A; Reprinted from Engineering Structures, 123, Drakatos, Muttoni and Beyer, Internal Slab-Column Connections Under monotonic and cyclic imposed rotations, 501-516, Copyright (2016), with permission from Elsevier

Table 9-5: Summary of Experimental Specimens (Concentric Shear Only [V Only] and Combined Concentric Shear and Monotonic Uniaxial Unbalanced Moment [V+M (Monotonic)]) Tested by Drakatos et al. [4]

Load Type	Slab	V_{test} (kN)	GSR	f_c' (MPa)	f_y (MPa)	ρ (%)	ρ' (%)	d (mm)
V only	PD7	983	-	39.2	507	0.80	0.35	200
	PD9	1040	-	34.3	593	1.61	0.74	195
V+M (monotonic)	PD1	253	0.26	37.9	559	0.79	0.35	204
	PD4	376	0.38	39.0	507	0.80	0.35	201
	PD5	517	0.55	37.5	507	0.81	0.35	198
	PD3	734	0.81	34.9	558	0.81	0.34	198
	PD12	517	0.58	35.5	546	1.61	0.72	195
	PD10	734	0.85	32.3	593	1.60	0.72	197

Note: maximum aggregate size of 16mm for all slabs; nominal cover of 20mm for both bottom and top reinforcing mats; GSR defined as ratio of applied vertical load (V_{test}) to concentric punching capacity predicted by ACI 318-19 (using a critical perimeter with ninety-degree corners)

The experimental boundary conditions for the specimens subjected to combined vertical loading and uniaxial unbalanced moment are shown in Figure 9-6 and Figure 9-7. In the tests, the supporting column was simulated by steel plates which were post-tensioned to the slab before loading was applied. The plates were post-tensioned to the slab to limit the separation of the slab and support plates [4], which differs from the PT [57] and AM [151] series, where the slabs were free to lift. Vertical loading was applied to the slab through eight steel load plates located at a radius of 1.504m around the column (approximately *0.22L*, where *L* is the slab span in the prototype structure considered by Drakatos et al. [4]), as shown in Figure 9-6. The loading was applied using a force-controlled procedure (for the V only specimens the load was increased until failure) [4] (note, in all simulations herein the vertical load plates were located at a radius of 1.5m to match the AM [151] and PT [57] series specimens as Drakatos et al. [4] did not provide the exact plate locations). For the specimens subjected to combined concentric vertical loading and unbalanced moment, the vertical load was applied first. After reaching the desired vertical load level, the unbalanced moment was introduced by applying equal and opposite forces (the lever arm of the couple forces was 7.2m as shown in Figure 9-6) to steel arms which were connected to the concrete slab. Due to this method of applying unbalanced moment, four 30mm diameter threaded steel bars (f_y=754MPa) were provided at each of the two slab edges parallel to section A-A in Figure 9-6. This additional edge

reinforcement, which is shown in Figure 9-8, was necessary to connect both the concrete slab and the steel arms used to the apply the unbalanced moment, but also to avoid the formation of global mechanisms which are not representative of the connection behaviour in a continuous structure [4, 107].

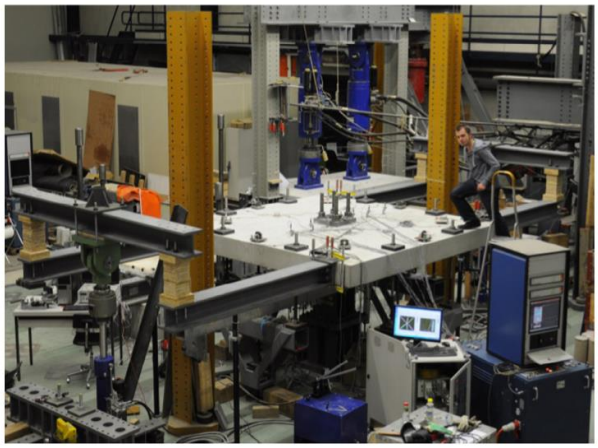


Figure 9-7: Example of Specimen Subjected to Combined Concentric Shear and Unbalanced Moment in Test Setup [4]; Reprinted from Engineering Structures, 123, Drakatos, Muttoni and Beyer, Internal Slab-Column Connections Under monotonic and cyclic imposed rotations, 501-516, Copyright (2016), with permission from Elsevier

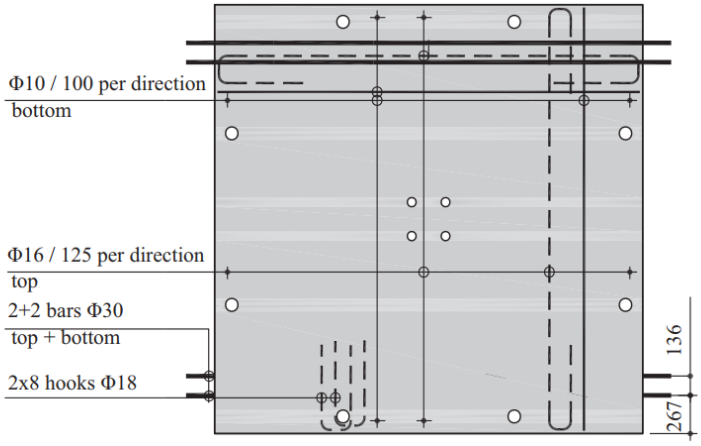


Figure 9-8: Overview of Reinforcement for Slabs Where ρ is approximately equal to 0.8% [4]; Reprinted from Engineering Structures, 123, Drakatos, Muttoni and Beyer, Internal Slab-Column Connections Under monotonic and cyclic imposed rotations, 501-516, Copyright (2016), with permission from Elsevier

9.3.2 Summary of FEM Calibration

In addition to having the same specimen geometry and similar vertical load conditions to the AM [151] and PT [57] series slabs, the PD [4] series slabs also have similar material properties and amounts of flexural reinforcement as shown in Table 9-6. The similarities between the specimens suggest that the calibrated FEM used herein should be similar to that used in the slab wall study (Chapter 6), though some changes, at a minimum to the boundary conditions, are required due to the introduction of the unbalanced moment. Therefore, the first step in the FEM calibration was to verify that the input parameters of the CDP model, which are summarized in Table 9-7 and are based on those from the FEM used in Chapter 6, applied to the PD specimens. Note, as done in Chapter 6 and Chapter 8, the post-peak response of the Hognestad parabola was terminated at a stress level of approximately $0.4f_c'$). Additionally, as commonly assumed in the analysis of cracked concrete, and consistent with the FEMs in Chapter 6, a value of 0 was used for the concrete's Poisson ratio.

To verify the applicability of the CDP model input parameters, slabs PD7 and PD9, which were subjected to concentric vertical loading only, were simulated first. As done in Chapter 6, quarter models were used in the analyses of these specimens to take advantage of symmetry. However, unlike Chapter 6, where the load and support plates were modelled as separate parts and the interaction between the slab and the plates was modelled with contacts, in Chapter 9, the load and support plates (and the steel arms used to introduce the moment for the V+M (monotonic) specimens) were extruded from the slab geometry. This change was made for two reasons. Firstly, removing the contacts simplifies the modelling and significantly reduces the required computational resources by reducing the number of variables in the analysis. Secondly, unlike the AM [151] and PT [57] series slabs, where the slab was free to lift off the supporting plate [26, 151], the supporting plates in the PD series [4] were post-tensioned to the slab surface, which prevented separation of the slab and supports.

The boundary conditions used in the analysis of the concentrically loaded specimens (PD7 and PD9) are shown in Figure 9-9 (the boundary conditions for the concentrically loaded specimens discussed in Sections 9.3.3 and 9.4 are the same as those shown in Figure 9-9, other than the removal of the symmetry boundary conditions due to the use of half and full models, respectively). As shown in Figure 9-9, a fixed boundary condition was applied to the top and bottom of the supporting plates. This boundary condition was assumed to match previous NLFEA of the PD specimens by Setiawan et al. [98] (though it should be noted that the rotational degrees of freedom are inactive for C3D8R elements in Abaqus).

Table 9-6: Comparison of Specimens Tested by Sagaseta et al. [57, 151] and Drakatos et al. [4] Considered in FEM Calibrations

Parameter	Experimental Specimens from Literature		
	PT22, PT31 and PT32 [57]	AM Series [151]	PD Series [4]
f_c' (MPa)	40.0-67.0	39.7-44.6	32.3-39.2
d (mm)	196-215	202-214	195-204
ρ (%) [(a)]	0.75-1.48	0.75	0.79-1.61
f_y (MPa) [(b)]	540-558	516	507-593
$c_{max} \times c_{min}$ (mm)	260x260	780x260	390x390

[(a)] Only average flexural reinforcement ratio reported for AM series slabs; [(b)] yield strength of flexural reinforcement on tension surface of slab under concentric loading

Table 9-7: Summary of Concrete Material Parameters in Calibrated FEM in Chapter 9

Calibrated Model – Concrete Specific Parameters		
Material Model – Concrete Damaged Plasticity Dilation Angle – 45° Eccentricity* – 0.1 σ_{bo}/σ_{co}* – 1.16 Damage Parameters – N.A.	Uniaxial Compression Model – Hognestad Parabola $E_c = 5000\sqrt{f_c'}$ (31225MPa for all simulations in Sections 9.3.3 and 9.4) Poisson's Ratio (ν) – 0 Tension Model – Bilinear tensile stress-crack width/displacement [327] G_f – Calculated according to Model Code 1990 [159] (0.0865N/mm for all simulations in Section s 9.3.3 and 9.4)	Element Size – 20mm Element Type – C3D8R *Abaqus Default Value

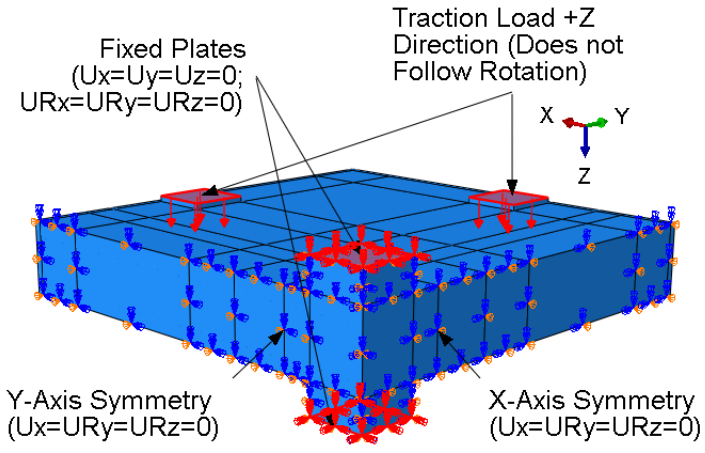


Figure 9-9: Boundary Conditions Used in FEM Calibration for Concentrically Loaded PD Specimens

Before presenting the results of the FEM calibration, it should be noted that Drakatos et al. [4] provided the experimental data in terms of load-connection rotation (concentric specimens), or moment-connection rotation (V+M (monotonic) specimens), instead of load-displacement or moment-displacement. For the concentrically loaded specimens, the connection rotation is calculated using equation 9-1, using the small angle assumption and assuming the deflection profile of the slab to be approximately linear (this assumption was found to apply to the NLFEA results as well)

$$\psi = \frac{\Delta}{[L_{iso}/2 - c/2]} \quad \text{9-1}$$

where Δ is the vertical deflection of the slab edge (mm), L_{iso} is the isolated specimen length (mm) and c is the column dimension in the same direction the rotation is being calculated (mm). Note, for the concentrically loaded experimental specimens the reported rotations are equal to the average rotation of the two locations shown in Figure 9-10 (averaging is not necessary in the FEA since the results are perfectly symmetric).

For the specimens subjected to combined concentric load and uniaxial unbalanced moment, the connection rotation is calculated according to equation 9-2

$$\psi_{scc} = \frac{(\psi_{max} - \psi_{min})}{2} - \psi_{col} \quad \text{9-2}$$

where ψ_{max} and ψ_{min} are the maximum and minimum connection rotations, respectively, and ψ_{col} is the column rotation [4]. Note, ψ_{max} and ψ_{min} were calculated using equation 9-1, considering the predicted deflections at the two locations shown in Figure 9-10 and ψ_{col} is equal to 0 in the FEA since the top and bottom support plates were fixed [98]. Note, in the experiments, ψ_{max} and ψ_{min} were calculated based on the measured deflections at points located at approximately 1380mm from the column centroid [4] instead of the slab edge (therefore the denominator of equation 9-1 is replaced with 1380-*c*/2). However, in the FEA, the deflections at the slab edge (1500mm from the column centroid) were used to calculate ψ_{max} and ψ_{min} for simplicity (a similar discussion also applies to the rotations for the concentrically loaded specimens). The influence of these different measurement locations on the rotation values was very minor, since the deflection profile of the slab in the FEA was approximately linear.

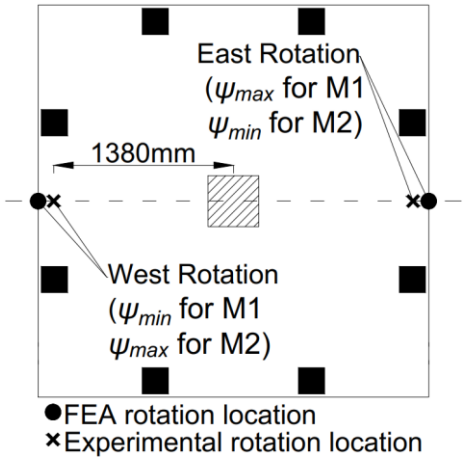


Figure 9-10: Rotation Output Locations Considered in Chapter 9

A comparison of the predicted and experimentally measured (experimental data is approximated from the plots in [4]) load-rotation responses for PD7 and PD9 is provided in Figure 9-11. As seen in Figure 9-11, the calibrated FEM accurately predicts the capacity and rotation at failure for both specimens (a summary of the experimental and numerical results is provided in Table 9-8). However, as was observed during the analysis of the AM [151] and PT [57] series slabs, the response predicted by the FEA is initially stiffer than that measured experimentally, though the stiffness predicted by the FEA does approach the experimental value as the load increases. The influence of numerous parameters including the parameters of the Hognestad Parabola (upper bound of the initial linear elastic region, initial stiffness and tangent stiffness), assumed concrete tensile strength, CDP model parameters (specifically ϵ, K_c and σ_{bo}/σ_{co}) and the concrete fracture energy (G_f) on the predicted initial stiffness was investigated. However, the influence of these parameters on the predicted initial stiffness was minor, or resulted in inaccurate predictions for higher load levels. Therefore, no changes to the calibrated FEM parameters were made to improve the agreement between the FEM predictions and experimental results for low load levels.

In Figure 9-11, the predictions based on a dynamic/explicit (quasi-static) analysis in Abaqus/Explicit and a general/static (implicit) analysis in Abaqus/Standard are also compared (note, in all static analyses presented herein a viscosity parameter, μ, of $1x10^{-5}$ was used based on recommendations by Genikomsou and Polak [25]). As seen in Figure 9-11, the results from explicit and implicit analyses agree well until the peak load predicted by the explicit analysis, regardless of the analysis timestep length in Abaqus/Explicit. Note, because force-based tractions were used to apply the vertical loads to the slab, as shown in Figure 9-9, the load in the static analysis will continue

to increase until the end of the analysis. Due to the agreement between the explicit and implicit results, and an analysis of the energy balance within the explicit FEAs, it can be concluded that the analysis in Abaqus/Explicit is indeed quasi-static, and accurately represents the behaviour of the concentrically loaded PD specimens. It should be noted that in all analyses presented in this chapter, and in the remainder of this thesis, the analysis timestep length of the vertical load application step was equal to 1s (as this significantly reduces the required computational resources compared to longer timesteps and did not influence the results significantly).

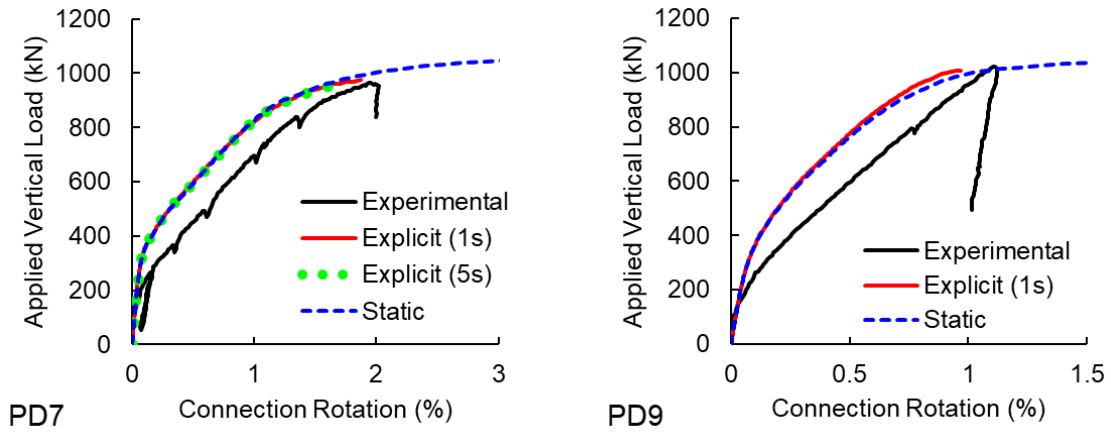


Figure 9-11: Comparison of Predicted and Measured Vertical Load-Rotation Responses for Concentrically Loaded Specimens, Experimental Responses Approximated from Plots in [4]

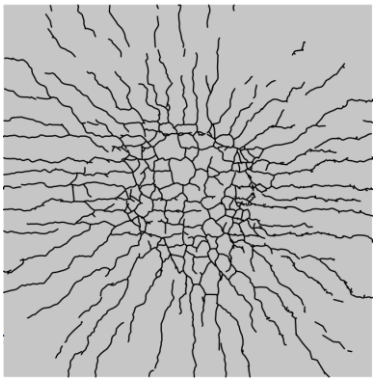
In addition to the predicted load-connection rotation response, the predicted tension surface crack patterns were also analyzed. For both PD7 and PD9, the crack patterns predicted by the FEA agreed well with those from the experiments (a comparison of the predicted and measured tension surface crack patterns for PD9, which is representative of both concentrically loaded specimens, is provided in Figure 9-12). For both specimens, cracking perpendicular to each column face and diagonal cracking extending from the column corners to the slab corners were predicted, which matches the experimental observations. Therefore, based on the comparisons of the load-connection rotation responses and tension surface crack patterns, it was concluded that the material properties of the FEM, originally calibrated to the results of the AM [151] and PT [57] series (as discussed in Chapter 6) were also applicable to the analysis of the PD specimens [4].

Table 9-8: Summary of Experimental and FEA Results for Selected PD [4] Specimens

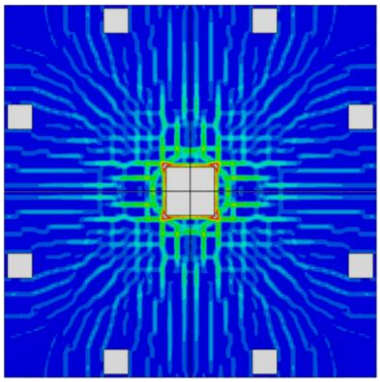
			Concentric Capacity, V (kN)			Connection Rotation, $\psi_{scc,max}$ (%)		
	Slab	Exp.	FEA	$\frac{V_{exp}}{V_{FEA}}$	Exp.	FEA	$\frac{Exp}{FEA}$
V Only	PD7	983	976.5	1.01	1.96	1.87	1.05
	PD9	1040	1006.3	1.03	1.11	0.97	1.15
			Avg.	1.02		Avg.	1.10

				Moment Capacity, M (kNm)			Connection Rotation, $\psi_{scc,max}$ (%)		
	Slab	V_{test} (kN)	GSR	Exp.	FEA	$\frac{M_{exp}}{M_{FEA}}$	Exp.	FEA	$\frac{Exp}{FEA}$
V+M (monotonic)	PD1	253	0.26	525	523.2	1.00	[a]	2.000	-
	PD4	376	0.38	527	471.5	1.12	2.01	1.675	1.200
	PD5	517	0.55	462	387.8	1.19	2.19	1.561	1.403
	PD3	734	0.81	200	197.5	1.01	0.45	0.875	0.514
	PD12	517	0.58	469	440.3	1.07	1.21	0.945	1.281
	PD10	734	0.85	290	284.4	1.02	0.49	0.693	0.707
					Avg.	1.07		Avg.[b]	1.021

[a] Inconsistent rotation measurements during the experiment; [b] not including PD1; Note: Length of vertical load application step (1s) in all simulations



Experimental



NLFEA

Figure 9-12: Comparison of Tension Surface Crack Pattern Experimentally Observed and Predicted by Calibrated FEM, Concentrically Loaded Specimen with High Flexural Reinforcement Ratio (PD9); Experimental Crack Pattern Reprinted from Engineering Structures, 123, Drakatos, Muttoni and Beyer, Internal Slab-Column Connections Under monotonic and cyclic imposed rotations, 501-516, Copyright (2016), with permission from Elsevier

However, before proceeding with the analysis of SS-SCCs subjected to combined concentric load and uniaxial unbalanced moment, the applicability of the calibrated FEM to the V+M (monotonic) PD specimens needed to be investigated. The boundary conditions used in the analysis of the V+M (monotonic) PD specimens (and the specimens in the calibration verification study discussed in Section 9.3.3) are shown in Figure 9-13. Note, the boundary conditions used in the parametric study discussed in Sections 9.2 and 9.4, shown in Figure 9-14, are the same as those shown in Figure 9-13, other than the removal of the symmetry boundary conditions due to the use of full slab specimens. The use of full slab specimens was required due to the nonsymmetric opening layouts. As previously discussed, the steel arms used to apply the unbalanced moment were extruded from the slab geometry in the FEM (similarly to the steel load and support plates). Since the dimensions of these steel arms were not provided by Drakatos et al. [4] or Setiawan et al. [98], the size of the steel arms was assumed. It should be noted that the assumed steel arm size was found to have a minimal influence on the FEA results.

Since the concentric load and unbalanced moment in the FEM were introduced using force-based tractions and pressures, respectively, the V+M (monotonic) PD specimens were also analyzed in Abaqus/Explicit (with Abaqus/Standard again used to verify the results). In these initial analyses, which were conducted for all six V+M (monotonic) specimens, the analysis timestep length for both the vertical load and unbalanced moment application steps was set to 1s. Also, in these initial analyses, the unbalanced moment was introduced through two equal and opposite tractions which did not follow the specimen rotation, instead of pressures which do follow the rotation as shown in Figure 9-13. The use of traction loads which do not follow the specimen rotation to introduce the unbalanced moment is problematic as the moment arm between the couple forces is unknown. Furthermore, in the experimental setup (see Figure 9-7) the actuators used to introduce the couple forces were connected to the steel arms via pins. As such, it was concluded that the use of pressure loads, which follow the specimen rotation, was a more accurate representation of the experimental boundary conditions. However, due to the long run time of the analyses presented herein, the initial simulations, based on analysis timestep lengths of 1s were not repeated using pressure loads to apply the unbalanced moment.

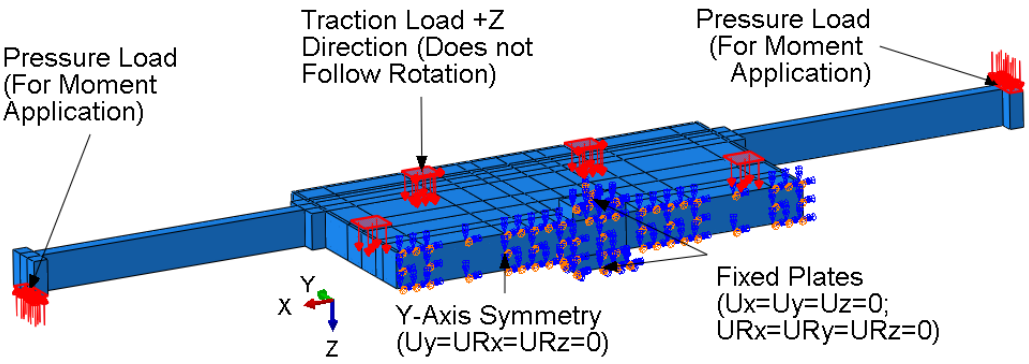


Figure 9-13: Boundary Conditions Used in FEM Calibration for PD Specimens Subjected to Combined Concentric Loading and Uniaxial Unbalanced Moment (Monotonic Moment)

A comparison of the experimental and initial numerical predictions from the dynamic/explicit analysis in Abaqus/Explicit (1s analysis timestep length) and the general/static analysis in Abaqus/Standard for specimen PD1, which is representative of the trend for all six specimens, is provided in Figure 9-15a. It should be noted that the moments for the FEA results in Figure 9-15a are approximations as they were calculated assuming a constant moment arm of 7.2m, which is incorrect for traction loads. As expected, the results from Abaqus/Explicit and Abaqus/Standard generally agreed well for most of the analysis. However, as shown in Figure 9-15a, the predictions from Abaqus/Explicit begin to deviate significantly from Abaqus/Standard predictions near the occurrence of failure (occurrence of failure determined by Abaqus/Explicit since the load/moment will continually increase in Abaqus/Standard).

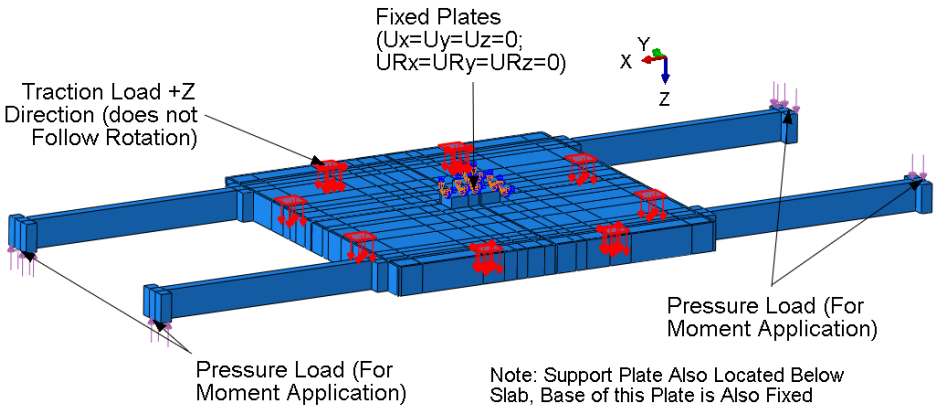


Figure 9-14: Representative Boundary Conditions Used in Special-Shaped Slab-Column Connection Study – Combined Shear and Unbalanced Moment (M1 Direction Shown, Pressure Loads Modified for M2 Direction)

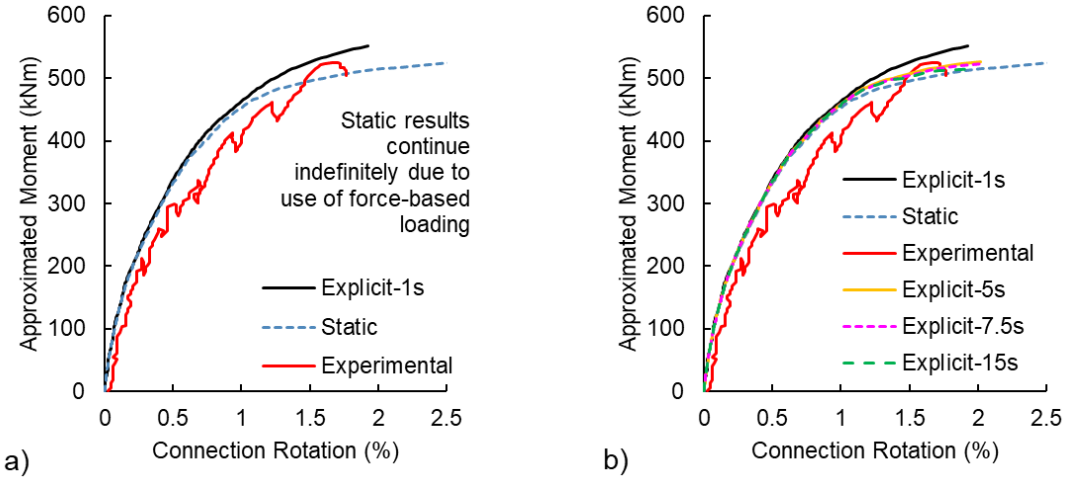


Figure 9-15: Comparison of Predicted and Measured Moment-Rotation Responses for PD1, Experimental Responses Approximated from Plots in [4]

The cause of the discrepancy between the Explicit and Standard results was initially unknown. Numerous parameters, such as bulk viscosity (which is a parameter of the explicit analysis step in Abaqus; default values used for all simulations presented in this thesis), hourglass controls (element property; defaults used for all simulations presented in this thesis), load amplitude definition (ramp function used for all analyses herein) and increment size (property of static analysis step in Abaqus) were investigated, but found to have a minimal influence. However, increasing the analysis timestep length of the moment application step was found to significantly decrease the difference between Explicit and Standard predictions, as shown in Figure 9-15b (note, in all simulations shown in Figure 9-15b traction loads which do not follow the slab rotation are used to apply the unbalanced moment). A summary of the predicted peak moments, connection rotations at failure and runtimes for the Abaqus/Explicit and Abaqus/Standard simulations for specimen PD1 is provided in Table 9-9. As seen in Table 9-9, the simulation runtime significantly increases as the analysis timestep length increases, but the predicted moment capacity and connection rotation at failure begin to approach approximately constant values. Therefore, there is a trade-off between simulation runtime and accuracy. Based on the results presented in Figure 9-15b and Table 9-9, an analysis timestep length of 7.5s for the moment application step (note, a 1s timestep is still used for the vertical load application step) was selected for the calibrated FEM (and all V+M simulations presented in Sections 9.3.3 and 9.4), as it significantly reduced the difference between the Explicit and Standard results, while maintaining a similar runtime to the Standard simulation (though Abaqus/Standard cannot predict failure due to the use of force-based loads).

Table 9-9: Comparison of Predictions for PD1 From Explicit and Static Analyses (Timestep of Moment Application Step Varied for Explicit Analyses)

Analysis Type	Timestep Length (s)	M_{FEA} (kNm)[a]	% Difference[b]	ψ_{scc} (%)	% Difference[b]	Runtime (hours)
Explicit	1	552.0	-	1.926	-	10.6
	5	526.1	-4.69	2.019	+4.82	31.3
	7.5	523.2	-5.21	2.033	+5.53	43.8
	10	520.4	-5.72	2.057	+6.78	56.5
	15	514.6	-6.77	1.980	+2.77	80.0
Static[c]	-	-	-	-	-	43.1

[a] Reported moment values are approximate since exact magnitude of moment arm is unknown due to use of tractions in place of pressure loads in initial simulations; [b] % difference calculated with respect to results for Explicit analysis with 1s timestep [c] Due to the use of force-based loading static analysis cannot be used to predict failure mode directly, reported runtime is that for the analysis to achieve the capacity predicted by Explicit analysis (1s timestep)

Comparisons of the moment-connection rotation responses for all six V+M (monotonic) specimens measured experimentally and predicted using the calibrated FEM (analysis timestep lengths of 1s and 7.5s for the vertical load and moment application steps, respectively, and pressure loads to apply the unbalanced moments; legend entry "Explicit-7.5s" in Figure 9-16) are provided in Figure 9-16 (comparisons to the FEA results of Setiawan et al. [98] are also provided for reference where available). For the specimens where the GSR is less than or equal to 0.6 (PD1, PD4, PD5 and PD12), the agreement between the FEA predictions and experimental results is generally quite good. As will be discussed, the calibrated FEM accurately predicts the unbalanced moment capacity of each specimen, though the connection rotation at failure is generally underpredicted. Additionally, for the specimens where the GSR is less than or equal to 0.6, the predictions from Abaqus/Explicit and Abaqus/Standard are also quite similar for most of the specimens. However, as seen for PD4, the Explicit results do deviate slightly from the Standard results in some cases just before the onset of failure (with the Explicit simulations predicting slightly lower deflections for the same moment magnitude). The slight deviation between the Explicit and Standard results suggests that the timestep length for the moment application step should be slightly longer, but the small increase in simulation accuracy is not justified by the large increase in runtime.

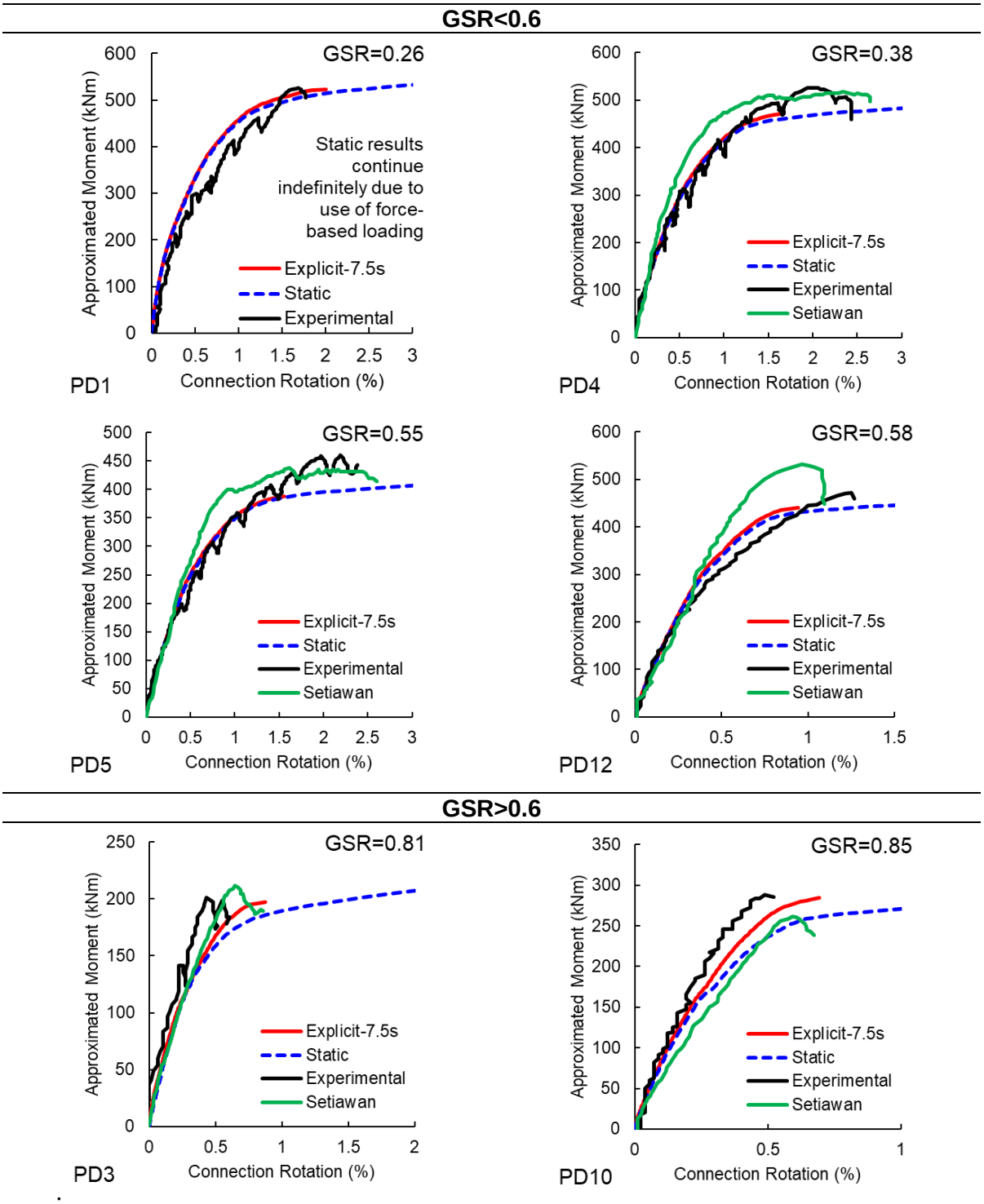


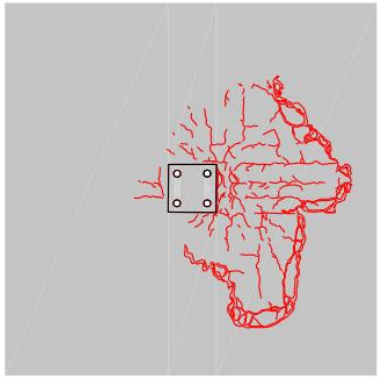
Figure 9-16: Comparison of Predicted and Measured Moment-Rotation Responses for Specimens Subjected to Combined Concentric Shear and Unbalanced Moment, Finalized Calibrated FEM, Experimental Responses Approximated from Plots in [4]

For the specimens where the GSR exceeds 0.6 (PD3 and PD10), the deviation between the Explicit and Standard results is larger. The cause of this deviation is unknown, and increasing the analysis timestep length (step lengths up to 12.5s were investigated) did not significantly reduce the difference between the Explicit and Standard predictions. It should be noted that some of the deviation could be due to errors in the Standard analyses as the results in Abaqus/Standard are dependent on the inputted viscosity parameter in the CDP model, which was not calibrated in this work. However, as previously mentioned, ACI 318-19 [2] does not allow connections to be subjected to such high GSRs without the inclusion of shear reinforcement, and therefore, it was decided that the calibrated FEM was adequate, even with the deviation between the Explicit and Standard results for the specimens with high GSRs (GSR > 0.8). It should also be noted that even with the deviation between the Explicit and Standard predictions, the trends for the high GSR specimens predicted by the calibrated FEM match those from the experiments (for example, significantly lower moment and connection rotation capacity). Additionally, an analysis of the energy balance suggests that the Explicit analyses for all V+M (monotonic) specimens are quasi-static until the onset of failure.

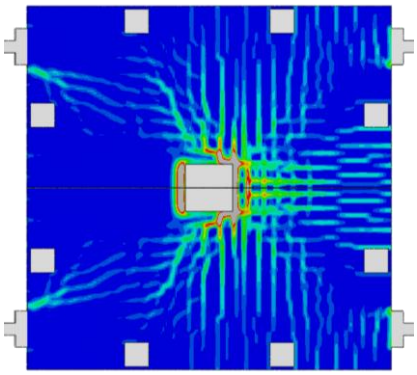
Representative comparisons of the predicted and measured tension surface crack patterns for the specimens with low ($\rho \approx 0.8\%$) and high ($\rho \approx 1.6\%$) flexural reinforcement ratios are provided in Figure 9-17 and Figure 9-18, respectively. Overall, the crack patterns predicted at failure agree well with those recorded experimentally. For all specimens, the overall extent and shape of the cracking are similar between the FEA and experiments. It should be noted that the FEA underpredicts the amount of cracking which occurs due to the application of the concentric load, particularly for the specimens where the GSR is less than approximately 0.4. This was expected since the initial response predicted by the FEA is stiffer than that observed experimentally.

Comparisons of the interior crack patterns parallel to the direction of the applied moment for the specimens whose ρ is approximately equal to 0.8% are provided in Figure 9-19. As with the tension surface crack patterns, the FEA predicts crack patterns which agree well with the experimental results. For the specimens where the GSR is less than approximately 0.6, a punching cone is predicted on the side of the column where the shear stresses due to the concentric load and unbalanced moment are additive. Only for PD3, where the GSR exceeds 0.8, is a punching cone predicted on both sides of the column (though that on the side where the shear stresses are additive is much larger). Both of these trends match the experimental observations and further demonstrate that the calibrated FEM is

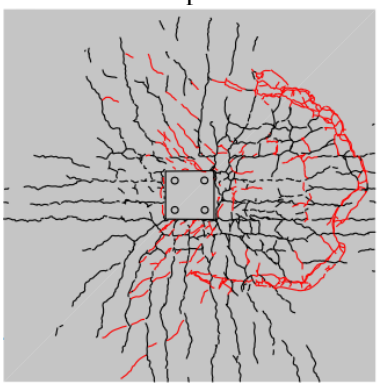
accurately predicting the behaviour of slab-column connections subjected to combined concentric vertical load and unbalanced moment.



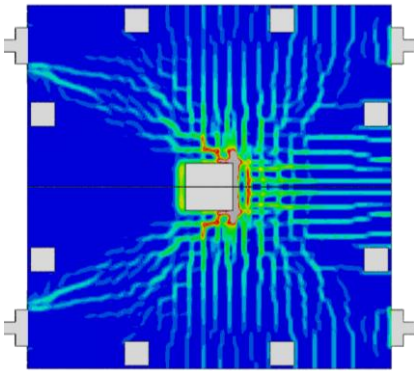
PD1 – Experimental



PD1 – NLFEA



PD4 – Experimental



PD4 – NLFEA

Figure 9-17: Representative Comparison of Experimentally Measured and Numerically Predicted Tension Surface Crack Patterns for Specimens Where ρ is Approximately Equal to 0.8%, PD1 and PD4 Shown (for Experimental Crack Patterns Black and Red Lines Denote Cracks Due to Concentric Load and Unbalanced Moment, Respectively); Experimental Crack Pattern Reprinted from Engineering Structures, 123, Drakatos, Muttoni and Beyer, Internal Slab-Column Connections Under monotonic and cyclic imposed rotations, 501-516, Copyright (2016), with permission from Elsevier

Finally, the peak moment and connection rotation capacities predicted by the calibrated FEM for all 6 V+M (monotonic) PD specimens are compared in Table 9-8. Overall, the calibrated FEM is found to accurately predict the moment capacity of each specimen with an average underprediction of 7% for the six specimens (maximum underprediction of 19% for PD5). On average, the connection rotations at failure predicted by the calibrated FEM are within approximately 2% of the experimental measurements. Nevertheless, looking at the results for the individual specimens, it is clear that the

calibrated FEM can struggle to accurately predict the connection rotation at failure, particularly when the GSR exceeds 0.8 (PD3 and PD10). However, since the primary goal of the study summarized in Section 9.2 is to determine if slab openings between the column flanges reduce the punching capacity of SS-SCCs subjected to combined concentric load and unbalanced moment, the calibrated FEM was deemed adequate, as it accurately predicts the capacity, crack patterns at failure and overall behaviour of slab-column connections under various load conditions (this is also demonstrated in the calibration verification study presented in Section 9.3.3).

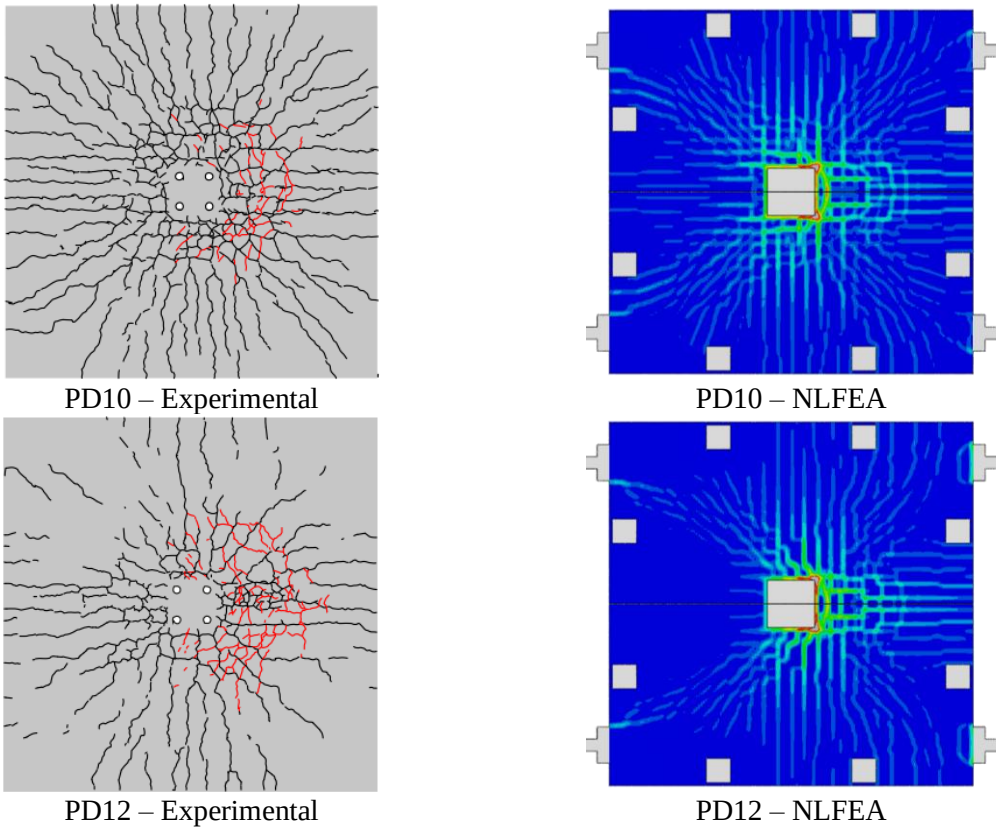


Figure 9-18: Representative Comparison of Experimentally Measured and Numerically Predicted Tension Surface Crack Patterns for Specimens Where ρ is Approximately Equal to 1.6%, PD10 and PD12 Shown (for Experimental Crack Patterns Black and Red Lines Denote Cracks Due to Concentric Load and Unbalanced Moment, Respectively); Experimental Crack Pattern Reprinted from Engineering Structures, 123, Drakatos, Muttoni and Beyer, Internal Slab-Column Connections Under monotonic and cyclic imposed rotations, 501-516, Copyright (2016), with permission from Elsevier

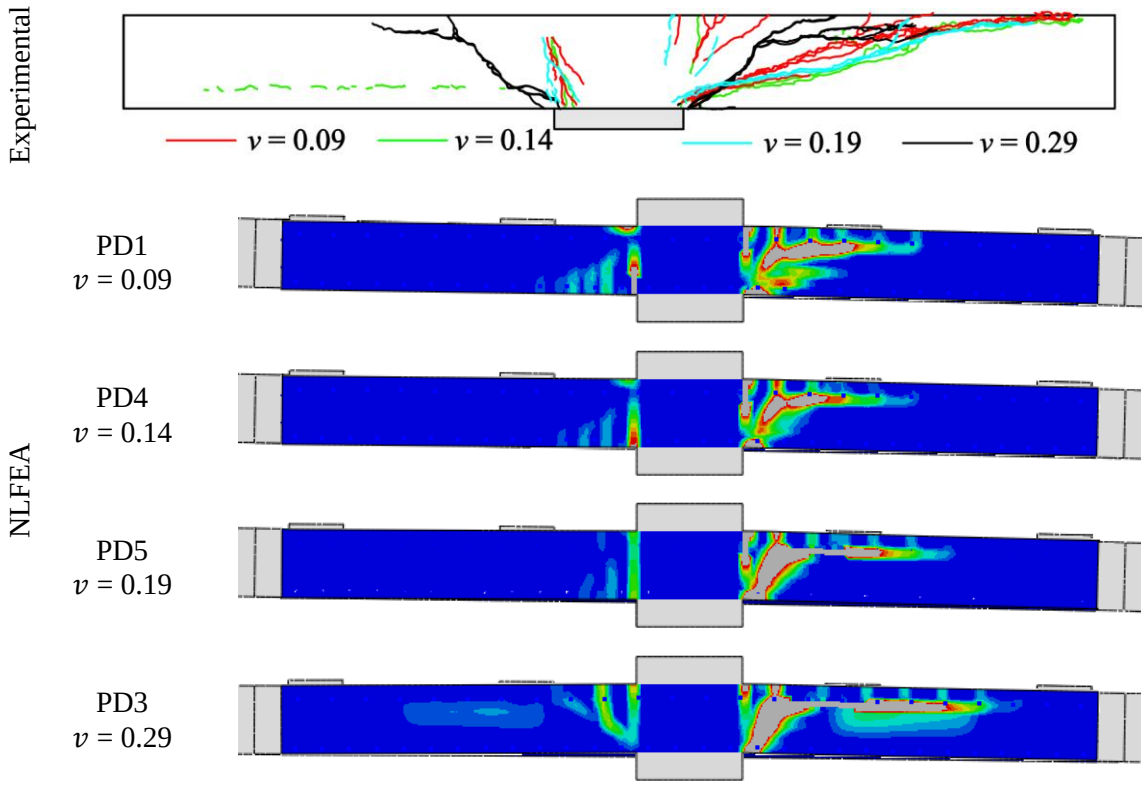


Figure 9-19: Comparison of Interior Crack Patterns Experimentally Observed and Predicted by Calibrated FEM, Specimens Subjected to Combined Shear and Unbalanced Moment Where ρ is Approximately Equal to 0.8%; Experimental Crack Pattern Reprinted from Engineering Structures, 123, Drakatos, Muttoni and Beyer, Internal Slab-Column Connections Under monotonic and cyclic imposed rotations, 501-516, Copyright (2016), with permission from Elsevier

9.3.3 Verification Study

9.3.3.1 Study Overview

Before using the calibrated FEM to conduct the study outlined in Section 9.2, a final calibration verification study, focused on studying the punching shear behaviour of square slab-column connections subjected to combined concentric vertical load and monotonically increasing uniaxial unbalanced moment, was conducted. The study, which is summarized in Table 9-10, is similar to that conducted by Drakatos et al. [4] in the fact that four GSRs (0.25, 0.4, 0.6 and 0.8) and two flexural reinforcement ratios (0.8% and 1.56%) were considered. However, unlike the experimental tests,

where variabilities between test specimens can make the identification of trends difficult, a consistent set of material parameters and reinforcing layouts were used in the verification study. Additionally, the verification study expands the experimental program of Drakatos et al. [4], as the punching shear behaviour of slab-column connections with high flexural reinforcement ratios (ρ >1.5%), but low GSRs (GSR≤0.4), is also investigated.

The material properties of the specimens (concrete compressive strength = 39MPa and flexural reinforcement yield strength = 507MPa) and effective depths of all specimens were based on slab PD4 tested by Drakatos et al. [4]. The properties of PD4 were selected for the verification study since they are the closest to those of slab AM04, tested by Sagaseta et al. [151], which was the slab originally used to calibrate the input parameters of the CDP used in the FEM, as discussed in Chapter 6. The flexural reinforcement on the top and bottom surfaces of the slabs where ρ equalled 0.8% consisted of 16mm diameter bars spaced at 125mm in both directions and 10mm diameter bars spaced at 100mm in both directions, respectively (this is the same reinforcement used in PD4 and in the connections analyzed in Section 9.4). The flexural reinforcement on the top and bottom surfaces of the slabs where ρ equalled 1.56% consisted of 20mm diameter bars spaced at 100mm in both directions and 14mm diameter bars spaced at 100mm in both directions, respectively (these rebar sizes and spacings match those of the connections with large amounts of flexural reinforcement tested by Drakatos et al. [4]).

Table 9-10:Summary of Specimens Considered in FEM Calibration Verification Study

	ID	V_{FEA} (kN)	GSR FEA	GSR ACI	f_c' (MPa)	f_y (MPa	ρ (%)	d (mm)	ρ' (%)	d' (mm)
Low ρ[(a)]	L0.25V	250	0.25	0.26	39	507	0.8	201	0.35	224
	L0.4V	400	0.40	0.41						
	L0.6V	600	0.60	0.61						
	L0.8V	800	0.80	0.82						
High ρ[(b)]	H0.25V	302	0.25	0.31	39	507	1.56	201	0.69[(c)]	224[(c)]
	H0.4V	483	0.40	0.49						
	H0.6V	725	0.60	0.74						
	H0.8V	967	0.80	0.99						

[(a)] Concentric punching capacity of low ρ specimen predicted by NLFEA – 999kN;
[(b)] Concentric punching capacity of high ρ specimen predicted by NLFEA – 1209kN;
[(c)] if constructed clear cover to reinforcement would not meet minimum code requirements;
390mm square columns to match Drakatos et al. [4]

It should be noted that in the verification study the applied vertical load levels, and GSRs, were calculated based on the concentric punching capacity predicted by the calibrated nonlinear FEM, instead of that predicted by ACI 318-19 [2]. For the specimens where ρ equalled 0.8%, the GSRs calculated using the concentric capacities predicted by the FEA and ACI 318-19 are similar as shown in Table 9-10. However, for the specimens where ρ equalled 1.56%, the concentric punching capacity predicted by ACI 318-19 is significantly lower than that predicted by the FEA. Therefore, for these specimens, the GSRs according to ACI 318-19 are significantly higher than that predicted by the FEA.

An additional benefit of the calibration verification study is that it allowed for an initial analysis of the accuracy of the ACI 318-19 [2] and ACI 421.1R-20 [5] punching shear design provisions for slab-column connections subjected to combined concentric shear force and applied unbalanced moment. Since most historic punching shear research has been focused on square slab-column connections, the existing provisions should be the most accurate for square connections. Therefore, if the existing provisions are sufficiently conservative for square slab-column connections they are potentially also conservative for alternate column geometries. But if the provisions are only slightly conservative for square slab-column connections, then they are likely unconservative for alternate column geometries where all sides of the connection are not equally effective in transferring load and significant stress concentrations exist.

9.3.3.2 Calibration Verification Study Results

The predicted moment-connection rotation responses (connection rotation was calculated using equation 9-2 in Section 9.3.2) for all specimens in the calibration verification study are provided in Figure 9-20. As the applied concentric shear force increased (i.e. GSR increased), the predicted moment and connection rotation capacity decreased (the applied moment and connection rotation at failure for all specimens are provided in Table 9-11). As observed by Laguta [246] in their NLFEA of square slab-column connections subjected to combined concentric shear load and uniaxial unbalanced moment, the predicted moment and connection rotation capacity decrease approximately linearly as the applied concentric load increases. However, it should be noted that the predicted connection rotations at failure for the connections where the GSR was less than or equal to 0.4 and ρ equalled 1.56% deviate from the approximately linear relationship, and instead display an approximate maximum connection rotation of 1.2%.

Also consistent with Laguta's findings [246], the predicted connection stiffness decreases as the applied concentric load increases. This is logical because a higher vertical shear force causes higher tensile stresses and more cracking (which lowers stiffness) before the application of the unbalanced moment. Also, the calibrated FEM predicts the connections with a higher flexural reinforcement ratio to be stiffer than those with a lower flexural reinforcement ratio, which is again logical.

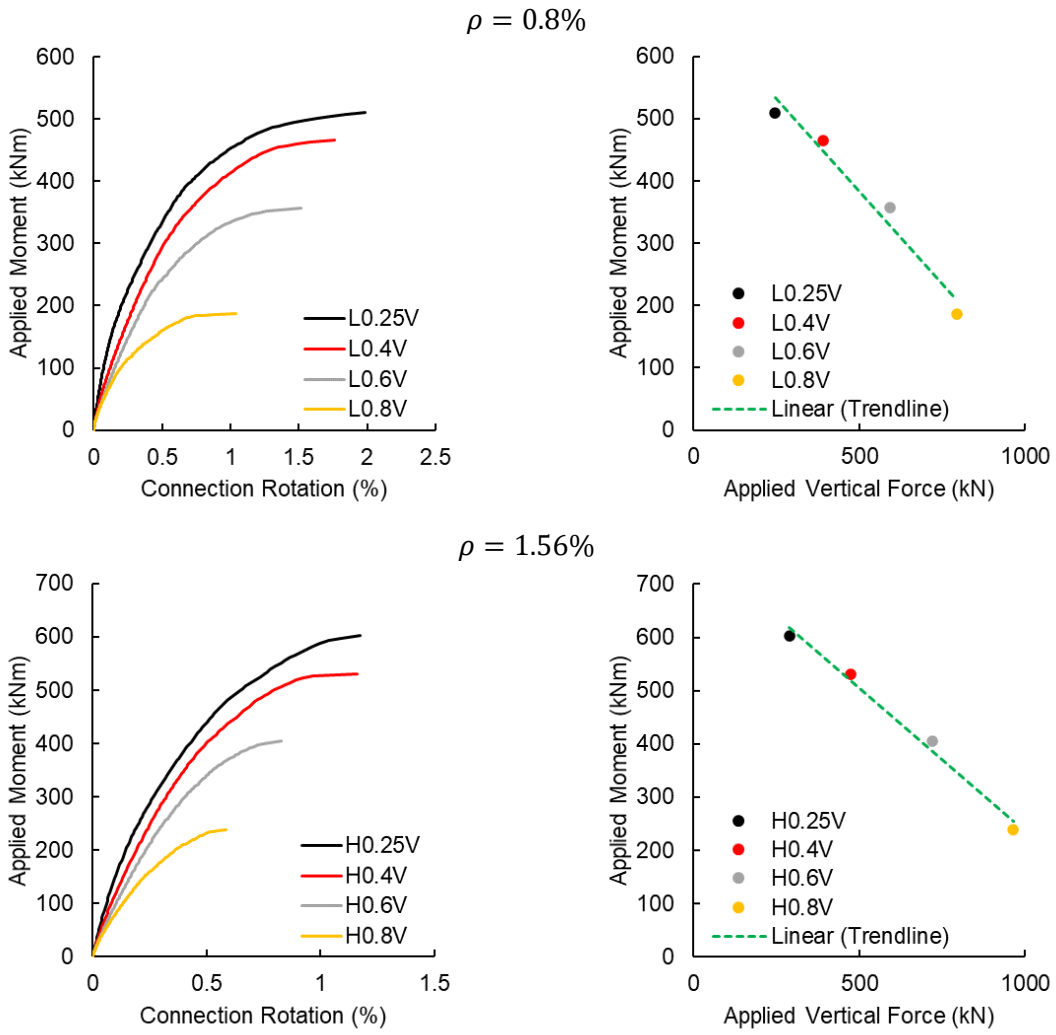


Figure 9-20: Comparison of Predicted Moment-Rotation Response and Moment vs Applied Vertical (Concentric) Load for Low ρ (0.8%) and High ρ (1.56%) Specimens in FEM Calibration Verification Study

The predicted relationship between the peak moment capacity and applied concentric vertical load for all specimens in the calibration verification study are also provided in Figure 9-20. For both

investigated flexural reinforcement ratios, the relationship between the predicted peak moment capacity and applied concentric shear force is approximately linear. As discussed by Laguta [246], the ACI 318-19 [2], Eurocode 2 (2004) [34], Model Code 2010 [35] LoA I, and Model Code 2010 LoA II punching shear design provisions also assume a linear relationship between the applied concentric load and the unbalanced moment capacity. NLFEA by Laguta [246] has also suggested that the relationship between the applied concentric shear force and unbalanced moment is approximately linear for connections where the failure mode is governed by punching shear, and not flexural failure of the slab reinforcement.

Table 9-11: Summary of NLFEA and ACI 318-19 Predictions, FEM Calibration Verification Study

	ID	V_{FEA} (kN)	M_{FEA} (kNm)	% Change	ψ_{scc} (%)	M_{ACI} (kNm)	M_{ACI}/M_{FEA}
Low ρ	L0.25V	250	510.0	-	1.987	369.5	0.725
	L0.4V	400	465.7	-8.7	1.764	293.5	0.630
	L0.6V	600	357.0	-30.0	1.516	192.2	0.538
	L0.8V	800	186.9	-63.4	1.038	90.8	0.486
High ρ	H0.25V	302	602.9	-	1.174	343.2	0.569
	H0.4V	483	531.0	-11.9	1.160	251.5	0.474
	H0.6V	725	404.4	-32.9	0.829	128.8	0.319
	H0.8V	967	238.5	-60.4	0.584	6.2	0.026[(a)]

[(a)] Concentric punching capacity predicted by ACI 318-19 is only slightly higher than applied load (which is based on concentric capacity predicted by NLFEA), hence very low moment capacity predicted

The trends in the predicted crack patterns are consistent with those for the experimental specimens tested by Drakatos et al. [4] and discussed in Section 9.3.2. Regardless of the flexural reinforcement ratio, the FEA generally predicts a minor amount of cracking due to the concentric load when the GSR is less than or equal to 0.4, due to the high initial stiffness predicted by the FEA (which is due to the assumed Hognestad parabola and lack of temperature and shrinkage cracking). However, the crack patterns at failure are similar with respect to shape and extent of cracking to those observed by Drakatos et al. [4] demonstrating that the FEA is accurately capturing the connection behaviour at failure. Furthermore, the extent of cracking increases as the applied concentric load and unbalanced moment increases, which is again logical as higher loads cause higher tensile stresses and more extensive cracking.

The unbalanced moment capacities predicted by ACI 318-19 are also provided in Table 9-11. In all cases, the ACI 318-19 predictions are very conservative compared to those from the FEA, particularly for the heavily reinforced specimens (ρ=1.56%) where the concentric shear capacity was significantly underpredicted by ACI 318-19. Therefore, it appears that the existing provisions, which have been largely unchanged since their introduction in ACI 318-63 [51, 287], can be significantly improved with further experimental and numerical analysis of slab-column connections subjected to combined concentric load and unbalanced moment.

Based on the above discussions, the calibrated FEM was found to predict behaviour which agrees with the overall trends of past experiments, worldwide design codes and previous, independently calibrated, NLFEA. As such, the FEM calibration was deemed adequate, and the calibrated FEM presented in Section 9.3.2 was used to conduct the study of the punching shear behaviour of R-SCCs and SS-SCCs subjected to combined concentric loading and monotonically increasing uniaxial unbalanced moment as outlined in Section 9.2. Finally, based on a comparison of the unbalanced moment capacities predicted by ACI 318-19 and the calibrated nonlinear FEM, it is anticipated that the existing provisions may result in conservative, yet inaccurate estimates of unbalanced moment capacity for alternate column geometries, though this is investigated in Section 9.4.

9.4 Study Results

9.4.1 Concentric Shear Loading (V Only) Specimens

The trends of the results for the concentrically loaded specimens considered in Chapter 9 are consistent with those discussed in Chapter 8, and therefore, only a brief discussion of the results for the concentric specimens is provided herein. Furthermore, since the overall trends are consistent with those presented in Chapter 8, the predicted load-displacement responses, crack patterns and shear stress distributions are not provided in the main body of this thesis (though these figures are provided in Appendix K for reference).

The calibrated FEA predicted all the concentrically loaded specimens to fail in punching shear. Consistent with the results in Chapter 8, slab openings near the slab-column connections resulted in a reduction in both punching capacity and connection stiffness. Furthermore, as shown in Figure 9-21, the X-SCCs were predicted to have the highest punching capacities. The T-SCCs were predicted to have the second highest punching shear capacities. The R-SCCs and L-SCCs, which were predicted to have approximately equal concentric punching capacities, had the lowest predicted capacities.

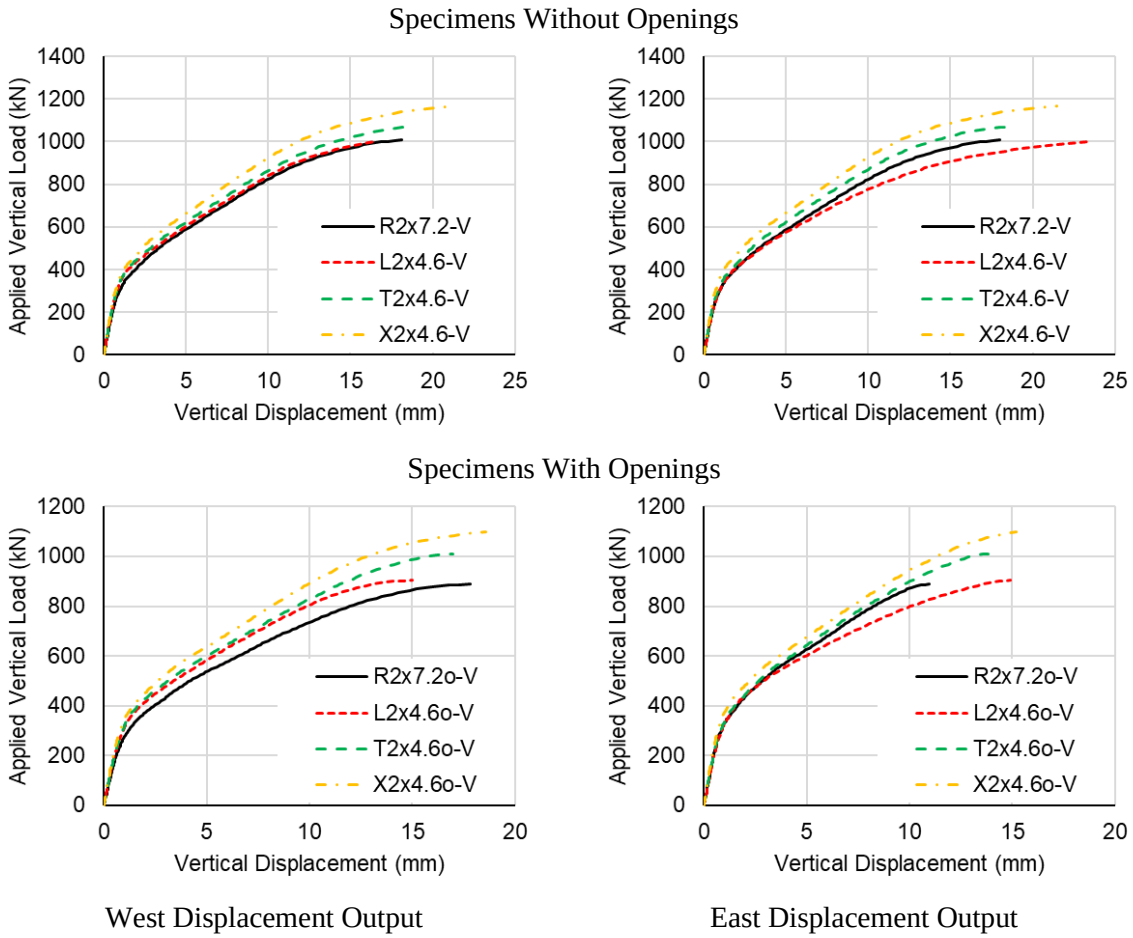


Figure 9-21: Comparison of Predicted Load-Displacement Responses for Concentrically Loaded R-SCCs and SS-SCCs, Displacement Measurement Locations Shown in Figure 9-5

A summary of the punching capacities and opening influences predicted by the FEA are provided in Table 9-12. For R2x7.2, the slab opening resulted in an approximately 11.9% lower punching capacity. This reduction is similar to that which was predicted for R1-S-o1 and R2-S-o1 (approximately 11.3% and 8.9% lower punching capacities than the reference specimens, respectively, see Chapter 8), which had similar opening layouts and were also predicted to fail in punching. For T2x4.6 and X2x4.6 the considered opening layout typically had a small influence on punching capacity (the opening reduced the punching capacity of T2x4.6 and X2x4.6 by approximately 5.4% and 6.0%, respectively). On the other hand, the influence of the opening was slightly larger for L2x4.6, with the capacity of the specimen with an opening being approximately 9.4% lower than that of the reference specimen without an opening.

Therefore, while the influence of the opening between the column flanges was minor for T2x4.6 and X2x4.6 (which is consistent with the observations of Chapter 8) the influence was slightly more significant for L2x4.6 (and slightly larger than that observed for similar specimens in Chapter 8). As such, the specimen shown in Figure 9-22 was analyzed to verify that openings along the outer edge are more detrimental than openings between the column flange for L2x4.6.

Table 9-12: Comparison of Capacities and Opening Influences Predicted by FEA, ACI 318-19 and ACI 421.1R-20 – Concentrically Loaded Specimens

	kN		mm	V_{ACI} (kN)			V_{ACI}/V_{FEA}			Opening Impact (%)			
ID	V_{FEA}	β	b_o[(a)]	318	318*	421	318	318*	421	FEA	318	318*	421
R2x7.2-V	1008.5	3.60	2644	877.7	-	877.7[(b)]	0.87	-	0.87	-	-	-	-
R2x7.2o-V	888.0		2203	731.4	-	581.7	0.82	-	0.66	-11.9	-16.7	-	-33.7
L2x4.6-V	997.3	1.39	2457	1017.9	831.1	954.1	1.02	0.83	0.96	-	-	-	-
L2x4.6o-V	903.0		1977	819.0	807.0	692.0	0.91	0.89	0.77	-9.4	-19.5	-2.9	-27.5
T2x4.6-V	1067.4	1.57	2790	1155.9	1113.2	1137.5	1.08	1.04	1.07	-	-	-	-
T2x4.6o-V	1009.6		2344	971.0	935.2	837.2	0.96	0.93	0.83	-5.4	-16.0	-16.0	-26.4
X2x4.6-V	1167.7	1.00	2937	1216.5	-	1216.5[(b)]	1.04	-	1.04	-	-	-	-
X2x4.6o-V	1097.8		2511	1040.2	-	889.0	0.95	-	0.81	-6.0	-14.5	-	-26.9

Note: 318: Capacity according to ACI 318-19 concentric punching provisions; 318*: Capacity according to initial design method recommended in Chapter 8 (modified concentric provisions); 421: Capacity according to ACI 421.1R-20 provisions; [(a)] b_o applies to 318 and 421 predictions only; [(b)] Capacity based on concentric provisions as column, slab and critical perimeter centroids aligned; Material safety factors set to 1 when calculating V_{ACI}

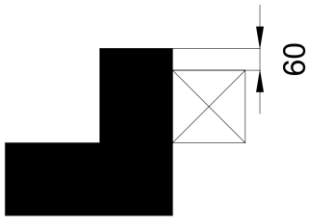


Figure 9-22: Additional Opening Layout Considered for L2x4.6 (200mm Square Opening) – Concentric Loading

When the same opening is located along the outer edge of the connection, as shown in Figure 9-22, the influence of the opening is nearly doubled (compared to its influence when located between the flanges), with the predicted punching capacity of the specimen being approximately 17.4% lower than the reference specimen without an opening. Therefore, even though the influence of openings located between the column flange can be significant in some cases for L-SCCs, the influence of such openings is still much lower than similarly sized openings located along the outer edges. As such, the opening layout previously shown in Figure 9-3 was considered in all further analyses presented in this chapter.

The trends in the predicted tension surface crack patterns for the specimens without openings match those from the concentric load study presented in Chapter 8. Even though R2x7.2 was predicted to fail in punching shear, significant one-way shear cracking parallel to the long sides of the column was predicted. The most significant cracking around L2x4.6 was predicted along and at the intersection of the outer edges (column sides 5 and 6, see Figure 8-10) and, as observed in Chapter 8, one-way shear appears to be the dominant force transfer mechanism along these sides. The most significant cracking around T2x4.6 was predicted around the base of the T (column sides 4, 5 and 6, see Figure 8-12). Consistent with the previously analyzed T-SCCs, significant one-way shear cracking parallel to side 5 was predicted, again demonstrating that one-way shear was the dominant force transfer mechanism parallel to the long dimension of the base of the T. For X2x4.6, the most significant cracking was predicted around the short sides or near the outer corners of the connection (intersection of the short and long sides of each flange). The most significant diagonal cracking in the region between the column flanges was predicted for X2x4.6, which is again consistent with Chapter 8.

Furthermore, the trends in the predicted tension surface crack patterns for the specimens with openings were also consistent with those presented in Chapter 8. Since the slab opening layouts are nonsymmetric, other than for L2x4.6, the resulting crack patterns are also nonsymmetric (note, for the specimens without openings the crack patterns are slightly nonsymmetric due to the inclusion of the additional edge reinforcement along two slab edges). For all specimens, crack concentrations are predicted near the opening, with the extent of the additional cracking typically being limited to a region approximately bounded by the additional flexural reinforcement placed around the opening.

It should also be noted that the overall extent of cracking predicted for the R2x7.2, L2x4.6, T2x4.6 and X2x4.6 specimens with and without openings was more severe than that predicted for the specimens analyzed in Chapter 8 (this can be seen by comparing the crack patterns provided in Appendix J and K). This is likely because the capacities of the specimens analyzed in Chapter 9 are much higher than those analyzed in Chapter 8, due to the larger slab thickness and inclusion of flexural reinforcement on both the compressive and tensile sides of the slab (the yield strength of the flexural reinforcement is also higher for the specimens in Chapter 9).

The trends in the column perimeter shear stress distributions at the peak load predicted by the FEA (figures are provided in Appendix K) are also consistent with those from Chapter 8. As expected, the shear stress distribution along the column perimeter is non-uniform, with significant concentrations at

the corners (particularly those at the outer edges). The percentages of the total peak load transferred along each column side for the four specimens without openings are provided in Figure 9-23. The sides which transfer the largest portion of the total load are consistent with those determined in Chapter 8 (long sides for R-SCCs, sides 5 and 6 for L-SCCs, sides 4, 5 and 6 for T-SCCs and short sides of each flange load for X-SCCs [see Figure 8-10 and Figure 8-12 for the side numbering for L-SCCs and T-SCCs, respectively]).

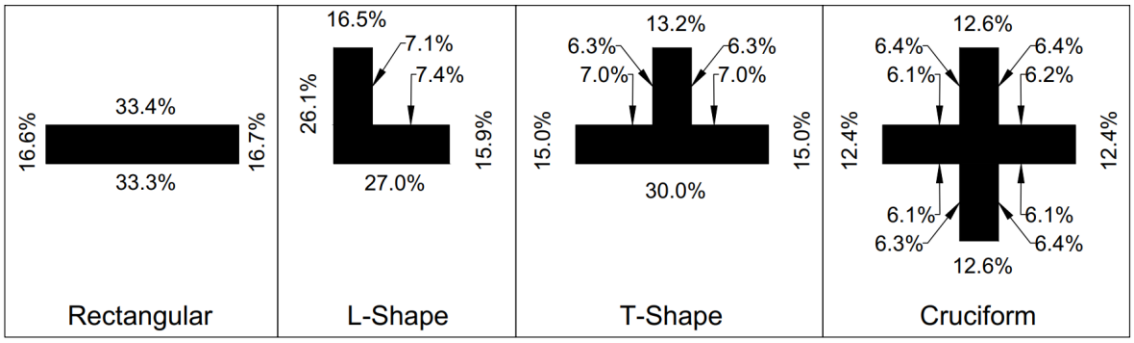


Figure 9-23: Comparison of Percent of Total Load Carried on Each Column Side for Different Column Shapes Predicted by FEA for Specimens Without Slab Openings (Data Recorded at Peak Load)

A comparison of the punching capacities and opening influences predicted by the FEA, ACI 318-19 concentric punching shear provisions ($V_{ACI\ 318}$), modified ACI 318-19 concentric punching shear provisions ($V_{ACI\ 318*}$, modification 1 for L-SCCs and modification 2 for T-SCCs) and ACI 421.1R-20 (V_{421}) are also provided in Table 9-12. Again, the overall trends of the predictions match those presented in detail in Chapter 8.

For the R-SCCs, the punching capacities predicted by ACI 318-19 are generally conservative, and fairly accurate compared to the FEA (which was also the case for most of the R-SCCs in Chapter 8), though the influence of openings along the long side is slightly overpredicted. Also consistent with Chapter 8, the punching capacities predicted by ACI 421.1R-20 are overly conservative, and the influence of the opening is greatly overpredicted compared to the FEA. Though it should be noted that both ACI 318-19 and 421.1R-20 predict the same capacity for the reference connection without an opening since there is no eccentricity between the column and critical perimeter centroids. Therefore, this provides further verification that the unbalanced moment generated due to eccentricity of the reduced critical perimeter and column centroids can be safely neglected in the punching shear design of R-SCCs with nonsymmetric slab openings.

For the analyzed SS-SCCs, the punching capacities predicted by the ACI 318-19 concentric punching shear provisions ($V_{ACI\ 318}$) generally agreed well with the FEA predictions, though some slight overpredictions exist (approximately 8% max overprediction for T2x4.6-V). This was expected since the column flanges of the analyzed columns (200x460mm) were similar to the flanges of the larger small column analyzed in Chapter 8 (2-S specimens, 200x420mm flanges), which were also overpredicted by ACI 318. Also as expected, the punching capacities and opening influences predicted by the ACI 421.1R-20 provisions (V_{421}) were more conservative than those from the concentric punching provisions, particularly when openings are present between the column flanges.

Punching capacities predicted according to the modified concentric punching shear provisions recommended in Chapter 8 for initial design ($V_{ACI\ 318*}$, modification 1 and modification 2 for L-SCCs and T-SCCs, respectively) also agreed well with the FEA predictions. Even though the slight overpredictions in punching capacity (T2x4.6-V) or somewhat large underpredictions of the influence of interior openings (L2x4.6o-V) exist, the general applicability of the proposed modifications for initial design is further demonstrated. Though, it should be noted that final design verification according to ACI 421.1R-20 is still necessary to satisfy the requirements of ACI 318-19 (it is also necessary as ACI 421.1R-20 generally results in lower capacity estimates).

9.4.2 Combined Shear and Unbalanced Moment (V+M (Monotonic)) Specimens

In the following subsections, the results for the connections subjected to V+M (monotonic) loading are presented. The results are first presented for each column geometry individually, and then a general discussion considering all column geometries is provided. Note, in the following sections moment-displacement responses are presented instead of moment-rotation responses. For square slab-column connections, such as those analyzed in the calibration and calibration verification study, the calculation of rotations is straightforward. However, for L-SCCs and T-SCCs calculation of the maximum rotation is more complicated, and therefore, for consistency moment-deflection responses are presented for all analyzed R-SCCs and SS-SCCs.

9.4.2.1 Rectangular Slab-Column Connections (R-SCCs)

The FEA predicted all 6 R-SCCs to fail in punching shear. The predicted moment-deflection responses at the east and west displacement output locations (the location of the output points was previously shown in Figure 9-5 and Figure 9-10) are provided in Figure 9-24, and a summary of the predicted unbalanced moment capacities is provided in Table 9-13. Note, as previously discussed, the

unbalanced moment capacities in the M1 and M2 directions are the same for the connection without opening due to symmetry. Consistent with the findings for the concentrically loaded specimens, slab openings result in a decrease in capacity, especially when the moment is applied towards the opening (i.e. the opening is located on the column side where the shear stresses due to the unbalanced moment and concentric loading are additive). For the connections with openings where the GSR was equal to 0.4 and 0.55, the unbalanced moment capacities in the M2 direction were approximately 9.2% and 11.9% lower than those in the M1 direction, respectively. Therefore, the influence of the opening on punching capacity is also influenced by the location of the opening with respect to the moment direction. Furthermore, consistent with the results for square slab-column connections, the unbalanced moment capacity of the R-SCCs decreased as the GSR increased. For example, for the connections without openings, the predicted unbalanced moment capacity decreased by approximately 15% when the GSR increased from 0.4 to 0.55.

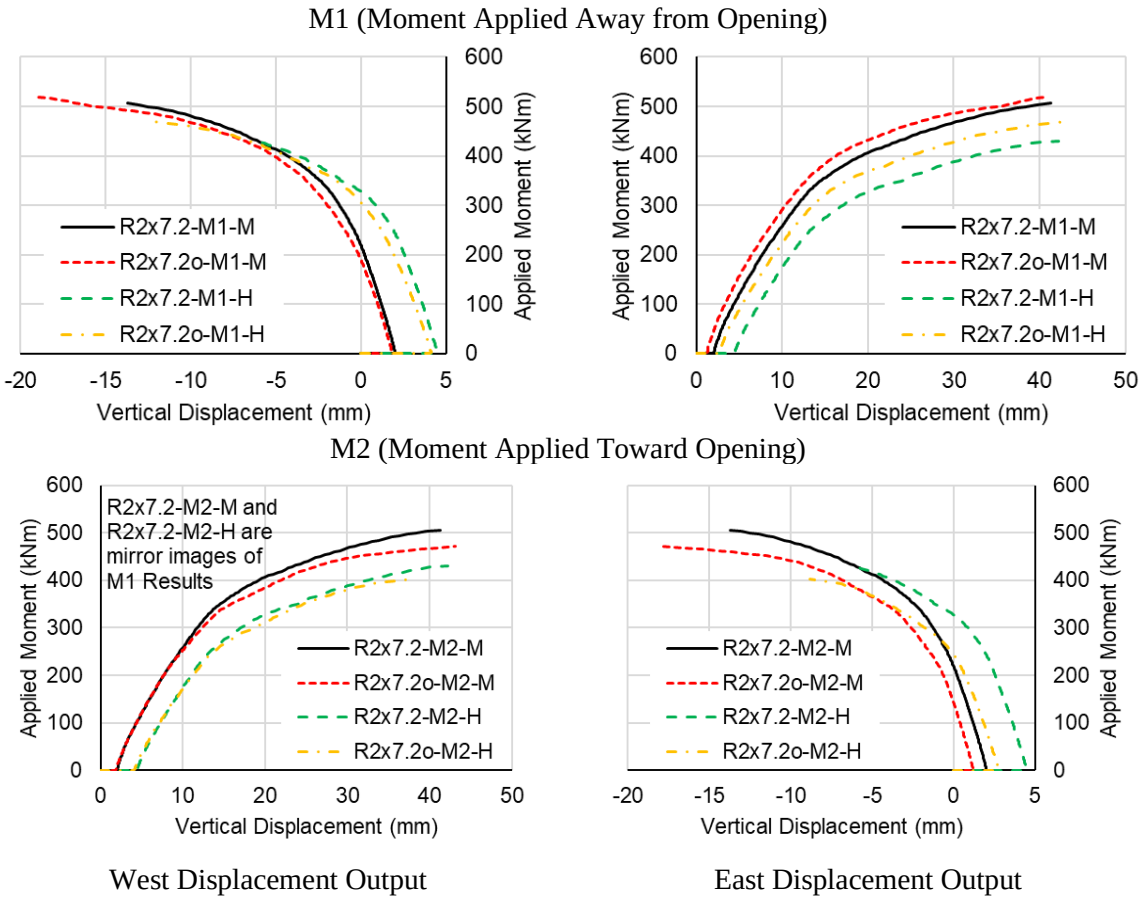


Figure 9-24: Predicted Moment-Displacement Responses for R-SCCs Subjected to V+M (Monotonic) Loading, Displacement Measurement Locations Shown in Figure 9-5

However, since the connections with and without openings are subjected to different vertical load levels (to maintain consistent GSRs between the connections), the unbalanced moment capacities of the connections with and without openings cannot be compared directly. Therefore, to quantify the influence of the openings on the unbalanced moment capacity, the capacity of a connection without an opening was approximated at the same vertical load level used in the analysis of the connections with openings. For GSR ratios of 0.4 and 0.55, these approximations correspond to a linear extrapolation and linear interpolation of the results for the connections without openings, respectively. As shown in Figure 9-25a, the results for the two connections without openings were used to generate a linear relationship between the unbalanced moment capacity (*M*) and the applied concentric load (*V*). The linear relationship was then used to estimate the capacity of the connection without an opening at the same vertical load levels used in the analysis of the connections with openings as shown in Figure 9-25b (the approximated moments, denoted M_{trend} herein, are also summarized in Table 9-13. It should be noted that assuming a linear relationship between *M* and *V* is consistent with current North American [2, 36] and European [34, 35] punching shear design provisions, and the results of square slab-column connections presented in Section 9.3.3.

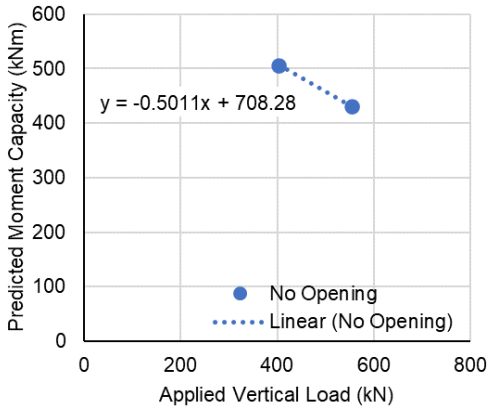
Table 9-13: Summary of Predicted Unbalanced Moment Capacities and Approximated Opening Influences, R-SCCs

		FEA Results		Approximated Opening Impact (Trendline Analysis)		
		kN	kNm	kN	kNm	%
	Specimen	*V*	M_{FEA}	$V^{(A)}$	M_{trend}[(a)]	Opening Influence
GSR = 0.4	R2x7.2-M1-M	403.2	506.2	355.2	530.3	-
	R2x7.2o-M1-M	355.2	518.7	-	-	-2.2
	R2x7.2o-M2-M		471.0	-	-	-11.2
GSR = 0.55	R2x7.2-M1-H	554.4	430.5	488.4	463.5	-
	R2x7.2o-M1-H	488.4	470.4	-	-	+1.5
	R2x7.2o-M2-H		401.8	-	-	-13.3

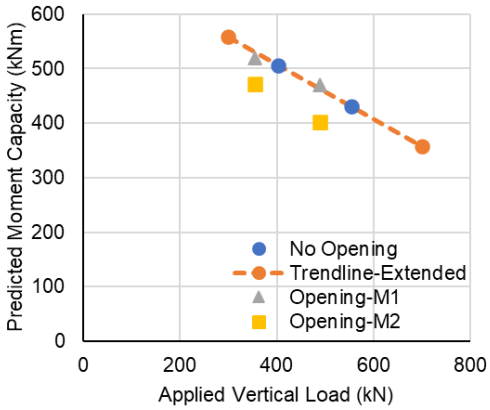
[(a)] M_{trend} is the approximated unbalanced moment capacity of the connection without opening at vertical load level used in the analysis of opening specimens ($V^{(A)}$)

As seen in Figure 9-25b, when the moment is applied away from the opening (i.e. the opening is located on the column side where the shear stresses due to the unbalanced moment and the concentric load are not additive), the opening has a very minor influence on the connection capacity. For the two analyzed connections a maximum decrease of 2.2% was predicted based on the approximated

capacities of the connections without openings. However, when the moment is applied towards the opening, the opening decreases the unbalanced moment capacity of the connection by more than 10%. Therefore, as observed for concentric loading, slab openings have a significant influence on the unbalanced moment capacity of R-SCCs, especially because in most practical applications it is not possible to ensure the moment will not be applied towards the opening.



a) Results for Specimens Without Openings and Trendline



b) Results for Specimens with Openings and Comparison to Trendline Predictions

Figure 9-25: Comparison of Unbalanced Moment Capacity of Specimens with Openings to Approximated Capacity Based on Trendline for Specimens Without Openings, R-SCCs

The predicted tension surface crack patterns at the peak unbalanced moment predicted by the FEA for the analyzed R-SCCs are provided in Figure 9-26. Overall, the trends in the predicted crack patterns are similar to those observed for the square slab-column connections in the calibration and verification studies. Firstly, as the GSR increases, the amount of cracking due to the concentric loading increases. Secondly, the cracks concentrate on the side of the connection where the shear stresses due to the concentric load and unbalanced moment are additive (the punching cone also develops on this side). However, there are also bands of cracks propagating from the column corners to the steel moment arms used to apply the upward force of the moment couple. Therefore, one needs to use caution when using this load method, in order to avoid failures in the region where the steel moment arms are connected to the slab.

For the connections with openings, the presence of nonsymmetric opening layouts results in nonsymmetric tension surface crack patterns. Furthermore, similarly to the overall connection capacity, the slab openings have a larger influence on the predicted tension surface crack patterns when the moment is applied toward the opening. Consistent with the results for the concentrically

loaded specimens, a concentration of cracking is observed around the opening, though this concentration is also more significant when the moment is applied toward the opening.

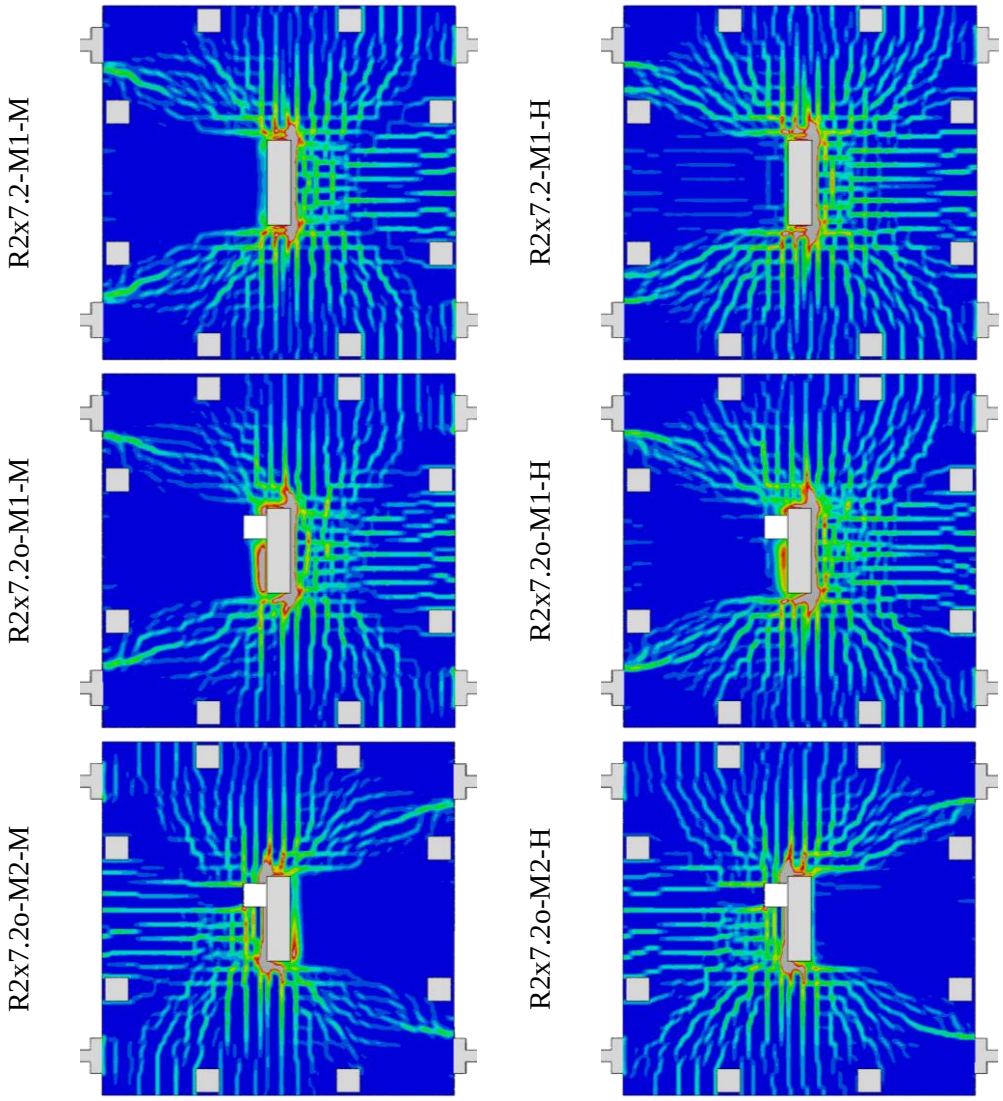


Figure 9-26: Predicted Tension Surface Crack Patterns at Failure, R-SCCs (Grey Regions Have Principal Plastic Strains > 0.02)

9.4.2.2 L Slab-Column Connections (L-SCCs)

The FEA predicted all 8 L-SCCs to fail in punching shear. The predicted moment-deflection responses at the east and west displacement output locations (the location of the output points was previously shown in Figure 9-5 and Figure 9-10) are provided in Figure 9-27, and a summary of the predicted unbalanced moment capacities is provided in Table 9-14. Consistent with the findings for

the concentrically loaded specimens, and for the R-SCCs subjected to V+M loading, slab openings result in a decreased capacity, especially when the moment is applied towards the opening. For the connections with openings where the GSR was equal to 0.4 and 0.55, the unbalanced moment capacities in the M2 direction were approximately 11.2% and 4.3% lower than those in the M1 direction, respectively. Therefore, the influence of the opening on punching capacity is also influenced by the location of the opening with respect to the moment direction regardless of the column geometry. Furthermore, consistent with the results for all other column geometries, the unbalanced moment capacity of the L-SCCs decreased as the GSR increased. For example, for the connections without openings, the predicted unbalanced moment capacities in the M1 and M2 directions decreased by approximately 18% and 19%, respectively, when the GSR increased from 0.4 to 0.55.

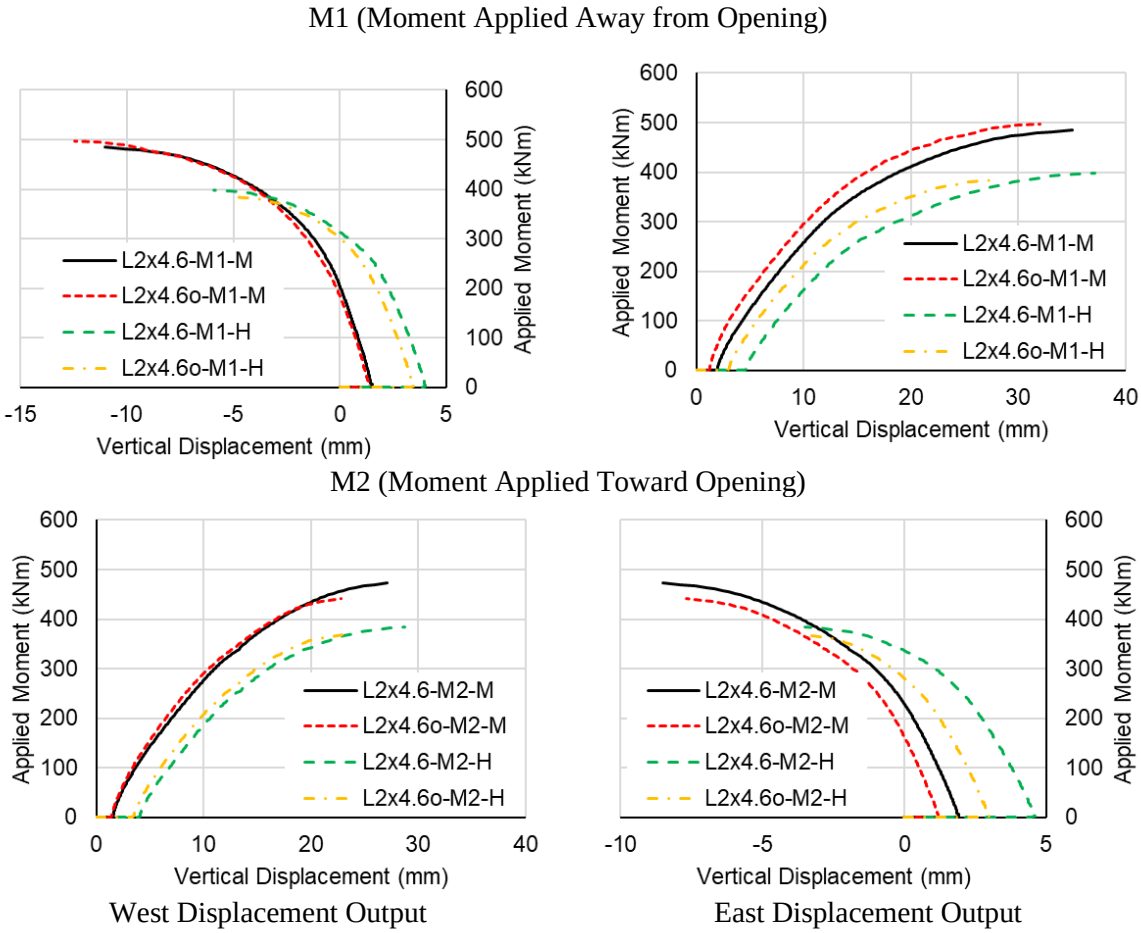


Figure 9-27: Predicted Moment-Displacement Responses for L-SCCs Subjected to V+M (Monotonic) Loading, Displacement Measurement Locations Shown in Figure 9-5

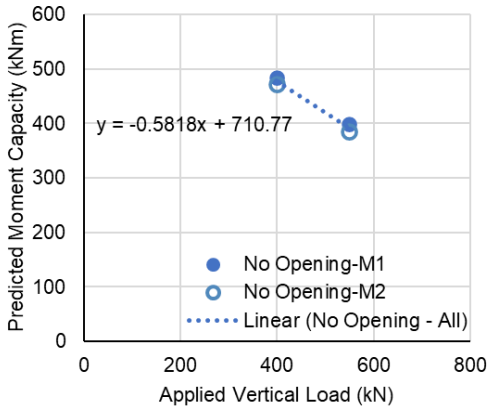
It should also be noted that the FEM predicts approximately equal unbalanced moment capacities in the M1 and M2 directions for the connections without openings. Therefore, while further studies are needed, it appears that the uniaxial unbalanced moment capacity of L-SCCs without openings is not significantly different when the moment is applied toward the interior of the connection or the outer edges.

Table 9-14: Summary of Predicted Unbalanced Moment Capacities and Approximated Opening Influences, L-SCCs

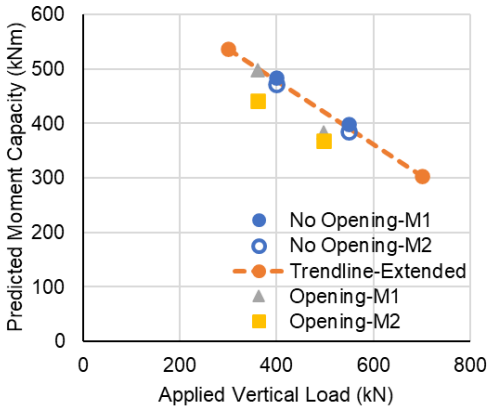
		FEA Results		Approximated Opening Impact (Trendline Analysis)		
		kN	kNm	kN	kNm	%
	Specimen	V	M_{FEA}	$V^{(A)}$	M_{trend}[(a)]	Opening Influence
GSR = 0.4	L2x4.6-M1-M	398.9	484.6	361.2	500.6	-
	L2x4.6-M2-M		472.8		500.6	-
	L2x4.6o-M1-M	361.2	497.5	-	-	-0.6
	L2x4.6o-M2-M		441.6	-	-	-11.8
GSR = 0.55	L2x4.6-M1-H	548.5	398.6	496.7	421.8	-
	L2x4.6-M2-H		384.7		421.8	-
	L2x4.6o-M1-H	496.7	384.3	-	-	-8.9
	L2x4.6o-M2-H		367.7	-	-	-12.8

[(a)] M_{trend} is the approximated unbalanced moment capacity of the connection without opening at vertical load level used in the analysis of opening specimens ($V^{(A)}$)

As was done for R-SCCs, the opening influence is quantified by approximating the unbalanced moment capacity of a connection without an opening at the vertical load levels used for the connections with openings. However, for the L-SCCs, the linear relationship between the unbalanced moment capacity and concentric load is based on predicted unbalanced moment capacities in the M1 and M2 directions as shown in Figure 9-28a. As discussed previously, the unbalanced moment capacities of the analyzed L-SCCs in the M1 and M2 directions were similar, and therefore, the decision to use a single trendline based on the four simulated connections without openings, instead of individual trendlines for the M1 and M2 directions was made. Coincidentally, the trendline based on all four connections is equal to the average of the individual trendlines for the M1 and M2 directions.



a) Results for Specimens Without Openings and Trendline



b) Results for Specimens with Openings and Comparison to Trendline Predictions

Figure 9-28: Comparison of Unbalanced Moment Capacity of Specimens with Openings to Approximated Capacity Based on Trendline for Specimens Without Openings (Note, Trendline Based on M1 and M2 Data), L-SCCs

The predicted moment capacities for the connections without openings at the vertical load levels corresponding to the connections with opening and the approximated opening influences are summarized in Table 9-14. For a GSR of 0.4, the opening between the column flanges has a negligible influence on the unbalanced moment capacity when the moment is applied away from the opening. However, for a GSR of 0.55, the analyzed opening layout results in an approximately 9% lower unbalanced moment capacity, demonstrating that when the GSR is high, openings between the column flanges of L-SCCs can have a significant influence even when the moment is applied away from the opening. Furthermore, when the moment is applied towards the opening, the opening reduces the unbalanced moment capacity by more than 10%, which is consistent with the results for the R-SCCs and other column geometries.

The predicted tension surface crack patterns at the peak unbalanced moment predicted by the FEA for the analyzed L-SCCs are provided in Figure 9-29. Overall, the trends in crack patterns are consistent with those previously discussed for the R-SCCs. However, for L-SCCs, and other SS-SCCs, slab openings between the column flanges interrupt the diagonal cracking in the region between the column flanges.

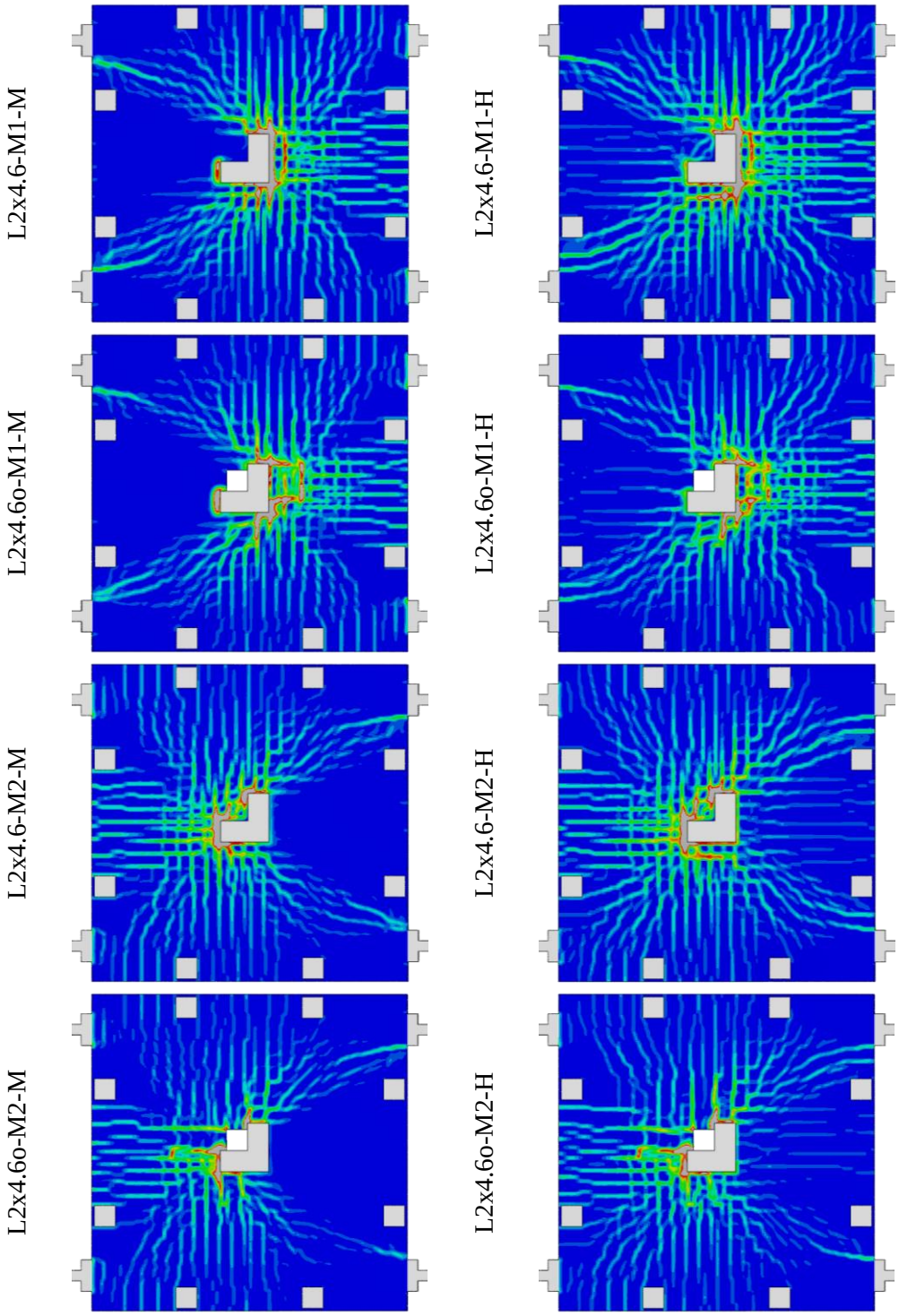


Figure 9-29: Predicted Tension Surface Crack Patterns at Failure, L-SCCs (Grey Regions Have Principal Plastic Strains > 0.02)

Note, the overall trends in crack patterns around L-SCCs are consistent with those for the T-SCCs and X-SCCs. Therefore, the crack patterns for these remaining two column geometries are not discussed further herein. The crack patterns for both column geometries are provided in Appendix K for completeness.

9.4.2.3 T Slab-Column Connections (T-SCCs)

The FEA predicted all 8 T-SCCs to fail in punching shear. The predicted moment-deflection responses at the east and west displacement output locations (the location of the output points was previously shown in Figure 9-5 and Figure 9-10) are provided in Figure 9-30, and a summary of the predicted unbalanced moment capacities is provided in Table 9-15. Consistent with the findings for the concentrically loaded specimens, and for the R-SCCs and L-SCCs subjected to V+M loading, slab openings result in a decreased capacity, especially when the moment is applied towards the opening. For the connections with openings where the GSR was equal to 0.4 and 0.55, the unbalanced moment capacities in the M2 direction were approximately 12.4% and 4.7% lower than those in the M1 direction, respectively. Therefore, the influence of the opening on punching capacity is also influenced by the location of the opening with respect to the moment direction regardless of the column geometry. Furthermore, consistent with the results for all other column geometries, the unbalanced moment capacity of the T-SCCs decreased as the GSR increased. For example, for the connections without openings, the predicted unbalanced moment capacities in the M1 and M2 directions decreased by approximately 21% and 15%, respectively, when the GSR increased from 0.4 to 0.55.

As was observed for the L-SCCs without openings, the FEM predicts approximately equal unbalanced moment capacities in the M1 and M2 directions for the T-SCCs without openings. Therefore, while further studies are needed, it appears that the uniaxial unbalanced moment capacity of T-SCCs without openings is not significantly different when the moment is applied towards the short side of the stem or the long side of the base of the T.

The same procedure used to quantify the influence of the slab openings for the L-SCCs is used for the analyzed T-SCCs. As shown in Figure 9-31a, the linear relationship between the unbalanced moment capacity and concentric load corresponds to the trendline of the results for the four specimens without openings, since the strengths in both moment directions are approximately equal.

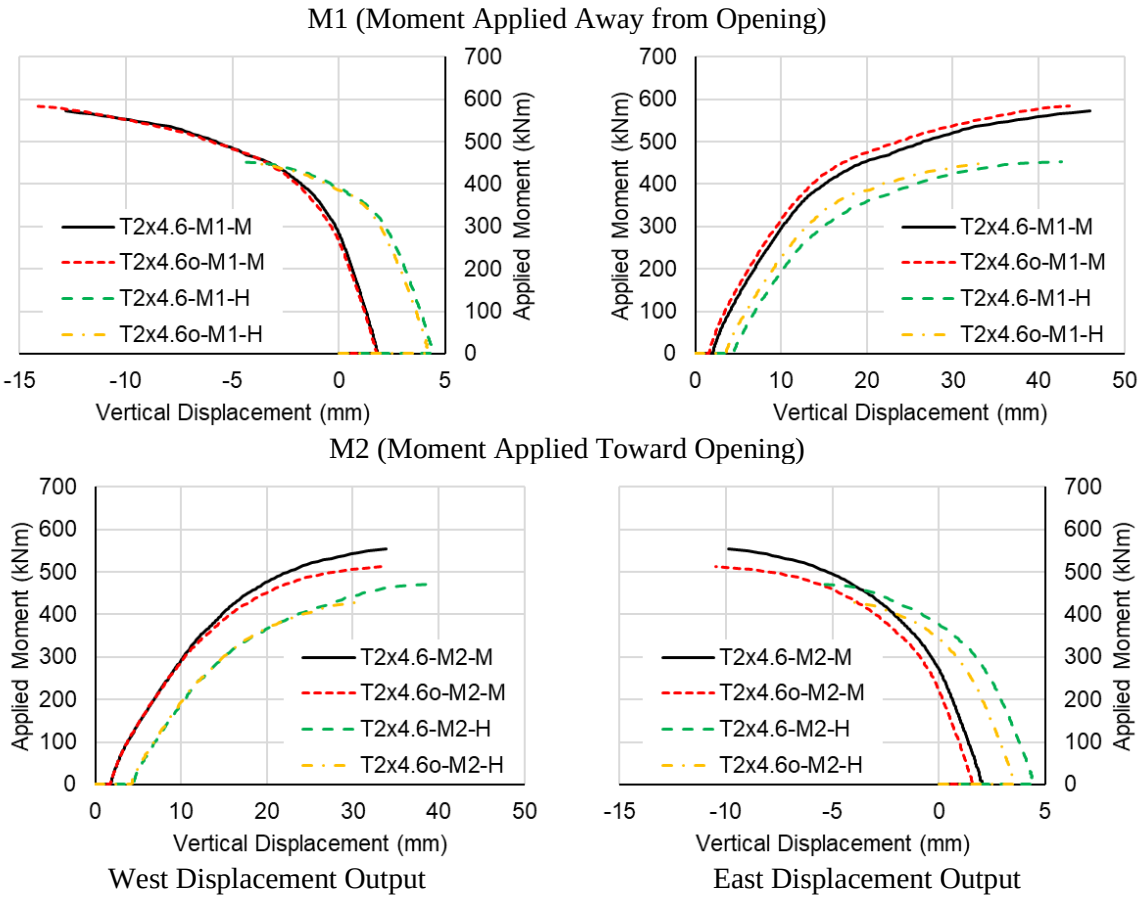


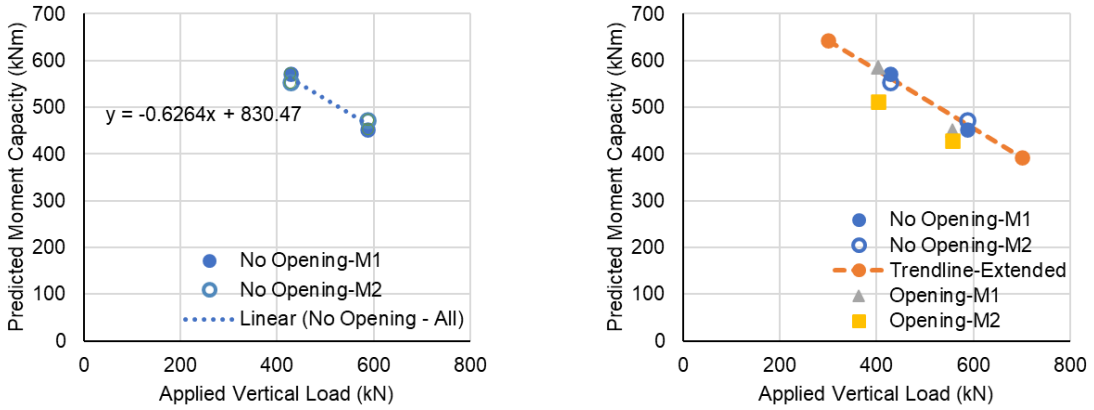
Figure 9-30: Predicted Moment-Displacement Responses for T-SCCs Subjected to V+M (Monotonic) Loading, Displacement Measurement Locations Shown in Figure 9-5

The predicted moment capacities for the connections without openings at the vertical load levels corresponding to the connections with opening and the approximated opening influences are summarized in Table 9-15. As discussed for the L-SCCs, for a GSR of 0.4, the opening between the column flanges has a negligible influence on the unbalanced moment capacity when the moment is applied away from the opening. However, for a GSR of 0.55, the analyzed opening layout results in an approximately 7% lower unbalanced moment capacity, demonstrating that when the GSR is high, openings between the column flanges of T-SCCs can have an influence even when the moment is applied away from the opening. Furthermore, when the moment is applied toward the opening, the unbalanced moment capacity of the connections is decreased by more than 10%, which is consistent with the results for all other column geometries analyzed herein.

Table 9-15: Summary of Predicted Unbalanced Moment Capacities and Approximated Opening Influences, T-SCCs

		FEA Results		Approximated Opening Impact (Trendline Analysis)		
		kN	kNm	kN	kNm	%
	Specimen	V	M_{FEA}	$V^{(A)}$	M_{trend}[(a)]	Opening Influence
GSR = 0.4	T2x4.6-M1-M	427.0	572.5	403.8	577.5	-
	T2x4.6-M2-M		553.6		577.5	-
	T2x4.6o-M1-M	403.8	585.0	-	-	+1.3
	T2x4.6o-M2-M		512.2	-	-	-11.3
GSR = 0.55	T2x4.6-M1-H	587.1	452.9	555.3	482.6	-
	T2x4.6-M2-H		472.6		482.6	-
	T2x4.6o-M1-H	555.3	450.0	-	-	-6.8
	T2x4.6o-M2-H		429.0	-	-	-11.1

[(a)] M_{trend} is the approximated unbalanced moment capacity of the connection without opening at vertical load level used in the analysis of opening specimens ($V^{(A)}$)



a) Results for Specimens Without Openings and Trendline

b) Results for Specimens with Openings and Comparison to Trendline Predictions

Figure 9-31: Comparison of Unbalanced Moment Capacity of Specimens with Openings to Approximated Capacity Based on Trendline for Specimens Without Openings (Note, Trendline Based on M1 and M2 Data), T-SCCs

9.4.2.4 Cruciform Slab-Column Connections (X-SCCs)

The FEA predicted all 6 X-SCCs to fail in punching shear. The predicted moment-deflection responses at the east and west displacement output locations (the location of the output points was previously shown in Figure 9-5 and Figure 9-10) are provided in Figure 9-32, and a summary of the

predicted unbalanced moment capacities is provided in Table 9-16 (note, as previously discussed, the unbalanced moment capacities in the M1 and M2 directions are the same for the connection without opening due to symmetry). Consistent with the findings for the concentrically loaded specimens, slab openings result in a decrease in capacity, especially when the moment is applied toward the opening. For the connections with openings where the GSR was equal to 0.4 and 0.55, the unbalanced moment capacities in the M2 direction were approximately 8.3% and 5.5% lower than those in the M1 direction, respectively. Therefore, the influence of the opening on punching capacity is also influenced by the location of the opening with respect to the moment direction regardless of the column geometry. Furthermore, consistent with the results for all other column geometries, the unbalanced moment capacity of the X-SCCs decreased as the GSR increased. For example, for the connections without openings, the predicted unbalanced moment capacity decreased by approximately 19% when the GSR increased from 0.4 to 0.55.

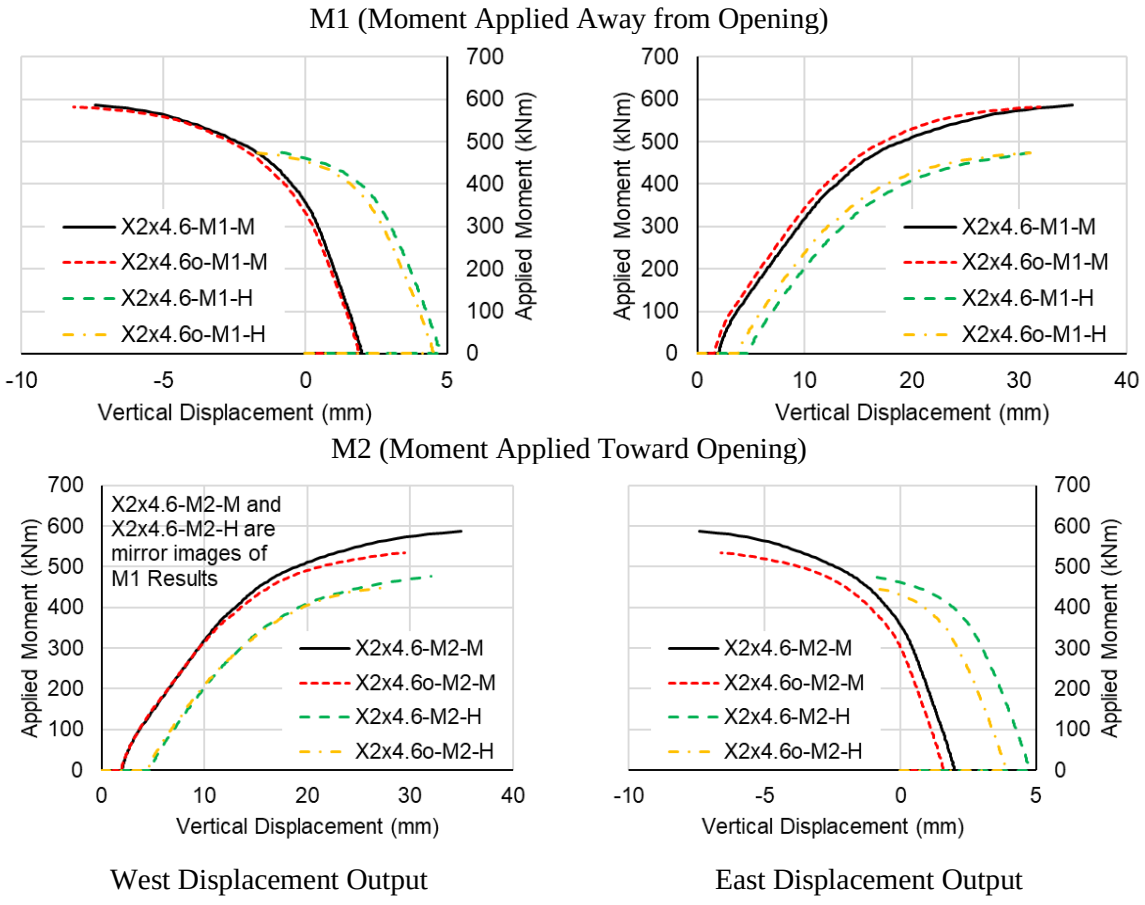
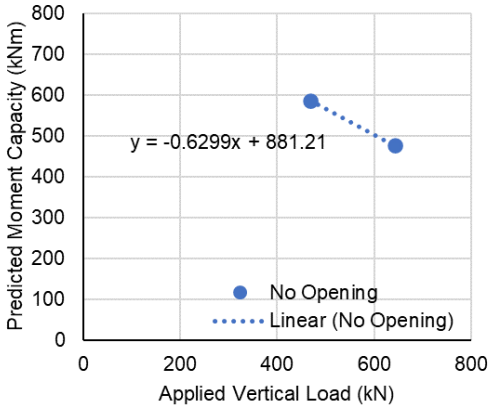


Figure 9-32: Predicted Moment-Displacement Responses for X-SCCs Subjected to V+M (Monotonic) Loading, Displacement Measurement Locations Shown in Figure 9-5

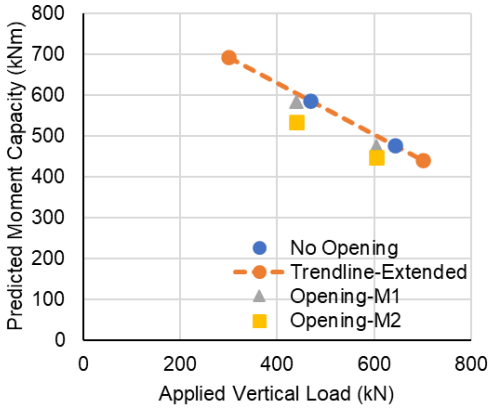
Table 9-16: Summary of Predicted Unbalanced Moment Capacities and Approximated Opening Influences, X-SCCs

		FEA Results		Approximated Opening Impact (Trendline Analysis)		
		kN	kNm	kN	kNm	%
	Specimen	V	M_{FEA}	$V^{(A)}$	M_{trend}[(a)]	Opening Influence
GSR = 0.4	X2x4.6-M1-M	467.1	587.0	439.1	604.6	-
	X2x4.6o-M1-M	439.1	583.2	-	-	-3.5
	X2x4.6o-M2-M		534.9	-	-	-11.5
GSR = 0.55	X2x4.6-M1-H	642.3	476.6	603.8	500.9	-
	X2x4.6o-M1-H	603.8	474.6	-	-	-5.2
	X2x4.6o-M2-H		448.4	-	-	-10.5

[(a)] M_{trend} is the approximated unbalanced moment capacity of the connection without opening at vertical load level used in the analysis of opening specimens ($V^{(A)}$)



a) Results for Specimens Without Openings and Trendline



b) Results for Specimens with Openings and Comparison to Trendline Predictions

Figure 9-33: Comparison of Unbalanced Moment Capacity of Specimens with Openings to Approximated Capacity Based on Trendline for Specimens Without Openings, X-SCCs

Again, the opening influence is quantified by estimating the capacity of the connection without an opening for the vertical load levels used in the simulations of the connections with openings assuming a linear relationship between the unbalanced moment capacity and concentric load as shown in Figure 9-33a. Based on the approximated moment capacities, which are summarized in Table 9-16 (M_{trend}), it is concluded that openings located between the column flanges have a minor influence on connection capacity (less than approximately 5% for the analyzed connections) when the moment is applied away from the opening. However, when the moment is applied toward the opening, the connection

capacity is reduced by approximately 10%, which is consistent with the results for the R-SCCs, L-SCCs and T-SCCs.

9.4.2.5 Comparison of Predicted Capacities from NLFEA and ACI 421.1R-20

The unbalanced moment capacities predicted by the calibrated FEM for all R-SCCs and SS-SCCs analyzed in Chapter 9 are provided in Table 9-17. Consistent with the predictions for the concentrically loaded specimens, the X-SCCs were predicted to be the strongest connections. Even though the X-SCCs were subjected to the highest concentric loads, the FEM also predicted them to have the highest unbalanced moment capacities. Again, consistent with the concentric results, the second-highest unbalanced moment capacities were predicted for the T-SCCs. However, unlike the concentric results, the R-SCCs were typically predicted to be slightly stronger than the L-SCCs.

The unbalanced moment capacities predicted according to the ACI 421.1R-20 provisions for all analyzed R-SCCs and SS-SCCs are also provided in Table 9-17. Overall, the ACI 421.1R-20 predictions are very conservative compared to the FEA (the ratio of M_{ACI}/M_{FEA} is less than approximately 0.7 for most of the analyzed connections), particularly for the specimens with openings. However, while the predictions are conservative, they are very inconsistent, as the ratio of M_{ACI}/M_{FEA} varies from 0.08-0.86 for the analyzed specimens. Therefore, it is clear that the ACI 421.1R-20 method is not accurately capturing the behaviour of slab-column connections subjected to combined concentric shear and unbalanced moment and requires revision.

Somewhat surprisingly, ACI 421.1R-20 was found to be the most conservative for the R-SCCs. This was unexpected as there is more literature related to the punching shear behaviour of R-SCCs than SS-SCCs. Though as discussed in Chapter 2, both areas are still lacking and most previous studies of R-SCCs with openings involve openings near or along the short side of the connection. The large discrepancy between the predictions from the FEA and ACI 421.1R-20 demonstrates that improvements to the opening and unbalanced moment provisions are needed, particularly for R-SCCs with openings, as the current provisions may lead to overly conservative designs.

However, in addition to being generally overly conservative and inconsistent, another major issue with the ACI 421.1R-20 provisions is that the influence of the moment direction with respect to the slab opening on punching shear capacity is not accurately captured. As previously discussed, the FEM predicted higher unbalanced moment capacities when the moment was applied away from the opening (i.e. the opening is on the side of the connection where the stresses due to the unbalanced

moment and concentric load are not additive), which matches experimental observations for square [204, 210] and rectangular [210, 220] slab-column connections. On the other hand, ACI 421.1R-20 predicts a higher unbalanced moment capacity when the moment is applied toward the opening (i.e. the opening is on the side of the connection where the stresses due to the unbalanced moment and concentric load are additive). However, it must be reiterated, that even though the influence of the moment direction is not accurately captured, the unbalanced moment capacities predicted by ACI 421.1R-20 are still very conservative compared to the FEA for all specimens with openings (maximum M_{ACI}/M_{FEA} ratio of 0.74 [T2x4.6o-M2-M]).

Table 9-17: Unbalanced Moment Capacities Predicted by ACI 421.1R-20 for Analyzed R-SCCs and SS-SCCs Subjected to V+M (Monotonic) Loading

GSR = 0.4					GSR = 0.55				
Specimen	kN V	kNm M_{FEA}	kNm M_{ACI}	$\frac{M_{ACI}}{M_{FEA}}$	Specimen	kN V	kNm M_{FEA}	kNm M_{ACI}	$\frac{M_{ACI}}{M_{FEA}}$
R2x7.2-M1-M	403.2	506.2	248.4	0.49	R2x7.2-M1-H	554.4	430.5	169.2	0.39
R2x7.2o-M1-M	355.2	518.7	95.7	0.18	R2x7.2o-M1-H	488.4	470.4	39.4	0.08
R2x7.2o-M2-M	355.2	471.0	183.8	0.39	R2x7.2o-M2-H	488.4	401.8	140.5	0.35
L2x4.6-M1-M	398.9	484.6	275.4	0.57	L2x4.6-M1-H	548.5	398.6	213.7	0.54
L2x4.6-M2-M	398.9	472.8	288.3	0.61	L2x4.6-M2-H	548.5	384.7	210.6	0.55
L2x4.6o-M1-M	351.2	497.5	125.6	0.25	L2x4.6o-M1-H	496.7	384.3	74.1	0.19
L2x4.6o-M2-M	351.2	441.6	225.6	0.51	L2x4.6o-M2-H	496.7	367.7	175.2	0.48
T2x4.6-M1-M	427.0	572.5	338.4	0.59	T2x4.6-M1-H	587.1	452.9	266.7	0.59
T2x4.6-M2-M	427.0	553.6	475.4	0.86	T2x4.6-M2-H	587.1	472.6	368.3	0.78
T2x4.6o-M1-M	403.8	585.0	185.3	0.32	T2x4.6o-M1-H	555.3	450.0	121.6	0.27
T2x4.6o-M2-M	403.8	512.2	380.2	0.74	T2x4.6o-M2-H	555.3	429.0	287.3	0.67
X2x4.6-M1-M	467.1	587.0	419.4	0.71	X2x4.6-M1-H	642.3	476.6	321.3	0.67
X2x4.6o-M1-M	439.1	583.2	238.7	0.41	X2x4.6o-M1-H	603.8	474.6	151.3	0.32
X2x4.6o-M2-M	439.1	534.9	379.7	0.71	X2x4.6o-M2-H	603.8	448.4	295.6	0.66

Note: Diagonal portion of critical perimeter included and β defined as a_n/b_n when calculating M_{ACI}; Material safety factors set to 1 when calculating M_{ACI}

Furthermore, ACI 421.1R-20 does not accurately capture the influence of the moment direction for T-SCCs without slab openings. Unlike the FEM, which predicts an approximately equal unbalanced

moment capacity when the moment is applied away (M1 direction) or toward (M2 direction) the stem of the T, ACI 421.1R-20 predicts the unbalanced moment capacity in the M2 direction to be approximately 28% higher. However, it should be noted that ACI 421.1R-20 predicts approximately equal unbalanced moment capacities in the M1 and M2 directions for L-SCCs, which matches the FEM predictions.

Based on the above discussion, ACI 421.1R-20, and by extension ACI 318-19, do not accurately capture the punching shear behaviour of R-SCCs or SS-SCCs subjected to combined concentric load and unbalanced moment. While the overall predictions are conservative, they are not consistently conservative. Additionally, the influence of the moment direction on the punching shear behaviour of T-SCCs without openings, or on all connection geometries when openings are present is not accurately captured. Future studies should focus on developing either modifications to the existing provisions, or entirely new design methods, to correct the issues highlighted above, and to improve the overall prediction accuracy to avoid overly conservative designs. However, due to the limited size of the study conducted herein, the development of alternate design methods for connections subjected to combined unbalanced moment and concentric load is beyond the scope of this work.

9.5 Summary and Contributions

In this chapter, the punching shear behaviour of R-SCCs and SS-SCCs, with and without slab openings, subjected to combined concentric shear and uniaxial unbalanced moment was studied using NLFEA. The work presented in this chapter builds on that presented in Chapter 8, which was focused on the connection behaviour under concentric loading only, and is important because most, if not all, connections are subjected to a combination of concentric shear and unbalanced moment in actual structures. While this is a common loading condition in practice, previous studies are limited, particularly for SS-SCCs or for slab-column connections with openings.

Based on NLFEA results, discussions of the influence of the vertical load level, direction of the unbalanced moment and slab openings on the capacity, stiffness and cracking of interior R-SCCs and SS-SCCs are provided. These discussions are currently lacking in the existing literature, and therefore the findings of this work are important contributions that can be used to improve future punching shear design provisions.

The accuracy of the ACI provisions for connections subjected to combined concentric shear and unbalanced moment was also evaluated in this work. Due to the connection geometry and presence of

slab openings, ACI 421.1R-20 was used to estimate the connection capacity. The ACI 421.1R-20 provisions were found to be overly conservative compared to the FEA. Additionally, the level of conservativeness was not consistent, suggesting that the ACI method is not accurately capturing the behaviour of connections subjected to combined shear and unbalanced moment. However, due to the limited size of the study presented herein, suggestions to improve the ACI provisions are beyond the scope of this work.

Chapter 10: Conclusions and Future Work

In this chapter, the conclusions related to the interior slab-wall connection study (Chapter 6), alternate punching shear design methods for elongated connections (Chapter 7), and special-shaped slab-column connection studies (Chapter 8 [concentric loading] and Chapter 9 [combined concentric shear and unbalanced moment]) are presented. A brief summary of the work conducted in this thesis, and recommendations for future work are also provided. The conclusions for each study are presented in individual sections.

10.1 Summary

Experimental tests of rectangular or special-shaped slab-column connections subjected to concentric loading only or combined concentric shear and unbalanced moment, with or without slab openings are limited. NLFEA, when properly calibrated to experimental results, is a cost and time-effective method to expand experimental databases and evaluate the influence of parameters which are difficult to study experimentally. The Concrete Damaged Plasticity model (CDP) model, available in the commercial FEA software Abaqus, has already been shown to be capable of accurately predicting the punching shear behaviour of square and rectangular slab-column connections by Genikomsou [235], Laguta [246], Beaulieu [247] and the author [1].

The work presented in this thesis was conducted to study the influence of support geometry on the punching shear behaviour of interior slab-column and slab-wall connections using slightly modified versions of the FEMs developed during the author's MASc studies. All nonlinear FEMs used in this work were based on the CDP model in Abaqus, with the model input parameters calibrated to experimental specimens from literature.

First, the punching shear behaviour of interior slab-wall connections (SWCs) with or without slab openings and subjected to concentric shear or combined concentric shear and uniaxial, monotonically increasing unbalanced moment was analyzed by extending the FEM originally developed to study the concentric punching shear behaviour of rectangular slab-column connections (R-SCCs). As discussed in [1], and briefly summarized herein, this FEM was calibrated to experimental results of four R-SCCs subjected to different loading conditions [151] and three square slab-column connections with different flexural reinforcing layouts [57]. Before the calibrated FEM was used to study the punching shear behaviour of SWCs, linear elastic FEA was used to estimate the radius of contraflexure around interior SWCs in continuous structures such that isolated slab-wall specimens, where the portion of

the slab included in the analysis approximates the extent of the negative moment region around the connection, could be analyzed. In the slab-wall connection study, the influence of loading conditions (concentric load only [including different application methods] and combined concentric shear and uniaxial, monotonically increasing unbalanced moment), wall size (thickness and length) and presence of symmetric slab opening layouts on the punching shear behaviour of SWCs were analyzed. The punching behaviour of SWCs and R-SCCs, with and without slab openings were compared (the punching behaviour of R-SCCs with openings was analyzed as part of this work).

Second, alternative punching shear design methods for interior R-SCCs and SWCs were developed as the FEA results presented herein and in [1] have demonstrated that the existing ACI 318-19 [2] provisions are inadequate for elongated connections. The proposed design methods were developed based on the FEA results and verified by comparisons to experiments where possible. For R-SCCs, three potential design methods were proposed. The first, Method 1, was based on an assumed effective critical perimeter, the extent of which was derived from the linear elastic shear stress distribution along the critical perimeter at *d/2* from the column face of isolated specimens predicted by the FEA. In the second, Method 2, the entire critical perimeter at *d/2* from the column face is assumed to be effective, but a non-uniform shear stress distribution is assumed. As Method 1 and 2 were found to be overly conservative for elongated and small columns, respectively, a third method, the Combined Method, which combines Method 1 and 2, was also proposed. The transition point between the two methods was determined based on NLFEA results for 77 isolated slab-column connections previously analyzed by the author [1]. The proposed design method for interior SWCs decomposes the wall into a combination of two-way shear regions, which are located near the wall ends (the extent of these regions was determined using NLFEA), and a one-way shear region along the remainder of the wall. Simple methods to estimate the capacity of two-way shear regions, one-way shear region and the applied punching load demand were presented.

Third, the punching shear behaviour of special-shaped slab-column connections (SS-SCCs) (specifically L, T and cruciform connections), with and without slab openings, subjected to concentric load only, were analyzed using a slightly modified version of the FEM originally calibrated to analyze the one square and eight rectangular slab-column connections tested by Hawkins et al. [3]. Note, at the time of the FEM calibration, the experimental tests of L slab-column connections (L-SCCs) by Pinto et al. [174] were not available. In this work, the original calibration, which was presented in [1] and based on the model by Genikomsou [235], was updated to improve the

agreement between the FEA results and experimental measurements. The FEM was used to study the influence of column size and shape on the concentric punching shear behaviour of SS-SCCs. The FEM was also used to analyze the influence of slab openings at various locations around L, T and cruciform slab-column connections. The FEA demonstrated that slab openings located between the column flanges typically had a minor influence on the concentric punching shear behaviour of SS-SCCs. The minor influence of openings between the column flanges suggests that the diagonal portion of the critical perimeter assumed in design codes is relatively ineffective in transferring load between the slab and the column. To further quantify the benefits of SS-SCCs, the punching shear behaviour of R-SCCs with and without slab openings was also analyzed as part of this study.

Finally, the punching shear behaviour of SS-SCCs and R-SCCs with and without slab openings when subjected to combined concentric shear and uniaxial, monotonically increasing unbalanced moment was also analyzed. Since the specimens tested by Hawkins et al. [3] lacked flexural reinforcement on both sides of the slab, this study was conducted using a nonlinear FEM calibrated to the experimental tests of square slab-column connections by Drakatos et al. [4]. As the Drakatos et al. [4] specimens had the same slab geometry and concentric loading conditions as those in [57, 151] the CDP parameters used in this study and in the slab-wall connection study were the same. However, due to the application of the unbalanced moment some modifications to the FEM were required. The primary goal of this study was to determine if openings located between the column flanges also had a minor influence on the punching shear behaviour of these connections when subjected to combined concentric shear and uniaxial, monotonic unbalanced moment. The influence of the moment direction with respect to the opening (away from or toward the opening) was also studied.

10.2 Conclusions of Interior Slab-Wall Connection Study

In Chapter 6, a three-dimensional nonlinear FEM implemented in Abaqus/Explicit, which was originally calibrated to study the punching shear behaviour of interior R-SCCs, was extended to study the punching shear behaviour of interior SWCs subjected to various loading conditions. The study was divided into two main parts, the concentric load study, outlined in Section 6.2.2, and the V+M study, outlined in Section 6.2.3. In addition to analyzing the influence of load conditions, the influence of symmetric slab opening layouts on the concentric punching shear behaviour of interior SWCs was also studied. This study, which was denoted the Symmetric Opening Study, was outlined in Section 6.2.4. It should be noted that specimens subjected to combined concentric shear and

uniaxial unbalanced moment were not analyzed in the Symmetric Opening Study due to the high computational resources required to analyze the necessary half models.

Brief summaries and the main conclusions of the concentric load type study, V+M study and the Symmetric Opening Study are provided in Sections 10.2.1, 10.2.2 and 10.2.3, respectively.

10.2.1 Concentric Load Study

In the concentric load study, the punching shear behaviour of interior SWCs subjected to concentric loading only was studied. In the first part of the concentric load study, which was denoted the Load Type Study, the punching shear behaviour of a SWC with a length of 13760mm and a thickness of 260mm ($\kappa = c_{min}/d$ =1.287) was studied for four different load cases. In the second part of the concentric load study, denoted the Parametric Study, the influence of connection size (wall length and thickness) on punching shear behaviour was studied through an analysis of eight hypothetical connections. Based on the results presented in Section 6.4.1, the following conclusions can be drawn:

1. Interior SWCs can fail in punching shear before failing in one-way shear. However, it should be noted that when subjected to concentric vertical loading one-way shear does have a significant impact on the overall connection response as extensive one-way shear cracking in the slab parallel to the long side of the wall is predicted. Furthermore, the occurrence of punching does not necessarily result in a significant decrease in load-carrying capacity as is observed for slab-column connections. Experimental tests of SWCs subjected to lateral loading have also demonstrated that punching failures of SWCs may not result in a catastrophic loss of load carrying capacity [29, 30].
2. The methodology used to apply the concentric vertical loading to the isolated slab-wall specimen had a significant impact on the predicted capacity and stiffness. For the connections which were loaded through discrete load plates approximately located along the radius of contraflexure increasing the load magnitude on the plate close to the wall toe (wall end) resulted in a decreased stiffness and lower punching capacity than when each load plate was equally loaded or had a load based on the tributary area of each plate. Applying a uniformly distributed load to the slab surface beyond *d/2* from the wall face resulted in a significantly higher punching capacity and stiffness than when the specimen was loaded through discrete load plates. Similar large increases in punching capacity and connection stiffness were also experimentally observed when a uniformly distributed load

was applied to isolated slab-column connections [330, 331]. It should be noted that the remainder of the conclusions presented in this section are based on the analyses where concentric loading was applied through equally loaded plates approximately located along the radius of contraflexure, as this load case is the most representative of typical experimental punching shear tests.

3. As the wall length, L, thickness (minimum plan dimension), c_{min}, and the ratio of wall thickness to effective slab depth, d ($\kappa = c_{min}/d$) increased so too did the connection stiffness and concentric punching capacity. The connection stiffness in the direction perpendicular to the short side of the wall increased at a faster rate than that in the direction perpendicular to the long side of the wall. This behaviour matched that predicted for R-SCCs subjected to concentric vertical loading previously studied by the author [1, 145].

4. The ACI 318-19 punching shear design provisions predict significantly higher punching shear capacities than the NLFEA. On average, the ACI 318-19 predictions were 2.36 times higher than those from the NLFEA for the eight analyzed SWCs ($f_c' = 44.6$MPa). While the ACI 318-19 provisions include equations relating the support aspect ratio, β, and the ratio of the critical perimeter length, b_o, to d, to the concrete's nominal shear capacity along the critical perimeter, v_c, these relationships were derived from experimental tests of isolated slab-column connections and do not appear to be accurate for SWCs.

5. The FEA predicted one-way shear to dominate the connection behaviour parallel to the long side of the wall. The one-way shear capacity predicted by ACI 318-19 parallel to the long side of the wall was 1.29 times higher on average than the total shear capacity predicted by the NLFEA for the eight specimens ($f_c' = 44.6$MPa). The one-way shear capacity predicted by ACI 318-19 parallel to the short side of the wall based on the dimensions of the isolated specimen was much lower than the total shear capacity predicted by the FEA. Therefore, the ACI 318-19 one-way shear provisions also do not appear to accurately capture the behaviour of SWCs predicted by the FEA, though this may be because the connections are failing in punching shear before the complete development of the one-way shear mechanism.

6. As observed in the author's previous analysis of interior R-SCCs [1], the nominal shear stress capacity along the critical perimeter at *d/2* from the wall predicted by ACI 318-19 is much higher than the shear stress magnitudes along the critical perimeter predicted by the

FEA, particularly along the long side of the wall. Comparing the shear stress distributions predicted by ACI 318-19 and the NLFEA, the assumption of uniform shear stress with a minimum magnitude of $0.17\sqrt{f_c'}$ (which is the value associated with one-way shear in ACI 318-19) is incorrect. The NLFEA predicted the shear stress distribution along the critical perimeter to be non-uniform, with a high concentration of shear stress near the wall toes (wall ends). At failure, the NLFEA predicted the shear stress magnitudes along most of the critical perimeter at *d/2* from the wall face to be less than 0.5MPa, which is much lower than the value of 1.135MPa predicted by ACI 318-19 for a f_c' value of 44.6MPa.

7. When an interior SWC is subjected to concentric vertical loading, the shear stresses along the wall perimeter concentrate along the short side of the wall and near the wall corner along the long side. As the ratio of the wall thickness to the effective slab depth ($\kappa = c_{min}/d$) increased, the concentration of shear stresses at the wall corner increased. The FEA predicted the shear stress magnitudes along the long side of the wall to decrease rapidly with increasing distance from the wall corner, approaching a magnitude of approximately 0MPa at a distance of approximately *5d* (approximately 1000mm for *d*=202mm) from the wall corner. This approximately zero shear stress region is assumed to mark the end of the portion of the connection which is influenced by two-way shear. Beyond this point, the shear stress magnitudes increase slightly towards an approximately constant value along the remainder of the long side of the wall (for the analyzed specimens where f_c' = 44.6MPa the shear stress magnitude in the approximately constant region was below 0.5MPa). It is also interesting that the peak shear stress magnitudes along the wall perimeter at the peak load level are of similar magnitude to those predicted in the previous NLFEA of R-SCCs subjected to concentric vertical load [1], which suggests that punching shear failures occur at a similar peak shear stress magnitude regardless of connection size.

8. While punching shear failures are predicted to occur before one-way shear failures, the predicted nominal concentric punching shear capacities are typically quite large, and also typically exceed the factored load demands determined in accordance with North American design provisions [332, 333]. If the ACI 318-19 strength reduction factor for shear failures (ϕ = 0.75) is applied to the capacities predicted by the NLFEA, the factored shear capacities are only less than the applied load demand determined in accordance with ASCE 7-16 [332] in cases where the walls are relatively thin ($\kappa < 1.782$), based on the large span

between supports in the prototype structure (L = 6.75m [56]), and the live load is high (4.8kPa). As such, the punching capacities predicted by the NLFEA confirm why punching failures of interior SWCs are exceedingly rare in practice, even though no widely adopted design method is currently available. Furthermore, while the factored capacities of the specified connections are lower than the factored applied loads, these connections would likely be adequate in practice due to the fact that the occurrence of the full factored design load is rare, and the significant benefits of compressive membrane action and moment/shear redistribution (which increase punching capacity) are neglected in the analysis of isolated specimens. Therefore, without the presence of large concentrated loads or slab openings near the wall toe, punching shear failures of SWCs are unlikely in practice.

9. While punching shear failures of SWCs are unlikely in practice for the reasons outlined above, a proper understanding of the connection behaviour is necessary for efficient design, and due to the fact that the SWCs are essential for the performance of both the gravity and lateral force resisting systems in many reinforced concrete structures. Additionally, while punching shear failures of SWCs that do occur are not expected to be catastrophic, due to the overall connection size, and are instead expected to be confined to regions near the wall ends, these failures should be avoided at all costs. Localized punching failures near the wall toes could lead to serviceability limit state failures as excessive slab cracking near the wall toes could damage any services installed in the slab, or lead to the public questioning overall structural safety.

10.2.2 Combined Shear and Unbalanced Moment Study (V+M Study)

In the V+M Study, the punching shear behaviour of an interior SWC with a length of 13760mm and a thickness of 260mm (κ = 1.287) when subjected to a vertical load equal to 40% and 65% of its concentric punching capacity and a monotonically increasing uniaxial unbalanced moment about an axis parallel to the short side of the wall was studied. Due to how the unbalanced moment was applied, these simulations required the use of half models, which greatly increased the computational demand, leading to only one connection being analyzed. Based on the FEA results presented in Section 6.4.2, the following conclusions can be drawn:

1. The shear stress distribution along the portion of the wall where the shear stresses due to concentric loading and uniaxial unbalanced moment are additive has a similar shape to that

predicted for a connection subjected to concentric load only. Additionally, the shear stress magnitudes at a similar distance from the wall corner are similar for both load conditions on this portion of the wall. The similarities in the wall perimeter shear stress distributions for concentric load only and combined concentric vertical load and uniaxial unbalanced moment about an axis parallel to the short side of the wall suggests that the same portion of the connection is effective for transferring shear stresses due to vertical loads and unbalanced moment. It also suggests that regardless of loading conditions that punching shear failures are triggered at a similar peak shear stress magnitude.

2. As with the concentric punching shear capacities, the unbalanced moment capacities of SWCs subjected to vertical load levels equal to 40% and 65% of their concentric punching capacity are very high and exceed the unbalanced moment demands which would be expected in most structures. Therefore, punching shear failures of SWCs are expected to be exceptionally rare in continuous flat plate structures even when the connections are subjected to combined concentric vertical loading and monotonically increasing uniaxial unbalanced moment about an axis parallel to the short side of the wall.

10.2.3 Influence of Slab Openings

In the Symmetric Opening Study, the influence of slab openings on the concentric punching shear behaviour of interior SWCs was studied. Like in the V+M Study, the SWC with a length of 13760mm and a thickness of 260mm was taken as the reference specimen. A total of six opening layouts were considered. Note, all slab opening layouts were doubly symmetric to allow for the use of quarter models to reduce the required computational demand. Seven R-SCCs, six of which had opening layouts similar to those considered for the SWCs, were also analyzed to allow the influence of openings on the punching behaviour of R-SCCs and SWCs to be compared. The maximum and minimum dimensions of the rectangular column were 780mm and 260mm, respectively. For both rectangular slab-column and slab-wall connections, the accuracy of the ACI 318-19 punching shear provisions was evaluated through comparisons to the FEA predictions. The accuracy of the radial approach (which is used in ACI 318-19), and the straight projection approach, which are intended to account for the negative influence of slab openings by reducing the critical perimeter length, were also evaluated. Based on the presented results, the following conclusions can be drawn:

1. Slab openings near elongated connections (rectangular slab-column and slab-wall connections) reduce connection capacity and stiffness. The negative influence of a

particular opening is dependent on both the opening's size and location (distance from the face of the elongated support and its location with respect to the support).

2. Openings which are adjacent to the long side of elongated connections can result in significant reductions in punching capacity (maximum reductions of approximately 18% and 39% for the analyzed R-SCCs and SWCs, respectively), and can be more detrimental than openings which are adjacent to or near the short sides of the support.

3. When the behaviour of slab-column connections is governed by punching shear, which occurs when the ratio of the maximum column dimension to the isolated specimen length is less than approximately 0.4 as discussed in [1, 145], openings in the vicinity of the connection should be avoided when possible. If openings must be located near the long side of the connection, they should be oriented such that the minimum dimension of the opening is parallel to the long side to minimize the opening's negative influence.

4. For connections where one-way shear is dominant, which occurs when the ratio of maximum support dimension to the isolated specimen length exceeds approximately 0.4, openings adjacent to the long side which are located at or near the end of the support should be avoided, as they result in significant reductions in punching capacity. If openings must be located along the long side, they should be located at a distance greater than $5d$ from each end of the support or near the support centerline to minimize their influence.

5. The punching capacities of the R-SCCs with slab openings in the Symmetric Opening Study predicted by ACI 318-19 when the reduced critical perimeters are calculated using the radial approach were conservative to those predicted by the NLFEA. However, the punching capacities predicted by ACI 318-19 are only conservative because the radial approach greatly overpredicts the influence of each opening layout, particularly when the openings are located adjacent to the long side of the column (note, that the punching capacity of the reference specimen without an opening was overpredicted by ACI 318-19).

6. When using the straight projection approach to determine the required critical perimeter reductions, the punching capacities predicted by ACI 318-19 are typically higher than those based on the radial approach. For the analyzed R-SCCs, the punching capacities based on the straight projection approach were typically unconservative compared to the FEA, but the predicted opening influences agreed well. Therefore, it appears that the

straight projection approach is only suitable for slab-column connections if the connection behaviour is governed by punching shear.

7. As concluded in the Concentric Load Study, ACI 318-19 greatly overpredicts the punching capacity of SWCs. Neither the radial nor straight projection approaches predict opening influences which agree well with those predicted by the FEA. Opening influences predicted according to the radial approach are typically much higher than those predicted by the FEA, though it should be noted that the influence of opening layout 3W, which is the most critical, was reasonably predicted. The straight projection approach is not adequate for SWCs as the influence of opening layout 3W is significantly underpredicted.
8. Finally, slab openings typically have a significant influence on the crack patterns predicted by the FEA. For R-SCCs, all investigated slab opening layouts had a noticeable impact on the predicted crack patterns. Significant crack concentrations are predicted around the openings in a region bounded by the additional rebar placed around the openings, regardless of the opening size and location (these observations are also applicable to the R-SCCs analyzed in the special-shaped connection study, see Sections 8.4.1 and 10.4.1). For SWCs, the influence of openings, other than those located adjacent to the long side and within *5d* of the wall end, on the predicted crack pattern was typically minor. For all elongated supports, even those governed by punching shear, one-way shear cracks are predicted parallel to the long side of the support.

10.3 Conclusions Related to the Development of Alternative Punching Shear Design Methods

Recent research has led to the development of accurate and robust punching shear design methods for interior elongated connections (R-SCCs and SWCs). However, in order to estimate punching capacity, these new methods require the use of two-dimensional FEA, specialized joint elements and the Critical Shear Crack Theory (CSCT) [158, 189], making them unsuitable for hand calculations and typical design scenarios. Additionally, as discussed herein and in [1, 161], the existing ACI 318-19 punching shear provisions (which are applicable to both R-SCCs and SWCs) can greatly overpredict the punching capacity of interior elongated connections compared to the calibrated NLFEA. Therefore, in Chapter 7, alternative punching shear design methods, developed from

NLFEA results, for interior elongated connections without shear reinforcement and subjected to concentric gravity loading, which are suitable for hand calculations, are presented.

Based on the results of the cut-wall model, the proposed design methods for R-SCCs and SWCs apply to connections where the maximum column dimension is less than or equal to and greater than *14d*, respectively. While the recommended punching shear design method for R-SCCs could also be used for SWCs, the predictions would become overly conservative as the increase in the average shear stress in the one-way shear region with increasing κ ($\kappa = c_{min}/d$) would be neglected.

The conclusions derived from the development of the punching shear design methods for rectangular slab-column and slab-wall connections are presented in Sections 10.3.1 and 10.3.2, respectively. It should be noted that all elongated connections considered in this work have effective slab depths less than 250mm, and therefore, the size effect factor (λ_s) in ACI 318-19 [2] was equal to 1. For any connections where the effective slab depth exceeds 250mm, the recommended shear stress magnitudes presented in Sections 7.1, 7.2, 10.3.1 and 10.3.2 should be multiplied by λ_s (see equation 3-5 in Section 3.3.2).

10.3.1 Rectangular Slab-Column Connections (R-SCCs)

1. The concentric punching shear capacity of square or rectangular slab-column connections can be conservatively estimated by using an effective critical perimeter (Method 1). In this work, the effective critical perimeter, whose length was determined using linear elastic FEA, is applicable when at least one column dimension exceeds *2.25d* in length and is located at a distance of *d/2* from the column face. Along the effective critical perimeter, a uniform shear stress distribution, with a magnitude of $0.33\sqrt{f_c'}$ (f_c' in MPa), which matches the maximum value assumed in ACI 318-19, is assumed. Based on a comparison to NLFEA predictions for 77 interior square/rectangular slab-column connections, Method 1 is found to approximately account for the influence of both the column aspect ratio, β, and the relative column size, κ ($\kappa = c_{min}/d$) on punching shear capacity. Additionally, Method 1, which predicts the same punching capacity as ACI 318-19 for connections where the column dimensions are less than or equal to *2.25d* and the ratio of the critical perimeter length to the effective slab depth is less than approximately 20.2 (which is beneficial as the adequacy of the existing provisions for such connections has been proven in practice), is found to be fairly accurate for small slab-column connections ($\beta < 5$).

However, due to the effective critical perimeter neglecting the influence of one-way shear, Method 1 becomes increasingly conservative as the slab-column connections become increasingly elongated. Furthermore, the use of an effective critical perimeter may also suggest to practitioners that slab openings can be located in the ineffective regions without negatively influencing punching capacity, which is untrue.

2. The punching shear design of square or rectangular slab-column connections with slab openings near the connection can be completed using Method 1 by converting the constant shear stress distribution along the effective perimeter to a nominal shear capacity along the entire unreduced critical perimeter length ($b_{0,unreduced} = 2[c_{max} + d] + 2[c_{min} + d]$), $v_{c,eff1}$. Once $v_{c,eff1}$ is determined the existing ACI 318-19 opening provisions can be applied to approximate the negative influence of the opening.

3. The punching shear capacity of square or rectangular slab-column connections can also be conservatively estimated by considering a non-uniform shear stress distribution along the critical perimeter length assumed in ACI 318-19. Along each side of the critical perimeter, the shear stress distribution is assumed to vary from a maximum magnitude of $0.33\sqrt{f_c'}$ to a minimum magnitude of $(0.1)0.33\sqrt{f_c'}$ (f_c' in MPa) over a distance of *3.75d*. Along portions of the critical perimeter which are located beyond a distance of *3.75d* from the corners of the critical perimeter, a uniform shear stress distribution, with a magnitude of $(0.1)0.33\sqrt{f_c'}$, is assumed. Unlike Method 1, Method 2 was found to be overly conservative for small connections (which are dominated by two-way shear), but became increasingly accurate as the columns become more elongated, as the influence of one-way shear is accounted for.

4. The punching shear capacity of square or rectangular slab-column connections can be most accurately estimated by using a combination of Method 1 and Method 2. The combination of both methods, denoted the Combined Method, has the advantages of each individual method, without becoming overly conservative for small or elongated connections. Based on the NLFEA for 77 square/rectangular slab-column connections Method 1 and Method 2 should be used to design connections where the maximum column dimension is less than *3.75d* and greater than or equal to *3.75d*, respectively.

10.3.2 Slab-Wall Connections (SWCs)

1. A tributary area, bounded by the slab centerlines around the SWC, can be used to accurately estimate the applied concentric shear demand for interior SWCs in continuous structures with equal slab bays which are subjected to uniformly distributed gravity loading. When the structure has less than five bays in each orthogonal direction, the tributary area calculated based on the slab centerlines around the connection may be a slight underprediction of the actual tributary area, but the underestimate of the applied load is expected to be less than 5%. If the SWC is a first interior support, or if pattern live loading is to be considered, the estimated tributary area should be increased in line with best engineering practices.

2. For structures with an inconsistent bay size or a non-uniform support layout linear elastic FEA using shell elements can be used to estimate the tributary area or applied load of a SWC.

3. During the development of the cut-wall model, it was found that approximately 40-50% of the total gravity load applied to the isolated slab is transferred to the supporting wall through the toe regions (the portions of the connection with *5d* from each wall end). As such, punching shear design methods for interior SWCs should consider the wall to be made up of two-way shear regions (near the wall toes), and a one-way shear region. Based on the results of NLFEA of isolated SWCs, the two-way shear regions are the portions of the connection within *5d* from each wall end, and the one-way shear region is the remaining portion of the connection beyond *7d* from each end. Note, a *2d* gap between the two-way and one-way shear regions is assumed to be conservative and because the NLFEA predicts the shear stress magnitudes in this region to be very low.

4. As with estimating the concentric punching shear capacity of R-SCCs, the punching capacity of the two-way shear (toe) regions can be estimated using an effective critical perimeter (Method 1W) or a non-uniform shear stress distribution (Method 2W). To make the design methods for SWCs and R-SCCs consistent, Method 2W, which assumes the shear stress distribution along the toe critical perimeter to vary from a maximum magnitude of $0.33\sqrt{f_c'}$ to a minimum magnitude of $(0.1)0.33\sqrt{f_c'}$ (f_c' is in MPa), is recommended. While the Method 2W predictions are more conservative than those from

Method 1W, the assumed stress distribution along the critical perimeter more accurately captures that predicted by the NLFEA.

5. The shear capacity of the one-way shear region can be estimated by assuming a uniform shear stress distribution along the critical perimeter at *d/2* from the wall face. Based on the average shear stress in this region predicted by the NLFEA, the magnitude of the uniform stress is assumed to be equal to $(0.1)0.33\sqrt{f_c'}$ and $(0.15)0.33\sqrt{f_c'}$ (f_c' in MPa) for κ values less than or equal to 0.594 and greater than or equal to 2.970, respectively. The shear stress magnitude for intermediate values of κ can be determined through linear interpolation between these two extreme values.

10.4 Conclusions of Special-Shaped Slab-Column Connection Study – Concentric Shear

In the first part of the special-shaped slab-column connection study, the concentric punching shear behaviour of L, T and cruciform slab-column connections with and without slab openings was studied using a three-dimensional, nonlinear FEM implemented in Abaqus. Due to a lack of experimental tests of SS-SCCs at the time of the calibration the FEM was calibrated to the experimental results of one square and eight rectangular slab-column connections tested by Hawkins et al. [3]. A total of 71 SS-SCCs, 59 of which had slab openings near the column, were simulated to study the influence of column size, column shape and presence of slab openings on concentric punching capacity. Due to the non-uniformity of the column perimeter shear force distribution for SS-SCCs without slab openings predicted by the FEA, the openings were located at various points around the connection to determine the ideal opening location for each column geometry. The punching capacities and opening influences predicted by the FEA were also used to evaluate the accuracy of the ACI 318-19 and ACI 421.1R-20 punching shear design provisions for SS-SCCs.

To allow for a comparison of the punching behaviour of SS-SCCs and more commonly used connection geometries, twenty-one R-SCCs, seventeen of which had slab openings near the column, were also simulated. Due to the smaller size of the specimens in the concentrically loaded special-shaped connection study the influence of nonsymmetric slab opening layouts on the concentric punching shear behaviour of R-SCCs could be evaluated. In addition to expanding the findings of the Symmetric Opening Study, the use of nonsymmetric opening layouts also has the benefit of allowing for the need to account for the unbalanced moment generated due to the eccentricity between the

column and reduced critical perimeter centroids to be evaluated. As was done for SS-SCCs, the punching capacities and opening influences predicted by the FEA, ACI 318-19 and ACI 421.1R-20 were compared to evaluate the accuracy of the ACI provisions. When calculating punching capacity according to the ACI 318-19 concentric punching shear provisions, reduced critical perimeters based on both the radial (which is used in ACI 318-19) and the straight projection approach were considered. However, due to the time-consuming nature of the ACI 421.1R-20 provisions reduced critical perimeters according to radial approach only were considered.

Conclusions related to the R-SCCs considered in the special-shaped connection study are provided in Section 10.4.1. General conclusions related to SS-SCCs, and specific conclusions for L-, T- and cruciform-shaped slab-column connections are provided in Sections 10.4.2, 10.4.3, 10.4.4 and 10.4.5, respectively.

10.4.1 Rectangular Slab-Column Connections (R-SCCs)

1. As concluded in the Symmetric Opening Study (see Section 10.2.3), slab openings near R-SCCs significantly reduce punching capacity and connection stiffness. In addition to the opening's size and location, the opening's negative influence is also dependent on the governing failure mode of the connection without an opening (punching shear or one-way shear).

2. Also consistent with the results of the Symmetric Opening Study, openings adjacent to the long side of R-SCCs can result in a significant reduction in punching capacity. When the behaviour of a R-SCC is governed by punching shear (which occurs when the ratio of the maximum column dimension to the isolated specimen length is less than approximately 0.4 as discussed in [1, 145]), openings along the long side of the connection should be avoided whenever possible. Regardless of their location along the long side, such openings result in significant reductions in punching capacity (maximum reduction of approximately 22% for the analyzed specimens). If an opening must be located along the long side of the connection, it should be oriented such that the minimum dimension of the opening is parallel to the long side of the column, to minimize the negative influence of the opening.

3. For the R1-L and R2-L specimens, openings which are located along the long side and at or near the column ends lead to significant capacity reduction (maximum reductions >10%). Therefore, when the connection behaviour is dominated by one-way shear (which occurs

when the ratio of the maximum support dimension to the isolated specimen length exceeds approximately 0.4) openings which start at or near the column ends should be avoided. This conclusion is consistent with the findings for SWCs in the Symmetric Opening Study.

4. For R-SCCs with nonsymmetric opening layouts, punching failures can occur around one end of the connection (typically the end closest to the opening). Note, similar behaviour was also observed by Teng et al. [147].

5. Consistent with the Symmetric Opening Study, the punching capacity of the analyzed R-SCCs predicted by ACI 318-19 based on reduced critical perimeters according to the radial approach were typically conservative compared to the FEA. Unlike the Symmetric Opening Study, where the opening influences were significantly overpredicted, the predicted opening influences for the R-SCCs in the special-shaped connection study were reasonably accurate, and conservative compared to those from the FEA. However, it should be noted that the influence of openings along the long side of the connections were significantly overpredicted in some cases, particularly when using the ACI 421.1R-20 method to estimate concentric punching capacity.

6. As observed in the Symmetric Opening Study, punching capacities according to ACI 318-19 calculated using a reduced critical perimeter based on the straight projection approach were typically higher than those based on the radial approach. For the four analyzed column sizes the predicted punching capacities were conservative on average. However, the accuracy of the predicted opening influences was dependent on the connection behaviour. For the small column specimens, R1-S and R2-S (which are governed by punching shear), the predicted opening influences agreed well with the FEA results. For the large column specimens, R1-L and R2-L (which are governed by one-way shear), the straight projection approach does not accurately predict the influence of openings adjacent to the long side of the connection, especially when the openings are near the column ends. The inability of the straight projection approach to accurately predict the influence of openings near the end of connections which are dominated by one-way shear was also observed in the Symmetric Opening Study for opening layout 3W. Therefore, the straight projection approach is not suitable to estimate the influence of openings around elongated connections which are governed by one-way shear (ratio of maximum column dimension to isolated specimen length greater than approximately 0.4).

7. The punching capacities and opening influences predicted by ACI 421.1R-20 are much more conservative compared to the FEA than those based on the ACI 318-19 concentric punching shear provisions. Therefore, it does not appear to be necessary to account for the unbalanced moment generated due to the misalignment of the column and reduced critical perimeter centroids for R-SCCs with nonsymmetric opening layouts when the connection is subjected to concentric gravity loading only.

10.4.2 General Conclusions for Special-Shaped Slab-Column Connections (SS-SCCs)

1. As with R-SCCs, the shear force distribution around the perimeter of L, T and cruciform (special-shaped) slab-column connections subjected to concentric gravity loading is non-uniform.
2. Again, consistent with the behaviour of R-SCCs, slab openings near SS-SCCs reduce the connection stiffness and concentric punching shear capacity. The negative influence of an opening on stiffness and capacity is dependent on both the opening size and location (distance from the column and location around the column).
3. Ideally, openings should be located as far away from the column as possible, but if openings must be located near SS-SCCs they should be located between the column flanges to minimize their negative influence. In addition to minimizing their influence on the connection's punching capacity, locating the openings between the column flanges also has architectural benefits, as any services routed through the opening can be hidden from view. Openings which are near the column should be placed near the diagonal portion of the critical perimeter assumed in ACI 318-19. Openings which must be located very close or adjacent to the column should be placed as close as possible to the inner vertices of the connection to minimize the opening's negative influence on concentric punching shear capacity, as the shear stresses along the column perimeter in these regions are typically low according to the FEA.
4. Revisions to the ACI 318-19 punching shear design provisions are needed to improve their accuracy for SS-SCCs. As currently formulated, the influence of openings between the column flanges is typically significantly overpredicted. Furthermore, the alternate definition of the column aspect ratio, β, for SS-SCCs results in higher nominal shear capacities along the critical perimeter than those predicted for R-SCCs of the same size. Finally, while the

ACI 421.1R-20 method can result in accurate and conservative estimates of punching capacity for SS-SCCs with and without slab openings, it is time-consuming and difficult to use, making it unsuitable for use in practice, particularly for initial design.

5. From the perspective of the expected influence of slab openings on concentric punching shear capacity, the structural benefit of using a SS-SCC over a R-SCC is dependent on both the column size and the location of the opening(s) with respect to the column. If the opening(s) would be located along the outer edges of a L-SCC (column side 4 or 5), or the base of a T-SCC (column sides 4, 5 and 6) then a R-SCC or X-SCC should be used. On the other hand, if the opening(s) would be located in the region between the column flanges, then it is always beneficial to use a SS-SCC over a R-SCC (particularly if the behaviour of the R-SCC is dominated by punching shear). Additionally, even when the influence of the opening(s) on concentric punching capacity is similar, the use of a SS-SCC would allow the opening(s) and service(s) to be hidden from view.

10.4.3 L Slab-Column Connections (L-SCCs)

1. The outer edges of L-SCCs (sides 5 and 6, see Figure 8-10 for column side numbering) transfer a significant amount of the total gravity load applied to the connection. Based on the crack patterns predicted by the NLFEA, the dominant method of force transfer along these sides is one-way shear. This conclusion is also supported by the work of Pinto et al. [174].

2. Openings located along the outer edges of the connection, especially those located at or near the intersection of the two outer edges, lead to severe reductions in connection stiffness and punching capacity. These openings also result in significant crack concentrations along the outer edges of the connection. Therefore, openings along the outer edges of L-SCCs should be avoided whenever possible.

3. Through comparisons to the NLFEA results, numerous issues with the ACI 318-19 opening provisions were found for L-SCCs. Firstly, when the column centroid falls within the opening the required critical perimeter reductions are unclear. Secondly, if the column centroid is very close to the opening, exceptionally large critical perimeter reductions are required, which suggests that interior openings have a significant influence on punching capacity, which contradicts the NLFEA. Finally, when the required critical perimeter reductions are clear, the existing opening provisions can overpredict the influence of openings between the flanges,

and underpredict the influence of openings along the outer edges (which are the most critical). Therefore, the ACI 318-19 opening provisions need to be modified to accurately represent the behaviour of L-SCCs.

4. The initial punching shear design of L-SCCs can be completed using the existing ACI 318-19 concentric punching shear design provisions if the diagonal portion of the critical perimeter is neglected when calculating the critical perimeter length, b_o, and the nominal concrete shear capacity along the critical perimeter, v_c, (modification 1). However, since this method is not yet approved by ACI 318, the design should then be verified using the ACI 421.1R-20 method to ensure the chosen column size satisfies the requirements of ACI 318-19.

10.4.4 T Slab-Column Connections (T-SCCs)

1. Unlike the other analyzed SS-SCCs, which all failed in punching shear, the failure mode of T slab-column connections (T-SCCs) subjected to concentric gravity loading predicted by the FEA was dependent on the column size. The failure mode of the small column specimens, T1-S and T2-S, was punching, whereas the failure mode of the majority of the large column specimens, T1-L and T2-L, was a simultaneous punching failure and one-way shear failure parallel to the long dimension of the base of the T (side 5, see Figure 8-12 for column side numbering). Regardless of the governing failure mode of the connection, a significant portion of the total load was transferred between the slab and column through the base of the T (sides 4, 5 and 6). On the tension surface of the slab, significant one-way shear cracking parallel to the outer long dimension of the base (side 5) was predicted. Therefore, the force transfer mechanism along side 5, which transfers a large portion of the total load transferred through the base, is one-way shear. This conclusion is also supported by the shear stress distribution along the column perimeter predicted by the FEA. The FEA also predicted significant crack concentrations around the short sides of the base of T, further demonstrating that the base of the T is transferring a significant portion of the total load.

2. On the tension surface of the slab, some diagonal cracking in the region between the column flanges is predicted by the NLFEA. Therefore, some of the diagonal portion of the critical perimeter assumed in ACI 318-19 is effective in transferring load between the slab and the column.

3. The majority of the load applied to the connection is transferred along the base of the T. At the peak load, column sides 4, 5 and 6 are predicted to transfer approximately 7.5-14.1%, 30.8-39.1% and 7.5-14.1% of the total load, respectively, for T-SCCs without slab openings. As such, openings should not be located near these column sides to avoid significant reductions in stiffness and capacity. In particular, openings along the outer long dimension of the base of the T (side 5) should be avoided whenever possible as openings along this side interrupt the one-way shear transfer mechanism along the base of the T, which significantly reduces connection capacity.

4. The vertical portions of the stem (sides 2 and 8) and inner edges of the base (sides 3 and 7) typically transfer a small portion of the total load. Therefore, openings located between the flanges of T-SCCs typically only result in minor reductions in punching capacity, unless the column is relatively small. For example, the punching capacity of T1-S-o1, which had one opening located between the flanges, was approximately 9.4% lower than that of the reference specimen without an opening. However, even for the T1-S specimens the influence of openings located along the outer edges of the connection is still at least two times larger than that for openings between the column flanges. Therefore, the ideal location for openings around T-SCCs which must be near the column is between the column flanges, regardless of column size.

5. ACI 421.1R-20 typically predicts punching capacities which are conservative to those predicted by the NLFEA for T-SCCs. As observed for the other analyzed SS-SCCs, the ACI 318-19 opening provisions typically overpredict the influence of openings located between the column flanges of T-SCCs. However, the predicted influence of openings along the outer edge of the base (sides 4, 5 and 6) typically agreed well with those predicted by the FEA.

6. The initial punching shear design of T-SCCs can be completed using the existing ACI 318-19 concentric punching shear provisions if β is redefined as the maximum of all individual column flanges (modification 2) (see Figure 8-12 for the definition of a column flange for T-SCCs). However, since this method is not yet approved by ACI 318 the design should then be verified using the ACI 421.1R-20 method to ensure the chosen column size satisfies the requirements of ACI 318-19.

10.4.5 Cruciform Slab-Column Connections (X-SCCs)

1. Unlike L-SCCs and T-SCCs where some sides of the connection are relatively ineffective, all sides of cruciform slab-column connections (X-SCCs) are relatively effective in transferring load between the slab and column. The shear stress distributions along the column perimeter and crack patterns on the tension surface of the slab predicted by the NLFEA suggest that most of the load is transferred through the short sides of each flange and along a portion of the long sides near the short sides. Therefore, openings near the short sides of X-SCCs should be avoided whenever possible.
2. The NLFEA predicted crack concentrations on the tension surface of the slab near the short sides and outer corners of each column flange for X-SCCs. A higher amount of diagonal cracking in the regions between the column flanges is also predicted compared to that for L-SCCs and T-SCCs. Therefore, most of the diagonal portion of the critical perimeter around X-SCCs assumed in ACI 318-19 can be assumed to be effective.
3. While the punching capacities predicted by ACI 421.1R-20 and the NLFEA typically displayed good agreement there are some issues with the ACI provisions. Firstly, the ACI 318-19 opening provisions can significantly overpredict the influence of openings located between the column flanges, particularly for small columns (as seen for the X1-S and X2-S specimens). Secondly, for doubly symmetric X-SCCs β is always equal to 1 regardless of the actual flange dimensions, due to the alternate definition of β for SS-SCCs. Therefore, the nominal shear stress capacity along the critical perimeter is higher around X-SCCs then similarly sized R-SCCs.
4. Unlike L-SCCs and T-SCCs, no modifications to the ACI 318-19 concentric punching shear provisions are required to use the provisions for the initial design of X-SCCs with slab openings. However, it should be reiterated that the influence of openings between the column flanges may be overpredicted and the design must be verified using the ACI 421.1R-20 method.

10.5 Conclusions of Special-Shaped Slab-Column Connection Study – Combined Shear and Unbalanced Moment

In the second part of the special-shaped slab-column connection study, the punching shear behaviour of rectangular slab-column connections and special-shaped slab-column connections (L, T and

cruciform) with and without slab openings subjected to combined concentric loading and uniaxial, monotonic unbalanced moment (V+M (monotonic) loading) was studied using a three-dimensional, nonlinear FEM implemented in Abaqus/Explicit. However, the FEM used in Chapter 9 is not the same as that used in Chapter 8 due to the fact that the nonlinear FEM in Chapter 8 was calibrated to experimental results of slab-column connections without flexural reinforcement on both sides of the slab. Therefore, the FEM used in Chapter 9 was calibrated to experimental tests of square slab-column connections subjected to combined concentric load and uniaxial unbalanced moment by Drakatos et al. [4].

However, due to large amount of computational resources needed to complete each simulation in Chapter 9, the overall study size was reduced compared to that in Chapter 8. In total, six rectangular slab-column connections (R-SCCs) and twenty-two special-shaped slab-column connections (SS-SCCs) (eight L, eight T and six cruciform connections) were simulated to study the punching shear behaviour of slab-column connections with and without openings under V+M (monotonic) loading. Additionally, the study was used to determine if openings located between the column flanges also have a minor influence on the punching shear behaviour of SS-SCCs under V+M (monotonic) loading. Finally, the unbalanced moment capacities predicted by the calibrated FEM were used to evaluated the accuracy of the ACI 421.1R-20 provisions for RSSCs and SS-SCCs subjected to V+M (monotonic) loading.

From the presented work the following conclusions can be drawn:

1. Consistent with the results of the concentric load study, the highest unbalanced moment capacities are predicted for the cruciform slab-column connections (X-SCCs), even though they are subjected to the largest concentric loads. The T slab-column connections (T-SCCs) are predicted to have the second highest unbalanced moment capacity, followed by the R-SCCs and the L slab-column connections (L-SCCs).
2. Consistent with the results for square slab-column connections, the unbalanced moment capacity of R-SCCs and SS-SCCs decreases as the applied concentric load increases (i.e. the unbalanced moment capacity decreases as the gravity shear ratio (GSR, which in this work was defined as the ratio of the applied vertical load to the concentric capacity predicted by the NLFEA) increases.

3. The calibrated FEM predicts approximately equal unbalanced moment capacities for L-SCCs without slab openings when the moment is applied toward the interior of the connection or toward the outer edges. Similarly, the calibrated FEM predicts approximately equal unbalanced moment capacities for T-SCCs without openings when the moment is applied toward the short side of the stem or toward the long side of the base of the T.

4. Consistent with the results for concentrically loaded specimens, slab openings result in a reduced punching shear capacity. However, the influence of the opening is typically more significant when the moment is applied toward the opening (i.e. the opening is located on the side of the connection where the shear stresses due to the concentric load and unbalanced moment are additive). For all investigated column shapes, the analyzed opening layout decreased the unbalanced moment capacity of the connection by more than 10% when the moment was applied toward the opening. On the other hand, when the moment was applied away from the opening (i.e. the opening is located on the side of the connection where the shear stresses due to the concentric loading and unbalanced moment counteract) the influence of the opening is typically less than 5%. Therefore, consistent with the results for square and rectangular slab-column connections, openings are more detrimental when the moment is applied toward the openings, though it should be noted that the direction of the applied moment cannot be controlled in most practical applications. Additionally, for the analyzed L-SCCs and T-SCCs, the investigated opening layout reduced the predicted unbalanced moment capacity by approximately 9% and 7%, respectively. As such, openings between the column flanges of L-SCCs and T-SCCs may have a significant influence on connection capacity even when the moment is applied away from the opening if the GSR is high, though further studies are necessary to confirm this.

5. Therefore, openings located between the column flanges of SS-SCCs do have an influence on the unbalanced moment capacity of the connection. The results presented herein suggest that the influence of openings between column flanges is consistent between different column shapes when the connection is subjected to combined concentric load and uniaxial monotonic unbalanced moment. For the analyzed column size and opening layout, the openings reduced the unbalanced moment capacity of the connections by a maximum of approximately 10% regardless of the column shape and GSR.

6. The unbalanced moment capacities predicted by ACI 421.1R-20 are typically very conservative compared to the NLFEA results, and become increasingly conservative for connections with slab openings. The most conservative predictions occur for R-SCCs, which was somewhat surprising as some experimental results of similar connections exist in literature. However, it should also be noted that the predictions are also very inconsistent, as the ratio of the capacity predicted by ACI 421.1R-20 to that predicted by the NLFEA varies from 0.08-0.86. Therefore, it is clear that the ACI 421.1R method is not accurately approximating the behaviour of connections subjected to combined concentric shear and unbalanced moment. Additionally, ACI 421.1R-20 does not accurately capture the influence of the moment direction for T-SCCs without openings. While the FEA predicts an approximately equal unbalanced moment capacity regardless of whether the moment is applied toward the short side of the stem or the long side of the base, ACI 421.1R-20 predicts the unbalanced moment capacity to be approximately 28% higher when the moment is applied toward the short side of the stem (M2 direction, see Figure 9-3). Furthermore, it should be noted that ACI 421.1R-20 predicts higher unbalanced moment capacities when the moment is applied toward the opening, which contradicts the FEA results, and previous experimental tests (though the predicted capacities are still very conservative). Therefore, revisions to the provisions to account for both column geometry and the presence of slab openings are necessary.

10.6 Recommendations for Future Work

While a significant amount of work related to the influence of column/support geometry on punching shear behaviour was conducted in this research program, there are still areas which could be expanded or require further research.

Firstly, the punching shear behaviour of SWCs should be studied further, with a particular emphasis on analyzing connections with different wall sizes and slab thicknesses. This would expand the database of sixteen interior SWCs presented herein, which would be beneficial to further refine the proposed design methods, or to develop more advanced design methods. Furthermore, due to limitations regarding available computational resources only one SWC subjected to combined concentric shear and unbalanced moment was analyzed as part of this work. Therefore, any additional studies should also consider SWCs which are subjected to combined concentric shear and unbalanced moment, as this load condition is of practical importance and requires further analysis.

Secondly, the influence of slab-openings on the punching shear behaviour of SWCs should also be studied to a greater extent in the future. Additional numerical simulations of various opening layouts around elongated connections would be beneficial to the development of opening provisions for elongated connections. In these future studies, particular attention should be paid to the influence of nonsymmetric slab opening layouts (as again the available computational resources limited the study of slab openings around SWCs to doubly symmetric opening layouts to facilitate the use of quarter models). Furthermore, SWCs with slab openings and subjected to combined concentric shear and unbalanced moment should be analyzed as the influence of openings on the unbalanced moment capacity of SWCs needs to be studied. These analyses could also be used to confirm that openings located at a distance greater than *5d* from the wall ends have a minimal influence on the punching behaviour of SWCs regardless of the load conditions (the limited impact of such openings on the concentric punching behaviour of SWCs was demonstrated in subsection 6.4.3.2).

Thirdly, analyses similar to those presented in Chapter 6 and recommended in the preceding paragraphs should be conducted for interior slab-wall corner connections and exterior edge or corner SWCs. Additionally, SWCs with shear reinforcement near the wall toe should also be analyzed for interior and exterior wall locations. Of particular importance is identifying the extent of the region which needs to be shear reinforced to avoid punching shear failures of SWCs, and if shear reinforcement can be used to reduce or mitigate the negative influence of slab openings located within *5d* of the wall ends.

Fourthly, the punching shear behaviour of SS-SCCs can be studied further. For example, the punching shear behaviour of SS-SCCs with unequal flange dimensions (examples of such columns are shown in Figure 10-1) could be studied for different loading conditions. Additionally, the influence of shear reinforcement or placing flexural reinforcement in non-orthogonal directions in the region between the column flanges, as shown in Figure 10-2, should be investigated. Both potential reinforcing details could potentially improve the effectiveness of the regions between the column flange in transferring load between the slab and column. In terms of rectangular and special-shaped slab-column connections subjected to combined concentric shear and unbalanced moments, additional analyses similar to those presented in Chapter 9 should be conducted for lower gravity shear ratios (such as a gravity shear ratio of 0.25). Additionally, the influence of exterior openings (see Figure 10-3 for examples), which was not studied herein due to the significant negative influence of these openings for concentric load conditions and due to limited computational resources, should be

conducted. Furthermore, the influence of alternate moment directions (see Figure 10-4 for examples, these alternate directions are also applicable for exterior opening layouts such as those shown in Figure 10-3), should be studied, particularly for R-SCCs and T-SCCs (with or without openings) and for L-SCCs and X-SCCs (with openings)

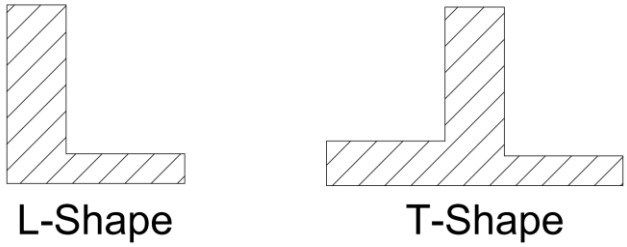


Figure 10-1: Examples of Special-Shaped Slab-Column Connections with Unequal Flange Dimensions

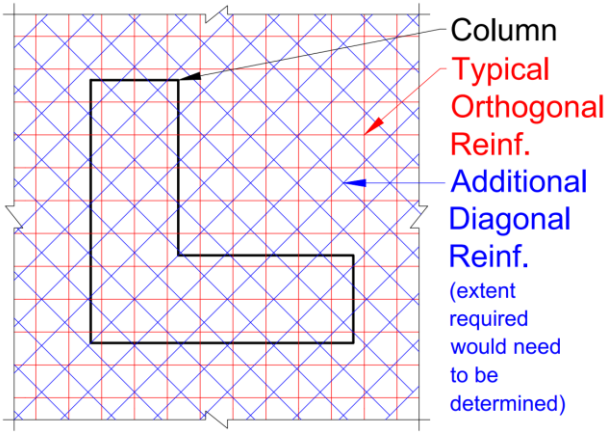


Figure 10-2: Potential Layout of Additional Diagonal Flexural Reinforcement Which Could be Placed Around Special-Shaped Slab-Column Connections

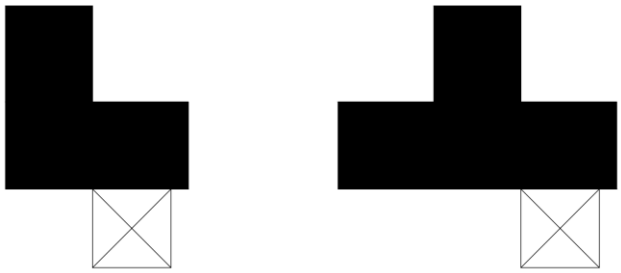


Figure 10-3: Examples of Exterior Openings Which Could be Considered for Special-Shaped Slab-Column Connections Subjected to Combined Concentric Shear and Unbalanced Moment

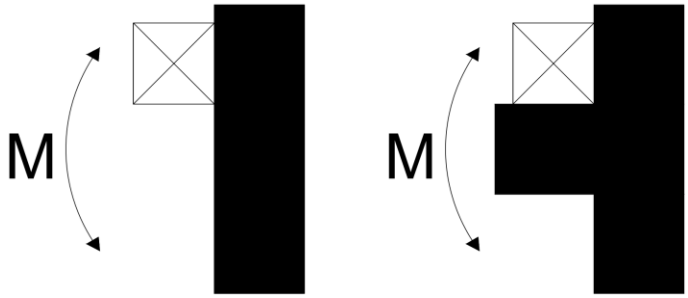


Figure 10-4: Examples of Alternate Moment Directions Which Could be Considered for Rectangular and Special-Shaped Slab-Column Connections Subjected to Combined Concentric Shear and Unbalanced Moment

Fifthly, the punching shear behaviour of SWCs, R-SCCs and SS-SCCs under combined concentric shear and cyclic unbalanced moment should be studied, as cyclically applied unbalanced moments have been found to be more detrimental to punching shear capacity than monotonically applied unbalanced moments [4, 23, 97, 99, 349, 350], as discussed in Chapter 2. However, before these analyses could be conducted, two modifications to the calibrated FEMs presented herein are required. Firstly, damage parameters, which account for compressive and tensile stiffness loss due to cracking, must be incorporated into the CDP, to properly capture the behaviour of concrete under cyclic loading. Secondly, the stress-strain relationship for the steel reinforcement must be updated. In the simulations presented herein, a linear elastic-perfectly plastic relationship was assumed for simplicity. However, for accurate cyclic analyses a stress-strain response which accounts for strain hardening and the Bauschinger effect should be incorporated into the FEM. The use of this refined stress-strain response for the steel reinforcement would also potentially allow the FEM to be used to study the flexural response of slab-wall and slab-column connections.

Sixthly, the influence of horizontal ducts and pipelines, which unlike openings do not penetrate through the entire slab thickness, on the punching shear behaviour of SWCs, R-SCCs and SS-SCCs should be studied. Though horizontal ducts within the slab thickness are common, as they are used to route piping and electrical services throughout a floor of a structure, their influence on punching shear has received much less interest [351, 352, 353] than slab openings. Additionally, as discussed in Section 3.6, *fib* Model Code 2010 [35] and prEC2 (2020) [280] estimate the influence of slab openings and embedded pipelines differently, but the validity of these recommendations should be studied.

Finally, experimental tests should be conducted the validate the FEA results and conclusions presented herein. Experimental testing of SWCs should focus on analyzing the shear force/stress distribution along the connection and critical perimeters to verify the proposed design methods. Additionally, the severe negative influence of openings located within *5d* of the wall ends, and the limited influence of openings beyond these toe regions, on the punching shear behaviour of SWCs should be experimentally verified. Experimental testing of SS-SCCs should initially focus on T and cruciform slab-column connections, as L-SCCs have been previously studied experimentally [174]. These tests should be used to verify that slab openings located between the column flanges have a limited influence on punching capacity for both concentric loading, and combined concentric shear and unbalanced moment loading conditions.

Letters of Copyright Permission

The letters/agreements granting permission to reproduce figures from previously published literature are provided on the following pages.

PEARSON ALWAYS LEARNING

PERMISSION TO REPRODUCE FOR EDUCATIONAL USE

To: Graeme Milligan – University of Waterloo

INVOICE- GPGREF-0014270-12-22_9780131014039

Title: Reinforced Concrete: Mechanism and Design (Canadian Edition)
Author: MacGregor, James G., Bartlett, F. Michael
ISBN: 9780131014039
Material: Figures 13.2 and 13.35 on page numbers 578 and 617
Purpose: Use in PhD thesis: Nonlinear Finite Element Analysis of Influence of Support Geometry on the Punching Shear Behaviour of Reinforced Concrete Slabs

Period: 1 December 2022 to 1 December 2023
Instructor: faculty
Permission Details: 2 pages @ $0.00
Permission Fee: $0.00
GST (reg.no. 5%): $0.00
PST (7%) $0.00
Total: $0.00

Pearson Canada HST # 104137526RT0001

Send payment and copy of this invoice to Pec.royalty@pearsoncanada.com

---

A credit line must be added to the material being copied. The credit line should include title, author, copyright date and publisher and indicate that the material is reproduced with the permission of Pearson Canada Inc.

NOTE: This permission does not allow the reproduction of any material copyrighted in or credited to the name of any person or entity other than Pearson Canada Inc. Should you desire to use such material, you must seek permission directly from the owner of that material. Pearson Canada disclaims all liability in connection with your use of such material without proper consent.

Authorization(s) granted under this one-time, pay-per use license does not in any way remove Financial Accounting Theory from the repertoire of Access Copyright that is licensed under the Access Copyright Post-Secondary Educational Institutions Interim Tariff (the "Interim Tariff") or the Proposed Access Copyright Post-Secondary Educational Institutions Tariff, 2011-2013 (the "Proposed Tariff"). Nor can the authorization(s) granted hereunder be construed in any way to mean that authorization is not required for any other uses of works in which copyright is owned by Pearson Canada Inc, including under the Interim Tariff or Proposed Tariff.

PEARSON ALWAYS LEARNING

Permission is granted to electronically post the content listed above from the Pearson Canada Inc. title *Reinforced Concrete: Mechanism and Design (Canadian Edition)*, on the university's access-controlled library repository.
This request is valid for the period 1 December 2022 to 1 December 2023 and applies to this use only. The material must be credited as indicated above.

Canada Royalties Department
Pearson Canada Inc. | 26 Prince Andrew Place | Toronto, ON | M3C 2T8 |
Email: Pec.royalty@pearsoncanada.com

Date: 1 December, 2022



Graeme Milligan
University of Waterloo – Doctor of Philosophy Graduate Student
200 University Avenue West
Waterloo, Ontario, Canada, N2L 3G1

September 16, 2022

Subject: Use of ACI Copyrighted Material

Your request to:

___X___ Use information/figures/tables indicated below. Please credit American Concrete Institute, author(s) and publication.

___X___ Reprint the information described in the quantity indicated. Please add a note to the reprint similar to: *Authorized reprint from (publication) (issue/volume/year as appropriate.)*

_____ Payment of Right-to-Reprint fee of ($0 per Table/Figure/Section) is required.

Permission is granted to reference and reprint
Fig. 4 from *ACI Structural Journal, July-August 2008, Vol. 105 No. 4, Title no. 105-S42*
Fig. 9 from *ACI Structural Journal, September-October 2008, Vol. 105 No. 5, Title no. 105-S50*
Fig. 4 from *ACI Structural Journal, May-June 1987, Vol. 84 No. 3, Title no. 84-S27*
Fig. 1 from *ACI Structural Journal, May-June 1992, Vol. 89 No. 3, Title no. 89-S32*

Signed: ***Ryan Jay*** Date: ***16 September 2022***

Ryan Jay
Supervisor/Graphic Designer, Publishing Services
Ryan.Jay@Concrete.org

American Concrete Institute
Always advancing

Graeme Milligan
Country: Canada (CAN)
Address: 200 University Avenue West
State: Ontario (ON)
City: Waterloo
Zip code: N2L3G1
January 11, 2023

Subject: Use of ACI Copyrighted Material

Your request to:

___X___ Use information/figures/tables indicated below. Please credit American Concrete Institute, author(s) and publication.

___X_____ Reprint the information described in the quantity indicated. Please add a note to the reprint similar to: *Authorized reprint from (publication) (issue/volume/year as appropriate.)*

_____ Payment of Right-to-Reprint fee of ($0 per Table/Figure/Section) is required.

Permission is granted to reference and reprint
Fig. 17 of Cyclic Lateral Loading of Nonductile Slab-Column Connections, ACI Structural Journal, May-June 2006, Vol. 103 No. 3, Title no. 103-S37.
Fig. 3.1 of Guide to Seismic Design of Punching Shear Reinforcement in Flat Plates, ACI 421.2R-10.

Signed: ***Ryan Jay***_____ Date: ***11 January 2023***

Ryan Jay
Supervisor/Graphic Designer, Publishing Services
Ryan.Jay@Concrete.org

SPRINGER NATURE LICENSE
TERMS AND CONDITIONS

Oct 28, 2022

This Agreement between University of Waterloo -- Graeme Milligan ("You") and Springer Nature ("Springer Nature") consists of your license details and the terms and conditions provided by Springer Nature and Copyright Clearance Center.

License Number	5417980173088
License date	Oct 28, 2022
Licensed Content Publisher	Springer Nature
Licensed Content Publication	Springer eBook
Licensed Content Title	On the Distribution of Shear Forces in Non-axisymmetric Slab-Column Connections
Licensed Content Author	Jürgen Einpaul, Robert L. Vollum, António Pinho Ramos
Licensed Content Date	Jan 1, 2018
Type of Use	Thesis/Dissertation
Requestor type	non-commercial (non-profit)
Format	print and electronic
Portion	figures/tables/illustrations
Number of figures/tables/illustrations	1
Will you be translating?	no

Circulation/distribution	100 - 199
Author of this Springer Nature content	no
Title	Nonlinear Finite Element Analysis of Influence of Support Geometry on the Punching Shear Behaviour of Reinforced Concrete Slabs
Institution name	University of Waterloo
Expected presentation date	Apr 2023
Portions	Fig. 1.
Requestor Location	University of Waterloo 200 University Avenue West Waterloo, ON N2L3G1 Canada Attn: Graeme Jacob Milligan
Total	0.00 CAD

Terms and Conditions

Springer Nature Customer Service Centre GmbH
Terms and Conditions

This agreement sets out the terms and conditions of the licence (the **Licence**) between you and **Springer Nature Customer Service Centre GmbH** (the **Licensor**). By clicking 'accept' and completing the transaction for the material (**Licensed Material**), you also confirm your acceptance of these terms and conditions.

1. Grant of License

1. 1. The Licensor grants you a personal, non-exclusive, non-transferable, world-wide licence to reproduce the Licensed Material for the purpose specified in your order only. Licences are granted for the specific use requested in the order and for no other use, subject to the conditions below.

1. 2. The Licensor warrants that it has, to the best of its knowledge, the rights to license reuse of the Licensed Material. However, you should ensure that the material you are requesting is original to the Licensor and does not carry the copyright of another entity (as credited in the published version).

1. 3. If the credit line on any part of the material you have requested indicates that it was reprinted or adapted with permission from another source, then you should also seek permission from that source to reuse the material.

2. Scope of Licence

2. 1. You may only use the Licensed Content in the manner and to the extent permitted by these Ts&Cs and any applicable laws.

2. 2. A separate licence may be required for any additional use of the Licensed Material, e.g. where a licence has been purchased for print only use, separate permission must be obtained for electronic re-use. Similarly, a licence is only valid in the language selected and does not apply for editions in other languages unless additional translation rights have been granted separately in the licence. Any content owned by third parties are expressly excluded from the licence.

2. 3. Similarly, rights for additional components such as custom editions and derivatives require additional permission and may be subject to an additional fee. Please apply to Journalpermissions@springernature.com/bookpermissions@springernature.com for these rights.

2. 4. Where permission has been granted **free of charge** for material in print, permission may also be granted for any electronic version of that work, provided that the material is incidental to your work as a whole and that the electronic version is essentially equivalent to, or substitutes for, the print version.

2. 5. An alternative scope of licence may apply to signatories of the STM Permissions Guidelines, as amended from time to time.

3. Duration of Licence

3. 1. A licence for is valid from the date of purchase ('Licence Date') at the end of the relevant period in the below table:

Scope of Licence	Duration of Licence
Post on a website	12 months
Presentations	12 months
Books and journals	Lifetime of the edition in the language purchased

4. Acknowledgement

4. 1. The Licensor's permission must be acknowledged next to the Licenced Material in print. In electronic form, this acknowledgement must be visible at the same time as the figures/tables/illustrations or abstract, and must be hyperlinked to the journal/book's homepage. Our required acknowledgement format is in the Appendix below.

5. Restrictions on use

5. 1. Use of the Licensed Material may be permitted for incidental promotional use and minor editing privileges e.g. minor adaptations of single figures, changes of format, colour and/or style where the adaptation is credited as set out in Appendix 1 below. Any

other changes including but not limited to, cropping, adapting, omitting material that affect the meaning, intention or moral rights of the author are strictly prohibited.

5. 2. You must not use any Licensed Material as part of any design or trademark.

5. 3. Licensed Material may be used in Open Access Publications (OAP) before publication by Springer Nature, but any Licensed Material must be removed from OAP sites prior to final publication.

6. Ownership of Rights

6. 1. Licensed Material remains the property of either Licensor or the relevant third party and any rights not explicitly granted herein are expressly reserved.

7. Warranty

IN NO EVENT SHALL LICENSOR BE LIABLE TO YOU OR ANY OTHER PARTY OR ANY OTHER PERSON OR FOR ANY SPECIAL, CONSEQUENTIAL, INCIDENTAL OR INDIRECT DAMAGES, HOWEVER CAUSED, ARISING OUT OF OR IN CONNECTION WITH THE DOWNLOADING, VIEWING OR USE OF THE MATERIALS REGARDLESS OF THE FORM OF ACTION, WHETHER FOR BREACH OF CONTRACT, BREACH OF WARRANTY, TORT, NEGLIGENCE, INFRINGEMENT OR OTHERWISE (INCLUDING, WITHOUT LIMITATION, DAMAGES BASED ON LOSS OF PROFITS, DATA, FILES, USE, BUSINESS OPPORTUNITY OR CLAIMS OF THIRD PARTIES), AND
WHETHER OR NOT THE PARTY HAS BEEN ADVISED OF THE POSSIBILITY OF SUCH DAMAGES. THIS LIMITATION SHALL APPLY NOTWITHSTANDING ANY FAILURE OF ESSENTIAL PURPOSE OF ANY LIMITED REMEDY PROVIDED HEREIN.

8. Limitations

8. 1. ***BOOKS ONLY:*** Where **'reuse in a dissertation/thesis'** has been selected the following terms apply: Print rights of the final author's accepted manuscript (for clarity, NOT the published version) for up to 100 copies, electronic rights for use only on a personal website or institutional repository as defined by the Sherpa guideline (www.sherpa.ac.uk/romeo/).

8. 2. For content reuse requests that qualify for permission under the STM Permissions Guidelines, which may be updated from time to time, the STM Permissions Guidelines supersede the terms and conditions contained in this licence.

9. Termination and Cancellation

9. 1. Licences will expire after the period shown in Clause 3 (above).

9. 2. Licensee reserves the right to terminate the Licence in the event that payment is not received in full or if there has been a breach of this agreement by you.

Appendix 1 — Acknowledgements:

For Journal Content:
Reprinted by permission from [**the Licensor**]: [**Journal Publisher** (e.g. Nature/Springer/Palgrave)] [**JOURNAL NAME**] [**REFERENCE CITATION** (Article name, Author(s) Name), [**COPYRIGHT**] (year of publication)

For **Advance Online Publication papers:**
Reprinted by permission from [**the Licensor**]: [**Journal Publisher** (e.g. Nature/Springer/Palgrave)] [**JOURNAL NAME**] [**REFERENCE CITATION** (Article name, Author(s) Name), [**COPYRIGHT**] (year of publication), advance online publication, day month year (doi: 10.1038/sj.[JOURNAL ACRONYM].)

For Adaptations/Translations:
Adapted/Translated by permission from [**the Licensor**]: [**Journal Publisher** (e.g. Nature/Springer/Palgrave)] [**JOURNAL NAME**] [**REFERENCE CITATION** (Article name, Author(s) Name), [**COPYRIGHT**] (year of publication)

Note: For any republication from the British Journal of Cancer, the following credit line style applies:

Reprinted/adapted/translated by permission from [**the Licensor**]: on behalf of Cancer Research UK: : [**Journal Publisher** (e.g. Nature/Springer/Palgrave)] [**JOURNAL NAME**] [**REFERENCE CITATION** (Article name, Author(s) Name), [**COPYRIGHT**] (year of publication)

For **Advance Online Publication** papers:
Reprinted by permission from The [**the Licensor**]: on behalf of Cancer Research UK: [**Journal Publisher** (e.g. Nature/Springer/Palgrave)] [**JOURNAL NAME**] [**REFERENCE CITATION** (Article name, Author(s) Name), [**COPYRIGHT**] (year of publication), advance online publication, day month year (doi: 10.1038/sj.[JOURNAL ACRONYM])

For Book content:
Reprinted/adapted by permission from [**the Licensor**]: [**Book Publisher** (e.g. Palgrave Macmillan, Springer etc) [**Book Title**] by [**Book author**(s)] [**COPYRIGHT**] (year of publication)

Other Conditions:

Version 1.3

Questions? customercare@copyright.com or +1-855-239-3415 (toll free in the US) or +1-978-646-2777.

ELSEVIER LICENSE
TERMS AND CONDITIONS

Nov 07, 2022

This Agreement between University of Waterloo -- Graeme Milligan ("You") and Elsevier ("Elsevier") consists of your license details and the terms and conditions provided by Elsevier and Copyright Clearance Center.

License Number	5423730533567
License date	Nov 07, 2022
Licensed Content Publisher	Elsevier
Licensed Content Publication	Structures
Licensed Content Title	Punching of RC slabs without transverse reinforcement supported on elongated columns
Licensed Content Author	Andri Setiawan,Robert L. Vollum,Lorenzo Macorini,Bassam A. Izzuddin
Licensed Content Date	Oct 1, 2020
Licensed Content Volume	27
Licensed Content Issue	n/a
Licensed Content Pages	21
Start Page	2048
End Page	2068

Type of Use	reuse in a thesis/dissertation
Portion	figures/tables/illustrations
Number of figures/tables/illustrations	1
Format	both print and electronic
Are you the author of this Elsevier article?	No
Will you be translating?	No
Title	Nonlinear Finite Element Analysis of Influence of Support Geometry on the Punching Shear Behaviour of Reinforced Concrete Slabs
Institution name	University of Waterloo
Expected presentation date	Apr 2023
Portions	Figure 4
Requestor Location	University of Waterloo 200 University Avenue West Waterloo, ON N2L3G1 Canada Attn: Graeme Jacob Milligan
Publisher Tax ID	GB 494 6272 12
Total	0.00 CAD
Terms and Conditions	

INTRODUCTION

1. The publisher for this copyrighted material is Elsevier. By clicking "accept" in connection with completing this licensing transaction, you agree that the following terms and conditions apply to this transaction (along with the Billing and Payment terms and conditions established by Copyright Clearance Center, Inc. ("CCC"), at the time that you opened your Rightslink account and that are available at any time at http://myaccount.copyright.com).

GENERAL TERMS

2. Elsevier hereby grants you permission to reproduce the aforementioned material subject to the terms and conditions indicated.

3. Acknowledgement: If any part of the material to be used (for example, figures) has appeared in our publication with credit or acknowledgement to another source, permission must also be sought from that source. If such permission is not obtained then that material may not be included in your publication/copies. Suitable acknowledgement to the source must be made, either as a footnote or in a reference list at the end of your publication, as follows:

"Reprinted from Publication title, Vol /edition number, Author(s), Title of article / title of chapter, Pages No., Copyright (Year), with permission from Elsevier [OR APPLICABLE SOCIETY COPYRIGHT OWNER]." Also Lancet special credit - "Reprinted from The Lancet, Vol. number, Author(s), Title of article, Pages No., Copyright (Year), with permission from Elsevier."

4. Reproduction of this material is confined to the purpose and/or media for which permission is hereby given.

5. Altering/Modifying Material: Not Permitted. However figures and illustrations may be altered/adapted minimally to serve your work. Any other abbreviations, additions, deletions and/or any other alterations shall be made only with prior written authorization of Elsevier Ltd. (Please contact Elsevier's permissions helpdesk here). No modifications can be made to any Lancet figures/tables and they must be reproduced in full.

6. If the permission fee for the requested use of our material is waived in this instance, please be advised that your future requests for Elsevier materials may attract a fee.

7. Reservation of Rights: Publisher reserves all rights not specifically granted in the combination of (i) the license details provided by you and accepted in the course of this licensing transaction, (ii) these terms and conditions and (iii) CCC's Billing and Payment terms and conditions.

8. License Contingent Upon Payment: While you may exercise the rights licensed immediately upon issuance of the license at the end of the licensing process for the transaction, provided that you have disclosed complete and accurate details of your proposed use, no license is finally effective unless and until full payment is received from you (either by publisher or by CCC) as provided in CCC's Billing and Payment terms and conditions. If full payment is not received on a timely basis, then any license preliminarily granted shall be deemed automatically revoked and shall be void as if never granted. Further, in the event that you breach any of these terms and conditions or any of CCC's Billing and Payment terms and conditions, the license is automatically revoked and shall be void as if never granted. Use of materials as described in a revoked license, as well as any use of the materials beyond the scope of an unrevoked license, may constitute copyright infringement

and publisher reserves the right to take any and all action to protect its copyright in the materials.

9. Warranties: Publisher makes no representations or warranties with respect to the licensed material.

10. Indemnity: You hereby indemnify and agree to hold harmless publisher and CCC, and their respective officers, directors, employees and agents, from and against any and all claims arising out of your use of the licensed material other than as specifically authorized pursuant to this license.

11. No Transfer of License: This license is personal to you and may not be sublicensed, assigned, or transferred by you to any other person without publisher's written permission.

12. No Amendment Except in Writing: This license may not be amended except in a writing signed by both parties (or, in the case of publisher, by CCC on publisher's behalf).

13. Objection to Contrary Terms: Publisher hereby objects to any terms contained in any purchase order, acknowledgment, check endorsement or other writing prepared by you, which terms are inconsistent with these terms and conditions or CCC's Billing and Payment terms and conditions. These terms and conditions, together with CCC's Billing and Payment terms and conditions (which are incorporated herein), comprise the entire agreement between you and publisher (and CCC) concerning this licensing transaction. In the event of any conflict between your obligations established by these terms and conditions and those established by CCC's Billing and Payment terms and conditions, these terms and conditions shall control.

14. Revocation: Elsevier or Copyright Clearance Center may deny the permissions described in this License at their sole discretion, for any reason or no reason, with a full refund payable to you. Notice of such denial will be made using the contact information provided by you. Failure to receive such notice will not alter or invalidate the denial. In no event will Elsevier or Copyright Clearance Center be responsible or liable for any costs, expenses or damage incurred by you as a result of a denial of your permission request, other than a refund of the amount(s) paid by you to Elsevier and/or Copyright Clearance Center for denied permissions.

LIMITED LICENSE

The following terms and conditions apply only to specific license types:

15. **Translation**: This permission is granted for non-exclusive world **English** rights only unless your license was granted for translation rights. If you licensed translation rights you may only translate this content into the languages you requested. A professional translator must perform all translations and reproduce the content word for word preserving the integrity of the article.

16. **Posting licensed content on any Website**: The following terms and conditions apply as follows: Licensing material from an Elsevier journal: All content posted to the web site must maintain the copyright information line on the bottom of each image; A hyper-text must be included to the Homepage of the journal from which you are licensing at http://www.sciencedirect.com/science/journal/xxxxx or the Elsevier homepage for books at http://www.elsevier.com; Central Storage: This license does not include permission for a scanned version of the material to be stored in a central repository such as that provided by Heron/XanEdu.

Licensing material from an Elsevier book: A hyper-text link must be included to the Elsevier homepage at http://www.elsevier.com . All content posted to the web site must maintain the copyright information line on the bottom of each image.

Posting licensed content on Electronic reserve: In addition to the above the following clauses are applicable: The web site must be password-protected and made available only to bona fide students registered on a relevant course. This permission is granted for 1 year only. You may obtain a new license for future website posting.

17. **For journal authors:** the following clauses are applicable in addition to the above:

Preprints:

A preprint is an author's own write-up of research results and analysis, it has not been peer-reviewed, nor has it had any other value added to it by a publisher (such as formatting, copyright, technical enhancement etc.).

Authors can share their preprints anywhere at any time. Preprints should not be added to or enhanced in any way in order to appear more like, or to substitute for, the final versions of articles however authors can update their preprints on arXiv or RePEc with their Accepted Author Manuscript (see below).

If accepted for publication, we encourage authors to link from the preprint to their formal publication via its DOI. Millions of researchers have access to the formal publications on ScienceDirect, and so links will help users to find, access, cite and use the best available version. Please note that Cell Press, The Lancet and some society-owned have different preprint policies. Information on these policies is available on the journal homepage.

Accepted Author Manuscripts: An accepted author manuscript is the manuscript of an article that has been accepted for publication and which typically includes author-incorporated changes suggested during submission, peer review and editor-author communications.

Authors can share their accepted author manuscript:

- immediately
  - via their non-commercial person homepage or blog
  - by updating a preprint in arXiv or RePEc with the accepted manuscript
  - via their research institute or institutional repository for internal institutional uses or as part of an invitation-only research collaboration work-group
  - directly by providing copies to their students or to research collaborators for their personal use
  - for private scholarly sharing as part of an invitation-only work group on commercial sites with which Elsevier has an agreement
- After the embargo period
  - via non-commercial hosting platforms such as their institutional repository
  - via commercial sites with which Elsevier has an agreement

In all cases accepted manuscripts should:

- link to the formal publication via its DOI
- bear a CC-BY-NC-ND license - this is easy to do
- if aggregated with other manuscripts, for example in a repository or other site, be shared in alignment with our hosting policy not be added to or enhanced in any way to

appear more like, or to substitute for, the published journal article.

Published journal article (JPA): A published journal article (PJA) is the definitive final record of published research that appears or will appear in the journal and embodies all value-adding publishing activities including peer review co-ordination, copy-editing, formatting, (if relevant) pagination and online enrichment.

Policies for sharing publishing journal articles differ for subscription and gold open access articles:

Subscription Articles: If you are an author, please share a link to your article rather than the full-text. Millions of researchers have access to the formal publications on ScienceDirect, and so links will help your users to find, access, cite, and use the best available version.

Theses and dissertations which contain embedded PJAs as part of the formal submission can be posted publicly by the awarding institution with DOI links back to the formal publications on ScienceDirect.

If you are affiliated with a library that subscribes to ScienceDirect you have additional private sharing rights for others' research accessed under that agreement. This includes use for classroom teaching and internal training at the institution (including use in course packs and courseware programs), and inclusion of the article for grant funding purposes.

Gold Open Access Articles: May be shared according to the author-selected end-user license and should contain a CrossMark logo, the end user license, and a DOI link to the formal publication on ScienceDirect.

Please refer to Elsevier's posting policy for further information.

18. **For book authors** the following clauses are applicable in addition to the above: Authors are permitted to place a brief summary of their work online only. You are not allowed to download and post the published electronic version of your chapter, nor may you scan the printed edition to create an electronic version. **Posting to a repository:** Authors are permitted to post a summary of their chapter only in their institution's repository.

19. **Thesis/Dissertation**: If your license is for use in a thesis/dissertation your thesis may be submitted to your institution in either print or electronic form. Should your thesis be published commercially, please reapply for permission. These requirements include permission for the Library and Archives of Canada to supply single copies, on demand, of the complete thesis and include permission for Proquest/UMI to supply single copies, on demand, of the complete thesis. Should your thesis be published commercially, please reapply for permission. Theses and dissertations which contain embedded PJAs as part of the formal submission can be posted publicly by the awarding institution with DOI links back to the formal publications on ScienceDirect.

Elsevier Open Access Terms and Conditions

You can publish open access with Elsevier in hundreds of open access journals or in nearly 2000 established subscription journals that support open access publishing. Permitted third party re-use of these open access articles is defined by the author's choice of Creative Commons user license. See our open access license policy for more information.

Terms & Conditions applicable to all Open Access articles published with Elsevier:

Any reuse of the article must not represent the author as endorsing the adaptation of the article nor should the article be modified in such a way as to damage the author's honour or reputation. If any changes have been made, such changes must be clearly indicated.

The author(s) must be appropriately credited and we ask that you include the end user license and a DOI link to the formal publication on ScienceDirect.

If any part of the material to be used (for example, figures) has appeared in our publication with credit or acknowledgement to another source it is the responsibility of the user to ensure their reuse complies with the terms and conditions determined by the rights holder.

Additional Terms & Conditions applicable to each Creative Commons user license:

CC BY: The CC-BY license allows users to copy, to create extracts, abstracts and new works from the Article, to alter and revise the Article and to make commercial use of the Article (including reuse and/or resale of the Article by commercial entities), provided the user gives appropriate credit (with a link to the formal publication through the relevant DOI), provides a link to the license, indicates if changes were made and the licensor is not represented as endorsing the use made of the work. The full details of the license are available at http://creativecommons.org/licenses/by/4.0.

CC BY NC SA: The CC BY-NC-SA license allows users to copy, to create extracts, abstracts and new works from the Article, to alter and revise the Article, provided this is not done for commercial purposes, and that the user gives appropriate credit (with a link to the formal publication through the relevant DOI), provides a link to the license, indicates if changes were made and the licensor is not represented as endorsing the use made of the work. Further, any new works must be made available on the same conditions. The full details of the license are available at http://creativecommons.org/licenses/by-nc-sa/4.0.

CC BY NC ND: The CC BY-NC-ND license allows users to copy and distribute the Article, provided this is not done for commercial purposes and further does not permit distribution of the Article if it is changed or edited in any way, and provided the user gives appropriate credit (with a link to the formal publication through the relevant DOI), provides a link to the license, and that the licensor is not represented as endorsing the use made of the work. The full details of the license are available at http://creativecommons.org/licenses/by-nc-nd/4.0. Any commercial reuse of Open Access articles published with a CC BY NC SA or CC BY NC ND license requires permission from Elsevier and will be subject to a fee.

Commercial reuse includes:

- Associating advertising with the full text of the Article
- Charging fees for document delivery or access
- Article aggregation
- Systematic distribution via e-mail lists or share buttons

Posting or linking by commercial companies for use by customers of those companies.

20. **Other Conditions**:

v1.10

Questions? customercare@copyright.com or +1-855-239-3415 (toll free in the US) or +1-978-646-2777.

JOHN WILEY AND SONS LICENSE TERMS AND CONDITIONS

Oct 06, 2022

This Agreement between University of Waterloo -- Graeme Milligan ("You") and John Wiley and Sons ("John Wiley and Sons") consists of your license details and the terms and conditions provided by John Wiley and Sons and Copyright Clearance Center.

License Number	5403250388186
License date	Oct 06, 2022
Licensed Content Publisher	John Wiley and Sons
Licensed Content Publication	Structural Concrete
Licensed Content Title	Punching shear design of RC flat slabs supported on wall corners
Licensed Content Author	Bassam A Izzuddin, Lorenzo Macorini, Robert L Vollum, et al
Licensed Content Date	Apr 3, 2020
Licensed Content Volume	21
Licensed Content Issue	3
Licensed Content Pages	16
Type of Use	Dissertation/Thesis
Requestor type	University/Academic
Format	Print and electronic
Portion	Figure/table
Number of figures/tables	2
Will you be translating?	No
Title	Nonlinear Finite Element Analysis of Influence of Support Geometry on the Punching Shear Behaviour of Reinforced Concrete Slabs
Institution name	University of Waterloo
Expected presentation date	Apr 2023
Portions	Fig 1 (entire figure); Figure 12a
Requestor Location	University of Waterloo 200 University Avenue West Waterloo, ON N2L3G1 Canada Attn: Graeme Jacob Milligan
Publisher Tax ID	EU826007151
Total	**0.00 CAD**
Terms and Conditions	

TERMS AND CONDITIONS

This copyrighted material is owned by or exclusively licensed to John Wiley & Sons, Inc. or one of its group companies (each a"Wiley Company") or handled on behalf of a society with which a Wiley Company has exclusive publishing rights in relation to a particular work (collectively "WILEY"). By clicking "accept" in connection with completing this licensing transaction, you agree that the following terms and conditions apply to this transaction (along with the billing and payment terms and conditions established by the Copyright Clearance Center Inc., ("CCC's Billing and Payment terms and conditions"), at the time that you opened your RightsLink account (these are available at any time at http://myaccount.copyright.com).

Terms and Conditions

- The materials you have requested permission to reproduce or reuse (the "Wiley Materials") are protected by copyright.
- You are hereby granted a personal, non-exclusive, non-sub licensable (on a stand-alone basis), non-transferable, worldwide, limited license to reproduce the Wiley Materials for the purpose specified in the licensing process. This license, **and any CONTENT (PDF or image file) purchased as part of your order,** is for a one-time use only and limited to any maximum distribution number specified in the license. The first instance of republication or reuse granted by this license must be completed within two years of the date of the grant of this license (although copies prepared before the end date may be distributed thereafter). The Wiley Materials shall not be used in any other manner or for any other purpose, beyond what is granted in the license. Permission is granted subject to an appropriate acknowledgement given to the

author, title of the material/book/journal and the publisher. You shall also duplicate the copyright notice that appears in the Wiley publication in your use of the Wiley Material. Permission is also granted on the understanding that nowhere in the text is a previously published source acknowledged for all or part of this Wiley Material. Any third party content is expressly excluded from this permission.

- With respect to the Wiley Materials, all rights are reserved. Except as expressly granted by the terms of the license, no part of the Wiley Materials may be copied, modified, adapted (except for minor reformatting required by the new Publication), translated, reproduced, transferred or distributed, in any form or by any means, and no derivative works may be made based on the Wiley Materials without the prior permission of the respective copyright owner.**For STM Signatory Publishers clearing permission under the terms of the STM Permissions Guidelines only, the terms of the license are extended to include subsequent editions and for editions in other languages, provided such editions are for the work as a whole in situ and does not involve the separate exploitation of the permitted figures or extracts,** You may not alter, remove or suppress in any manner any copyright, trademark or other notices displayed by the Wiley Materials. You may not license, rent, sell, loan, lease, pledge, offer as security, transfer or assign the Wiley Materials on a stand-alone basis, or any of the rights granted to you hereunder to any other person.

- The Wiley Materials and all of the intellectual property rights therein shall at all times remain the exclusive property of John Wiley & Sons Inc, the Wiley Companies, or their respective licensors, and your interest therein is only that of having possession of and the right to reproduce the Wiley Materials pursuant to Section 2 herein during the continuance of this Agreement. You agree that you own no right, title or interest in or to the Wiley Materials or any of the intellectual property rights therein. You shall have no rights hereunder other than the license as provided for above in Section 2. No right, license or interest to any trademark, trade name, service mark or other branding ("Marks") of WILEY or its licensors is granted hereunder, and you agree that you shall not assert any such right, license or interest with respect thereto

- NEITHER WILEY NOR ITS LICENSORS MAKES ANY WARRANTY OR REPRESENTATION OF ANY KIND TO YOU OR ANY THIRD PARTY, EXPRESS, IMPLIED OR STATUTORY, WITH RESPECT TO THE MATERIALS OR THE ACCURACY OF ANY INFORMATION CONTAINED IN THE MATERIALS, INCLUDING, WITHOUT LIMITATION, ANY IMPLIED WARRANTY OF MERCHANTABILITY, ACCURACY, SATISFACTORY QUALITY, FITNESS FOR A PARTICULAR PURPOSE, USABILITY, INTEGRATION OR NON-INFRINGEMENT AND ALL SUCH WARRANTIES ARE HEREBY EXCLUDED BY WILEY AND ITS LICENSORS AND WAIVED BY YOU.

- WILEY shall have the right to terminate this Agreement immediately upon breach of this Agreement by you.

- You shall indemnify, defend and hold harmless WILEY, its Licensors and their respective directors, officers, agents and employees, from and against any actual or threatened claims, demands, causes of action or proceedings arising from any breach of this Agreement by you.

- IN NO EVENT SHALL WILEY OR ITS LICENSORS BE LIABLE TO YOU OR ANY OTHER PARTY OR ANY OTHER PERSON OR ENTITY FOR ANY SPECIAL, CONSEQUENTIAL, INCIDENTAL, INDIRECT, EXEMPLARY OR PUNITIVE DAMAGES, HOWEVER CAUSED, ARISING OUT OF OR IN CONNECTION WITH THE DOWNLOADING, PROVISIONING, VIEWING OR USE OF THE MATERIALS REGARDLESS OF THE FORM OF ACTION, WHETHER FOR BREACH OF CONTRACT, BREACH OF WARRANTY, TORT, NEGLIGENCE, INFRINGEMENT OR OTHERWISE (INCLUDING, WITHOUT LIMITATION, DAMAGES BASED ON LOSS OF PROFITS, DATA, FILES, USE, BUSINESS OPPORTUNITY OR CLAIMS OF THIRD PARTIES), AND WHETHER OR NOT THE PARTY HAS BEEN ADVISED OF THE POSSIBILITY OF SUCH DAMAGES. THIS LIMITATION SHALL APPLY NOTWITHSTANDING ANY FAILURE OF ESSENTIAL PURPOSE OF ANY LIMITED REMEDY PROVIDED HEREIN.

- Should any provision of this Agreement be held by a court of competent jurisdiction to be illegal, invalid, or unenforceable, that provision shall be deemed amended to achieve as nearly as possible the same economic effect as the original provision, and the legality, validity and enforceability of the remaining provisions of this Agreement shall not be affected or impaired thereby.

- The failure of either party to enforce any term or condition of this Agreement shall not constitute a waiver of either party's right to enforce each and every term and condition of this Agreement. No breach under this agreement shall be deemed waived or excused by either party unless such waiver or consent is in writing signed by the party granting such waiver or consent. The waiver by or consent of a party to a breach of any provision of this Agreement shall not operate or be construed as a waiver of or consent to any other or subsequent breach by such other party.

- This Agreement may not be assigned (including by operation of law or otherwise) by you without WILEY's prior written consent.

- Any fee required for this permission shall be non-refundable after thirty (30) days from receipt by the CCC.

- These terms and conditions together with CCC's Billing and Payment terms and conditions (which are incorporated herein) form the entire agreement between you and WILEY concerning this licensing transaction and (in the absence of fraud) supersedes all prior agreements and representations of the parties, oral or written. This Agreement may not be amended except in writing signed by both parties. This Agreement shall be binding upon and inure to the benefit of the parties' successors, legal representatives, and authorized assigns.

- In the event of any conflict between your obligations established by these terms and conditions and those established by CCC's Billing and Payment terms and conditions, these terms and conditions shall prevail.

- WILEY expressly reserves all rights not specifically granted in the combination of (i) the license details provided by you and accepted in the course of this licensing transaction, (ii) these terms and conditions and (iii) CCC's Billing and Payment terms and conditions.

- This Agreement will be void if the Type of Use, Format, Circulation, or Requestor Type was misrepresented during the licensing process.
- This Agreement shall be governed by and construed in accordance with the laws of the State of New York, USA, without regards to such state's conflict of law rules. Any legal action, suit or proceeding arising out of or relating to these Terms and Conditions or the breach thereof shall be instituted in a court of competent jurisdiction in New York County in the State of New York in the United States of America and each party hereby consents and submits to the personal jurisdiction of such court, waives any objection to venue in such court and consents to service of process by registered or certified mail, return receipt requested, at the last known address of such party.

WILEY OPEN ACCESS TERMS AND CONDITIONS

Wiley Publishes Open Access Articles in fully Open Access Journals and in Subscription journals offering Online Open. Although most of the fully Open Access journals publish open access articles under the terms of the Creative Commons Attribution (CC BY) License only, the subscription journals and a few of the Open Access Journals offer a choice of Creative Commons Licenses. The license type is clearly identified on the article.

The Creative Commons Attribution License

The Creative Commons Attribution License (CC-BY) allows users to copy, distribute and transmit an article, adapt the article and make commercial use of the article. The CC-BY license permits commercial and non-

Creative Commons Attribution Non-Commercial License

The Creative Commons Attribution Non-Commercial (CC-BY-NC)License permits use, distribution and reproduction in any medium, provided the original work is properly cited and is not used for commercial purposes.(see below)

Creative Commons Attribution-Non-Commercial-NoDerivs License

The Creative Commons Attribution Non-Commercial-NoDerivs License (CC-BY-NC-ND) permits use, distribution and reproduction in any medium, provided the original work is properly cited, is not used for commercial purposes and no modifications or adaptations are made. (see below)

Use by commercial "for-profit" organizations

Use of Wiley Open Access articles for commercial, promotional, or marketing purposes requires further explicit permission from Wiley and will be subject to a fee.

Further details can be found on Wiley Online Library http://olabout.wiley.com/WileyCDA/Section/id-410895.html

Other Terms and Conditions:

v1.10 Last updated September 2015

Questions? customercare@copyright.com or +1-855-239-3415 (toll free in the US) or +1-978-646-2777.



This is a License Agreement between Graeme Milligan ("User") and Copyright Clearance Center, Inc. ("CCC") on behalf of the Rightsholder identified in the order details below. The license consists of the order details, the Marketplace Order General Terms and Conditions below, and any Rightsholder Terms and Conditions which are included below.

All payments must be made in full to CCC in accordance with the Marketplace Order General Terms and Conditions below.

Order Date	21-Nov-2022	**Type of Use**	Republish in a thesis/dissertation
Order License ID	1292445-1		
ISSN	1084-0680	**Publisher**	American Society of Civil Engineers
		Portion	Chart/graph/table/figure

LICENSED CONTENT

Publication Title	PRACTICE PERIODICAL ON STRUCTURAL DESIGN AND CONSTRUCTION	**Country**	United States of America
		Rightsholder	American Society of Civil Engineers
Author/Editor	American Society of Civil Engineers Structural Division, American Society of Civil Engineers Construction Division	**Publication Type**	Journal
Date	12/31/1996		
Language	English		

REQUEST DETAILS

Portion Type	Chart/graph/table/figure	**Distribution**	Worldwide
Number of Charts / Graphs / Tables / Figures Requested	1	**Translation**	Original language of publication
		Copies for the Disabled?	No
Format (select all that apply)	Print, Electronic	**Minor Editing Privileges?**	No
Who Will Republish the Content?	Academic institution	**Incidental Promotional Use?**	No
Duration of Use	Current edition and up to 15 years	**Currency**	CAD
Lifetime Unit Quantity	Up to 44,999		
Rights Requested	Main product		

NEW WORK DETAILS

Title	Nonlinear Finite Element Analysis of Influence of Support Geometry on the Punching Shear Behaviour of Reinforced Concrete Slabs	**Institution Name**	University of Waterloo
		Expected Presentation Date	2023-03-30

Instructor Name	Graeme Milligan

ADDITIONAL DETAILS

Order Reference Number	N/A	**The Requesting Person/Organization to Appear on the License**	Graeme Milligan

REUSE CONTENT DETAILS

Title, Description or Numeric Reference of the Portion(s)	Figure 2	**Title of the Article/Chapter the Portion Is From**	Comparative Investigation of Concrete Plasticity Models for Nonlinear Finite-Element Analysis of Reinforced Concrete Specimens
Editor of Portion(s)	N/A	**Author of Portion(s)**	Hadi Panahi and Aikaterini S. Genikomsou
Volume of Serial or Monograph	27	**Issue, if Republishing an Article From a Serial**	2
Page or Page Range of Portion	04021083	**Publication Date of Portion**	2021-12-24

Marketplace Order General Terms and Conditions

The following terms and conditions ("General Terms"), together with any applicable Publisher Terms and Conditions, govern User's use of Works pursuant to the Licenses granted by Copyright Clearance Center, Inc. ("CCC") on behalf of the applicable Rightsholders of such Works through CCC's applicable Marketplace transactional licensing services (each, a "Service").

1) **Definitions.** For purposes of these General Terms, the following definitions apply:

"License" is the licensed use the User obtains via the Marketplace platform in a particular licensing transaction, as set forth in the Order Confirmation.

"Order Confirmation" is the confirmation CCC provides to the User at the conclusion of each Marketplace transaction. "Order Confirmation Terms" are additional terms set forth on specific Order Confirmations not set forth in the General Terms that can include terms applicable to a particular CCC transactional licensing service and/or any Rightsholder-specific terms.

"Rightsholder(s)" are the holders of copyright rights in the Works for which a User obtains licenses via the Marketplace platform, which are displayed on specific Order Confirmations.

"Terms" means the terms and conditions set forth in these General Terms and any additional Order Confirmation Terms collectively.

"User" or "you" is the person or entity making the use granted under the relevant License. Where the person accepting the Terms on behalf of a User is a freelancer or other third party who the User authorized to accept the General Terms on the User's behalf, such person shall be deemed jointly a User for purposes of such Terms.

"Work(s)" are the copyright protected works described in relevant Order Confirmations.

2) **Description of Service.** CCC's Marketplace enables Users to obtain Licenses to use one or more Works in accordance with all relevant Terms. CCC grants Licenses as an agent on behalf of the copyright rightsholder identified in the relevant Order Confirmation.

3) **Applicability of Terms.** The Terms govern User's use of Works in connection with the relevant License. In the event of any conflict between General Terms and Order Confirmation Terms, the latter shall govern. User acknowledges that

Rightsholders have complete discretion whether to grant any permission, and whether to place any limitations on any grant, and that CCC has no right to supersede or to modify any such discretionary act by a Rightsholder.

4) **Representations; Acceptance.** By using the Service, User represents and warrants that User has been duly authorized by the User to accept, and hereby does accept, all Terms.

5) **Scope of License; Limitations and Obligations.** All Works and all rights therein, including copyright rights, remain the sole and exclusive property of the Rightsholder. The License provides only those rights expressly set forth in the terms and conveys no other rights in any Works

6) **General Payment Terms.** User may pay at time of checkout by credit card or choose to be invoiced. If the User chooses to be invoiced, the User shall: (i) remit payments in the manner identified on specific invoices, (ii) unless otherwise specifically stated in an Order Confirmation or separate written agreement, Users shall remit payments upon receipt of the relevant invoice from CCC, either by delivery or notification of availability of the invoice via the Marketplace platform, and (iii) if the User does not pay the invoice within 30 days of receipt, the User may incur a service charge of 1.5% per month or the maximum rate allowed by applicable law, whichever is less. While User may exercise the rights in the License immediately upon receiving the Order Confirmation, the License is automatically revoked and is null and void, as if it had never been issued, if CCC does not receive complete payment on a timely basis.

7) **General Limits on Use.** Unless otherwise provided in the Order Confirmation, any grant of rights to User (i) involves only the rights set forth in the Terms and does not include subsequent or additional uses, (ii) is non-exclusive and non-transferable, and (iii) is subject to any and all limitations and restrictions (such as, but not limited to, limitations on duration of use or circulation) included in the Terms. Upon completion of the licensed use as set forth in the Order Confirmation, User shall either secure a new permission for further use of the Work(s) or immediately cease any new use of the Work(s) and shall render inaccessible (such as by deleting or by removing or severing links or other locators) any further copies of the Work. User may only make alterations to the Work if and as expressly set forth in the Order Confirmation. No Work may be used in any way that is defamatory, violates the rights of third parties (including such third parties' rights of copyright, privacy, publicity, or other tangible or intangible property), or is otherwise illegal, sexually explicit, or obscene. In addition, User may not conjoin a Work with any other material that may result in damage to the reputation of the Rightsholder. User agrees to inform CCC if it becomes aware of any infringement of any rights in a Work and to cooperate with any reasonable request of CCC or the Rightsholder in connection therewith.

8) **Third Party Materials.** In the event that the material for which a License is sought includes third party materials (such as photographs, illustrations, graphs, inserts and similar materials) that are identified in such material as having been used by permission (or a similar indicator), User is responsible for identifying, and seeking separate licenses (under this Service, if available, or otherwise) for any of such third party materials; without a separate license, User may not use such third party materials via the License.

9) **Copyright Notice.** Use of proper copyright notice for a Work is required as a condition of any License granted under the Service. Unless otherwise provided in the Order Confirmation, a proper copyright notice will read substantially as follows: "Used with permission of [Rightsholder's name], from [Work's title, author, volume, edition number and year of copyright]; permission conveyed through Copyright Clearance Center, Inc." Such notice must be provided in a reasonably legible font size and must be placed either on a cover page or in another location that any person, upon gaining access to the material which is the subject of a permission, shall see, or in the case of republication Licenses, immediately adjacent to the Work as used (for example, as part of a by-line or footnote) or in the place where substantially all other credits or notices for the new work containing the republished Work are located. Failure to include the required notice results in loss to the Rightsholder and CCC, and the User shall be liable to pay liquidated damages for each such failure equal to twice the use fee specified in the Order Confirmation, in addition to the use fee itself and any other fees and charges specified.

10) **Indemnity.** User hereby indemnifies and agrees to defend the Rightsholder and CCC, and their respective employees and directors, against all claims, liability, damages, costs, and expenses, including legal fees and expenses, arising out of any use of a Work beyond the scope of the rights granted herein and in the Order Confirmation, or any use of a Work which has been altered in any unauthorized way by User, including claims of defamation or infringement of rights of copyright, publicity, privacy, or other tangible or intangible property.

11) **Limitation of Liability.** UNDER NO CIRCUMSTANCES WILL CCC OR THE RIGHTSHOLDER BE LIABLE FOR ANY DIRECT, INDIRECT, CONSEQUENTIAL, OR INCIDENTAL DAMAGES (INCLUDING WITHOUT LIMITATION DAMAGES FOR LOSS OF BUSINESS PROFITS OR INFORMATION, OR FOR BUSINESS INTERRUPTION) ARISING OUT OF THE USE OR INABILITY TO USE A WORK, EVEN IF ONE OR BOTH OF THEM HAS BEEN ADVISED OF THE POSSIBILITY OF SUCH DAMAGES. In any event, the

total liability of the Rightsholder and CCC (including their respective employees and directors) shall not exceed the total amount actually paid by User for the relevant License. User assumes full liability for the actions and omissions of its principals, employees, agents, affiliates, successors, and assigns.

12) **Limited Warranties.** THE WORK(S) AND RIGHT(S) ARE PROVIDED "AS IS." CCC HAS THE RIGHT TO GRANT TO USER THE RIGHTS GRANTED IN THE ORDER CONFIRMATION DOCUMENT. CCC AND THE RIGHTSHOLDER DISCLAIM ALL OTHER WARRANTIES RELATING TO THE WORK(S) AND RIGHT(S), EITHER EXPRESS OR IMPLIED, INCLUDING WITHOUT LIMITATION IMPLIED WARRANTIES OF MERCHANTABILITY OR FITNESS FOR A PARTICULAR PURPOSE. ADDITIONAL RIGHTS MAY BE REQUIRED TO USE ILLUSTRATIONS, GRAPHS, PHOTOGRAPHS, ABSTRACTS, INSERTS, OR OTHER PORTIONS OF THE WORK (AS OPPOSED TO THE ENTIRE WORK) IN A MANNER CONTEMPLATED BY USER; USER UNDERSTANDS AND AGREES THAT NEITHER CCC NOR THE RIGHTSHOLDER MAY HAVE SUCH ADDITIONAL RIGHTS TO GRANT.

13) **Effect of Breach.** Any failure by User to pay any amount when due, or any use by User of a Work beyond the scope of the License set forth in the Order Confirmation and/or the Terms, shall be a material breach of such License. Any breach not cured within 10 days of written notice thereof shall result in immediate termination of such License without further notice. Any unauthorized (but licensable) use of a Work that is terminated immediately upon notice thereof may be liquidated by payment of the Rightsholder's ordinary license price therefor; any unauthorized (and unlicensable) use that is not terminated immediately for any reason (including, for example, because materials containing the Work cannot reasonably be recalled) will be subject to all remedies available at law or in equity, but in no event to a payment of less than three times the Rightsholder's ordinary license price for the most closely analogous licensable use plus Rightsholder's and/or CCC's costs and expenses incurred in collecting such payment.

14) **Additional Terms for Specific Products and Services.** If a User is making one of the uses described in this Section 14, the additional terms and conditions apply:

a) ***Print Uses of Academic Course Content and Materials (photocopies for academic coursepacks or classroom handouts).*** For photocopies for academic coursepacks or classroom handouts the following additional terms apply:

i) The copies and anthologies created under this License may be made and assembled by faculty members individually or at their request by on-campus bookstores or copy centers, or by off-campus copy shops and other similar entities.

ii) No License granted shall in any way: (i) include any right by User to create a substantively non-identical copy of the Work or to edit or in any other way modify the Work (except by means of deleting material immediately preceding or following the entire portion of the Work copied) (ii) permit "publishing ventures" where any particular anthology would be systematically marketed at multiple institutions.

iii) Subject to any Publisher Terms (and notwithstanding any apparent contradiction in the Order Confirmation arising from data provided by User), any use authorized under the academic pay-per-use service is limited as follows:

A) any License granted shall apply to only one class (bearing a unique identifier as assigned by the institution, and thereby including all sections or other subparts of the class) at one institution;

B) use is limited to not more than 25% of the text of a book or of the items in a published collection of essays, poems or articles;

C) use is limited to no more than the greater of (a) 25% of the text of an issue of a journal or other periodical or (b) two articles from such an issue;

D) no User may sell or distribute any particular anthology, whether photocopied or electronic, at more than one institution of learning;

E) in the case of a photocopy permission, no materials may be entered into electronic memory by User except in order to produce an identical copy of a Work before or during the academic term (or analogous period) as to which any particular permission is granted. In the event that User shall choose to retain materials that are the subject of a photocopy permission in electronic memory for purposes of producing identical copies more than one day after such retention (but still within the scope of any permission granted), User must notify CCC of such fact in the applicable permission request and such retention shall constitute one copy actually sold for purposes of calculating permission fees due; and

F) any permission granted shall expire at the end of the class. No permission granted shall in any way include any right by User to create a substantively non-identical copy of the Work or to edit or in any other way modify the Work (except by means of deleting material immediately preceding or following the entire portion of the Work copied).

iv) Books and Records; Right to Audit. As to each permission granted under the academic pay-per-use Service, User shall maintain for at least four full calendar years books and records sufficient for CCC to determine the numbers of copies made by User under such permission. CCC and any representatives it may designate shall have the right to audit such books and records at any time during User's ordinary business hours, upon two days' prior notice. If any such audit shall determine that User shall have underpaid for, or underreported, any photocopies sold or by three percent (3%) or more, then User shall bear all the costs of any such audit; otherwise, CCC shall bear the costs of any such audit. Any amount determined by such audit to have been underpaid by User shall immediately be paid to CCC by User, together with interest thereon at the rate of 10% per annum from the date such amount was originally due. The provisions of this paragraph shall survive the termination of this License for any reason.

b) ***Digital Pay-Per-Uses of Academic Course Content and Materials (e-coursepacks, electronic reserves, learning management systems, academic institution intranets).*** For uses in e-coursepacks, posts in electronic reserves, posts in learning management systems, or posts on academic institution intranets, the following additional terms apply:

i) The pay-per-uses subject to this Section 14(b) include:

A) **Posting e-reserves, course management systems, e-coursepacks for text-based content,** which grants authorizations to import requested material in electronic format, and allows electronic access to this material to members of a designated college or university class, under the direction of an instructor designated by the college or university, accessible only under appropriate electronic controls (e.g., password);

B) **Posting e-reserves, course management systems, e-coursepacks for material consisting of photographs or other still images not embedded in text,** which grants not only the authorizations described in Section 14(b)(i)(A) above, but also the following authorization: to include the requested material in course materials for use consistent with Section 14(b)(i)(A) above, including any necessary resizing, reformatting or modification of the resolution of such requested material (provided that such modification does not alter the underlying editorial content or meaning of the requested material, and provided that the resulting modified content is used solely within the scope of, and in a manner consistent with, the particular authorization described in the Order Confirmation and the Terms), but not including any other form of manipulation, alteration or editing of the requested material;

C) **Posting e-reserves, course management systems, e-coursepacks or other academic distribution for audiovisual content,** which grants not only the authorizations described in Section 14(b)(i)(A) above, but also the following authorizations: (i) to include the requested material in course materials for use consistent with Section 14(b)(i)(A) above; (ii) to display and perform the requested material to such members of such class in the physical classroom or remotely by means of streaming media or other video formats; and (iii) to "clip" or reformat the requested material for purposes of time or content management or ease of delivery, provided that such “clipping” or reformatting does not alter the underlying editorial content or meaning of the requested material and that the resulting material is used solely within the scope of, and in a manner consistent with, the particular authorization described in the Order Confirmation and the Terms. Unless expressly set forth in the relevant Order Conformation, the License does not authorize any other form of manipulation, alteration or editing of the requested material.

ii) Unless expressly set forth in the relevant Order Confirmation, no License granted shall in any way: (i) include any right by User to create a substantively non-identical copy of the Work or to edit or in any other way modify the Work (except by means of deleting material immediately preceding or following the entire portion of the Work copied or, in the case of Works subject to Sections 14(b)(1)(B) or (C) above, as described in such Sections) (ii) permit "publishing ventures" where any particular course materials would be systematically marketed at multiple institutions.

iii) Subject to any further limitations determined in the Rightsholder Terms (and notwithstanding any apparent contradiction in the Order Confirmation arising from data provided by User), any use authorized under the electronic course content pay-per-use service is limited as follows:

A) any License granted shall apply to only one class (bearing a unique identifier as assigned by the institution, and thereby including all sections or other subparts of the class) at one institution;

B) use is limited to not more than 25% of the text of a book or of the items in a published collection of essays, poems or articles;

C) use is limited to not more than the greater of (a) 25% of the text of an issue of a journal or other periodical or (b) two articles from such an issue;

D) no User may sell or distribute any particular materials, whether photocopied or electronic, at more than one institution of learning;

E) electronic access to material which is the subject of an electronic-use permission must be limited by means of electronic password, student identification or other control permitting access solely to students and instructors in the class;

F) User must ensure (through use of an electronic cover page or other appropriate means) that any person, upon gaining electronic access to the material, which is the subject of a permission, shall see:

- a proper copyright notice, identifying the Rightsholder in whose name CCC has granted permission,
- a statement to the effect that such copy was made pursuant to permission,
- a statement identifying the class to which the material applies and notifying the reader that the material has been made available electronically solely for use in the class, and
- a statement to the effect that the material may not be further distributed to any person outside the class, whether by copying or by transmission and whether electronically or in paper form, and User must also ensure that such cover page or other means will print out in the event that the person accessing the material chooses to print out the material or any part thereof.

G) any permission granted shall expire at the end of the class and, absent some other form of authorization, User is thereupon required to delete the applicable material from any electronic storage or to block electronic access to the applicable material.

iv) Uses of separate portions of a Work, even if they are to be included in the same course material or the same university or college class, require separate permissions under the electronic course content pay-per-use Service. Unless otherwise provided in the Order Confirmation, any grant of rights to User is limited to use completed no later than the end of the academic term (or analogous period) as to which any particular permission is granted.

v) Books and Records; Right to Audit. As to each permission granted under the electronic course content Service, User shall maintain for at least four full calendar years books and records sufficient for CCC to determine the numbers of copies made by User under such permission. CCC and any representatives it may designate shall have the right to audit such books and records at any time during User's ordinary business hours, upon two days' prior notice. If any such audit shall determine that User shall have underpaid for, or underreported, any electronic copies used by three percent (3%) or more, then User shall bear all the costs of any such audit; otherwise, CCC shall bear the costs of any such audit. Any amount determined by such audit to have been underpaid by User shall immediately be paid to CCC by User, together with interest thereon at the rate of 10% per annum from the date such amount was originally due. The provisions of this paragraph shall survive the termination of this license for any reason.

c) ***Pay-Per-Use Permissions for Certain Reproductions (Academic photocopies for library reserves and interlibrary loan reporting) (Non-academic internal/external business uses and commercial document delivery).*** The License expressly excludes the uses listed in Section (c)(i)-(v) below (which must be subject to separate license from the applicable Rightsholder) for: academic photocopies for library reserves and interlibrary loan reporting; and non-academic internal/external business uses and commercial document delivery.

i) electronic storage of any reproduction (whether in plain-text, PDF, or any other format) other than on a transitory basis;

ii) the input of Works or reproductions thereof into any computerized database;

iii) reproduction of an entire Work (cover-to-cover copying) except where the Work is a single article;

iv) reproduction for resale to anyone other than a specific customer of User;

v) republication in any different form. Please obtain authorizations for these uses through other CCC services or directly from the rightsholder.

Any license granted is further limited as set forth in any restrictions included in the Order Confirmation and/or in these Terms.

d) ***Electronic Reproductions in Online Environments (Non-Academic-email, intranet, internet and extranet).*** For "electronic reproductions", which generally includes e-mail use (including instant messaging or other electronic transmission to a defined group of recipients) or posting on an intranet, extranet or Intranet site (including any display or performance incidental thereto), the following additional terms apply:

i) Unless otherwise set forth in the Order Confirmation, the License is limited to use completed within 30 days for any use on the Internet, 60 days for any use on an intranet or extranet and one year for any other use, all as measured from the "republication date" as identified in the Order Confirmation, if any, and otherwise from the date of the Order Confirmation.

ii) User may not make or permit any alterations to the Work, unless expressly set forth in the Order Confirmation (after request by User and approval by Rightsholder); provided, however, that a Work consisting of photographs or other still images not embedded in text may, if necessary, be resized, reformatted or have its resolution modified without additional express permission, and a Work consisting of audiovisual content may, if necessary, be "clipped" or reformatted for purposes of time or content management or ease of delivery (provided that any such resizing, reformatting, resolution modification or “clipping” does not alter the underlying editorial content or meaning of the Work used, and that the resulting material is used solely within the scope of, and in a manner consistent with, the particular License described in the Order Confirmation and the Terms.

15) **Miscellaneous.**

a) User acknowledges that CCC may, from time to time, make changes or additions to the Service or to the Terms, and that Rightsholder may make changes or additions to the Rightsholder Terms. Such updated Terms will replace the prior terms and conditions in the order workflow and shall be effective as to any subsequent Licenses but shall not apply to Licenses already granted and paid for under a prior set of terms.

b) Use of User-related information collected through the Service is governed by CCC's privacy policy, available online at www.copyright.com/about/privacy-policy/.

c) The License is personal to User. Therefore, User may not assign or transfer to any other person (whether a natural person or an organization of any kind) the License or any rights granted thereunder; provided, however, that, where applicable, User may assign such License in its entirety on written notice to CCC in the event of a transfer of all or substantially all of User's rights in any new material which includes the Work(s) licensed under this Service.

d) No amendment or waiver of any Terms is binding unless set forth in writing and signed by the appropriate parties, including, where applicable, the Rightsholder. The Rightsholder and CCC hereby object to any terms contained in any writing prepared by or on behalf of the User or its principals, employees, agents or affiliates and purporting to govern or otherwise relate to the License described in the Order Confirmation, which terms are in any way inconsistent with any Terms set forth in the Order Confirmation, and/or in CCC's standard operating procedures, whether such writing is prepared prior to, simultaneously with or subsequent to the Order Confirmation, and whether such writing appears on a copy of the Order Confirmation or in a separate instrument.

e) The License described in the Order Confirmation shall be governed by and construed under the law of the State of New York, USA, without regard to the principles thereof of conflicts of law. Any case, controversy, suit, action, or proceeding arising out of, in connection with, or related to such License shall be brought, at CCC's sole discretion, in any federal or state court located in the County of New York, State of New York, USA, or in any federal or state court whose geographical jurisdiction covers the location of the Rightsholder set forth in the Order Confirmation. The parties expressly submit to the personal jurisdiction and venue of each such federal or state court.

ELSEVIER LICENSE
TERMS AND CONDITIONS

Nov 21, 2022

This Agreement between University of Waterloo -- Graeme Milligan ("You") and Elsevier ("Elsevier") consists of your license details and the terms and conditions provided by Elsevier and Copyright Clearance Center.

License Number	5433721117024
License date	Nov 21, 2022
Licensed Content Publisher	Elsevier
Licensed Content Publication	Engineering Structures
Licensed Content Title	New methodology for calculating damage variables evolution in Plastic Damage Model for RC structures
Licensed Content Author	B. Alfarah,F. López-Almansa,S. Oller
Licensed Content Date	Feb 1, 2017
Licensed Content Volume	132
Licensed Content Issue	n/a
Licensed Content Pages	17
Start Page	70
End Page	86

Type of Use	reuse in a thesis/dissertation
Portion	figures/tables/illustrations
Number of figures/tables/illustrations	1
Format	both print and electronic
Are you the author of this Elsevier article?	No
Will you be translating?	No
Title	Nonlinear Finite Element Analysis of Influence of Support Geometry on the Punching Shear Behaviour of Reinforced Concrete Slabs
Institution name	University of Waterloo
Expected presentation date	Apr 2023
Portions	Fig. 3.
Requestor Location	University of Waterloo 200 University Avenue West Waterloo, ON N2L3G1 Canada Attn: Graeme Jacob Milligan
Publisher Tax ID	GB 494 6272 12
Total	0.00 CAD
Terms and Conditions	

INTRODUCTION

1. The publisher for this copyrighted material is Elsevier. By clicking "accept" in connection with completing this licensing transaction, you agree that the following terms and conditions apply to this transaction (along with the Billing and Payment terms and conditions established by Copyright Clearance Center, Inc. ("CCC"), at the time that you opened your Rightslink account and that are available at any time at http://myaccount.copyright.com).

GENERAL TERMS

2. Elsevier hereby grants you permission to reproduce the aforementioned material subject to the terms and conditions indicated.

3. Acknowledgement: If any part of the material to be used (for example, figures) has appeared in our publication with credit or acknowledgement to another source, permission must also be sought from that source. If such permission is not obtained then that material may not be included in your publication/copies. Suitable acknowledgement to the source must be made, either as a footnote or in a reference list at the end of your publication, as follows:

"Reprinted from Publication title, Vol /edition number, Author(s), Title of article / title of chapter, Pages No., Copyright (Year), with permission from Elsevier [OR APPLICABLE SOCIETY COPYRIGHT OWNER]." Also Lancet special credit - "Reprinted from The Lancet, Vol. number, Author(s), Title of article, Pages No., Copyright (Year), with permission from Elsevier."

4. Reproduction of this material is confined to the purpose and/or media for which permission is hereby given.

5. Altering/Modifying Material: Not Permitted. However figures and illustrations may be altered/adapted minimally to serve your work. Any other abbreviations, additions, deletions and/or any other alterations shall be made only with prior written authorization of Elsevier Ltd. (Please contact Elsevier's permissions helpdesk here). No modifications can be made to any Lancet figures/tables and they must be reproduced in full.

6. If the permission fee for the requested use of our material is waived in this instance, please be advised that your future requests for Elsevier materials may attract a fee.

7. Reservation of Rights: Publisher reserves all rights not specifically granted in the combination of (i) the license details provided by you and accepted in the course of this licensing transaction, (ii) these terms and conditions and (iii) CCC's Billing and Payment terms and conditions.

8. License Contingent Upon Payment: While you may exercise the rights licensed immediately upon issuance of the license at the end of the licensing process for the transaction, provided that you have disclosed complete and accurate details of your proposed use, no license is finally effective unless and until full payment is received from you (either by publisher or by CCC) as provided in CCC's Billing and Payment terms and conditions. If full payment is not received on a timely basis, then any license preliminarily granted shall be deemed automatically revoked and shall be void as if never granted. Further, in the event that you breach any of these terms and conditions or any of CCC's Billing and Payment terms and conditions, the license is automatically revoked and shall be void as if never granted. Use of materials as described in a revoked license, as well as any use of the materials beyond the scope of an unrevoked license, may constitute copyright infringement and publisher reserves the right to take any and all action to protect its copyright in the materials.

9. Warranties: Publisher makes no representations or warranties with respect to the licensed material.

10. Indemnity: You hereby indemnify and agree to hold harmless publisher and CCC, and their respective officers, directors, employees and agents, from and against any and all claims arising out of your use of the licensed material other than as specifically authorized pursuant to this license.

11. No Transfer of License: This license is personal to you and may not be sublicensed, assigned, or transferred by you to any other person without publisher's written permission.

12. No Amendment Except in Writing: This license may not be amended except in a writing signed by both parties (or, in the case of publisher, by CCC on publisher's behalf).

13. Objection to Contrary Terms: Publisher hereby objects to any terms contained in any purchase order, acknowledgment, check endorsement or other writing prepared by you, which terms are inconsistent with these terms and conditions or CCC's Billing and Payment terms and conditions. These terms and conditions, together with CCC's Billing and Payment terms and conditions (which are incorporated herein), comprise the entire agreement between you and publisher (and CCC) concerning this licensing transaction. In the event of any conflict between your obligations established by these terms and conditions and those established by CCC's Billing and Payment terms and conditions, these terms and conditions shall control.

14. Revocation: Elsevier or Copyright Clearance Center may deny the permissions described in this License at their sole discretion, for any reason or no reason, with a full refund payable to you. Notice of such denial will be made using the contact information provided by you. Failure to receive such notice will not alter or invalidate the denial. In no event will Elsevier or Copyright Clearance Center be responsible or liable for any costs, expenses or damage incurred by you as a result of a denial of your permission request, other than a refund of the amount(s) paid by you to Elsevier and/or Copyright Clearance Center for denied permissions.

LIMITED LICENSE

The following terms and conditions apply only to specific license types:

15. **Translation**: This permission is granted for non-exclusive world **English** rights only unless your license was granted for translation rights. If you licensed translation rights you may only translate this content into the languages you requested. A professional translator must perform all translations and reproduce the content word for word preserving the integrity of the article.

16. **Posting licensed content on any Website**: The following terms and conditions apply as follows: Licensing material from an Elsevier journal: All content posted to the web site must maintain the copyright information line on the bottom of each image; A hyper-text must be included to the Homepage of the journal from which you are licensing at http://www.sciencedirect.com/science/journal/xxxxx or the Elsevier homepage for books at http://www.elsevier.com; Central Storage: This license does not include permission for a scanned version of the material to be stored in a central repository such as that provided by Heron/XanEdu.

Licensing material from an Elsevier book: A hyper-text link must be included to the Elsevier homepage at http://www.elsevier.com . All content posted to the web site must maintain the copyright information line on the bottom of each image.

Posting licensed content on Electronic reserve: In addition to the above the following clauses are applicable: The web site must be password-protected and made available only to bona fide students registered on a relevant course. This permission is granted for 1 year only. You may obtain a new license for future website posting.

17. **For journal authors:** the following clauses are applicable in addition to the above:

Preprints:

A preprint is an author's own write-up of research results and analysis, it has not been peer-reviewed, nor has it had any other value added to it by a publisher (such as formatting, copyright, technical enhancement etc.).

Authors can share their preprints anywhere at any time. Preprints should not be added to or enhanced in any way in order to appear more like, or to substitute for, the final versions of articles however authors can update their preprints on arXiv or RePEc with their Accepted Author Manuscript (see below).

If accepted for publication, we encourage authors to link from the preprint to their formal publication via its DOI. Millions of researchers have access to the formal publications on ScienceDirect, and so links will help users to find, access, cite and use the best available version. Please note that Cell Press, The Lancet and some society-owned have different preprint policies. Information on these policies is available on the journal homepage.

Accepted Author Manuscripts: An accepted author manuscript is the manuscript of an article that has been accepted for publication and which typically includes author-incorporated changes suggested during submission, peer review and editor-author communications.

Authors can share their accepted author manuscript:

- immediately
    - via their non-commercial person homepage or blog
    - by updating a preprint in arXiv or RePEc with the accepted manuscript
    - via their research institute or institutional repository for internal institutional uses or as part of an invitation-only research collaboration work-group
    - directly by providing copies to their students or to research collaborators for their personal use
    - for private scholarly sharing as part of an invitation-only work group on commercial sites with which Elsevier has an agreement
- After the embargo period
    - via non-commercial hosting platforms such as their institutional repository
    - via commercial sites with which Elsevier has an agreement

In all cases accepted manuscripts should:

- link to the formal publication via its DOI
- bear a CC-BY-NC-ND license - this is easy to do
- if aggregated with other manuscripts, for example in a repository or other site, be shared in alignment with our hosting policy not be added to or enhanced in any way to appear more like, or to substitute for, the published journal article.

Published journal article (JPA): A published journal article (PJA) is the definitive final record of published research that appears or will appear in the journal and embodies all

value-adding publishing activities including peer review co-ordination, copy-editing, formatting, (if relevant) pagination and online enrichment.

Policies for sharing publishing journal articles differ for subscription and gold open access articles:

Subscription Articles: If you are an author, please share a link to your article rather than the full-text. Millions of researchers have access to the formal publications on ScienceDirect, and so links will help your users to find, access, cite, and use the best available version.

Theses and dissertations which contain embedded PJAs as part of the formal submission can be posted publicly by the awarding institution with DOI links back to the formal publications on ScienceDirect.

If you are affiliated with a library that subscribes to ScienceDirect you have additional private sharing rights for others' research accessed under that agreement. This includes use for classroom teaching and internal training at the institution (including use in course packs and courseware programs), and inclusion of the article for grant funding purposes.

Gold Open Access Articles: May be shared according to the author-selected end-user license and should contain a CrossMark logo, the end user license, and a DOI link to the formal publication on ScienceDirect.

Please refer to Elsevier's posting policy for further information.

18. **For book authors** the following clauses are applicable in addition to the above: Authors are permitted to place a brief summary of their work online only. You are not allowed to download and post the published electronic version of your chapter, nor may you scan the printed edition to create an electronic version. **Posting to a repository:** Authors are permitted to post a summary of their chapter only in their institution's repository.

19. **Thesis/Dissertation**: If your license is for use in a thesis/dissertation your thesis may be submitted to your institution in either print or electronic form. Should your thesis be published commercially, please reapply for permission. These requirements include permission for the Library and Archives of Canada to supply single copies, on demand, of the complete thesis and include permission for Proquest/UMI to supply single copies, on demand, of the complete thesis. Should your thesis be published commercially, please reapply for permission. Theses and dissertations which contain embedded PJAs as part of the formal submission can be posted publicly by the awarding institution with DOI links back to the formal publications on ScienceDirect.

Elsevier Open Access Terms and Conditions

You can publish open access with Elsevier in hundreds of open access journals or in nearly 2000 established subscription journals that support open access publishing. Permitted third party re-use of these open access articles is defined by the author's choice of Creative Commons user license. See our open access license policy for more information.

Terms & Conditions applicable to all Open Access articles published with Elsevier:

Any reuse of the article must not represent the author as endorsing the adaptation of the article nor should the article be modified in such a way as to damage the author's honour or reputation. If any changes have been made, such changes must be clearly indicated.

The author(s) must be appropriately credited and we ask that you include the end user license and a DOI link to the formal publication on ScienceDirect.

If any part of the material to be used (for example, figures) has appeared in our publication with credit or acknowledgement to another source it is the responsibility of the user to ensure their reuse complies with the terms and conditions determined by the rights holder.

Additional Terms & Conditions applicable to each Creative Commons user license:

CC BY: The CC-BY license allows users to copy, to create extracts, abstracts and new works from the Article, to alter and revise the Article and to make commercial use of the Article (including reuse and/or resale of the Article by commercial entities), provided the user gives appropriate credit (with a link to the formal publication through the relevant DOI), provides a link to the license, indicates if changes were made and the licensor is not represented as endorsing the use made of the work. The full details of the license are available at http://creativecommons.org/licenses/by/4.0.

CC BY NC SA: The CC BY-NC-SA license allows users to copy, to create extracts, abstracts and new works from the Article, to alter and revise the Article, provided this is not done for commercial purposes, and that the user gives appropriate credit (with a link to the formal publication through the relevant DOI), provides a link to the license, indicates if changes were made and the licensor is not represented as endorsing the use made of the work. Further, any new works must be made available on the same conditions. The full details of the license are available at http://creativecommons.org/licenses/by-nc-sa/4.0.

CC BY NC ND: The CC BY-NC-ND license allows users to copy and distribute the Article, provided this is not done for commercial purposes and further does not permit distribution of the Article if it is changed or edited in any way, and provided the user gives appropriate credit (with a link to the formal publication through the relevant DOI), provides a link to the license, and that the licensor is not represented as endorsing the use made of the work. The full details of the license are available at http://creativecommons.org/licenses/by-nc-nd/4.0. Any commercial reuse of Open Access articles published with a CC BY NC SA or CC BY NC ND license requires permission from Elsevier and will be subject to a fee.

Commercial reuse includes:

- Associating advertising with the full text of the Article
- Charging fees for document delivery or access
- Article aggregation
- Systematic distribution via e-mail lists or share buttons

Posting or linking by commercial companies for use by customers of those companies.

20. **Other Conditions**:

v1.10

Questions? customercare@copyright.com or +1-855-239-3415 (toll free in the US) or +1-978-646-2777.

Re: Obtain permission request - Journal (1323307) [221116-020207]

Rights and Permissions (ELS) <Permissions@elsevier.com>
Thu 11/17/2022 1:42 PM
To: Graeme Jacob Milligan <gjmillig@uwaterloo.ca>

Dear Mr. Graeme Milligan,

Thank you for your email.

We hereby grant you permission to reprint the material below at no charge in your thesis subject to the following conditions:

1. If any part of the material to be used (for example, figures) has appeared in our publication with credit or acknowledgement to another source, permission must also be sought from that source. If such permission is not obtained then that material may not be included in your publication/copies.

2. Suitable acknowledgment to the source must be made, either as a footnote or in a reference list at the end of your publication, as follows:
"This article was published in Publication title, Vol number, Author(s), Title of article, Page Nos, Copyright Elsevier (or appropriate Society name) (Year)."

3. Your thesis may be submitted to your institution in either print or electronic form.

4. Reproduction of this material is confined to the purpose for which permission is hereby given

5. This permission is granted for non-exclusive world English rights only. For other languages please reapply separately for each one required. Permission excludes use in an electronic form other than submission. Should you have a

specific electronic project in mind please reapply for permission.

6. Should your thesis be published commercially, please reapply for permission.

This includes permission for the Library and Archives of Canada to supply single copies, on demand, of the complete thesis. Should your thesis be published commercially, please reapply for permission- Canada
This includes permission for UMI to supply single copies, on demand, of the complete thesis. Should your thesis be published commercially, please reapply for permission-ROW

7. Posting of the full article online is not permitted. You may post an abstract with a link to the Elsevier website www.elsevier.com, or to the article on ScienceDirect if it is available on that platform.

8. Article can used be in the University library if it is embedded in the thesis and not used commercially.

Kind regards,

Thomas Rexson Yesudoss
Copyrights Coordinator
ELSEVIER | HCM - Health Content Management

Visit Elsevier Permissions

From: Administrator
Date: Wednesday, November 16, 2022 03:06 PM GMT

Dear ,

Thank you for contacting the Permissions Granting Team.

We acknowledge the receipt of your request and we aim to respond within seven business days. Your unique reference number is 221116-020207.

Please avoid changing the subject line of this email when replying to avoid delay with your query.

Regards,

Permission Granting Team

From:
Date: Wednesday, November 16, 2022 03:06 PM GMT

Submission ID: 1323307
Date: 16 Nov 2022 3:06pm

Name: Mr. Graeme Milligan
Institute/company: University of Waterloo
Address: 200 University Avenue West
Post/Zip Code: N2L 3G1
City: Waterloo
State/Territory: ONTARIO
Country: Canada
Telephone: 9055184711
Email: gjmillig@uwaterloo.ca

Type of Publication: Journal

Title: Archives of Civil and Mechanical Engineering
Auhtors: Adam Wosatko, Andrzej Winnicki, Maria Anna Polak and Jerzy Pamin
Year: 2019
From page: 1268
To page: 1283
ISSN: 1644-9665
Volume: 19
Issue: 4
Article title: Role of dilatancy angle in plasticity-based models of concrete

I would like to use: Figure(s)

Quantity of material: 4
I am the author of the Elsevier material: No
Elsevier author is involved in my project: Yes
Involvement: Professor Maria Anna Polak is my PhD supervisor.

In what format will you use the material: Print and Electronic
Translation: No

Proposed use: Reuse in a thesis/dissertation

Material can be extracted: Yes

Additional Comments / Information:

This email is for use by the intended recipient and contains information that may be confidential. If you are not the intended recipient, please notify the sender by return email and delete this email from your inbox. Any unauthorized use or distribution of this email, in whole or in part, is strictly prohibited and may be unlawful. Any price quotes contained in this email are merely indicative and will not result in any legally binding or enforceable obligation. Unless explicitly designated as an intended e-contract, this email does not constitute a contract offer, a contract amendment, or an acceptance of a contract offer.

Elsevier Limited. Registered Office: The Boulevard, Langford Lane, Kidlington, Oxford, OX5 1GB, United Kingdom, Registration No. 1982084, Registered in England and Wales. Privacy Policy

ELSEVIER LICENSE
TERMS AND CONDITIONS

Sep 16, 2022

This Agreement between University of Waterloo -- Graeme Milligan ("You") and Elsevier ("Elsevier") consists of your license details and the terms and conditions provided by Elsevier and Copyright Clearance Center.

License Number	5390811318466
License date	Sep 16, 2022
Licensed Content Publisher	Elsevier
Licensed Content Publication	Engineering Structures
Licensed Content Title	Internal slab-column connections under monotonic and cyclic imposed rotations
Licensed Content Author	Ioannis-Sokratis Drakatos,Aurelio Muttoni,Katrin Beyer
Licensed Content Date	Sep 15, 2016
Licensed Content Volume	123
Licensed Content Issue	n/a
Licensed Content Pages	16
Start Page	501
End Page	516

Type of Use	reuse in a thesis/dissertation
Portion	figures/tables/illustrations
Number of figures/tables/illustrations	9
Format	both print and electronic
Are you the author of this Elsevier article?	No
Will you be translating?	No
Title	Nonlinear Finite Element Analysis of Influence of Support Geometry on the Punching Shear Behaviour of Reinforced Concrete Slabs
Institution name	University of Waterloo
Expected presentation date	Apr 2023
Portions	Fig. 3 and Fig. 4 (entire figure); Fig. 15 (a), Fig. 15 (c); Fig. 16(a), Fig. 16 (c); Fig. 17(a), Fig 17(b)
Requestor Location	University of Waterloo 200 University Avenue West Waterloo, ON N2L3G1 Canada Attn: Graeme Jacob Milligan
Publisher Tax ID	GB 494 6272 12
Total	0.00 CAD
Terms and Conditions	

INTRODUCTION

1. The publisher for this copyrighted material is Elsevier. By clicking "accept" in connection with completing this licensing transaction, you agree that the following terms and conditions apply to this transaction (along with the Billing and Payment terms and conditions established by Copyright Clearance Center, Inc. ("CCC"), at the time that you opened your Rightslink account and that are available at any time at http://myaccount.copyright.com).

GENERAL TERMS

2. Elsevier hereby grants you permission to reproduce the aforementioned material subject to the terms and conditions indicated.

3. Acknowledgement: If any part of the material to be used (for example, figures) has appeared in our publication with credit or acknowledgement to another source, permission must also be sought from that source. If such permission is not obtained then that material may not be included in your publication/copies. Suitable acknowledgement to the source must be made, either as a footnote or in a reference list at the end of your publication, as follows:

"Reprinted from Publication title, Vol /edition number, Author(s), Title of article / title of chapter, Pages No., Copyright (Year), with permission from Elsevier [OR APPLICABLE SOCIETY COPYRIGHT OWNER]." Also Lancet special credit - "Reprinted from The Lancet, Vol. number, Author(s), Title of article, Pages No., Copyright (Year), with permission from Elsevier."

4. Reproduction of this material is confined to the purpose and/or media for which permission is hereby given.

5. Altering/Modifying Material: Not Permitted. However figures and illustrations may be altered/adapted minimally to serve your work. Any other abbreviations, additions, deletions and/or any other alterations shall be made only with prior written authorization of Elsevier Ltd. (Please contact Elsevier's permissions helpdesk here). No modifications can be made to any Lancet figures/tables and they must be reproduced in full.

6. If the permission fee for the requested use of our material is waived in this instance, please be advised that your future requests for Elsevier materials may attract a fee.

7. Reservation of Rights: Publisher reserves all rights not specifically granted in the combination of (i) the license details provided by you and accepted in the course of this licensing transaction, (ii) these terms and conditions and (iii) CCC's Billing and Payment terms and conditions.

8. License Contingent Upon Payment: While you may exercise the rights licensed immediately upon issuance of the license at the end of the licensing process for the transaction, provided that you have disclosed complete and accurate details of your proposed use, no license is finally effective unless and until full payment is received from you (either by publisher or by CCC) as provided in CCC's Billing and Payment terms and conditions. If full payment is not received on a timely basis, then any license preliminarily granted shall be deemed automatically revoked and shall be void as if never granted. Further, in the event that you breach any of these terms and conditions or any of CCC's Billing and Payment terms and conditions, the license is automatically revoked and shall be void as if never granted. Use of materials as described in a revoked license, as well as any use of the materials beyond the scope of an unrevoked license, may constitute copyright infringement

and publisher reserves the right to take any and all action to protect its copyright in the materials.

9. Warranties: Publisher makes no representations or warranties with respect to the licensed material.

10. Indemnity: You hereby indemnify and agree to hold harmless publisher and CCC, and their respective officers, directors, employees and agents, from and against any and all claims arising out of your use of the licensed material other than as specifically authorized pursuant to this license.

11. No Transfer of License: This license is personal to you and may not be sublicensed, assigned, or transferred by you to any other person without publisher's written permission.

12. No Amendment Except in Writing: This license may not be amended except in a writing signed by both parties (or, in the case of publisher, by CCC on publisher's behalf).

13. Objection to Contrary Terms: Publisher hereby objects to any terms contained in any purchase order, acknowledgment, check endorsement or other writing prepared by you, which terms are inconsistent with these terms and conditions or CCC's Billing and Payment terms and conditions. These terms and conditions, together with CCC's Billing and Payment terms and conditions (which are incorporated herein), comprise the entire agreement between you and publisher (and CCC) concerning this licensing transaction. In the event of any conflict between your obligations established by these terms and conditions and those established by CCC's Billing and Payment terms and conditions, these terms and conditions shall control.

14. Revocation: Elsevier or Copyright Clearance Center may deny the permissions described in this License at their sole discretion, for any reason or no reason, with a full refund payable to you. Notice of such denial will be made using the contact information provided by you. Failure to receive such notice will not alter or invalidate the denial. In no event will Elsevier or Copyright Clearance Center be responsible or liable for any costs, expenses or damage incurred by you as a result of a denial of your permission request, other than a refund of the amount(s) paid by you to Elsevier and/or Copyright Clearance Center for denied permissions.

LIMITED LICENSE

The following terms and conditions apply only to specific license types:

15. **Translation**: This permission is granted for non-exclusive world **English** rights only unless your license was granted for translation rights. If you licensed translation rights you may only translate this content into the languages you requested. A professional translator must perform all translations and reproduce the content word for word preserving the integrity of the article.

16. **Posting licensed content on any Website**: The following terms and conditions apply as follows: Licensing material from an Elsevier journal: All content posted to the web site must maintain the copyright information line on the bottom of each image; A hyper-text must be included to the Homepage of the journal from which you are licensing at http://www.sciencedirect.com/science/journal/xxxxx or the Elsevier homepage for books at http://www.elsevier.com; Central Storage: This license does not include permission for a scanned version of the material to be stored in a central repository such as that provided by Heron/XanEdu.

Licensing material from an Elsevier book: A hyper-text link must be included to the Elsevier homepage at http://www.elsevier.com . All content posted to the web site must maintain the copyright information line on the bottom of each image.

Posting licensed content on Electronic reserve: In addition to the above the following clauses are applicable: The web site must be password-protected and made available only to bona fide students registered on a relevant course. This permission is granted for 1 year only. You may obtain a new license for future website posting.

17. **For journal authors:** the following clauses are applicable in addition to the above:

Preprints:

A preprint is an author's own write-up of research results and analysis, it has not been peer-reviewed, nor has it had any other value added to it by a publisher (such as formatting, copyright, technical enhancement etc.).

Authors can share their preprints anywhere at any time. Preprints should not be added to or enhanced in any way in order to appear more like, or to substitute for, the final versions of articles however authors can update their preprints on arXiv or RePEc with their Accepted Author Manuscript (see below).

If accepted for publication, we encourage authors to link from the preprint to their formal publication via its DOI. Millions of researchers have access to the formal publications on ScienceDirect, and so links will help users to find, access, cite and use the best available version. Please note that Cell Press, The Lancet and some society-owned have different preprint policies. Information on these policies is available on the journal homepage.

Accepted Author Manuscripts: An accepted author manuscript is the manuscript of an article that has been accepted for publication and which typically includes author-incorporated changes suggested during submission, peer review and editor-author communications.

Authors can share their accepted author manuscript:

- immediately
  - via their non-commercial person homepage or blog
  - by updating a preprint in arXiv or RePEc with the accepted manuscript
  - via their research institute or institutional repository for internal institutional uses or as part of an invitation-only research collaboration work-group
  - directly by providing copies to their students or to research collaborators for their personal use
  - for private scholarly sharing as part of an invitation-only work group on commercial sites with which Elsevier has an agreement
- After the embargo period
  - via non-commercial hosting platforms such as their institutional repository
  - via commercial sites with which Elsevier has an agreement

In all cases accepted manuscripts should:

- link to the formal publication via its DOI
- bear a CC-BY-NC-ND license - this is easy to do
- if aggregated with other manuscripts, for example in a repository or other site, be shared in alignment with our hosting policy not be added to or enhanced in any way to

appear more like, or to substitute for, the published journal article.

Published journal article (JPA): A published journal article (PJA) is the definitive final record of published research that appears or will appear in the journal and embodies all value-adding publishing activities including peer review co-ordination, copy-editing, formatting, (if relevant) pagination and online enrichment.

Policies for sharing publishing journal articles differ for subscription and gold open access articles:

Subscription Articles: If you are an author, please share a link to your article rather than the full-text. Millions of researchers have access to the formal publications on ScienceDirect, and so links will help your users to find, access, cite, and use the best available version.

Theses and dissertations which contain embedded PJAs as part of the formal submission can be posted publicly by the awarding institution with DOI links back to the formal publications on ScienceDirect.

If you are affiliated with a library that subscribes to ScienceDirect you have additional private sharing rights for others' research accessed under that agreement. This includes use for classroom teaching and internal training at the institution (including use in course packs and courseware programs), and inclusion of the article for grant funding purposes.

Gold Open Access Articles: May be shared according to the author-selected end-user license and should contain a CrossMark logo, the end user license, and a DOI link to the formal publication on ScienceDirect.

Please refer to Elsevier's posting policy for further information.

18. **For book authors** the following clauses are applicable in addition to the above: Authors are permitted to place a brief summary of their work online only. You are not allowed to download and post the published electronic version of your chapter, nor may you scan the printed edition to create an electronic version. **Posting to a repository:** Authors are permitted to post a summary of their chapter only in their institution's repository.

19. **Thesis/Dissertation**: If your license is for use in a thesis/dissertation your thesis may be submitted to your institution in either print or electronic form. Should your thesis be published commercially, please reapply for permission. These requirements include permission for the Library and Archives of Canada to supply single copies, on demand, of the complete thesis and include permission for Proquest/UMI to supply single copies, on demand, of the complete thesis. Should your thesis be published commercially, please reapply for permission. Theses and dissertations which contain embedded PJAs as part of the formal submission can be posted publicly by the awarding institution with DOI links back to the formal publications on ScienceDirect.

Elsevier Open Access Terms and Conditions

You can publish open access with Elsevier in hundreds of open access journals or in nearly 2000 established subscription journals that support open access publishing. Permitted third party re-use of these open access articles is defined by the author's choice of Creative Commons user license. See our open access license policy for more information.

Terms & Conditions applicable to all Open Access articles published with Elsevier:

Any reuse of the article must not represent the author as endorsing the adaptation of the article nor should the article be modified in such a way as to damage the author's honour or reputation. If any changes have been made, such changes must be clearly indicated.

The author(s) must be appropriately credited and we ask that you include the end user license and a DOI link to the formal publication on ScienceDirect.

If any part of the material to be used (for example, figures) has appeared in our publication with credit or acknowledgement to another source it is the responsibility of the user to ensure their reuse complies with the terms and conditions determined by the rights holder.

Additional Terms & Conditions applicable to each Creative Commons user license:

CC BY: The CC-BY license allows users to copy, to create extracts, abstracts and new works from the Article, to alter and revise the Article and to make commercial use of the Article (including reuse and/or resale of the Article by commercial entities), provided the user gives appropriate credit (with a link to the formal publication through the relevant DOI), provides a link to the license, indicates if changes were made and the licensor is not represented as endorsing the use made of the work. The full details of the license are available at http://creativecommons.org/licenses/by/4.0.

CC BY NC SA: The CC BY-NC-SA license allows users to copy, to create extracts, abstracts and new works from the Article, to alter and revise the Article, provided this is not done for commercial purposes, and that the user gives appropriate credit (with a link to the formal publication through the relevant DOI), provides a link to the license, indicates if changes were made and the licensor is not represented as endorsing the use made of the work. Further, any new works must be made available on the same conditions. The full details of the license are available at http://creativecommons.org/licenses/by-nc-sa/4.0.

CC BY NC ND: The CC BY-NC-ND license allows users to copy and distribute the Article, provided this is not done for commercial purposes and further does not permit distribution of the Article if it is changed or edited in any way, and provided the user gives appropriate credit (with a link to the formal publication through the relevant DOI), provides a link to the license, and that the licensor is not represented as endorsing the use made of the work. The full details of the license are available at http://creativecommons.org/licenses/by-nc-nd/4.0. Any commercial reuse of Open Access articles published with a CC BY NC SA or CC BY NC ND license requires permission from Elsevier and will be subject to a fee.

Commercial reuse includes:

- Associating advertising with the full text of the Article
- Charging fees for document delivery or access
- Article aggregation
- Systematic distribution via e-mail lists or share buttons

Posting or linking by commercial companies for use by customers of those companies.

20. **Other Conditions**:

v1.10

Questions? customercare@copyright.com or +1-855-239-3415 (toll free in the US) or +1-978-646-2777.

Bibliography

[1] G. J. Milligan, "Nonlinear Finite Element Analysis of Punching Shear of Reinforced Concrete Slabs Supported on Rectangular Columns," Master's Thesis, University of Waterloo, Waterloo, Ontario, Canada, 2018.

[2] ACI Committee 318, Building Code Requirements for Structural Concrete (ACI 318-19) and Commentary on Building Code Requirements for Structural Concrete (ACI 318R-19), Farmington Hills, Michigan: American Concrete Institute, 2019.

[3] N. M. Hawkins, H. B. Fallsen and R. C. Hinojosa, "Influence of Column Rectangularity on the Behavior of Flat Plate Structures," *ACI Symposium Publication,* vol. 30, pp. 127-146, 1971.

[4] I.-S. Drakatos, A. Muttoni and K. Beyer, "Internal slab-column connections under monotonic and cyclic imposed rotations," *Engineering Structures,* vol. 123, pp. 501-516, 2016.

[5] Joint ACI-ASCE Committee 421, ACI 421.1R-20 Guide for Shear Reinforcement for Slabs, Farmington Hills, MI: American Concrete Institute, 2020.

[6] D. A. Gasparini, "Contributions of C.A.P. Turner to development of reinforced concrete flat slabs 1905-1909," *Journal of Structural Engineering,* vol. 128, no. 10, pp. 1243-1252, 2002.

[7] M. A. Sozen and C. P. Siess, "Investigation of multiple-panel reinforced concrete floor slabs design methods - their evolution and comparison," *Journal of the American Concrete Institute,* vol. 60, no. 8, pp. 999-1028, 1963.

[8] Turner, C.A.P., *Engineering News,* 1905, pp. 383-384.

[9] FIB, "Punching of structural concrete slabs," *fib Bulletin 12,* 2001.

[10] J. G. MacGregor and F. M. Bartlett, Reinforced Concrete Mechanics and Design - First Canadian Edition, Toronto: Pearson Education Canada Inc., 2000.

[11] A. Muttoni, "Punching shear strength of reinforced concrete slabs without transverse reinforcement," *ACI Structural Journal,* vol. 105, no. 4, pp. 440-450, 2008.

[12] N. J. Gardner, "Verification of punching shear provisions for reinforced concrete flat slabs," *ACI Structural Journal,* vol. 108, no. 5, pp. 572-580, 2011.

[13] N. Gardner, J. Huh and L. Chung, "Lessons from the Sampoong department store collapse," *Cement and Concrete Composites,* vol. 24, no. 6, pp. 523-529, 2002.

[14] I. Robertson and G. Johnson, "Cyclic Lateral Loading of Nonductile Slab-Column Connections," *ACI Structural Journal,* vol. 103, no. 3, pp. 356-364, 2006.

[15] A. D. Pan and J. P. Moehle, "An Experimental Study of Slab-Column Connections," *ACI Structural Journal,* vol. 89, no. 6, pp. 626-638, 1992.

[16] S. Megally and A. Ghali, "Design Considerations for Slab-Column Connections in Seismic Zones," *ACI Structural Journal,* vol. 91, no. 3, pp. 303-314, 1994.

[17] S. Megally and A. Ghali, "Punching Shear Design of Earthquake Resistant Slab-Column Connections," *ACI Structural Journal,* vol. 97, no. 5, pp. 720-730, 2000.

[18] T. H.-K. Kang and J. W. Wallace, "Dynamic Responses of Flat Plate Systems with Shear Reinforcement," *ACI Structural Journal,* vol. 102, no. 5, pp. 763-773, 2005.

[19] T. H. Kang and J. W. Wallace, "Seismic Performance of Reinforced Concrete Slab-Column Connections with Thin Plate Stirrups," *ACI Structural Journal,* vol. 105, no. 5, pp. 617-625, 2008.

[20] M.-Y. Cheng and G. J. Parra-Montesinos, "Evaluation of Steel Fiber Reinforcement for Punching Shear Resistance in Slab-Column Connections—Part II: Lateral Displacement Reversals," *ACI Structural Journal,* vol. 107, no. 1, pp. 110-118, 2010.

[21] A. Ghali and R. B. Gayed, "Lateral Stiffness of Flat-Plate Buildings: Punching Shear Consideration," *Canadian Journal of Civil Engineering,* vol. 39, no. 5, pp. 536-545, 2012.

[22] E. M. Matzke, R. D. Lequesne, G. J. Parra-Montesinos and C. K. Shield, "Behavior of Biaxially Loaded Slab-Column Connections with Shear Studs," *ACI Structural Journal,* vol. 112, no. 3, pp. 335-346, 2015.

[23] I.-S. Drakatos, A. Muttoni and K. Beyer, "Mechanical Model for Drift-Induced Punching of Slab Column Connections without Transverse Reinforcement," *ACI Structural Journal,* vol. 115, no. 2, pp. 463-474, 2018.

[24] D. Topuzi, M. A. Polak and S. Narasimhan, "A New Technique for the Seismic Retrofit of Slab-Column Connections," *ACI Structural Journal,* vol. 114, no. 6, pp. 1471-1481, 2017.

[25] A. S. Genikomsou and M. A. Polak, "Finite element analysis of punching shear of concrete slabs using damaged plasticity model in ABAQUS," *Engineering Structures,* vol. 98, pp. 38-48, 2015.

[26] J. Shu, B. Belletti, A. Muttoni, M. Scolari and M. Plos, "Internal force distribution in RC slabs subjected to punching shear," *Engineering Structures,* vol. 153, pp. 766-781, 2017.

[27] M. Plos, J. Shu, K. Zandi and K. Lundgren, "A multi-level structural assessment strategy for reinforced concrete bridge deck slabs," *Structure and Infrastructure Engineering,* vol. 13, no. 2, pp. 223-241, 2017.

[28] Y.-C. Chang, "Slabs in Shear Wall Buildings," Master's Thesis, University of Toronto, Toronto, Ontario, Canada, 1969.

[29] C. M. Szalwinski, "Inter-Connecting Slabs in Shear Wall Structures," Master's Thesis, University of Toronto, Toronto, Ontario, Canada, 1976.

[30] J. Schwaighofer and M. P. Collins, "Experimental Study of the Behaviour of Reinforced Concrete Coupling Slabs," *Journal Proceedings,* vol. 74, no. 3, pp. 123-127, 1977.

[31] T. Paulay and R. Taylor, "Slab Coupling of Earthquake-Resisting Shearwalls," *Journal Proceedings,* vol. 78, no. 2, pp. 130-140, 1981.

[32] A. Coull and W. Y. Chee, "Design of Floor Slabs Coupling Shear Walls," *Journal of Structural Engineering,* vol. 109, no. 1, pp. 109-125, 1983.

[33] M. S. Mirza and A. K. Lim, "Behaviour and design of coupled slab – structural wall systems," *Canadian Journal of Civil Engineering,* vol. 17, no. 5, pp. 705-723, 1990.

[34] European Committee for Standardization, EN 1992-1-1 (2004) (English): Eurocode 2: Design of Concrete Structures - Part 1-1: General Rules and Rules for Buildings, Brussels, Belgium , 2004.

[35] fédération internationale du béton (fib), fib Model Code for Concrete Structures 2010, Lausanne, Switzerland, 2013.

[36] Canadian Standards Association (CSA Group), CSA A23.3:19 Design of Concrete Structures, Toronto, Ontario: CSA Group, 2019.

[37] FIB, fib Bulletin 52: Structural Concrete Textbook on behaviour, design and performance, 2 ed., vol. 2, Lausanne, Switzerland: International federation for structural concrete (fib), 2010.

[38] P. Regan and M. Braestrup, Punching Shear in Reinforced Concrete - Bulletin D'Information 168, Lausanne: Comite Euro International Du Beton, 1985.

[39] S. D. Alexander and S. H. Simmonds, "Ultimate Strength of Slab-Column Connections," *ACI Structural Journal*, vol. 84, no. 3, pp. 255-261, 1987.

[40] D. Theodorakopoulos and R. Swamy, "Ultimate punching shear strength analysis of slab-column connections," *Cement and Concrete Composites*, vol. 24, no. 6, pp. 509-521, 2002.

[41] R. Park and W. Gamble, Reinforced Concrete slabs, Toronto: John Wiley & Sons Inc., 1980.

[42] E. Anggadjaja and S. Teng, "Edge-Column Slab Connections under Gravity and Lateral Loading," *ACI Structural Journal*, vol. 105, no. 5, pp. 541-551, 2008.

[43] J. Moe, Shearing strength of reinforced concrete slabs and footings under concentrated loads, Skokie, Illinois: Portland Cement Association, 1961.

[44] C. E. Ospina, G. Birkle, Y. W. Widianto, S. R. Fernando, S. Fernando, A. C. Catlin and S. Pujol, "NEES: ACI 445 Punching Shear Collected Databank," 2015.

[45] O. S. Paiva, M. P. Ferreira, D. C. Oliveira, A. F. Lima Neto and M. R. Teixeira, "Influence of the column rectangularity index and of the boundary conditions in the punching resistance of slab-column connections," *Ibracon Structures and Materials Journal*, vol. 8, no. 3, pp. 260-295, 2015.

[46] W. Zhang, J. Xue, J. Xu, X. Xi, B. Li and K. Liu, "Yield-Line solutions for flexural failure of flat slabs on columns of different shapes," *Structures*, vol. 40, pp. 936-945, 2022.

[47] R. C. Elstner and E. Hognestad, "Shearing Strength of Reinforced Concrete Slabs," *Journal Proceedings*, vol. 53, no. 7, pp. 29-58, 1956.

[48] R. D. Mowrer and M. D. Vanderbilt, "Shear strength of lightweight aggregate reinforced concrete flat plates," *Journal Proceedings*, vol. 64, no. 11, pp. 722-729, 1967.

[49] P. E. Regan, "Symmetric punching of reinforced concrete slabs," *Magazine of Concrete Research*, vol. 38, no. 136, pp. 115-128, 1986.

[50] ASCE-ACI Committee 426, "The shear strength of reinforced concrete members - slabs," *Journal of the Structural Divison*, vol. 100, no. 8, pp. 1543-1591, 1974.

[51] ACI Committee 318, Building Code Requirements for Reinforced Concrete (ACI 318-63), Detroit, Michigan: American Concrete Institute, 1963.

[52] M. D. Vanderbilt, "Shear Strength of Continuous Plates," *Journal of the Structural Division*, vol. 98, no. 5, pp. 961-973, 1972.

[53] Comité Euro-International Du Béton, "CEB-FIP Model Code for Concrete Structures," in *Bulletin D'Information N. 124/125-E*, vol. II, Paris, Comité Euro-International Du Béton, 1978.

[54] ACI Committee 318, Building Code Requirements for Reinforced Concrete (ACI 318-83), Detroit, Michigan: American Concrete Institute, 1983.

[55] T. Yamada, A. Nanni and K. Endo, "Punching Shear Resistance of Flat Slabs: Influence of Reinforcement Type and Ratio," *ACI Structural Journal,* vol. 88, no. 4, pp. 555-563, 1992.

[56] S. Guandalini, O. L. Burdet and A. Muttoni, "Punching Tests of Slabs with Low Reinforcement Ratios," *ACI Structural Journal,* vol. 106, no. 1, pp. 87-95, 2009.

[57] J. Sagaseta, A. Muttoni, M. Fernández Ruiz and L. Tassinari, "Non-axis-symmetrical punching shear around internal columns of RC slabs without transverse reinforcement," *Magazine of Concrete Research,* vol. 63, no. 6, pp. 441-457, 2011.

[58] S. Lips, M. Fernández Ruiz and A. Muttoni, "Experimental investigation on punching strength and deformation capacity of shear-reinforced slabs," *ACI Structural Journal,* vol. 109, no. 6, pp. 889-900, 2012.

[59] J. Einpaul, J. Bujnak, M. Fenández Ruiz and A. Muttoni, "Study on influence of column size and slab slenderness on punching strength," *ACI Structural Journal,* vol. 113, no. 1, pp. 135-146, 2016.

[60] H. Marzouk and A. Hussein, "Punching shear analysis of reinforced high-strength concrete slabs," *Canadian Journal of Civil Engineering,* vol. 18, no. 6, pp. 594-963, 1991.

[61] B. Adetifa and M. Polak, "Retrofit of Interior Slab connections for punching using shear bolts," *ACI Structural Journal,* vol. 102, no. 2, pp. 268-274, 2005.

[62] G. Birkle and W. H. Dilger, "Influence of Slab Thickness on Punching Shear Strength," *ACI Structural Journal,* vol. 105, no. 2, pp. 180-188, 2008.

[63] A. J. Alam, K. M. Amanat and S. M. Seraj, "An Experimental Study on Punching Shear Behavior of Concrete Slabs," *Advances in Structural Engineering,* vol. 12, no. 2, pp. 257-265, 2009.

[64] C. L. Moreno and A. M. Sarmento, "Punching shear analysis of slab-column connections," *Engineering Computations,* vol. 30, no. 6, pp. 802-814, 2013.

[65] M. M. Inácio, A. F. Almeida, D. M. Faria, V. J. Lúcio and A. P. Ramos, "Punching of high strength concrete flat slabs without shear reinforcement," *Engineering Structures,* vol. 103, pp. 275-284, 2015.

[66] R. Vaz Rodrigues, "Shear Strength of Reinforced Concrete Bridge Deck Slabs," Lausanne, Switzerland, 2007.

[67] R. Vaz Rodrigues, M. Fernández Ruiz and A. Muttoni, "Shear strength of R/C bridge cantilever slabs," *Engineering Structures,* vol. 30, no. 11, pp. 3024-3033, 2008.

[68] N. J. Gardner and X.-y. Shao, "Punching Shear of Continuous Flat Reinforced Concrete Slabs," *ACI Structural Journal,* vol. 96, no. 2, pp. 218-228, 1996.

[69] D. R. Fick, M. A. Sozen and M. E. Kreger, "Cyclic Lateral Load Test and the Estimation of Elastic Drift Response of a Full-Scale Three-Story Flat-Plate Structure," *Symposium Paper,* vol. 296, pp. 1-14, 2014.

[70] D. R. Fick, M. A. Sozen and M. E. Kreger, "Response of Full-Scale Three-Story Flat-Plate Test Structure to Cycles of Increasing Lateral Load," *ACI Structural Journal,* vol. 114, no. 6, pp. 1507-1517, 2017.

[71] D. Coronelli, M. L. Tornaghi, L. Martinelli, M. Molina, A. Muttoni, I. R. Pascu, P. Pegon, M. Peroni, A. P. Ramos, G. Tsionis and T. Netti, "Testing of a full-scale flat slab building for gravity and lateral loads," *Engineering Structures,* vol. 243, p. 112551, 2021.

[72] J. Hegger, M. Ricker and A. G. Sherif, "Punching Strength of Reinforced Concrete Footings," *ACI Structural Journal,* vol. 106, no. 5, pp. 706-716, 2009.

[73] C. Siburg and J. Hegger, "Experimental Investigations on the Punching Behaviour of Reinforced Concrete Footings With Structural Dimensions," *Structural Concrete,* vol. 15, no. 3, pp. 331-339, 2014.

[74] S.-M. Kang, S.-J. Na and H.-J. Hwang, "Two-way Shear Strength of Reinforced Concrete Transfer Slab-Column Connections," *Engineering Structures,* vol. 231, p. 111693, 2021.

[75] E. Rizk, H. Marzouk and A. Hussein, "Punching Shear of Thick Plates with and Without Shear Reinforcement," *ACI Structural Journal,* vol. 108, no. 5, pp. 581-591, 2011.

[76] Z. P. Bažant and A. Dönmez, "Size Effect on Punching Shear Strength of RC Slabs With and Without Shear Reinforcement," *ACI Symposium Publication,* vol. 315, pp. 23-34, 2017.

[77] A. Dönmez and Z. P. Bažant, "Size Effect on Punching Strength of Reinforced Concrete Slabs with and Without Shear Reinforcement," *ACI Structural Journal,* vol. 114, no. 4, pp. 875-886, 2017.

[78] N. M. Hawkins and C. E. Ospina, "Effect of Slab Flexural Reinforcement and Depth on Punching Strength," *ACI Symposium Publication,* vol. 315, pp. 117-140, 2017.

[79] M. F. Ruiz and A. Muttoni, "Size Effect on Punching Shear Strength: Differences and Analogies With Shear in One-Way Slabs," *Symposium Paper,* vol. 315, pp. 59-72, 2017.

[80] M. F. Ruiz and A. Muttoni, "Size Effect in Shear and Punching Shear Failures of Concrete Members Without Transverse Reinforcement: Differences Between Statically Determinate Members and Redundant Structures," *Structural Concrete,* vol. 19, no. 1, pp. 65-75, 2018.

[81] D. W. Menna and A. S. Genikomsou, "Punching Shear Response of Concrete Slabs Strengthened with Ultrahigh-Performance Fiber-Reinforced Concrete Using Finite-Element Methods," *Practice Periodical on Structural Design and Construction,* vol. 26, no. 1, p. 04020057, 2021.

[82] A. M. de Sousa, E. O. Lantsoght, A. S. Genikomsou, P. A. Krahl and M. K. El Debs, "Behavior and punching capacity of flat slabs with the rational use of UHPFRC: NLFEA and analytical predictions," *Engineering Structures,* vol. 244, p. 112774, 2021.

[83] A. Sine, M. Pimentel and S. Nunes, "Experimental Investigation on punching shear behaviour of RC-(R)UHPFRC composite flat slabs without transverse reinforcement," *Engineering Structures,* vol. 255, p. 113951, 2022.

[84] ACI Committee 318, Building Code Requirements for Structural Concrete (ACI 318M-14) and Commentary (ACI 318RM-14), Farmington Hills, MI: American Concrete Institute, 2014.

[85] S. Teng, K. Chanthabouala, D. T. Lim and R. Hidayat, "Punching Shear Strength of Slabs and Influence of Low Reinforcement Ratio," *ACI Structural Journal,* vol. 115, no. 1, pp. 139-150, 2018.

[86] T. Stein, A. Ghali and W. Dilger, "Distinction between Punching and Flexural Failure Modes of Flat Plates," *ACI Structural Journal,* vol. 104, no. 3, pp. 357-365, 2007.

[87] E. Rizk, H. Marzouk, A. Hussein and M. Hossin, "Effect of reinforcement ratio on punching capacity of RC plates," *Canadian Journal of Civil Engineering,* vol. 38, no. 7, pp. 729-740, 2011.

[88] T. X. Dam and J. K. Wight, "Flexurally-triggered punching shear failure of reinforced concrete slab–column connections reinforced with headed shear studs arranged in orthogonal and radial layouts," *Engineering Structures,* vol. 110, pp. 258-268, 2016.

[89] T. X. Dam, J. K. Wight and G. J. Parra-Montesinos, "Behavior of Monotonically Loaded Slab-Column Connections Reinforced with Shear Studs," *ACI Structural Journal,* vol. 114, no. 1, pp. 221-232, 2017.

[90] R. B. Gayed, C. Peiris and A. Ghali, "Flexure Induced Punching of Concrete Flat Plates," *ACI Symposium Publication,* vol. 315, pp. 73-99, 2017.

[91] A. Ghali and R. B. Gayed, "Universal Design for Punching Resistance of Concrete Slabs," *ACI Structural Journal,* vol. 116, no. 1, pp. 207-212, 2019.

[92] A. Torabian, B. Isufi, D. Mostofinejad and A. P. Ramos, "Behavior of thin lightly reinforced flat slabs under concentric loading," *Engineering Structures,* vol. 196, p. 109327, 2019.

[93] N. W. Hawkins and W. Corley, "Moment Transfer to Columns in Slabs with Shearhead Reinforcement," *ACI Symposium Publication,* vol. 42, pp. 847-880, 1974.

[94] S. Islam and R. Park, "Tests on Slab-Column Connections with Shear and Unbalanced Flexure," *Journal of the Structural Division,* vol. 102, no. 3, pp. 549-568, 1976.

[95] R. K. S. Al-Hamd, M. Gille, L. S. Cunningham, H. Warren and A. S. Albostami, "Novel shearhead reinforcement for slab-column connections subject to eccentic load and fire," *Archives of Civil and Mechanical Engineering,* vol. 19, no. 2, pp. 503-524, 2019.

[96] A. Pan and J. P. Moehle, "Lateral Displacement Ductility of Reinforced Concrete Flat Plates," *ACI Structural Journal,* vol. 86, no. 3, pp. 250-258, 1989.

[97] A. F. Almeida, M. M. Inácio, V. J. Lúcio and A. P. Ramos, "Punching behaviour of RC flat slabs under reversed horizontal cyclic loading," *Engineering Structures,* vol. 117, pp. 204-219, 2016.

[98] A. Setiawan, R. L. Vollum and L. Macorini, "Numerical and analytical investigation of internal slab-column connections subject to cyclic loading," *Engineering Structures,* vol. 184, pp. 535-554, 2019.

[99] C. Rha, T. H. Kang, M. Shin and J. Bae Yoon, "Gravity and Lateral Load Carrying Capacities of Reinforced Concrete Flat Plates Systems," *ACI Structural Journal,* vol. 111, no. 4, pp. 753-764, 2014.

[100] International Code Council, Internation Building Code 2006, Country Club Hills, IL 60478-5795: International Code Council, 2006.

[101] Joint ACI-ASCE Committee 421, ACI 421.2R-10 Guide to Seismic Design of Punching Shear Reinforcement in Flat Plates, Farmington Hills, MI: American Concrete Institute, 2010.

[102] A. Ghali, W. Dilger and R. B. Gayed, "Punching of Concrete Slabs: Interpretation of Test Results," *Journal of Structural Engineering,* vol. 139, no. 6, pp. 869-874, 2013.

[103] M. A. Sözen, "Review of Earthquake Response of R.C. Buildings With a View to Drift Control," *State-of-the-art in Earthquake Engineering 1981 - 7th World Conference on Earthquake Engineering, Istanbul Turkey,* pp. 383-418, 1981.

[104] Joint ACI-ASCE Committee 352, ACI 352.1R-11 Guide for Design of Slab-Column Connections in Monolithic Concrete Structures, Farmington Hills, MI: American Concrete Institute, 2012.

[105] M. B. D. Hueste and J. K. Wight, "Nonlinear Punching Shear Failure Model for Interior Slab-Column Connections," *Journal of Structural Engineering,* vol. 125, no. 9, pp. 997-1008, 1999.

[106] C. E. Broms, "Design Method for Imposed Rotations of Interior Slab-Column Connections," *ACI Structural Journal,* vol. 106, no. 5, pp. 636-645, 2009.

[107] I. S. Drakatos, "Seismic behaviour of slab-column connections without," Lausanne, Switzerland, 2016.

[108] L. Secci, M. Lapi, E. Teoni, A. Pinho Ramos and M. Orlando, "Eccentric punching strength of continuous flat slabs—Analysis of different experimental setups," *Structural Concrete,* vol. 22, no. 2, pp. 1183-1204, 2021.

[109] J. Einpaul, R. L. Vollum and A. P. Ramos, "On the Distribution of Shear Forces in Non-axisymmetric Slab-Column Connections," in *In: Hordijk, D., Luković, M. (eds) High Tech Concrete: Where Technology and Engineering Meet*, 2018.

[110] Joint ACI-ASCE Committee 421, ACI 421.3R-15 Guide to Design of Reinforced Two-Way Slab Systems, Farmington Hills, MI: American Concrete Institute, 2015.

[111] S. Megally and A. Ghali, "Seismic behavior of slab–column connections," *Canadian Journal of Civil Engineering,* vol. 27, no. 1, pp. 84-100, 2000.

[112] S. Megally and A. Ghali, "Cautionary Note on Shear Capitals," *Concrete International,* vol. 24, no. 3, pp. 75-82, 2002.

[113] A. J. Durrani and E. H. Wey, "Seismic Response of Interior Slab-Column Connections with Shear Capitals," *ACI Structural Journal,* vol. 89, no. 6, pp. 682-691, 1992.

[114] W. G. Corley and N. M. Hawkins, "Shearhead Reinforcement for Slabs," *Journal Proceedings,* vol. 65, no. 10, pp. 811-824, 1968.

[115] A. Ghali and N. Hammill, "Effectiveness of Shear Reinforcement in Slabs," *Concrete International,* vol. 14, no. 1, pp. 60-65, 1992.

[116] D. R. Oliveira, G. S. Melo and P. E. Regan, "Punching Strengths of Flat Plates with Vertical or Inclined Stirrups," *ACI Structural Journal,* vol. 97, no. 3, pp. 485-491, 2000.

[117] R. T. Mabrouk, A. Bakr and H. Abdalla, "Effect of flexural and shear reinforcement on the punching behavior of reinforced concrete flat slabs," *Alexandria Engineering Journal,* vol. 56, no. 4, pp. 591-599, 2017.

[118] H. Lima, R. Palhares, G. S. de Melo and M. Oliveira, "Experimental analysis of punching shear in flat slabs with variation in the anchorage of shear reinforcement," *Structural Concrete,* vol. 22, no. 2, pp. 1165-1182, 2020.

[119] i. H. D. de Oliveira, H. J. N. de Lima and G. S. Melo, "Punching shear resistance of flat slabs with different types of stirrup anchorages such as shear reinforcement," *Engineering Structures,* vol. 253, p. 113671, 2022.

[120] N. M. Hawkins, D. Mitchell and S. N. Hanna, "The Effects of Sher Reinforcement on the Reversed Cyclic Loading Behaviour of Flat Plate Structures," *Canadian Journal of Civil Engineering,* vol. 2, no. 4, pp. 575-582, 1975.

[121] I. N. Robertson, T. Kawai, J. Lee and B. Enomoto, "Cyclic Testing of Slab-Column Connections With Shear Reinforcement," *ACI Structural Journal,* vol. 99, no. 5, pp. 605-613, 2002.

[122] J. Hegger, A. G. Sherif, D. Kueres and C. Siburg, "Efficiency of Various Punching Shear Reinforcement Systems for Flat Slabs," *ACI Structural Journal,* vol. 114, no. 3, pp. 631-642, 2017.

[123] S.-M. Kang, H.-G. Park and Y.-N. Kim, "Lattice-Reinforced Slab-Column Connections Under Cyclic Lateral Loading," *ACI Structural Journal,* vol. 110, no. 6, pp. 929-940, 2013.

[124] K. Pilakoutas and X. Li, "Alternative Shear Reinforcement for Reinforced Concrete Flat Slabs," *Journal of Structural Engineering,* vol. 129, no. 9, pp. 1164-1172, 2003.

[125] J.-K. Song, J. Kim, H.-B. Song and J.-W. Song, "Effecting Punching Shear and Moment Capacity of Flat Plate Column Connections With Shear Reinforcements for Lateral Loading," *International Journal of Concrete Structures and Materials,* vol. 6, no. 1, pp. 19-29, 2012.

[126] M. P. Ferreira, M. J. Pereira Filho, M. V. Freitas, A. F. Lima Neto and G. S. Melo, "Experimental resistance of slab-column connections with prefabricated truss bars as punching shear reinforcement," *Engineering Structures,* vol. 233, p. 111903, 2021.

[127] N. Lawler and M. A. Polak, "Development of FRP Shear Bolts for Punching Shear Retrofit of Reinforced Concrete Slabs," *Journal of Composites for Construction,* vol. 15, no. 4, pp. 591-601, 2011.

[128] E. F. El-Salakawy, M. A. Polak and K. A. Soudki, "New Shear Strengthening Technique for Concrete Slab-Column Connections," *ACI Structural Journal,* vol. 100, no. 3, pp. 297-304, 2003.

[129] W. Bu and M. A. Polak, "Seismic Retrofit of Reinforced Concrete Slab-Column Connections Using Shear Bolts," *ACI Structural Journal,* vol. 106, no. 4, pp. 514-522, 2009.

[130] A. F. V. D. Voet, W. H. Dilger and A. Ghali, "Concrete flat plates with well-anchored shear reinforcement elements," *Canadian Journal of Civil Engineering,* vol. 9, no. 1, pp. 107-114, 1982.

[131] H. Guan and Y.-C. Loo, "Failure analysis of column–slab connections with stud shear reinforce," *Canadian Journal of Civil Engineering,* vol. 30, no. 5, pp. 934-944, 2003.

[132] D. I. Mclean, L. T. Phan, H. Hew and R. N. White, "Punching Shear Behavior of Lightweight Concrete Slabs and Shells," *ACI Structural Journal,* vol. 87, no. 4, pp. 386-392, 1990.

[133] M. P. Ferreira, G. S. Melo, P. E. Regan and R. L. Vollum, "Punching of Reinforced Concrete Flat Slabs with Double Headed Shear Reinforcement," *ACI Structural Journal,* vol. 111, no. 2, pp. 363-374, 2014.

[134] M. de Pina Ferreira, M. H. Oliveira and G. S. S. Melo, "Tests on the punching resistance of flat slabs with unbalanced moments," *Engineering Structures,* vol. 196, p. 109311, 2019.

[135] G. E. Polo, O. Bayrak and T. D. Hrynyk, "Shear-Resisting Performance of Reinforced Concrete Flat Plates with Different Headed Stud Layouts," *ACI Structural Journal,* vol. 118, no. 1, pp. 5-16, 2021.

[136] A.-S. Mokhtar, A. Ghali and W. Dilger, "Stud Shear Reinforcement for Flat Concrete Plates," *Journal Proceedings,* vol. 82, no. 5, pp. 676-683, 1985.

[137] A. A. Elgabry and A. Ghali, "Tests on Concrete Slab-Column Connections with Stud-Shear Reinforcement Subjected to Shear-Moment Transfer," *ACI Structural Journal,* vol. 84, no. 5, pp. 433-442, 1987.

[138] B. Isufi, A. P. Ramos and V. Lúcio, "Reversed horizontal cyclic loading tests of flat slab specimens with studs as shear reinforcement," *Structural Concrete,* vol. 20, no. 1, pp. 330-347, 2019.

[139] J. D. Mortin and A. Ghali, "Connection of Flat Plates to Edge Columns," *ACI Structural Journal,* vol. 88, no. 2, pp. 191-198, 1991.

[140] F. K. Lim and B. Vijaya Rangan, "Studies on Concrete Slabs with Stud Shear Reinforcement in Vicinity of Edge and Corner Columns," *ACI Structural Journal,* vol. 92, no. 5, pp. 515-525, 1995.

[141] S. Megally and A. Ghali, "Seismic Behavior of Edge Column-Slab Connections with Stud Shear Reinforcement," *ACI Structural Journal,* vol. 97, no. 1, pp. 53-60, 2000.

[142] M. Husain, A. S. Eisa and R. Roshdy, "Alternative to Enhance Flat Slab Ductility," *International Journal of Concrete Structures and Materials,* vol. 11, no. 1, pp. 161-169, 2017.

[143] A. A. Elgabry and A. Ghali, "Design of Stud-Shear Reinforcement For Slabs," *ACI Structural Journal,* vol. 87, no. 3, pp. 350-361, 1990.

[144] N. W. Hanson and J. M. Hanson, "Shear and Moment Transfer Between Concrete Slabs and Columns," *Journal of the PCA Research and Development Laboratories,* vol. 10, no. 1, pp. 2-16, 1968.

[145] G. J. Milligan, M. A. Polak and C. Zurell, "Finite Element Analysis of Punching Shear Behaviour of Concrete Slabs Supported on Rectangular Columns," *Engineering Structures,* vol. 224, p. 111189, 2020.

[146] D. R. Oliveira, P. E. Regan and G. S. Melo, "Punching resistance of RC slabs with rectangular columns," *Magazine of Concrete Research,* vol. 56, no. 3, pp. 123-138, 2004.

[147] S. Teng, H. K. Cheong, K. L. Kuang and J. Z. Geng, "Punching Shear Strength of Slabs with Openings and Supported on Rectangular Columns," *ACI Structural Journal,* vol. 101, no. 5, pp. 678-687, 2004.

[148] H. Erdogan, B. Binici and G. Ozcebe, "Effect of column rectangularity on CFRP-strengthened RC flat plates," *Magazine of Concrete Research*, vol. 63, no. 7, pp. 511-525, 2011.

[149] V. Alves, L. Oliveira, A. Santos and L. Trautwein, "Experimental Evaluation of the Load Carrying Capacity of SFRC Flat Slabs Varying the Rectangularity Index of Columns," *KSCE Journal of Civil Engineering*, vol. 25, no. 2, pp. 574-585, 2021.

[150] A. T. Al-Yousif and P. E. Regan, "Punching Resistance of RC slabs supported by large/or elongated columns," *Structural Engineer*, vol. 81, no. 5, pp. 30-34, 2003.

[151] J. Sagaseta, L. Tassinari, M. Fernández Ruiz and A. Muttoni, "Punching of flat slabs supported on rectangular columns," *Engineering Structures*, vol. 77, pp. 17-33, 2014.

[152] T.-S. Eom, J.-W. Song, J.-K. Song, G.-S. Kang, J.-K. Yoon and S.-M. Kang, "Punching-shear behavior of slabs with bar truss shear reinforcement on rectangular columns," *Engineering Structures*, vol. 134, pp. 390-399, 2017.

[153] F. Habibi, E. Redl, M. Egberts, W. D. Cook and D. Mitchell, "Assessment of CSA A23.3 structural integrity requirements for two-way slabs," *Canadian Journal of Civil Engineering*, vol. 39, no. 4, pp. 351-361, 2012.

[154] V. Filatov and E. Bubnov, "Experimental Investigation of the Deformability of Reinforced Concrete Slabs under Punching," in *MATEC Web of Conferences*, 2016.

[155] P. E. Regan and H. Rezai-Jorabi, "Shear Resistance of One-Way Slabs under Concentrated Loads," *ACI Structural Journal*, vol. 85, no. 2, pp. 150-157, 1988.

[156] S. H. Simmonds, "Flat Slabs Supported On Columns Elongated in Plan," *Journal Proceedings*, vol. 67, no. 12, pp. 967-976, 1970.

[157] G. A. Hartley and M. F. El Kafrawy, "Elongated columns and column offsets in reinforced concrete building frames," *Canadian Journal of Civil Engineering*, vol. 11, no. 1, pp. 8-18, 1984.

[158] A. Setiawan, R. L. Vollum, L. Macorini and B. A. Izzuddin, "Punching of RC slabs without transverse reinforcement supported on elongated columns," *Structures*, vol. 27, pp. 2048-2068, 2020.

[159] Comité Euro-International du Béton, CEB-FIP Model Code 1990: Design Code, London: Thomas Telford, 1993.

[160] G. J. Milligan and M. A. Polak, "Finite Element Investigation on the Effect of Column Rectangularity on Punching Shear Strength of Concrete Slabs, The International Federation for Structural Concrete," *fib Congress, Melbourne,* p. 12 pages, 2018.

[161] G. J. Milligan, M. A. Polak and C. Zurell, "Impact of Column Rectangularity on Punching Shear Strength - Code Predictions Versus FEA," *Journal of Structural Engineering,* vol. 147, no. 2, p. 04020331, 2021.

[162] S. Sarvaicova, V. Borzovic and T. Augustin, "The influence of a column shape cross-section on the punching capacity," *Proceedings of the 13th International conference "Modern Building Materials, Structures and Techniques (MBMST 2019),* pp. 455-462, 2019.

[163] N. M. Hawkins, A. Bao and J. Yamazaki, "Moment Transfer from Concrete Slabs to Columns," *ACI Structural Journal,* vol. 86, no. 6, pp. 705-716, 1989.

[164] W. Dilger, "Flat slab-column connections," *Progress in Structural Engineering and Materials,* vol. 2, no. 3, pp. 386-399, 2000.

[165] A. G. Sherif, M. B. Emara, A. H. Ibrahim and S. A. Magd, "Effect of the Column Dimensions on the Punching Shear Strength of Edge Column-Slab Connections," *ACI Special Publication 232* , pp. 175-192, 2005.

[166] S. Megally and A. Ghali, "Punching of Concrete Slabs Due to Column Moment Transfer," *Journal of Structural Engineering,* vol. 126, no. 2, pp. 180-189, 2000.

[167] Y. Tan and S. Teng, "Interior Slab-Rectangular Column Connections Under Biaxial Lateral Loadings," *ACI Symposium Publication,* vol. 232, pp. 147-174, 2005.

[168] A. Himawan and S. Teng, "Cyclic Behaviour of Post-Tensioned Slab-Rectangular Column Connections," *ACI Structural Journal,* vol. 111, no. 1, pp. 177-188, 2014.

[169] ACI Committee 318, Commentary on Building Code Requirements for Reinforced Concrete (ACI 318-77), Detroit, Michigan: American Concrete Institute, 1977.

[170] ACI Committee 318, Building Code Requirements for Reinforced Concrete (ACI 318-77), Detroit, Michigan: American Concrete Institute, 1977.

[171] W. Liu and C. Huang, "Experimental investigation on punching shear behaviour of concrete slab-nonrectangular column connections," *Journal of Building Structures,* vol. 25, no. 4, pp. 26-33, 2004.

[172] J. Cai, G. Li, C. Yang and F. Lin, "Tests on Unbonded Post-Tensioned Concrete Flat Plate with T-shaped Column Connections," *Advances in Structural Engineering,* vol. 9, no. 5, pp. 671-685, 2006.

[173] Z. A. Abou-Saleh, "Punching Shear Strength of Post-Tensioned Concrete Flat Plates With L-Shaped Columns," Master's Thesis, University of Miami, Coral Gables, Florida, 2007.

[174] V. C. Pinto, V. Branco and D. R. Oliveira, "Punching in two-way RC flat slabs with openings and L section columns," *Engineering Computations,* vol. 36, no. 7, pp. 2430-2444, 2019.

[175] J. Xue, W. Zhang, J. Xu, Z. Yuan, F. Zhao and C. Zhang, "Investigation of the punching shear behaviors of reinforced concrete slab–steel reinforced concrete L-shaped column connections," *Advances in Structural Engineering,* vol. Forthcoming, 2022.

[176] Z.-j. Wang, W.-q. Liu, J. Wang, Y.-s. Jing and C. Xu, "Shaking table test for a mid-highrise big-bay RC frame model," *Earthquake Engineering and Engineering Vibration,* vol. 19, no. 3, pp. 59-64, 1999.

[177] ACI Committee 318, Building Code Requirements For Structural Concrete (ACI 318-95) and Commentary (ACI 318R-95), Farmington Hills, MI: American Concrete Institute, 1995.

[178] I. N. Robertson, "Analysis of Flat Slab Structures Subjected to Combined Lateral and Gravity Loads," *ACI Structural Journal,* vol. 94, no. 6, pp. 723-729, 1997.

[179] Y. M. Park, S. W. Han and Y. H. Rew, "Stiffness reduction factor for post-tensioned flat plate slabs," *Magazine of Concrete Research,* vol. 64, no. 1, pp. 83-92, 2012.

[180] K. S. Kim, S.-H. Choi, H. Ju, D. H. Lee, J.-Y. Lee and M. Shin, "Unified equivalent frame method for flat plate slab structures under combined gravity and lateral loads – Part 1: derivation," *Earthquakes and Structures,* vol. 7, no. 5, pp. 719-733, 2014.

[181] S. Pantazopoulou and I. Imran, "Slab-Wall Connections Under Lateral Forces," *ACI Structural Journal,* vol. 89, no. 5, pp. 515-527, 1992.

[182] H. Beck, "Contribution to the Analysis of Coupled Shear Walls," *Journal Proceedings,* vol. 59, no. 8, pp. 1055-1070, 1962.

[183] A. Coull and J. Choudhury, "Analysis of Coupled Shear Walls," *Journal Proceedings,* vol. 64, no. 9, pp. 587-593, 1967.

[184] D. C. Black, V. Pulmano and A. Kabaila, "Flat Plates Supported on Walls," *Memoires, International Association for Bridge and Structural Engineering, Swiss Federal Institute Of Technology, Zurich,* vol. 36, no. I, pp. 79-91, 1976.

[185] A. Coull and A. A. El Hag, "Effective Coupling of Shearwalls by Floor Slabs," *Journal Proceedings,* vol. 72, no. 8, pp. 429-431, 1975.

[186] A. Coull and Y. Wong, "Bending stiffness of floor slabs in cross-wall structures," *Proceedings of the Institution of Civil Engineers,* vol. 71, no. 1, pp. 17-35, 1981.

[187] A. Qadeer and B. S. Smith, "The Bending Stiffness of Slabs Connecting Shear WaIIs," *Journal Proceedings,* vol. 66, no. 6, pp. 464-473, 1969.

[188] L. Jaeger, A. Mufti and J. Mamet, "The structural analysis of tall buildings having irregularly positioned shear walls," *Building Science,* vol. 8, no. 1, pp. 11-22, 1973.

[189] A. Setiawan, R. L. Vollum, L. Macorini and B. A. Izzuddin, "Punching Shear Design of RC Flat Slabs Supported on Wall Corners," *Structural Concrete,* vol. 21, no. 3, pp. 859-874, 2020.

[190] H.-K. Choi, "Experimental Study on Shear Wall with Slab and Openings," *International Journal of Civil Engineering,* vol. 15, no. 4, pp. 451-471, 2017.

[191] E. Hognestad, R. C. Elstner and J. Hanson, "Sheer Strength of Reinforced Structural Lightweight Aggregate Concrete Slabs," *Journal Proceedings,* vol. 61, no. 6, pp. 643-656, 1964.

[192] F. Roll, S. Zaidi, G. Sabnis and K. Chuang, "Shear Resistance of Perforated Reinforced Concrete Slabs," *ACI Symposium Publication,* vol. 30, pp. 77-102, 1971.

[193] J. Di Stasio and M. P. Van Buren, "Transfer of Bending Moment Between Flat Plate Floor and Column," *Journal Proceedings,* vol. 57, no. 9, pp. 299-314, 1960.

[194] J. Di Stasio and M. P. Van Buren, "Landmark Series: Transfer of Bending Moment Between Flat Plate Floor and Column," *Concrete International,* vol. 25, no. 7, pp. 57-72, 2003.

[195] E. F. El-Salakawy, M. A. Polak and M. H. Soliman, "Reinforced concrete slab-column edge connections with shear studs," *Canadian Journal of Civil Engineering,* vol. 27, no. 2, pp. 338-348, 2000.

[196] H. Guan and M. A. Polak, "Finite element studies of reinforced concrete slab – edge column connections with openings," *Canadian Journal of Civil Engineering,* vol. 34, no. 8, pp. 952-965, 2007.

[197] H. Guan, "Prediction of Punching Shear Failure Behaviour of Slab-Edge Column Connections with Varying Opening and Column Parameters," *Advances in Structural Engineering,* vol. 12, no. 1, pp. 19-36, 2009.

[198] Ö. Anil, T. Kina and V. Salmani, "Effect of opening size and location on punching shear behaviour of two-way RC slabs," *Magazine of Concrete Research,* vol. 66, no. 18, pp. 955-966, 2014.

[199] T. Ha, M.-H. Lee, J. Park and D.-J. Kim, "Effects of openings on the punching shear strength of RC flat-plate slabs without shear reinforcement," *The Structural Design of Tall and Special Buildings,* vol. 24, no. 15, pp. 895-911, 2015.

[200] A. S. Genikomsou and M. A. Polak, "Effect of Openings on Punching Shear Strength of Reinforced Concrete Slabs—Finite Element Investigation," *ACI Structural Journal,* vol. 114, no. 5, pp. 1249-1262, 2017b.

[201] G. P. Balomenos, A. S. Genikomsou and M. A. Polak, "Investigation of the effect of openings of interior reinforced concrete flat slabs," *Structural Concrete,* vol. 19, no. 6, pp. 1672-1681, 2018.

[202] E. A. P. Liberati, M. G. Marques, E. D. Leonel, L. C. Almeida and L. M. Trautwein, "Failure analysis of punching in reinforced concrete flat slabs with openings adjacent to the column," *Engineering Structures,* vol. 182, pp. 331-343, 2019.

[203] A. M. Yousef, S. E. El-Metwally, H. H. Askar and M. A. El-Mandouh, "Behaviour of high-strength concrete interior slab-column connections with openings under seismic loading," *Construction and Building Materials,* vol. 214, pp. 619-630, 2019.

[204] S. Živković, M. Bešević, M. V. Purčar and L. Kozarić, "Nonlinear Finite Element Analysis of Punching Shear Strength of Eccentrically Loaded RC Flat Slabs with Opening," *KSCE Journal of Civil Engineering,* vol. 23, no. 11, pp. 4771-4780, 2019.

[205] Ö. Anıl and B. Ulusoy, "Nonlinear FEA of Two-Way RC Slabs' Punching Behaviour with Openings," *Iranian Journal of Science and Technology, Transactions of Civil Engineering,* vol. 44, no. 4, pp. 1109-1124, 2020.

[206] T. Augustin, L. Fillo and J. Halvonik, "Punching resistance of slab-column connections with openings," *Structural Concrete,* vol. 21, no. 1, pp. 278-290, 2020.

[207] M. G. Marques, E. A. P. Liberati, R. B. Gomes, L. C. Almeida and L. M. Trautwein, "Study of Failure Mode of Reinforced Concrete Flat Slabs with Openings and Studs," *ACI Structural Journal*, vol. 117, no. 4, pp. 39-48, 2020a.

[208] M. G. Marques, E. A. P. Liberati, M. J. Pimentel, R. A. de Souza and L. M. Trautwein, "Nonlinear finite element analysis (NLFEA) of reinforced concrete flat slabs with holes," *Structures*, vol. 27, pp. 1-11, 2020b.

[209] D. Mostofinejad, N. Jafarian, A. Naderi, A. Mostofinejad and S. Mohamad, "Effects of openings on the punching shear strength of reinforced concrete slabs," *Structures*, vol. 25, pp. 760-773, 2020.

[210] S. Bursać, M. Bešević, M. V. Purčar, L. Kozarić and N. Đurić, "Experimental analysis of punching shear strength of eccentrically loaded slab with the opening along the face of the internal column," *Engineering Structures*, vol. 249, p. 113359, 2021.

[211] D. d. S. Lourenço, E. A. P. Liberati, M. G. Marques, L. C. d. Almeida and L. M. Trautwein, "Reinforced concrete flat slabs with openings at different distances from the column," *IBRACON Structures and Materials Journal*, vol. 14, no. 1, 2021.

[212] M. G. Marques, E. A. P. Liberati, R. B. Gomes, A. L. Carvalho and L. M. Trautwein, "Punching Shear Strength Model for Reinforced Concrete Flat Slabs with Openings," *Journal of Structural Engineering*, vol. 147, no. 7, p. 04021090, 2021.

[213] N. T. Trung and P. T. Tung, "Investigation of the effects of opening size and location on punching shear resistance of flat slabs using Abaqus," *Journal of Science and Technology in Civil Engineering (STCE) - HUCE*, vol. 15, no. 4, pp. 136-147, 2021.

[214] E. Yooprasertchai, Y. Tiawilai, T. Wittayawanitchai, J. Angsumalee, P. Joyklad and Q. Hussain, "Effect of Shape, Number, and Location of Openings on Punching Shear Capacity of Flat Slabs," *Buildings*, vol. 11, no. 10, p. 484, 2021.

[215] T. Yılmaz, Ö. Anil and R. T. Erdem, "Experimental and numerical investigation of impact behaviour of RC slab with different opening size and layout," *Structures*, vol. 35, pp. 818-832, 2022.

[216] G. M. Mateus, A. J. Aguiar, M. P. Ferreira and D. R. C. Oliveira, "Two-way ribbed flat slabs with shafts," *Ibracon Structures and Materials Journal*, vol. 7, no. 4, pp. 572-591, 2014.

[217] M. Elsayed, B. A. Tayeh and D. Kamal, "Effect of crumb rubber on the punching shear behaviour of reinforced concrete slabs with openings," *Construction and Building Materials,* vol. 311, p. 125345, 2021.

[218] M. A. El-Mandouh and K. Abu el-hassan, "Cyclic behavior of high strength lightweight concrete slab-edge column connections with and without openings," *Case Studies in Construction Materials,* vol. 16, p. e00832, 2022.

[219] L. L. Borges, G. S. Melo and R. B. Gomes, "Punching shear of reinforced concrete flat plates with openings," *ACI Structural Journal,* vol. 110, no. 4, pp. 547-556, 2013.

[220] D. C. Oliveira, R. B. Gomes and G. S. Melo, "Punching shear in reinforced concrete flat slabs with hole adjacent to the column and moment transfer," *Ibracon Structures and Materials Journal,* vol. 7, no. 3, pp. 414-467, 2014.

[221] J. A. Silva, M. G. Marques, L. M. Trautwein, R. B. Gomes and G. N. Guimarães, "Punching of reinforced concrete flat slabs with holes and shear reinforcement," *REM-International Engineering Journal,* vol. 70, no. 4, pp. 407-413, 2017.

[222] A. Aguiar, D. Oliveria, L. Reis and A. Nzambi, "Punching shear strength of waffle flat slabs with openings adjacent to elongated columns," *Engineering Structures,* vol. 243, p. 112641, 2021.

[223] Ľ. Kormošová and J. Halvonik, "Behavior of the Experimental Flat Slab Specimen Supported by an Elongated Column," *Solid State Phenomena,* vol. 322, pp. 87-93, 2021.

[224] Ľ. Kormošová, T. Augustin and J. Halvonik, "Comparison of the Test Results on Flat Slabs Weakened by Openings with Punching Shear Capacities Assessed by the Model in the 2nd Generation of EC2," *Key Engineering Materials,* vol. 930, pp. 119-126, 2022.

[225] J. B. Santos, R. M. Souza, G. S. Melo and R. B. Gomes, "Punching Resistance of Flat Slabs With Openings Adjacent to the Columns," *ACI Structural Journal,* vol. 119, no. 1, pp. 41-53, 2022.

[226] N. K. Oukaili and T. S. Salman, "Punching Shear Strength of Reinforced Concrete Flat Plates with Openings," *Journal of Engineering,* vol. 20, no. 1, pp. 1-20, 2014.

[227] S. M. Rashied, "Punching Shear Resistance of Flat Slabs With Opening," *International Journal of Civil Engineering and Technology (IJCIET),* vol. 6, no. 4, pp. 1-12, 2015.

[228] T. F. El-Shafiey, A. M. Atta and M. Elnasharty, "Effect of opening shape, size and location on the punching shear behaviour of RC flat slabs," *Structures,* vol. 44, pp. 1138-1151, 2022.

[229] P. Regan, "Design for punching shear," *The Structural Engineer,* vol. 52, no. 5, pp. 197-207, 1974.

[230] D. M. Masterson and A. E. Long, "The Punching Strength of Slabs, A Flexural Approach Using Finite Elements," *ACI Symposium Publication,* vol. 42, pp. 767-768, 1974.

[231] F. González-Vidosa, M. D. Kotsovos and M. N. Pavlovic, "Symmetrical Punching of Reinforced Concrete Slabs: An Analytical Investigation Based on Nonlinear Finite Element Modeling," *ACI Structural Journal,* vol. 85, no. 3, pp. 241-250, 1988.

[232] P. Menétrey, R. Walther, T. Zimmermann, K. J. Willam and P. E. Regan, "Simulation of punching failure in reinforced-concrete structures," *Journal of Structural Engineering,* vol. 123, no. 5, pp. 652-659, 1997.

[233] M. Hallgren and M. Bjerke, "Non-linear finite element analyses of punching shear failure of column footings," *Cement & Concrete Composites,* vol. 24, no. 6, pp. 491-496, 2002.

[234] C. Bédard and M. D. Kotsovos, "Application of NLFEA to concrete structures," *Journal of Structural Engineering,* vol. 111, no. 12, pp. 2691-2707, 1985.

[235] A. Genikomsou, "Nonlinear finite element analysis of punching shear of reinforced concrete slab-column connections," Doctoral Thesis, University of Waterloo, Waterloo, Ontario, Canada, 2015.

[236] J. Shu, M. Plos, K. Zandi, M. Johansson and F. Nilenius, "Prediction of punching behaviour of RC slabs using continuum non-linear FE analysis," *Engineering Structures,* vol. 125, pp. 15-25, 2016.

[237] M. A. Polak, "Modeling Punching Shear of Reinforced Concrete Slabs Using Layered Finite Elements," *ACI Structural Journal,* vol. 95, no. 1, pp. 71-80, 1998.

[238] M. A. Eder, R. L. Vollum, A. Y. Elghazouli and T. Abdel-Fattah, "Modelling and experimental assessment of punching shear in flat slabs with shearheads," *Engineering Structures,* vol. 32, no. 12, pp. 3911-3924, 2010.

[239] R. Abolhelm, "Shell-Based Finite Element Analysis of Reinforced Concrete Slabs Subjected to Non-uniform Stress Distribution at Column Connection Regions," Master's Thesis, University of Waterloo, Waterloo, Ontario, Canada, 2022.

[240] C. Y. M. Goh and T. D. Hrynyk, "Numerical investigation of the punching resistance of Reinforced Concrete Flat Plates," *Journal of Structural Engineering,* vol. 144, no. 10, p. 04018166, 2018.

[241] C. Y. M. Goh and T. D. Hrynyk, "Nonlinear finite element analysis of reinforced concrete flat plate punching using a thick-shell modelling approach," *Engineering Structures,* vol. 224, p. 111250, 2020.

[242] A. Setiawan, R. L. Vollum, L. Macorini and B. Izzuddin, "Efficient 3-D modelling of punching shear failure at slab-column connections by means of nonlinear joint elements," *Engineering Structures,* vol. 197, p. 109372, 2019.

[243] A. J. Alam and K. M. Amanat, "Finite Element Simulation on Punching Shear Behaviour of Reinforced Concrete Slabs," *ISRN Civil Engineering,* vol. 2012, pp. 1-9, 2012.

[244] A. Wosatko, J. Pamin and M. A. Polak, "Application of damage-plasticity models in finite element analysis of punching shear," *Computers and Structures,* vol. 151, pp. 73-85, 2015.

[245] J. Shu, D. Fall, M. Plos, K. Zandi and K. Lundgren, "Development of modelling strategies for two-way RC slabs," *Engineering Structures,* vol. 101, pp. 439-449, 2015.

[246] M. Laguta, "Effect of Unbalanced Moment on Punching Shear Strength of Slab-Column Joints," Master's Thesis, University of Waterloo, Waterloo, Ontario, Canada, 2020.

[247] P. M. Beaulieu, "Nonlinear Finite Element Analysis of Reinforced Concrete Slab-Column Connections with Headed Stud/Bolt Shear Reinforcement Subjected to Punching Shear," Master's Thesis, University of Waterloo, Waterloo, Ontario, Canada, 2022.

[248] K. Winkler and F. Stangenberg, "Numerical analysis of punching shear failure of reinforced concrete slabs," *Abaqus Users' Conference,* 2008.

[249] M. Navarro, S. Ivorra and F. B. Varona, "Parametric computational analysis for punching shear in RC slabs," *Engineering Structures,* vol. 165, pp. 254-263, 2016.

[250] D. V. Bompa and T. Onet, "Punching shear strength of RC flat slabs at interior connections to columns," *Magazine of Concrete Research,* vol. 68, no. 1, pp. 24-42, 2016.

[251] M. Tang, W.-J. Yi and Y.-F. Wu, "Numerical and analytical investigation on the moment and deformation capacity of interior slab-column connections without shear reinforcement," *Advances in Structural Engineering,* vol. 24, no. 16, pp. 3707-3723, 2021.

[252] W. Nana, T. Bui, A. Limam and S. Abouri, "Experimental and Numerical Modelling of Shear Behaviour of Full-scale RC Slabs Under Concentrated Loads," *Structures*, vol. 10, pp. 96-116, 2017.

[253] H. Madkour, M. Maher and O. Ali, "Finite element analysis for interior slab-column connections reinforced with GFRP bars using damage plasticity model," *Journal of Building Engineering*, vol. 48, p. 104013, 2022.

[254] R. de Azevedo Palhares, F. Weitzel Rossignoli, G. Sales de Melo and H. Jorge Nery de Lima, "A numerical model capable of accurately simulating the punching shear behavior of a reinforced concrete slab," *Structural Concrete*, vol. 23, no. 2, pp. 1134-1150, 2022.

[255] A. S. Genikomsou and M. A. Polak, "Finite-element analysis of reinforced concrete slabs with punching shear reinforcement," *Journal of Structural Engineering*, vol. 142, no. 12, p. 04016129, 2016.

[256] A. S. Genikomsou and M. A. Polak, "3D finite element investigation of the compressive membrane action effect in reinforced concrete flat slabs," *Engineering Structures*, vol. 136, pp. 233-244, 2017a.

[257] A. Genikomsou and M. A. Polak, "Finite element simulation of concrete slabs with various placement and amount of shear bolts," *Procedia Engineering*, vol. 193, pp. 313-320, 2017c.

[258] D. Topuzi, "Large Scale Testing and Modelling of Reinforced Concrete Flat Plates in Seismic Areas," PhD Thesis, University of Waterloo, Waterloo, Ontario, Canada, 2015.

[259] G. J. Milligan, Q. Zhang and M. A. Polak, "Effect of Support Geometry on the Punching Shear Behaviour of Reinforced Concrete Flat Slabs," *ACI Symposium Publication*, vol. 353, pp. 29-49, 2022.

[260] A. Marí, A. Cladera, E. Oller and J. M. Bairán, "A punching shear mechanical model for reinforced concrete flat slabs with and without shear reinforcement," *Engineering Structures*, vol. 166, pp. 413-426, 2018.

[261] S. Kinnunen and H. S. E. Nylander, "Punching of concrete slabs without shear reinforcement," *Transactions of the Royal Institute of Technology, Stockholm, Sweden*, vol. 158, p. 112, 1960.

[262] P. Menétrey, "Analytical computation of the punching strength of reinforced concrete," *ACI Structural Journal*, vol. 93, no. 5, pp. 503-511, 1996.

[263] S. D. Alexander and S. H. Simmonds, "Bond model for concentric punching shear," *ACI Structural Journal,* vol. 89, no. 3, pp. 325-334, 1992.

[264] E. O. Lantsoght, C. van der Veen, J. C. Walraven and A. de Boer, "Transition from one-way to two-way shear in slabs under concentrated loads," *Magazine of Concrete Research,* vol. 67, no. 17, pp. 909-922, 2015.

[265] G. Rankin and A. Long, "Predicting the punching strength of conventional slab-column specimens," *Proceedings of the Institution of Civil Engineers (London),* vol. 82, no. 1, pp. 327-346, 1987.

[266] G. Rankin and A. Long, "Punching strength of conventional slab-column specimens," *Engineering Structures,* vol. 178, pp. 37-54, 2019.

[267] A. Shehata and P. E. Regan, "Punching in R.C. slabs," *Journal of Structural Engineering,* vol. 115, no. 7, pp. 1726-1740, 1989.

[268] A. Muttoni and J. Schwartz, "behaviour of beams and punching in slabs without shear reinforcement," *IABSE Colloquium,* vol. 62, pp. 703-708, 1991.

[269] A. Muttoni, M. Fernández Ruiz, E. Bentz, S. Foster and V. Sigrist, "Background to fib Model Code 2010 shear provisions - Part II: Punching shear," *Structural Concrete,* vol. 14, no. 3, pp. 204-214, 2013.

[270] A. Muttoni and M. Fernández Ruiz, "Shear strength of members without transverse reinforcement as function of critical shear crack width," *ACI Structural Journal,* vol. 105, no. 2, pp. 163-172, 2008.

[271] J. Halvonik, J. Kalická, L. Majtánová and M. Minárová, "Safety factor for the punching shear resistance model in 2nd Generation of Eurocode 2," *Journal of Building Engineering,* vol. 46, p. 103788, 2022.

[272] A. Muttoni, M. F. Ruiz and J. T. Simões, "Recent improvements of the Critical Shear Crack Theory for punching shear design and its simplification for code provisions," *fib Congress, Melbourne,* p. 10 pages, 2018.

[273] M. Fernández Ruiz and A. Muttoni, "Applications of critical shear crack theory to punching of reinforced concrete slabs with transverse reinforcement," *ACI Structural Journal,* vol. 106, no. 4, pp. 485-494, 2009.

[274] M. F. Ruiz, A. Muttoni and J. Kunz, "Strengthening of Flat Slabs Against Punching Shear Using Post-Installed Shear Reinforcement," *ACI Structural Journal,* vol. 107, no. 4, pp. 434-442, 2010.

[275] A. Muttoni, M. F. Ruiz and J. T. Simões, "The theoretical principles of the critical shear crack theory for punching shear failures and derivation of consistent closed-form design expressions," *Structural Concrete,* vol. 19, no. 1, pp. 174-190, 2019.

[276] M. F. Ruiz, A. Muttoni and J. Sagaseta, "Shear strength of concrete members without transverse reinforcement: A mechanical approach to consistently account for size and strain effects," *Engineering Structures,* vol. 99, pp. 360-372, 2015.

[277] J. Einpaul, M. F. Ruiz and A. Muttoni, "Influence of moment redistribution and compressive membrane action on punching strength of flat slabs," *Engineering Structures,* vol. 86, pp. 43-57, 2015.

[278] T. Clément, A. P. Ramos, M. F. Ruiz and A. Muttoni, "Influence of prestressing on the punching strength of post-tensioned slabs," *Engineering Structures,* vol. 72, pp. 56-69, 2014.

[279] F. Natário, M. F. Ruiz and A. Muttoni, "Shear strength of RC slabs under concentrated loads near clamped linear supports," *Engineering Structures,* vol. 76, pp. 10-23, 2014.

[280] CEN/TC 250, Eurocode 2: Design of Concrete Structures—Part 1-1: General Rules - Rules for buildings, bridges and civil engineering structures, prEN 1992-1-1:2021 (E), Brussels, Belgium, 2021-09.

[281] D. Kueres, C. Siburg, M. Herbrand, M. Classen and J. Hegger, "Uniform design method for punching shear in flat slabs and column bases," *Engineering Structures,* vol. 136, pp. 149-164, 2017.

[282] Committee of Laws and Ordinances, Requirements for Reinforced Concrete or Concrete-Steel Constructed Buildings Recommended by the National Board of Fire Underwriters, National Association of Cement Users , 1908.

[283] American Concrete Institute, Standard Specification No. 23 Standard Building Regulations for the Use of Reinforced Concrete, American Concrete Institute, 1920.

[284] ACI Committee E-1, Tentative Building Regulations for the Use of Reinforced Concrete (E-1A-27T), American Concrete Institute, 1927.

[285] ACI Committee 501, Building Regulations for Reinforced Concrete (A.C.I. 501-36T), American Concrete Institute, 1936.

[286] ACI Committee 318, Building Code Requirements for Reinforced Concrete (ACI 318-56), Detroit, Michigan: American Concrete Institute, 1956.

[287] ACI Committee 318, Special Publication 10 Commentary on Building Code Requirements for Reinforced Concrete (ACI 318-63), Detroit, Michigan: American Concrete Institute, 1965.

[288] ACI Committee 318, Building Code Requirements for Reinforced Concrete (ACI 318-89) And Commentary - ACI 318R-89, Farmington Hills, MI: American Concrete Institute, 1989.

[289] D. Mitchell, W. Cook and W. Dilger, "Effects of size, geometry and material properties on punching shear resistance," *ACI Symposium Publication*, vol. 232, pp. 39-56, 2005.

[290] ACI Committee 318, Building Code Requirements for Reinforced Concrete (ACI 318-71), Detroit, Michigan: American Concrete Institute, 1970.

[291] R. P. Johnson, "Eurocodes, 1970-2010: why 40 years?," *Proceedings of the Institution of Civil Engineers-Structures and Buildings*, vol. 162, no. 6, pp. 371-379, 2009.

[292] European Comittee for Standardization (CEN), ENV 1992-1-1: 1991 Eurocode 2 Design of Concrete Structures - Part 1: General Rules and Rules for Buldings (English Language Version), London, UK: British Standard Insitute, 1993.

[293] The Concrete Centre, part of the MPA, "Background to Eurocode 2," [Online]. Available: https://www.concretecentre.com/Concrete-Design/Design-Codes/Eurocode-2/Background-to-Eurocode-2.aspx.

[294] European Concrete Platform ASBL, Eurocode 2 Commentary, 2008.

[295] M. Ricker and C. Siburg, "Punching shear strength of flat slabs - critical review of Eurocode 2 and fib Model Code 2010 design provisions," *Structural Concrete*, vol. 17, no. 3, pp. 457-468, 2016.

[296] T. C. Zsutty, "Beam Shear Strength Prediction by Analysis of Existing Data," *Journal Proceedings*, vol. 65, no. 11, pp. 943-951, 1968.

[297] J. Halvonik, L. Majtánová and M. Minarova, "Safety factor for the Eurocode 2 punching resistance model," *Magazine of Concrete Research*, vol. 74, no. 5, pp. 225-235, 2022.

[298] J. Walraven and A. Bigaj, "The 2010 fib model code for concrete structures: a new approach to structural engineering," *Structural Concrete,* vol. 12, no. 3, pp. 139-147, 2011.

[299] A. Muttoni and M. Fernández Ruiz, "The levels-of-approximation approach in MC 2010: application to punching shear provisions," *Structural Concrete,* vol. 13, no. 1, pp. 32-41, 2012.

[300] L. Soares and R. Vollum, "Comparison of punching shear requirements in BS 8110, EC2 and MC2010," *Magazine of Concrete Research,* vol. 67, no. 24, pp. 1315-1328, 2015.

[301] B. Belletti, M. Pimentel, M. Scolari and J. C. Walraven, "Safety assessment of punching shear failure according to the level of approximation approach," *Structural Concrete,* vol. 16, no. 3, pp. 366-380, 2015.

[302] Comite Euro-International Du Beton, Bulletin D'Information 137 Complement to CEB-FIp Model Code 1978 Final Draft English Version, Paris: Comite Euro-International Du Beton, 1980.

[303] Dassault Systemes Simulia Corp., ABAQUS Analysis User's Guide 6.13, Providence, RI, USA, 2013.

[304] Dassault Systemes Simulia Corp., Abaqus Theory Guide (6.13), Providence, RI, USA, 2013.

[305] J. G. Stoner, "Finite Element Modelling of GFRP Reinforced Concrete Beams," Waterloo, Ontario, Canada, 2015.

[306] W. Chen, Plasticity in Reinforced Concrete, New York: McGraw Hill, 1982.

[307] W.-F. Chen and D. Han, Plasticity for Structural Engineers, New York: Springer-Verlag, 1988.

[308] H. Kupfer, H. K. Hilsdorf and H. Rüsch, "Behavior of Concrete Under Biaxial Stresses," *Journal Proceedings,* vol. 66, no. 8, pp. 656-666, 1969.

[309] J. Lubliner, J. Oliver, S. Oller and E. Oñate, "A plastic-damage model for concrete," *International Journal of Solids and Structures,* vol. 25, no. 3, pp. 299-326, 1989.

[310] J. Lee and G. L. Fenves, "Plastic-damage model for cyclic loading of concrete structures," *Journal of engineering mechanics,* vol. 124, no. 8, pp. 892-900, 1998a.

[311] W. A. Labib, "An Experimental Study and Finite Element Analysis of Punching Shear Failure in Steel Fibre-Reinforced Concrete Ground-Suspended Floor Slabs," Doctoral Thesis, Liverpool John Moores University, Liverpool, United Kingdom, 2008.

[312] R. Barrage, "Finite Element Modelling of FRP Reinforced Concrete Beams and Comparative Analysis of Current Strength Prediction Models," Waterloo, Ontario, Canada, 2017.

[313] H. Panahi and A. S. Genikomsou, "Comparative evaluation of concrete constitutive models in non-linear finite element simulations of slabs with different flexural reinforcement ratios," *Engineering Structures,* vol. 252, p. 113617, 2022.

[314] A. Hillerborg, M. Modéer and P. Petersson, "Analysis of crack formation and crack growth in concrete by means of fracture mechanics and finite elements," *Cement and Concrete Research,* vol. 6, no. 6, pp. 773-781, 1976.

[315] B. Alfarah, F. López-Almansa and S. Oller, "New methodology for calculating damage variables evolution in Plastic Damage Model for RC Structures," *Engineering Structures,* vol. 132, pp. 70-86, 2017.

[316] T. Yu, J. Teng, Y. Wong and S. Dong, "Finite element modeling of confined concrete-II: Plastic-damage model," *Engineering Structures,* vol. 32, no. 3, pp. 680-691, 2010.

[317] R. Malm, "Shear Cracks in Concrete Structures Subjected to in-plane Stresses," Licentiate Thesis, Royal Institute of Technology (KTH), Stockholm, Sweden, 2006.

[318] H.-T. Hu and W. C. Schnobrich, "Constitutive Modelling of Concrete by Using Nonassociated Plasticity," *Journal of Materials in Civil Engineering,* vol. 1, no. 4, pp. 199-216, 1989.

[319] P. Kmiecik and M. Kamiński, "Modelling of reinforced concrete structures and composite structures with concrete strength degradation taken into consideration," *Archives of Civil and Mechanical Engineering,* vol. 11, no. 3, pp. 623-636, 2011.

[320] A. Wosatko, A. Winnicki, M. A. Polak and J. Pamin, "Role of dilatancy angle in plasticity-based models of concrete," *Archives of Civil and Mechanical Engineering,* vol. 19, no. 4, pp. 1268-1283, 2019.

[321] J. Lee and G. L. Fenves, "A plastic-damage concrete model for earthquake analysis of dams," *Earthquake Engineering & Structural Dynamics,* vol. 27, no. 9, pp. 937-956, 1998b.

[322] J. Y. Wu, J. Li and R. Faria, "An energy release rate-based plastic-damage model for concrete," *International Journal of Solids and Structures,* vol. 43, no. 3-4, pp. 583-612, 2006.

[323] G. J. Milligan, M. A. Polak and C. Zurell, "Finite Element Analysis of Punching Shear Behaviour of Reinforced Concrete Slabs Supported on Walls," *Structural Concrete,* vol. 23, no. 2, pp. 1118-1133, 2022.

[324] G. J. Milligan and M. A. Polak, "Finite Element Analysis of Shear Behaviour of Concrete Slabs Partially Supported on Walls," *Proceedings of the fib Symposium 2019*, pp. 1803-1810, 2019.

[325] G. J. Milligan and M. A. Polak, "Finite Element Analysis of Shear Behaviour of Concrete Slabs Partially Supported on Walls," in *Concrete innovations in materials, design and structures: proceedings of the 2019 fib symposium*, held in Krakow, Poland, 2019.

[326] A. S. Genikomsou, G. J. Milligan and M. A. Polak, "Modeling Parameters in Punching Shear Finite Element Analysis of Concrete Slabs," *ACI Symposium Publication*, vol. 328, pp. 12.1-12.24, 2018.

[327] E. Petersson, "Crack Growth and Development of Fracture Zones in Plain Concrete and Similar Materials," Lund, Sweden, 1981.

[328] H. Cornelissen, D. Hordijk and H. Reinhardt, "Experimental determination of crack softening characteristics of normalweight and lightweight concrete," *HERON*, vol. 31, no. 2, pp. 45-56, 1986.

[329] R. De Azevedo Palhares, F. Weitzel Rossignoli, G. Sales De Melo and H. Jorge Nery De Lima, "A numerical model capable of accurately simulating the punching shear behavior of a reinforced concrete slab," *Structural Concrete*, vol. 23, no. 2, pp. 1134-1150, 2022.

[330] G. E. Polo, "Punching shear of reinforced concrete flat plates : behavior and design considerations," Doctoral Thesis - University of Texas at Austin, Austin, Texas, United States of America, 2018.

[331] L. S. Montagna, "Two-way Shear Strength of Reinforced Concrete Slab-Column Connections: Influence of Testing Conditions in Isolated Specimens," Master's Thesis, The University of Texas at Austin, Austin, Texax, United States of America, 2018.

[332] American Society of Civil Engineers, ASCE/SEI 7-16 Minimum Design Loads and Associated Criteria for Buildings and Other Structures, Reston, Virginia: American Society of Civil Engineers, 2017.

[333] Canadian Commission on Building and Fire Codes/National Research Council of Canada, National Building Code of Canada 2015, Ottawa, Ontario, 2015.

[334] A. F. Lima Neto, "Análise experimental na fase de pós-puncionamento de lajes cogumelo de concreto armado," Master's Thesis, Universidade de Brasília, Brasília, Brazil, 2003.

[335] C. Forssell and A. Holmberg, "Stämpellast pa plattor av betong," 1946.

[336] A. S. Carvalho, "de Análise Experimental de Laje Lisa de Concreto Armado de Alta Resistência com Metacaulim Apoiadas em Pilares Retangulares e Armada à Punção," Master's Thesis, Universidade Federal do Pará Centro Tecnológico, Belém, Pará, Brazil, 2006.

[337] L. S. R. Damasceno, "Análise Experimental de Lajes Lisas Unidirecionais de Concreto Armado Com Pilares Retangulares ao Puncionamento," Master's Thesis, Universidada Federal Do Pará Instituto de Tecnologia, Belém - Pará, Brazil, 2007.

[338] A. Vilhena, K. Nahun, M. Peres and D. Oliveira, "Análise Experimental de Lajes Unidirecionais com Pilares Retangulares ao Puncionamento Simétrico," *48º Congresso Brasileiro do Concreto,* 2006.

[339] B. N. Moraes Neto, "Análise Experimental de Lajes Lisas Bidirecionais de Concreto Armado com Estribos Inclinados e Pilares Retangulares Sujeitas a Puncionamento Simétrico," Master's Thesis, Universidade Federal do Pará Centro Tecnológico, Belém, Pará, Brazil, 2006.

[340] V. C. Mouro, "Punção em lajes cogumelo: estudo de retangularidade dos pilares," Master's Thesis, Universidade Federal de Goiás, Goiânia, Brazil, 2006.

[341] L. d. L. J. Borges, "Comportamento ao puncionamento de lajes cogumelo de concreto armado com pilares retangulares e furos de grandes dimensões," Doctoral Thesis, Universidade de Brasília, Brasília, Brazil, 2007.

[342] T. Urban, Nośność na Przebicie w Aspekcie Proporcji Boków Słupa, Łódź, Poland: Wydawnictwo Politechniki Łódzkiej (in Polish), 1994.

[343] D. Yitzhaki, "Punching Strength of Reinforced Concrete Slabs," *Journal Proceedings,* vol. 63, no. 5, pp. 527-542, 1966.

[344] I. Rosenthal, "Experimental Investigation of Flat Plate Floors," *Journal Proceedings,* vol. 56, no. 8, pp. 153-166, 1959.

[345] Swiss Society of engineers and architects SIA, Code 262 for concrete structres, Zürich: Swiss Society of Engineers and Architects, 2013.

[346] DIN EN 1992-1-1/NA:2013-04: Nationaler Anhang – National festgelegte Parameter – Eurocode 2: Bemessung und Konstruktion von Stahlbeton- und Spannbetontragwerken – Teil 1-1: Allgemeine Bemessungsregeln und Regeln für den Hochbau., Deutsche Fassung EN 1992-1-1/NA:2013-04, 2013. (in German).

[347] Q. Zhang, G. J. Milligan and M. A. Polak, "Nonlinear finite element analysis of punching shear strength of reinforced concrete slabs supported on L-shaped columns," *Budownictwo i Architektura*, vol. 19, no. 4, pp. 125-138, 2020.

[348] G. J. Milligan and M. A. Polak, "Influence of Slab Openings on the Punching Shear Behaviour of Reinforced Concrete Slabs Supported on L-Shaped Columns," *ACI Symposium Publication*, 2023 (In Press).

[349] Y. Tian, J. O. Jirsa and O. Bayrak, "Nonlinear Modeling of Slab-Column Connections under Cyclic Loading," *ACI Structural Journal*, vol. 106, no. 1, pp. 30-38, 2009.

[350] M. Eladawy, M. Hassan and B. Benmokrane, "Experimental Study of Interior Glass Fiber-Reinforced Polymer-Reinforced Concrete Slab-Column Connections under Lateral Cyclic Load," *ACI Structural Journal*, vol. 116, no. 6, pp. 165-180, 2019.

[351] J. M. Hanson, "Influence of embedded service ducts on strength of flat-plate structures," *Portland Cement Association Research and Development Bulletin*, vol. RD 005.01D, 1970.

[352] J. Schnell and C. Thiele, "Shear Load Capacity of Concrete Slabs With Embedded Ducts," in *Tailor Made Concrete Structures*, London, UK, Taylor and Francis Group, 2008, pp. 1183-1184.

[353] H. A. Al-Tameemi, M. A. Habelalmateen and A. A. Alalikhan, "Effect of Embedded Pipelines within Slab Thickness on Punching Shear Capacity of Flat Slabs," *KSCE Journal of Civil Engineering*, vol. 25, no. 1, pp. 208-218, 2021.

[354] C. L. Hamberg and R. Vavrinek, "Shoelace Algorithm," *IMSA Math Journal*, vol. 2, no. 1, pp. 3-7, 1993.

[355] G. J. Milligan and M. A. Polak, "Influence of Openings on the Punching Shear Behaviour of Concrete Slabs Supported on Special-Shaped Columns," *Engineering Structures*, p. Submitted, 20xx.

[356] G. J. Milligan, M. A. Polak and C. Zurell, "Influence of Openings on the Punching Shear Behaviour of Concrete Slabs Supported on Rectangular Columns and Walls," *Journal of Structural Engineering*, p. Submitted, 20xx.

[357] G. J. Milligan, M. A. Polak and C. Zurell, "Punching Shear Design Methods for Reinforced Concrete Slab-Wall Connections," Submitted.

[358] G. J. Milligan, M. A. Polak and C. Zurell, "Alternative Punching Shear Design Methods for Concrete Slabs on Rectangular Columns," Submitted.

Appendix A

Calculation of Shear Stress Distribution from Abaqus Results

In this appendix, the methodology used to calculate the shear stress distribution from the Abaqus results using a Python 2.7 script created by the author is discussed. The text and figures in this appendix are mostly taken verbatim from Appendix B of the author's MASc thesis [1]. In addition to modifications to figure and equation numbers for consistency with this thesis, additional discussions have been added to clarify the procedure. The procedure and discussion are focused on isolated rectangular slab-column connections but a similar procedure was applied for the isolated slab-wall connections and special-shaped slab-column connections.

For reference, a top view of the quarter model for the AM series (AM04 is shown) and the parametric study models (for rectangular columns in the author's MASc thesis [1]) is provided in Figure A-1. In the Abaqus model, the X-axis is parallel to the long side of the steel plate and the Y-axis is parallel to the short side of the steel plate, which is opposite of the experimental setup. However, the experimental convention was used when referring to the stress distributions and the load-rotation or load-deflection responses in this thesis. Therefore, the Y-direction was parallel to the long side of the steel plate and the X-direction was parallel to the short side of the steel plate.

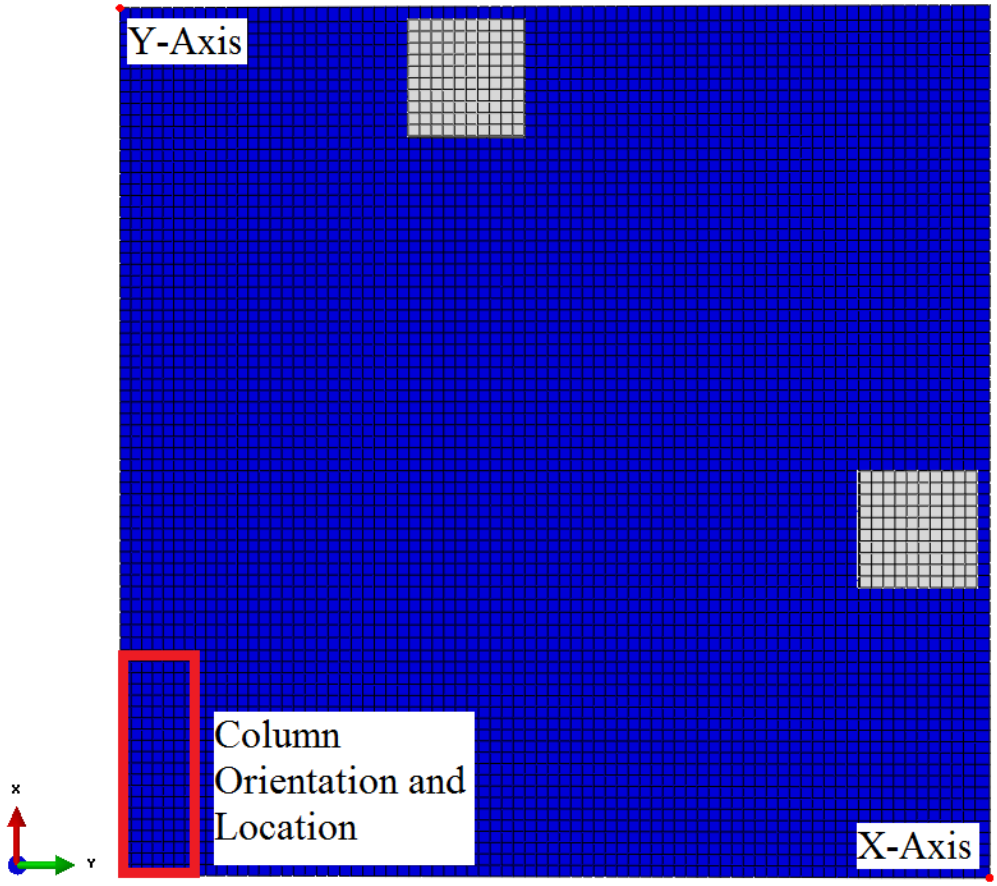


Figure A-1: Overview of AM04 Quarter Model

The location of the elements considered in the calculation of the shear stress distribution in the slab around the perimeter of the steel support plate ("column") and the ACI 318 critical perimeter are shown in Figure A-2. The elements parallel to the short side of the supported area were denoted "Parallel to X" or "Parallel to X ACI." The elements parallel to the long side of the supported area were denoted "Parallel to Y" or "Parallel to Y ACI." In all models, the support plate/column

perimeter elements were located along the outer edge of the supported area as shown in Figure A-2. In all models except for the AM04 model, the ACI critical perimeter elements were located at a distance of 100mm from the outer edge of the supported area. Since the elements only have one integration point, located at the element centroid, the stress values used are calculated at a distance of 90mm away from the edge of the supported area, which is slightly less than *d/2* (101mm). In the AM04 model the ACI critical perimeter elements were located at 110mm from the edge of the supported area, and therefore, the integration points are approximately located 100mm from the edge of the supported area. However, the distance of 110mm was not used for all models because it led to meshing issues due to the use of a 20mm global mesh size. For the elements parallel to the short side of the supported area shear stress S13 (τ_{xz}) was recorded during the analysis. For the elements parallel to the long side of the supported area shear stress S23 (τ_{yz}) was recorded.

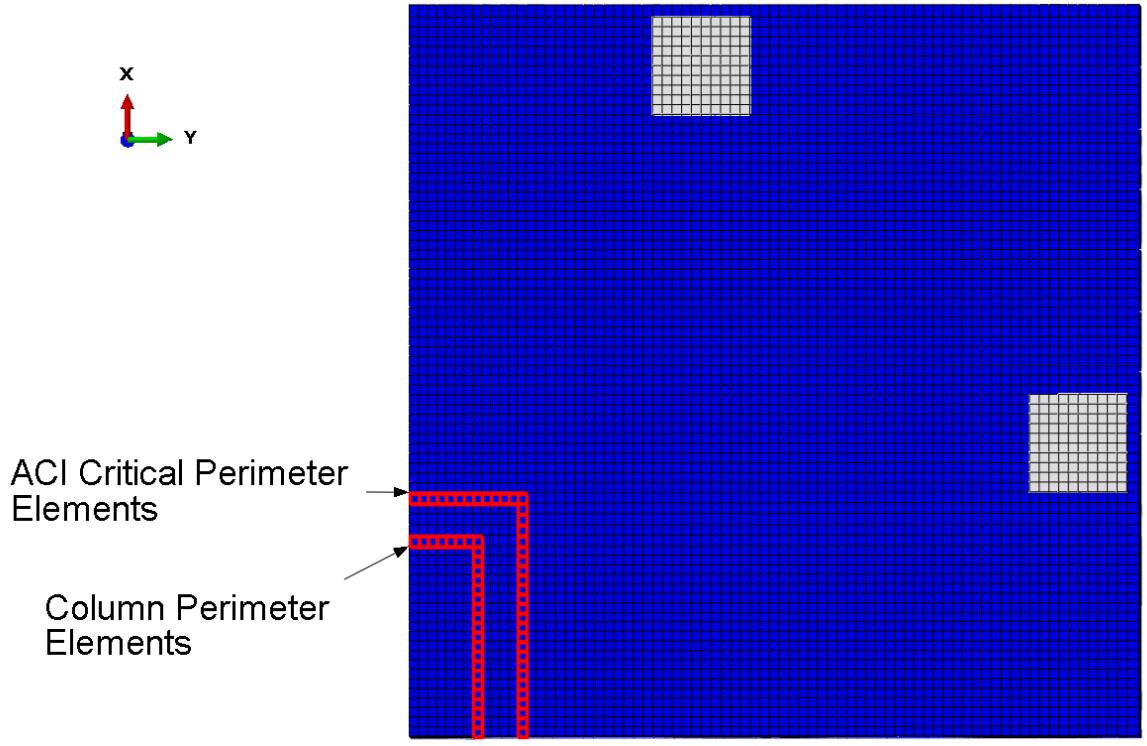


Figure A-2: Top View of Elements Considered in Shear Stress Distribution Calculations

A side view of slab showing the elements considered when calculating the shear stress distribution is shown in Figure A-3. As previously discussed, the elements along the perimeter of the supported

area were located along the outer edge of the support plate. All elements through the slab depth were included when calculating the shear stress distribution.

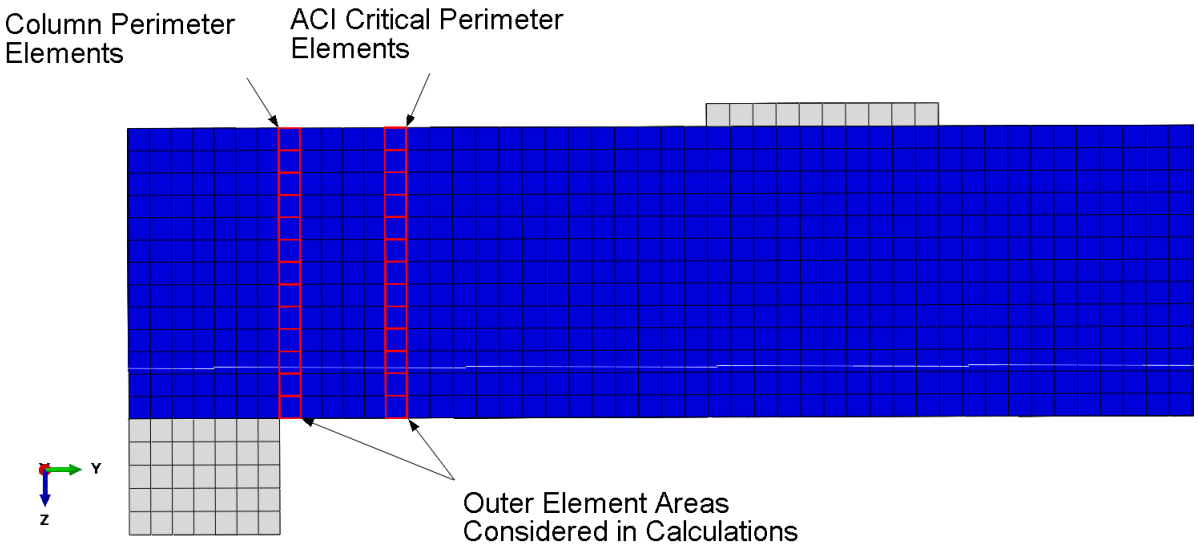


Figure A-3: Side View of Elements Considered in Stress Distribution Calculations

Since the element area is not a variable which can be extracted from Abaqus it must be calculated using the deformed nodal coordinates of each element. As noted in Figure A-3, the outer element face area was used instead of the inner face area or average face area. Only using the area of the outer element face was found to have a minimal impact on the predicted shear stress distribution but greatly increased the computational efficiency of the Python post processing code.

The Shoelace algorithm, provided in equation *A1*, was used to calculate the outer element face area from the four deformed nodal coordinates at each step during the analysis. The area of a closed polygon with four non-intersecting sides was calculated according to equation *A2*.

$$A = \frac{1}{2}\left|(x_1y_2 + x_2y_3 + \cdots + x_ny_1) - (x_2y_1 + x_3y_2 + \cdots + x_1y_n)\right| \qquad (A1)$$

$$A = \frac{1}{2}\left|(x_1y_2 + x_2y_3 + x_3y_4 + x_4y_1) - (x_2y_1 + x_3y_2 + x_4y_1 + x_1y_4)\right| \qquad (A2)$$

where x_i and y_i are the nodal coordinates of each node of the polygon (1-n) in a Cartesian plane and the nodes are numbered in a counterclockwise or clockwise direction [354].

Using the element area and shear stress at the element integration point, the shear force acting on each element was calculated as shown in Figure A-4. The total shear stress on each column of elements was then calculated as the total force in the column of elements divided by the total area. This process was repeated for each column of elements along the support plate and critical perimeter. As shown in Figure A-2, the elements considered in each direction intersect at the corner of the supported area or the critical perimeter. Therefore, the procedure outlined above was implemented twice for the corner elements considering the S13 and S23 stresses and the results were summed.

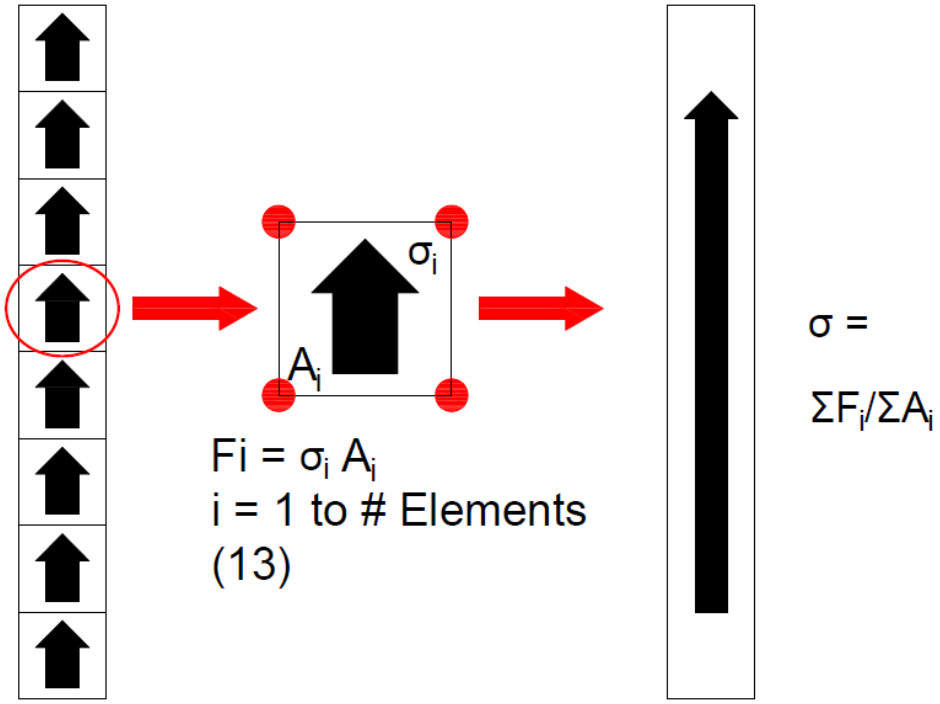


Figure A-4: Procedure to Calculate Total Stress on a Column of Elements

To summarize, the local shear stresses (τ_{xz} and τ_{yz}) were averaged over the slab depth for each vertical band of elements around the considered perimeter. At the corners, the local shear stresses from the two adjoining faces were summed. Ideally, the shear stress distributions should represent the principal shear stresses along the investigated perimeter. However, the additional data required to calculate the principal shear stresses would have been prohibitive from both an analysis and post-processing perspective. As such, the simplified procedure outlined above was used. The use of local shear stresses greatly simplified the post processing, and only introduced minor errors in the predicted shear stress distributions (the error in the total force computed from the shear stress distributions and the reaction force predicted by Abaqus was typically between 5-10%).

Appendix B
Additional Figures from Parametric Study of Isolated Slab-Wall Connections

In this appendix, additional load-displacement plots, crack patterns and slab shear stress distributions along the wall perimeter not included in Chapter 6 are provided. These additional figures are for the other displacement locations studied, different c_{min}/d ratios and the uniformly distributed loading (UDL) models. The figures contained in this appendix were considered in the observations and conclusions discussed in Chapter 6.

Additional plots for the equal load plate loading models (V study, subsection 6.4.1.2) are presented first. Then plots for the UDL models, and the key differences between the equal load plate and UDL model results are discussed. Finally, the crack patterns for the remaining symmetric opening specimens (rectangular columns and walls) are provided. These plots are supplemental to those presented in Section 6.4.3.

Additional Plots for Equal Load Plate Models (V Study, subsection 6.4.1.2)

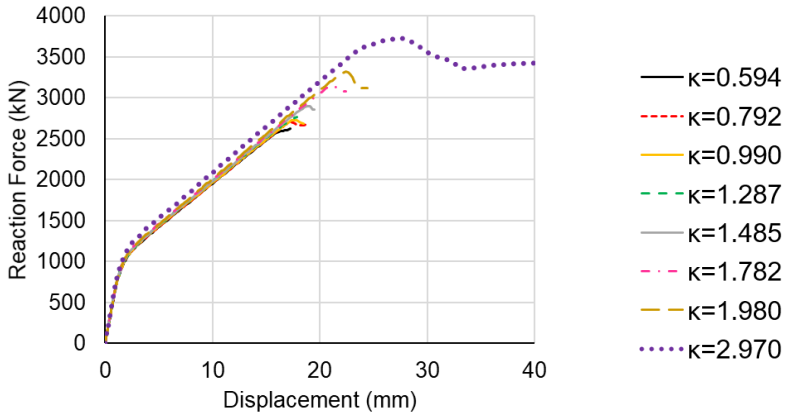


Figure B-1: Predicted Load-Displacement Response Perpendicular to the Long Side of the Wall at the Wall Centerline (X-Wall CL Location, see Figure 6-4), Equal Load Plate Loading, all *κ*

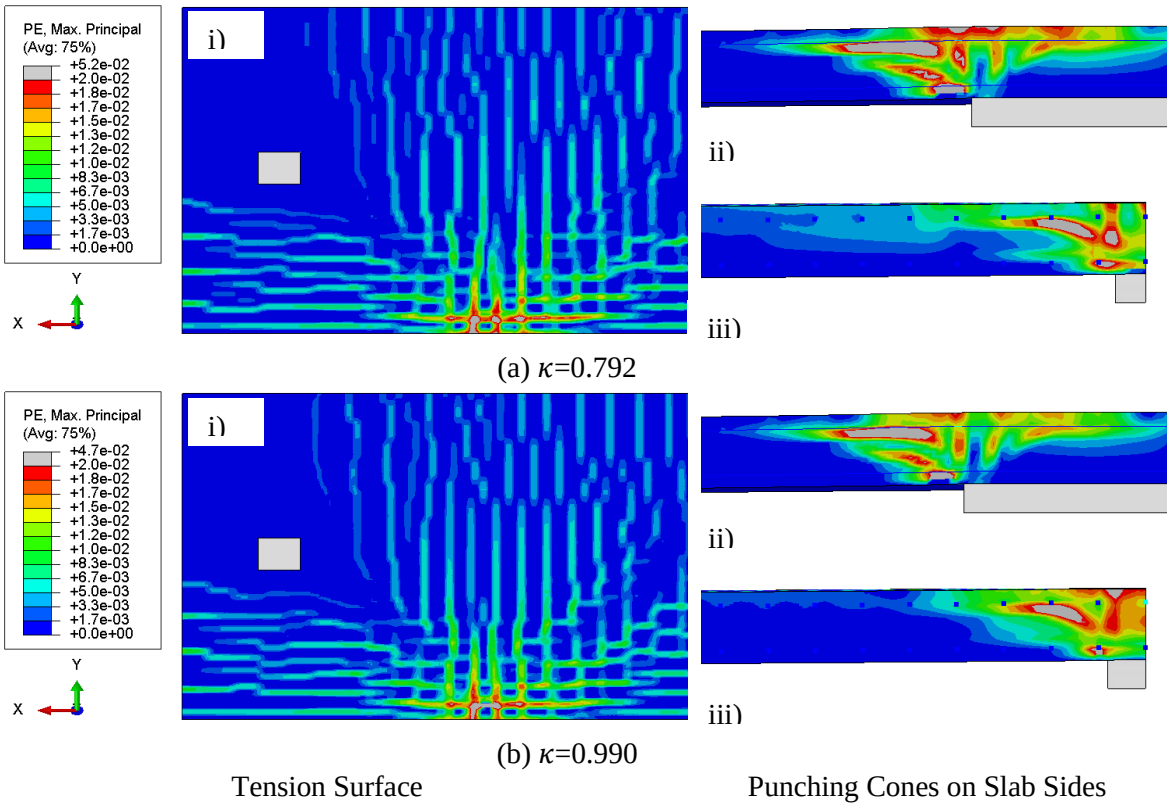


Figure B-2: Predicted Crack Pattern Near Wall Toe, (a) *κ* = 0.792, (b) *κ* = 0.990, i) Tension Surface, ii) Slab Side Surface Parallel to Long Side of Wall, iii) Slab Side Parallel to Short Side of Wall, Equal Load Plate Loading (Entire Isolated Slab-Wall Specimen not Shown)

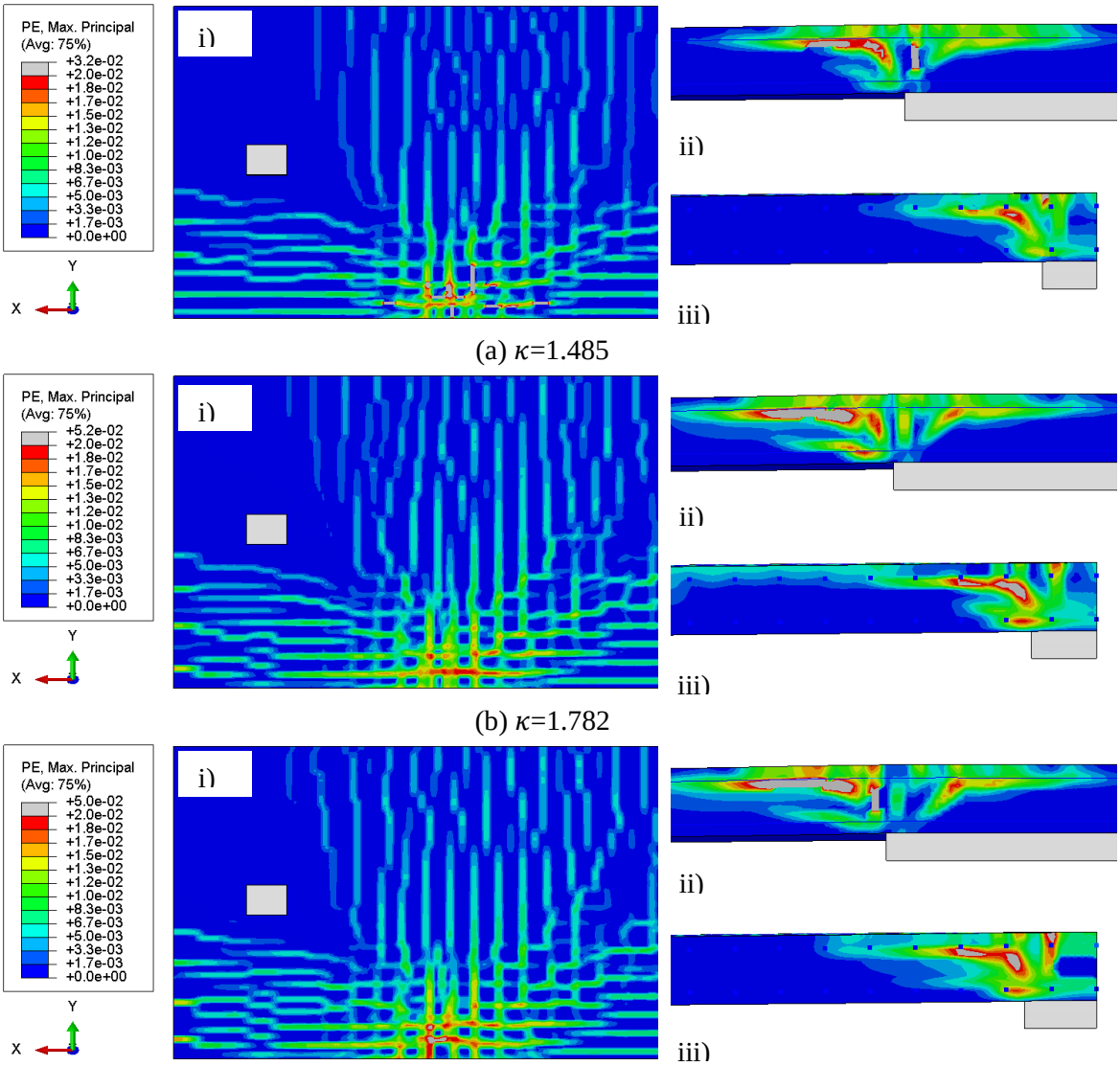


Figure B-3: Predicted Crack Pattern Near Wall Toe, (a) κ = 1.485, (b) κ = 1.782, (c) κ = 1.980, i) Tension Surface, ii) Slab Side Surface Parallel to Long Side of Wall, iii) Slab Side Parallel to Short Side of Wall, Equal Load Plate Loading (Entire Isolated Slab-Wall Specimen not Shown)

Uniformly Distributed Loading (UDL) Results and Comparison to Equal Load Plate Models

The predicted load-displacement responses perpendicular to the long side of the wall (X-Wall Corner and X-Wall CL) and perpendicular to the short side of the wall (Y-Wall CL, see Figure 6-4 for location of displacement output locations) for all 8 slab-wall connections (SWCs) subjected to uniformly distributed loading (UDL models) are provided in Figure B-4. As for rectangular slab-column connections (R-SCCs) [1], and isolated slab-wall connections (SWCs) subjected to equal load plate loads, the connection capacity and stiffness increased as κ increased. The stiffness increase in both directions at the wall toe (X-Wall Corner and Y-Wall CL) was larger than that at the wall centerline perpendicular to the long side of the wall (X-Wall CL). The stiffness increase in the direction perpendicular to the short side of the wall (Y-Wall CL) was the largest, which is also consistent with the R-SCCs results [1]. Additionally, the stiffness was higher perpendicular to the short side of the wall, which is also consistent with the R-SCCs results [1].

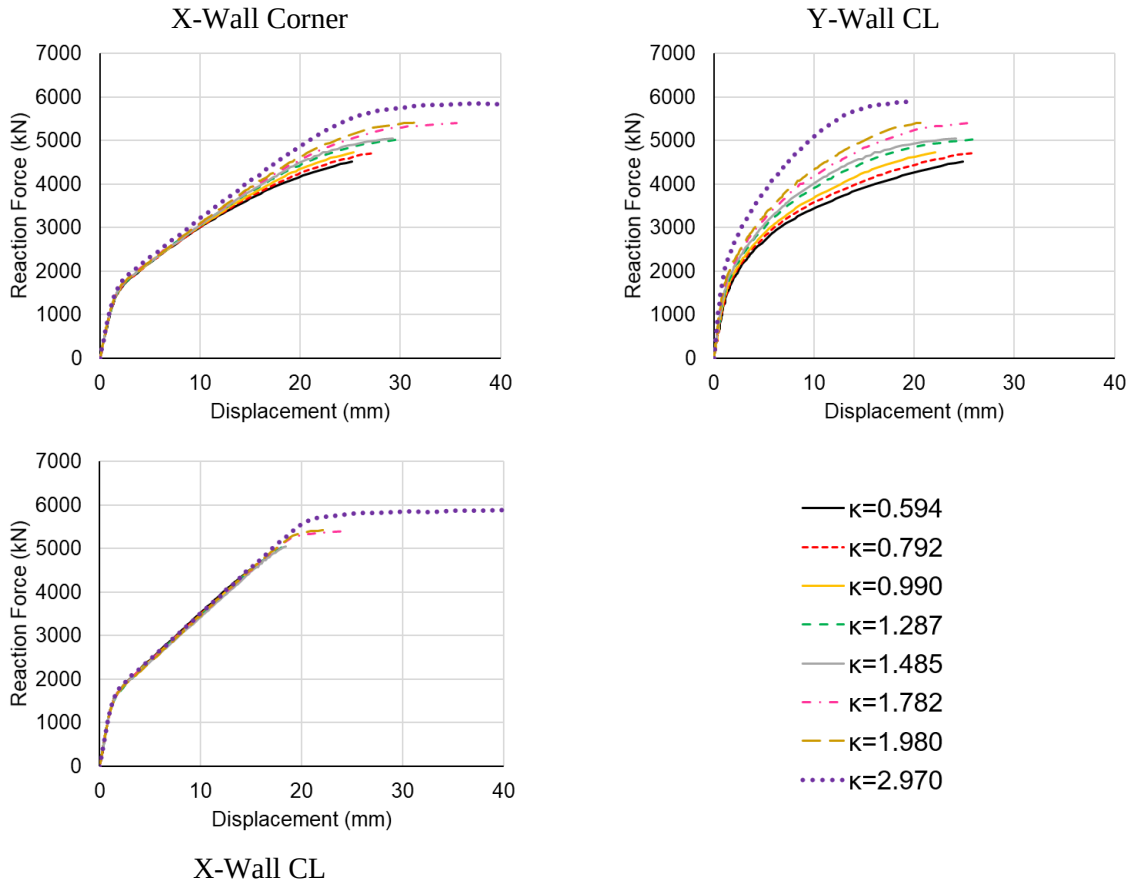


Figure B-4: Predicted Load-Displacement Responses at Selected Locations (see Figure 6-4), Uniformly Distributed Loading (UDL), all κ Values

The punching capacities predicted by the FEA for the equal load plate and uniformly distributed loading cases are compared in Table B-1. Consistent with the results of the load type study, presented in subsection 6.4.1.1, the predicted capacities for the specimens subjected to uniformly distributed loading (UDL) are significantly higher than those which were loaded using a finite number of equally loaded plates.

The loading type also has an impact on the predicted failure mode as seen in Table B-1. All 8 specimens were predicted to fail via punching when the concentric load was applied through equally loaded plates. When subjected to uniformly distributed loading beyond *d/2* from the wall face all connections where κ was less than or equal to 1.782 were predicted to fail in punching. The isolated SWC where κ equalled 1.980 was predicted to simultaneously fail in punching and one-way shear parallel to the long side of the wall, and the connection where κ equalled 2.970, was predicted to fail in one-way shear parallel to the long side of the wall.

Table B-1: Comparison of Predicted Capacities for Analyzed Slab-Wall Connections for Different Load Conditions

κ	Wall Parameters (mm)			V_{FEA} (kN)		V_{ACI} (kN)	
(c_{min}/d)	Thickness	Length	Aspect Ratio, β	Equal Load Plates	UDL	Punching Shear	One-way Shear
0.594	120	13620	113.5	2595.3	4518.2	6601.7	
0.792	160	13660	85.4	2699.9	4715.2	6676.9	
0.990	200	13700	68.5	2729.8	4731.3	6752.3	
1.287	260	13760	52.9	2764.1	5020.9	6865.8	3781.7[(a)]
1.485	300	13800	46.0	2869.9	5052.7	6941.7	938.0[(b)]
1.782	360	13860	38.5	3148.5	5405.0	7056.0	
1.980	400	13900	34.8	3316.0	5429.3[(c)]	7132.4	
2.970	600	14100	23.5	3727.4	5885.0[(d)]	7517.3	

[(a)] Assuming one-way failure along the long side of the wall (matches FEA predictions)
[(b)] Assuming one-way failure along the short side of the wall
[(c)] Simultaneous punching and one-way shear failure parallel to the long side predicted by FEA
[(d)] One-way shear failure parallel to the long side predicted by FEA

For the specimens which were predicted to fail in punching, the predicted capacities from the UDL models are approximately 75% higher than those from the equal load plate models. For the connections predicted to fail in one-way shear, the predicted capacities for the UDL models are approximately 60% higher. It should be noted that the punching capacities predicted by ACI 318-19 are higher than those from the UDL model as shown in Table B-1.

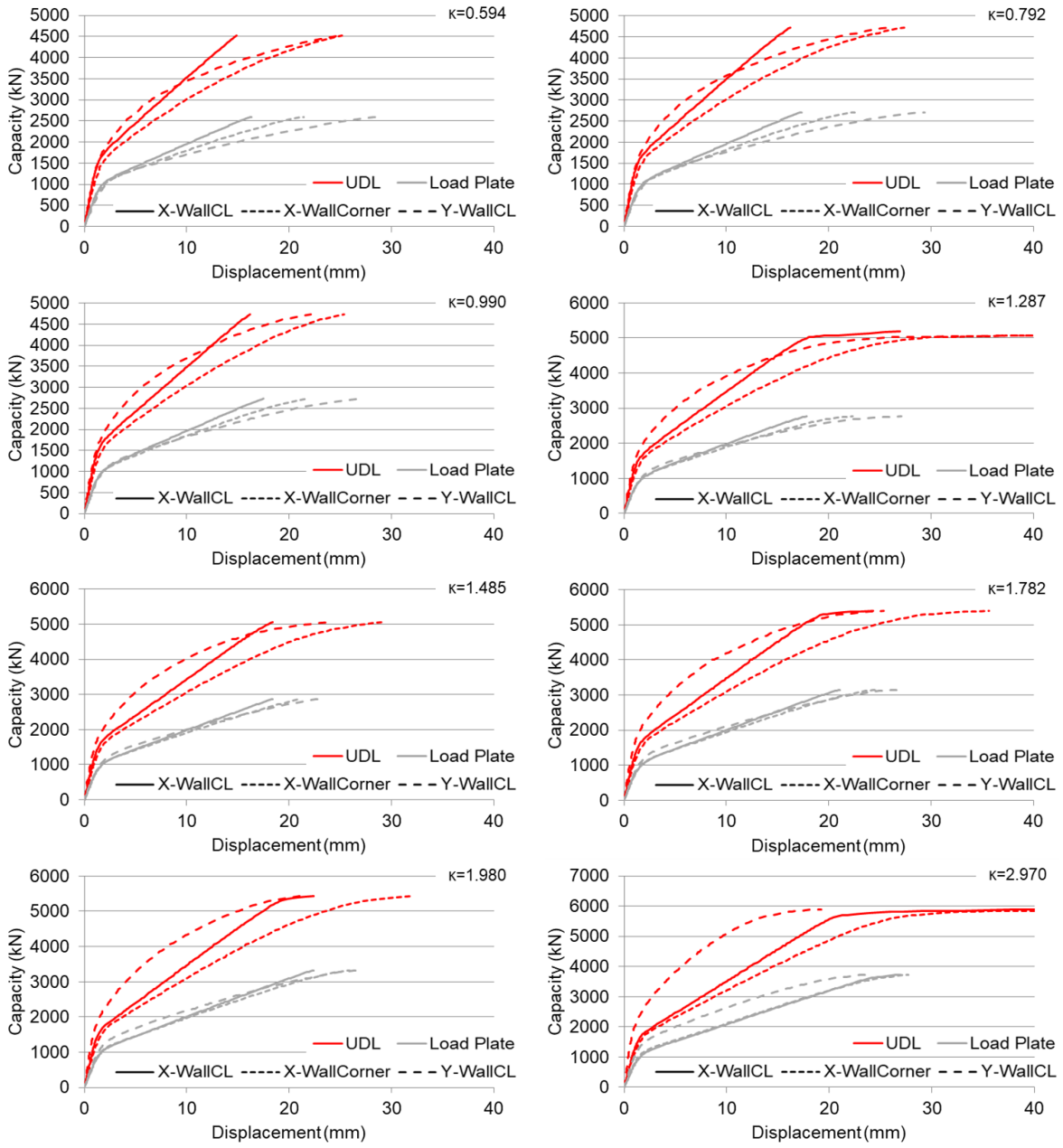


Figure B-5: Comparison of Predicted Load-Displacement Response at Chosen Locations (see Figure 6-4) from Equal Load Plate and UDL Models

A comparison of the predicted load-displacement responses at the chosen output locations for the UDL and equal load plate models for all 8 slab-wall specimens is provided in Figure B-5. For the UDL models the predicted response perpendicular to the short side of the wall (Y-Wall CL) is always stiffer than the predicted response perpendicular to the long side of the wall (X-Wall Corner and X-

Wall CL). This is consistent with the rectangular column results [1] (note the R-SCCs were loaded through equally loaded plates). For the equal load plate models the response perpendicular to the short side of the wall is not always the stiffest, though this is likely due to the assumed load plate locations.

The predicted crack patterns near the end of the wall for the UDL models are provided in Figure B-6, Figure B-7, and Figure B-8 (note, the crack patterns for the equal load plate models were previously provided in Figure 6-16, Figure 6-19, Figure B-2 and Figure B-3). On the tension surface of the slab a concentration of cracking near the wall toe is predicted. Cracks which are perpendicular to the long and short sides of the wall originate from this region of high cracking near the wall toe and extend the towards the edges of the isolated specimen. As κ increases, the extent of the crack concentration near the wall toe increases, and the one-way shear cracks parallel to the long side of the wall become larger and denser.

The trends in the internal cracking perpendicular to the short side of the wall are consistent with those from the rectangular column study [1]. As κ increases, the punching cone perpendicular to the short side of the wall thins and becomes more inclined. This change shows that one-way shear parallel to the long side of the wall is becoming more dominant. For the connections which are predicted to fail in punching, a punching cone is also observed perpendicular to the long side of the wall near the end of the wall.

The tension surface crack patterns from the equal load plate and UDL models are similar with some differences. Firstly, the cracks perpendicular to the long side of the wall at the wall toe extend to the slab edge in the equal load plate models, but do not in the models under UDL. Additionally, the cracks parallel to the long side of the wall extending from the wall centerline are present across more of the slab width in the load plate models compared to the UDL models. Both of these differences are likely caused by the load plates being at the edge of the slab, which causes more bending of the slab, due to the increased moment arm of the resultant force, compared to that from the UDL.

The overall trends in the internal crack patterns perpendicular to the short and long sides of the wall are similar for both load cases. The only difference occurs for the connections where κ equals 1.980 and 2.970 subjected to uniformly distributed loading. For these large connections, significant one-way shear cracking along the long side of the wall is predicted in the UDL models.

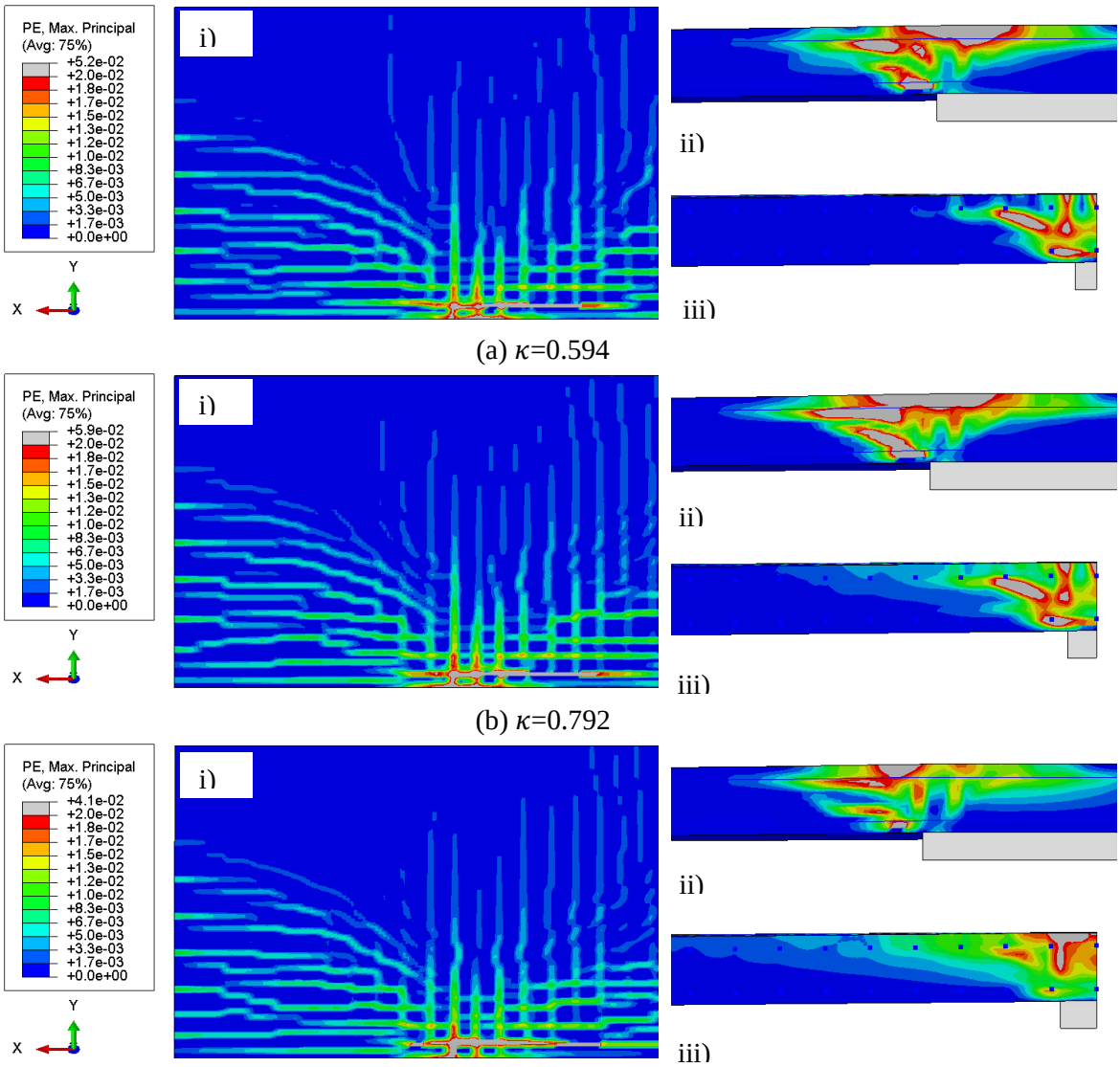


Figure B-6: Predicted Crack Pattern Near Wall Toe, (a) κ = 0.594, (b) κ = 0.792, (c) κ = 0.990, i) Tension Surface, ii) Slab Side Surface Parallel to Long Side of Wall, iii) Slab Side Parallel to Short Side of Wall, UDL (Entire Isolated Slab-Wall Specimen not Shown)

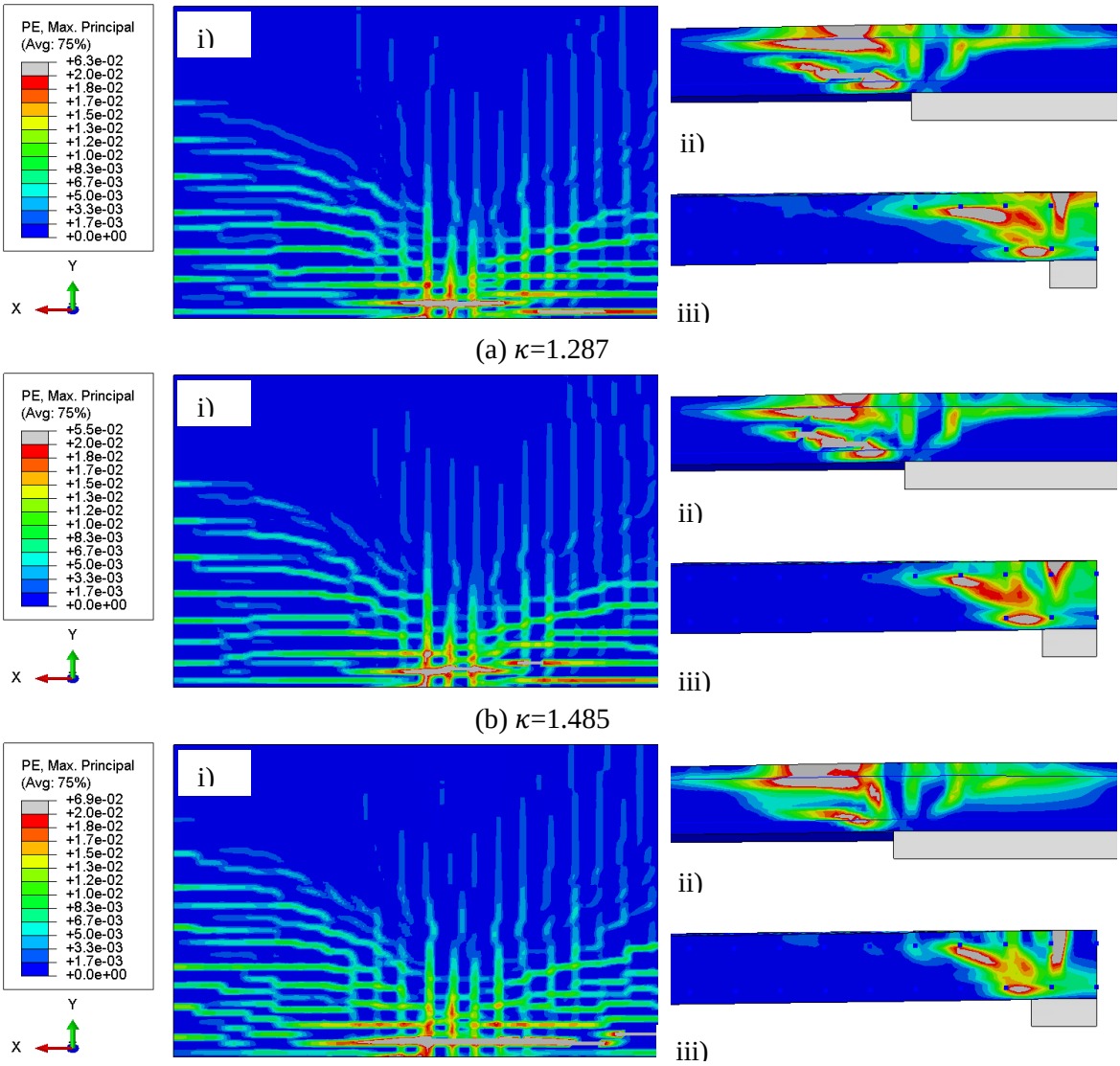


Figure B-7: Predicted Crack Pattern Near Wall Toe, (a) κ = 1.287, (b) κ = 1.485, (c) κ = 1.782, i) Tension Surface, ii) Slab Side Surface Parallel to Long Side of Wall, iii) Slab Side Parallel to Short Side of Wall, UDL (Entire Isolated Slab-Wall Specimen not Shown)

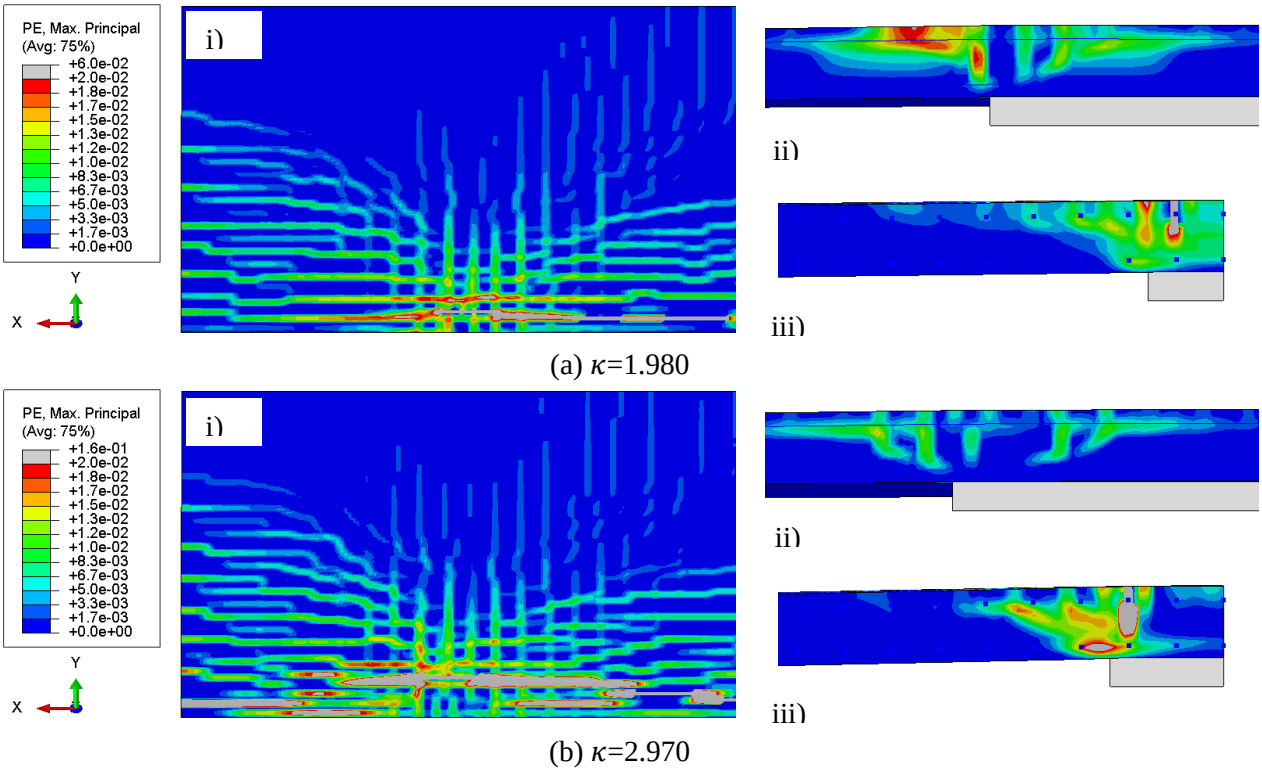


Figure B-8: Predicted Crack Pattern Near Wall Toe, (a) κ = 1.980, (b) κ = 2.970, i) Tension Surface, ii) Slab Side Surface Parallel to Long Side of Wall, iii) Slab Side Parallel to Short Side of Wall, UDL (Entire Isolated Slab-Wall Specimen not Shown)

The shear stress distributions along the wall perimeter at the peak load predicted by the FEA for the 8 SWCs when subjected to UDL are provided in Figure B-9 (note, the methodology used to calculate the shear stress distributions from the FEA results is discussed in Appendix A). As observed in the equal load plate simulations, the overall shape and magnitude of the predicted shear stress distributions are similar for all κ values. Along the long side of the connection, the shear stress magnitudes decrease rapidly with increasing distance from the end of the wall, before increasing slightly towards an approximately constant value along the remainder of the wall. However, unlike the equal load plate models, where the shear stress magnitude in the low stress region was approximately 0, the shear stress magnitude in this region is higher in the UDL models (though still slightly lower than that in the constant stress region). Also, as shown in Figure B-10 (which is representative of all the trend for all κ values), the shear stress magnitudes are typically higher in the UDL models than those in the equal load plate models. However, as shown in Figure B-11, the shear

stress magnitude at the intersection of the short and long sides of the wall, which is typically the peak shear stress magnitude along the wall perimeter, are similar for the two loading conditions. Therefore, it can be concluded that the equal load plate loading condition is an accurate representation of the behaviour of isolated SWCs.

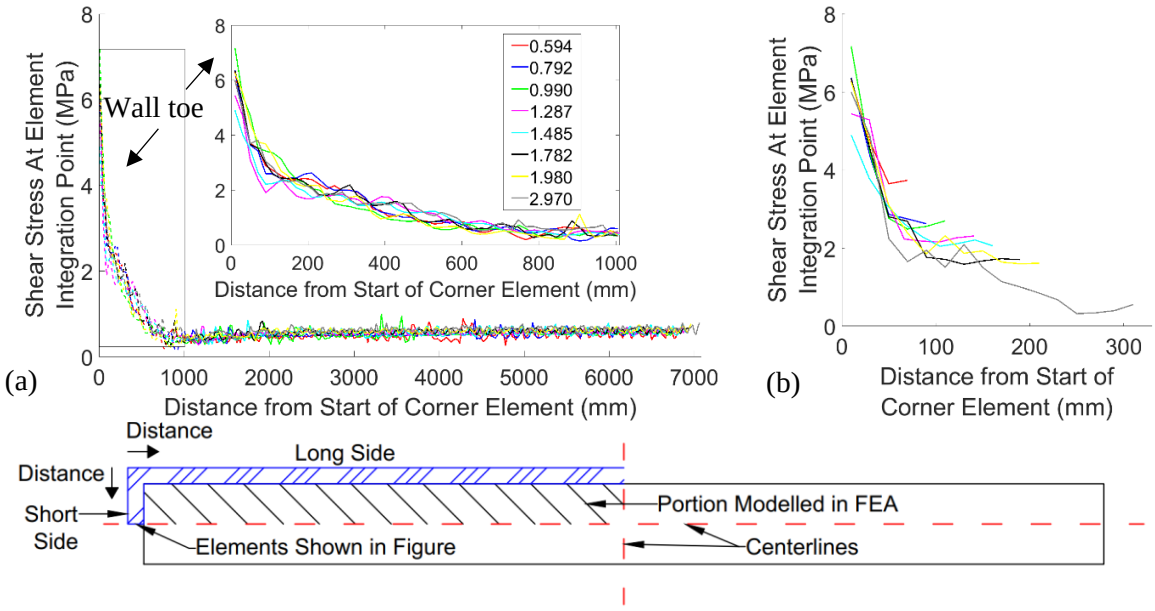


Figure B-9: Predicted Shear Stress Distribution Along Wall Perimeter, 100% of Peak Load, all *κ*; (a) Long Side, (b) Short Side (¼ of Wall Shown), UDL Models (Stresses Averaged Over Depth)

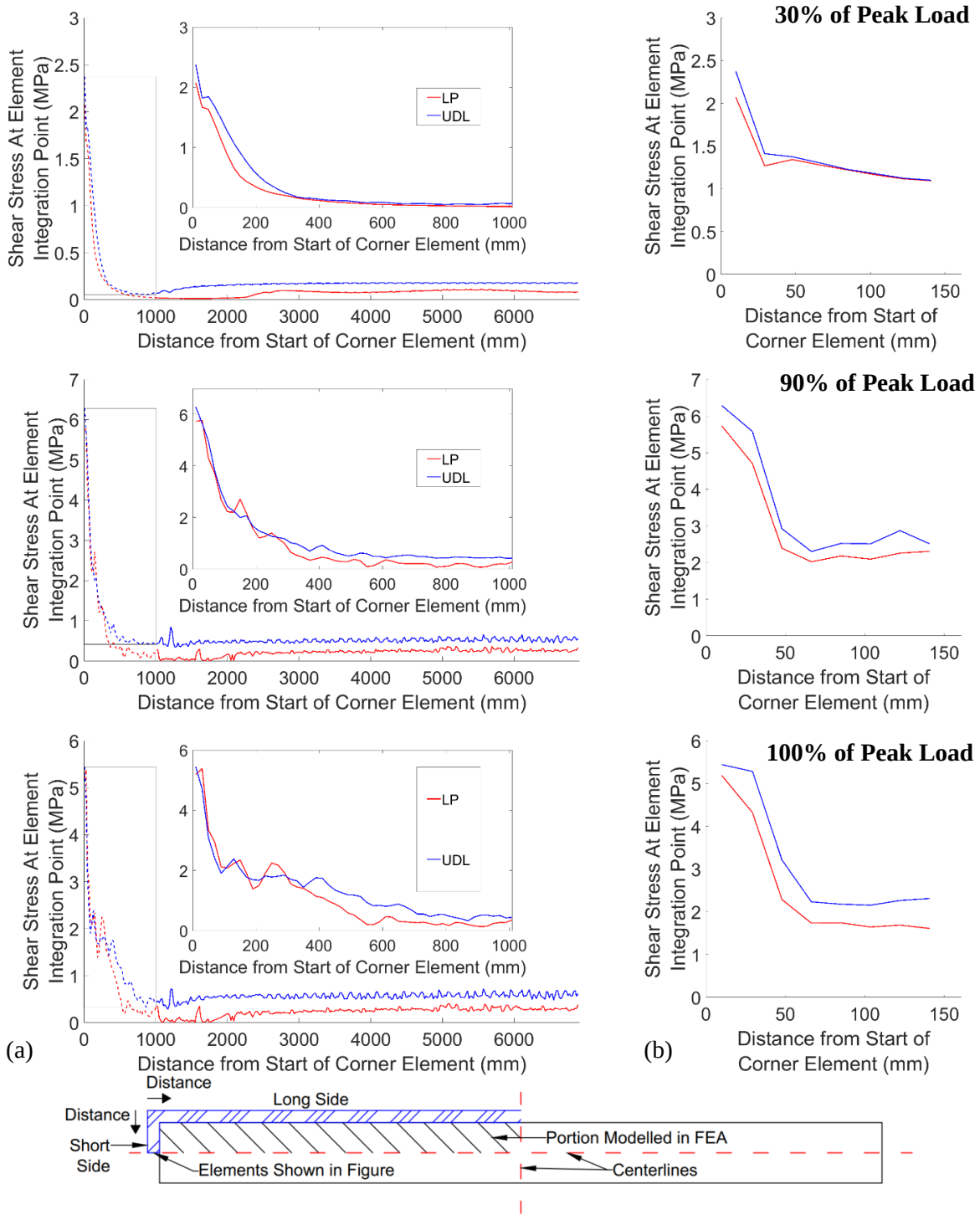


Figure B-10: Comparison of Predicted Shear Stress Distribution Along Wall Perimeter for UDL and Equal Load Plate Models, Various Load Levels, κ=1.287; (a) Long Side, (b) Short Side (¼ of Wall Shown, Stresses Averaged Over Depth)

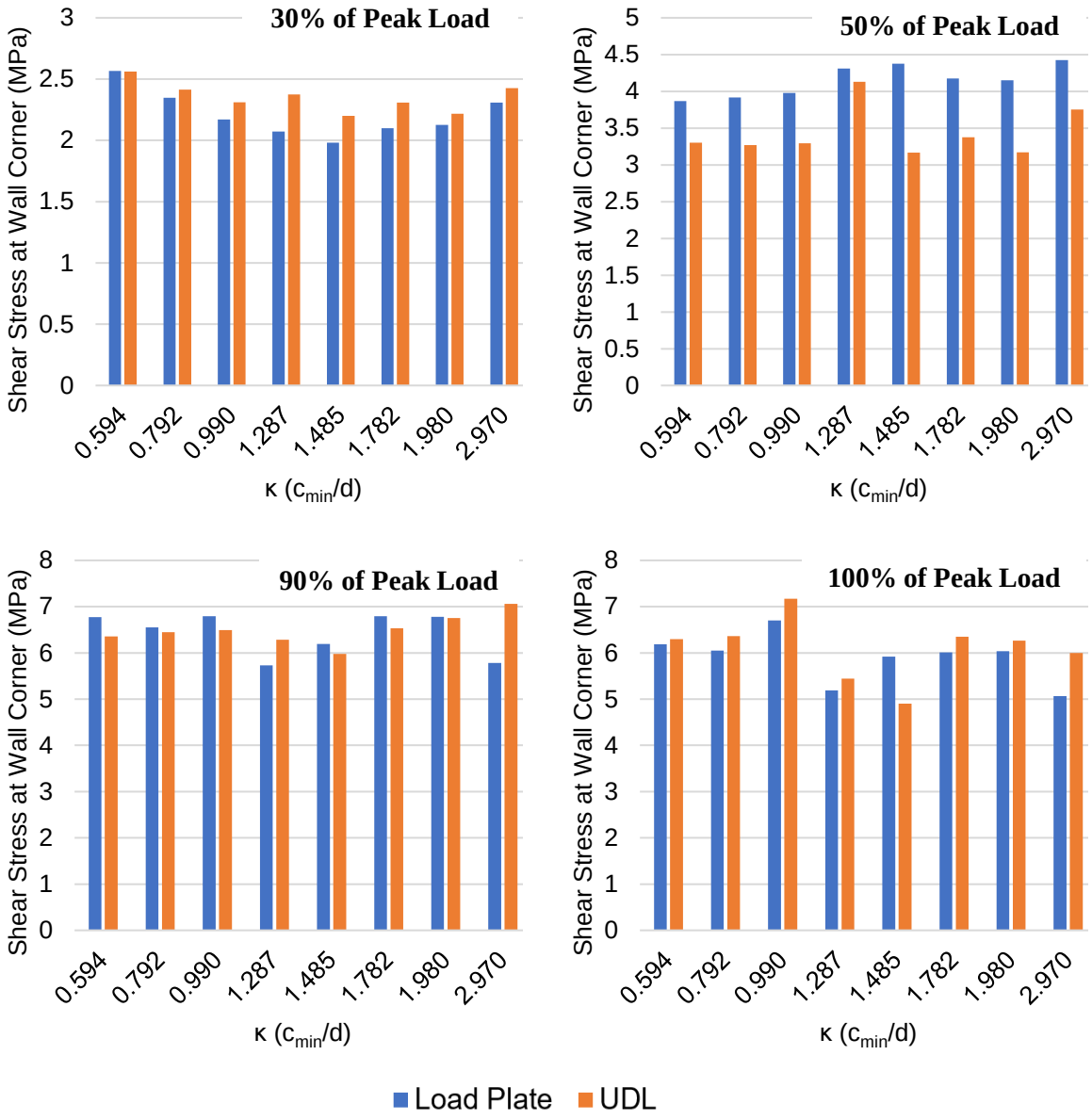


Figure B-11: Comparison of Shear Stress at the Corner of Supported Area for Equal Load Plate and UDL Loading, Multiple Load Levels, all *κ*

Additional Crack Patterns from Symmetric Opening Study (Concentric Loading, Section 6.4.3)

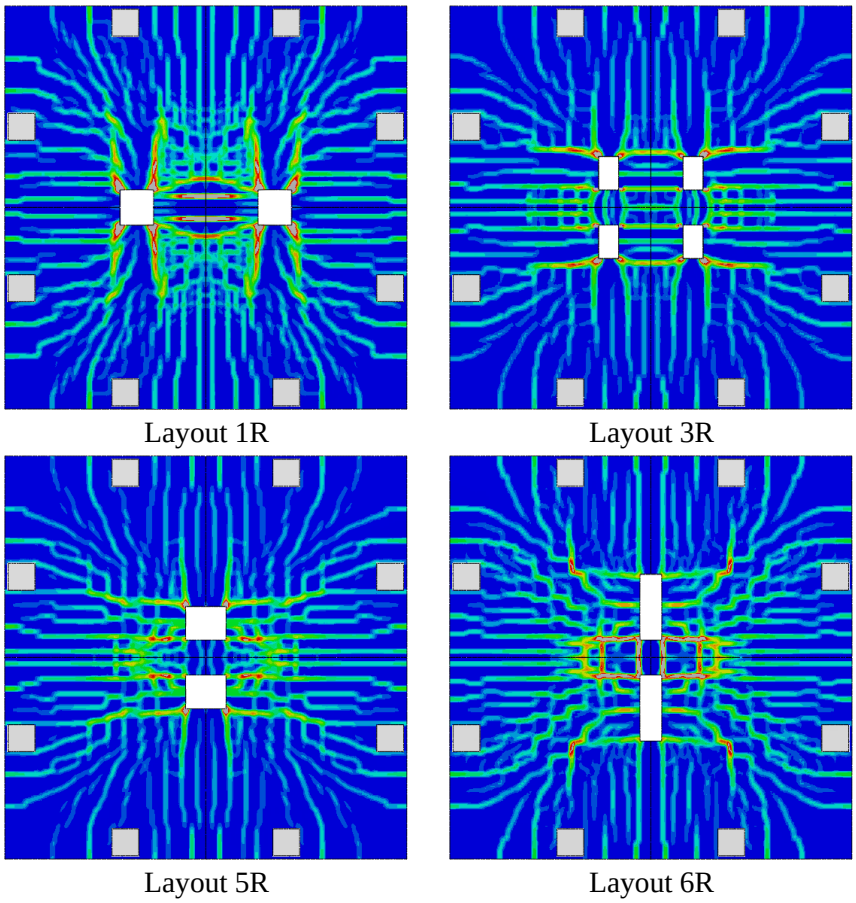


Figure B-12: Tension Surface Crack Patterns Around Remaining R-SCCs in Symmetric Opening Study

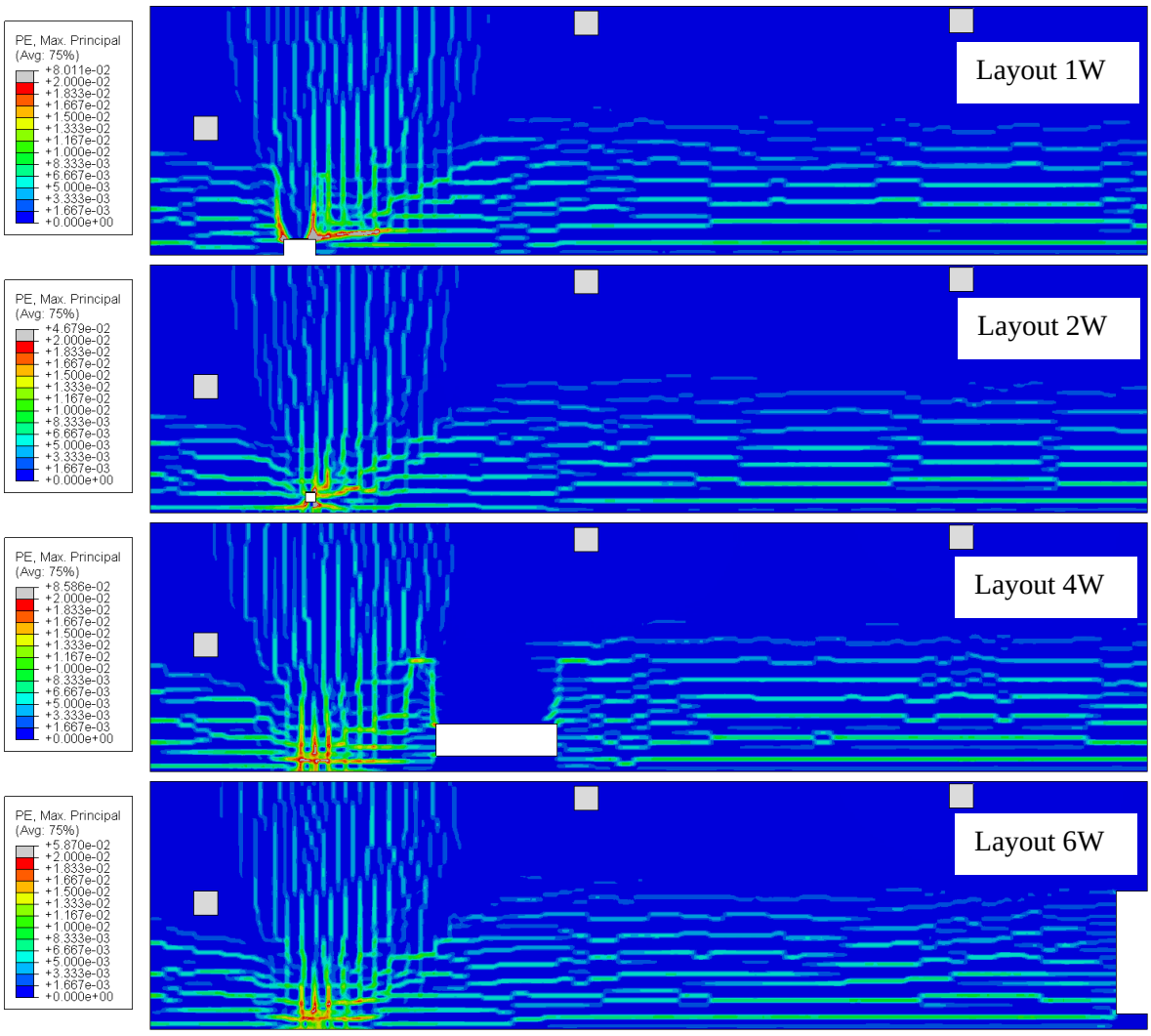


Figure B-13: Tension Surface Crack Patterns for Remaining SWCs in Symmetric Opening Study (¼ Model Shown)

Appendix C
Summary of Column Dimensions Considered in Parametric Study of Impact of Column Rectangularity on Punching Shear Conducted During Author's MASc Studies

In this appendix, the column sizes considered in the column rectangularity study conducted by the author during their MASc work [1] are summarized. These isolated square and rectangular slab-column connections were considered in the development of alternative design methods for rectangular slab-column connections (R-SCCs).

Table C-1: Summary of 77 Isolated-Slab Column Specimens Simulated During Author's MASc Work [1]

κ=0.594		
c_{min}	c_{max}	β
120	120	1
120	200	1.667
120	240	2
120	320	2.667
120	360	3
120	440	3.667
120	480	4
120	560	4.667
120	600	5
120	680	5.667
120	720	6
120	800	6.667
120	840	7
120	920	7.667
120	960	8
120	1040	8.667
120	1080	9
120	1160	9.667
120	1200	10

κ=0.792		
c_{min}	c_{max}	β
160	160	1
160	240	1.5
160	320	2
160	400	2.5
160	480	3
160	560	3.5
160	640	4
160	720	4.5
160	800	5
160	880	5.5
160	960	6
160	1040	6.5
160	1120	7
160	1200	7.5
160	1280	8

κ=0.990		
c_{min}	c_{max}	β
200	200	1
200	320	1.6
200	400	2
200	520	2.6
200	600	3
200	720	3.6
200	800	4
200	920	4.6
200	1000	5
200	1120	5.6
200	1200	6
200	1320	6.6

κ=1.287		
c_{min}	c_{max}	β
260	260	1.0
260	390	1.5
260	520	2.0
260	640	2.462
260	780	3.0
260	920	3.538
260	1040	4.0
260	1160	4.462
260	1320	5.077

κ=1.485		
c_{min}	c_{max}	β
300	300	1.0
300	450	1.5
300	600	2.0
300	760	2.533
300	920	3.067
300	1040	3.467
300	1200	4.00

κ=1.782		
c_{min}	c_{max}	β
360	360	1.000
360	540	1.500
360	720	2.000
360	920	2.556
360	1080	3.000
360	1280	3.556

κ=1.980		
c_{min}	c_{max}	β
400	400	1.000
400	600	1.500
400	800	2.000
400	1000	2.500
400	1200	3.000

κ=2.970		
c_{min}	c_{max}	β
600	600	1.000
600	920	1.533
600	1200	2.000

All dimensions are given in mm

Appendix D

Details of Selected Experimental Specimens Which Failed in Punching Considered in Development of Alternative Design Methods for Rectangular Slab-Column Connections

In this appendix, the relevant details of all 86 experimental specimens which failed in punching and were considered in the development of the alternative punching shear design methods for rectangular slab-column connections, which were summarized in Table 7-2, are provided. The table in this appendix is taken from the manuscript related to the alternate punching shear design methods for rectangular slab-column connections, which has been submitted for publication.

Table D-1: Detailed of Selected Databank Specimens Without Shear Reinforcement Which Failed in Punching and are Supported on Square or Rectangular Columns (86 Specimens)

Reference	Specimen ID	c_{min} (mm)	c_{max} (mm)	κ	β	d (mm)	f_c' (MPa)	V_{exp} (kN)
[3]	2	203.2	406.4	1.73	2.00	117.3	26.3	351.4
	3	152.4	457.2	1.30	3.00	117.3	32.0	333.2
	4	114.3	495.3	0.97	4.33	117.3	31.0	330.5
	5	152.4	457.2	1.30	3.00	117.3	26.9	355.0
	7	152.4	457.2	1.30	3.00	117.3	25.9	319.8
	8	114.3	495.3	0.95	4.33	120.7	26.1	314.5
	9	152.4	304.8	1.26	2.00	120.7	29.5	315.4
[146]	L1b	120	120	1.11	1.00	108	59	322.4
	L1c	120	120	1.12	1.00	107	59	318
	L2b	120	240	1.13	2.00	106	58	361
	L2c	120	240	1.12	2.00	107	57	330.8
	L3b	120	360	1.12	3.00	107	60	400
	L3c	120	360	1.13	3.00	106	54	357.6
	L4b	120	480	1.13	4.00	106	54	395
	L4c	120	480	1.12	4.00	107	56	404
	L5b	120	600	1.11	5.00	108	67	426.4
	L5c	120	600	1.10	5.00	109	63	446.4
[155]	14R	75	100	0.95	1.33	79	31	154
	15R	100	150	1.27	1.50	79	30.8	172
	19R	100	150	1.27	1.50	79	29	170
[147]	OC11	200	200	1.90	1.00	105.3	36.01	423
	OC13	200	600	1.86	3.00	107.3	35.81	568
	OC15	200	1000	1.95	5.00	102.8	40.15	649
[150]	1	100	500	1.25	5.00	80	25.7[(a)]	163
	2	100	500	1.25	5.00	80	25.2[(a)]	209
	3	100	500	1.25	5.00	80	23.0[(a)]	189
	4	300	300	3.75	1.00	80	23.9[(a)]	242
[47]	A7	254	254	2.22	1.00	114.5	28.5	400
	A8	356	356	3.11	1.00	114.5	21.9	436
	A2a	254	254	2.22	1.00	114.5	13.7	334
	A2b	254	254	2.22	1.00	114.5	19.5	400
	A2c	254	254	2.22	1.00	114.5	37.4	467
	A7b	254	254	2.22	1.00	114.5	27.9	512
	A5	356	356	3.11	1.00	114.5	27.8	534
[334]	AL1	150	170	1.50	1.13	100	42	300
	AL2	150	170	1.47	1.13	102	44	380
	AL3	150	170	1.50	1.13	100	41	340
	AL4	150	170	1.58	1.13	95	47	310
[335]	10	25	300	0.24	12.00	104	17.6	186
	11	140	540	1.25	3.86	112	17.6	279
	12	140	340	1.30	2.43	108	17.6	265
[336]	1	85	85	1.00	1.00	85	52	185
	2	85	255	0.99	3.00	86	52	226
	3	85	425	1.00	5.00	85	50	239
[337]	L1A	85	85	0.95	1.00	89.3	41.3	188.5

	L1B	85	85	0.87	1.00	98.1	41.4	172
	L2B	85	255	0.94	3.00	90.5	42	194.5
[338]	L1a	85	85	1.31	1.00	65	51.2	123
	L1b	85	85	1.31	1.00	65	51.2	122
[339]	L1	85	85	0.98	1.00	87	39.4	224
	L2	85	255	0.97	3.00	87.5	39.8	241
	L3	85	425	0.98	5.00	86.5	40.9	294
[340]	L1	250	250	2.66	1.00	94	29	375
	L2	230	270	2.47	1.17	93	29	390
	L3	215	285	2.29	1.33	94	29	375
	L4	200	300	2.22	1.50	90	29	395
	L5	165	335	1.81	2.03	91	22	385
	L6	125	375	1.37	3.00	91	22	350
	L7	110	390	1.21	3.55	91	22	300
	L8	100	400	1.06	4.00	94	22	275
[341]	L42	200	400	1.44	2.00	139	43.2	657
	L42a	200	400	1.22	2.00	164	36.2	693
	L45	200	600	1.30	3.00	154	42	798
	L46	200	800	1.22	4.00	164	39.3	911
	L41	150	250	1.08	1.67	139	44.7	563
	L41a	150	250	0.91	1.67	164	38.9	600
	L43	150	450	0.91	3.00	164	38.7	726
	L44	150	600	0.91	4.00	164	40	761
[151]	AM04	260	780	1.29	3.00	202	44.6	1067
[52]	2S1-1	76.2	76.2	2.00	1.00	38.1	45.6	42.9
	3S1-2	114.3	114.3	3.00	1.00	38.1	46.6	46.6
	4S1-3	152.4	152.4	4.00	1.00	38.1	47.6	51.3
	6S1-5	228.6	228.6	6.00	1.00	38.1	48.6	78.3
	8S1-6	304.8	304.8	8.00	1.00	38.1	49.6	90.2
	2S2-7	76.2	76.2	2.00	1.00	38.1	50.6	49.5
	4S2-8	152.4	152.4	4.00	1.00	38.1	51.6	69.1
	8S2-10	304.8	304.8	8.00	1.00	38.1	52.6	114.1
	6S2-14	228.6	228.6	6.00	1.00	38.1	53.6	80.1
[342]	Pm 1/1-1.5	160	160	1.62	1.00	99	27.2	260.0
	Pd 1/1-1.5	320	320	3.23	1.00	99	32.8	360.0
	P 1/2-1.5	133	267	1.46	2.01	91	22.3	252.0
	P 1/3-1.5	100	300	1.09	3.00	92	20.5	220.0
	P 1/4-1.5	80	320	0.87	4.00	92	18.3	210.0
[343]	II-3	201	402	2.45	2.00	82	14.7[(a)]	244.0
[43]	R1	152	457	1.33	3.01	114.3	27.6	394.0
[344]	II/3	229	432	2.86	1.89	80	17.4[(a)]	245.0

[(a)] $f'c$ estimated as cube strength divided by 1.15; Note: $f'c$: concrete compressive strength, d: effective slab depth, β: column aspect ratio, $\kappa=c_{min}/d$: ratio of minimum column dimension to effective slab depth

Appendix E

Supplemental Comparisons of Shear Stress Distribution Predicted by NLFEA And Method 2 for Rectangular Columns

In this appendix, comparisons of the shear stress distributions around rectangular columns assumed in Method 2 to that predicted by the NLFEA (at the peak load) for the remaining seven κ values are provided. These plots are supplemental to those provided in Figure 7-12 and demonstrate the adequacy of the assumed shear stress distribution for all κ values. Note, the methodology used to calculate the shear stress distributions from the FEA results is discussed in Appendix A.

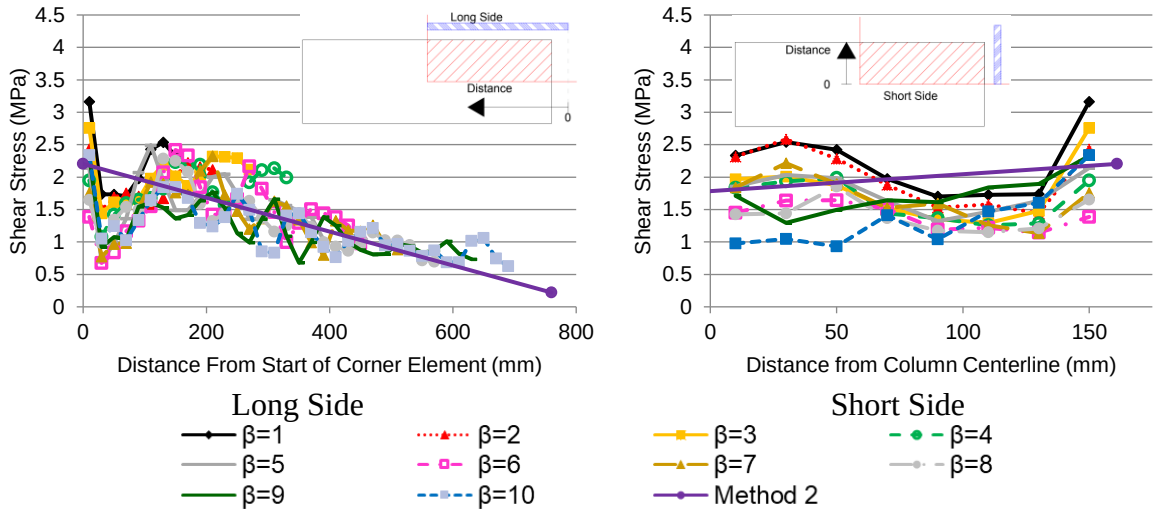


Figure E-1: Critical Perimeter Shear Stress Distribution Predicted by NLFEA and Method 2 (Assumed Distribution in Purple), κ = 0.594, Rectangular Column (¼ Column Shown, Stresses Averaged Over Depth)

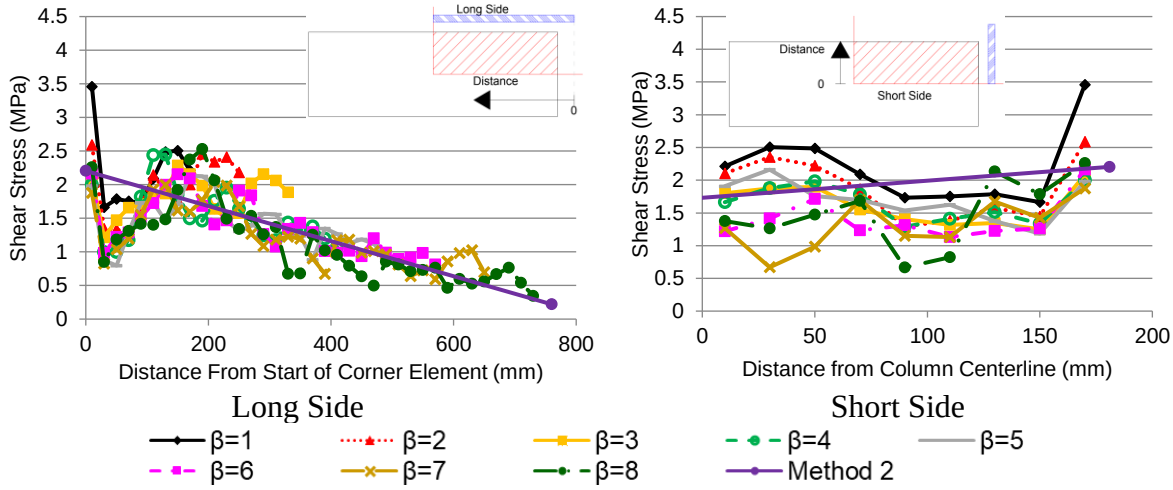


Figure E-2: Critical Perimeter Shear Stress Distribution Predicted by NLFEA and Method 2 (Assumed Distribution in Purple), κ = 0.792, Rectangular Column (¼ Column Shown, Stresses Averaged Over Depth)

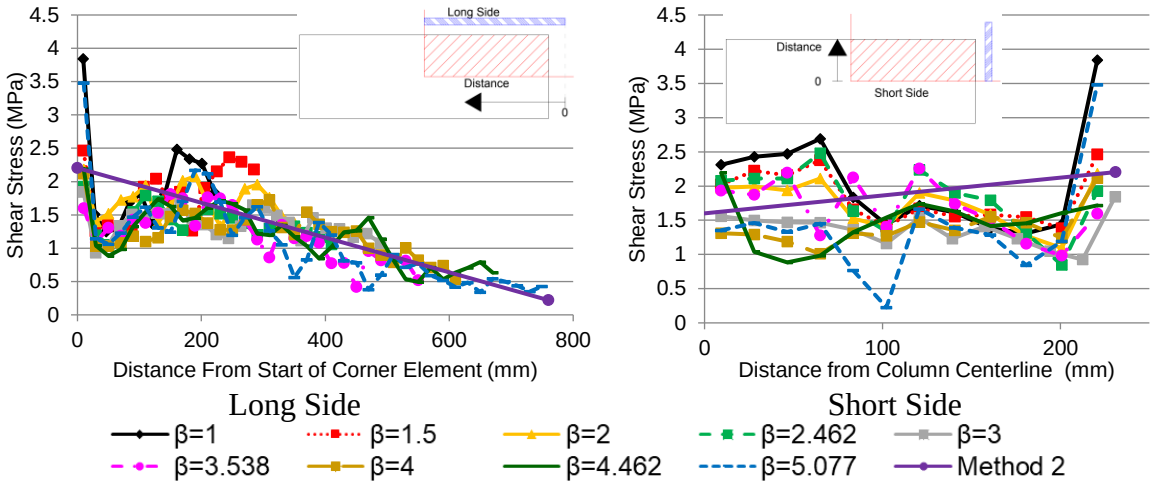


Figure E-3: Critical Perimeter Shear Stress Distribution Predicted by NLFEA and Method 2 (Assumed Distribution in Purple), κ = 1.287, Rectangular Column (¼ Column Shown, Stresses Averaged Over Depth)

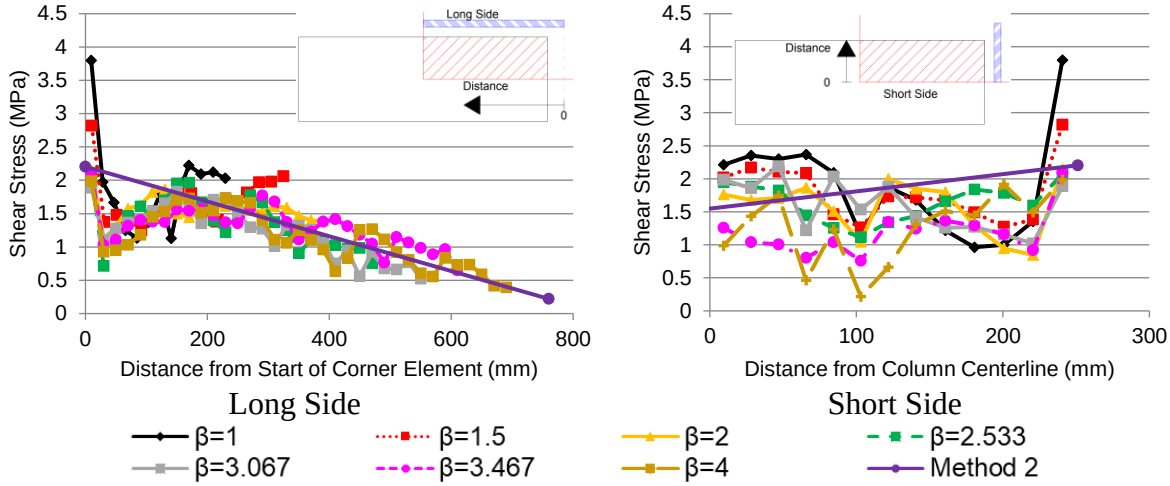


Figure E-4: Critical Perimeter Shear Stress Distribution Predicted by NLFEA and Method 2 (Assumed Distribution in Purple), κ = 1.485, Rectangular Column (¼ Column Shown, Stresses Averaged Over Depth)

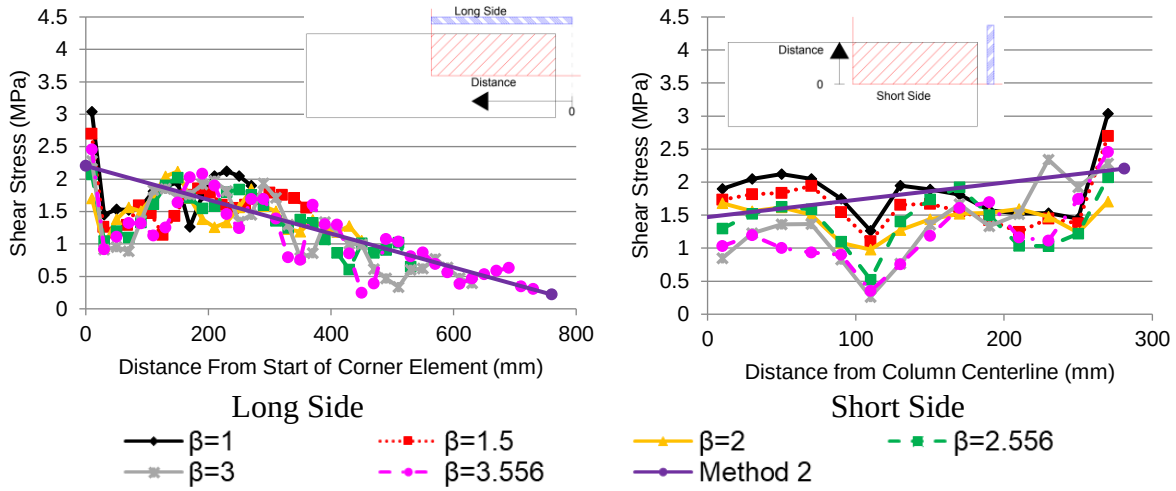


Figure E-5: Critical Perimeter Shear Stress Distribution Predicted by NLFEA and Method 2 (Assumed Distribution in Purple), κ = 1.782, Rectangular Column (¼ Column Shown, Stresses Averaged Over Depth)

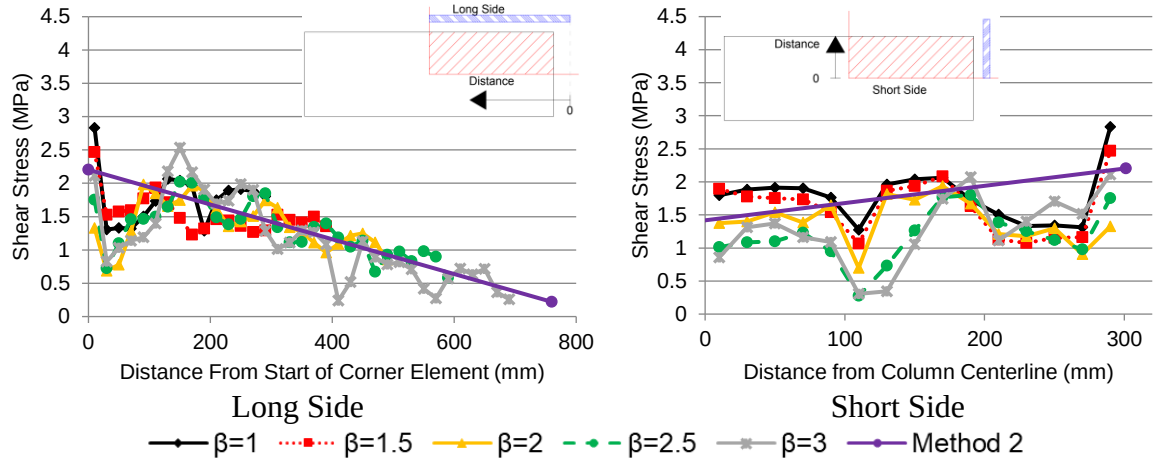


Figure E-6: Critical Perimeter Shear Stress Distribution Predicted by NLFEA and Method 2 (Assumed Distribution in Purple), κ = 1.980, Rectangular Column (¼ Column Shown, Stresses Averaged Over Depth)

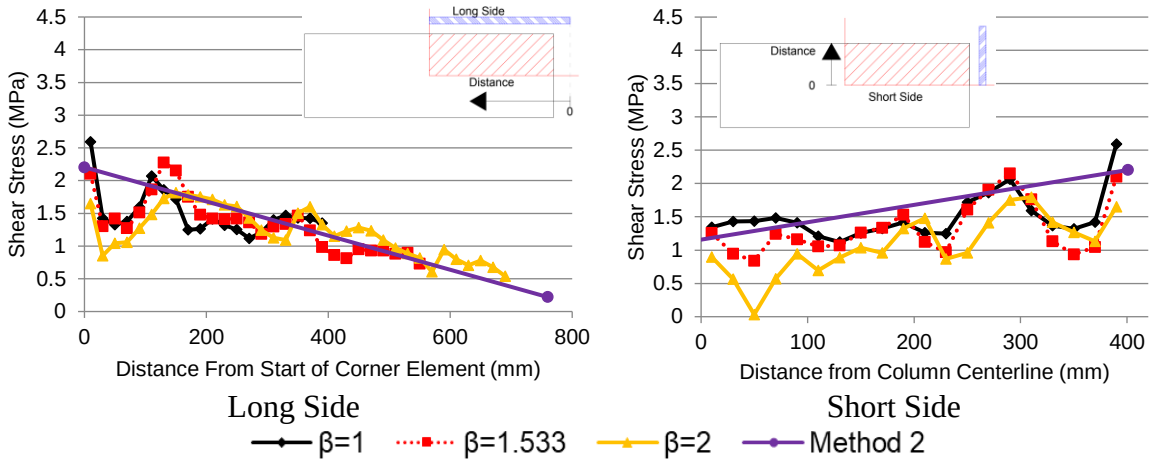
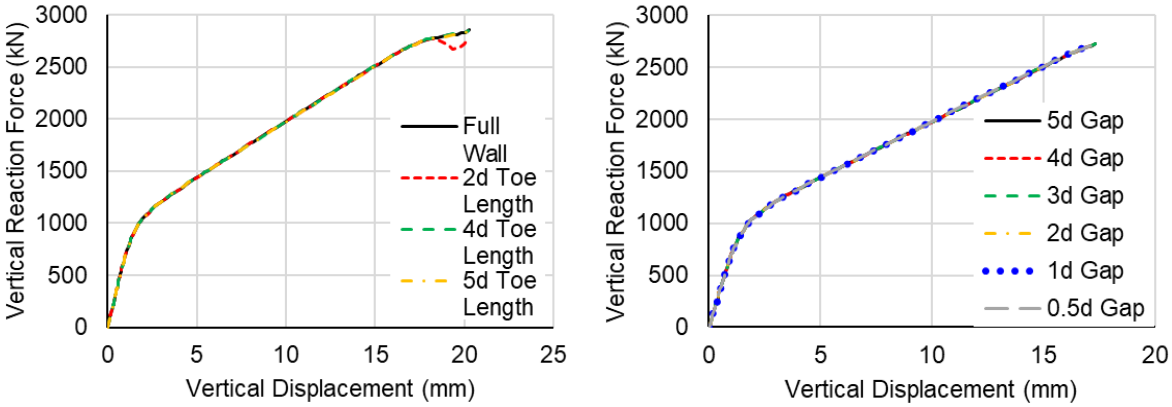


Figure E-7: Critical Perimeter Shear Stress Distribution Predicted by NLFEA and Method 2 (Assumed Distribution in Purple), κ = 2.970, Rectangular Column (¼ Column Shown, Stresses Averaged Over Depth)

Appendix F

Additional Load-Displacement Responses, Crack Patterns and Shear Stress Distributions from Parametric Study Using Proposed Cut-Wall Model

In this appendix, the additional figures for the parametric study conducted using the proposed cut-wall model discussed in Section 7.2.5 are provided. Note, the methodology used to calculate the shear stress distributions from the FEA results is discussed in Appendix A.



Toe Length Study (Gap Length: *5d*, no Slab Opening)

Gap Length Study (Toe Length: *5d*, no Slab Opening)

Figure F-1: Comparison of Predicted Load-Displacement Response at Wall CL (X-Wall CL, see Figure 7-25 for Displacement Location) for toe and gap Length Studies, κ =1.287, Predicted Response cut off at Peak Load)

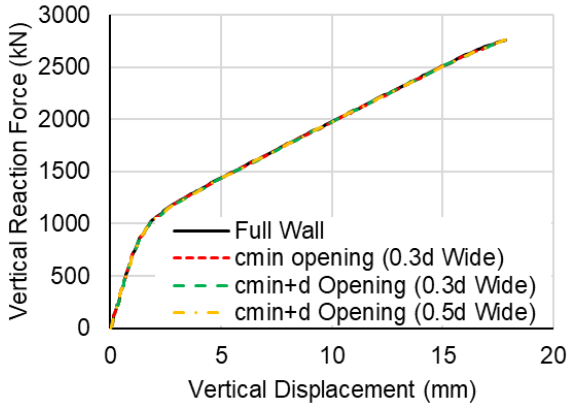


Figure F-2: Comparison of Predicted Load-Displacement Response at Wall CL (X-Wall CL, see Figure 7-25 for Displacement Location), Opening Size Study, κ = 1.287 (Toe Length Set to *5d*, Gap Length set to *2d*, Predicted Response cut off at Peak Load)

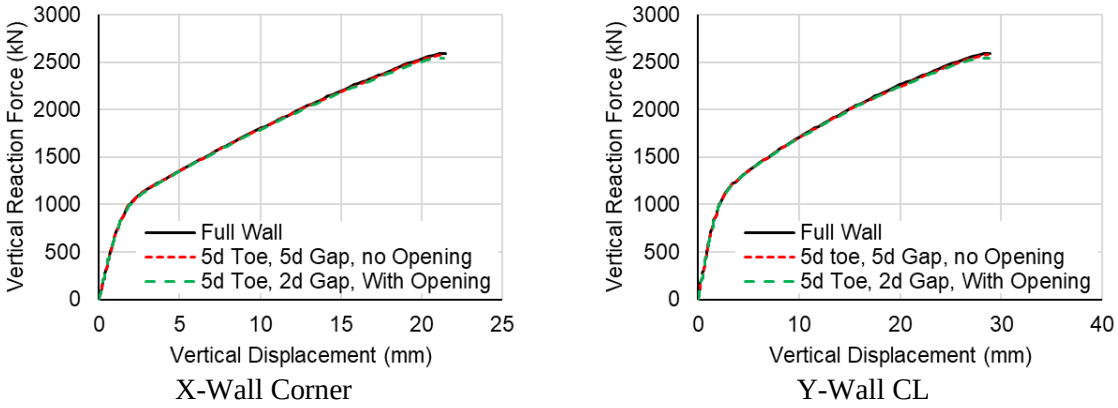


Figure F-3: Comparison of Predicted Load Displacement Response at Wall Toe from Full Wall, Original Cut-Wall Model (*5d* toe and gap Lengths, no Slab Opening) and Finalized Cut-Wall Model (*5d* toe, *2d* gap, c_{min}+*d* High and *0.5d* Slab Opening), κ = 0.594 (see Figure 6-4 and Figure 7-25 for Displacement Locations)

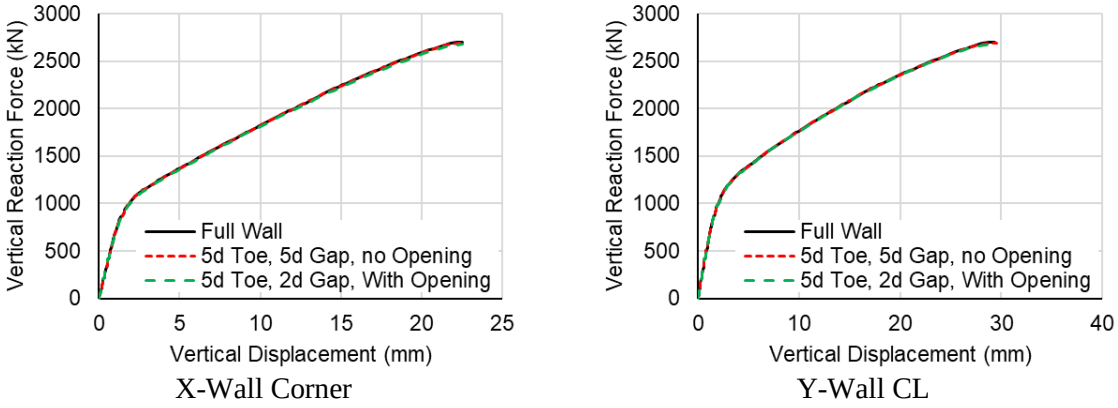


Figure F-4: Comparison of Predicted Load Displacement Response at Wall Toe from Full Wall, Original Cut-Wall Model (*5d* toe and gap Lengths, no Slab Opening) and Finalized Cut-Wall Model (*5d* toe, *2d* gap, c_{min}+*d* High and *0.5d* Slab Opening), κ = 0.792 (see Figure 6-4 and Figure 7-25 for Displacement Locations)

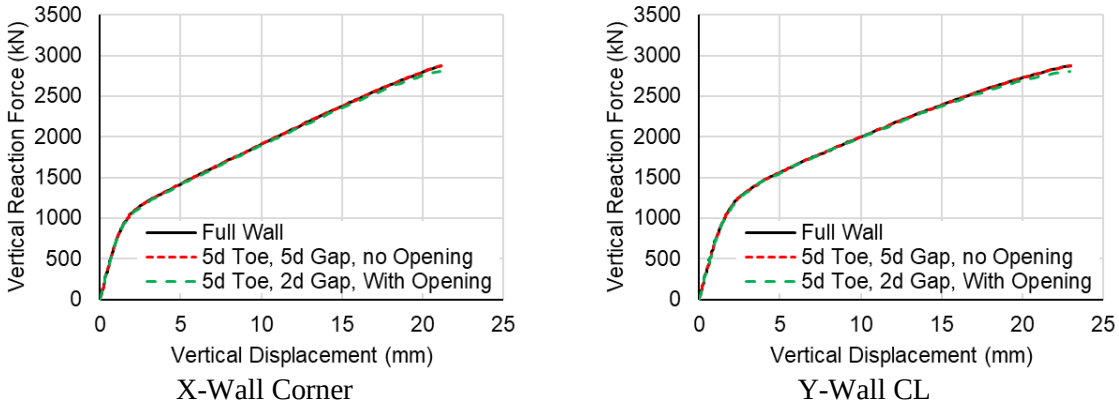


Figure F-5: Comparison of Predicted Load Displacement Response at Wall Toe from Full Wall, Original Cut-Wall Model (*5d* toe and gap Lengths, no Slab Opening) and Finalized Cut-Wall Model (*5d* toe, *2d* gap, c_{min}+*d* High and *0.5d* Slab Opening), κ = 1.485 (see Figure 6-4 and Figure 7-25 for Displacement Locations)

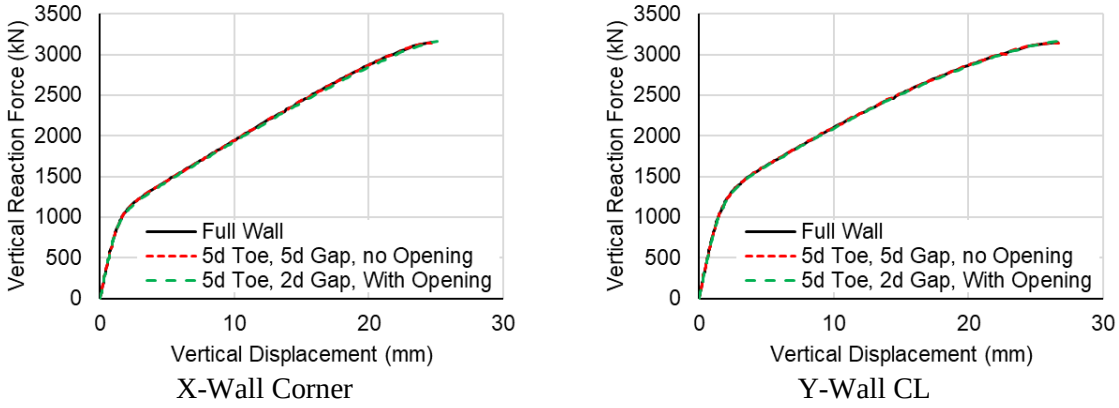


Figure F-6: Comparison of Predicted Load Displacement Response at Wall Toe from Full Wall, Original Cut-Wall Model (*5d* toe and gap Lengths, no Slab Opening) and Finalized Cut-Wall Model (*5d* toe, *2d* gap, c_{min}+*d* High and *0.5d* Slab Opening), κ = 1.782 (see Figure 6-4 and Figure 7-25 for Displacement Locations)

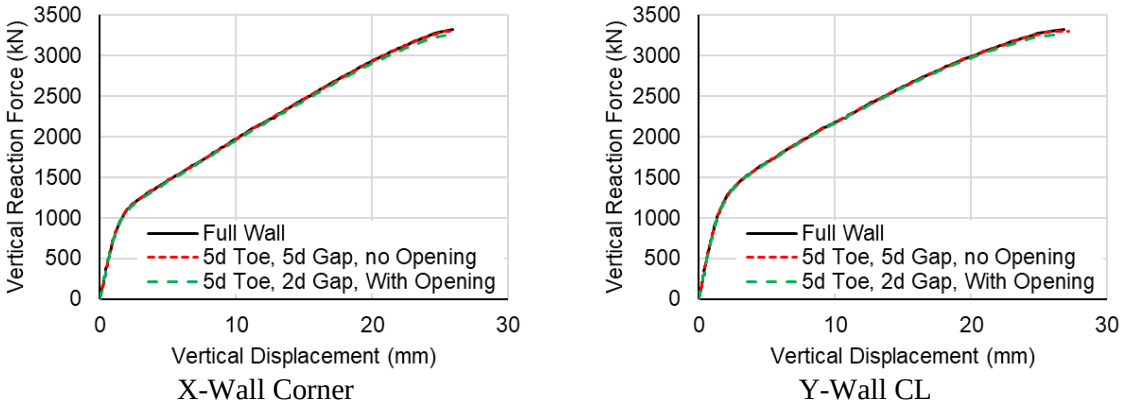


Figure F-7: Comparison of Predicted Load Displacement Response at Wall Toe from Full Wall, Original Cut-Wall Model (*5d* toe and gap Lengths, no Slab Opening) and Finalized Cut-Wall Model (*5d* toe, *2d* gap, c_{min}+*d* High and *0.5d* Slab Opening), κ = 1.980 (see Figure 6-4 and Figure 7-25 for Displacement Locations)

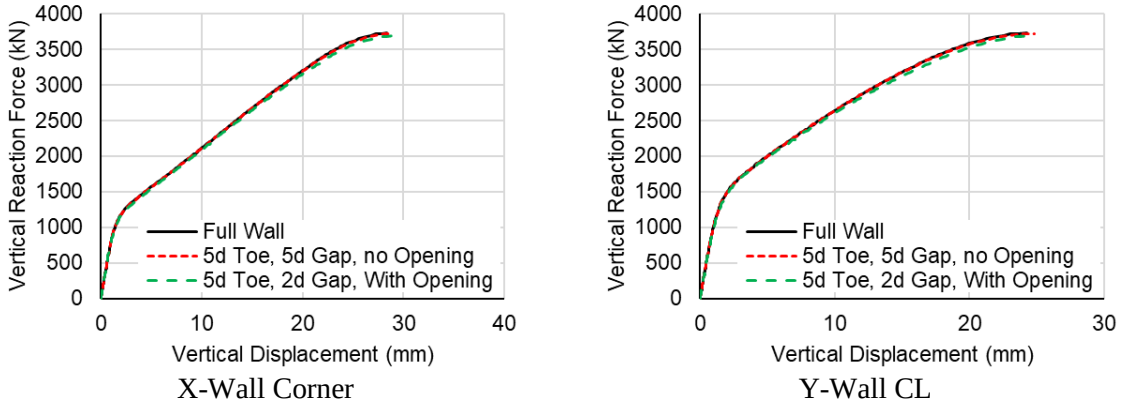


Figure F-8: Comparison of Predicted Load Displacement Response at Wall Toe from Full Wall, Original Cut-Wall Model (*5d* toe and gap Lengths, no Slab Opening) and Finalized Cut-Wall Model (*5d* toe, *2d* gap, c_{min}+*d* High and *0.5d* Slab Opening), κ = 2.970 (see Figure 6-4 and Figure 7-25 for Displacement Locations)

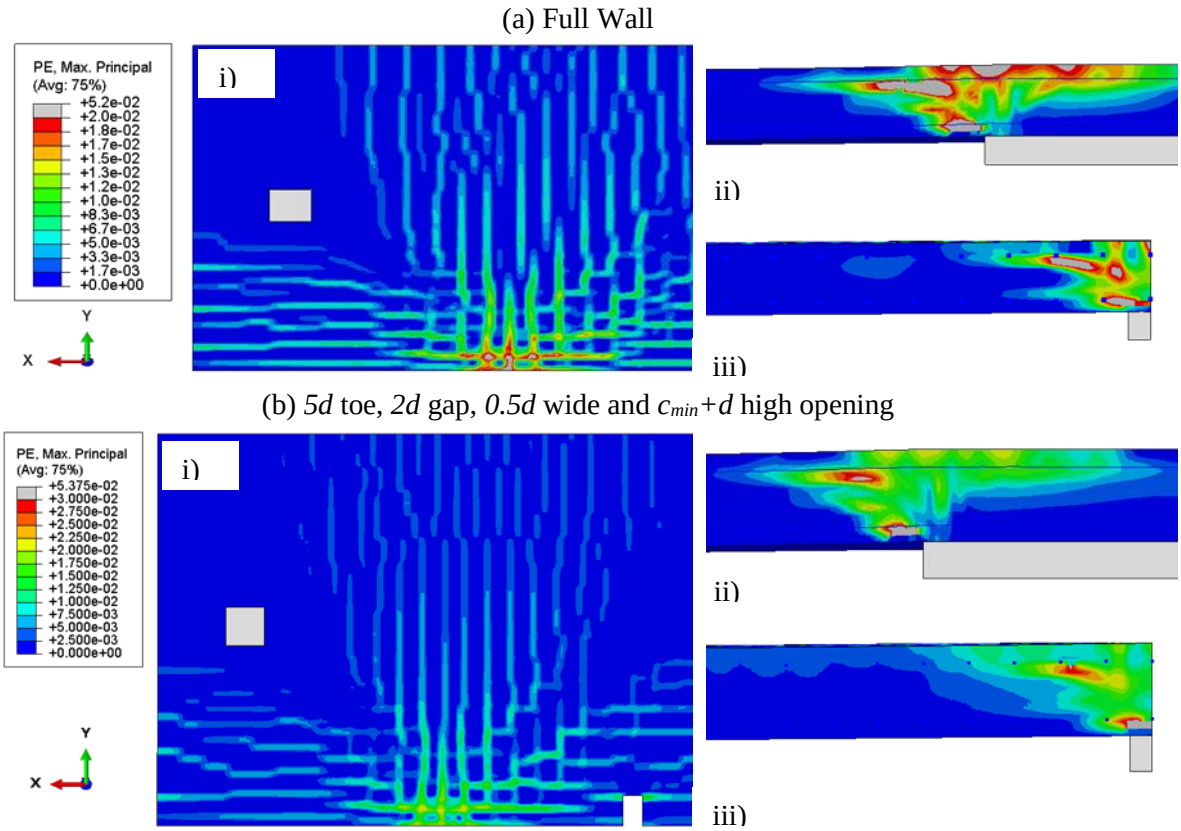
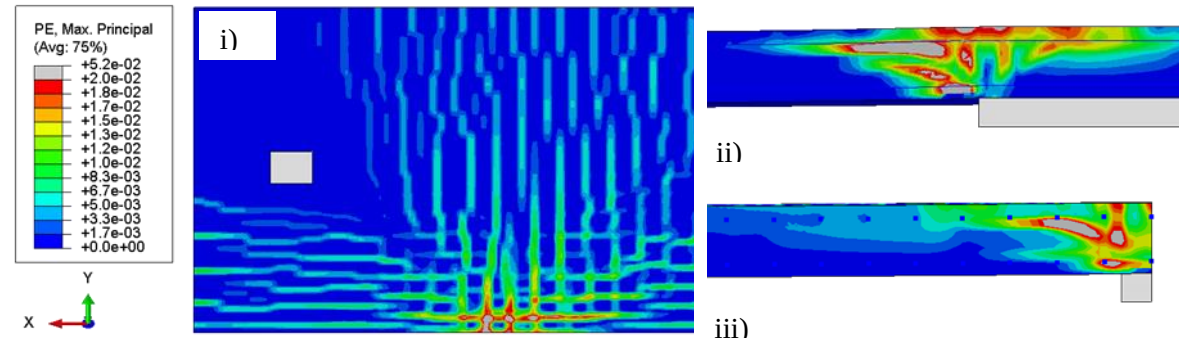
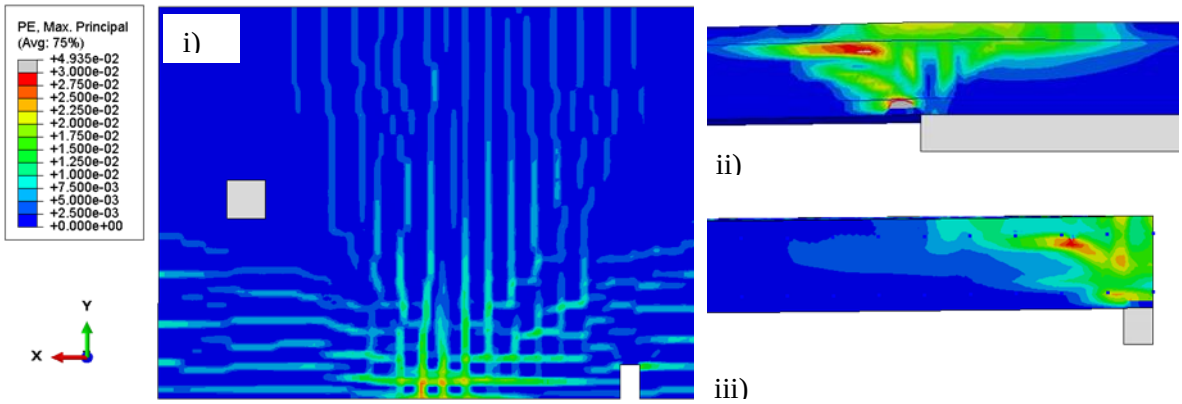


Figure F-9: Comparison of Crack Pattern From (a) Full Wall and (b) Finalized Cut-Wall Model, κ = 0.594, i) Tension Surface, ii) Slab Side Parallel to Long Side of Wall, iii) Slab Side Parallel to Short Side of Wall (Entire Isolated Slab-Wall Specimen not Shown

(a) Full Wall



(b) *5d* toe, *2d* gap, *0.5d* wide and c_{min}+*d* high opening



κ=0.792

Tension Surface Punching Cones on Slab Sides

Figure F-10: Comparison of Crack Pattern From (a) Full Wall and (b) Finalized Cut-Wall Model, κ = 0.792, i) Tension Surface, ii) Slab Side Parallel to Long Side of Wall, iii) Slab Side Parallel to Short Side of Wall (Entire Isolated Slab-Wall Specimen not Shown

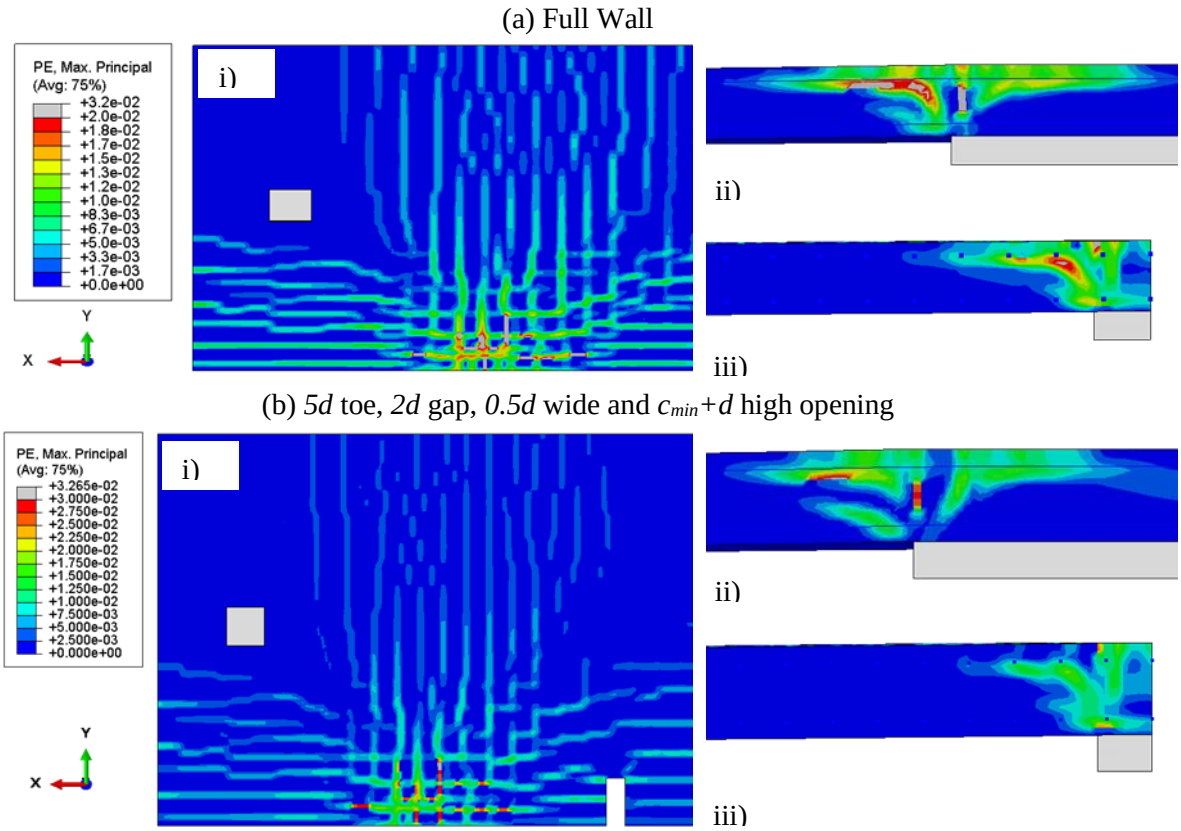
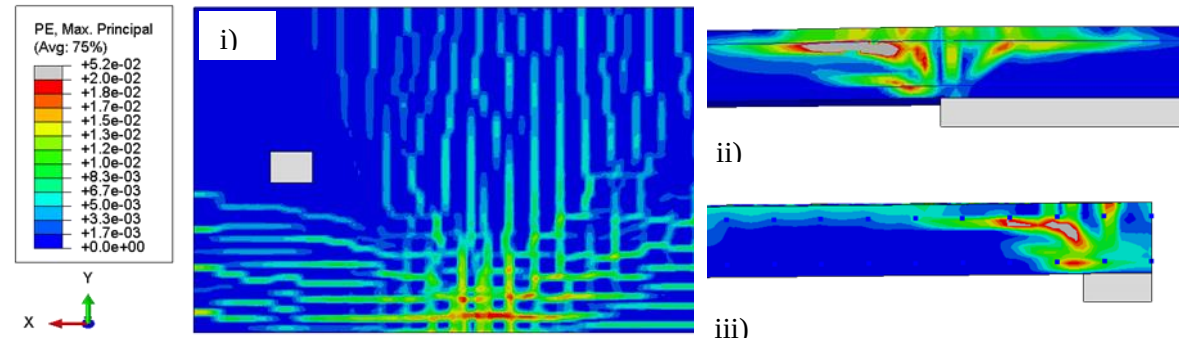
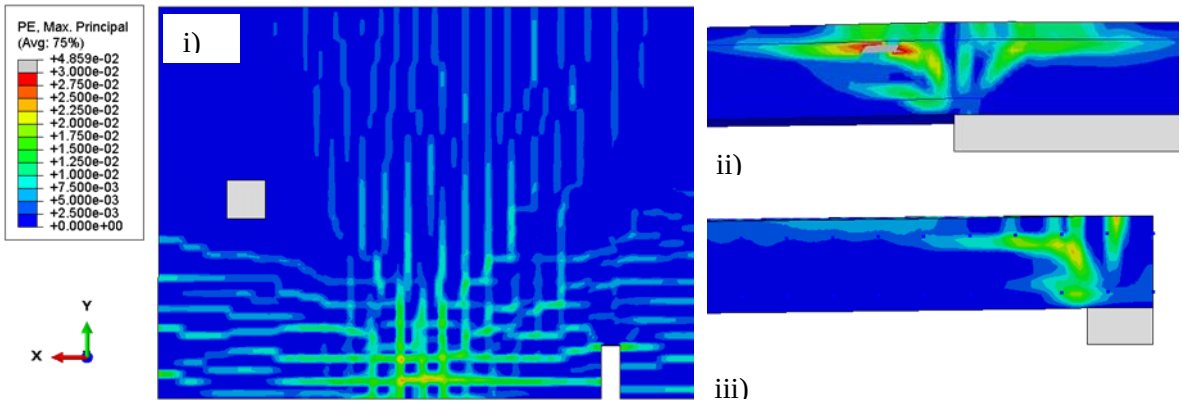


Figure F-11: Comparison of Crack Pattern From (a) Full Wall and (b) Finalized Cut-Wall Model, κ = 1.485, i) Tension Surface, ii) Slab Side Parallel to Long Side of Wall, iii) Slab Side Parallel to Short Side of Wall (Entire Isolated Slab-Wall Specimen not Shown

(a) Full Wall



(b) *5d* toe, *2d* gap, *0.5d* wide and c_{min}+*d* high opening



κ=1.782

Tension Surface Punching Cones on Slab Sides

Figure F-12: Comparison of Crack Pattern From (a) Full Wall and (b) Finalized Cut-Wall Model, κ = 1.782, i) Tension Surface, ii) Slab Side Parallel to Long Side of Wall, iii) Slab Side Parallel to Short Side of Wall (Entire Isolated Slab-Wall Specimen not Shown

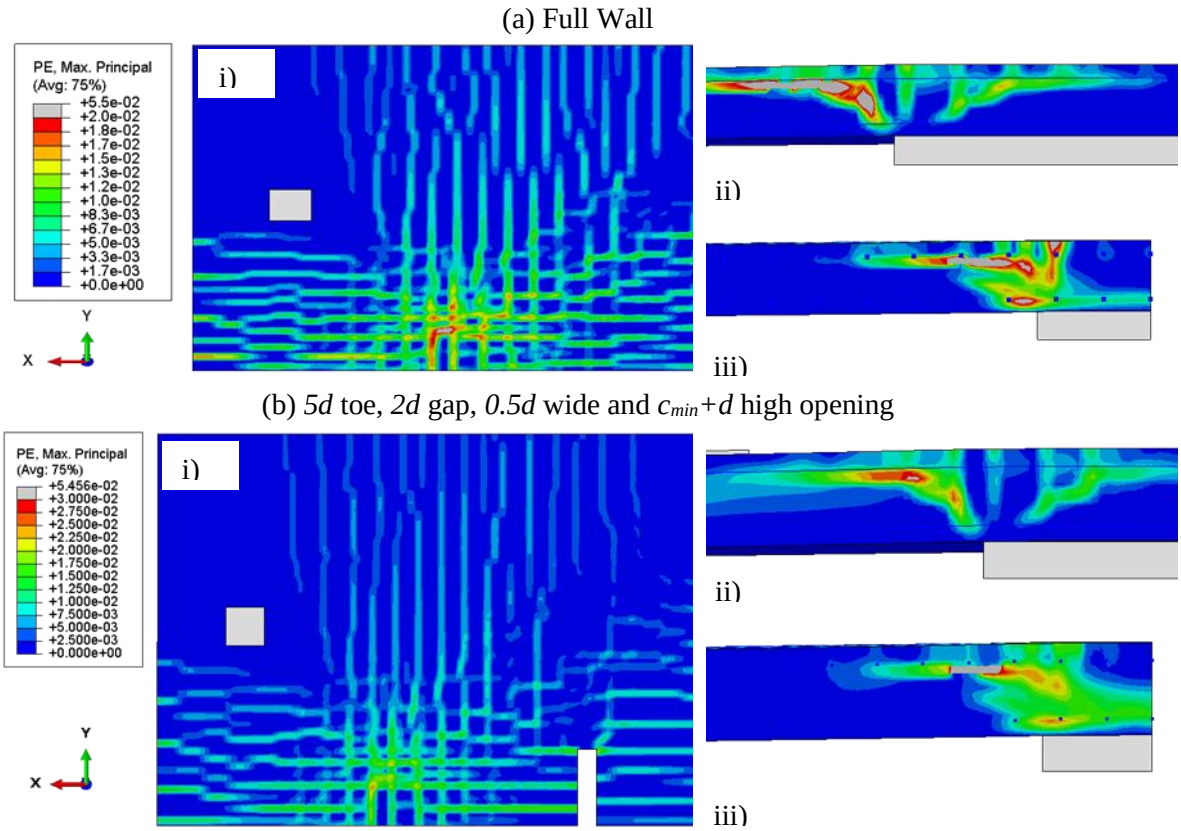


Figure F-13: Comparison of Crack Pattern From (a) Full Wall and (b) Finalized Cut-Wall Model, κ = 2.970, i) Tension Surface, ii) Slab Side Parallel to Long Side of Wall, iii) Slab Side Parallel to Short Side of Wall (Entire Isolated Slab-Wall Specimen not Shown

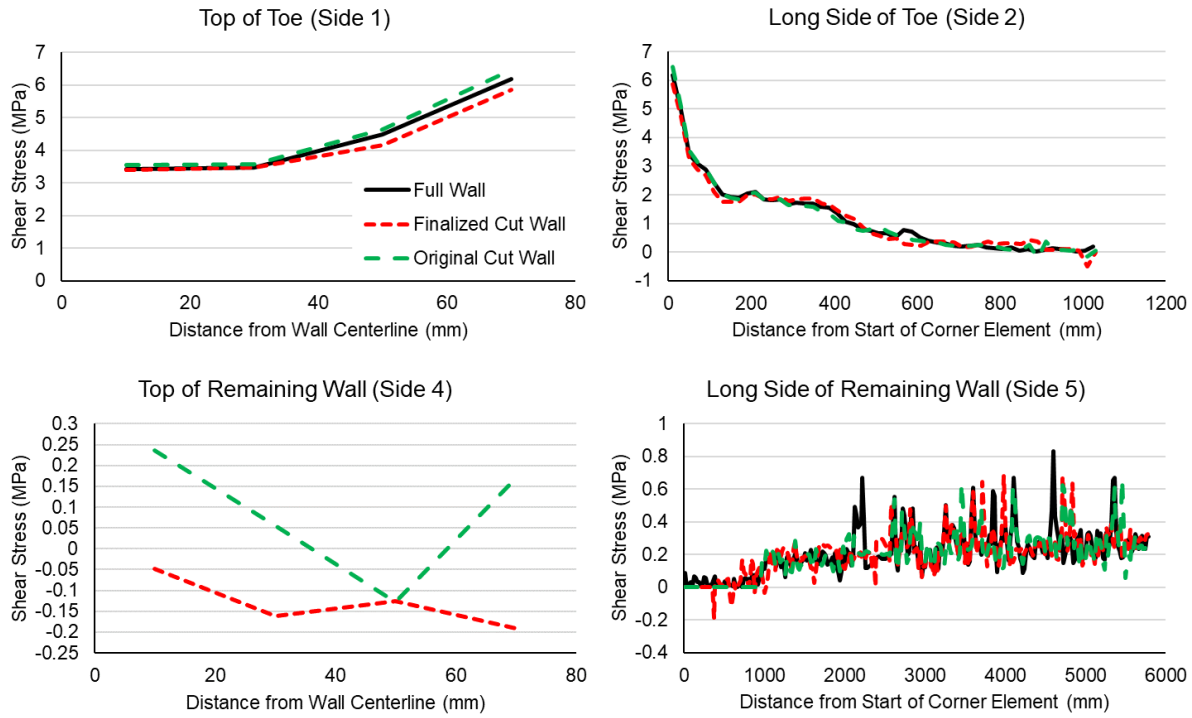


Figure F-14: Comparison of Shear Stress Distribution Along Wall Perimeter from Full Wall and Cut-Wall Models (no Bottom of Toe (Side 3) since c_{min}/d High Opening Removes all Elements), κ = 0.594 (see Figure 7-36 for Side Numbering Convention, ¼ Wall Shown, Stresses Averaged Over Depth)

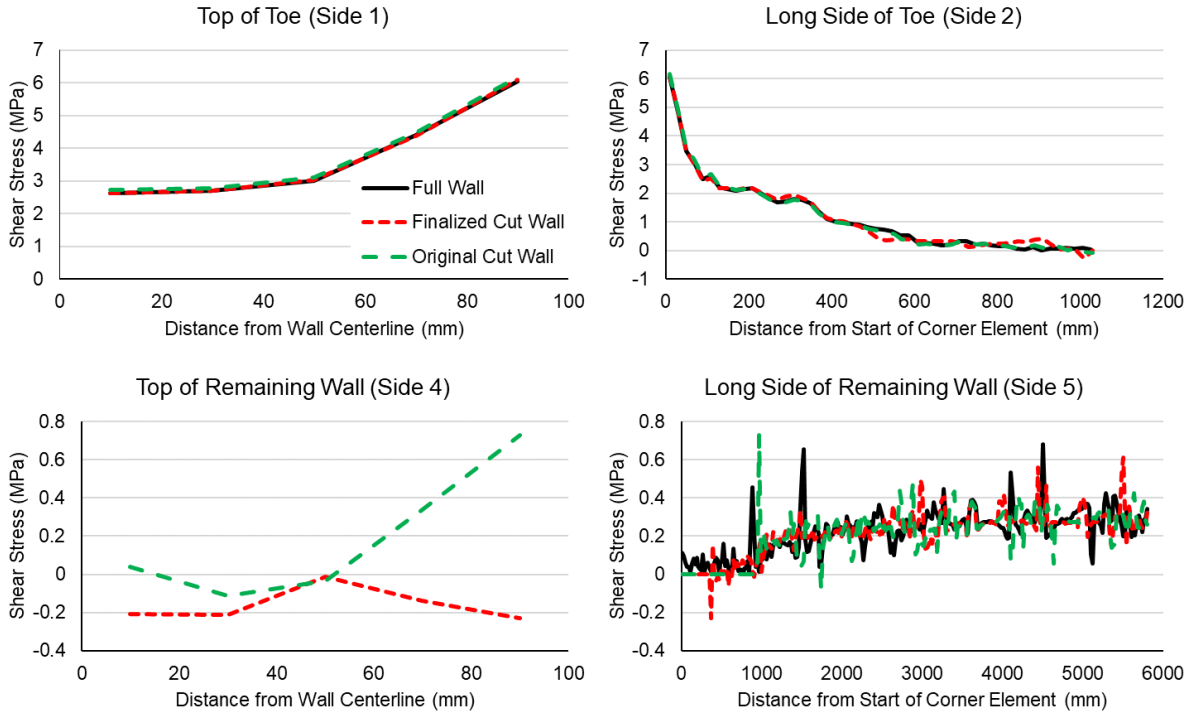


Figure F-15: Comparison of Shear Stress Distribution Along Wall Perimeter from Full Wall and Cut-Wall Models (no Bottom of Toe (Side 3) since c_{min}/d High Opening Removes all Elements), κ = 0.792 (see Figure 7-36 for Side Numbering Convention, ¼ Wall Shown, Stresses Averaged Over Depth)

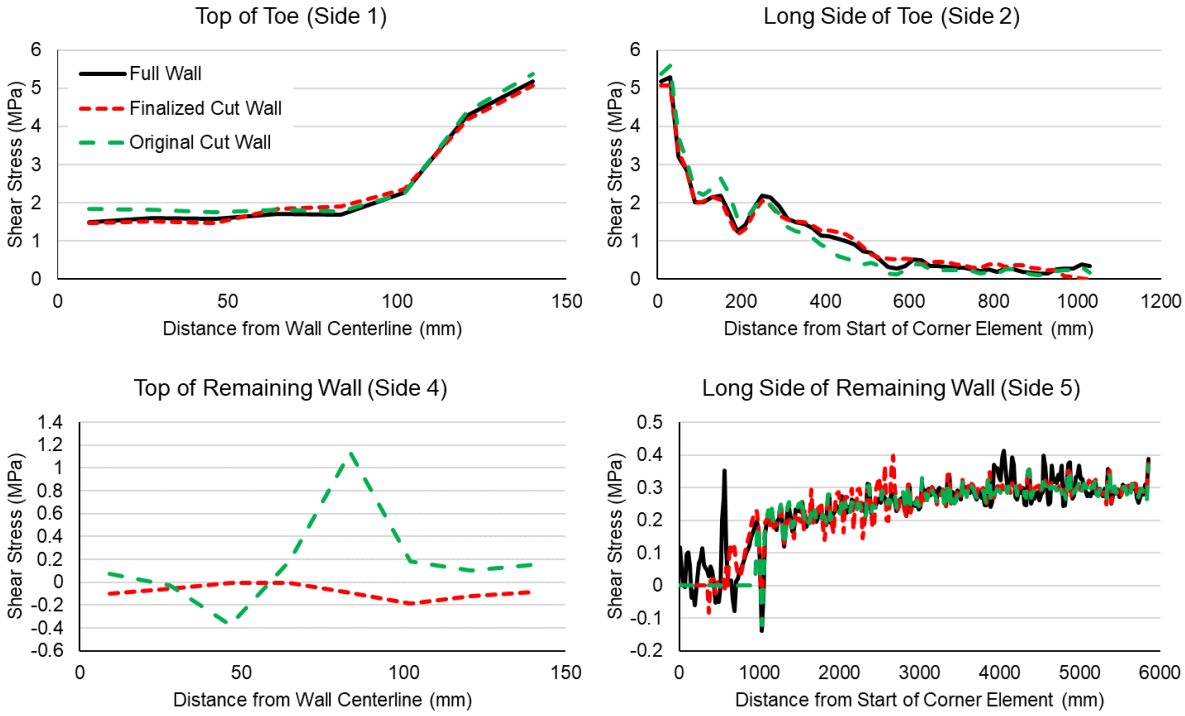


Figure F-16: Comparison of Shear Stress Distribution Along Wall Perimeter from Full Wall and Cut-Wall Models (no Bottom of Toe (Side 3) since c_{min}/d High Opening Removes all Elements), κ = 1.287 (see Figure 7-36 for Side Numbering Convention, ¼ Wall Shown, Stresses Averaged Over Depth)

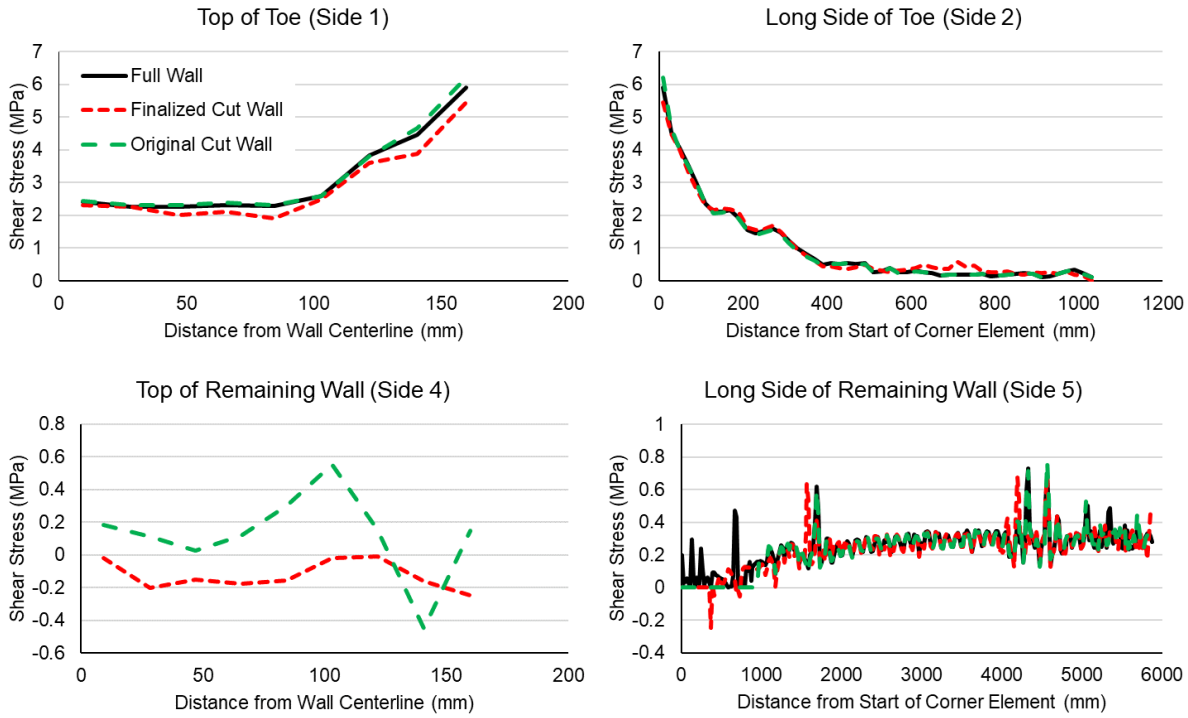


Figure F-17: Comparison of Shear Stress Distribution Along Wall Perimeter from Full Wall and Cut-Wall Models (no Bottom of Toe (Side 3) since c_{min}/d High Opening Removes all Elements), κ = 1.485 (see Figure 7-36 for Side Numbering Convention, ¼ Wall Shown, Stresses Averaged Over Depth)

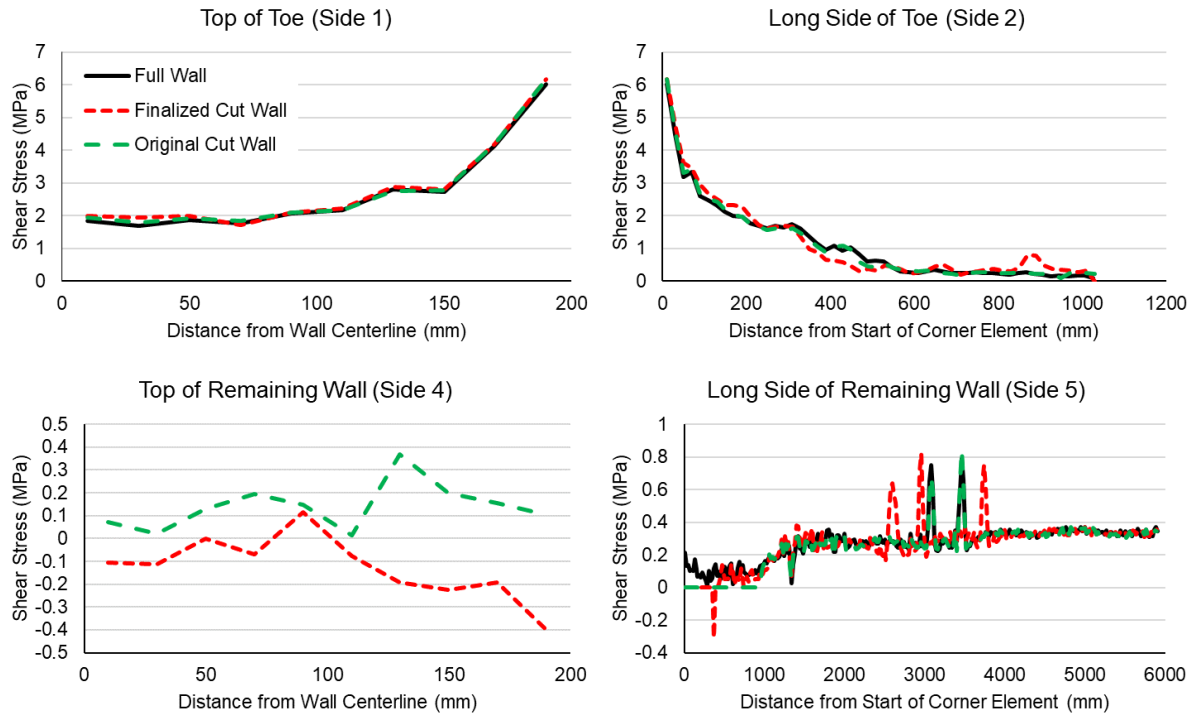


Figure F-18: Comparison of Shear Stress Distribution Along Wall Perimeter from Full Wall and Cut-Wall Models (no Bottom of Toe (Side 3) since c_{min}/d High Opening Removes all Elements), κ = 1.782 (see Figure 7-36 for Side Numbering Convention, ¼ Wall Shown, Stresses Averaged Over Depth)

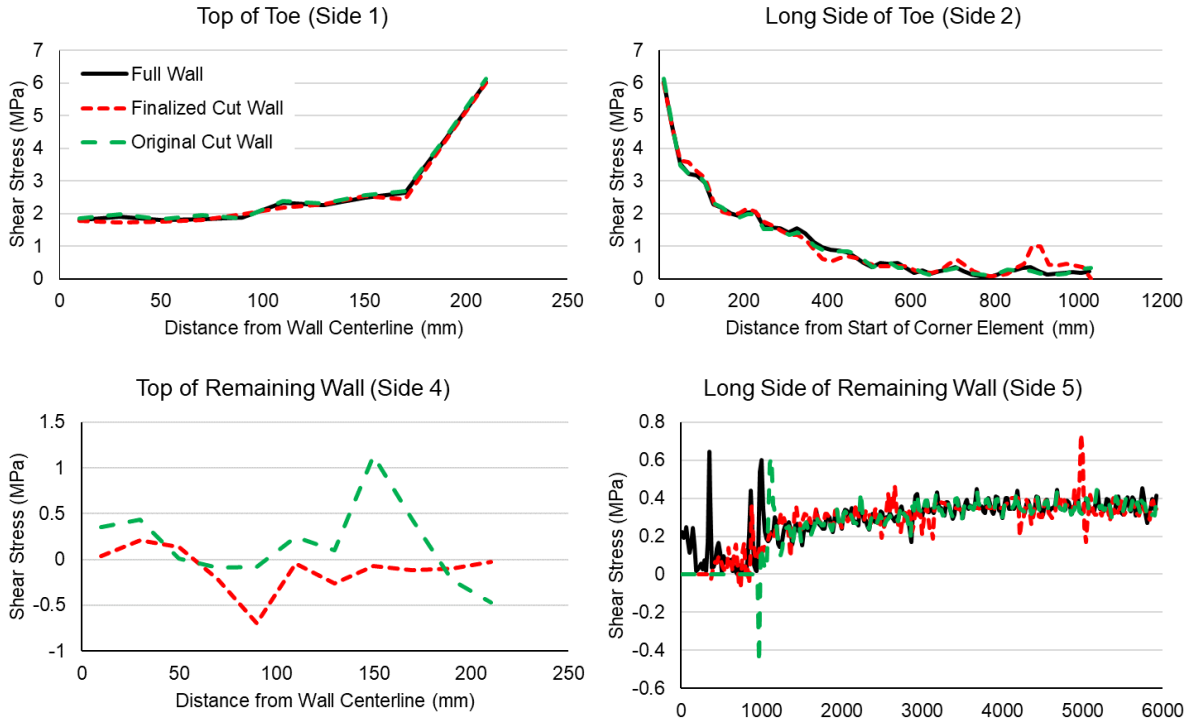


Figure F-19: Comparison of Shear Stress Distribution Along Wall Perimeter from Full Wall and Cut-Wall Models (no Bottom of Toe (Side 3) since c_{min}/d High Opening Removes all Elements), κ = 1.980 (see Figure 7-36 for Side Numbering Convention, ¼ Wall Shown, Stresses Averaged Over Depth)

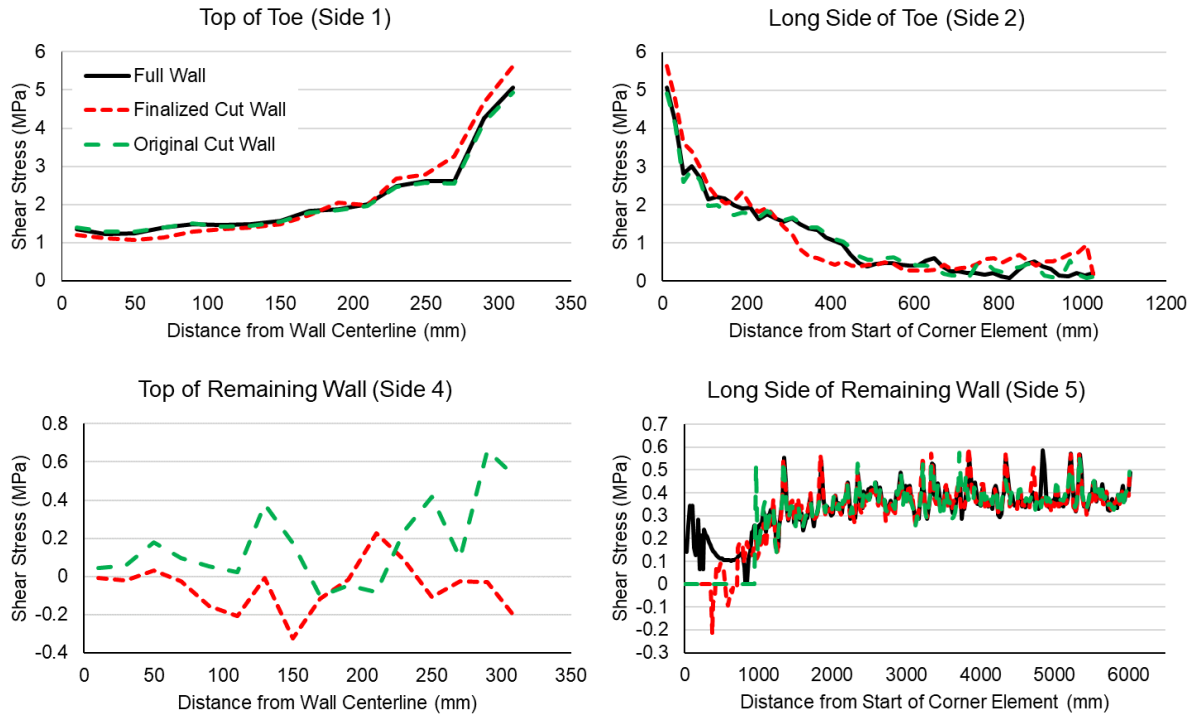


Figure F-20: Comparison of Shear Stress Distribution Along Wall Perimeter from Full Wall and Cut-Wall Models (no Bottom of Toe (Side 3) since c_{min}/d High Opening Removes all Elements), κ = 2.970 (see Figure 7-36 for Side Numbering Convention, ¼ Wall Shown, Stresses Averaged Over Depth)

Appendix G
Calculation of Parameters of Critical Perimeters Assumed in ACI 318-19

In this appendix, the notation and equations for calculating the parameters b_o, J and γ_v for the inner and outer critical perimeters around shear reinforced connections assumed in ACI 318-19 are presented. The equations in this section are compiled from [2, 101, 143] and are also applicable to special-shaped slab-column connections without shear reinforcement.

The inner and outer critical perimeters, located at *d/2* from the column face and the center of the outermost peripheral line of shear reinforcement, respectively, assumed in ACI 318-19 are shown in Figure G-1. The precise dimensions of the critical perimeter are not explicitly provided in ACI 318, but are discussed in [143].

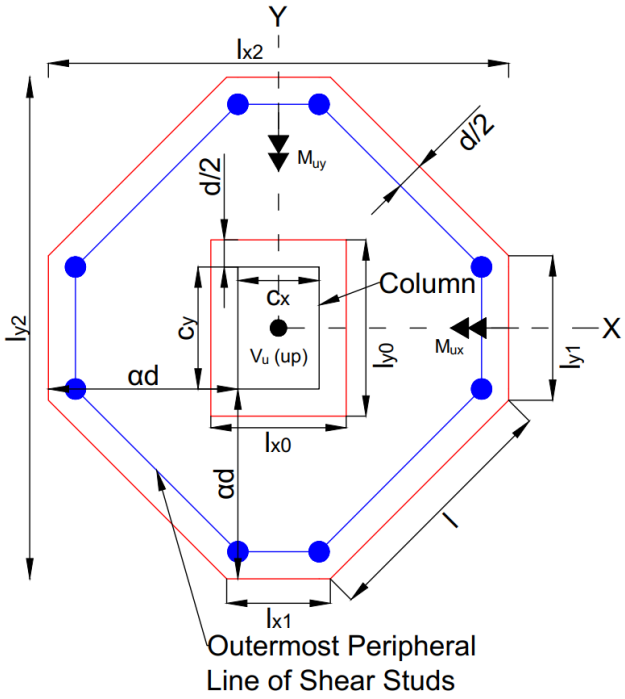


Figure G-1: Notation Used in Calculation of J and γ_v

The side lengths of the inner critical perimeter are calculated according to equations *G1a* and *G1b*, respectively

$$l_{x0} = c_x + d \qquad (G1a)$$

$$l_{y0} = c_y + d \qquad (G1b)$$

where c_x and c_y are the column dimensions in the *x* and *y* directions (mm), respectively, and d is the effective slab depth (mm).

The side lengths of the outer critical perimeter are calculated according to equations *G2a*, *G2b* and *G3*, respectively.

$$l_{x1} = c_x + 0.414d \qquad (G2a)$$

$$l_{y1} = c_y + 0.414d \qquad (G2b)$$

$$l = \sqrt{\frac{1}{2}(l_{x2} - l_{x1})^2} \tag{G3}$$

The overall dimensions of the outer critical perimeter, l_{x2} and l_{y2}, used in the calculation of γ_v are calculated according to Equation *G4a* and *G4b*, respectively

$$l_{x2} = c_x + 2(\alpha d) \tag{G4a}$$

$$l_{y2} = c_y + 2(\alpha d) \tag{G4b}$$

where αd is the distance from the column face to the outer critical perimeter.

The length of the inner critical perimeter, b_o, the parameters of the assumed critical perimeter analogous to the polar moments of inertia, J_{cy} and J_{cx}, and the factors used to determine the fraction of the unbalanced moment transferred by eccentric shear in the *x* and *y* directions, γ_{vy} and γ_{vx}, are calculated using equations *G5*, *G6a*, *G6b*, *G7a* and *G7b*, respectively.

$$b_o = 2(c_x + d) + 2\big(c_y + d\big) \tag{G5}$$

$$J_{cy} = \frac{d(c_x + d)^3}{6} + \frac{(c_x + d)d^3}{6} + \frac{d\big(c_y + d\big)(c_x + d)^2}{2} \tag{G6a}$$

$$J_{cx} = \frac{d\big(c_y + d\big)^3}{6} + \frac{\big(c_y + d\big)d^3}{6} + \frac{d(c_x + d)\big(c_y + d\big)^2}{2} \tag{G6b}$$

$$\gamma_{vy} = 1 - \gamma_f = 1 - \frac{1}{1 + \left(\frac{2}{3}\right)\sqrt{\frac{l_{x0}}{l_{y0}}}} \tag{G7a}$$

$$\gamma_{vx} = 1 - \gamma_f = 1 - \frac{1}{1 + \left(\frac{2}{3}\right)\sqrt{\frac{l_{y0}}{l_{x0}}}} \tag{G7b}$$

The length of the outer critical perimeter, $b_{o,out}$ is calculated using equation *G8*.

$$b_{o,out} = 4l + 2l_{x1} + 2l_{y1} \tag{G8}$$

For the outer critical perimeter, ACI 318-19 [2] does not provide equations to calculate J_{cx} or J_{cy}. ACI 421.2R-10 [101] recommends that J can be calculated as the product of the effective slab depth, d, and the second moment of inertia of the outer critical perimeter about its centroidal principal axes.

Equations *G9a* and *G9b* can be used to calculate J_x and J_y depending on the direction of the applied moment.

$$J_x = \frac{d}{3}\left(\sum\left\{l_{ij}\left[y_i^2 + y_i y_j + y_j^2\right]\right\}\right) \qquad (G9a)$$

$$J_y = \frac{d}{3}\left(\sum\left\{l_{ij}\left[x_i^2 + x_i x_j + x_j^2\right]\right\}\right) \qquad (G9b)$$

where l_{ij} is the length of segment ij of the critical perimeter (mm), x_i and y_i are the coordinates of point i of segment ij, and x_j and y_j are the coordinates of point j of segment ij [101].

For the outer critical perimeter γ_{vy} and γ_{vx} can be calculated using equations *G10a* and *G10b*.

$$\gamma_{vy} = 1 - \gamma_f = 1 - \frac{1}{1 + \left(\frac{2}{3}\right)\sqrt{\frac{l_{x2}}{l_{y2}}}} \qquad (G10a)$$

$$\gamma_{vx} = 1 - \gamma_f = 1 - \frac{1}{1 + \left(\frac{2}{3}\right)\sqrt{\frac{l_{y2}}{l_{x2}}}} \qquad (G10b)$$

Appendix H
Sample Punching Shear Capacity Calculations According to ACI 318-19 and ACI 421.1R-20 for Special-Shaped Slab-Column Connections

In this appendix, sample calculations demonstrating the ACI 318-19 concentric punching shear provisions ($V_{ACI}^{(A)}$), modified ACI 318-19 concentric shear provisions ($V_{ACI}^{(B)}$ and $V_{ACI}^{(C)}$) and the ACI 421.1R-20 method (V_{421}) are provided. These sample calculations are related to the values provided in Chapter 8 but a similar procedure can be used to calculate the moment capacities according to ACI 318-19 and 421.1R-20 in Chapter 9.

Sample calculations are provided for L slab-column connections (L-SCCs) and T slab-column connections (T-SCCs). The portion of this appendix related to L-SCCs is taken from a manuscript accepted for publication in an ACI Symposium Paper [348] (though the specimen naming has been revised to be consistent with the that used in this thesis). For both sets of sample calculations, the column flanges are 200x600mm, the effective slab depth is 117mm and the concrete compressive strength is 30.3MPa. Sample calculations are provided in SI units only. Also, $\lambda = \lambda_s = 1$ for all connections in this work as normal density concrete is assumed and *d* is less than 250mm. Specimens L2-L-o9 and T2-L-o9 are considered in the sample calculations for the L-SCCs and the T-SCCs, respectively.

Sample Calculations for L Slab-Column Connections (L-SCCs)

Sample Concentric Punching Shear Calculations for Unmodified ACI 318-19 Provisions ($V_{ACI}^{(A)}$)

The overall column dimensions and definition of the effective loaded area according to ACI 318-19 for L2-L-o9 are provided in Figure H-1. The values of a_n and b_n according to ACI 318-19, which are used to determine β for L columns, are also shown in Figure H-1.

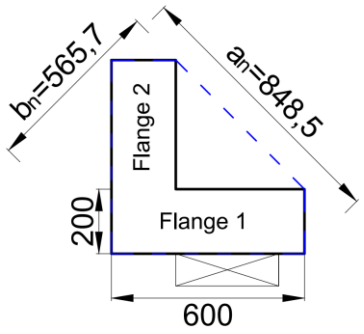


Figure H-1: Overall Column Dimensions and Values of a_n and b_n According to ACI 318-19 for L2-L-o9 (Effective Load Area Shown with Blue Dashed Line)

Step 1 – Determine the Reduced Critical Perimeter Length (b_o)

Due to the presence of a slab opening within *4h* of the column face, the critical perimeter length must be reduced. The portion of the critical perimeter to be neglected is bounded by straight projections from the column centroid (sample calculations for locating the column centroid are provided when discussing the 421.1R-20 method) which are tangent to the opening boundaries. The reduced critical perimeter according to ACI 318-19 for L2-L-o9 is shown in Figure H-2.

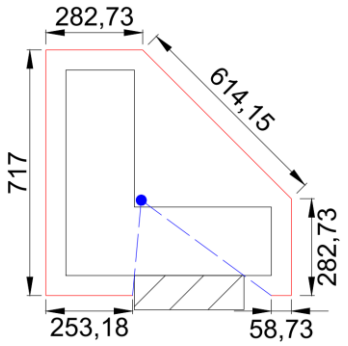


Figure H-2: Reduced Critical Perimeter According to ACI 318-19 for L2-L-o9

Step 2 – Calculate v_c according to ACI 318-19

The nominal shear capacity provided by the concrete along the critical perimeter, v_c, is calculated according to equations 3-2-3-4 (see Section 3.3) for a connection without shear reinforcement (note α_s=40 for interior columns). For L and other special-shaped columns, β is calculated as a_n/b_n.

$$v_c = min\begin{Bmatrix} 0.33\sqrt{30.3} = 1.816 \\ 0.17\left(1 + (2/[848.5/565.7])\sqrt{30.3}\right) = 2.183 \\ 0.083\left(2 + 40[117/2209]\sqrt{30.3}\right) = 1.882 \end{Bmatrix} \rightarrow v_c = 1.816\text{MPa}$$

Step 3 – Calculate concentric punching shear capacity, *V*

The maximum concentric punching shear capacity, *V*, is found by setting the shear resistance, v_r (which is equal to v_c for connections without shear reinforcement) to the shear demand, v_f. Since the shear stress distribution along the critical perimeter is assumed to be uniform for concentric conditions, *V* is found as follows:

$$v_c = v_f = V/b_o d \rightarrow \therefore V = v_c b_o d = (1.816)(2209)(117) \div 1000 = 469.4\text{kN}$$

Sample Concentric Punching Shear Calculations When Neglecting the Diagonal Portion of the Critical Perimeter ($V_{ACI}^{(B)}$)

The concentric punching shear calculations when neglecting the diagonal portion of the critical perimeter follow the same steps shown previously. However, the reduced critical perimeter shown in Figure H-3 is now used when determining b_o and v_c.

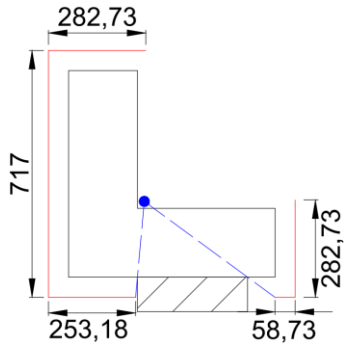


Figure H-3: Reduced Critical Perimeter for L2-L-o9 When Diagonal Portion is Neglected

Using the reduced value of b_o, v_c and *V* are calculated as follows:

$$v_c = min\begin{Bmatrix} 0.33\sqrt{30.3} = 1.816 \\ 0.17\big(1 + (2/[848.5/565.7])\sqrt{30.3}\big) = 2.183 \\ 0.083\big(2 + 40[117/1594]\sqrt{30.3}\big) = 2.255 \end{Bmatrix} \rightarrow v_c = 1.816\text{MPa}$$

$$V = (1.816)(1594)(117) \div 1000 = 338.9\text{kN}$$

Sample Concentric Punching Shear Calculations When Redefining β as Maximum of Individual Column Flanges ($V_{ACI}^{(C)}$)

When calculating $V_{ACI}^{(C)}$, β is redefined as the maximum aspect ratio of the individual column flanges. Aside from this change, the calculations and critical perimeter are the same as those used when finding $V_{ACI}^{(A)}$.

For L2-L-o9, β would be calculated as follows:

$$\beta = \max\begin{Bmatrix} \beta_{flange1} = 600/200 = 3 \\ \beta_{flange2} = 600/200 = 3 \end{Bmatrix} \rightarrow \therefore \beta = 3 \text{ (flange 1 and 2 are defined in Figure H-1)}$$

Finally, v_c and *V* would be calculated as follows:

$$v_c = min\begin{Bmatrix} 0.33\sqrt{30.3} = 1.816 \\ 0.17\big(1 + (2/3)\sqrt{30.3}\big) = 1.560 \\ 0.083\big(2 + 40[117/2209]\sqrt{30.3}\big) = 1.882 \end{Bmatrix} \rightarrow v_c = 1.560\text{MPa}$$

$$V = (1.560)(2209)(117) \div 1000 = 403.0\text{kN}$$

Sample Punching Shear Calculations for ACI 421.1R-20 Method (V_{421})

Once again, the shear capacity of a connection, *V*, is found by setting $v_f = v_c$. However, since the ACI 421.1R-20 method accounts for the unbalanced moment applied to the connection the shear stress demand, v_f, is now calculated using equation *H1*

$$v_f = \frac{V}{b_o d} + \frac{\gamma_{vy} M_{u-y}}{J_{cy}} x + \frac{\gamma_{vx} M_{u-x}}{J_{cx}} y \qquad (H1)$$

where J_{cx} and J_{cy} are properties of the assumed critical perimeter of any shape, equal to *d* multiplied by the second moment of perimeter about the *x* or *y* axis respectively (mm^4), γ_{vx} and γ_{vy} are factors used to determine the moment about the axes *x* and *y* between the slab and column that is transferred

by shear stress at the assumed critical perimeter, *x* and *y* are coordinates of a point along the assumed critical perimeter with respect to the centroidal principal axes *x* and *y* (mm) and M_{u-x} and M_{u-y} are the factored slab moments resisted by the supporting column about the centroidal principal axes *x* and *y* of the assumed critical perimeter [5].

Step 1 – Determine the location of the centroidal principal axes of the assumed critical perimeter (*x* and *y* axes)

The first step of the ACI 421.1R-20 method is to determine the location and orientation of the centroidal principal axes (*x* and *y*) of the critical perimeter. The location of the centroidal principal axis with respect to the arbitrary axes *x'* and *y'* can be found using equations *H2* and *H3*

$$x'_{cp} = \frac{\sum l_{ij} x'_{ij}}{\sum l_{ij}} \qquad (H2)$$

$$y'_{cp} = \frac{\sum l_{ij} y'_{ij}}{\sum l_{ij}} \qquad (H3)$$

where x'_{cp} and y'_{cp} are the location of the centroid of the critical perimeter with respect to *x'* and *y'* axes respectively, l_{ij} is the length of segment *ij* of the critical perimeter, x'_{ij} is the location of the centroid of segment *ij* with respect to the x' axis and y'_{ij} is the location of the centroid of segment *ij* with respect to the y' axis. The assumed critical perimeter, critical points of the perimeter and location of the assumed *x'* and *y'* axes for L2-L-o9 are shown in Figure H-4 (note the slab-column connection has been oriented to match the sign convention used in ACI 421.1R-20 [5]). The coordinates of the critical points with respect to the *x'* and *y'* axes are provided in Table H-1, and the segment lengths and centroids are provided in Table H-2.

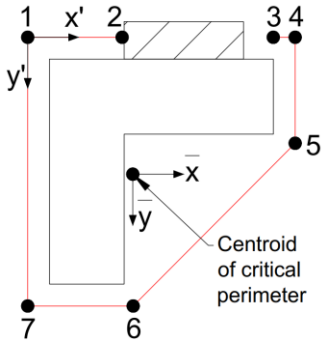


Figure H-4: Definition of *x'*, $\bar{x}$, *y'* and $\bar{y}$ axes and Numbering of Critical Points of Assumed Critical Perimeter

Table H-1: Summary of Coordinates of Critical Perimeter About Different axes and Summary of Computed Shear Stress Values at Critical Points for *V*=388.0kN, Specimen L2-L-o9

Point	*x'*	*y'*	$\bar{x}$	$\bar{y}$	*X*	*y*	v_f (MPa)
1	0	0	-281.7	-365.3	-60.0	-457.4	1.816
2	253.2	0	-28.5	-365.3	158.9	-330.1	1.791
3	658.3	0	376.6	-365.3	509.1	-126.6	1.751
4	717	0	435.3	-365.3	559.9	-97.1	1.745
5	717	282.7	435.3	-82.5	417.8	147.4	1.522
6	282.7	717	1.04	351.7	-175.8	304.6	1.225
7	0	717	-281.7	351.7	-420.3	162.5	1.253

All coordinates are given in mm

Table H-2: Summary of Lengths and Centroids of Each Segment of Critical Perimeter With Respect to *x'* and *y'* Coordinate System, Specimen L2-L-o9

Segment	l_{ij}	x'_{ij}	y'_{ij}
12	253.2	126.6	0
34	58.7	687.6	0
45	282.7	717	141.4
56	614.1	499.9	499.9
67	282.7	141.4	717
71	717	0	358.5

*Lengths and coordinates are in mm

For specimen L2-L-o9, x'_{cp} =281.7mm and y'_{cp} =365.3mm (with respect to the *x'* and *y'* axes shown in Figure H-4.

Step 2 – Determine the orientation of the centroidal principal axes of the assumed critical perimeter (*x* and *y* axes)

Now that the location of the centroidal principal axes has been determined, their orientation, θ, can be determined using equation *H4*

$$\tan(2\theta) = \frac{-2J_{c\bar{x}\bar{y}}}{J_{c\bar{x}} - J_{c\bar{y}}} \qquad (H4)$$

where $J_{c\bar{x}}$ and $J_{c\bar{y}}$ are properties of the assumed critical perimeter equal to *d* multiplied by the second moment of perimeter about the $\bar{x}$ and $\bar{y}$ axis respectively (the $\bar{x}$ and $\bar{y}$ axes are located at the centroid of the critical perimeter and oriented as shown in Figure H-4 to match the convention used in ACI

421.1R-20 [5]) (mm^4) and $J_{c\bar{x}\bar{y}}$ is equal to *d* multiplied by the product of inertia of the assumed critical perimeter about the nonprincipal axes $\bar{x}$ and $\bar{y}$ (mm^4) [5] $J_{c\bar{x}}$, $J_{c\bar{y}}$ and $J_{c\bar{x}\bar{y}}$ are calculated according to equations *H5*, *H6* and *H7*, respectively.

$$J_{c\bar{x}} = d\sum\left[\frac{l_{ij}}{3}\left(\bar{y}_i^2 + \bar{y}_i\bar{y}_j + \bar{y}_j^2\right)\right] \qquad (H5)$$

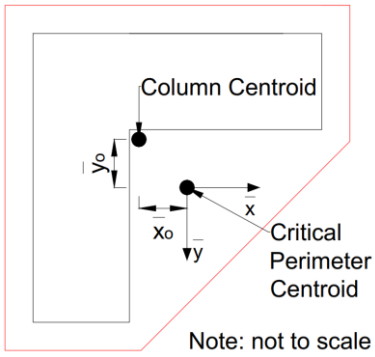
$$J_{c\bar{y}} = d\sum\left[\frac{l_{ij}}{3}\left(\bar{x}_i^2 + \bar{x}_i\bar{x}_j + \bar{x}_j^2\right)\right] \qquad (H6)$$

$$J_{c\bar{x}\bar{y}} = d\sum\left[\frac{l_{ij}}{6}\left(2\bar{x}_i\bar{y}_i + \bar{x}_i\bar{y}_j + \bar{x}_j\bar{y}_i + 2\bar{x}_j\bar{y}_j\right)\right] \qquad (H7)$$

where $\bar{x}_i$, $\bar{x}_j$, $\bar{y}_i$ and $\bar{y}_j$ are the coordinates of segment *ij* of the critical perimeter with respect to the centroidal nonprincipal axes $\bar{x}$ and $\bar{y}$ [5] (these coordinates are also provided in Table H-1 for L2-L-o9).

For L2-L-o9, $J_{c\bar{x}}$, $J_{c\bar{y}}$, $J_{c\bar{x}\bar{y}}$ and θ are equal to 1.687*x*10^{10}mm^4, 2.035*x*10^{10}mm^4, -3.057*x*10^{9}mm^4 and -30.17°, respectively. Note, that since the sign convention and orientation of the $\bar{x}$ and $\bar{y}$ axes from ACI 421.1R-20 was followed a negative θ value corresponds to a counterclockwise rotation of the axes. Therefore, for specimen L2-L-o9 the location and orientation of the principal centroidal axes *x* and *y* are as shown in Figure H-5b.

a)



b)

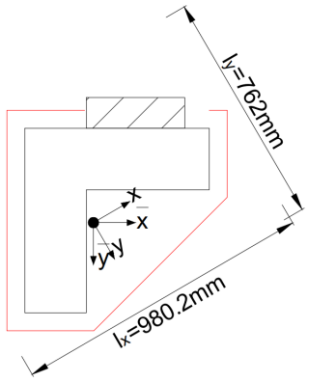


Figure H-5: a) Determination of $\overline{x_o}$, $\overline{y_o}$ (both Negative for the Example Shown); b) Determination of l_x and l_y and Orientation of Principal Centroidal Axes *x* and *y*

Step 3 – Calculate the parameters J_{cx} and J_{cy}

Now that the location and orientation of the *x* and *y* axes is known the coordinates of the critical perimeter with respect to the *x* and *y* axes can be determined using equations *H8* and *H9* [5].

$$x = \bar{x}cos\theta + \bar{y}sin\theta \qquad (H8)$$

$$y = -\bar{x}sin\theta + \bar{y}cos\theta \qquad (H9)$$

The coordinates of the critical perimeter for L2-L-o9 with respect to the *x* and *y* axes are also provided in Table H-1.

J_{cx} and J_{cy} can then be calculated according to equations *H10* and *H11*.

$$J_{cx} = d\sum \left[\frac{l_{ij}}{3}(y_i^2 + y_i y_j + y_j^2\right] \qquad (H10)$$

$$J_{cy} = d\sum \left[\frac{l_{ij}}{3}(x_i^2 + x_i x_j + x_j^2\right] \qquad (H11)$$

For specimen L2-L-o9, J_{cx} and J_{cy} are equal to 1.509*x*10^{10}mm^4 and 2.213*x*10^{10}mm^4, respectively.

Step 4 – Determination of γ_{vx} and γ_{vy}

The parameters γ_{vx} and γ_{vy} can also be determined after finding the location and orientation of the centroidal principal axes. According to ACI 421.1R-20 [5], γ_{vx} and γ_{vy} can be calculated according to equations *H12* and *H13* respectively for interior slab-column connections (ACI 421.1R-20 provides different equations for edge and corner slab-column connections which are not presented herein).

$$\gamma_{vx} = 1 - \frac{1}{1 + \frac{2}{3}\sqrt{l_y/l_x}} \qquad (H12)$$

$$\gamma_{vy} = 1 - \frac{1}{1 + \frac{2}{3}\sqrt{l_x/l_y}} \qquad (H13)$$

where l_x and l_y are the projections of the assumed critical perimeter on the principal *x* and *y* axes (mm). Based on the values for l_x and l_y for specimen L2-L-o9, which are provided in Figure H-5b, γ_{vx} and γ_{vy} equal 0.370 and 0.431, respectively.

Step 5 – Calculation of unbalanced moments, M_{u-x} and M_{u-y}

The final unknown components of equation *H1* are the factored slab moments resisted by the supporting column about the centroidal principal axes *x* and *y* of the assumed critical perimeter, M_{u-x} and M_{u-y}, which are calculated according to equation *H14* and *H15*, respectively (the sign convention for moments assumed in ACI 421.1R-20 [5] is provided in Figure H-6).

$$M_{u-x} = (M_{u-\bar{x}})cos\theta - \left(M_{u-\bar{y}}\right)sin\theta \qquad (H14)$$

$$M_{u-y} = (M_{u-\bar{x}})sin\theta + \left(M_{u-\bar{y}}\right)cos\theta \qquad (H15)$$

where $M_{u-\bar{x}}$ (Nmm) and $M_{u-\bar{y}}$ (Nmm) are the factored slab moments resisted by the column about the centroidal nonprincipal $\bar{x}$ and $\bar{y}$ axes, which are calculated according to equations *H16* and *H17*, respectively.

$$M_{u-\bar{x}} = M_{u0\bar{x}} + V\overline{y_o} \qquad (H16)$$

$$M_{u-\bar{y}} = M_{u0\bar{y}} + V\overline{x_o} \qquad (H17)$$

where $M_{u0\bar{x}}$ (Nmm) and $M_{u0\bar{y}}$ (Nmm) are the factored slab moments resisted by the column about axes parallel to the centroidal nonprincipal $\bar{x}$ and $\bar{y}$ axes through the column's centroid (point 0), and $\overline{x_o}$ (mm) and $\overline{y_o}$ (mm) are the eccentricity of the column and critical perimeter centroids with respect to the $\bar{x}$ and $\bar{y}$ axes (the definitions of $\overline{x_o}$ and $\overline{y_o}$ are shown in Figure H-5a).



Figure H-6: Positive Sign Convention for θ, M_{u-x} and M_{u-y} Assumed in ACI 421.1R-20 [5]

For L2-L-o9, $M_{u0\bar{x}}$ and $M_{u0\bar{y}}$ are both equal to 0Nmm (as the column and slab centroid are perfectly aligned) and $\overline{x_o}$ (mm) and $\overline{y_o}$ are equal to -3.19mm and -86.78mm, respectively (as calculated according to Figure H-5a). Since *V* is unknown, $M_{u-\bar{x}}$ and $M_{u-\bar{y}}$ and M_{u-x} and M_{u-y} are functions of *V*.

Step 6 – Calculation of shear capacity, *V*

Now that all components of equation *H1* are known or functions of *V* equation *H1* can be solved iteratively at each critical point of the critical perimeter (summarized in Table H-1) to find the maximum possible *V*. For L2-L-o9, point 1 is critical. When *V* is equal to 388.0kN v_f at point 1 is equal to v_c. The calculated shear stress values at the other critical points for *V*=388.0kN are provided in Table H-1.

Sample Calculations for T Slab-Column Connections (T-SCCs)

The procedure to calculate the concentric punching capacity of T-SCCs is similar to that shown for L-SCCs. Therefore, the sample calculations for T2-L-o9 are less detailed than those for L2-L-o9.

Sample Concentric Punching Shear Calculations for Unmodified ACI 318-19 Provisions ($V_{ACI}^{(A)}$)

The overall column dimensions and definition of the effective loaded area according to ACI 318-19 for T2-L-o9 are provided in Figure H-7. The values of a_n and b_n according to ACI 318-19, which are used to determine β for T-SCCs are also shown in Figure H-7.

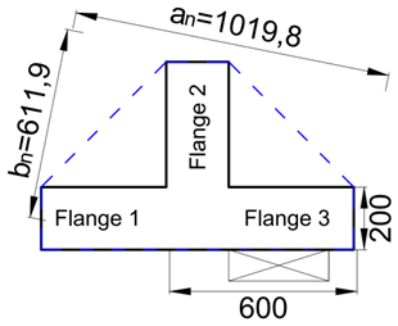


Figure H-7: Overall Column Dimensions and Values of a_n and b_n According to ACI 318-19 for T2-L-o9 (Effective Load Area Shown with Blue Dashed Line)

Step 1 – Determine the Reduced Critical Perimeter Length (b_o)

Due to the presence of a slab opening within *4h* of the column face, the critical perimeter length must be reduced. The portion of the critical perimeter to be neglected is bounded by straight projections from the column centroid which are tangent to the opening boundaries. The reduced critical perimeter according to ACI 318-19 for T2-L-o9 is shown in Figure H-8.

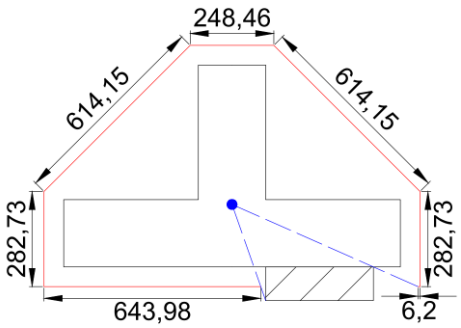


Figure H-8: Reduced Critical Perimeter According to ACI 318-19 for T2-L-o9

Step 2 – Calculate v_c according to ACI 318-19

$$v_c = min\begin{Bmatrix} 0.33\sqrt{30.3} = 1.816 \\ 0.17\left(1 + (2/[1019.8/611.9])\sqrt{30.3}\right) = 2.059 \\ 0.083\left(2 + 40[117/2692]\sqrt{30.3}\right) = 1.708 \end{Bmatrix} \rightarrow v_c = 1.708\text{MPa}$$

Step 3 – Calculate concentric punching shear capacity, *V*

$$v_c = v_f = V/b_o d \rightarrow \therefore V = v_c b_o d = (1.708)(2692)(117) \div 1000 = 538.0\text{kN}$$

Sample Concentric Punching Shear Calculations When Neglecting the Diagonal Portion of the Critical Perimeter ($V_{ACI}^{(B)}$)

The concentric punching shear calculations when neglecting the diagonal portion of the critical perimeter follow the same steps as previously shown for L2-L-o9. However, the reduced critical perimeter shown in Figure H-9 is now used when determining b_o and v_c.

Using the reduced value of b_o, v_c and *V* are calculated as follows:

$$v_c = min\begin{Bmatrix} 0.33\sqrt{30.3} = 1.816 \\ 0.17\left(1 + (2/[1019.8/611.9])\sqrt{30.3}\right) = 2.059 \\ 0.083\left(2 + 40[117/1464]\sqrt{30.3}\right) = 2.374 \end{Bmatrix} \rightarrow v_c = 1.816\text{MPa}$$

$$V = (1.816)(1464)(117) \div 1000 = 311.2\text{kN}$$

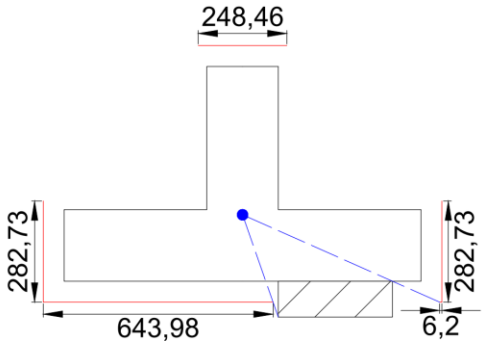


Figure H-9: Reduced Critical Perimeter for T2-L-o9 When Diagonal Portion is Neglected

Sample Concentric Punching Shear Calculations When Redefining β as Maximum of Individual Column Flanges ($V_{ACI}^{(C)}$)

As shown previously for L2-L-o9, β is redefined as the maximum aspect ratio of the individual column flanges when calculating $V_{ACI}^{(C)}$. Aside from this change the calculations and critical perimeter are the same as those used when finding $V_{ACI}^{(A)}$.

Therefore, for T2-L-o9, β would be calculated as follows:

$$\beta = \max\begin{Bmatrix}\beta_{flange1} = 600/200 = 3\\ \beta_{flange2} = 600/200 = 3\\ \beta_{flange3} = 600/200 = 3\end{Bmatrix} \rightarrow \therefore \beta = 3 \text{ (flange 1, 2 and 3 are defined in Figure H-7)}$$

Finally, v_c and V would be calculated as follows:

$$v_c = min\begin{Bmatrix}0.33\sqrt{30.3} = 1.816\\ 0.17\left(1 + (2/3)\sqrt{30.3}\right) = 1.560\\ 0.083\left(2 + 40[117/2692]\sqrt{30.3}\right) = 1.708\end{Bmatrix} \rightarrow v_c = 1.560\text{MPa}$$

$$V = (1.560)(2692)(117) \div 1000 = 491.3\text{kN}$$

Sample Punching Shear Calculations for ACI 421.1R-20 Method (V_{421})

As was done for L-SCCs, the shear capacity of the connection, V, is found by setting $v_f = v_c$ (note v_f is calculated according to equation *H1*).

Step 1 – Determine the location of the centroidal principal axes of the assumed critical perimeter (*x* and *y* axes)

The same procedure presented for L2-L-o9 is used to locate the centroidal principal axes with respect to the arbitrary axes *x'* and *y'*. The assumed critical perimeter, critical points of the perimeter and location of the assumed *x'* and *y'* axes for T2-L-o9 are shown in Figure H-10 (note the axes have been oriented to match the sign convention used in ACI 421.1R-20 [5]). The coordinates of the critical points with respect to the *x'* and *y'* axes are provided in Table H-3, and the segment lengths and centroids are provided in Table H-4.

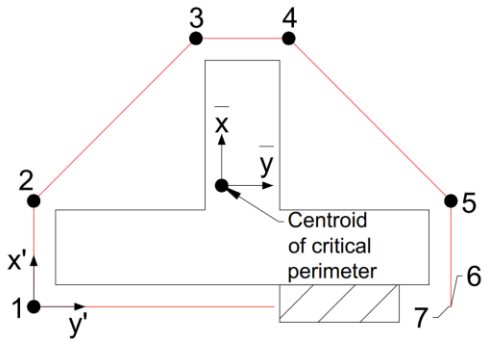


Figure H-10: Definition of x', $\bar{x}$, y' and $\bar{y}$ axes and Numbering of Critical Points of Assumed Critical Perimeter

Table H-3: Summary of Coordinates of Critical Perimeter About Different axes and Summary of Computed Shear Stress Values at Critical Points for V=424.0kN, Specimen T2-L-o9

Point	x'	y'	$\bar{x}$	$\bar{y}$	x	y	v_f (MPa)
1	0	0	-323.9	-503.2	-206.6	-561.6	1.392
2	282.7	0	-41.2	-503.2	69.3	-500.1	1.228
3	717	434.3	393.1	-68.9	398.7	18.3	1.097
4	717	682.7	393.1	179.5	344.6	260.8	1.168
5	282.7	1117	-41.2	613.8	-173.8	590.1	1.543
6	0	1117	-323.9	613.8	-449.7	528.6	1.708
7	0	1110.8	-323.9	607.6	-448.4	522.5	1.706
8	0	644.0	-323.9	140.8	-346.8	66.9	1.574

*All coordinates are given in mm

Table H-4: Summary of Lengths and Centroids of Each Segment of Critical Perimeter With Respect to x' and y' Coordinate System, Specimen T2-L-o9

Segment	l_{ij}	x'_{ij}	y'_{ij}
12	282.7	141.4	0
23	614.1	499.9	217.1
34	248.5	717	558.5
45	614.1	499.9	899.9
56	282.7	141.4	1117
67	6.2	0	1113.9
81	644.0	0	322.0

*Lengths and coordinates are in mm

For specimen T2-L-o9, x'_{cp} =323.9mm and y'_{cp} =503.2mm (with respect to the x' and y' axes shown in Figure H-10).

Step 2 – Determine the orientation of the centroidal principal axes of the assumed critical perimeter (*x* and *y* axes)

Again, equations *H4-H7* are applied to determine the orientation of the centroidal principal axes, θ (the same sign convention shown in Figure H-6 applies). For T2-L-o9, $J_{c\bar{x}}$, $J_{c\bar{y}}$, $J_{c\overline{xy}}$ and θ are equal to $4.587x10^{10}$mm^4, $2.183x10^{10}$mm^4, $5.641x10^{9}$mm^4 and -12.57°, respectively. As a negative θ value corresponds to a counterclockwise rotation of the axes (based on the sign convention assumed in ACI 421.1R-20 [5]) the location and orientation of the principal centroidal axes for T2-L-o9 are as shown in Figure H-11b.

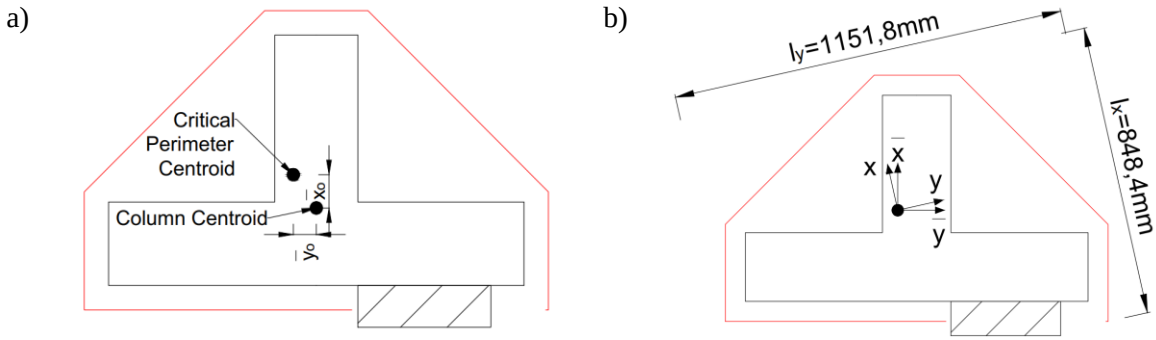


Figure H-11: a) Determination of $\overline{x_o}$, $\overline{y_o}$ (Negative $\overline{x_o}$ and Positive $\overline{y_o}$ for the Example Shown (T2-L-o9)); b) Determination of l_x and l_y and Orientation of Principal Centroidal Axes *x* and *y*

Step 3 – Calculate the parameters J_{cx} and J_{cy}

Equations *H8-H11* are used to calculate J_{cx} and J_{cy} (the coordinates of the vertices of the critical perimeter with respect to the *x* and *y* axes are also provided in Table H-3). For specimen T2-L-o9, J_{cx} and J_{cy} are equal to $4.713x10^{10}$mm^4 and $2.057x10^{10}$mm^4, respectively.

Step 4 – Determination of γ_{vx} and γ_{vy}

Based on the values of l_x and l_y for T2-L-o9, which are provided in Figure H-11b, and equations *H12* and *H13*, γ_{vx} and γ_{vy} equal 0.437 and 0.364, respectively.

Step 5 – Calculation of unbalanced moments, M_{u-x} and M_{u-y}

Equations *H14-H17* are again used to calculate the factored slab moments resisted by the supporting column about the centroidal principal axes *x* and *y* of the assumed critical perimeter, M_{u-x} and M_{u-y}. However, for T2-L-o9 a small eccentricity between the isolated slab and column centroids exists. Therefore, unlike L2-L-o9 where $M_{u0\bar{x}}$ and $M_{u0\bar{y}}$ were equal to 0 since the slab and column centroids were aligned, $M_{u0\bar{x}}$ and $M_{u0\bar{y}}$ are calculated using equations *H18* and *H19*, respectively (assuming the same sign convention as that shown in Figure H-6)

$$M_{uo\bar{x}} = Ve_y \qquad (H18)$$

$$M_{u0\bar{y}} = Ve_x \qquad (H19)$$

where e_y and e_x are the eccentricities of the slab and column centroids with respect to axes originating at the column centroid which are parallel to the $\bar{x}$ and $\bar{y}$ axes. For the T2-L specimens, e_x and e_y are equal to 6mm and 0mm, respectively, as shown in Figure H-12.

Based on the axes shown in Figure H-11a $\overline{x_o}$ (mm) and $\overline{y_o}$ are equal to -79.69mm and 55.29mm, respectively. Again, as *V* is unknown all moments are expressed as functions of *V*.

Step 6 – Calculation of shear capacity, *V*

Now that all components of equation *H1* are known or functions of *V* equation *H1* can be solved iteratively at each critical point of the critical perimeter (summarized in Table H-3) to find the maximum possible *V*. For T2-L-o9 point 6 is critical. When *V* is equal to 424.0kN v_f at point 6 is equal to v_c. The calculated shear stress values at the other critical points for *V*=424.0kN are provided in Table H-3.

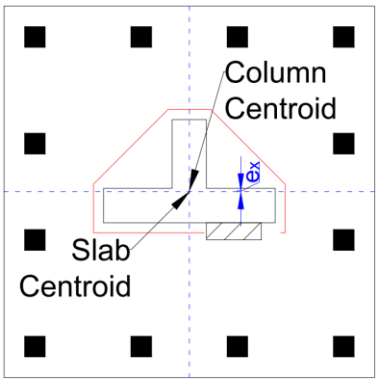


Figure H-12: Determination of e_x for T2-L Specimens (Note: e_x is Positive in This Case)

Appendix I

Critical Perimeters Around Slab-Column and Slab-Wall Connections With Slab Openings Analyzed in Chapter 6, Chapter 8, and Chapter 9 According to ACI 318-19

In this appendix, the reduced critical perimeters around the slab-column and slab-wall connections with openings analyzed in Chapter 6, Chapter 8, and Chapter 9 according to ACI 318-19 are provided.

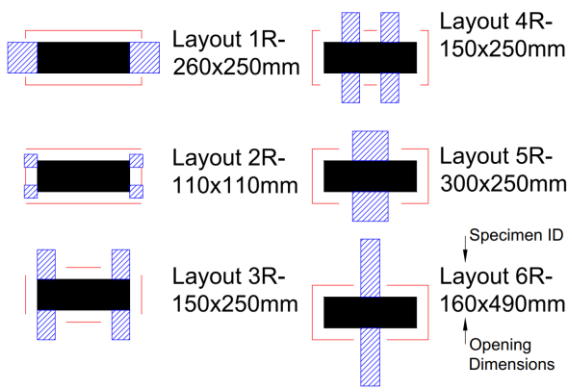


Figure I-1: Reduced Critical Perimeters Around Rectangular Slab-Column Connections with Openings According to ACI 318-19 (Radial Approach)

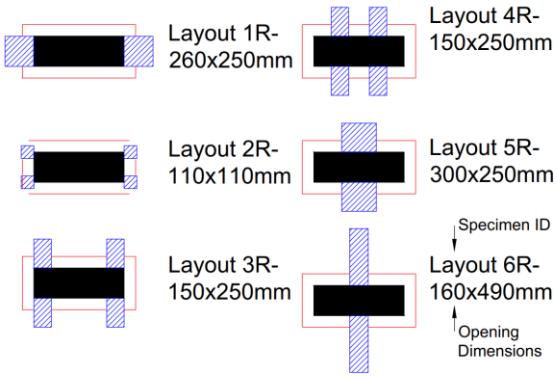


Figure I-2: Reduced Critical Perimeters Around Rectangular Slab-Column Connections with Openings According to ACI 318-19 (Straight Projection Approach)

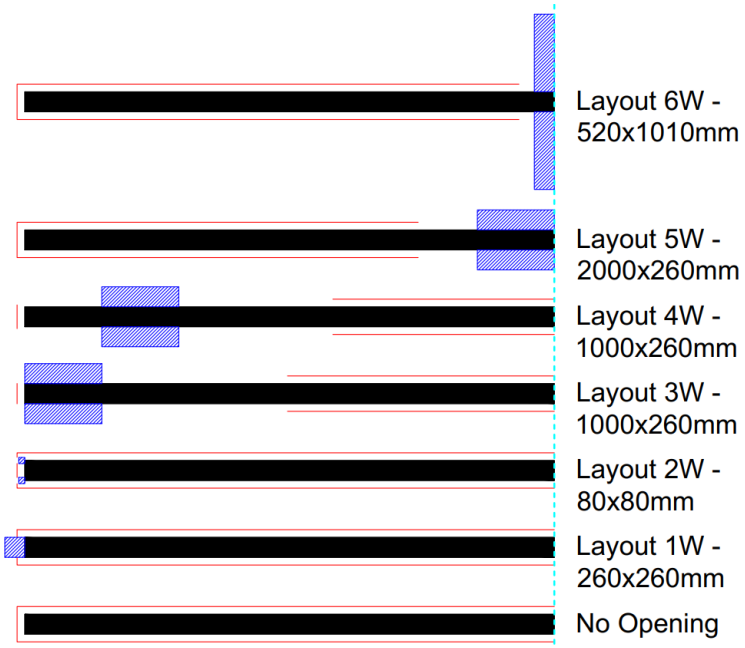


Figure I-3: Reduced Critical Perimeters Around Slab-Wall Connections with Openings According to ACI 318-19 (Half-Wall Shown, Radial Approach)

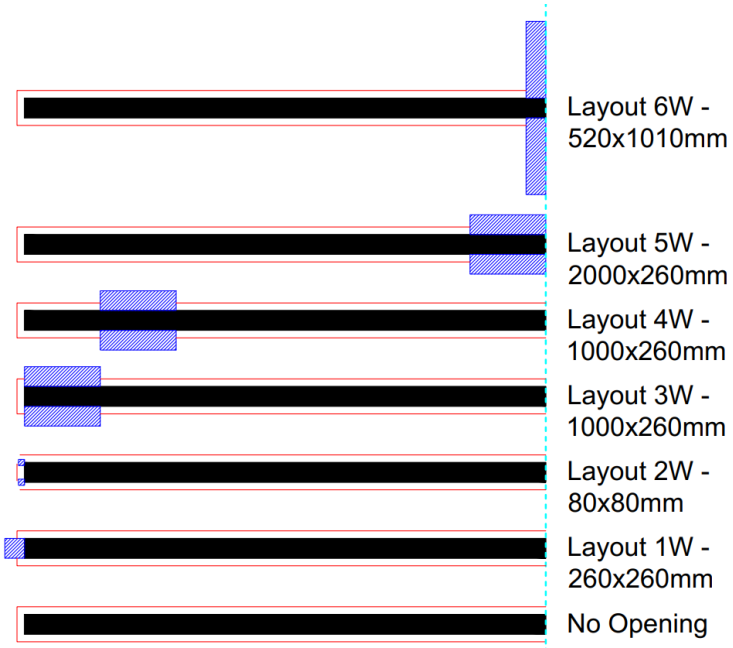


Figure I- 4: Reduced Critical Perimeters Around Slab-Wall Connections with Openings According to ACI 318-19 (Half-Wall Shown, Straight Projection Approach)

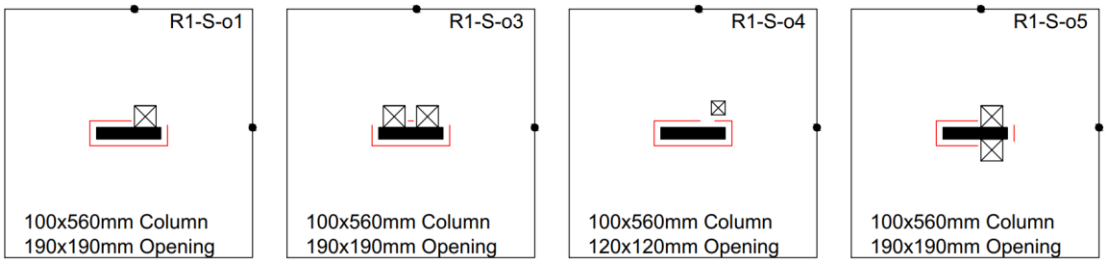


Figure I-5: Reduced Critical Perimeters for Slab-Column Connections with Openings According to ACI 318-19 – R1-S Specimens (Radial Approach)

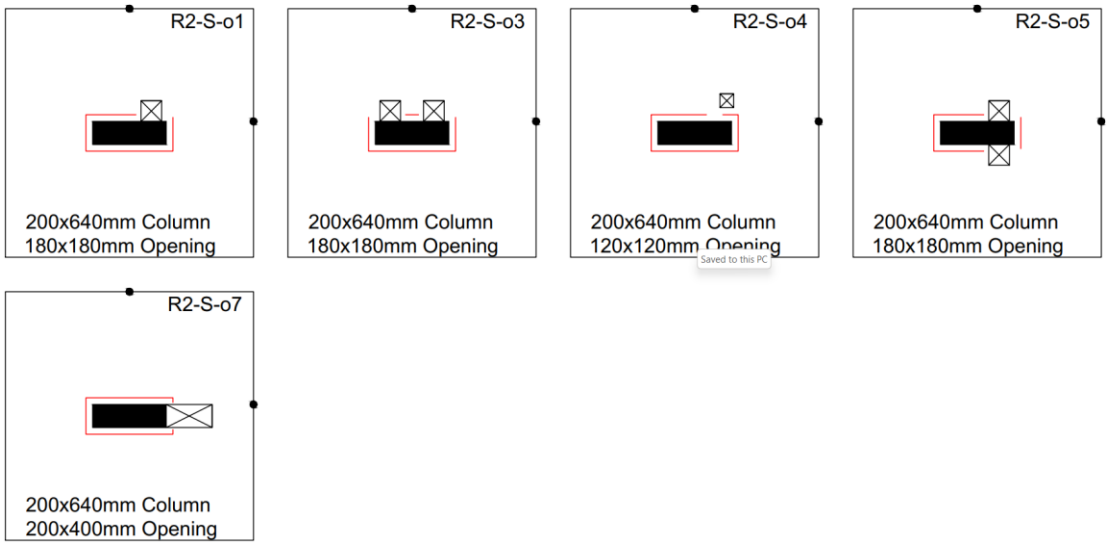


Figure I-6: Reduced Critical Perimeters for Slab-Column Connections with Openings According to ACI 318-19 – R2-S Specimens (Radial Approach)

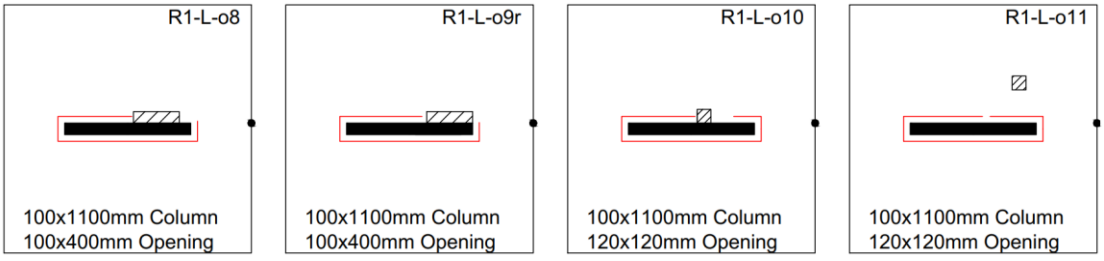


Figure I-7: Reduced Critical Perimeters for Slab-Column Connections with Openings According to ACI 318-19 – R1-L Specimens (Radial Approach)

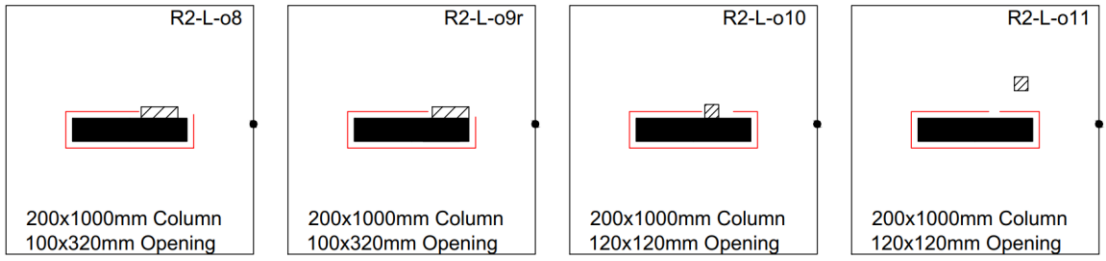


Figure I-8: Reduced Critical Perimeters for Slab-Column Connections with Openings According to ACI 318-19 – R2-L Specimens (Radial Approach)

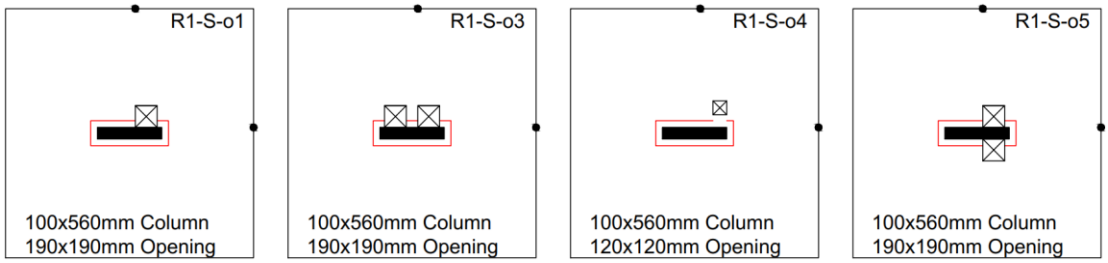


Figure I-9: Reduced Critical Perimeters for Slab-Column Connections with Openings According to ACI 318-19 – R1-S Specimens (Straight Projection Approach)

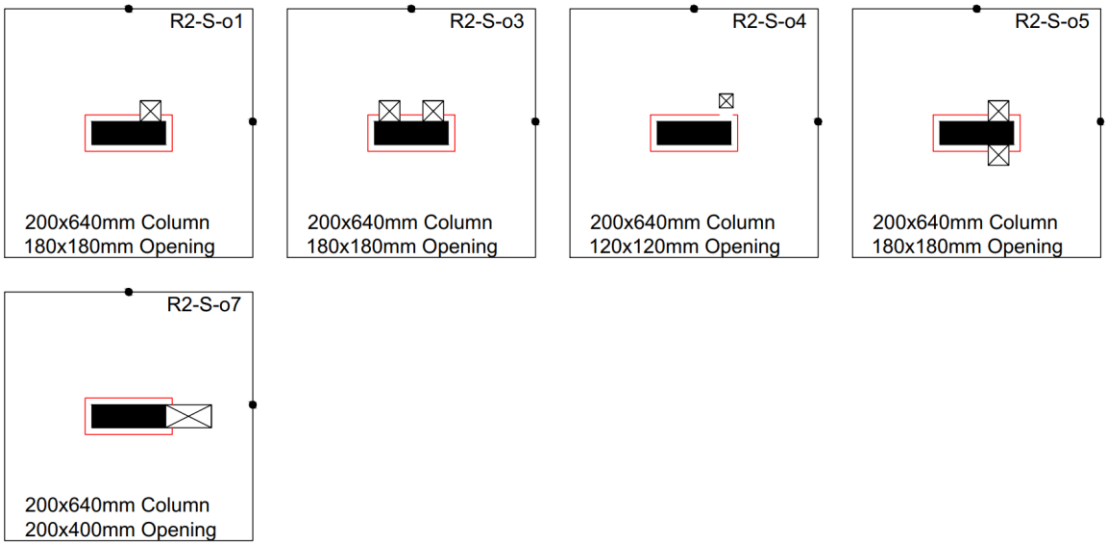


Figure I-10: Reduced Critical Perimeters for Slab-Column Connections with Openings According to ACI 318-19 – R2-S Specimens (Straight Projection Approach)

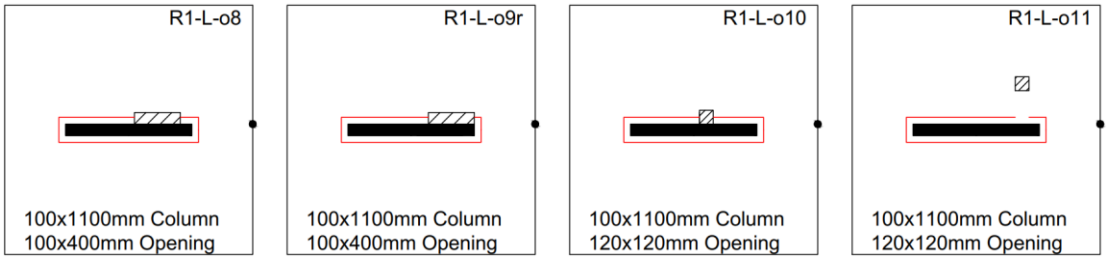


Figure I-11: Reduced Critical Perimeters for Slab-Column Connections with Openings According to ACI 318-19 – R1-L Specimens (Straight Projection Approach)

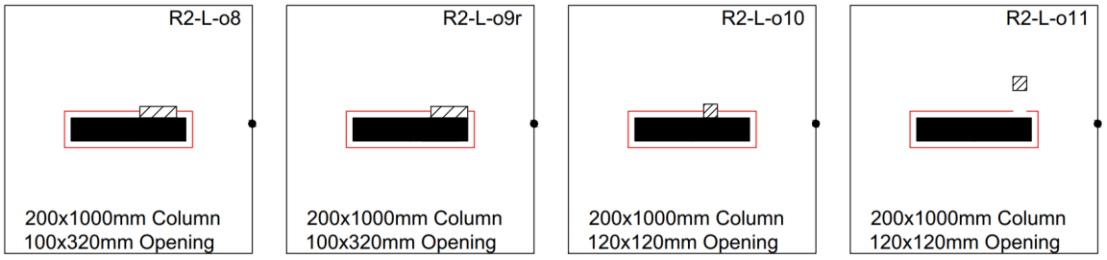


Figure I-12: Reduced Critical Perimeters for Slab-Column Connections with Openings According to ACI 318-19 – R2-L Specimens (Straight Projection Approach)

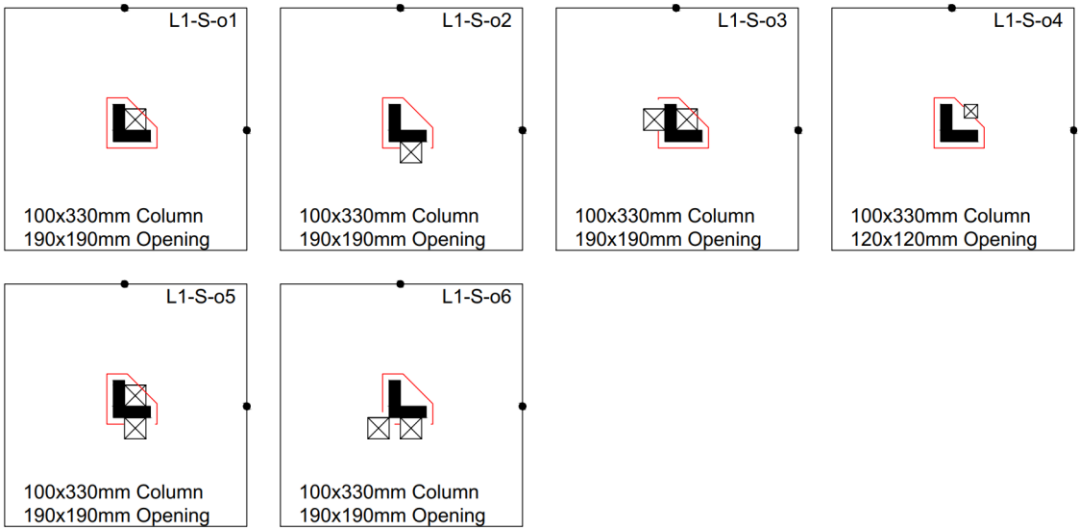


Figure I-13: Reduced Critical Perimeters for Slab-Column Connections with Openings According to ACI 318-19 – L1-S Specimens

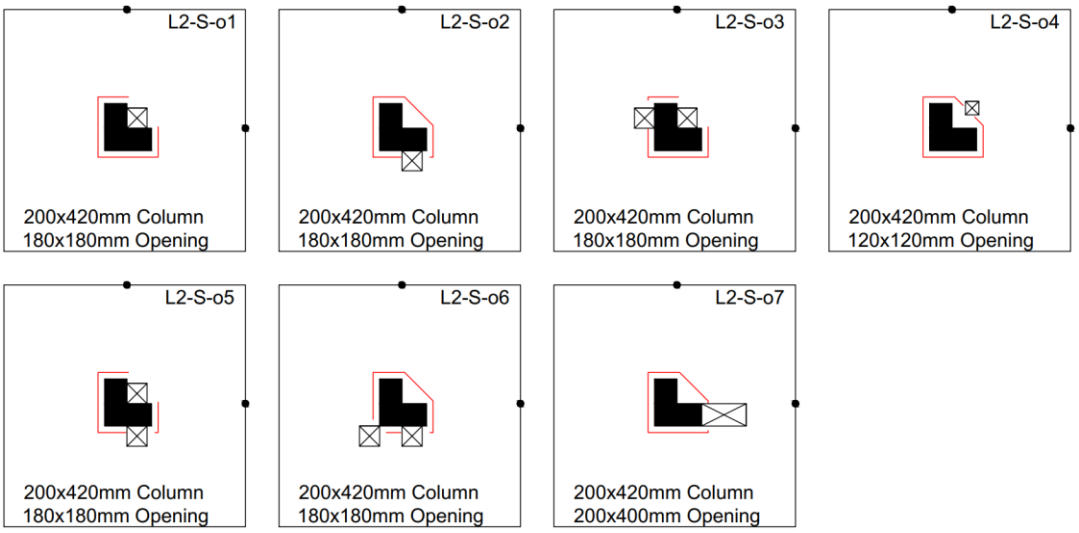


Figure I-14: Reduced Critical Perimeters for Slab-Column Connections with Openings According to ACI 318-19 – L2-S Specimens

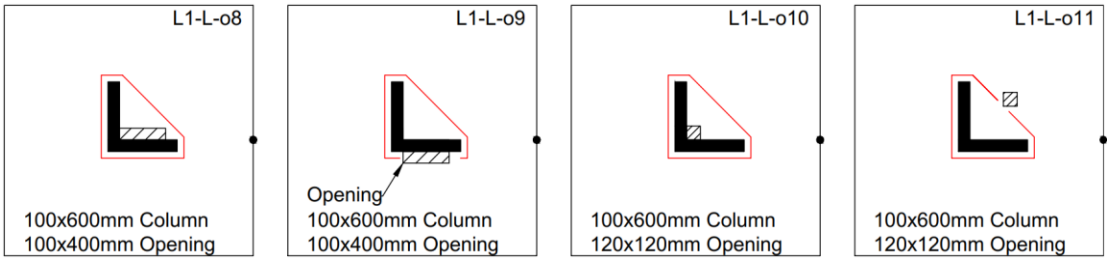


Figure I-15: Reduced Critical Perimeters for Slab-Column Connections with Openings According to ACI 318-19 – L1-L Specimens

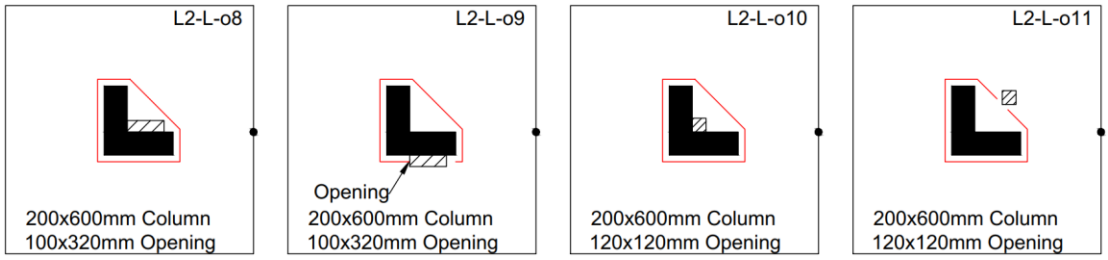


Figure I-16: Reduced Critical Perimeters for Slab-Column Connections with Openings According to ACI 318-19 – L2-L Specimens

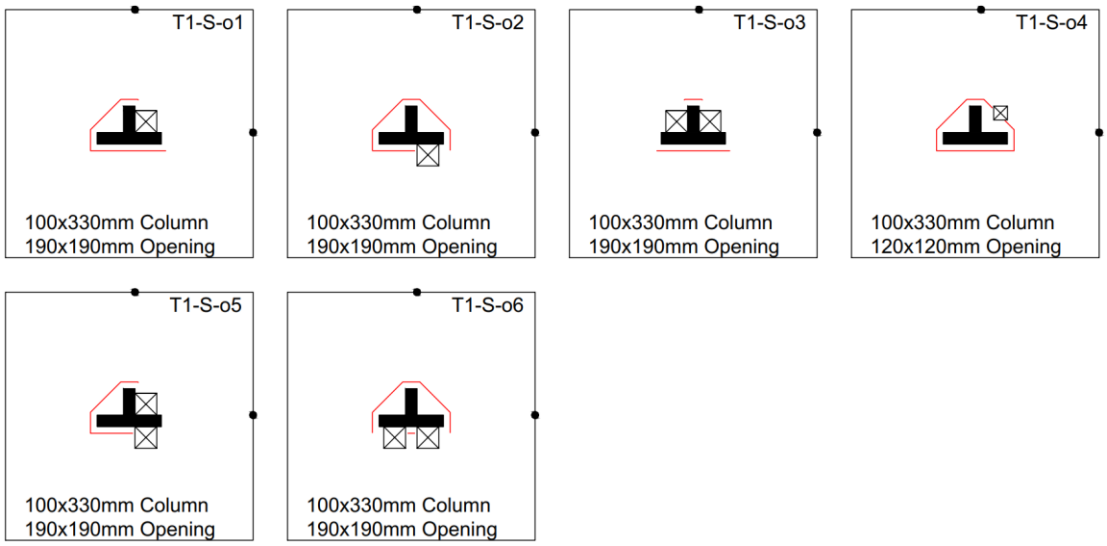


Figure I-17: Reduced Critical Perimeters for Slab-Column Connections with Openings According to ACI 318-19 – T1-S Specimens

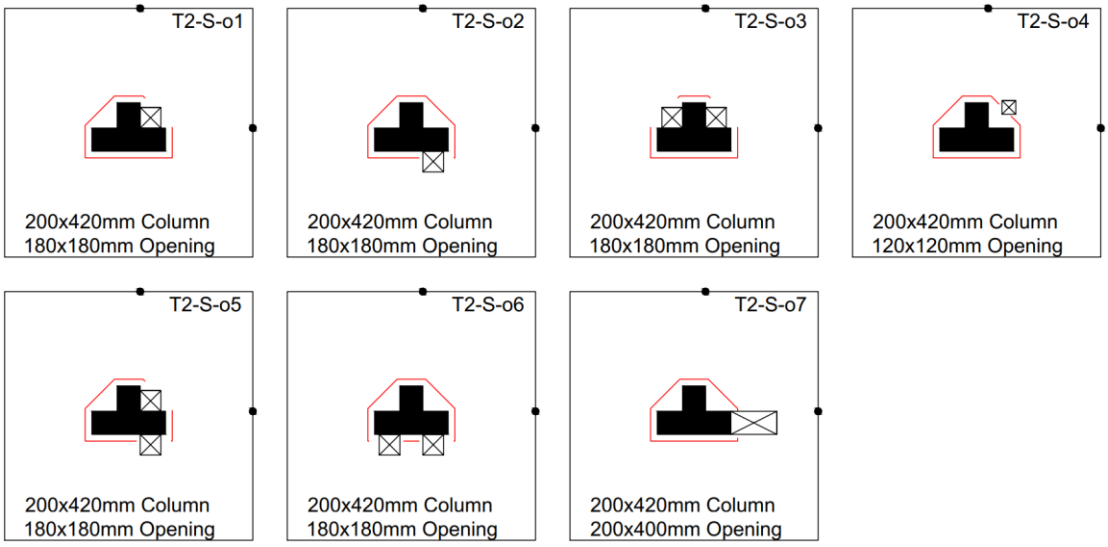


Figure I-18: Reduced Critical Perimeters for Slab-Column Connections with Openings According to ACI 318-19 – T2-S Specimens

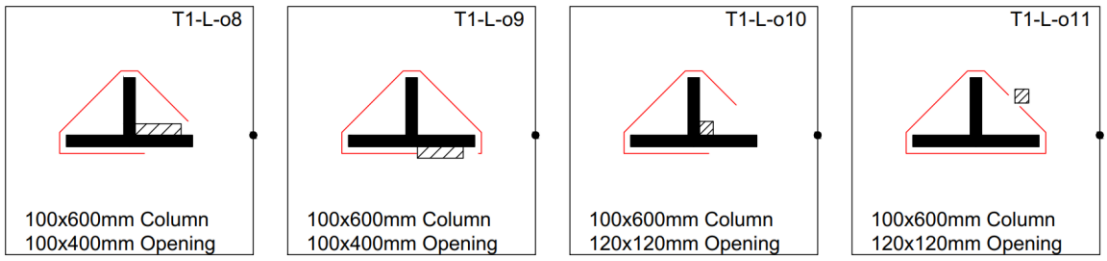


Figure I-19: Reduced Critical Perimeters for Slab-Column Connections with Openings According to ACI 318-19 – T1-L Specimens

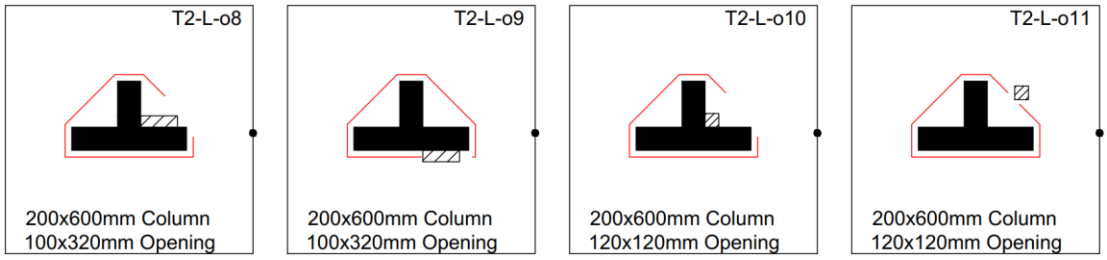


Figure I-20: Reduced Critical Perimeters for Slab-Column Connections with Openings According to ACI 318-19 – T2-L Specimens

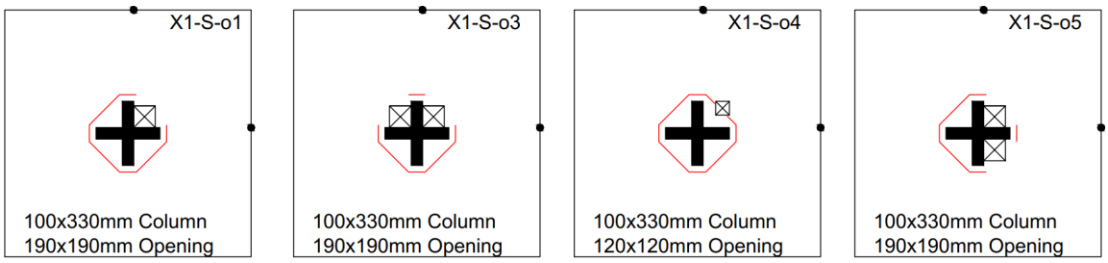


Figure I-21: Reduced Critical Perimeters for Slab-Column Connections with Openings According to ACI 318-19 – X1-S Specimens

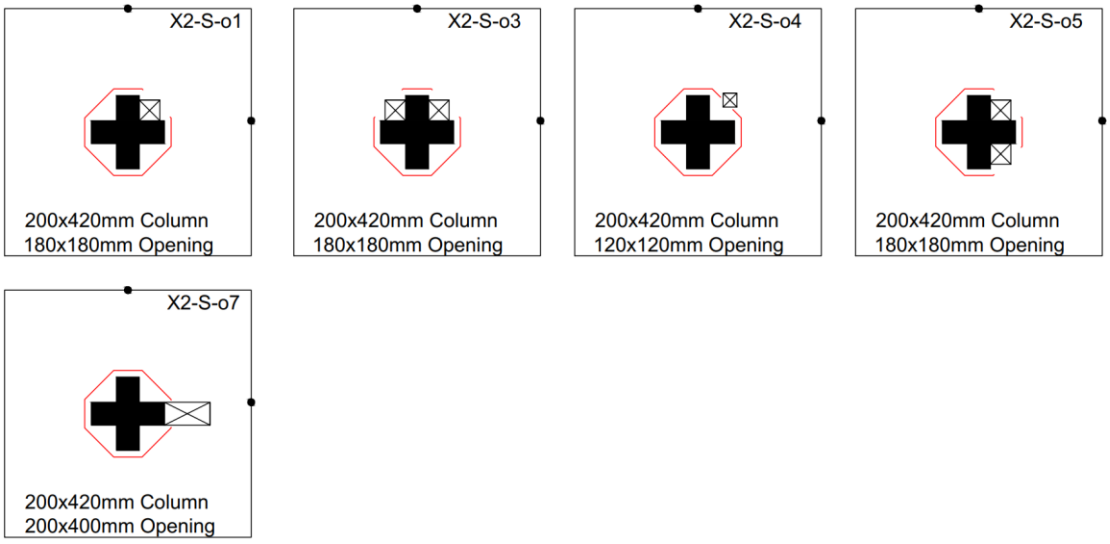


Figure I-22: Reduced Critical Perimeters for Slab-Column Connections with Openings According to ACI 318-19 – X2-S Specimens

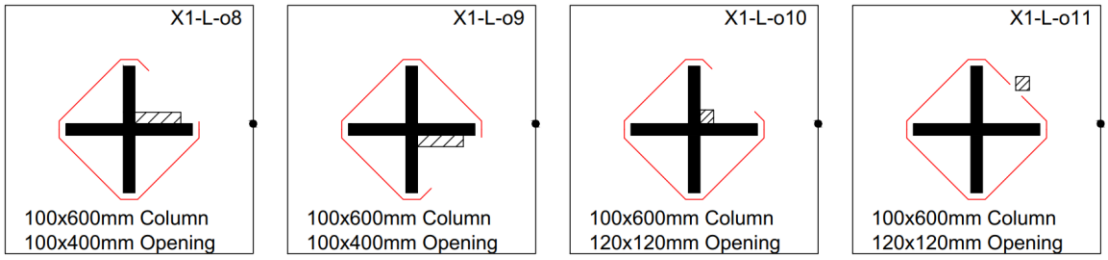


Figure I-23: Reduced Critical Perimeters for Slab-Column Connections with Openings According to ACI 318-19 – X1-L Specimens

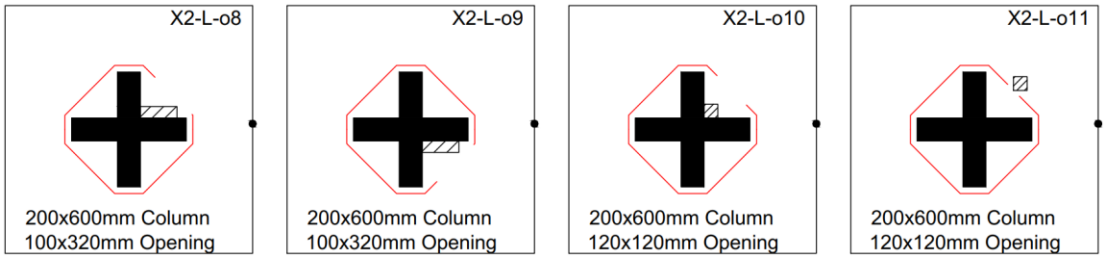


Figure I-24: Reduced Critical Perimeters for Slab-Column Connections with Openings According to ACI 318-19 – X2-L Specimens

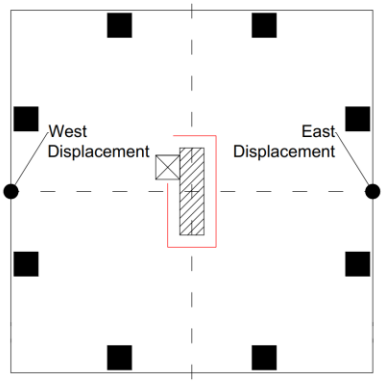


Figure I-25: Reduced Critical Perimeters for R2x7.2o Specimens According to ACI 318-19 (Radial Approach)

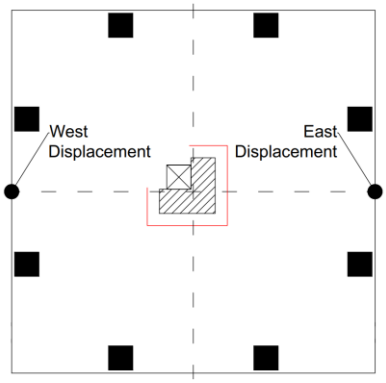


Figure I-26: Reduced Critical Perimeters for L2x4.6o Specimens According to ACI 318-19

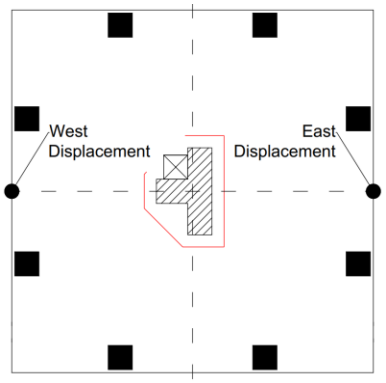


Figure I-27: Reduced Critical Perimeters for T2x4.6o Specimens According to ACI 318-19

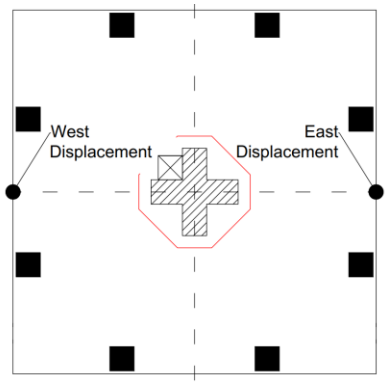


Figure I-28: Reduced Critical Perimeters for X2x4.6o Specimens According to ACI 318-19

Appendix J

Predicted Crack Patterns and Shear Stress Distributions – Special-Shaped and Rectangular Slab-Column Connections – Concentric Loading Study

In this appendix, the crack patterns and shear stress distributions along the column perimeter at the peak load level predicted by the NLFEA for all specimens discussed in Chapter 8 are provided. These plots are supplemental to the representative figures which were provided in Chapter 8. Note, the methodology used to calculate the shear stress distributions from the FEA results is discussed in Appendix A.

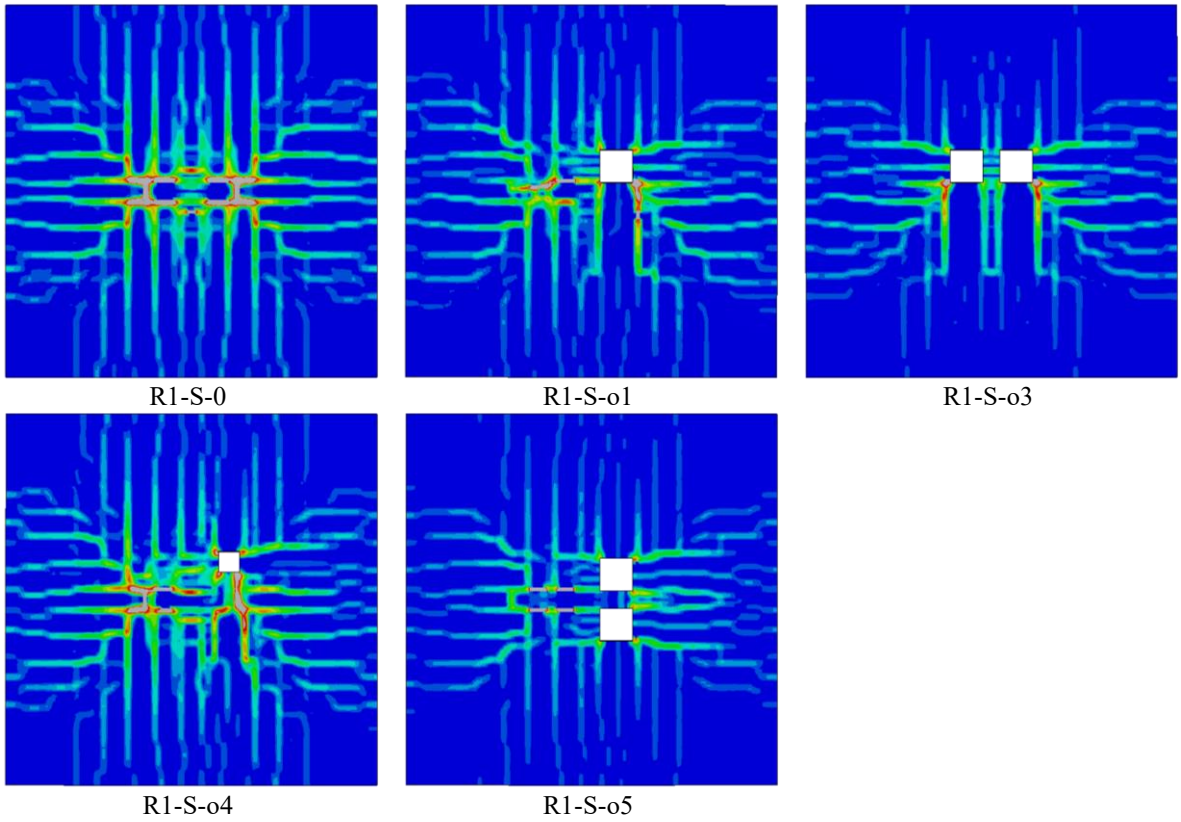


Figure J-1: Predicted Tension Surface Crack Patterns, R1-S Specimens (Grey Regions Have Principal Plastic Strains > 0.02)

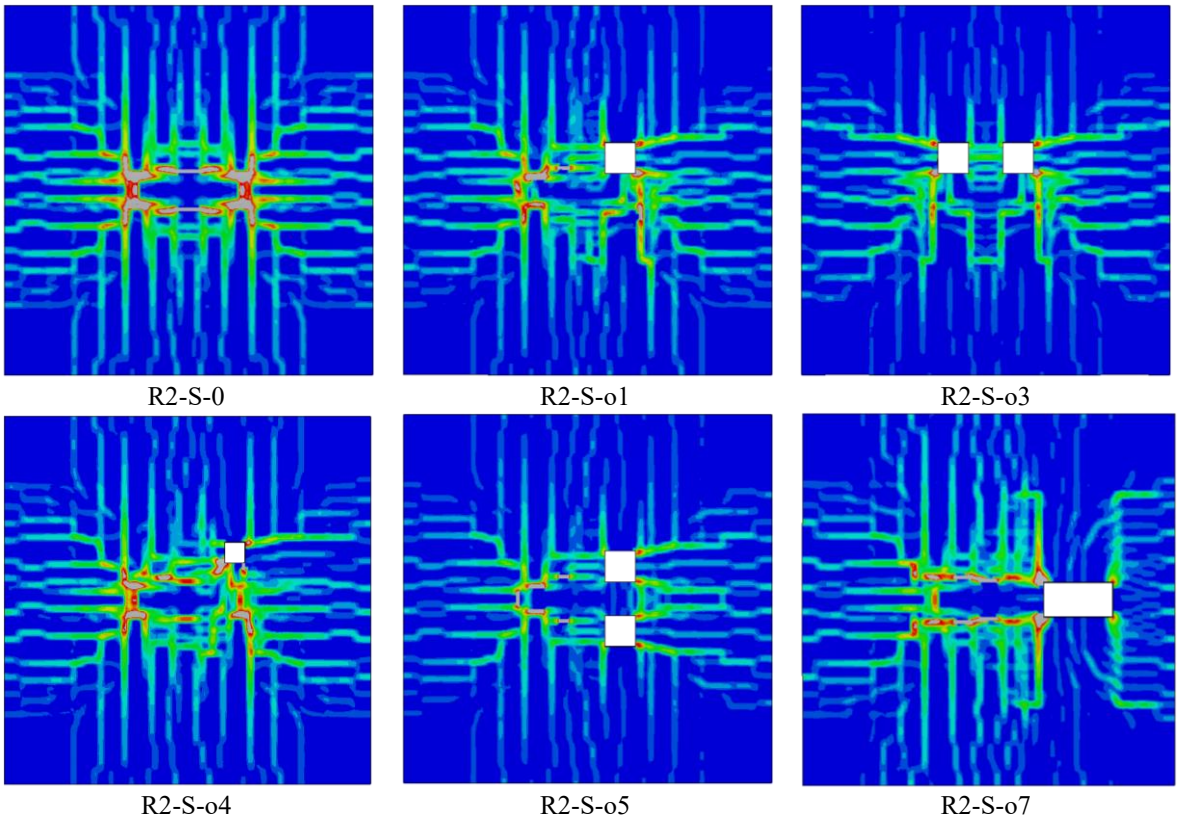


Figure J-2: Predicted Tension Surface Crack Patterns, R2-S Specimens (Grey Regions Have Principal Plastic Strains > 0.02)

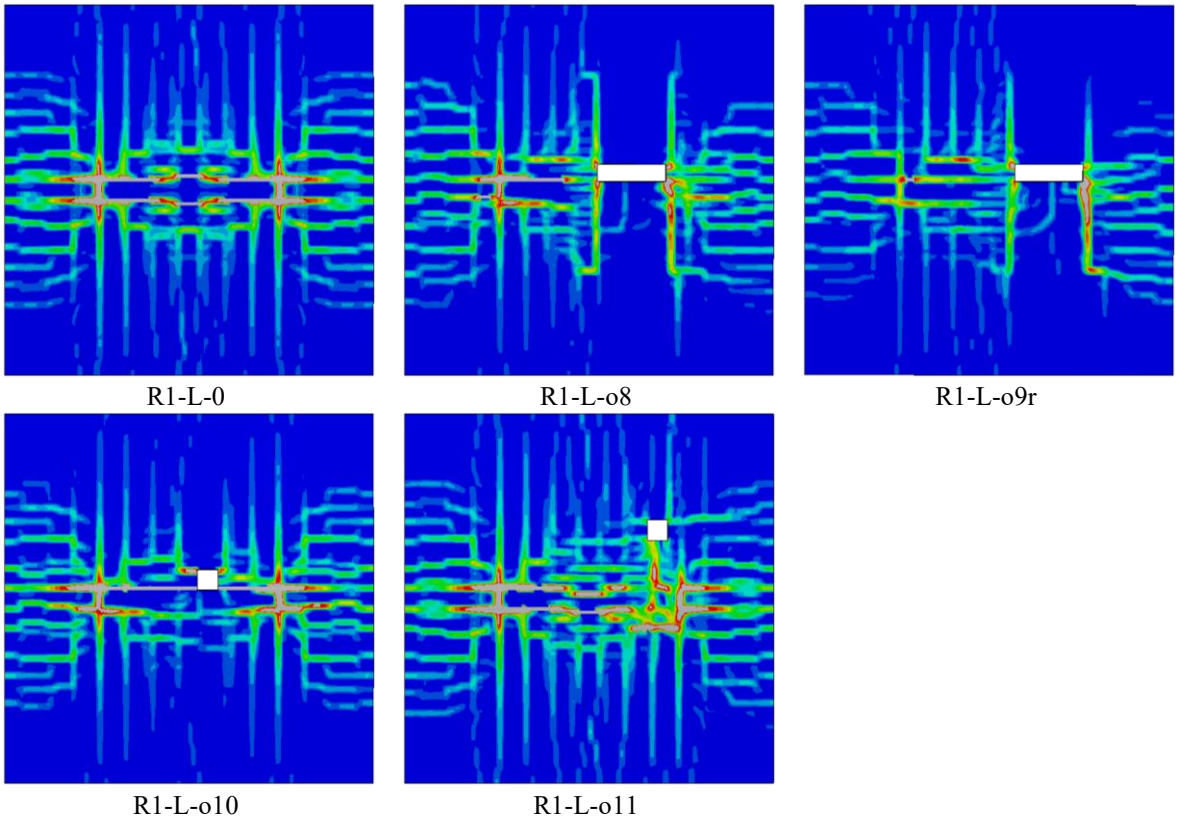


Figure J-3: Predicted Tension Surface Crack Patterns, R1-L Specimens (Grey Regions Have Principal Plastic Strains > 0.02)

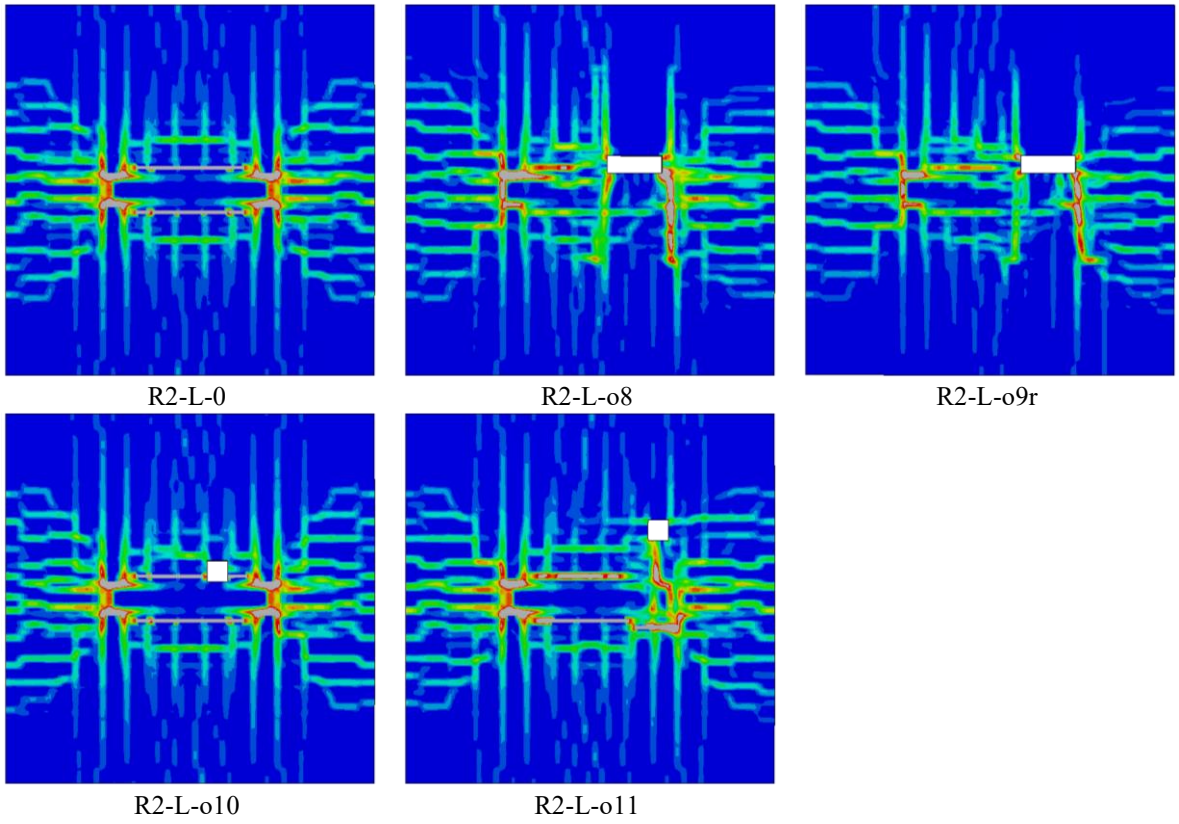


Figure J-4: Predicted Tension Surface Crack Patterns, R2-L Specimens (Grey Regions Have Principal Plastic Strains > 0.02)

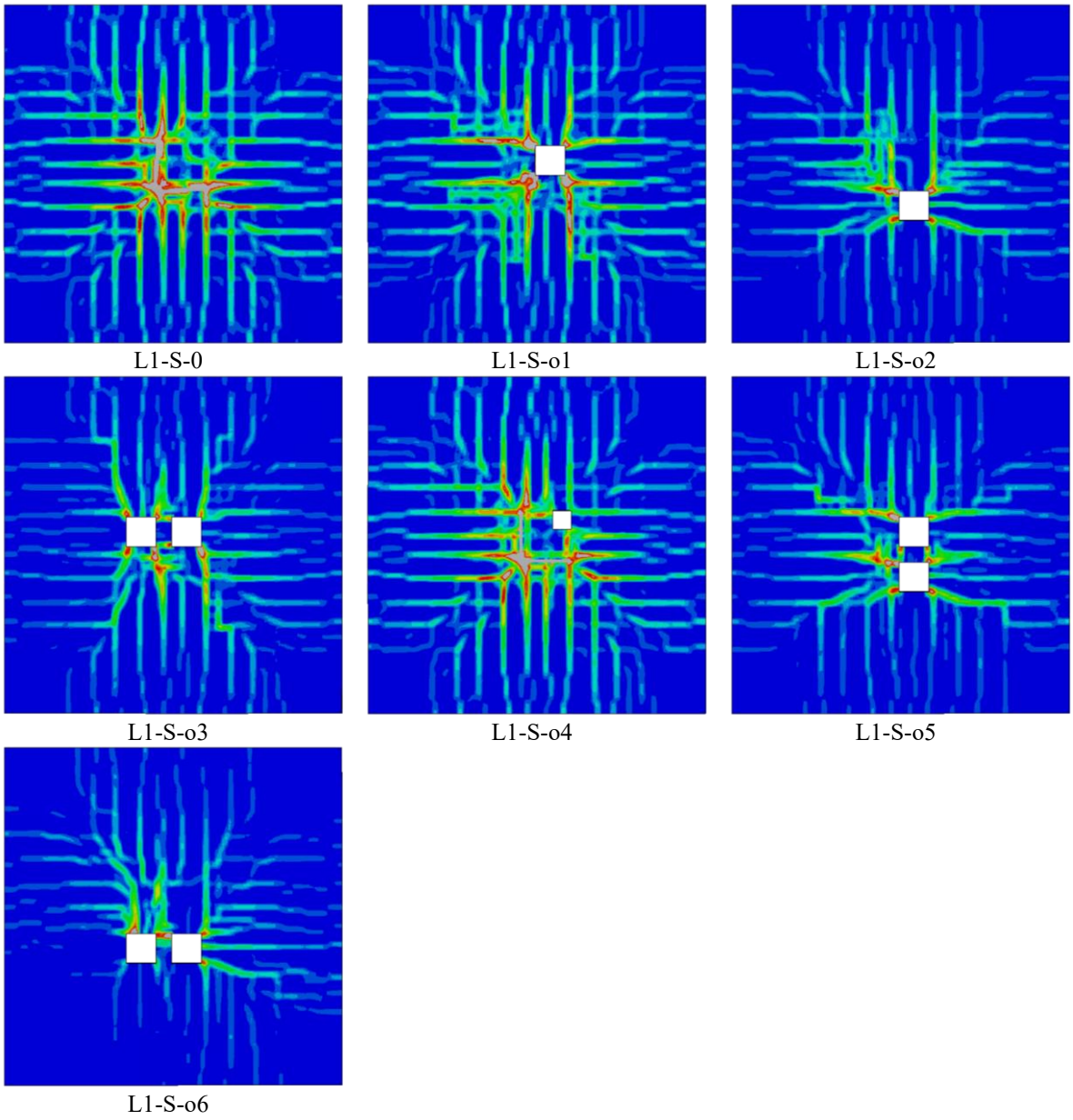


Figure J-5: Predicted Tension Surface Crack Patterns, L1-S Specimens (Grey Regions Have Principal Plastic Strains > 0.02)

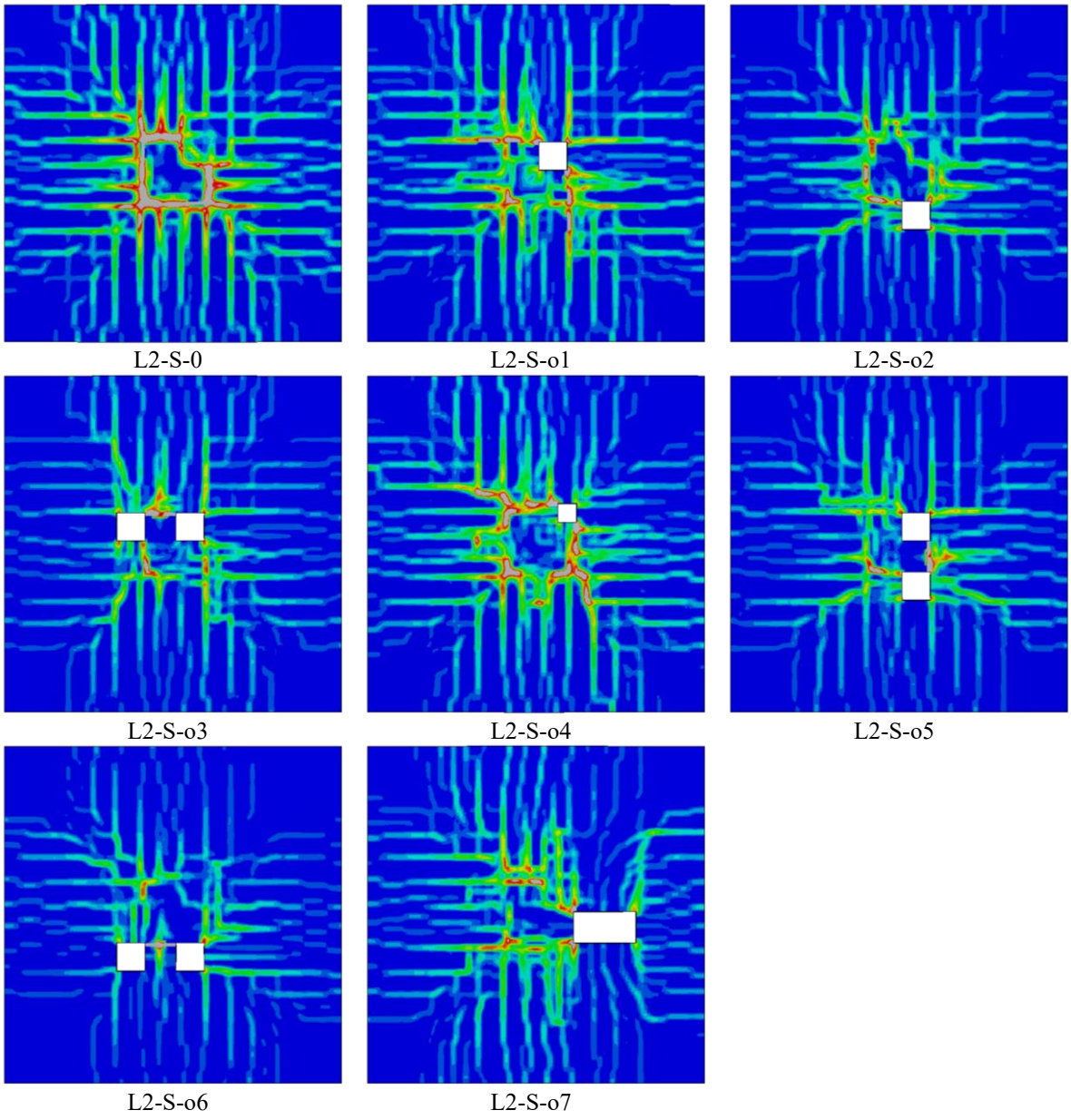


Figure J-6: Predicted Tension Surface Crack Patterns, L2-S Specimens (Grey Regions Have Principal Plastic Strains > 0.02)

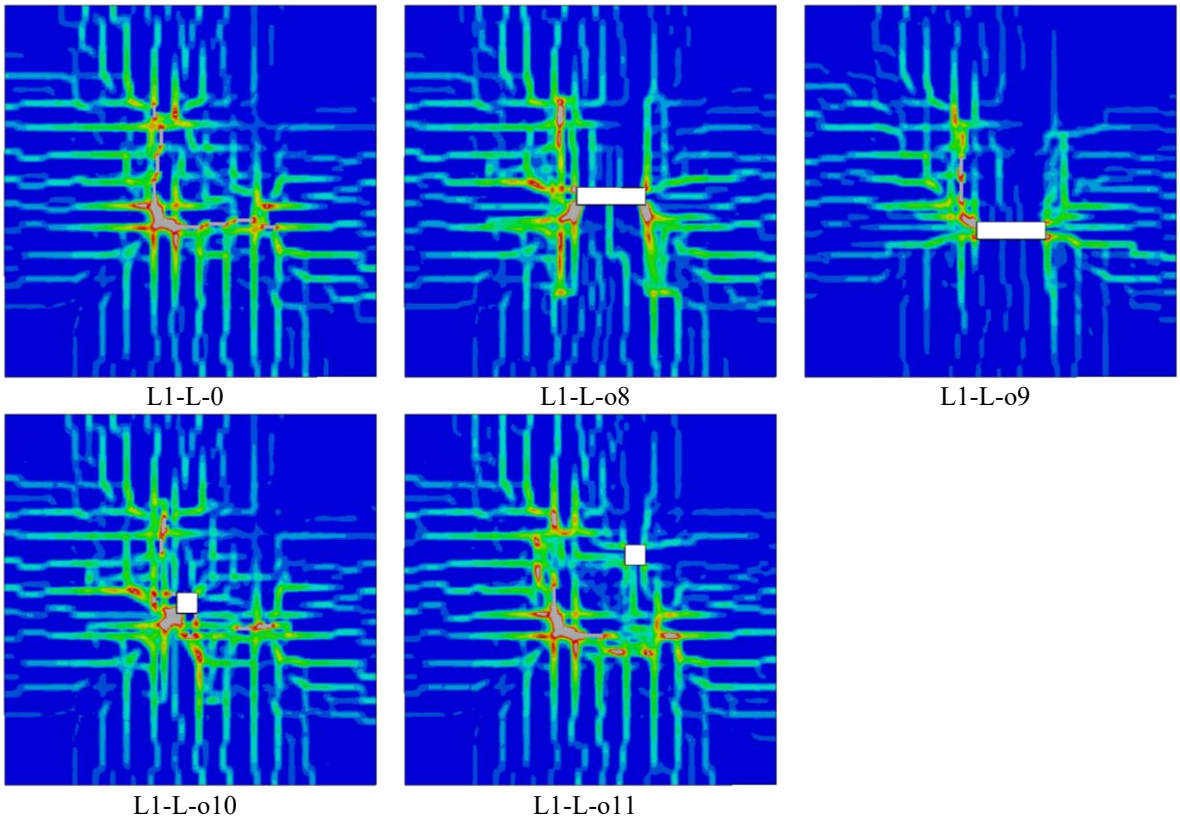


Figure J-7: Predicted Tension Surface Crack Patterns, L1-L Specimens (Grey Regions Have Principal Plastic Strains > 0.02)

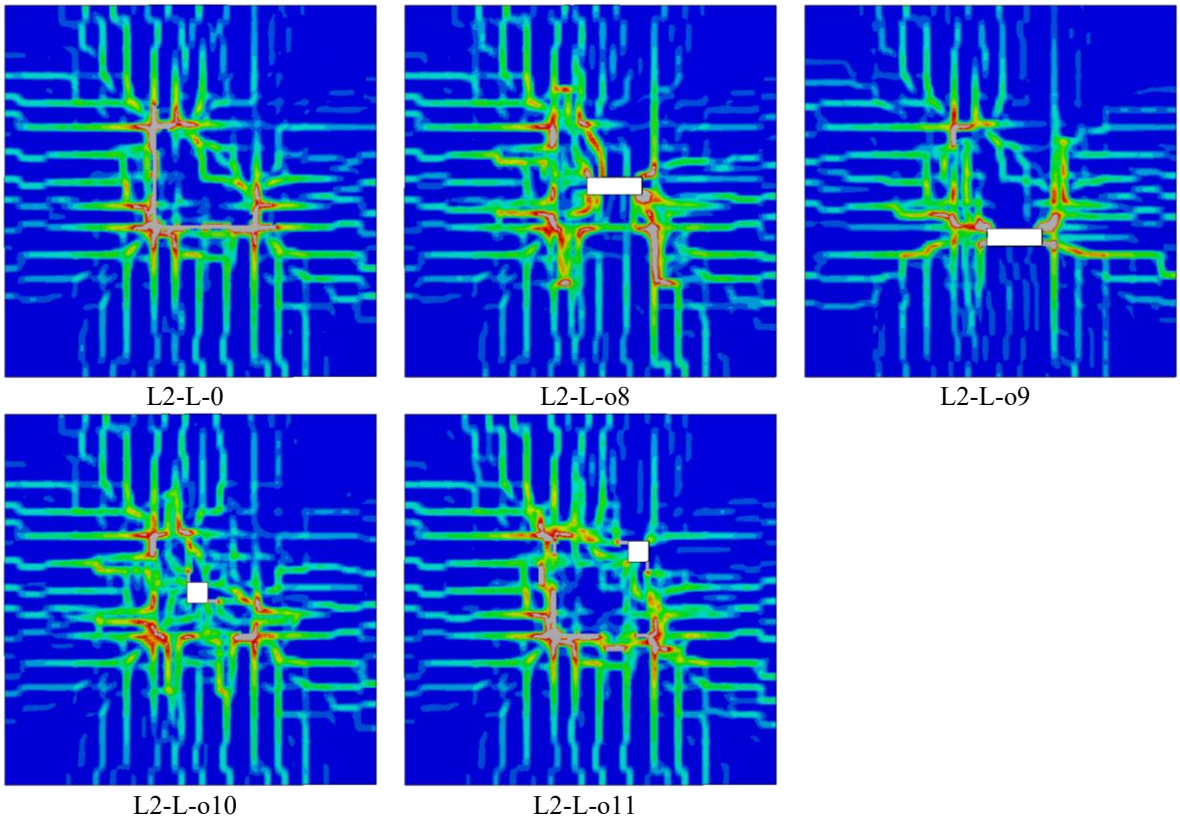


Figure J-8: Predicted Tension Surface Crack Patterns, L2-L Specimens (Grey Regions Have Principal Plastic Strains > 0.02)

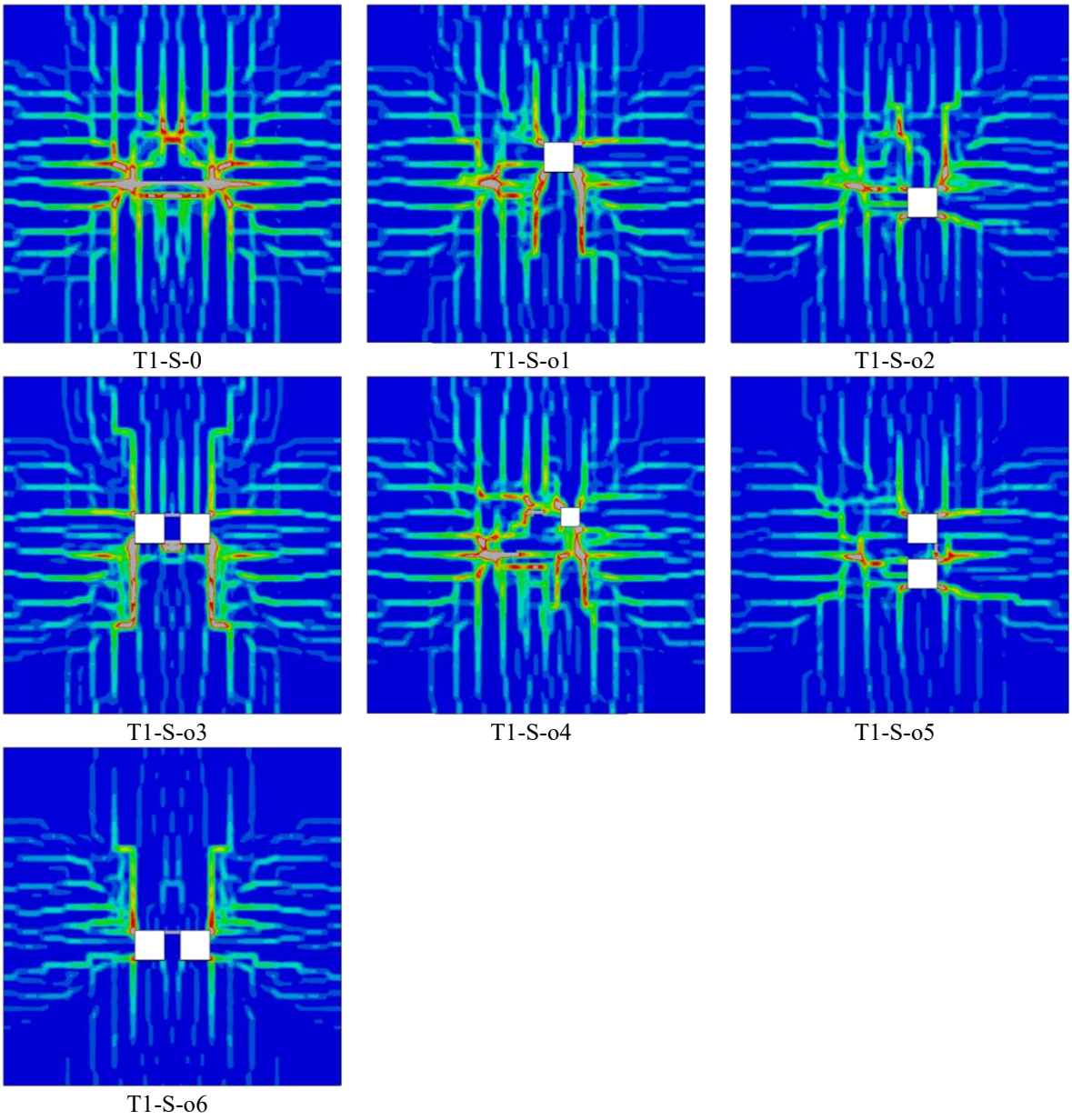


Figure J-9: Predicted Tension Surface Crack Patterns, T1-S Specimens (Grey Regions Have Principal Plastic Strains > 0.02)

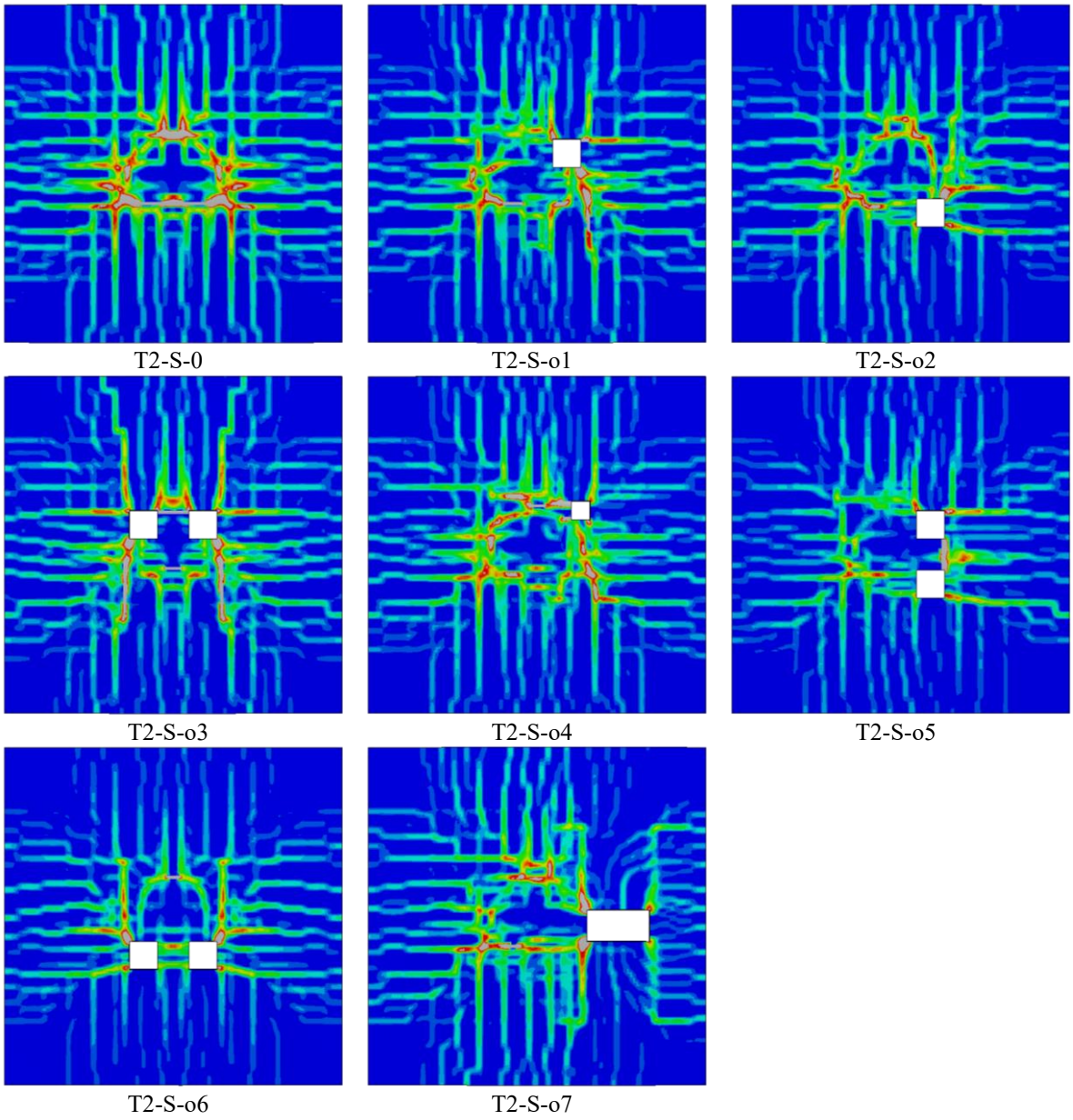


Figure J-10: Predicted Tension Surface Crack Patterns, T2-S Specimens (Grey Regions Have Principal Plastic Strains > 0.02)

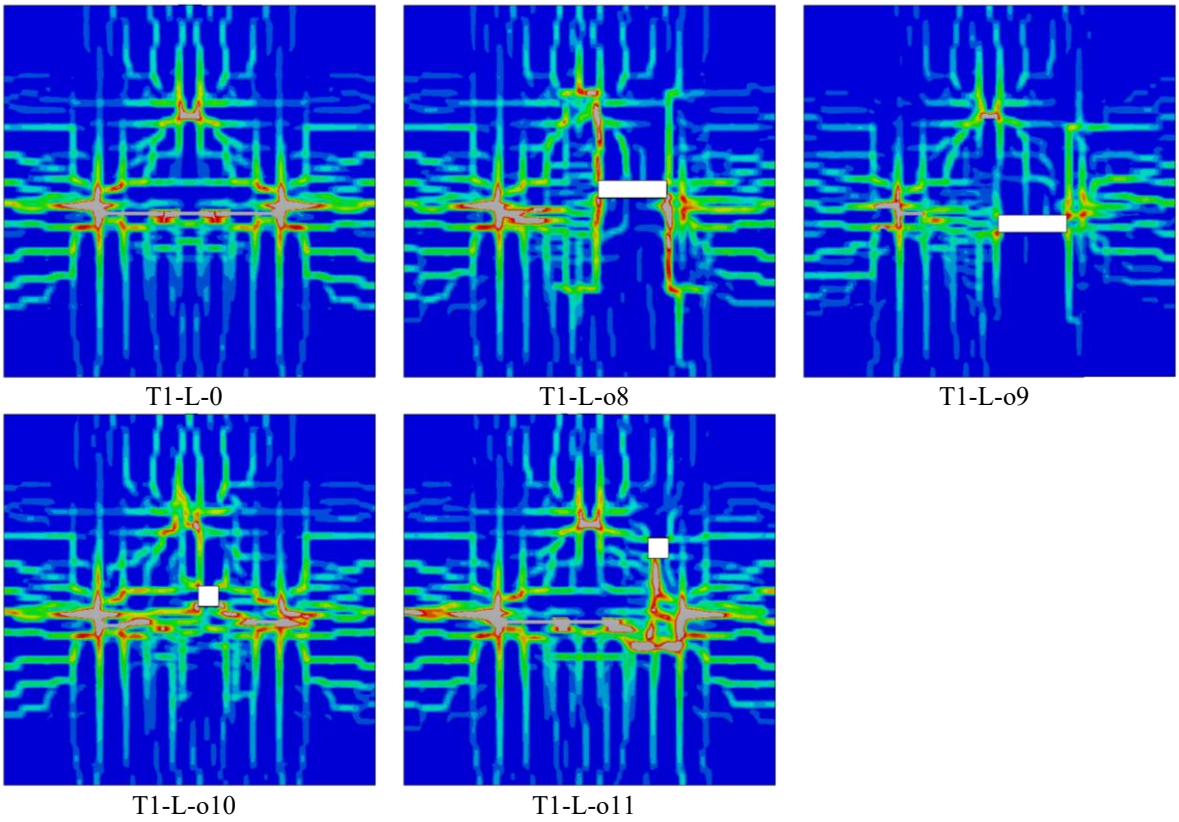


Figure J-11: Predicted Tension Surface Crack Patterns, T1-L Specimens (Grey Regions Have Principal Plastic Strains > 0.02)

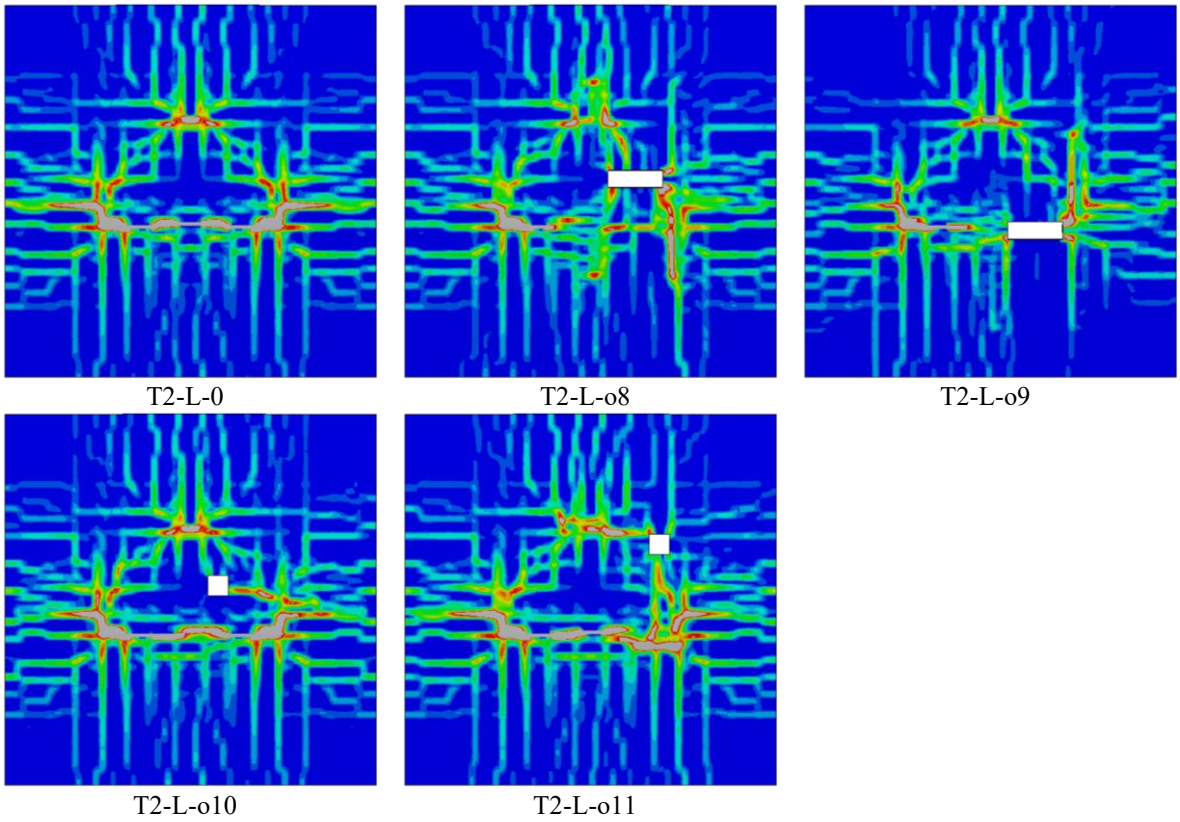


Figure J-12: Predicted Tension Surface Crack Patterns, T2-L Specimens (Grey Regions Have Principal Plastic Strains > 0.02)

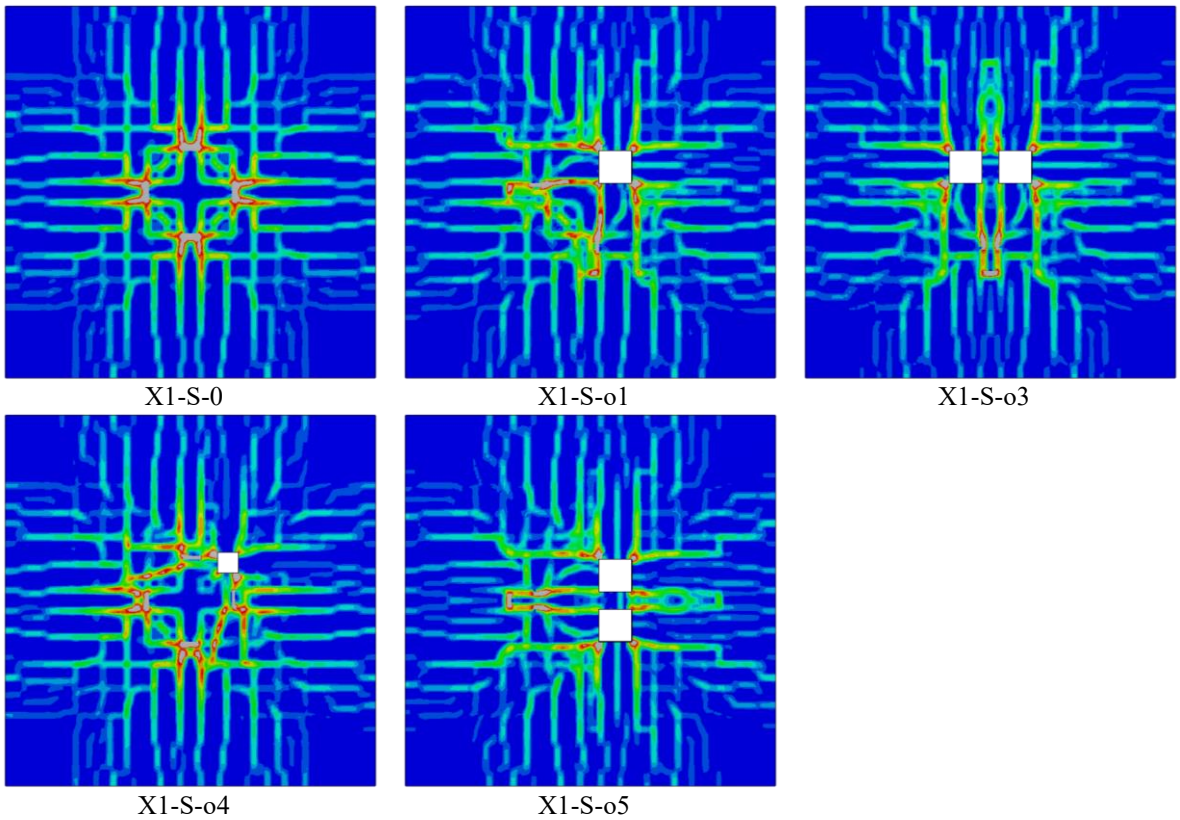


Figure J-13: Predicted Tension Surface Crack Patterns, X1-S Specimens (Grey Regions Have Principal Plastic Strains > 0.02)

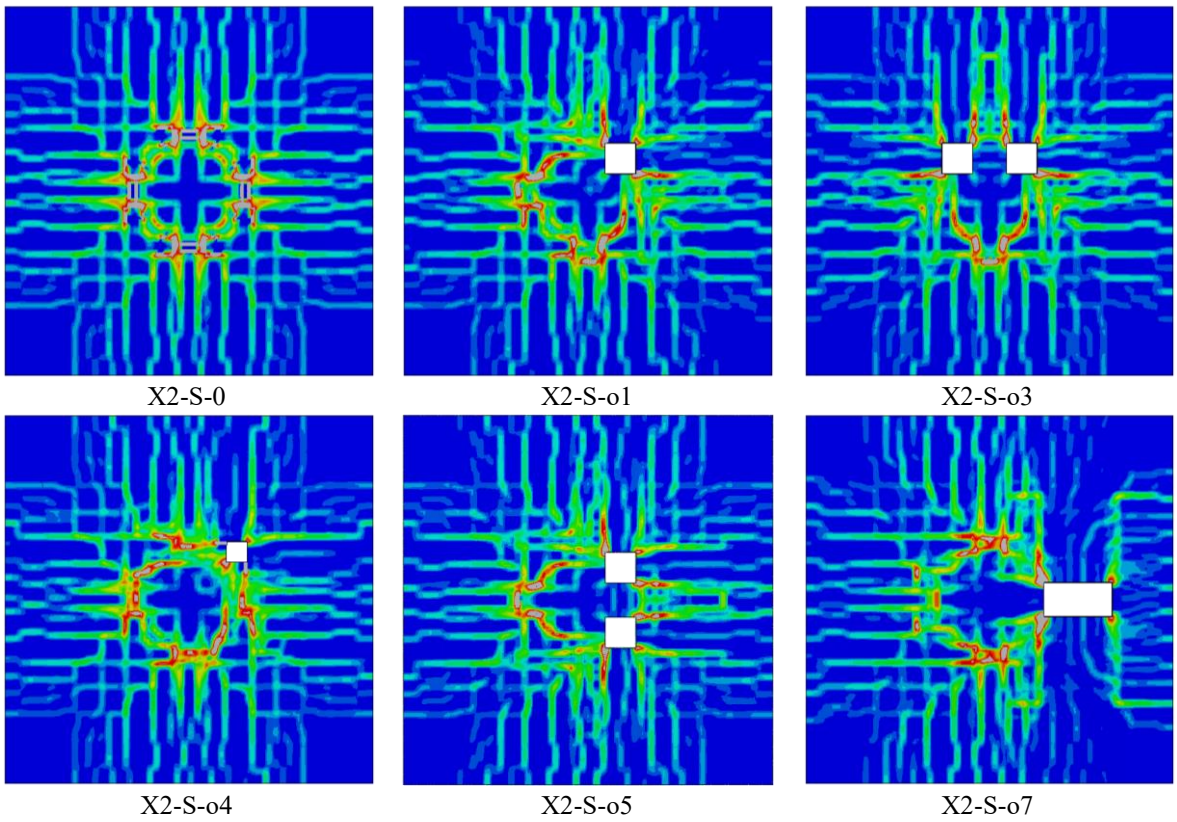


Figure J-14: Predicted Tension Surface Crack Patterns, X2-S Specimens (Grey Regions Have Principal Plastic Strains > 0.02)

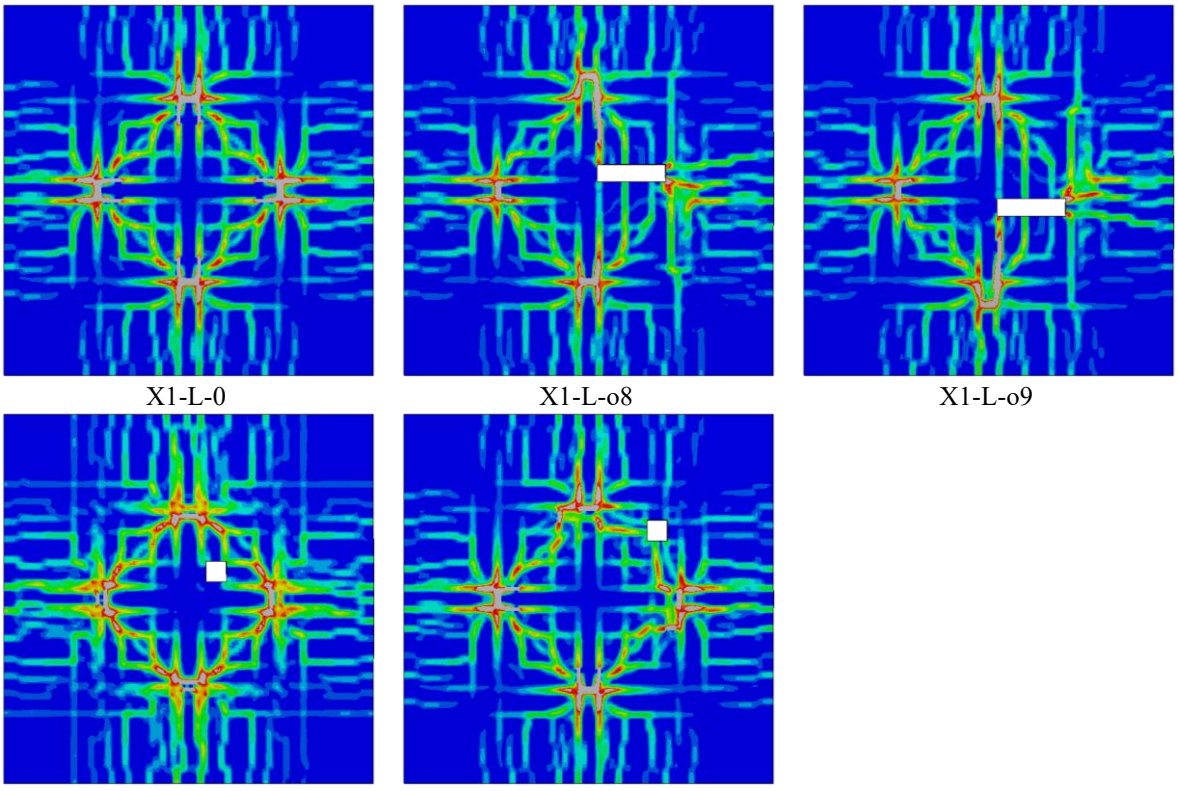


Figure J-15: Predicted Tension Surface Crack Patterns, X1-L Specimens (Grey Regions Have Principal Plastic Strains > 0.02)

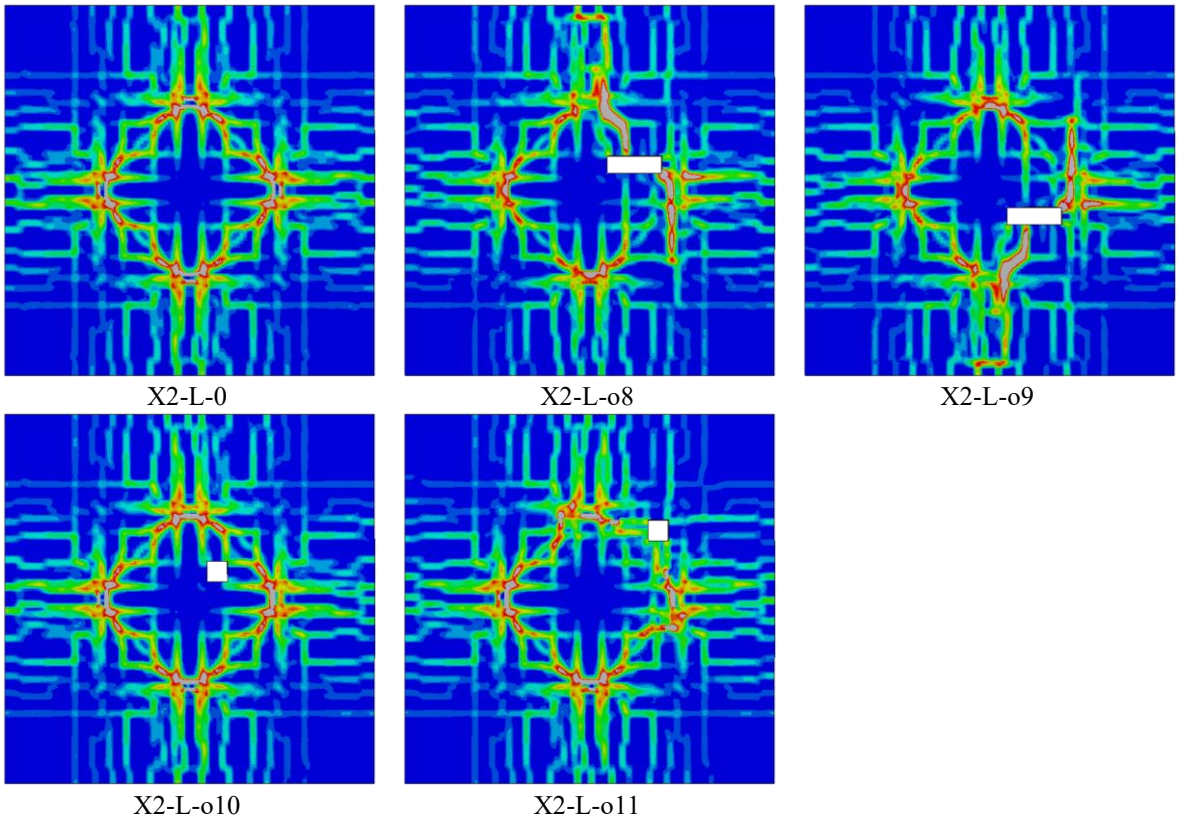


Figure J-16: Predicted Tension Surface Crack Patterns, X2-L Specimens (Grey Regions Have Principal Plastic Strains > 0.02)

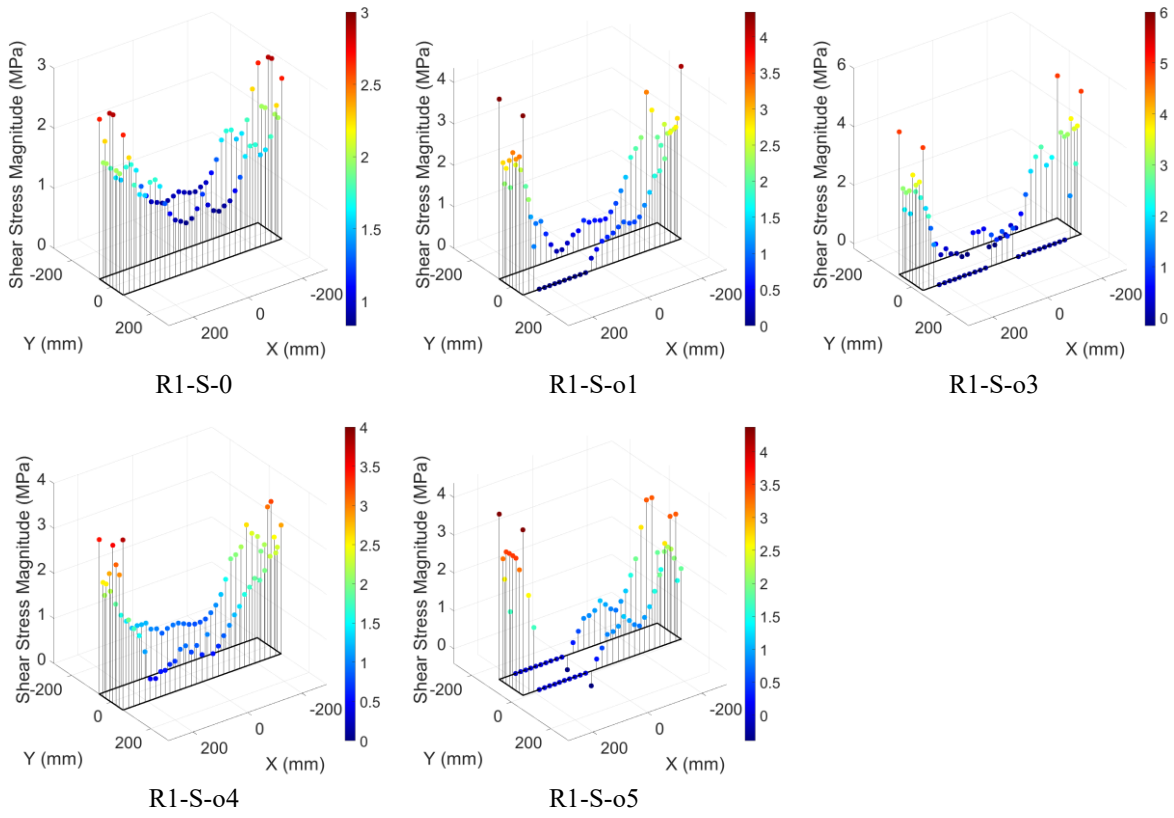


Figure J-17: Column Perimeter Shear Stress Distributions at Peak Load – R1-S Specimens (Stresses Averaged Over Depth)

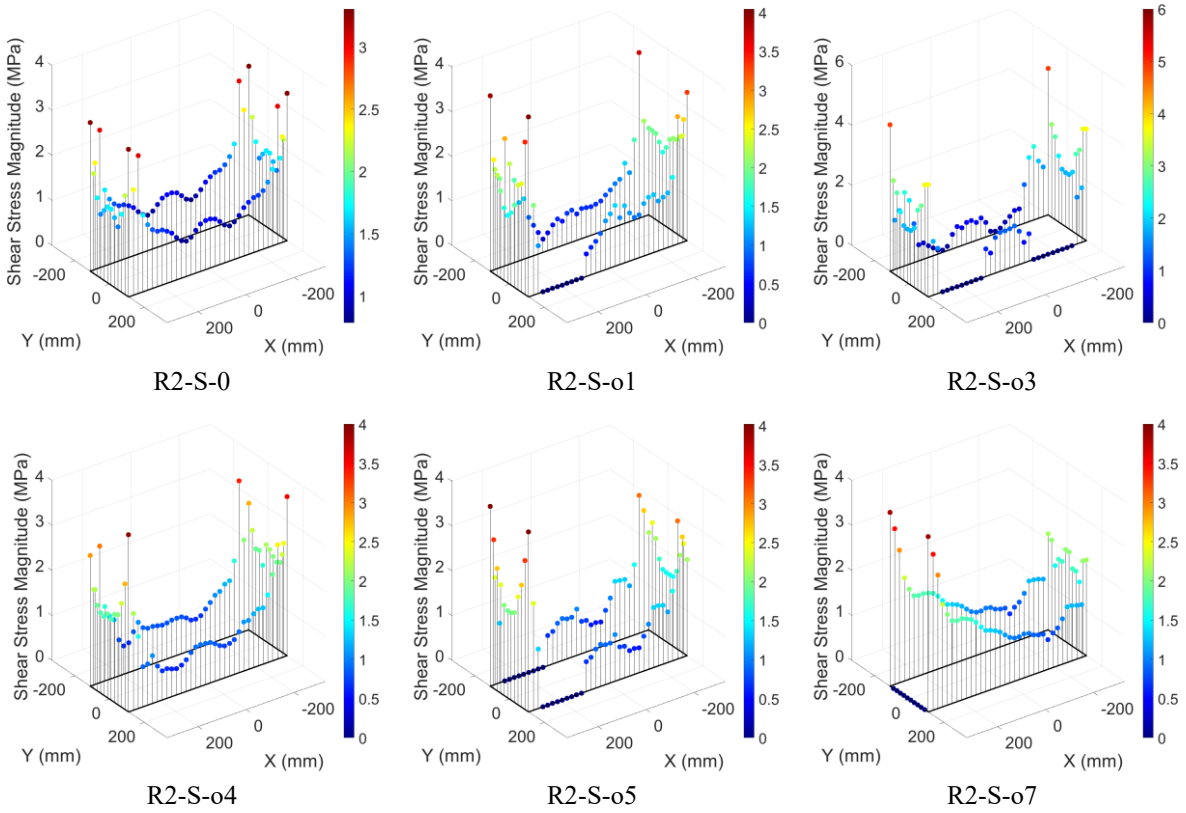


Figure J-18: Column Perimeter Shear Stress Distributions at Peak Load – R2-S Specimens (Stresses Averaged Over Depth)

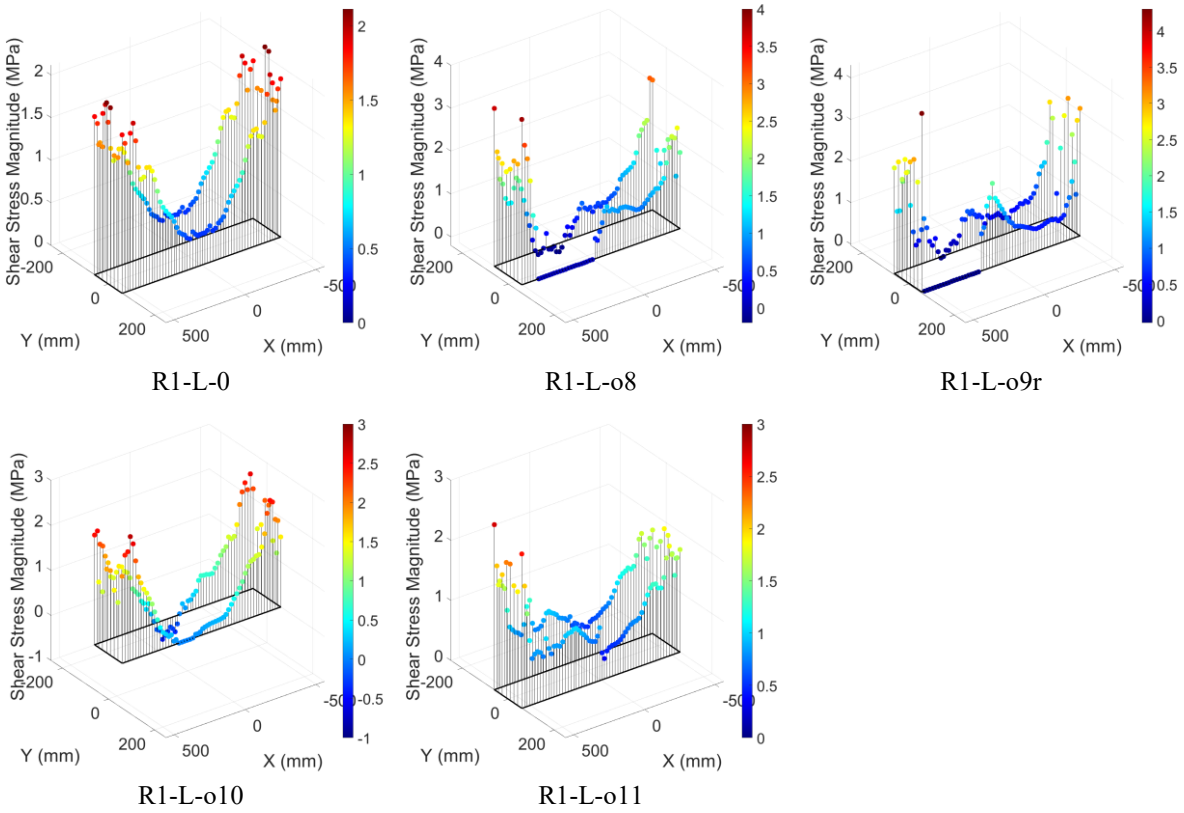


Figure J-19: Column Perimeter Shear Stress Distributions at Peak Load – R1-L Specimens (Stresses Averaged Over Depth)

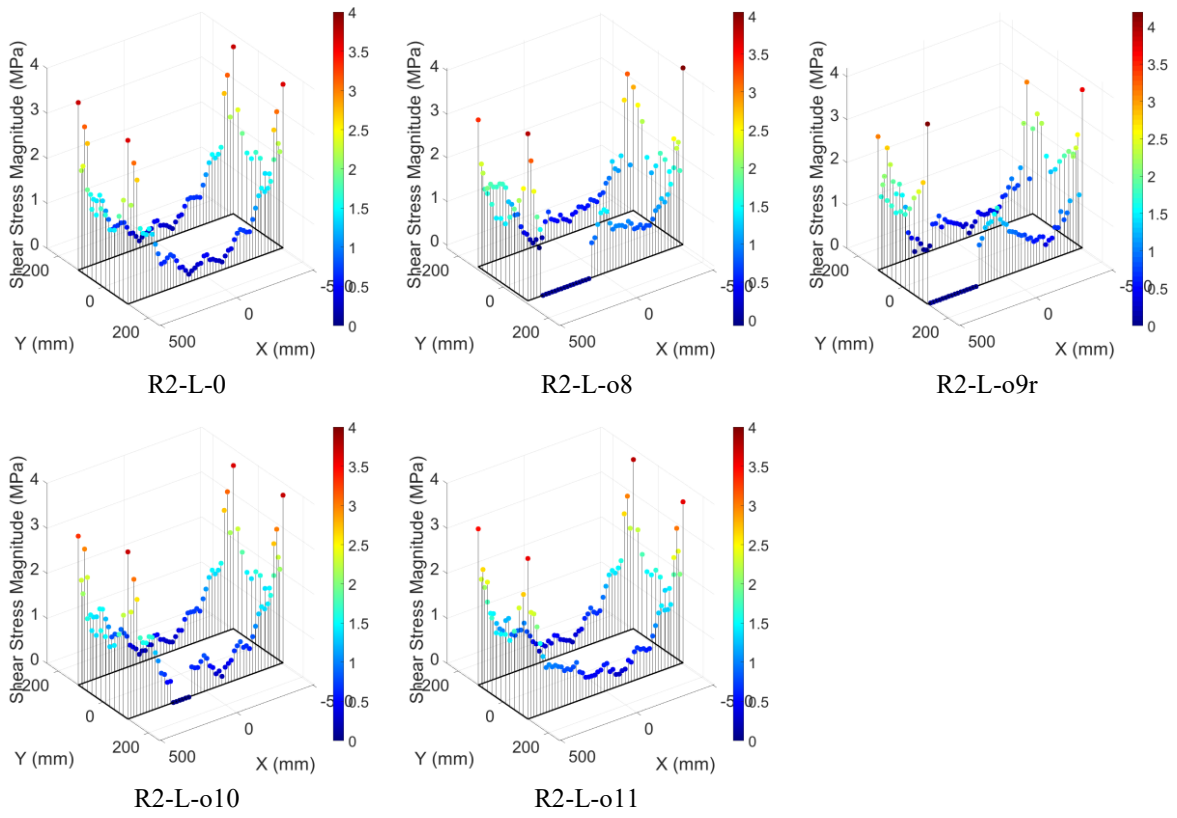


Figure J-20: Column Perimeter Shear Stress Distributions at Peak Load – R2-L Specimens (Stresses Averaged Over Depth)

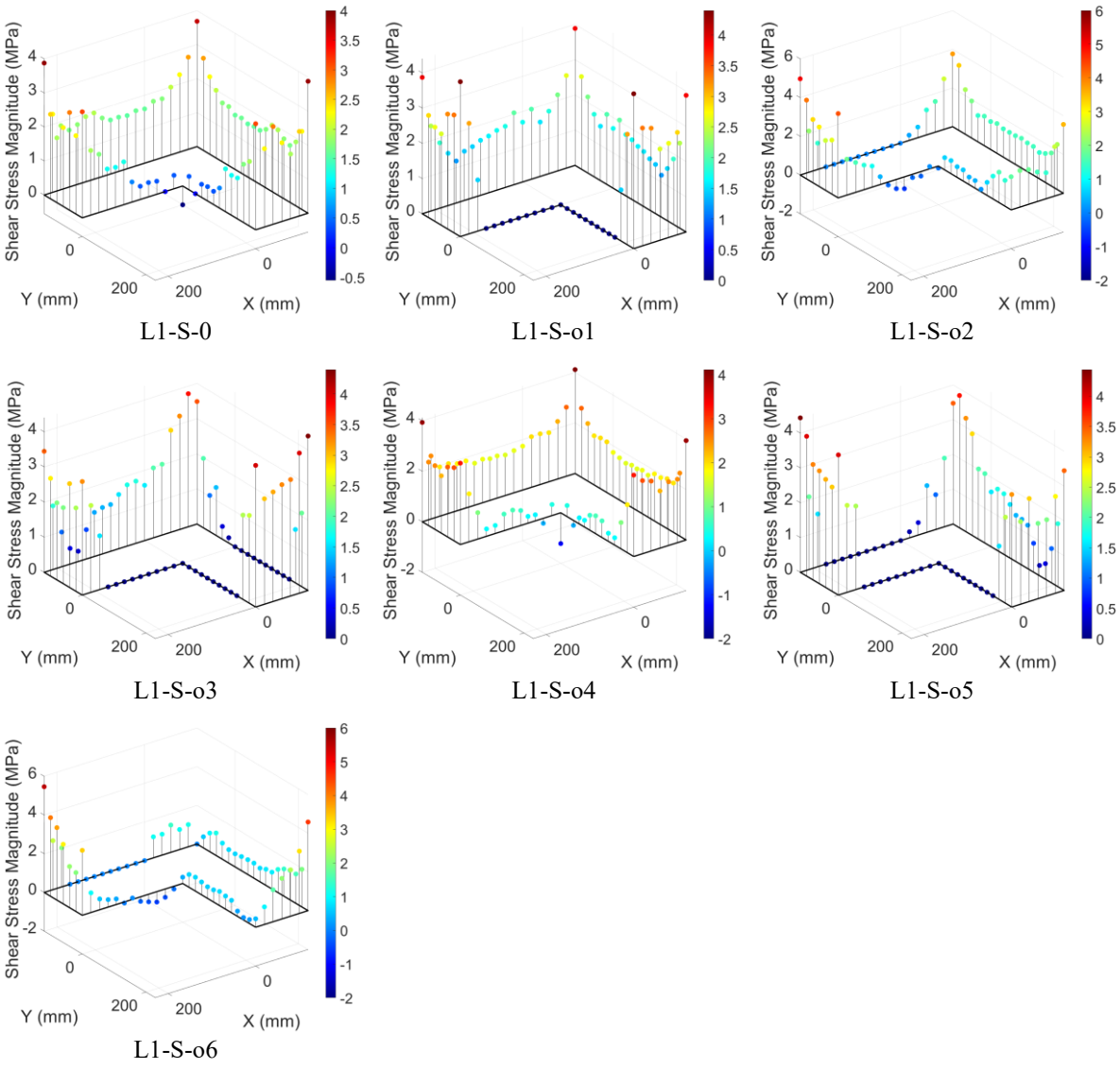


Figure J-21: Column Perimeter Shear Stress Distributions at Peak Load – L1-S Specimens (Stresses Averaged Over Depth)

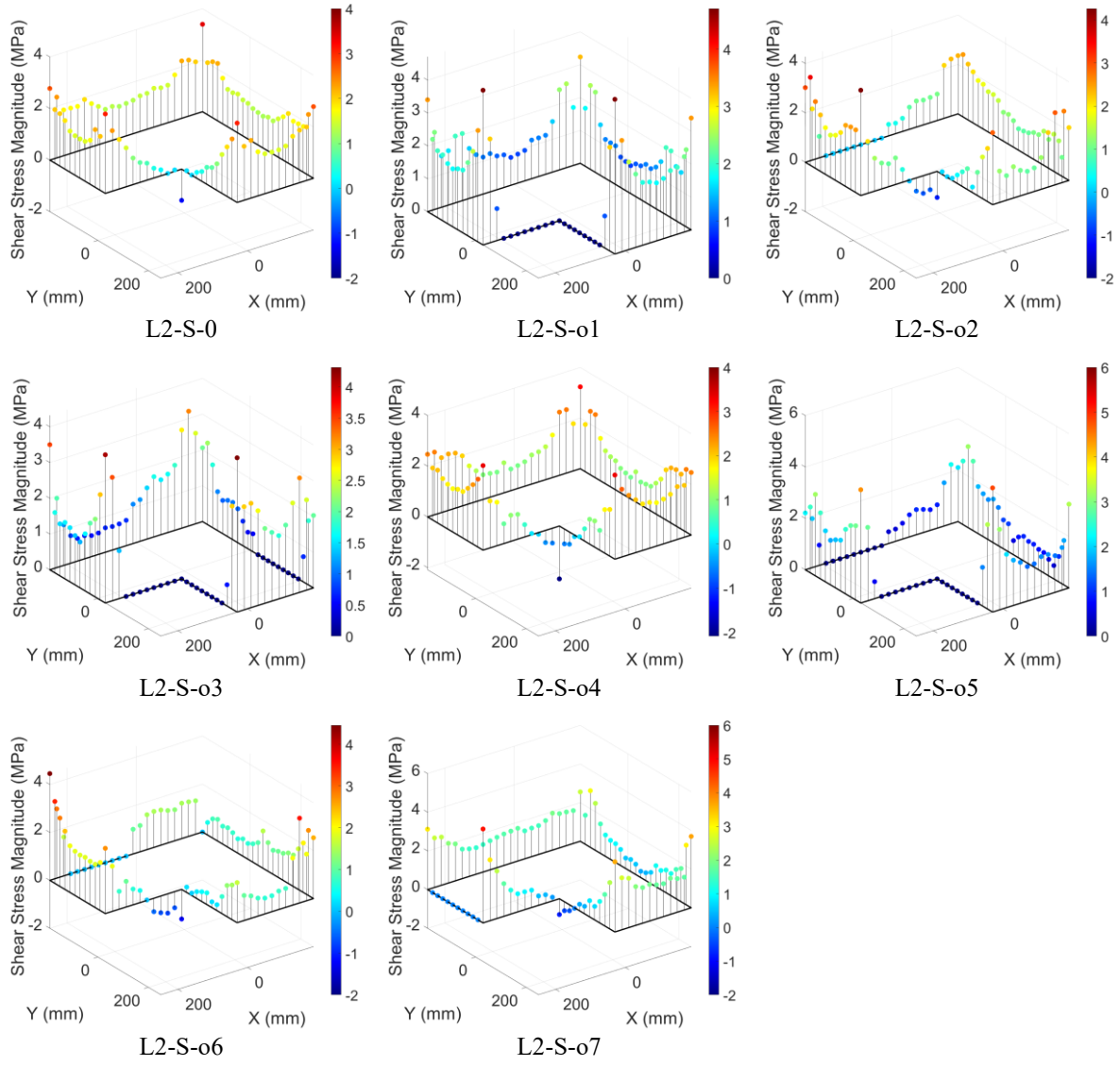


Figure J-22: Column Perimeter Shear Stress Distributions at Peak Load – L2-S Specimens (Stresses Averaged Over Depth)

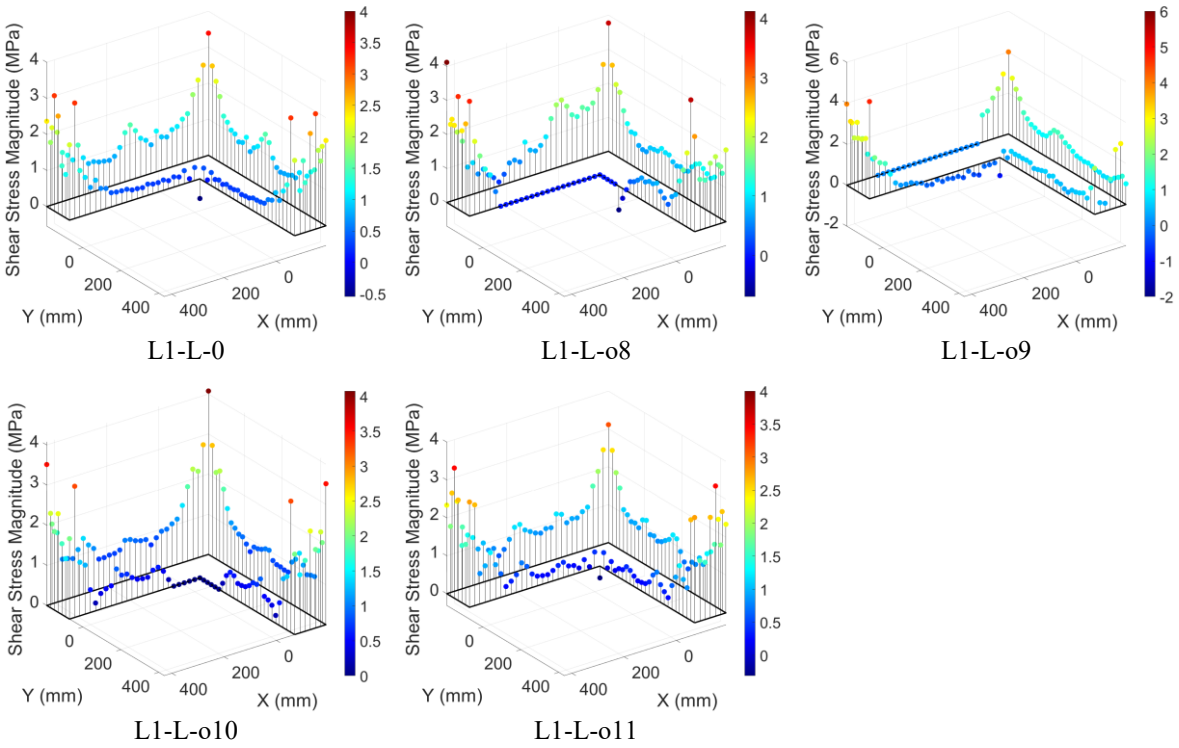


Figure J-23: Column Perimeter Shear Stress Distributions at Peak Load – L1-L Specimens (Stresses Averaged Over Depth)

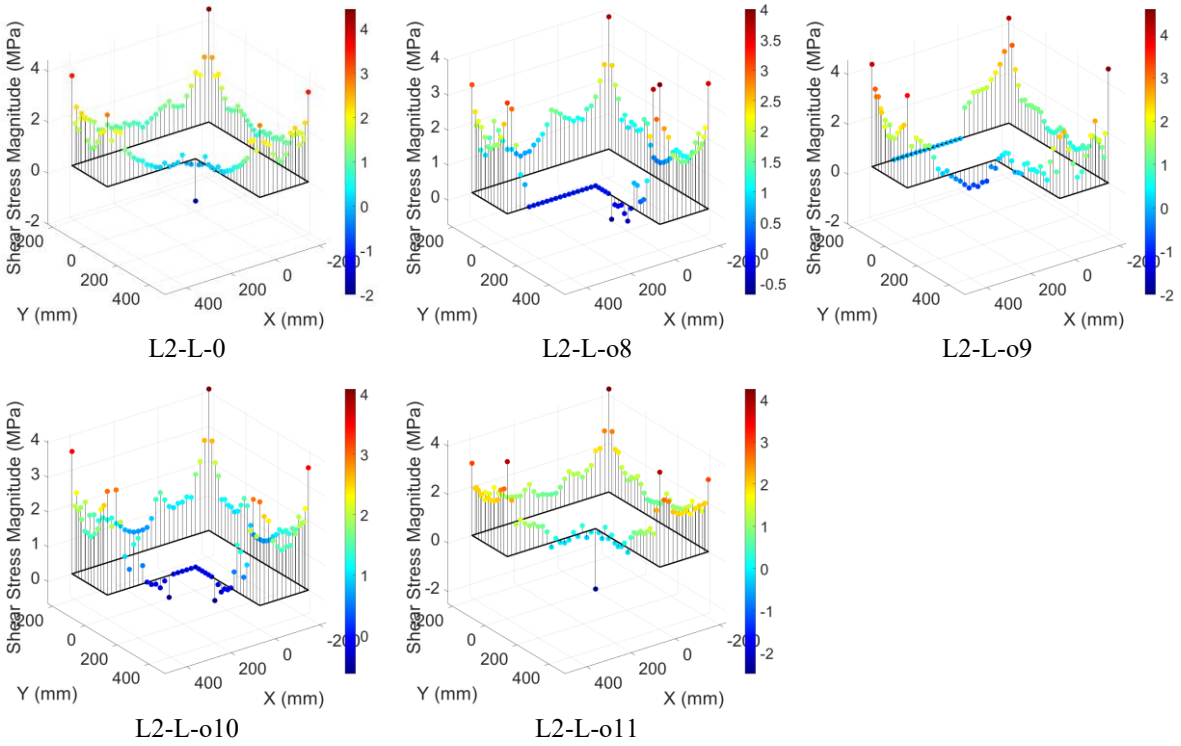


Figure J-24: Column Perimeter Shear Stress Distributions at Peak Load – L2-L Specimens (Stresses Averaged Over Depth)

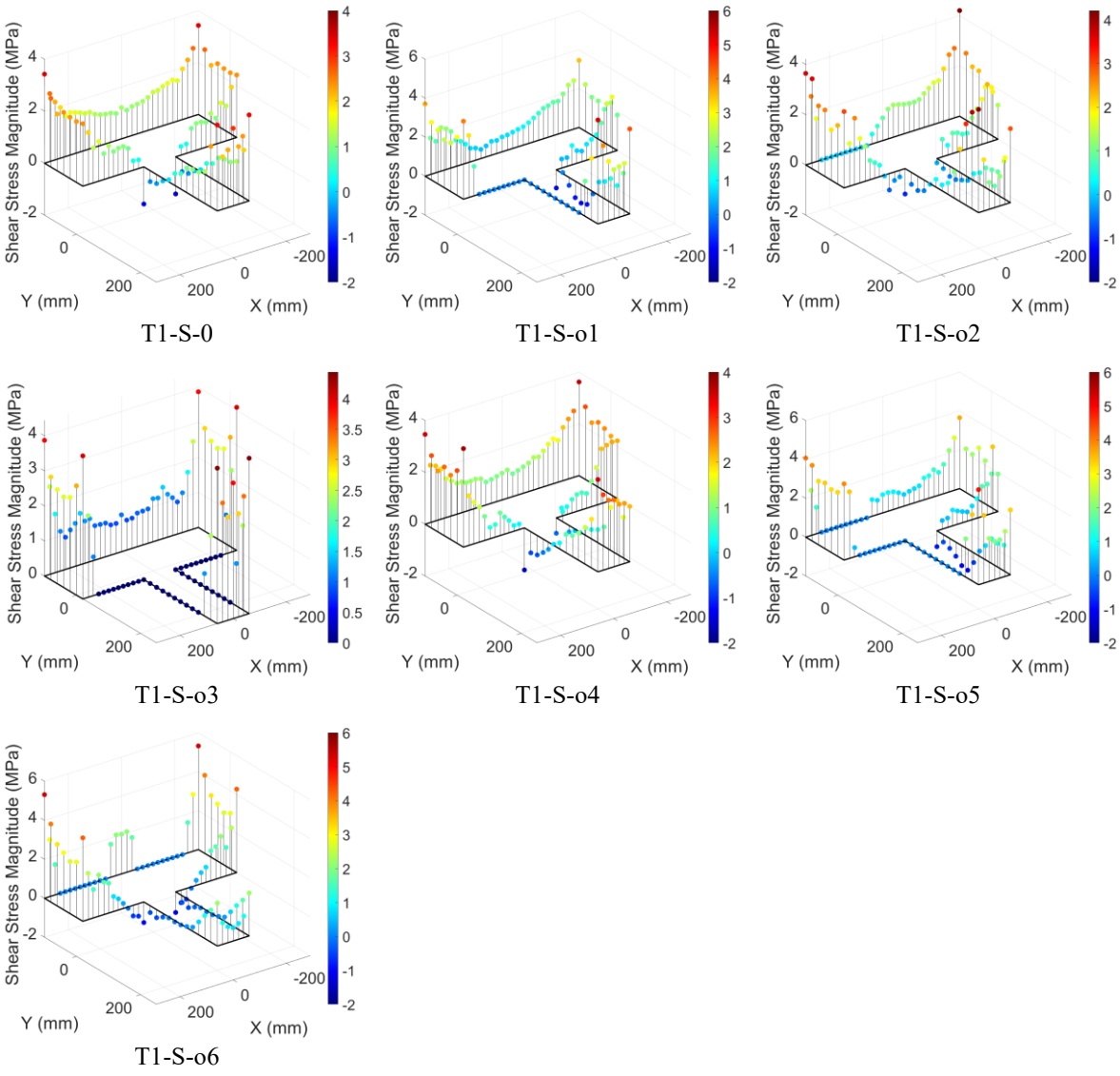


Figure J-25: Column Perimeter Shear Stress Distributions at Peak Load – T1-S Specimens (Stresses Averaged Over Depth)

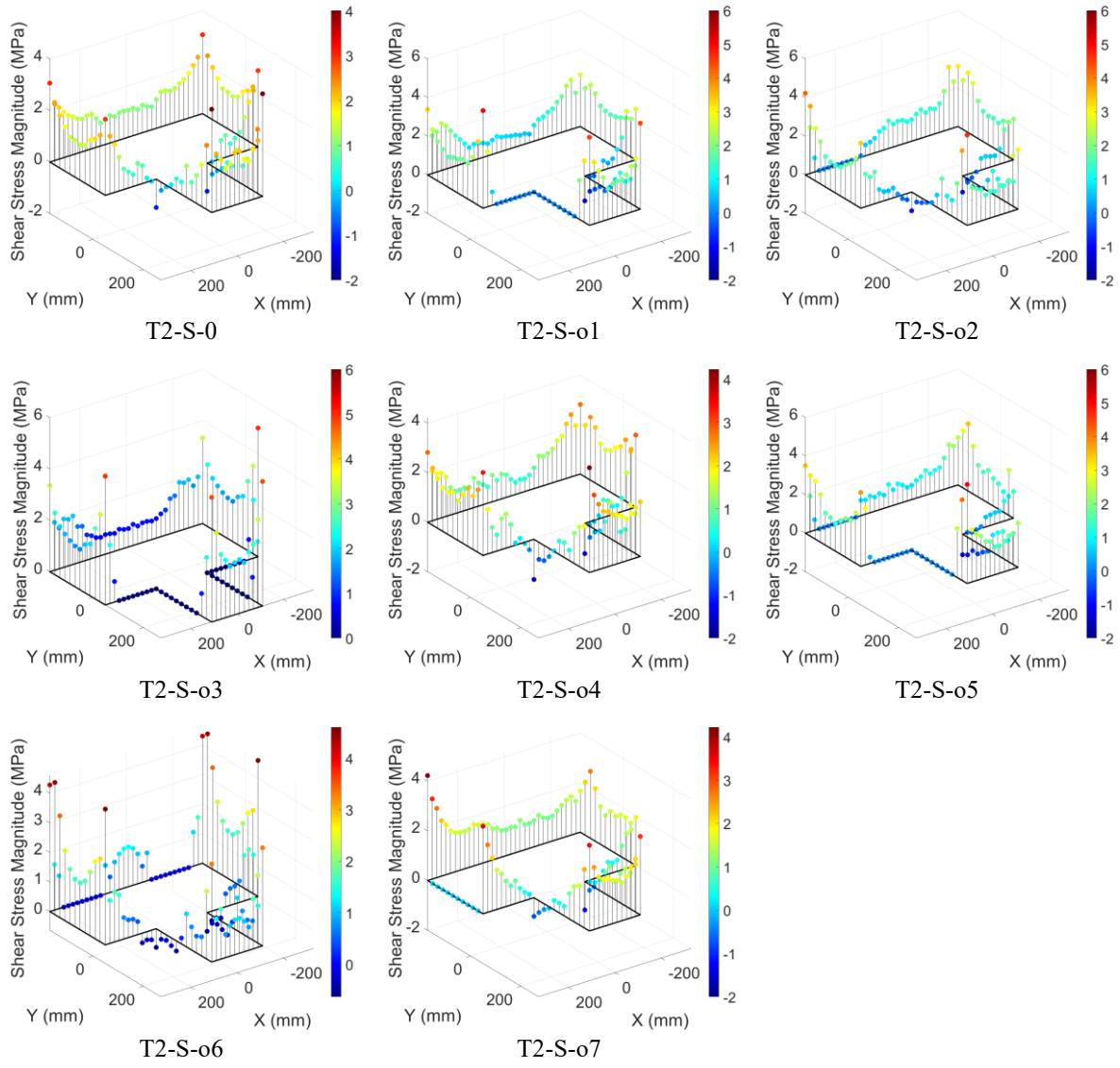


Figure J-26: Column Perimeter Shear Stress Distributions at Peak Load – T2-S Specimens (Stresses Averaged Over Depth)

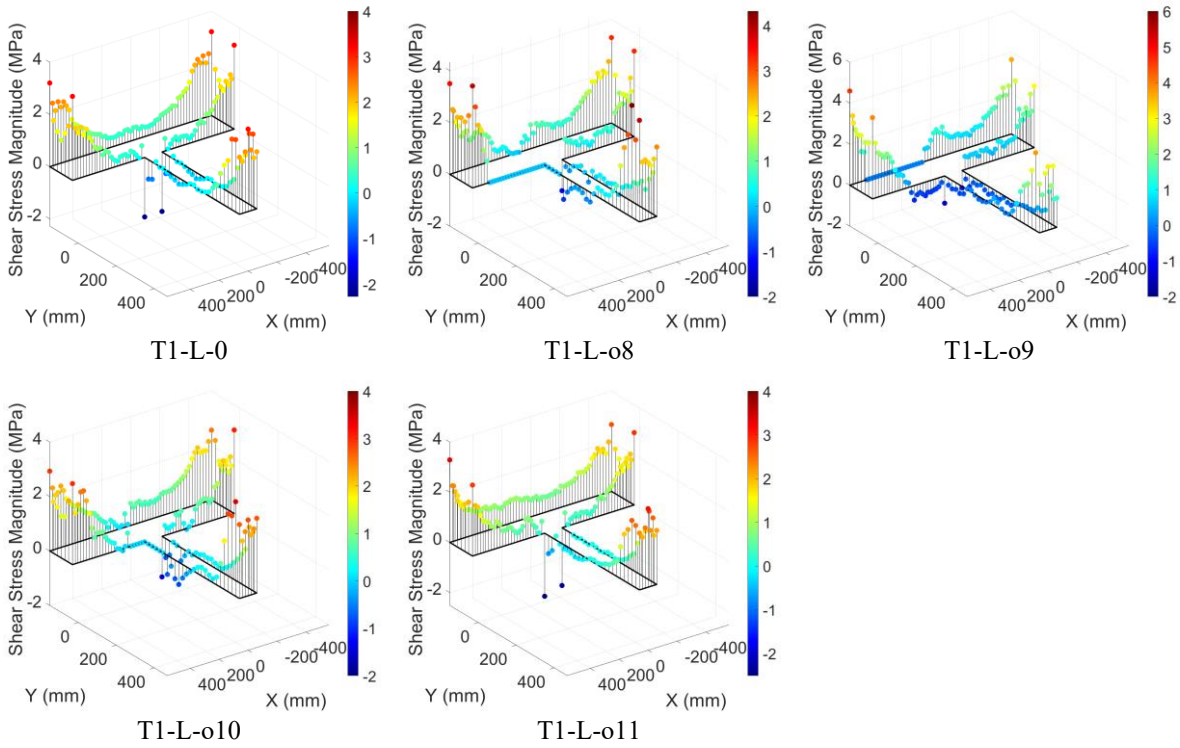


Figure J-27: Column Perimeter Shear Stress Distributions at Peak Load – T1-L Specimens (Stresses Averaged Over Depth)

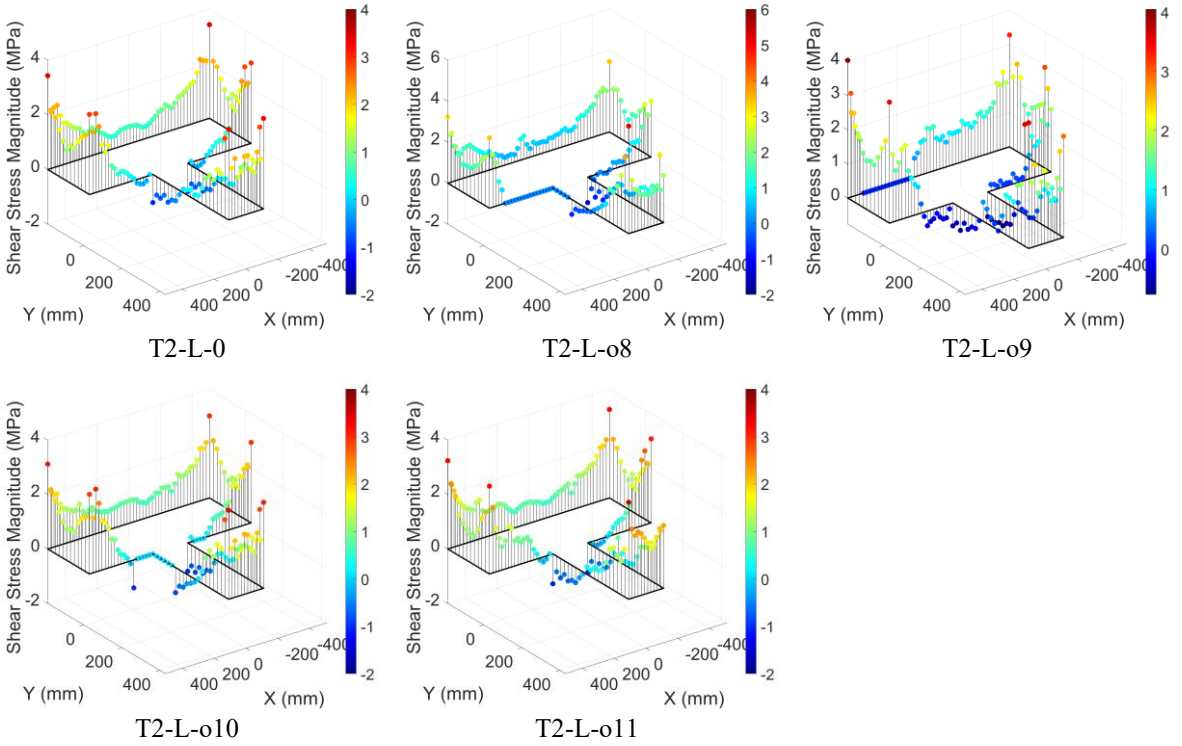


Figure J-28: Column Perimeter Shear Stress Distributions at Peak Load – T2-L Specimens (Stresses Averaged Over Depth)

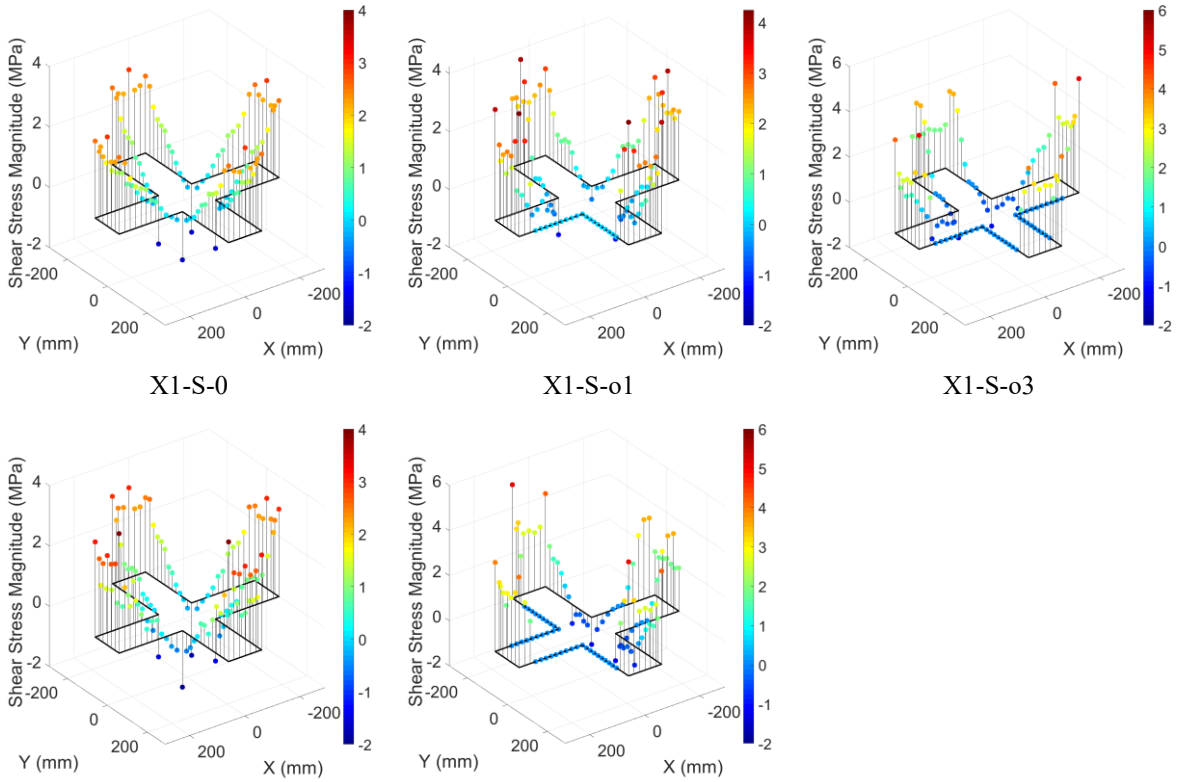


Figure J-29: Column Perimeter Shear Stress Distributions at Peak Load – X1-S Specimens (Stresses Averaged Over Depth)

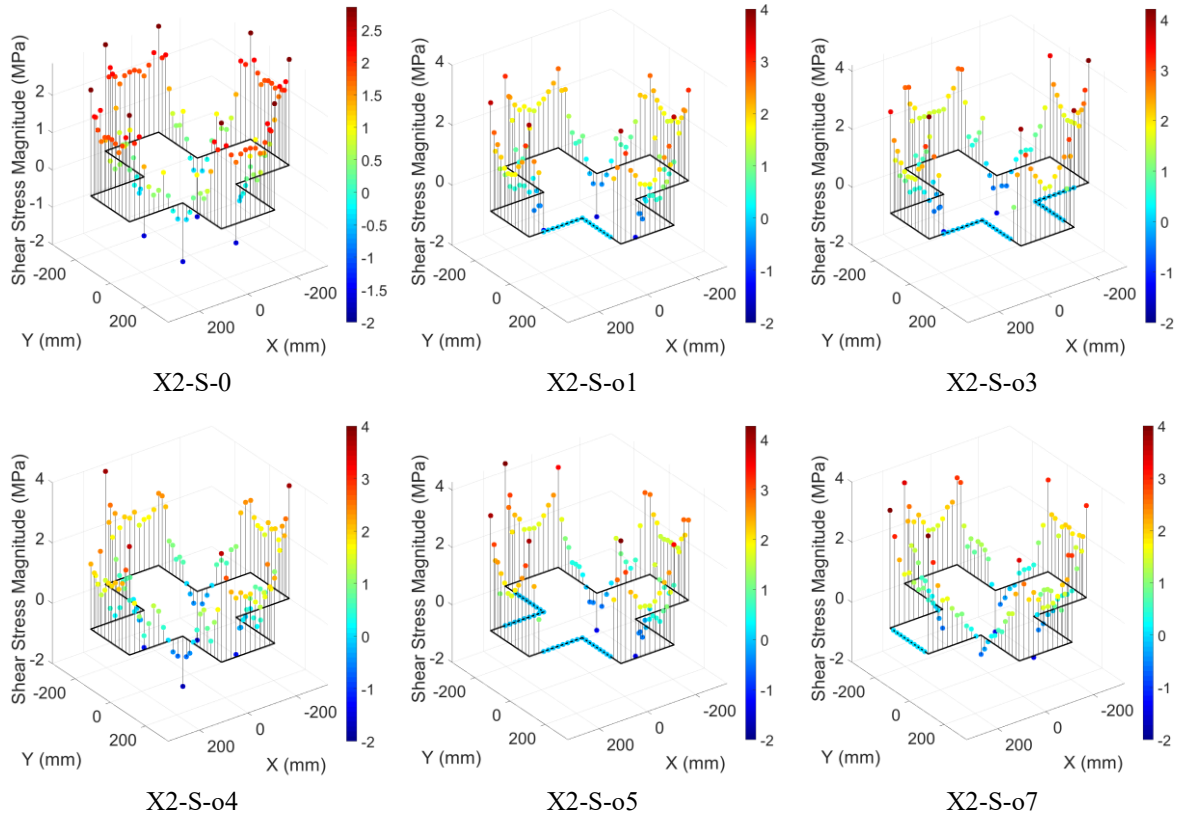


Figure J-30: Column Perimeter Shear Stress Distributions at Peak Load – X2-S Specimens (Stresses Averaged Over Depth)

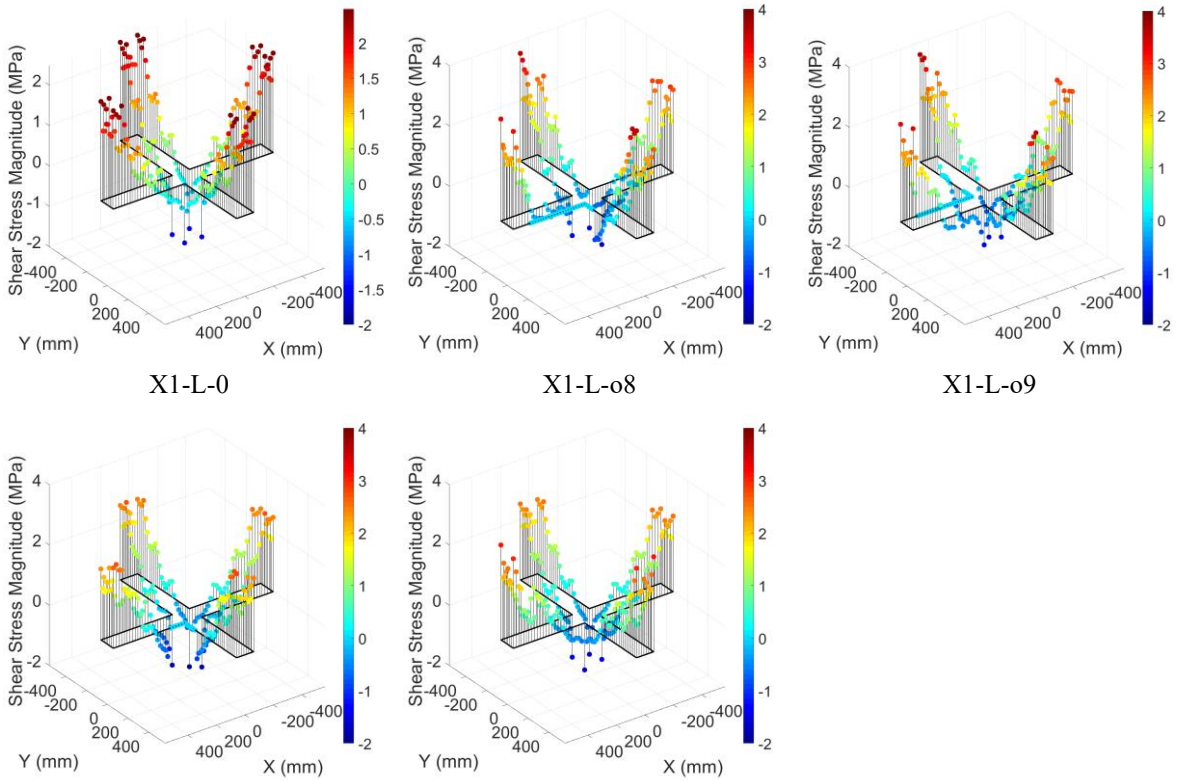


Figure J-31: Column Perimeter Shear Stress Distributions at Peak Load – X1-L Specimens (Stresses Averaged Over Depth)

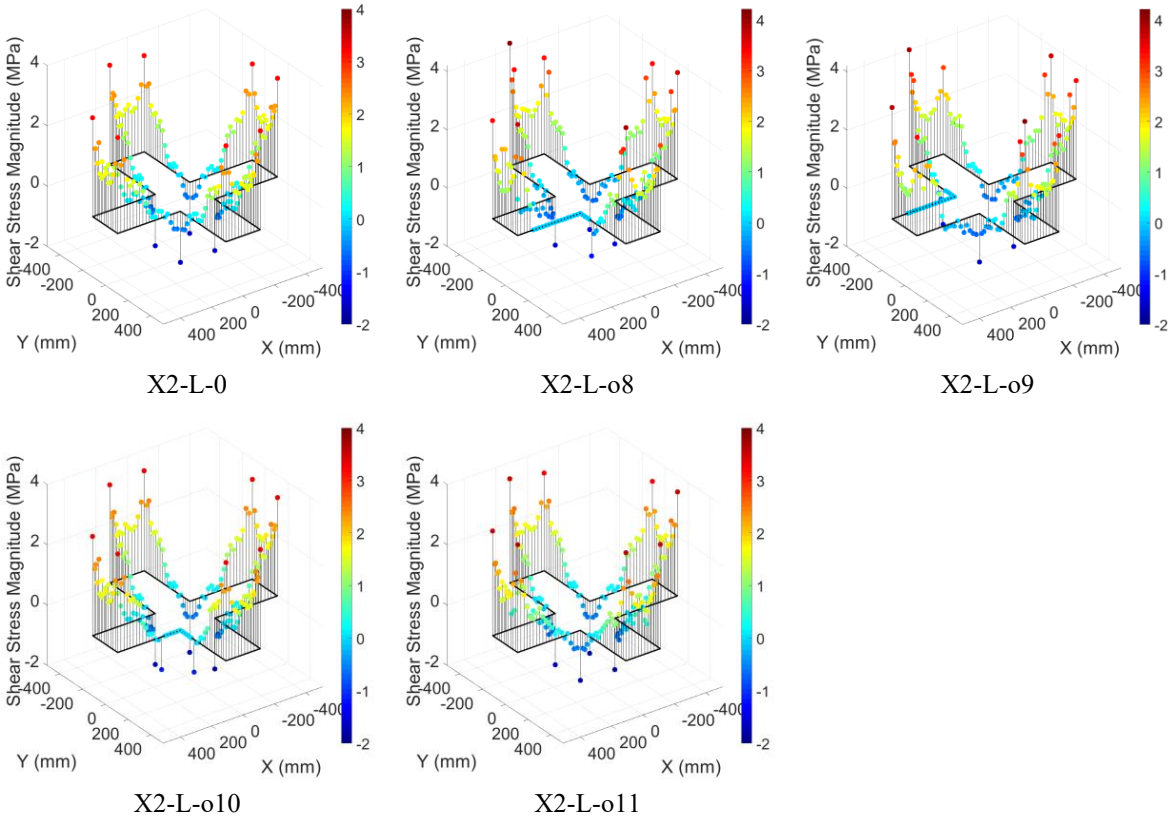


Figure J-32: Column Perimeter Shear Stress Distributions at Peak Load – X2-L Specimens (Stresses Averaged Over Depth)

Appendix K

Additional Load-Deflection Responses, Moment-Deflection Responses, Predicted Crack Patterns and Shear Stress Distributions – Special-Shaped and Rectangular Slab-Column Connections – Combined Shear and Unbalanced Moment Study

In this appendix, supplemental load-deflection responses, moment-deflection responses, crack patterns and shear stress distributions along the column perimeter at the peak load level predicted by the NLFEA supplemental to those in Chapter 9 are provided. Figures for both the concentric loading (V only) and combined shear and unbalanced moment (V+M (monotonic)) are provided. Note, the methodology used to calculate the shear stress distributions from the FEA results is discussed in Appendix A.

Concentric Loading (V Only) Specimens

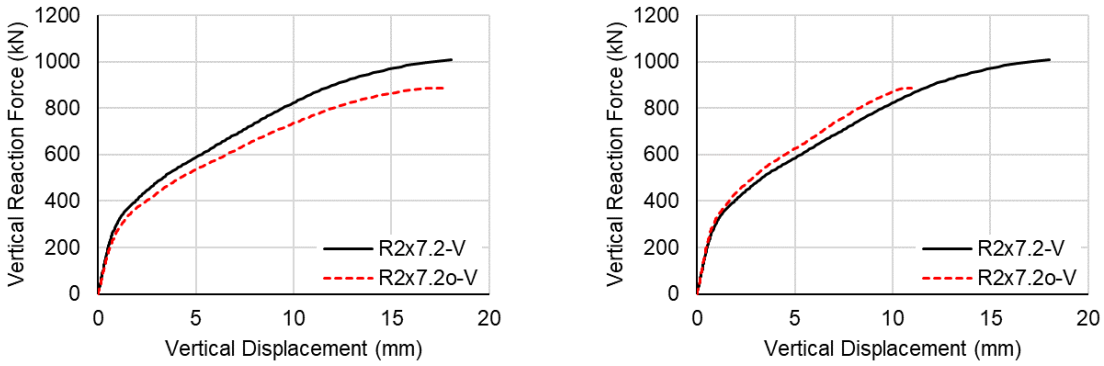


Figure K-1: Comparison of Predicted Load-Displacement Responses for Concentrically Loaded R-SCCs in Chapter 9, Displacement Measurement Locations Shown in Figure 9-5

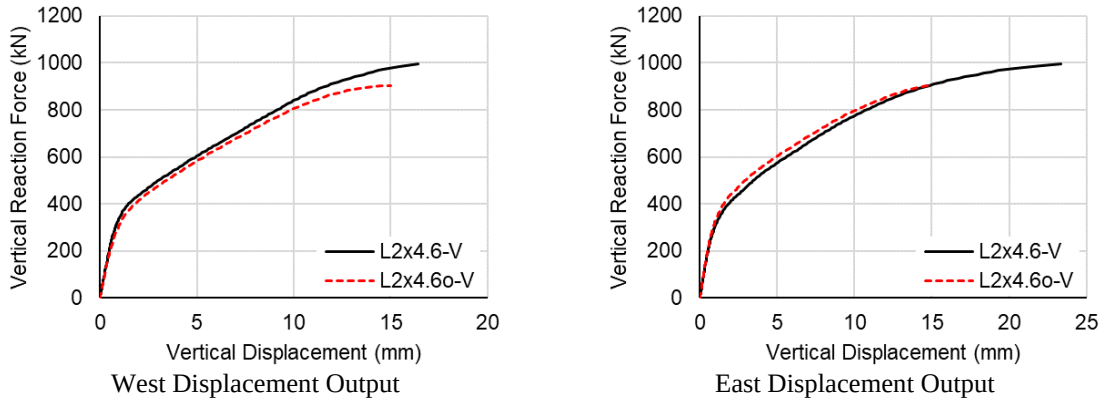


Figure K-2: Comparison of Predicted Load-Displacement Responses for Concentrically Loaded L-SCCs in Chapter 9, Displacement Measurement Locations Shown in Figure 9-5

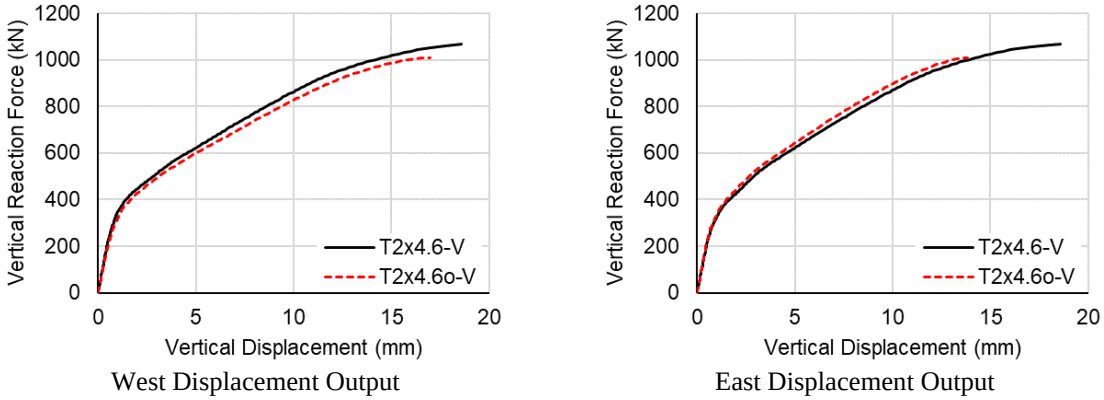
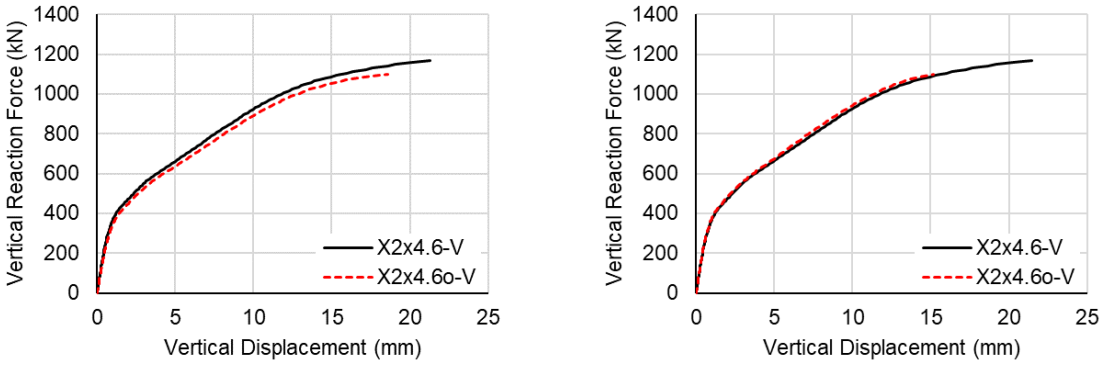
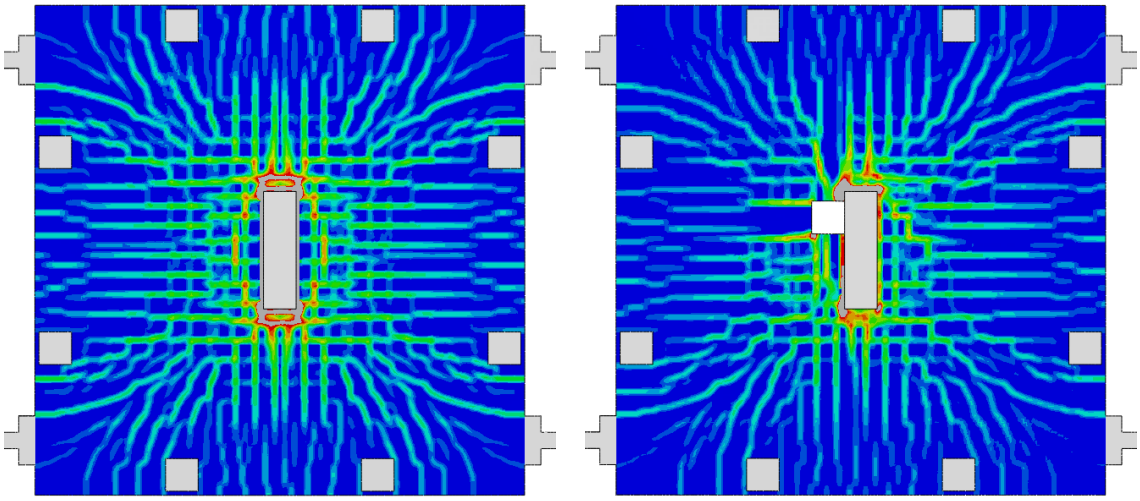


Figure K-3: Comparison of Predicted Load-Displacement Responses for Concentrically Loaded T-SCCs in Chapter 9, Displacement Measurement Locations Shown in Figure 9-5



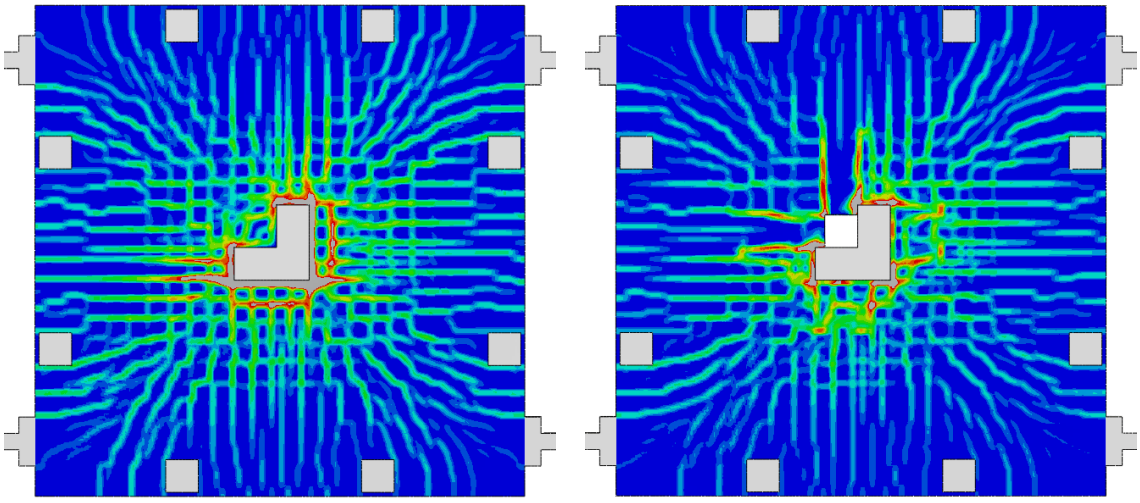
West Displacement Output East Displacement Output

Figure K-4: Comparison of Predicted Load-Displacement Responses for Concentrically Loaded X-SCCs in Chapter 9, Displacement Measurement Locations Shown in Figure 9-5



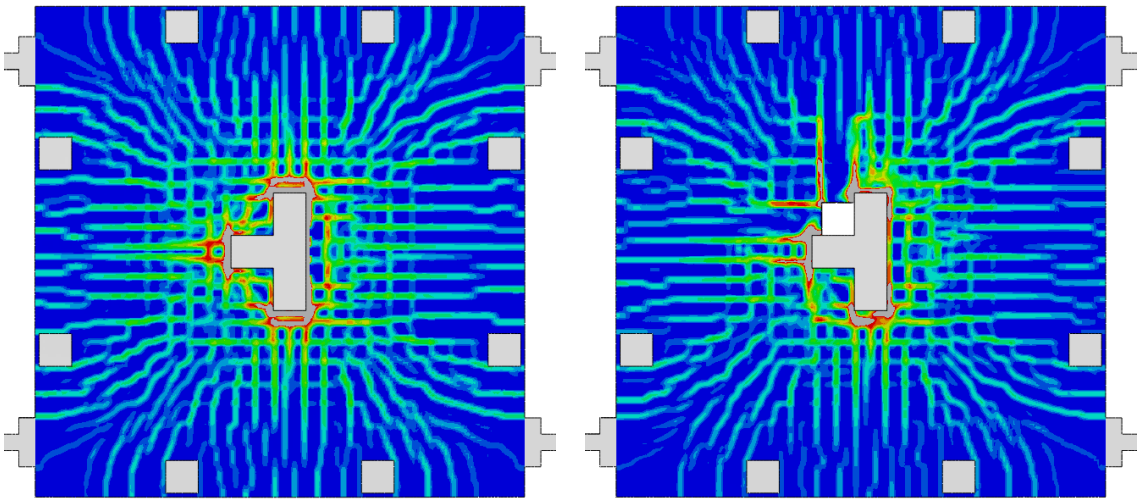
Reference Specimen (No Opening), R2x7.2-V Specimen With Opening, R2x7.2o-V

Figure K-5: Comparison of Predicted Tension Surface Crack Patterns for Concentrically Loaded R-SCCs in Chapter 9



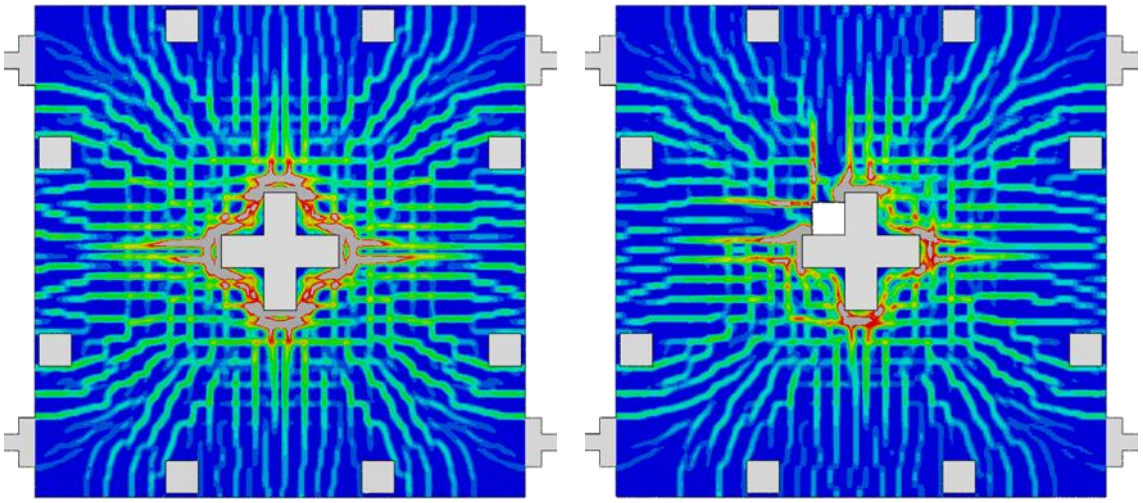
Reference Specimen (No Opening), L2x4.6-V Specimen With Opening, L2x4.6o-V

Figure K-6: Comparison of Predicted Tension Surface Crack Patterns for Concentrically Loaded L-SCCs in Chapter 9



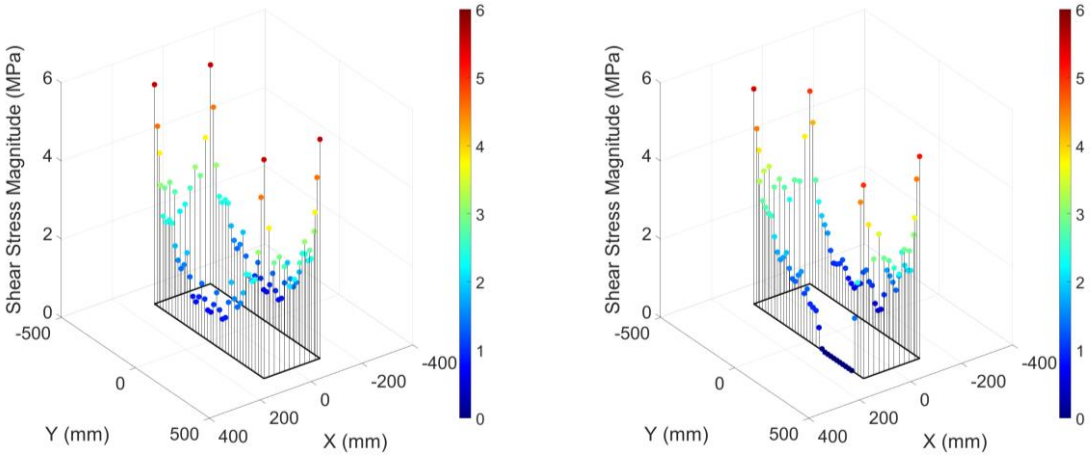
Reference Specimen (No Opening), T2x4.6-V Specimen With Opening, T2x4.6o-V

Figure K-7: Comparison of Predicted Tension Surface Crack Patterns for Concentrically Loaded T-SCCs in Chapter 9



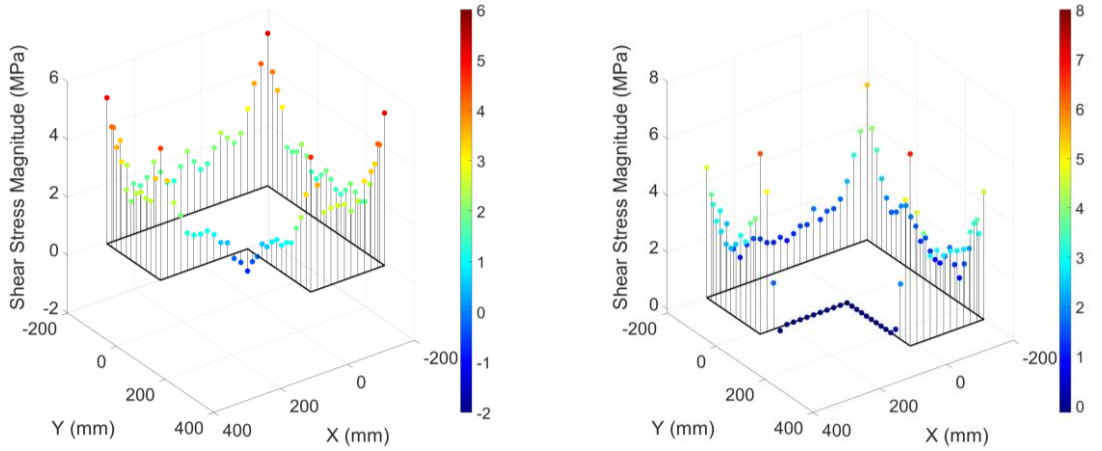
Reference Specimen (No Opening), X2x4.6-V Specimen With Opening, X2x4.6o-V

Figure K-8: Comparison of Predicted Tension Surface Crack Patterns for Concentrically Loaded X-SCCs in Chapter 9



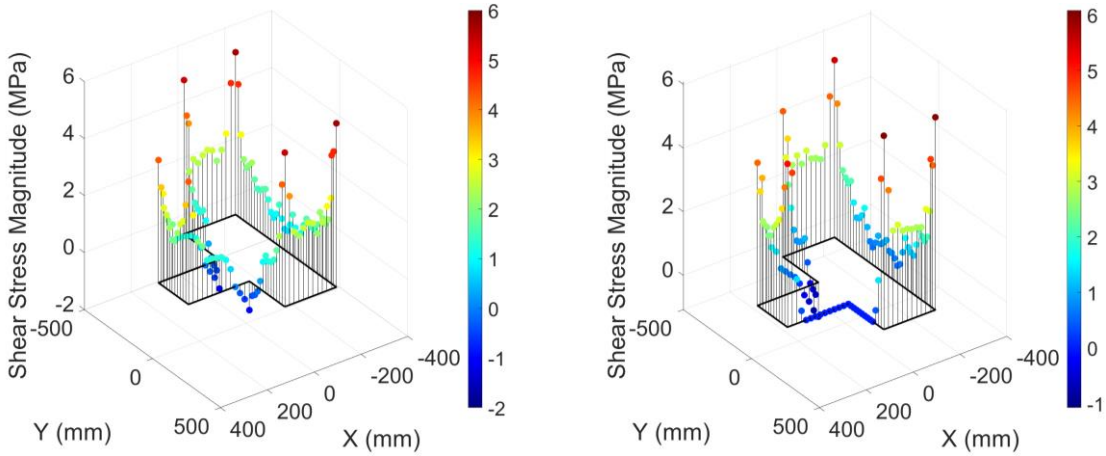
R2x7.2-V R2x7.2o-V

Figure K-9: Column Perimeter Shear Stress Distributions for Concentrically Loaded R-SCCs (Chapter 9) – Peak Load (Stresses Averaged Over Depth)



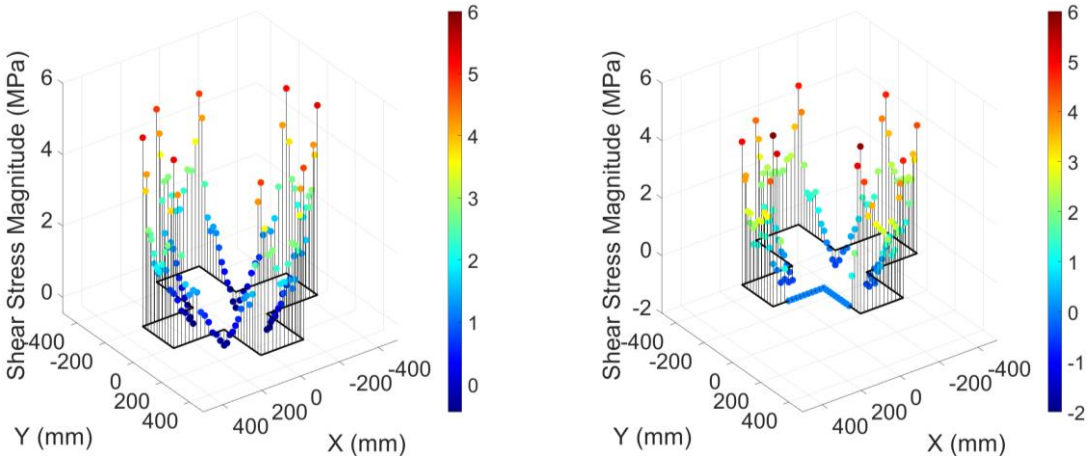
L2x4.6-V L2x4.6o-V

Figure K-10: Column Perimeter Shear Stress Distributions for Concentrically Loaded L-SCCs (Chapter 9) – Peak Load (Stresses Averaged Over Depth)



T2x4.6-V T2x4.6o-V

Figure K-11: Column Perimeter Shear Stress Distributions for Concentrically Loaded T-SCCs (Chapter 9) – Peak Load (Stresses Averaged Over Depth)



X2x4.6-V X2x4.6o-V

Figure K-12: Column Perimeter Shear Stress Distributions for Concentrically Loaded X-SCCs (Chapter 9) – Peak Load (Stresses Averaged Over Depth)

Combined Shear and Unbalanced Moment (V+M (monotonic)) Specimens

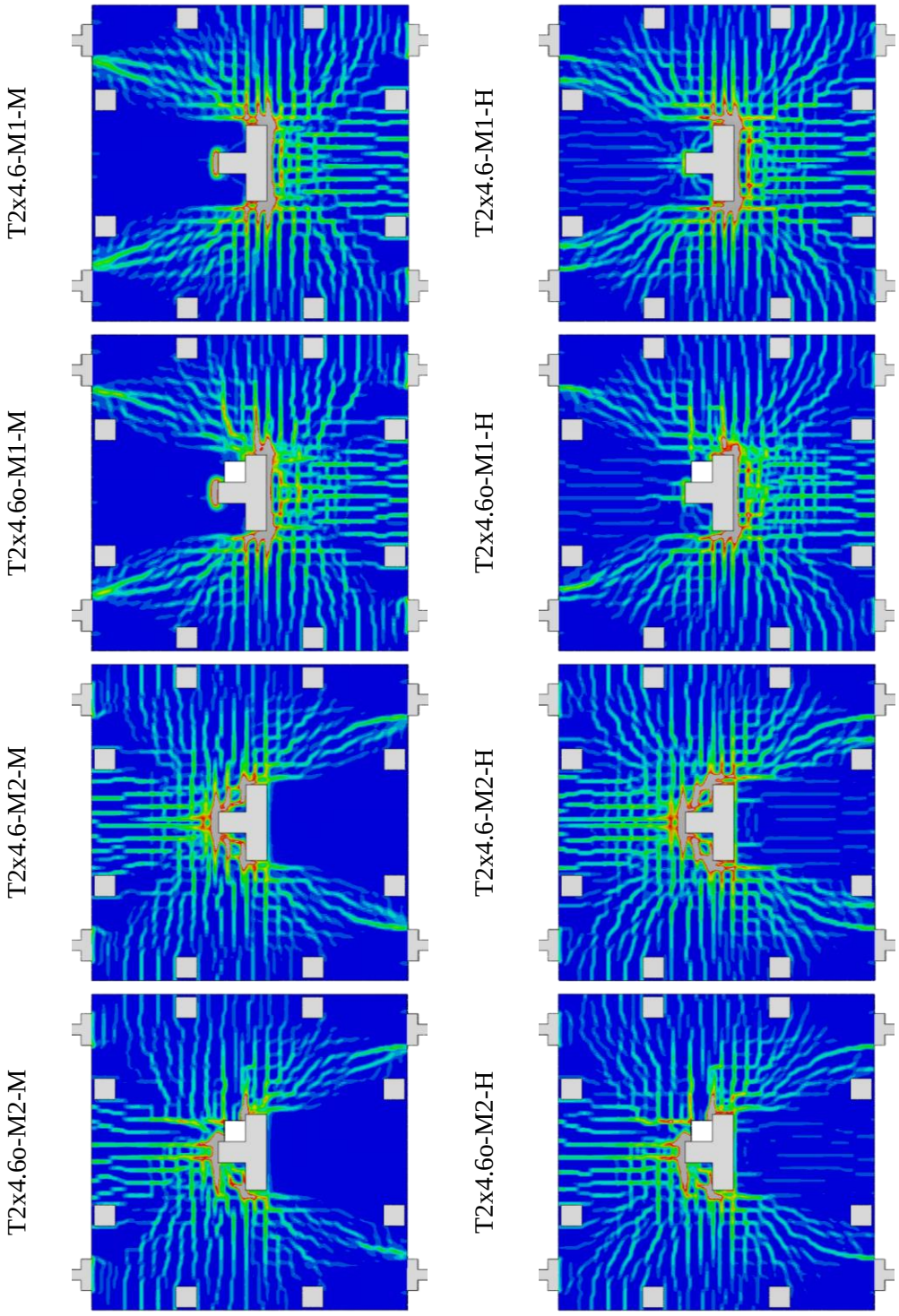


Figure K-13: Predicted Tension Surface Crack Patterns at Failure, T-SCCs (Grey Regions Have Principal Plastic Strains > 0.02)

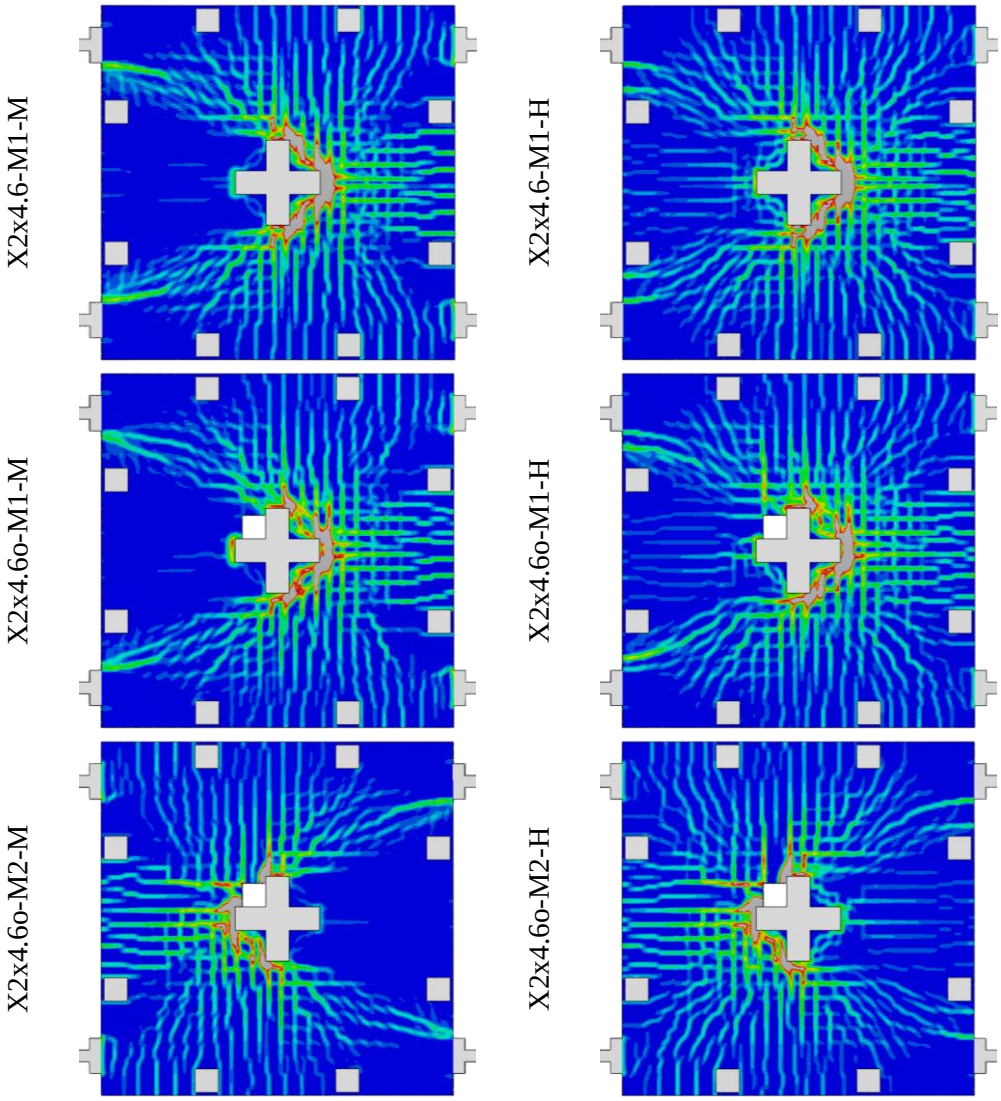


Figure K-14: Predicted Tension Surface Crack Patterns at Failure, X-SCCs (Grey Regions Have Principal Plastic Strains > 0.02)